Digitized by the Internet Archive
in 2024

https://archive.org/details/physica-scripta_1954_7

QC
1
S923

634

ARKIV FÖR FYSIK

UTGIVET AV

K. SVENSKA VETENSKAPSAKADEMIEN

Band 7

Med 46 avhandlingar

STOCKHOLM
ALMQVIST & WIKSELLS BOKTRYCKERI AB

LONDON
H. K. LEWIS & CO., LTD
136, GOWER STREET

1954

PARIS
LIBRAIRIE C. KLINCKSIECK
11 RUE DE LILLE

SJUNDE BANDETS INNEHÅLL

Sid.

1. **Brogren**, G. and **Adell**, Ö., The transmission and absorption of X-rays in calcite near the Bragg angle .... 1— 5
2. **Glad**, S., The spectrum of singly-ionized carbon, C II .... 7— 32
3. **Mileikowsky**, C., A nuclear spectrometer for heavy particles. Part II. Performance and focusing properties .... 33— 46
4. **Brogren**, G., A determination of the Avogadro number .... 47— 55
5. **Mileikowsky**, C., Astigmatic two-directional focusing in a nuclear spectrometer as a means of eliminating line broadening due to angular energy spread of transmutation particles. A nuclear spectrometer for heavy particles. Part III .... 57— 68
6. **Wiedling**, T., The angular correlation of Ni^{60} .... 69— 71
7. **Borelius**, G. and **Rudberg**, E., Reports from the Conference of the Swedish National Committee for Physics in 1952 .... 73— 88
8. **Mileikowsky**, C., Reaction energy of O^{18} (p, α) N^{15} and the atomic mass of oxygen 18 .... 89—108
9. **Lidén**, K. and **Starfelt**, N., Gamma-rays, X-rays and bremsstrahlung from Tm^{170} sources .... 109—116
10. **Mileikowsky**, C., Reaction energy of Ne^{20} (d, α) F^{18} by magnetic analysis 117—119
11. **Waller**, I. and **Lundqvist**, S. O., Some remarks on the rôle of overlapping in the X-ray scattering by crystals .... 121—124
12. **Uhler**, U., On the band-spectrum of silver oxide .... 125—147
13. **Ahnlund**, K., Determination of the radiation hazards from a 1.5 MeV high voltage accelerator .... 149—153
14. **Ahnlund**, K., Proton groups from deuteron bombardment of Ne^{20} by magnetic analysis. Transitions to the ground state and first excited state of Ne^{21} .... 155—163
15. **Fischer-Hjalmars**, I., Hybridization of atomic orbitals in formation of molecules .... 165—183
16. **Rasmussen**, Jr., J. O., The strong surface coupling nuclear model and hindered alpha decay .... 185—188
17. **Erlandsson**, G., Microwave spectrum and molecular structure of fluorobenzene .... 189—192
18. **Lidén**, K. and **Starfelt**, N., Characteristic X-rays from thick β-ray sources .... 193—196
19. **Adell**, Ö., **Brogren**, G. and **Haeggblom**, L.-E., The X-ray diffraction from quartz .... 197—211
20. **Wikström**, S., Studies of the heterocharges of electrets .... 213—220
21. **Karlson**, E., On regularization by means of analytic continuation .... 221—237
22. **Bergström**, I., **Nybö**, K., **Thulin**, S., **Wapstra**, A. H., and **Åström**, B., Measurements of conversion coefficients with a scintillation spectrometer. *A series of 8 papers* .... 239—291
23. **Lindgren**, E. R., Some aspects of the change between laminar and turbulent flow of liquids in cylindrical tubes .... 293—308

Sid.

24. Ingelstam, E., An optical uncertainty principle and its application to the amount of information obtainable from multiple-beam interferences .. 309—322
25. Larsson, K.-E., A critical comparison between some methods for measuring the strength of a Ra-Be neutron source absolutely .... 323—342
26. Kronqvist, E. and Giansoldati, A., Paramagnetic susceptibility measurements on AgMn and AuMn alloys .... 343—351
27. Krisement, O., Zur Kohlenstoffausscheidung aus dem α-Eisen .... 353—356
28. von Dardel, G., Time dependence of boron absorption coefficient for neutrons slowed down in water at room temperature .... 357—373
29. Sjölander, A., On the scattering of slow neutrons by crystals near the Bragg angles .... 375—390
30. Moreau, J., Étude de la radioactivité de Sb_{51}^{125} .... 391—397
31. Hertz, C. H., Point corona against a plane covered by an insulating film .... 399—400
32. Flinta, J. & Eklund, S., On the radioactivity of Rb^{87} .... 401—411
33. Minnhagen, L., Improved wavelengths for some infrared lines in the arc spectrum of carbon .... 413—414
34. Ericsson, G., Synthetic sodium chloride crystals; refractive index and lattice constant .... 415—421
35. Alburger, D. E. & Hedgran, A., Internal conversion of the zero-zero transition in RaC′ .... 423—425
36. Lidén, K. & Starfelt, N., Scintillation spectrometry of continuous γ- and x-ray spectra below 1 MeV .... 427—457
37. Ahnlund, K., The reaction energy of Ne^{22} (d, p) Ne^{23} and the atomic mass of Ne^{23} .... 459—462
38. Smårs, E. & Wernholm, O., Design study of a strong-focusing electron-synchrotron .... 463—472
39. Lagerqvist, A., The energy of dissociation of BeO .... 473—474
40. Waldeskog, B., Photo-electric determination of the charge of heavy primaries in the cosmic radiation .... 475—485
41. Klein, O., On a class of spherically symmetric solutions of Einstein's gravitational equations .... 487—496
42. Fröberg, C.-E., On a mathematical model of a photographic emulsion 497—502
43. Atterling, H., Acceleration of heavy ions in the 225-cm cyclotron at the Nobel Institute of Physics .... 503—506
44. Welander, P., On the temperature jump in a rarefied gas........... 507—553
45. Welander, P., Heat conduction in a rarefied gas: the cylindrically symmetrical case .... 555—564
46. Claesson, A., On the renormalization of the Salpeter-Bethe equation ... 565—585

ARKIV FÖR FYSIK Band 7 nr 1

Communicated 11 March 1953 by Axel E. Lindh and Gunnar Hägg

The transmission and absorption of X-rays in calcite near the Bragg angle

By Gösta Brogren and Öved Adell

With 6 figures in the text

In crystal diffraction of X-rays, it is customary when calculating the intensity of the reflected beam to apply corrections for absorption by using the normal coefficient of absorption. During recent years it has been shown that anomalous intensities are obtained when X-rays are transmitted through a perfect crystal in the direction of the incident beam at a position where Laue diffraction occurs (1, 2). Investigations of these transmitted and reflected intensities have recently been made both theoretically (3–6) and experimentally (7–10). Previous experimental results published are few, and such that they are less suitable as a basis for theoretical calculations. We are investigating this effect in calcite and quartz crystals in the region 700–1800 X.U., and we are able to report some observations for calcite.

The experimental arrangement is shown in Fig. 1. The investigations were carried out with a two-crystal spectrometer (11) with the reflecting crystal planes in the (1–1) position. The monochromator crystal (A) was a calcite crystal with the surface parallel to the cleavage plane (211). The analysator crystal (B) was another calcite crystal 0.41 mm thick with the same surface orientation. B was mounted in a crystal holder which permitted it to be adjusted so that both plane (211) and the equivalent plane (121), which cut each other at an angle 105° 3′ could be made parallel to the axis of revolution. Parallelism was achieved by tilting crystal B until minimum widths of the rocking curves were obtained both with plane (211) and with plane (121). The spectrometer was provided with two Geiger-Müller counters so that both the transmitted and the Laue diffracted intensities could be registered simultaneously. In order to eliminate surface deficiencies both crystals were etched with 0.7 normal hydrochloric acid for seven seconds.

The quality of the crystals was controlled by measuring the full width of the rocking curve with crystal B in surface reflection. With Mo $K\alpha_1$-radiation we got 5.2″, in good agreement with earlier measurements.

The voltage of the X-ray tube was always kept below the double threshold voltage so that no overlapping could occur. Registrations were performed with wavelengths corresponding to the following characteristic X-ray lines: Mo $K\alpha_1$, Au $L\beta_1$, Au $L\alpha_1$, Cu $K\alpha_1$, and Co $K\alpha_1$. Figures 2–6 show the results. ϑ is the angle between the incident X-radiation and the reflecting atomic plane, R_T is the intensity of the transmitted radiation, and R_L that of the Laue diffracted radiation. As the reflecting plane (121) cuts the surface at an angle of 75°, the paths of the two X-ray beams are not

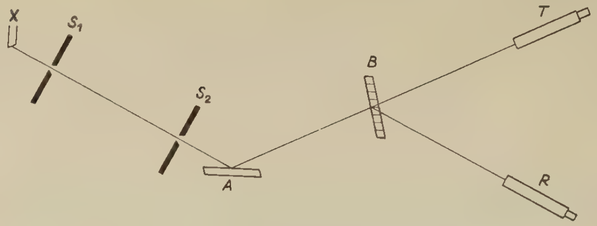

Fig. 1. The experimental arrangement.

the same. For this reason R_T and R_L are not directly comparable. R_T and R_L were recorded as a function of ϑ in the region of about one degree around the Bragg angle ϑ_B. As may be seen from the figures, the anomalous absorption appears only within a very small region around ϑ_B. When the normal absorption is small, so that $\mu_l \cdot d$ is small, a maximum in transmission is obtained in the region $\vartheta < \vartheta_B$ and a pronounced minimum on the other side of ϑ_B. When μ_l increases, the maximum increases but the minimum becomes less apparent. At 1540 X.U. (Cu $K\alpha_1$-radiation) the minimum has completely disappeared, and above this wavelength only a maximum can be seen in the transmission curve.

The following observations may be derived from the results:

1. The transmission curve is asymmetric in all cases. The region of anomalous transmission is wider below ϑ_B than above ϑ_B.

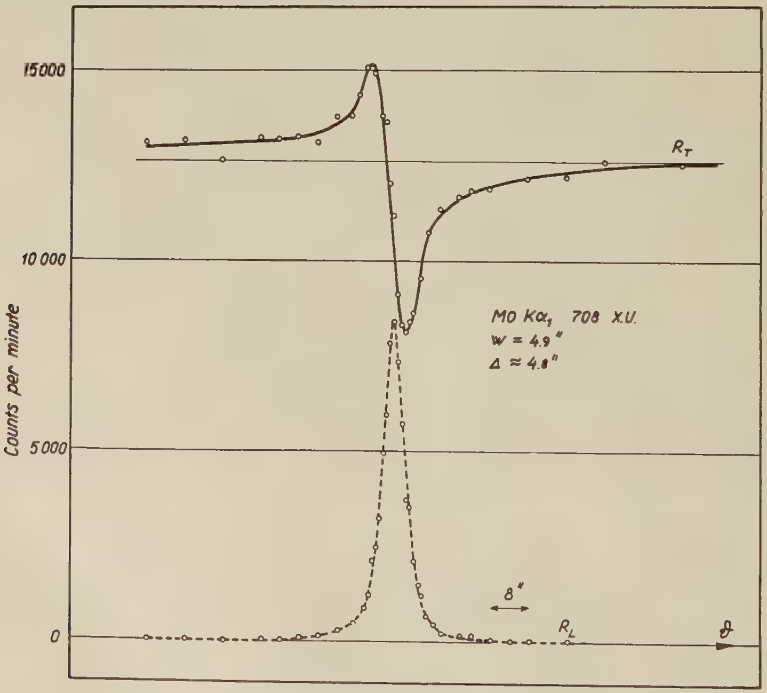

Fig. 2–6. The transmitted and reflected intensities at different wavelengths.

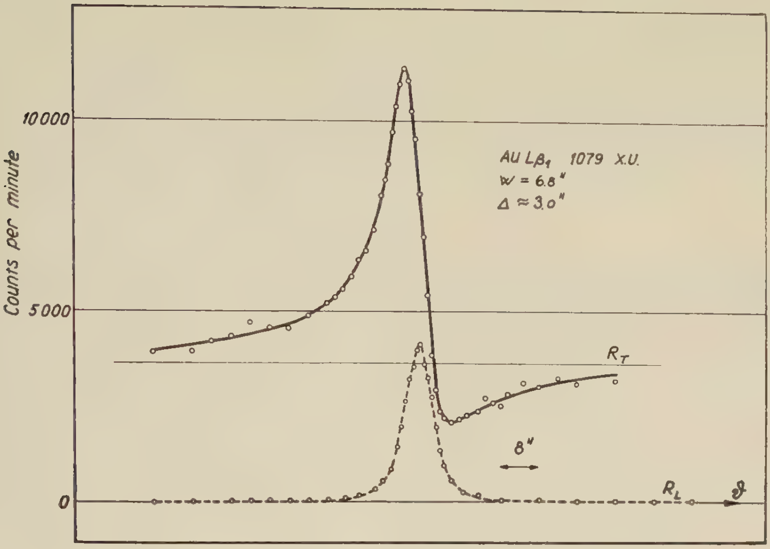
10000
5000
0
Counts per minute
Au $L\beta_1$ 1079 X.U.
W = 6.8"
Δ ≈ 3.0"
R_T
8"
R_L
ϑ

Fig. 3.

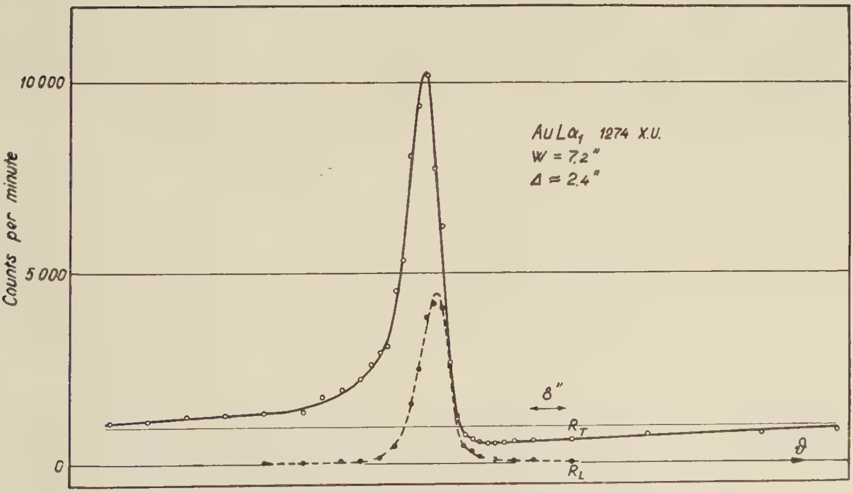
10000
5000
0
Counts per minute
Au $L\alpha_1$ 1274 X.U.
W = 7.2"
Δ = 2.4"
8"
R_T
R_L
ϑ

Fig. 4.

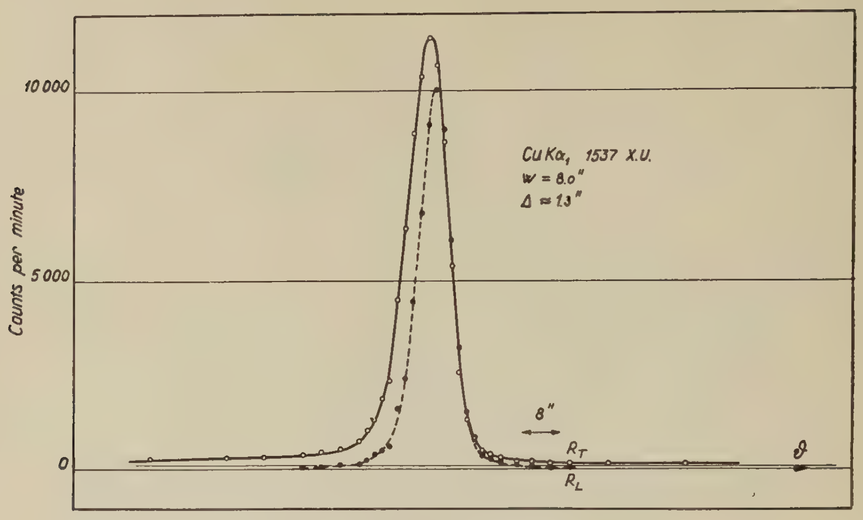
10 000
5 000
0
Counts per minute
$CuK\alpha_1$ 1537 X.U.
W = 8.0"
Δ ≈ 1.3"
8"
R_T
R_L
ϑ

Fig. 5.

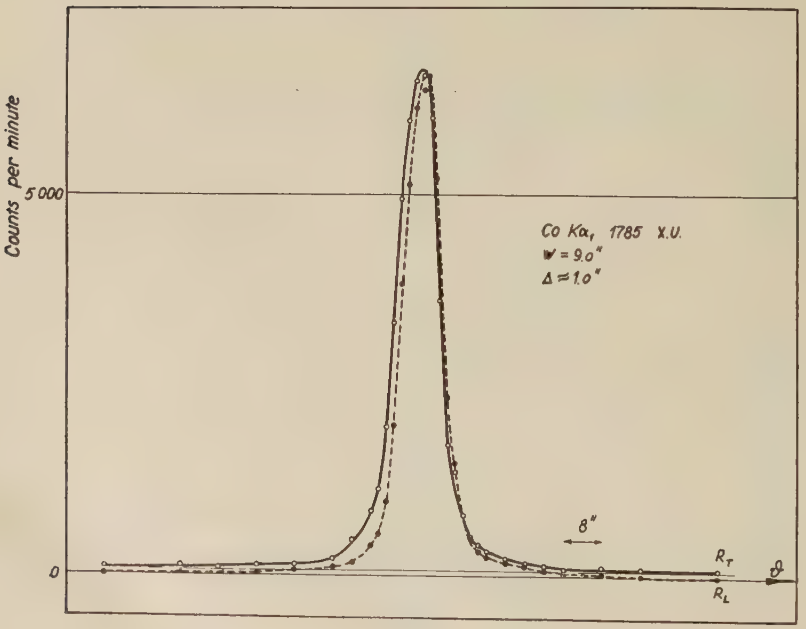
5 000
0
Counts per minute
$Co\ K\alpha_1$ 1785 X.U.
W = 9.0"
Δ ≈ 1.0"
8"
R_T
R_L
ϑ

Fig. 6.

2. If R_T and R_L are added together, there remains a region where $R_T + R_L$ is less than the normally transmitted intensity in all cases where there is a minimum in R_T. This effect may be due to the difference in paths for the two X-ray beams, but it will be studied carefully with crystals where the diffracting planes are perpendicular to the surface of the crystal, in which case both beams have the same paths in the crystal. Preliminary investigations with such a crystal, using plane (655), verify the above observation.

3. The angular distance Δ between the maxima of R_T and R_L decreases with increasing wavelength.

4. All rocking curves in the transmission (Laue) case are asymmetric. The full widths w at half maximum intensities are less than what is obtained when the surface of the second crystal is parallel to the diffracting planes. But for Mo $K\alpha_1$-radiation, the values are also less than those calculated (using the normal absorption coefficient). As the ϑ-value for the maximum of R_T is always less than ϑ_B, the intensity of the Laue diffracted radiation must be affected so that the rocking curve becomes asymmetric. It is possible that the peak of the rocking curve is displaced towards a smaller glancing angle. It may be mentioned as an example that for Cu $K\alpha_1$ the width of the Laue diffracted rocking curve is 8.0″, the normal width 10.2″ and the theoretical width 9.8″. The last two values refer to the case where the diffracting planes are parallel to the surface in both crystals.

As R_T and R_L are not comparable for reasons mentioned above, no absorption coefficients and no values of the integrated reflection are calculated here. They will be examined in a present investigation with the atomic planes perpendicular to the surface.

The shapes of the above curves have been calculated by HIRSCH (5) and RAMACHANDRAN (6) and the agreement with our results is in general good. In one point — viz. the forms and the widths of the rocking curves — it is not possible to make a comparision, as the theoretical curves are too rough. For Cu $K\alpha_1$-radiation Hirsch calculated the angular distance Δ between the peaks of R_L and R_T for a calcite crystal 0.4 mm thick to be about 1″, which is near our value 1.3″. There also seems to be a deviation in the region $\vartheta < \vartheta_B$, where the distance between the experimental curves is less than the theoretical ones.

The quartz investigations indicate effects of the same kind. A detailed report about all measurements will be given later.

Institute of Physics, University of Uppsala, Sweden, December 1952.

REFERENCES

1. G. BORRMAN, Phys. Zs. *43*, 157, 1941.
2. —— Zs. f. Phys. *127*, 297, 1950.
3. M. v. LAUE, Acta Cryst. *2*, 106, 1949.
4. —— Acta Cryst. *5*, 619, 1952.
5. P. B. HIRSCH, Acta Cryst. *5*, 176, 1952.
6. G. N. RAMACHANDRAN, J. Appl. Phys. *23*, 500, 1952.
7. H. N. CAMPBELL, J. Appl. Phys. *22*, 1139, 1951.
8. —— Acta Cryst. *4*, 180. 1951.
9. G. L. ROGOSA and G. SCHWARZ, Phys. Rev. *86*, 421, 1952.
10. —— Phys. Rev. *87*, 995, 1952.
11. G. BROGREN, Arkiv för Fysik, *3*, 507, 1951.

Tryckt den 5 maj 1953

Uppsala 1953. Almqvist & Wiksells Boktryckeri AB

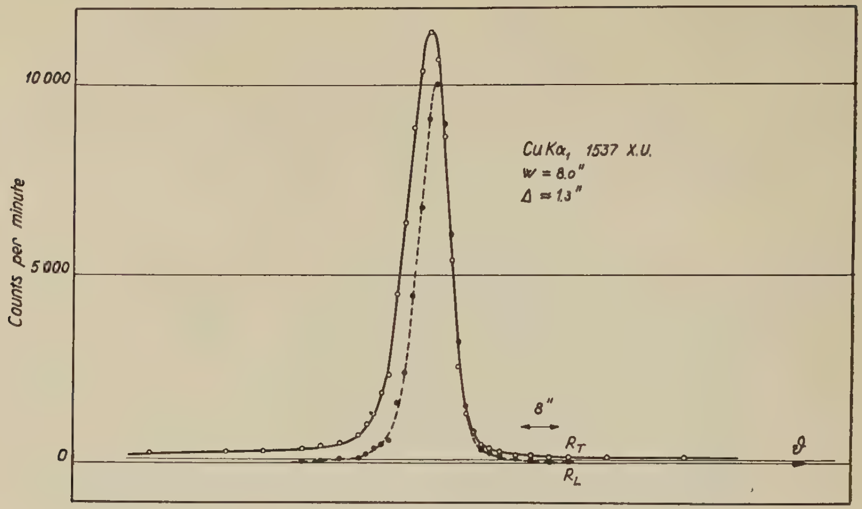
10 000
5 000
0
Counts per minute
Cu Kα₁ 1537 X.U.
w = 8.0"
Δ ≈ 1.3"
8"
R_T
R_L
ϑ

Fig. 5.

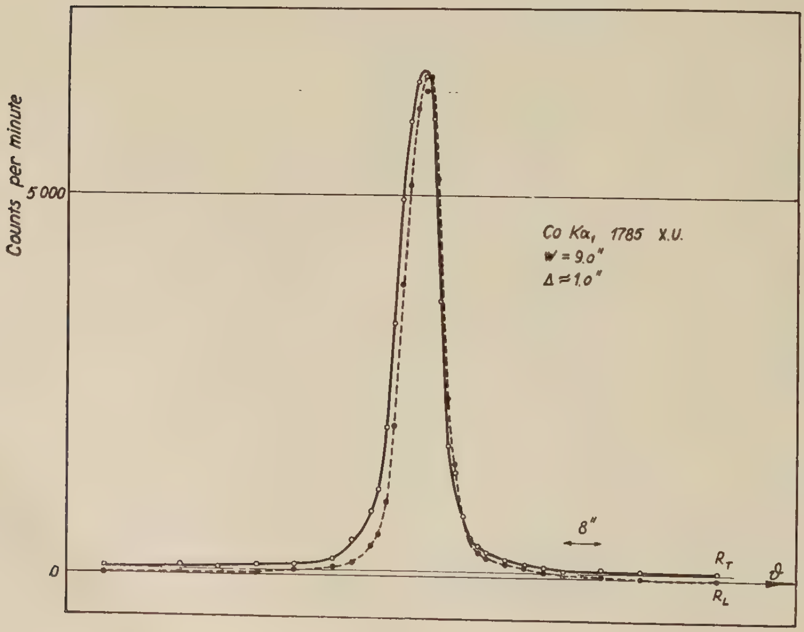
5 000
0
Counts per minute
Co Kα₁ 1785 X.U.
w = 9.0"
Δ ≈ 1.0"
8"
R_T
R_L
ϑ

Fig. 6.

2. If R_T and R_L are added together, there remains a region where $R_T + R_L$ is less than the normally transmitted intensity in all cases where there is a minimum in R_T. This effect may be due to the difference in paths for the two X-ray beams, but it will be studied carefully with crystals where the diffracting planes are perpendicular to the surface of the crystal, in which case both beams have the same paths in the crystal. Preliminary investigations with such a crystal, using plane (655), verify the above observation.

3. The angular distance Δ between the maxima of R_T and R_L decreases with increasing wavelength.

4. All rocking curves in the transmission (Laue) case are asymmetric. The full widths w at half maximum intensities are less than what is obtained when the surface of the second crystal is parallel to the diffracting planes. But for Mo $K\alpha_1$-radiation, the values are also less than those calculated (using the normal absorption coefficient). As the ϑ-value for the maximum of R_T is always less than ϑ_B, the intensity of the Laue diffracted radiation must be affected so that the rocking curve becomes asymmetric. It is possible that the peak of the rocking curve is displaced towards a smaller glancing angle. It may be mentioned as an example that for Cu $K\alpha_1$ the width of the Laue diffracted rocking curve is 8.0″, the normal width 10.2″ and the theoretical width 9.8″. The last two values refer to the case where the diffracting planes are parallel to the surface in both crystals.

As R_T and R_L are not comparable for reasons mentioned above, no absorption coefficients and no values of the integrated reflection are calculated here. They will be examined in a present investigation with the atomic planes perpendicular to the surface.

The shapes of the above curves have been calculated by HIRSCH (5) and RAMACHANDRAN (6) and the agreement with our results is in general good. In one point — viz. the forms and the widths of the rocking curves — it is not possible to make a comparision, as the theoretical curves are too rough. For Cu $K\alpha_1$-radiation Hirsch calculated the angular distance Δ between the peaks of R_L and R_T for a calcite crystal 0.4 mm thick to be about 1″, which is near our value 1.3″ There also seems to be a deviation in the region $\vartheta < \vartheta_B$, where the distance between the experimental curves is less than the theoretical ones.

The quartz investigations indicate effects of the same kind. A detailed report about all measurements will be given later.

Institute of Physics, University of Uppsala, Sweden, December 1952.

REFERENCES

1. G. BORRMAN, Phys. Zs. *43*, 157, 1941.
2. —— Zs. f. Phys. *127*, 297, 1950.
3. M. v. LAUE, Acta Cryst. *2*, 106, 1949.
4. —— Acta Cryst. *5*, 619, 1952.
5. P. B. HIRSCH, Acta Cryst. *5*, 176, 1952.
6. G. N. RAMACHANDRAN, J. Appl. Phys. *23*, 500, 1952.
7. H. N. CAMPBELL, J. Appl. Phys. *22*, 1139, 1951.
8. —— Acta Cryst. *4*, 180. 1951.
9. G. L. ROGOSA and G. SCHWARZ, Phys. Rev. *86*, 421, 1952.
10. —— Phys. Rev. *87*, 995, 1952.
11. G. BROGREN, Arkiv för Fysik, *3*, 507, 1951.

Tryckt den 5 maj 1953

Uppsala 1953. Almqvist & Wiksells Boktryckeri AB

ARKIV FÖR FYSIK Band 7 nr 2

Communicated 4 June 1952 by Nils Zeilon and Bengt Edlén

The spectrum of singly-ionized carbon, C II

By Sven Glad

With 2 plates and 4 figures in the text

Summary. The spectrum of singly-ionized carbon in the region 8800–1987 A has been studied by means of a condensed hollow cathode discharge. About 60 new energy levels have been determined. From several intercombination lines observed an exact linking up of the doublet and quartet systems has been obtained. The distance between the two limits $2s\ ^1S_0$ and $2p\ ^3P_2$ has been established to be $52\,423 \pm 7$ cm^{-1}.

Introduction

In investigating the spectrum of doubly-ionized iron the light source employed was a condensed hollow cathode discharge. This produced the Fe III spectrum with good intensity and at the same time it was possible to separate the Fe III lines from those of Fe I and Fe II by studying the shape of the lines. The hollow cathode consisted of a graphite tube containing a thin-walled iron cylinder. In addition to the iron lines the spectrograms contained lines belonging to the first three spectra of carbon. Since the carbon lines had the same shape as the Fe III lines there was some risk of the carbon lines being classed as Fe III. Therefore, in order to obtain a pure carbon spectrum by means of which the carbon lines could be picked out from the Fe III lines, spectrograms were taken with a pure graphite cylinder as the cathode. The wavelength data thus obtained form the basis for the present work on the C II spectrum.

Experimental procedure

The graphite tube used as a hollow cathode had a length of 45 mm and an inner diameter of 8 mm. It was placed in a large pyrex bulb, introduced into a vacuum circulating system of the type described by Paschen and Campbell (1). The pressure of the filling gas (helium with 0.1 % neon) was 6–12 mm. A full-wave rectifier charged a 10 μF condenser which was connected to the discharge tube through a rotating spark gap. Operating conditions were 800–1800 V and 20–30 sparks per second. An increase of the voltage led to a great increase of the brilliance of the discharge but at the same time some lines were strongly shaded to longer or shorter waves. This must essentially depend on the increase in the electric field inside the hollow cathode. In the side of the graphite tube a 3 mm hole was bored. The discharge was rather intense in the gas just outside this hole and the strongest C II lines were excited here also. This is clearly seen on Plate I b. The lower part of the spectrogram shows the discharge inside the cathode while the upper part contains the lines which appeared outside the hole. The line λ 6461 which is shaded to longer waves inside the cathode is sharp in the field-free space outside the tube. Its shape differs, however, from that of the other C II lines appearing in the upper part of Plate I b.

Because the helium contained 0.1 % neon, the strongest Ne I lines appeared on the plates and gave a suitable reference spectrum in the long wavelength range, use being made of the interferometer wavelengths reported by BURNS, ADAMS and LONGWELL (2). In order to get more standard lines in the region above 7000 A some plates were also supplied with an argon spectrum, obtained by admitting a small amount of argon into the system. Since argon is quickly absorbed by the liquid air cooled charcoal trap, gas-circulation was shut off during the time required to get a suitable argon spectrum. This time varied from 1 to 5 minutes. The wavelengths of argon were taken from MEGGERS and HUMPHREYS (3). By introducing a very small quantity of iron powder into the graphite tube the strongest lines of the first three spectra of iron were obtained. Fe I and Fe II lines (4, 5) were used as standard lines in the region 6000–2200 A and Fe III lines (6) in the region 2200–1900 A.

Most of the measured spectrograms were taken with a stigmatic concave grating spectrograph (Ja 70–15 m, Jarrell-Ash Company). The grating has 15000 lines per inch and a radius of curvature of 21 feet. The dispersion in the first order ranges from 5.1 A/mm to 4.7 A/mm. In the visible region additional spectrograms were obtained with a large glass prism spectrograph, previously described by MINNHAGEN (7). The dispersion is 7.7 A/mm at 6800 A and 1.0 A/mm at 4100 A. The faintest lines in the region 2500–2200 A have been measured on plates taken with a large quartz spectrograph, Hilger E478, dispersion 2.6 A/mm at 2500 A and 1.7 A/mm at 2200 A.

Eastman spectroscopic plates of different types were used in the region 9000 A to 2500 A. Below 2500 A Ilford Q2 and Q3 plates were used. The longest obtainable exposure time was about 3 hours. After that time the graphite tube became perforated and the discharge was no longer concentrated inside the hollow cathode. In most regions the exposure time varied from 1 to 90 minutes.

Wavelengths

The strongest bands from C_2 appear on the spectrograms, but their intensity is fairly weak as compared with that of the C II lines. It is usually easy to distinguish between the atomic lines and the bands. The measurement of certain C II lines, however, was made more difficult by their proximity to band lines. Since the graphite contained small amounts of vanadium and titanium, the strongest lines of V I–III and Ti I–III were recorded on the plates, but they are very sharp and easy to separate from C II lines. The experimental distinction between the different ionization stages of carbon is somewhat uncertain. Only the strongest C I and C III lines appear, however, and therefore they can easily be picked out by comparing with earlier investigations of these spectra. In the region above 6000 A, where no observations of the C III spectrum have been published, I have had the opportunity of using spectrograms taken by Bockasten. On these plates the intensity ratio C III/C II is much higher than on my plates. Knowledge of the C I spectrum between 8100 and 7000 A is evidently very incomplete. In this region EDLÉN (8) has classified three C I lines measured by RYDE (9). Each of these three lines has now been resolved into two or more lines and a few other lines have been found in spite of the light source not being ideal for the excitation of the C I spectrum.

All C II lines which have now been measured are given in Table 1. The wavelengths are, as a rule, weighted means of measurements on two or more spectrograms. Some of the faintest lines have been measured on one plate only. The estimated uncertainty, depending on the spectral range and the sharpness of the lines, lies between 0.005 and 0.1 A. The wave-numbers in column 4 have been calculated from wavelengths with three decimal places, even in cases where only two decimal places in the wavelength have been retained in column 2 of the table. Vacuum corrections to three decimal places were taken from a table calculated by Edlén and based on the formulae:

$$\Delta\lambda = \lambda_{\mathrm{vac}} - \lambda_{\mathrm{air}} = \lambda_{\mathrm{air}}(n-1),$$

$$10^7(n-1) = 643.28 + 294\,981\,(146-\nu^2)^{-1} + 2\,554.0\,(41-\nu^2)^{-1},$$

ν being the vacuum wave-number in units of μ^{-1} and $n-1$ the refractivity of dry air at 15° C and 760 mm Hg. ν_{calc} in column 5 has been obtained from the revised set of term values, given in Table 3. The notation in column 6 is that used by EDLÉN (10).

As mentioned above the shape of some lines indicates that certain levels are sensitive to Stark effect. This is generally true for terms with high quantum numbers. The two lines 6461 and 6454 on Plate I b are chosen as an example. The former one, identified as $4f\,^2\mathrm{F} - 6g\,^2\mathrm{G}$, is shaded to longer waves. This shading must depend on perturbation of the term $6g\,^2\mathrm{G}$, since $4f\,^2\mathrm{F}$ in combination with $3d\,^2\mathrm{D}$ gives symmetrical lines. The perturbing terms in this case are $6f\,^2\mathrm{F}$ and $6h\,^2\mathrm{H}$, situated on both sides of $6g\,^2\mathrm{G}$. The greater influence of $6h\,^2\mathrm{H}$, which lies nearest to $6g\,^2\mathrm{G}$, causes a displacement of $6g\,^2\mathrm{G}$ to larger term values and consequently a shading of the line $4f\,^2\mathrm{F} - 6g\,^2\mathrm{G}$ to longer waves. At the same time $6h\,^2\mathrm{H}$ is shifted in the opposite direction. This causes a shading to shorter waves of the line 6454, which represents the forbidden transition $4f\,^2\mathrm{F} - 6h\,^2\mathrm{H}$.

An obvious case of Stark effect perturbation is found in the term $3p'\,^2\mathrm{D}$ (8043 – – 77 cm^{-1}) of the (^{3}P) system. The lines that arise from transitions where $3p'\,^2\mathrm{D}$ is the initial term are strongly shaded to longer waves. This must chiefly depend on Stark effect perturbation from $8p\,^2\mathrm{P}$ with an estimated term value of about 7500cm^{-1}.

The shaded lines show a tendency to displacement of the wavelength with increasing voltage across the hollow cathode, as may be seen from Table 2. The combinations $2p''\,^2\mathrm{P} - 3p'\,^2\mathrm{D}$ and $4p\,^2\mathrm{P} - 3p'\,^2\mathrm{D}$ are chosen as an example. Columns 2 and 3 in Table 2 contain the wavelengths ($\lambda_{\min}$ and $\lambda_{\max}$) which have been obtained from spectrograms taken with the minimum and maximum voltages, respectively, across the light source. The wave-number difference $\Delta\nu$ corresponding to $\lambda_{\min} - \lambda_{\max}$ is inserted in column 4. The relatively small displacements of λ 5040 and λ 3836 may be due to the fact that it has not been possible to determine $\lambda_{\min}$ for these faint lines at the same low voltage as for the others.

This sensitivity to the electric field is still more evident on comparing the wavelength values obtained from the hollow cathode with those from the vacuum spark. The fifth column of Table 2 contains the wavelength values given by EDLÉN (10) for the vacuum spark and the last column gives the differences between the wave-numbers obtained from the vacuum spark and the hollow cathode.

Table 1

Wavelengths of C II lines in the region 8 800—1 987 A.†

h = hazy
l = slightly shaded to longer waves
s = slightly shaded to shorter waves
u = unsymmetrical
w = wide
unr = unresolved (= separation very uncertain)
m = masked by
bl = blended by

blg = blended by grating ghost
hul = hazy, unsymmetrical, shaded to longer waves
hus = hazy, unsymmetrical, shaded to shorter waves
ul = unsymmetrical, shaded to longer waves
us = unsymmetrical, shaded to shorter waves
wh = wide, hazy

Intensity	λ_{air}, *A*	Previous measurements*	ν_{obs}, cm^{-1}	ν_{calc}	Combination
0 very h	8 799.9		11 360.7	0.16	$3p'\ ^2D_2 - 3d'\ ^2F_3$
1 very h	8 793.8		11 368.5	8.17	$^2D_3 - \ ^2F_4$
5	8 696.71		11 495.44	5.46	$4s\ ^2S_1 - 2p''\ ^2P_1$
8	8 682.56		11 514.18	4.23	$^2S_1 - \ ^2P_2$
1 h	8 414.49		11 881.00	1.1	$4d'\ ^4F_3 - 5f'\ ^4G_4$
				1.1	$^4F_2 - \ ^4G_3$
2 h	8 413.42		11 882.51	2.4	$^4F_5 - \ ^4G_6$
				2.7	$^4F_4 - \ ^4G_5$
8	8 076.64		12 377.98	7.98	$3p'\ ^4P_3 - 3d'\ ^4P_3$
6	8 062.78		12 399.26	9.23	$^4P_3 - \ ^4P_2$
5	8 062.12		12 400.27	0.31	$^4P_2 - \ ^4P_3$
3	8 048.32		12 421.54	1.56	$^4P_2 - \ ^4P_2$
6	8 039.39		12 435.34	5.32	$^4P_2 - \ ^4P_1$
5	8 037.76		12 437.86	7.90	$^4P_1 - \ ^4P_2$
2	8 028.86		12 451.64	1.66	$^4P_1 - \ ^4P_1$
2	7 530.60		13 275.51	5.56	$2p''\ ^2P_2 - 3p'\ ^2P_1$
4 l	7 519.86		13 294.46	3.86	$5p\ ^2P_1 - 3p'\ ^2D_2$
				4.33	$2p''\ ^2P_1 - 3p'\ ^2P_1$
7	7 519.50		13 295.10	5.11	$^2P_2 - \ ^2P_2$
3	7 508.90		13 313.86	3.88	$^2P_1 - \ ^2P_2$
2 h u l	7 505.31		13 320.23	0.32	$5p\ ^2P_2 - 3p'\ ^2D_3$
7	7 237.17		13 813.75	3.75	$3p\ ^2P_2 - 3d\ ^2D_2$
20	7 236.42	6.19 F	13 815.18	5.18	$^2P_2 - \ ^2D_3$
18	7 231.32	1.12 F	13 824.93	4.90	$^2P_1 - \ ^2D_2$
1	7 144.19		13 993.53	3.44	$3p'\ ^4D_4 - 3d'\ ^4F_3$
6	7 134.11	3.52 F	14 013.31	3.33	$^4D_4 - \ ^4F_4$
1	7 132.45		14 016.56	6.53	$^4D_3 - \ ^4F_2$
7	7 125.73	5.49 F	14 029.78	9.80	$^4D_3 - \ ^4F_3$
12	7 119.90	9.45 F	14 041.26	1.25	$^4D_4 - \ ^4F_5$
				1.55	$^4D_2 - \ ^4F_2$
10	7 115.63	5.13 F	14 049.70	9.69	$^4D_3 - \ ^4F_4$

† A few lines of longer wavelengths have been added in proof (see page 32).
* References to previous measurements:

F = A. Fowler and E. W. H. Selwyn, Proc. Roy. Soc. London, A *120*, 312, 1928.
E = B. Edlén, Nova Acta Reg. Soc. Sci. Ups. *9*, No. 6, 74, 1934; B. Edlén, ZS. f. Phys. *98*, 561, 1936.

(Table 1, cont.)

Intensity	λ_{air}, A	Previous measurements*	ν_{obs}, cm^{-1}	ν_{calc}	Combination
7	7 113.04	2.36 F	14 054.82	4.82	$3p'\ {}^4D_2 - 3d'\ {}^4F_3$
6	7 112.48		14 055.91	5.92	${}^4D_1 - {}^4F_2$
8	7 063.70	3.4 F	14 152.99	3.02	$3p'\ {}^4S_2 - 3d'\ {}^4P_3$
6	7 053.09	2.9 F	14 174.27	4.27	${}^4S_2 - {}^4P_2$
4	7 046.26	5.8 F	14 188.02	8.03	${}^4S_2 - {}^4P_1$
3	6 812.29	2.19 F	14 675.30	5.32	$3s'\ {}^4P_3 - 3p'\ {}^4D_2$
7	6 800.68	0.50 F	14 700.36	0.34	${}^4P_3 - {}^4D_3$
3	6 798.11	8.04 F	14 705.90	5.93	${}^4P_2 - {}^4D_1$
7	6 791.47	1.30 F	14 720.30	0.30	${}^4P_2 - {}^4D_2$
6	6 787.22	7.09 F	14 729.51	9.53	${}^4P_1 - {}^4D_1$
10	6 783.90	3.75 F	14 736.72	6.70	${}^4P_3 - {}^4D_4$
5	6 780.61	0.27 F	14 743.87	3.90	${}^4P_1 - {}^4D_2$
8	6 779.93	9.74 F	14 745.34	5.32	${}^4P_2 - {}^4D_3$
3	6 755.16	4.75 F	14 799.42	9.41	$3p'\ {}^4D_4 - 3d'\ {}^4D_3$
8	6 750.55	0.22 F	14 809.52	9.55	${}^4D_4 - {}^4D_4$
3	6 742.43	2.05 F	14 827.37	7.36	${}^4D_3 - {}^4D_2$
6	6 738.62	8.36 F	14 835.75	5.77	${}^4D_3 - {}^4D_3$
2	6 734.00	3.56 F	14 845.92	5.91	${}^4D_3 - {}^4D_4$
2	6 733.58		14 846.84	6.84	${}^4D_2 - {}^4D_1$
5	6 731.07	0.79 F	14 852.38	2.38	${}^4D_2 - {}^4D_2$
4	6 727.19	6.84 F	14 860.95	0.79 1.21	${}^4D_2 - {}^4D_3$ ${}^4D_1 - {}^4D_1$
2	6 724.56		14 866.75	6.75	${}^4D_1 - {}^4D_2$
1 h	6 723.65		14 868.77	8.78	$4d\ {}^2D_3 - 6p\ {}^2P_2$
1 very h	6 622.05		15 096.90	6.60	$4f\ {}^2F_{3,4} - 6d\ {}^2D_{2,3}$
15	6 582.88	2.85 F	15 186.72	6.72	$3s\ {}^2S_1 - 3p\ {}^2P_1$
18	6 578.05	8.03 F	15 197.88	7.87	${}^2S_1 - {}^2P_2$
5 very h u l	6 461.95		15 470.93	0.93	$4f\ {}^2F_{3,4} - 6g\ {}^2G_{4,5}$
1 very h u s	6 454.77		15 488.1	8.1	$4f\ {}^2F - 6h\ {}^2H$
1 h	6 385.72		15 655.61	5.7	$4p'\ {}^4D_4 - 5d'\ {}^4F_5$
0	6 295.20		15 880.73	0.90	$3d'\ {}^4P_1 - 4p'\ {}^4D_1$
1	6 290.01		15 893.83	3.83	${}^4P_1 - {}^4D_2$
0	6 284.56		15 907.61	7.59	${}^4P_2 - {}^4D_2$
1	6 275.79		15 929.84	30.02	${}^4P_2 - {}^4D_3$
4 h	6 259.59		15 971.07	1.08	$4p\ {}^2P_2 - 5d\ {}^2D_{2,3}$
2 h	6 257.18		15 977.22	7.22	${}^2P_1 - {}^2D_2$
2	6 256.54		15 978.85	8.90	$3d'\ {}^2D_2 - 4p'\ {}^2P_1$
2	6 253.84		15 985.75	5.77	$3d'\ {}^4P_3 - 4p'\ {}^4D_4$
4	6 250.74		15 993.68	3.64	$3d'\ {}^2D_3 - 4p'\ {}^2P_2$
1 bl Ne	6 246.57		16 004.36	4.52	${}^2D_2 - {}^2P_2$
4 very h u l	6 151.43		16 251.89	1.89	$4d\ {}^2D_{2,3} - 6f\ {}^2F_{3,4}$
4	6 102.56	2.59 F	16 382.02	2.02	$3p'\ {}^2P_2 - 3d'\ {}^2D_2$
9	6 098.51	8.62 F	16 392.90	2.90	${}^2P_2 - {}^2D_3$
7	6 095.29	5.37 F	16 401.57	1.57	${}^2P_1 - {}^2D_2$

(Table 1, cont.)

Intensity	λ_{air}, A	Previous measurements*	ν_{obs}, cm^{-1}	ν_{calc}	Combination
0 h	6 037.96		16 557.30	7.6	$4d'\ {}^4D_4 - 6f'\ {}^4F_5$
3	5 919.45	9.60 F	16 888.77	8.76	$3d'\ {}^4P_1 - 4p'\ {}^4S_2$
4	5 914.64	4.92 F	16 902.50	2.52	${}^4P_2 -\ {}^4S_2$
6	5 907.21	7.36 F	16 923.78	3.77	${}^4P_3 -\ {}^4S_2$
12	5 891.59	1.65 F	16 968.65	8.62	$3d\ {}^2D_2 - 4p\ {}^2P_1$
15	5 889.77	9.97 F	16 973.88	3.87	${}^2D_3 -\ {}^2P_2$
6	5 889.27		16 975.33	5.30	${}^2D_2 -\ {}^2P_2$
5	5 856.04	6.09 F	17 071.66	1.59	$3p'\ {}^4D_4 - 3d'\ {}^4P_3$
2	5 843.61	3.77 F	17 107.98	7.95	${}^4D_3 -\ {}^4P_3$
4	5 836.35	6.31 F	17 129.24	9.20	${}^4D_3 -\ {}^4P_2$
2	5 827.85	7.80 F	17 154.23	4.22	${}^4D_2 -\ {}^4P_2$
2	5 823.14	3.13 F	17 168.10	7.98 8.59	${}^4D_2 -\ {}^4P_1$ ${}^4D_1 -\ {}^4P_2$
2	5 818.30	7.87 F	17 182.39	2.35	${}^4D_1 -\ {}^4P_1$
1 very h	5 791.77		17 261.09	1.3	$4d'\ {}^4F_5 - 6f'\ {}^4G_6$
0	5 713.56		17 497.36	7.59	$3d'\ {}^4P_2 - 4p'\ {}^4P_1$
1	5 712.51		17 500.60	0.58	${}^4P_1 -\ {}^4P_2$
0	5 708.03		17 514.32	4.34	${}^4P_2 -\ {}^4P_2$
2 w	5 701.16		17 535.42	5.32 5.59	${}^4P_2 -\ {}^4P_3$ ${}^4P_3 -\ {}^4P_2$
2	5 694.30		17 556.54	6.57	${}^4P_3 -\ {}^4P_3$
12	5 662.47	2.51 F	17 655.24	5.27	$3s'\ {}^4P_3 - 3p'\ {}^4S_2$
10	5 648.07	8.08 F	17 700.24	0.25	${}^4P_2 -\ {}^4S_2$
8	5 640.55	0.50 F	17 723.83	3.85	${}^4P_1 -\ {}^4S_2$
3	5 537.61	6.0 E	18 053.32	3.32	$4s\ {}^2S_1 - 5p\ {}^2P_1$
5	5 535.35		18 060.69	0.68	${}^2S_1 -\ {}^2P_2$
1	5 490.16		18 209.36	9.43	$3d'\ {}^4D_2 - 4p'\ {}^4D_2$
1	5 488.95		18 213.38	3.31	${}^4D_4 -\ {}^4D_3$
2	5 485.90		18 223.50	3.45	${}^4D_3 -\ {}^4D_3$
1	5 483.35		18 231.95	1.86	${}^4D_2 -\ {}^4D_3$
4	5 478.59	8.6 F	18 247.79	7.81	${}^4D_4 -\ {}^4D_4$
1 w h	5 368.58		18 621.74	1.7	$4d\ {}^2D_{2,3} - 7p\ {}^2P_{1,2}$
1 h	5 367.67		18 624.88	4.65	$4s'\ {}^4P_3 - 5p'\ {}^4D_4$
2 very h u l	5 342.40		18 713.0	3.0	$4f\ {}^2F_{3,4} - 7g^2\ G_{4,5}$
1 very h u s	5 339.85		18 721.9	2	$4f\ {}^2F - 7h\ {}^2H$
6 u l	5 334.79	6.7 E	18 739.67	9.67	$4p\ {}^2P_2 - 6s\ {}^2S_1$
4 u l	5 332.89		18 746.35	6.35	${}^2P_1 -\ {}^2S_1$
0 h	5 290.09		18 898.01	8.0 8.0	$4p'\ {}^4D_3 - 6s'\ {}^4P_2$ ${}^4D_2 -\ {}^4P_1$
1 h	5 286.47		18 910.95	0.9	${}^4D_4 -\ {}^4P_3$

(Table 1, cont.)

Intensity	λ_{air}, A	Previous measurements*	ν_{obs}, cm^{-1}	ν_{calc}	Combination
5	5 259.71	9.62 F	19 007.15	6.99	$3d'\ {}^4\mathrm{F}_3 - 4p'\ {}^4\mathrm{D}_2$
				7.33	${}^4\mathrm{F}_2 -\ {}^4\mathrm{D}_1$
5	5 259.06		19 009.50	9.53	${}^4\mathrm{F}_4 -\ {}^4\mathrm{D}_3$
7	5 257.24	7.36 F	19 016.11	6.11	${}^4\mathrm{F}_5 -\ {}^4\mathrm{D}_4$
2	5 256.09		19 020.26	0.26	${}^4\mathrm{F}_2 -\ {}^4\mathrm{D}_2$
4 bl C III	5 253.57	3.55 F	19 029.37	9.42	${}^4\mathrm{F}_3 -\ {}^4\mathrm{D}_3$
2	5 249.51	9.43 F	19 044.09	4.03	${}^4\mathrm{F}_4 -\ {}^4\mathrm{D}_4$
13	5 151.09	1.08 F	19 407.98	7.98	$3s'\ {}^4\mathrm{P}_3 - 3p'\ {}^4\mathrm{P}_2$
15	5 145.16	5.16 F	19 430.33	0.31	${}^4\mathrm{P}_3 -\ {}^4\mathrm{P}_3$
12	5 143.49	3.49 F	19 436.64	6.62	${}^4\mathrm{P}_2 -\ {}^4\mathrm{P}_1$
9	5 139.17	9.21 F	19 452.96	2.96	${}^4\mathrm{P}_2 -\ {}^4\mathrm{P}_2$
7	5 137.26	7.26 F	19 460.21	0.22	${}^4\mathrm{P}_1 -\ {}^4\mathrm{P}_1$
12	5 133.28	3.29 F	19 475.30	5.29	${}^4\mathrm{P}_2 -\ {}^4\mathrm{P}_3$
12	5 132.94	2.96 F	19 476.58	6.56	${}^4\mathrm{P}_1 -\ {}^4\mathrm{P}_2$
2	5 126.93		19 499.40	9.29	$4p\ {}^2\mathrm{P}_2 - 3p'\ {}^2\mathrm{P}_1$
4	5 125.20		19 506.01	5.97	${}^2\mathrm{P}_1 -\ {}^2\mathrm{P}_1$
2 very h u l	5 122.15		19 517.6	7.4	$4d\ {}^2\mathrm{D}_{2,3} - 7f\ {}^2\mathrm{F}_{3,4}$
5	5 121.82	1.69 F	19 518.88	8.84	$4p\ {}^2\mathrm{P}_2 - 3p'\ {}^2\mathrm{P}_2$
3 u l	5 120.10		19 525.43	5.17	$3d'\ {}^2\mathrm{P}_1 - 4f'\ {}^4\mathrm{D}_2$
				5.52	$4p\ {}^2\mathrm{P}_1 - 3p'\ {}^2\mathrm{P}_2$
4 h	5 119.45	9.55 F	19 527.92	7.86	$3d'\ {}^2\mathrm{P}_2 - 4f'\ {}^2\mathrm{D}_3$
2 h	5 116.75		19 538.20	8.27	${}^2\mathrm{P}_1 -\ {}^4\mathrm{D}_1$
4 h	5 114.26	4.07 F	19 547.72	7.74	${}^2\mathrm{P}_1 -\ {}^2\mathrm{D}_2$
4 h	5 113.69		19 549.89	9.84	${}^2\mathrm{P}_2 -\ {}^4\mathrm{D}_2$
				50.07	${}^2\mathrm{P}_2 -\ {}^4\mathrm{D}_3$
1 h bl band	5 107.91		19 572.04	2.41	${}^2\mathrm{P}_2 -\ {}^2\mathrm{D}_2$
2	5 049.24		19 799.43	9.43	$3d'\ {}^4\mathrm{D}_2 - 4p'\ {}^4\mathrm{P}_1$
3	5 047.11	7.2 E	19 807.79	7.77	${}^4\mathrm{D}_3 -\ {}^4\mathrm{P}_2$
1	5 044.98		19 816.14	6.18	${}^4\mathrm{D}_2 -\ {}^4\mathrm{P}_2$
5	5 044.35	4.8 E	19 818.63	8.61	${}^4\mathrm{D}_4 -\ {}^4\mathrm{P}_3$
2 bl C I	5 041.76		19 828.80	8.75	${}^4\mathrm{D}_3 -\ {}^4\mathrm{P}_3$
2 h u l	5 040.74		19 832.83	2.95	$2p''\ {}^2\mathrm{P}_2 - 3p'\ {}^2\mathrm{D}_2$
5 h u l	5 035.91	7.0 E	19 851.87	1.72	${}^2\mathrm{P}_1 -\ {}^2\mathrm{D}_2$
7 h u l	5 032.07	3.2 E	19 866.99	6.77	${}^2\mathrm{P}_2 -\ {}^2\mathrm{D}_3$
4	4 964.73	4.90 F	20 136.45	6.44	$3p'\ {}^2\mathrm{P}_2 - 3d'\ {}^2\mathrm{P}_2$
1	4 959.92	9.52 E	20 156.00	5.99	${}^2\mathrm{P}_1 -\ {}^2\mathrm{P}_2$
1	4 958.67		20 161.08	1.11	${}^2\mathrm{P}_2 -\ {}^2\mathrm{P}_1$
3	4 953.85	4.16 E	20 180.67	0.66	${}^2\mathrm{P}_1 -\ {}^2\mathrm{P}_1$
2	4 867.07		20 540.52	0.52	$4s\ {}^2\mathrm{S}_1 - 3s'\ {}^2\mathrm{P}_1$
4	4 862.57		20 559.52	9.47	${}^2\mathrm{S}_1 -\ {}^2\mathrm{P}_2$
1 very h	4 802.70		20 815.8	5.8	$4f\ {}^2\mathrm{F}_{3,4} - 8g\ {}^2\mathrm{G}_{4,5}$
2	4 747.28		21 058.80	8.81	$2p'\ {}^2\mathrm{P}_2 - 3p\ {}^2\mathrm{P}_1$
5	4 744.77	4.90 E	21 069.95	9.96	${}^2\mathrm{P}_2 -\ {}^2\mathrm{P}_2$
3	4 737.97	8.11 E	21 100.19	0.20	${}^2\mathrm{P}_1 -\ {}^2\mathrm{P}_1$
2	4 735.46		21 111.36	1.35	${}^2\mathrm{P}_1 -\ {}^2\mathrm{P}_2$

(Table 1, cont.)

Intensity	λ_{air}, A	Previous measurements*	ν_{obs}, cm^{-1}	ν_{calc}	Combination
2 h bl band	4 734.60	4.75 E	21 115.19	4.68	$3d'\ {}^2F_4 - 4f'\ {}^2F_4$
2 h	4 727.41	7.21 E	21 147.34	7.47	${}^2F_3 -\ {}^2F_3$
2 h u l	4 638.91		21 550.75	0.71	$4p\ {}^2P_2 - 6d\ {}^2D_3$
1 h u l	4 637.63		21 556.70	6.70	${}^2P_1 -\ {}^2D_2$
2 h	4 629.98	30.52 E	21 592.32	2.37	$3d'\ {}^2F_4 - 4f'\ {}^4G_5$
1 h	4 627.44		21 604.15	3.88	${}^2F_4 -\ {}^2G_4$
3 h	4 625.56	5.71 E	21 612.95	2.58	${}^2F_3 -\ {}^4G_4$
8 h unr	4 619.23	8.85 F	21 642.57	2.48	${}^2F_4 -\ {}^2G_5$
6 h	4 618.40		21 646.46	5.71	${}^2F_3 -\ {}^2G_4$
1	4 413.255		22 652.65	2.57	$3d'\ {}^2D_3 - 4f'\ {}^2F_3$
7	4 411.506	1.52 F	22 661.63	1.61	${}^2D_3 -\ {}^2F_4$
6	4 411.163	1.20 F	22 663.39	3.45	${}^2D_2 -\ {}^2F_3$
5	4 409.979	10.06 F	22 669.48	9.42	${}^2D_3 -\ {}^4F_4$
2	4 409.161		22 673.69	3.68	${}^2D_2 -\ {}^4F_3$
5 h	4 376.562	6.78 E	22 842.57	2.46	$3d'\ {}^4P_2 - 4f'\ {}^2D_3$
4	4 375.009		22 850.68	0.68	${}^4P_1 -\ {}^4D_2$
9	4 374.272	4.28 F	22 854.53	4.48	${}^4P_3 -\ {}^4D_4$
7 unr	4 372.487	2.49 F	22 863.85	3.71	${}^4P_3 -\ {}^2D_3$
				3.78	${}^4P_1 -\ {}^4D_1$
6	4 372.350		22 864.57	4.44	${}^4P_2 -\ {}^4D_2$
				4.67	${}^4P_2 -\ {}^4D_3$
1 h	4 370.661		22 873.41	3.25	${}^4P_1 -\ {}^2D_2$
2	4 369.857		22 877.62	7.54	${}^4P_2 -\ {}^4D_1$
4 unr	4 368.263	8.14 E	22 885.96	5.69	${}^4P_3 -\ {}^4D_2$
				5.92	${}^4P_3 -\ {}^4D_3$
1 h	4 368.047		22 887.09	7.01	${}^4P_2 -\ {}^2D_2$
5	4 326.156	5.88 E	23 108.71	8.67	$3p'\ {}^4P_2 - 4s'\ {}^4P_1$
4	4 325.827		23 110.47	0.44	${}^4P_3 -\ {}^4P_2$
3	4 323.102		23 125.03	5.01	${}^4P_1 -\ {}^4P_1$
3	4 321.647	1.95 E	23 132.82	2.77	${}^4P_2 -\ {}^4P_2$
5	4 318.600	8.92 E	23 149.14	9.11	${}^4P_1 -\ {}^4P_2$
8	4 317.260	7.42 E	23 156.33	6.30	${}^4P_3 -\ {}^4P_3$
6	4 313.100	3.50 E	23 178.66	8.63	${}^4P_2 -\ {}^4P_3$
2 h u l	4 307.59		23 208.32	8.36	$4p\ {}^2P_2 - 7s\ {}^2S_1$
1 h u l	4 306.33		23 215.10	5.04	${}^2P_1 -\ {}^2S_1$
4 h	4 295.920	6.11 E	23 271.35	1.40	$3d'\ {}^2D_3 - 4f'\ {}^2D_3$
3 h	4 291.819	2.00 E	23 293.59	3.38	${}^2D_3 -\ {}^4D_2$
				3.61	${}^2D_3 -\ {}^4D_3$
2 h	4 289.876		23 304.14	4.26	${}^2D_2 -\ {}^4D_2$
				4.49	${}^2D_2 -\ {}^4D_3$
3 h	4 285.704	5.96 E	23 326.83	6.83	${}^2D_2 -\ {}^2D_2$
20	4 267.258	7.27 F	23 427.66	7.64	$3d\ {}^2D_3 - 4f\ {}^2F_4$
18	4 267.003	7.02 F	23 429.06	9.07	${}^2D_2 -\ {}^2F_3$
4 unr	4 077.778		24 516.24	5.96	$3d'\ {}^4D_4 - 4f'\ {}^2F_4$
2	4 077.625		24 517.16	7.06	${}^4D_3 -\ {}^2F_3$
				7.15	${}^4D_4 -\ {}^4F_3$

(Table 1, cont.)

Intensity	λ_{air}, Å	Previous measurements*	ν_{obs}, cm^{-1}	ν_{calc}	Combination
0	4 076.83		24 521.95	2.13	$3d'\ {}^4D_3 - 4f'\ {}^4F_2$
4	4 076.526		24 523.77	3.77	${}^4D_4 - {}^4F_4$
3 } unr	4 076.251		24 525.42	5.47	${}^4D_2 - {}^2F_3$
5	4 076.142		24 526.08	6.10	${}^4D_3 - {}^2F_4$
12 l	4 075.851	6.00 E	24 527.83	7.29 7.82	${}^4D_3 - {}^4F_3$ ${}^4D_4 - {}^4F_5$
4	4 075.395		24 530.57	0.54	${}^4D_2 - {}^4F_2$
8	4 074.845	4.89 F	24 533.89	3.91	${}^4D_3 - {}^4F_4$
10	4 074.518	4.53 F	24 535.86	5.70 6.08	${}^4D_2 - {}^4F_3$ ${}^4D_1 - {}^4F_2$
3	4 021.167	1.13 F	24 861.37	1.38	$3p'\ {}^4S_2 - 4s'\ {}^4P_1$
5	4 017.278	7.27 F	24 885.45	5.48	${}^4S_2 - {}^4P_2$
7	4 009.884	9.90 F	24 931.33	1.34	${}^4S_2 - {}^4P_3$
1	4 001.717		24 982.21		} impurity?
2	3 999.890		24 993.62		
8	3 980.323	0.35 F	25 116.48	6.52	$3d'\ {}^4D_4 - 4f'\ {}^4D_4$
4 h	3 978.759	8.87 E	25 126.36	5.75 6.66	${}^4D_4 - {}^2D_3$ ${}^4D_3 - {}^4D_4$
5 h	3 977.269	7.30 E	25 135.77	5.89	${}^4D_3 - {}^2D_3$
1 h	3 975.953		25 144.09	4.30	${}^4D_2 - {}^2D_3$
2 h	3 975.341		25 147.96	7.96	${}^4D_4 - {}^4D_3$
7 h	3 973.760	3.84 E	25 157.97	7.87 8.10	${}^4D_3 - {}^4D_2$ ${}^4D_3 - {}^4D_3$
6 h	3 972.439	2.44 E	25 166.33	6.28 6.51	${}^4D_2 - {}^4D_2$ ${}^4D_2 - {}^4D_3$
2	3 971.574		25 171.81	1.82	${}^4D_1 - {}^4D_2$
4 u s	3 970.386	0.20 E	25 179.35	9.38 80.44	${}^4D_2 - {}^4D_1$ ${}^4D_3 - {}^2D_2$
3	3 969.520	9.38 E	25 184.84	4.92	${}^4D_1 - {}^4D_1$
0 h	3 968.92	8.63 E	25 188.65	8.85	${}^4D_2 - {}^2D_2$
0	3 953.95		25 283.99	4.26	$3d'\ {}^4F_5 - 4f'\ {}^2F_4$
1	3 952.679		25 292.14	2.07	${}^4F_5 - {}^4F_4$
9	3 952.058	2.08 F	25 296.12	6.12	${}^4F_5 - {}^4F_5$
4 } unr	3 949.530	} 9.45 E	25 312.30	2.18	${}^4F_4 - {}^2F_4$
1	3 949.373		25 313.31	3.37	${}^4F_4 - {}^4F_3$
6	3 948.333	8.15 E	25 319.97	9.99	${}^4F_4 - {}^4F_4$
6 l	3 947.715	7.60 E	25 323.94	3.03 4.04	${}^4F_3 - {}^2F_3$ ${}^4F_4 - {}^4F_5$
2	3 947.079		25 328.02	8.10	${}^4F_3 - {}^4F_2$
1 } unr	3 946.429	} 6.35 E	25 332.19	2.07	${}^4F_3 - {}^2F_4$
5	3 946.278		25 333.16	3.26	${}^4F_3 - {}^4F_3$
4	3 945.197	} 5.10 E	25 340.10	39.88	${}^4F_3 - {}^4F_4$
5	3 945.003		25 341.35	1.37	${}^4F_2 - {}^4F_2$
3	3 944.193		25 346.56	6.53	${}^4F_2 - {}^4F_3$
18	3 920.693	0.677 F	25 498.48	8.55	$3p\ {}^2P_2 - 4s\ {}^2S_1$
15	3 918.978	8.977 F	25 509.63	9.70	${}^2P_1 - {}^2S_1$
1	3 883.824		25 740.52	0.33	$3d'\ {}^4F_5 - 4f'\ {}^4G_4$
— blg	—		25 759	9.07	${}^4F_4 - {}^4G_3$
7	3 880.588	0.59 E	25 761.99	1.95	${}^4F_5 - {}^4G_5$

(Table 1, cont.)

Intensity	λ_{air}, A	Previous measure-ments*	ν_{obs}, cm^{-1}	ν_{calc}	Combination
7	3 879.640	9.60 E	25 768.28	8.25	$3d'\ {}^4F_4 - 4f'\ {}^4G_4$
7	3 878.028	8.22 E	25 779.00	8.96	${}^4F_3 - {}^4G_3$
12	3 876.664	6.670 F	25 788.06	8.14	${}^4F_3 - {}^4G_4$
12	3 876.408	6.409 F	25 789.77	9.87	${}^4F_4 - {}^4G_5$
12	3 876.187	6.188 F	25 791.24	1.24	${}^4F_5 - {}^4G_6$
9	3 876.055	6.051 F	25 792.11	2.23	${}^4F_2 - {}^4G_3$
2 h	3 874.666		25 801.36	1.38	${}^4F_4 - {}^2G_4$
0 h	3 873.067		25 812.01	2.06	${}^4F_5 - {}^2G_5$
7 h	3 871.669	1.62 E	25 821.34	1.27	${}^4F_3 - {}^2G_4$
6 h	3 868.874	8.84 E	25 839.99	9.98	${}^4F_4 - {}^2G_5$
2	3 862.181		25 884.77	4.82	$3d'\ {}^4F_5 - 4f'\ {}^4D_4$
0 h	3 856.62		25 922.09	1.97	${}^4F_4 - {}^2D_3$
2 h u l	3 836.683		26 056.79	6.68	$4p\ {}^2P_2 - 3p'\ {}^2D_2$
6 h u l	3 835.730	6.10 E	26 063.26	3.36	${}^2P_1 - {}^2D_2$
8 h u l	3 831.743	2.12 E	26 090.38	0.50	${}^2P_2 - {}^2D_3$
8 w	3 590.862	0.87 F	27 840.52	0.41 1.33	$3p'\ {}^4D_3 - 4s'\ {}^4P_2$ ${}^4D_2 - {}^4P_1$
9	3 589.657	9.67 F	27 849.88	9.91	${}^4D_4 - {}^4P_3$
5	3 588.915	8.92 F	27 855.63	5.70	${}^4D_1 - {}^4P_1$
6	3 587.657	7.68 F	27 865.39	5.43	${}^4D_2 - {}^4P_2$
3	3 585.809	5.83 F	27 879.76	9.80	${}^4D_1 - {}^4P_2$
7	3 584.977	4.98 F	27 886.22	6.27	${}^4D_3 - {}^4P_3$
3	3 581.763	1.80 E	27 911.25	1.29	${}^4D_2 - {}^4P_3$
2 very h	3 406.361		29 348.41	8.54	$3d'\ {}^2P_2 - 5f'\ {}^2D_3$
1 very h unr	3 404.33		29 365.90	5.8	${}^2P_1 - {}^2D_2$
1 very h unr	3 403.66		29 371.68	1.3	${}^2P_2 - {}^4D_{3,2}$
0 very h	3 401.53		29 390.07	0.5	${}^2P_2 - {}^2D_2$
1 h	3 393.946		29 455.78	5.78	$3d'\ {}^2D_2 - 5p'\ {}^2P_1$
2 h	3 392.146		29 471.40	1.40	${}^2D_3 - {}^2P_2$
6	3 361.721	1.75 F	29 738.12	8.12	$3d\ {}^2D_2 - 5p\ {}^2P_1$
8	3 361.051	1.09 F	29 744.05	4.05	${}^2D_3 - {}^2P_2$
3	3 360.891		29 745.47	5.48	${}^2D_2 - {}^2P_2$
0 h	3 357.19		29 778.26	7.83	$3d'\ {}^4P_1 - 5p'\ {}^4S_2$
1 h	3 355.690		29 791.57	1.59	${}^4P_2 - {}^4S_2$
2 h	3 353.302		29 812.78	2.84	${}^4P_3 - {}^4S_2$
0 very h	3 174.58		31 491.1	0.2	$3d'\ {}^2F_4 - 5f'\ {}^4G_5$
1 very h	3 172.62		31 510.55	09.9	${}^2F_3 - {}^4G_4$
2 very h unr	3 170.03		31 536.3	5.9	${}^2F_4 - {}^2G_5$
1 very h unr	3 169.66		31 539.9	9.3	${}^2F_3 - {}^2G_4$
8	3 167.931	7.95 F	31 557.21	7.17	$2p''\ {}^2D_2 - 3p'\ {}^2P_1$
4	3 165.974	5.99 E	31 576.72	6.72	${}^2D_2 - {}^2P_2$
9	3 165.467	5.51 F	31 581.78	1.83	${}^2D_3 - {}^2P_2$
0 h	3 157.13		31 665.19	5.01	$3d'\ {}^4D_4 - 5p'\ {}^4D_4$
0 h	3 142.04		31 817.24	7.67	$4d\ {}^2D_2 - 3d'\ {}^2F_3$
1 h	3 137.92		31 859.00	8.79	${}^2D_3 - {}^2F_4$

(Table 1, cont.)

Intensity	λ_{air}, A	Previous measurements*	ν_{obs}, cm^{-1}	ν_{calc}	Combination
2 h u s	3 124.133		31 999.60	9.44	$3p'\ ^2D_3 - 4d'\ ^2D_3$
1 h u s	3 122.086		32 020.59	0.28	$^2D_2 -\ ^2D_2$
2	3 100.570		32 242.78	2.84	$3d\ ^2D_3 - 3s'\ ^2P_2$
0 h	3 087.90		32 375.1	5.1	$3d'\ ^4D_3 - 5p'\ ^4P_2$
1 h	3 086.903		32 385.53	5.53	$^4D_4 -\ ^4P_3$
2 w h	3 083.052		32 425.98	6.0	$3d'\ ^4F_4 - 5p'\ ^4D_3$
				6.0	$^4F_3 -\ ^4D_2$
				6.0	$^4F_2 -\ ^4D_1$
2 h	3 082.381		32 433.04	3.31	$^4F_5 -\ ^4D_4$
1 h	3 060.64		32 663.39	3.14	$3d'\ ^4P_2 - 5f'\ ^2D_3$
0 h	3 059.83		32 672.05	2.2	$^4P_1 -\ ^4D_2$
3 h	3 059.091	9.24 E	32 679.95	9.87	$^4P_3 -\ ^4D_4$
2 w h	3 058.45		32 686.79	5.9	$^4P_2 -\ ^4D_2$
				5.9	$^4P_2 -\ ^4D_3$
				7.8	$^4P_1 -\ ^4D_1$
1 very w h	3 056.85		32 703.91	691.3	$^4P_1 -\ ^2D_2$
				707.2	$^4P_3 -\ ^4D_2$
				7.2	$^4P_3 -\ ^4D_3$
3	3 049.671	9.44 E	32 780.89	0.89	$3d'\ ^2D_3 - 5f'\ ^2F_4$
3	3 049.398		32 783.82	3.82	$^2D_2 -\ ^2F_3$
2	3 048.933		32 788.82	8.82	$^2D_3 -\ ^4F_4$
0	3 048.69		32 791.44	1.19	$^2D_2 -\ ^4F_3$
2 h	3 040.512	39.67 E	32 879.63	9.63	$3p'\ ^2D_2 - 4d'\ ^2F_3$
3 h	3 039.714		32 888.26	8.26	$^2D_3 -\ ^2F_4$
18 h	2 992.618	2.63 F	33 405.81	5.81	$3d\ ^2D_{2,3} - 5f\ ^2F_{3,4}$
0	2 969.59		33 664.91	4.84	$3p'\ ^4P_3 - 4d'\ ^4D_2$
2	2 968.836	8.83 E	33 673.40	3.39	$^4P_3 -\ ^4D_3$
7	2 967.868	7.91 F	33 684.38	4.47	$^4P_3 -\ ^4D_4$
3	2 967.629		33 687.09	7.17	$^4P_2 -\ ^4D_2$
5	2 966.871	6.88 E	33 695.71	5.72	$^4P_2 -\ ^4D_3$
3	2 966.655		33 698.16	8.16	$^4P_1 -\ ^4D_1$
3	2 966.187	6.25 E	33 703.48	3.51	$^4P_1 -\ ^4D_2$
3	2 910.729	0.82 E	34 345.60	5.67	$3p'\ ^4P_3 - 4d'\ ^4P_3$
2 w	2 908.957	9.03 E	34 366.52	6.13	$^4P_3 -\ ^4P_2$
				8.00	$^4P_2 -\ ^4P_3$
1	2 907.09		34 388.59	8.46	$^4P_2 -\ ^4P_2$
2	2 906.011	5.97 E	34 401.36	1.38	$^4P_2 -\ ^4P_1$
2	2 905.715		34 404.86	4.80	$^4P_1 -\ ^4P_2$
6 w	2 885.469	5.50 E	34 646.25	5.38	$3d'\ ^4D_3 - 5f'\ ^2F_4$
				5.84	$^4D_2 -\ ^2F_3$
				6.71	$^4D_4 -\ ^4F_5$
4 w	2 884.808	4.93 E	34 654.19	3.21	$^4D_2 -\ ^4F_3$
				3.31	$^4D_3 -\ ^4F_4$
				5.2	$^4D_1 -\ ^4F_2$

(Table 1, cont.)

Intensity	λ_{air}, A	Previous measurements*	ν_{obs}, cm^{-1}	ν_{calc}	Combination
2 h	2 861.060		34 941.82	1.91	$3d'\ {}^4D_4 - 5f'\ {}^4D_4$
1 h	2 858.00		34 979.20	9.4	${}^4D_3 - {}^4D_3$
18	2 837.603	7.602 F	35 230.66	0.63	$2p'\ {}^2S_1 - 3p\ {}^2P_1$
20	2 836.710	6.710 F	35 241.74	1.78	${}^2S_1 - {}^2P_2$
2	2 822.812		35 415.24	5.01	$3d'\ {}^4F_5 - 5f'\ {}^4F_5$
1 w	2 821.54		35 431.17	0.88	${}^4F_4 - {}^4F_3$
				1.46	${}^4F_4 - {}^2F_4$
1 w	2 820.70		35 441.83	39.39	${}^4F_4 - {}^4F_4$
				43.40	${}^4F_3 - {}^2F_3$
1	2 820.00		35 450.51	0.77	${}^4F_3 - {}^4F_3$
1 w	2 819.13		35 461.53	59.28	${}^4F_3 - {}^4F_4$
				60.5	${}^4F_2 - {}^4F_2$
				64.04	${}^4F_2 - {}^4F_3$
0 h	2 803.45		35 659.8	9.8	$3d'\ {}^4F_5 - 5f'\ {}^4G_5$
0 h	2 802.95		35 666.2	5.5	${}^4F_4 - {}^4G_4$
0 h	2 802.39		35 673.3	1.8	${}^4F_3 - {}^4G_3$
3 w } unr	2 801.43	1.31 E	35 685.57	5.1	${}^4F_2 - {}^4G_3$
				5.4	${}^4F_3 - {}^4G_4$
5 w	2 801.21		35 688.35	7.7	${}^4F_4 - {}^4G_5$
				8.6	${}^4F_5 - {}^4G_6$
1 h	2 799.15		35 714.7	4.8	${}^4F_3 - {}^2G_4$
1 h	2 797.70		35 733.1	3.4	${}^4F_4 - {}^2G_5$
3	2 767.673	7.75 F	36 120.77	0.71	$3p'\ {}^4S_2 - 4d'\ {}^4P_3$
2	2 766.118	6.18 F	36 141.07	1.17	${}^4S_2 - {}^4P_2$
1	2 765.120	5.27 F	36 154.11	4.09	${}^4S_2 - {}^4P_1$
12 u l	2 747.282	7.31 F	36 388.86	8.86	$3p\ {}^2P_2 - 4d\ {}^2D_{2,3}$
10	2 746.488	6.50 F	36 399.37	9.37	${}^2P_1 - {}^2D_2$
1	2 730.61		36 610.99	0.79	$3s'\ {}^2P_2 - 4p'\ {}^2P_1$
2	2 729.213		36 629.75	9.74	${}^2P_1 - {}^2P_1$
4	2 728.707	8.72 E	36 636.55	6.41	${}^2P_2 - {}^2P_2$
2 w	2 727.36		36 654.61	5.36	${}^2P_1 - {}^2P_2$
0 very w h	2 712.32		36 857.9	9.9	$3d'\ {}^2F_4 - 6f'\ {}^4G_5$
1 very w h	2 710.59		36 881.4	1.9	${}^2F_3 - {}^4G_4$
1 very w h	2 708.4		36 912	06.4	${}^2F_4 - {}^2G_5$
				15.2	${}^2F_3 - {}^2G_4$
3 u l	2 669.960		37 442.61	2.53	$3d\ {}^2D_3 - 6p\ {}^2P_2$
3	2 643.427	3.42 E	37 818.42	8.35	$3p'\ {}^4D_4 - 4d'\ {}^4F_4$
3	2 642.331	2.32 E	37 834.10	4.10	${}^4D_3 - {}^4F_3$
8 w	2 641.425	1.44 F	37 847.08	5.51	${}^4D_2 - {}^4F_2$
				7.47	${}^4D_4 - {}^4F_5$
5	2 640.894	0.93 F	37 854.68	4.71	${}^4D_3 - {}^4F_4$
6	2 640.560	0.58 F	37 859.47	9.12	${}^4D_2 - {}^4F_3$
				9.88	${}^4D_1 - {}^4F_2$
1 very w h	2 628.46		38 033.8	3.8	$3d'\ {}^4P_3 - 6f'\ {}^4D_4$

(Table 1, cont.)

Intensity	λ_{air}, A	Previous measurements*	ν_{obs}, cm^{-1}	ν_{calc}	Combination
2 h u l	2 622.90		38 114.3	4.56	$2p''\ ^2D_2 - 3p'\ ^2D_2$
3 h u l	2 620.20		38 153.6	3.49	$^2D_3 - \ ^2D_3$
2 very w h	2 612.45		38 266.9	66.	$3d'\ ^2D_3 - 6f'\ ^2F_4$
				67.	$^2D_2 - \ ^2F_3$
1	2 605.62		38 367.1	7.00	$3p'\ ^4D_4 - 4d'\ ^4D_3$
4	2 604.863	4.89 E	38 378.27	8.08	$^4D_4 - \ ^4D_4$
1	2 603.72		38 395.1	4.81	$^4D_3 - \ ^4D_2$
3	2 603.161	3.18 E	38 403.36	3.36	$^4D_3 - \ ^4D_3$
2	2 602.39	2.32 E	38 414.7	4.44	$^4D_3 - \ ^4D_4$
				4.48	$^4D_2 - \ ^4D_1$
2	2 602.02		38 420.2	19.83	$^4D_2 - \ ^4D_2$
2	2 601.42	1.49 E	38 429.0	8.38	$^4D_2 - \ ^4D_3$
				8.85	$^4D_1 - \ ^4D_1$
1	2 601.05		38 434.5	4.20	$^4D_1 - \ ^4D_2$
1	2 592.71		38 558.2	8.12	$3p'\ ^2P_2 - 4d'\ ^2D_2$
4	2 591.845	1.96 E	38 571.02	1.10	$^2P_2 - \ ^2D_3$
2	2 591.410	1.53 E	38 577.49	7.67	$^2P_1 - \ ^2D_2$
10 h u l	2 574.826	4.86 F	38 825.95	5.93	$3d\ ^2D_{2,3} - 6f\ ^2F_{3,4}$
1 h	2 571.76		38 872.2	2.2	$3d'\ ^4D_4 - 6p'\ ^4P_3$
2 w h	2 570.57		38 890.2		
0	2 556.12		39 110.0	09.58	$5p\ ^2P_2 - 4p'\ ^2P_1$
1	2 555.66		39 117.1	6.94	$^2P_1 - \ ^2P_1$
3	2 554.478		39 135.21	5.20	$^2P_2 - \ ^2P_2$
1 h	2 547.35		39 244.7	45.	$3d'\ ^4F_4 - 6p'\ ^4D_3$
				45.	$^4F_3 - \ ^4D_2$
				45.	$^4F_2 - \ ^4D_1$
2 h	2 546.81		39 253.1	3.1	$^4F_5 - \ ^4D_4$
2	2 543.45	3.5 E	39 304.9	4.3	$3p'\ ^4P_2 - 5s'\ ^4P_1$
				5.8	$^4P_3 - \ ^4P_2$
1	2 540.88	0.6 E	39 344.6	4.4	$^4P_1 - \ ^4P_2$
3	2 540.39		39 352.2	1.8	$^4P_3 - \ ^4P_3$
2	2 538.98		39 374.0	4.1	$^4P_2 - \ ^4P_3$
12	2 512.065	2.03 F	39 795.91	6.02	$2p'\ ^2P_2 - 2p''\ ^2D_3$
5	2 511.734	1.71 F	39 801.15	1.13	$^2P_2 - \ ^2D_2$
10	2 509.121	9.11 F	39 842.59	2.52	$^2P_1 - \ ^2D_2$
2 w h	2 491.37		40 126.4	6.1	$3d'\ ^4D_4 - 6f'\ ^4F_5$
2 w h	2 490.87		40 134.5	34.	$^4D_2 - \ ^4F_3$
				35.	$^4D_3 - \ ^4F_4$
				35.	$^4D_1 - \ ^4F_2$
1 w h	2 434.81		41 058.5	57.4	$3d'\ ^4F_4 - 6f'\ ^4G_5$
				57.4	$^4F_3 - \ ^4G_4$
				60.	$^4F_2 - \ ^4G_3$
2 w h	2 434.24		41 068.1	67.5	$^4F_5 - \ ^4G_6$

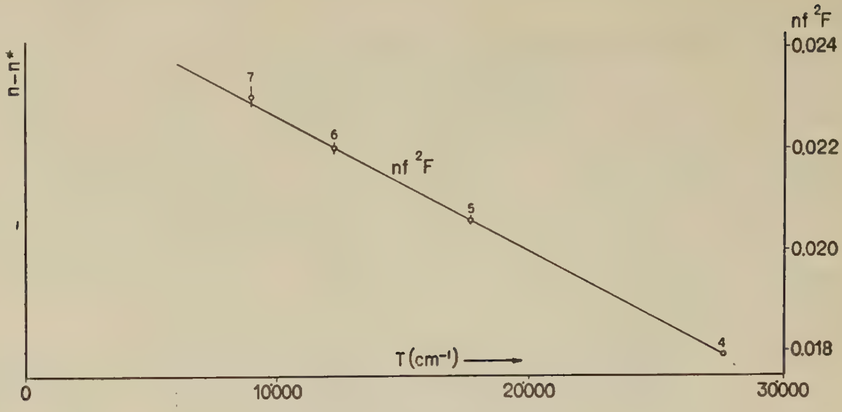

Fig. 1. The series *nf* ²F.

in the same way. The procedure was repeated until no further change in the values occurred. To the level system thus obtained the remaining levels were then attached individually.

For the determination of the series limit an unperturbed series must be selected. All series with the limit $2s\ {}^1S_0$ may be perturbed by doublet terms in the $({}^3P)$ system. For the series $nf\ {}^2F$ and $ng\ {}^2G$, however, the perturbing levels $3d'\ {}^2F$ and $4f'\ {}^2G$ are situated so far above the series limit that only very small perturbations can be expected. Since $nf\ {}^2F$ is known with much greater accuracy than $ng\ {}^2G$ the former was chosen as the basis of the limit determination. This has been done in the usual way, employing a Ritz formula $n - n^* = \alpha + \beta T_n$. The effective quantum numbers, $n^* = \sqrt{4R/T_n}$, have been calculated using the Rydberg constant for carbon, $R = 109\,732.34$ cm⁻¹. Fig. 1 shows the plot of $n - n^*$ against the term values for the series $nf\ {}^2F$. The old determination proved to be correct within ± 3 cm⁻¹.

Fig. 2 shows the two series $ns\ {}^2S_1$ and $nd\ {}^2D_3$, which deviate considerably from the Ritz formula. The beginning of the series $ns\ {}^2S$ is perturbed by $2p'\ {}^2S$, situated about 20000 cm⁻¹ below $3s\ {}^2S$. At the end of the series a second perturbation in the reverse direction appears, which is undoubtedly due to the term $3p'\ {}^2S$. This has earlier been determined from the lines $\lambda\lambda$ 6115.21, 3871.62 and 3868.84. However, the first one of these lines has not been found in the present spectrograms and therefore certainly cannot be assigned to C II, and the two other lines are now otherwise identified. Therefore, the previous identification of the level $3p'\ {}^2S_1$ must be discarded. The position of this level may be estimated from its perturbing effect on $ns\ {}^2S$. According to SHENSTONE and RUSSELL (12) a series perturbed by a foreign term can be represented by the formula

$$T_n = RZ_0^2 (n^*)^{-2} = RZ_0^2 [n - \alpha - \beta T_n - \gamma (T_n - T_0)^{-1}]^{-2},$$

where T_0 is the value of the foreign level and γ is a perturbing parameter. Since $2p'\ {}^2S$ lies far below the first member of the series $ns\ {}^2S$ it may be expected to cause only small displacements of the higher series members. The appearance of the series for $n \geq 4$ should, therefore, be influenced chiefly by $3p'\ {}^2S$. A value of this perturbing term together with values of the other constants α, β and γ in the above formula have been calculated from the four observed terms $ns\ {}^2S_1$ ($n = 4, 5, 6,$ and 7),

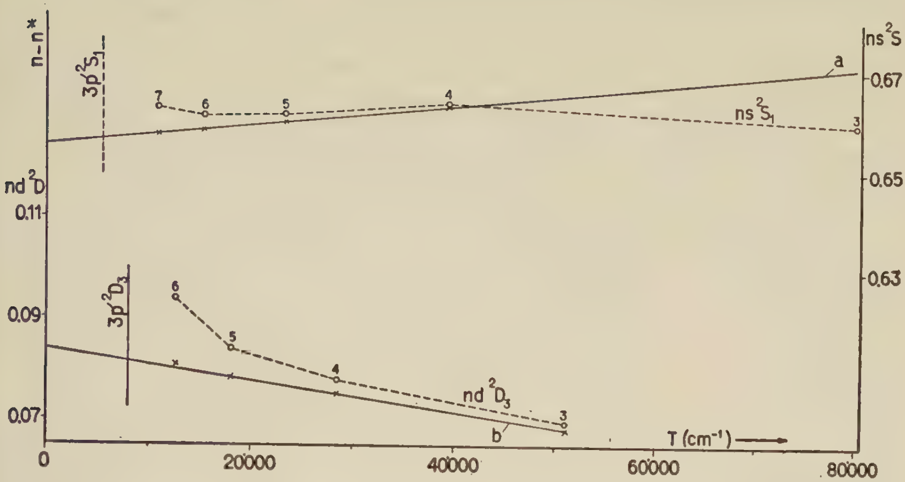

Fig. 2. The perturbation of the series *ns* $^2S_1$ and *nd* $^2D_3$ by the levels $3p'$ $^2S_1$ and $3p'$ $^2D_3$. The straight, solid lines represent the "unperturbed" series.

using the formulae given by EDLÉN (13). The following values have been obtained: $\alpha = 0.6543$, $\beta = 2.08 \cdot 10^{-7}$, $\gamma = 27.8$, $T_0 = 5500$. The straight line (a) in Fig. 2 represents $\alpha + \beta T_n$ and the crosses show the remainders after the subtraction of $\gamma (T_n - T_0)^{-1}$ from the observed $n - n^*$, thus representing the "unperturbed" series. The calculated position of the perturbing term $3p'$ $^2S_1$ is indicated by a vertical dashed line. Of course, this value is very uncertain, owing to the approximations made. All attempts to locate $3p'$ $^2S_1$ experimentally have been fruitless. This may possibly be due to the fact that $3p'$ $^2S_1$, through strong interaction with the high members of *ns* $^2S_1$, has partly adopted the character of these levels, thus giving rise only to combinations of very low intensity.

The series *nd* ^2D is perturbed by the term $3p'$ ^2D. With the values of $3d$ $^2D_3$, $4d$ $^2D_3$, and $5d$ $^2D_3$ given in Table 3 and with $T_0 = 3p'$ $^2D_3 = 8044$, the following values have been obtained: $\alpha = 0.0840$, $\beta = -3.11 \cdot 10^{-7}$, $\gamma = 58.7$. Again, the line (b) in Fig. 2 indicates the "unperturbed" series.

The series *np* $^2P_2$ is plotted in Fig. 3 on the same scale as the one used for *ns* ^2S and *nd* ^2D. The strong perturbation of this series is mainly caused by the terms $2p''$ ^2P and $3s'$ ^2P marked by two vertical lines in Fig. 3. Being perturbed by two terms the series *np* ^2P must be represented by a formula containing two γ's. An approximate calculation suggests the order of magnitude of the γ's to be: $\gamma_1 = 10$ ($T_0 = 2p''$ $^2P_2 = 27910$), and $\gamma_2 = 200$ ($T_0 = 3s'$ $^2P_2 = 18865$).

For $3s'$ ^2P a new value has been adopted. After the rejection of the term $3p'$ ^2S the old identification of $3s'$ ^2P is based upon 3 lines, λ 1223.99, λ 1223.59 ($2p'$ $^2S_1 - 3s'$ $^2P_{2,1}$) and λ 968.16 ($2p'$ $^2D_3 - 3s'$ $^2P_2$). The intensity ratio of the two first-mentioned lines requires the term $3s'$ ^2P to be inverted and at the same time λ 968.16 should represent the weaker component $2p'$ $^2D_2 - 3s'$ $^2P_1$, which is improbable. A new value of $3s'$ ^2P which is about 425 cm^{-1} greater than the old one has now been found from combinations with $4s$ ^2S, $3d$ ^2D and $4p'$ ^2P. The lines $\lambda\lambda$ 1223.99, 1223.59, and 968.16, for which no new identification has been found, are probably not belonging to C II.

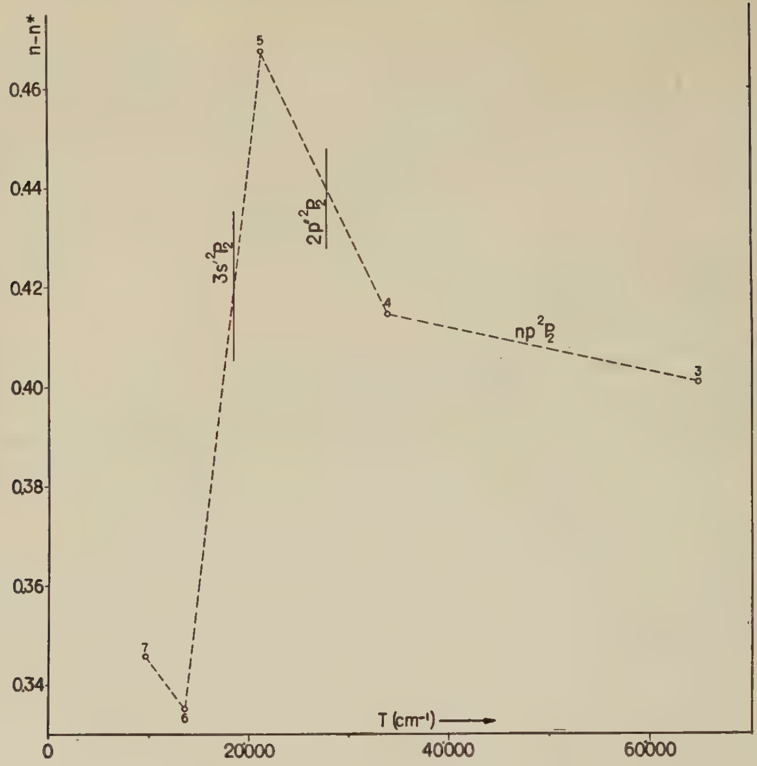

Fig. 3. The perturbation of the series $np\ ^2P_2$ by the levels $2p''\ ^2\mathrm{P}_2$ and $3s'\ ^2\mathrm{P}_2$.

The 4f′ levels. In the (^{3}P) system it is particularly interesting to study the $4f'$ levels. They deviate considerably from the LS-coupling and give fairly strong intercombination lines of the type $3d' - 4f'$ which make an exact linking up of the doublet and quartet systems possible. The analysis of the $4f'$ terms is rather difficult because of their anomalous structure and small intervals. According to the analysis of the transitions $3d'\ ^4\mathrm{P} - 4f'\ ^4\mathrm{D}$ suggested here, the two levels $4f'\ ^4\mathrm{D}_3$ and $4f'\ ^4\mathrm{D}_2$ will have nearly the same value, 25071 cm^{-1}. This may be due to perturbation from the doublet levels $4f'\ ^2\mathrm{D}_3$ and $4f'\ ^2\mathrm{D}_2$ which lie at 25049 and 25093 cm^{-1}, respectively, and thus tend to reduce the distance between $^4\mathrm{D}_3$ and $^4\mathrm{D}_2$. The anomalous level separations in $4f'\ ^4\mathrm{F}$ can be explained analogously. The difficulty of separating the multiplet components increases with increasing value of n. The analysis of $3d' - 5f'$ and $3d' - 6f'$ has been possible only on the assumption that the $5f'$ and $6f'$ levels have the same general structure as the $4f'$ levels.

The quartet system. The quartet levels were calculated in the same way as the doublet levels using EDLÉN's value of $3s'\ ^4\mathrm{P}_3$ as a starting point. The quartet system was then connected with the doublet system through the intercombination lines of the type $3d' - 4f'$. A determination of the limit $2p\ ^3\mathrm{P}$ is of interest since no intercombination lines have been observed in C III, and, therefore, the distance $2s\ ^1\mathrm{S}_0 - 2p\ ^3\mathrm{P}_2$ is known only approximately. In Fig. 4 $n - n^*$ has been plotted against the term values

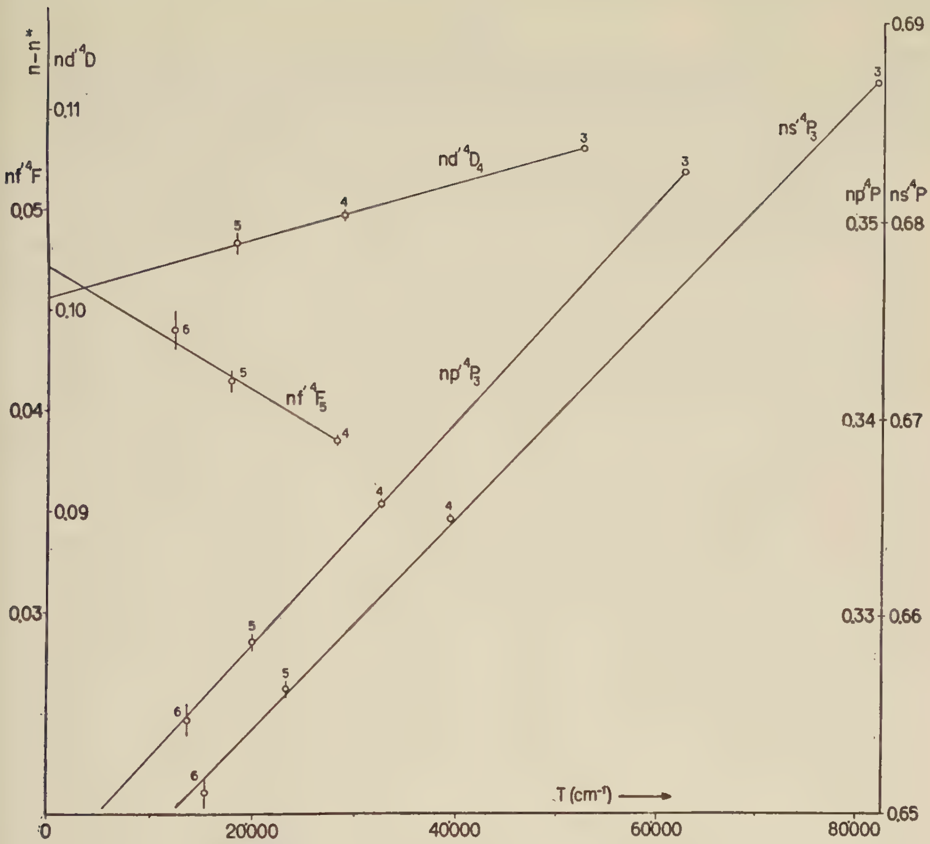

Fig. 4. The series $ns'\ ^4P_3$, $np'\ ^4P_3$, $nd'\ ^4D_4$ and $nf'\ ^4F_5$. The vertical lines show the deviation of $n-n^*$ caused by a change of $\pm 4\ \mathrm{cm}^{-1}$ in the limit.

(T) for the series $ns'\ ^4P_3$, $np'\ ^4P_3$, $nd'\ ^4D_4$, and $nf'\ ^4F_5$. The vertical lines show Δn^* corresponding to $\Delta T = \pm 4\ \mathrm{cm}^{-1}$. The quartet levels with the highest J value are the most suitable for a determination of the limit, as they are in general the best established, especially for high n values, and are essentially unperturbed. The present determinations of the series limits of the doublet terms built on $2s\ ^1S_0$ and the quartets built on $2p\ ^3P$ fix the distance $2s\ ^1S_0 - 2p\ ^3P_2$ to 52423 cm⁻¹ with an uncertainty of $\pm$ 7 cm⁻¹.

The term table. The deepest terms $2p\ ^2P$, $2p'\ ^4P$, $2p'\ ^2D$, and $2p''\ ^4S$ do not give any combinations in the region now investigated. They have been tied up with the remaining term system through lines in the vacuum ultraviolet, measured by EDLÉN (10) and by BOYCE, MORE and RIEKE (14, 15). The values for $4p'\ ^2D_3$, $4d'\ ^2P_{2,1}$, $6d'\ ^4D_4$ and $6d'\ ^4P_3$ were derived from combinations with the deep terms only.

Table 3 contains the complete term system of C II. An asterisk (*) marks the newly identified levels. The effective quantum number has been calculated for the

Table 3

The term system of C II.

$2p\ ^2P_2$	196 595.2	*64.0*	$2p'\ ^4P_3$	153 605.2	*28.3*	$2p''\ ^4S_2$	54 631.7	
$^2P_1$	196 659.2		$^4P_2$	153 633.5	*22.0*	$^2D_3$	46 197.19	*−5.11*
			$^4P_1$	153 655.5		$^2D_2$	46 192.08	
			$^2D_3$	121 728.6	*−2.5*	$^2P_2$	27 910.47	*18.77*
			$^2D_2$	121 726.1		$^2P_1$	27 929.24	
			$^2P_2$	85 993.21	*41.39*			
			$^2P_1$	86 034.60				
			$^2S_1$	100 165.03				

Term symbol	Term value, cm^{-1}		n^*	Term symbol	Term value, cm^{-1}		n^*
Limit: $2s\ ^1S_0\ (=0)$							
$3s\ ^2S_1$	80 121.12		2.34058	$3d\ ^2D_3$	51 108.07	*1.43*	2.93057
$4s\ ^2S_1$	39 424.70		3.33667	$^2D_2$	51 109.50		
$5s\ ^2S_1$	23 310.93		4.33928	$4d\ ^2D_3$	28 534.32	*0.71*	3.92205
$6s\ ^2S_1$	15 394.53		5.3397	$^2D_2$	28 535.03		
$7s\ ^2S_1$	*10 925.84		6.3383	$5d\ ^2D_3$	18 163.06	*0.60*	4.91589
				$^2D_2$	*18 163.66		
$3p\ ^2P_2$	64 923.25	*11.15*	2.60014	$6d\ ^2D_3$	12 583.49	*0.69*	5.9061
$^2P_1$	64 934.40			$^2D_2$	*12 584.18		
$4p\ ^2P_2$	34 134.20	*6.68*	3.58594				
$^2P_1$	34 140.88			$4f\ ^2F_{4,3}$	27 680.43		3.98209
$5p\ ^2P_2$	21 364.02	*7.36*	4.53269	$5f\ ^2F_{4,3}$	17 702.83		4.97939
$^2P_1$	21 371.38			$6f\ ^2F_{4,3}$	12 282.71		5.9779
$6p\ ^2P_2$	*13 665.54		5.6674	$7f\ ^2F_{4,3}$	* 9 017.2		6.9769
$7p\ ^2P_{2,1}$	* 9 912.9		6.6542				
				$5g\ ^2G_{5,4}$	*17 585.72		4.99594
				$6g\ ^2G_{5,4}$	*12 209.50		5.9958
				$7g\ ^2G_{5,4}$	* 8 967.4		6.9962
				$8g\ ^2G_{5,4}$	* 6 864.6		7.9963
				$6h\ ^2H_{6,5}$	*12 192.3		6.0001
				$7h\ ^2H_{6,5}$	* 8 958		7.000
Limits: $2p\ ^3P_2\ (-52\,422.8)$; $^3P_1\ (-52\,366.0)$; $^3P_0\ (-52\,343.0)$							
$3s'\ ^4P_3$	29 623.06	*44.98*	2.3130 ($^3P_2$)	$3p'\ ^4S_2$	11 967.79		2.6120 ($^3P_1$)
$^4P_2$	29 668.04	*23.60*					
$^4P_1$	29 691.64			$^4P_3$	10 192.75	*22.33*	2.6476 ($^3P_2$)
$^2P_2$	*18 865.23	*18.95*	2.4814 ($^3P_2$)	$^4P_2$	10 215.08	*16.34*	
$^2P_1$	*18 884.18			$^4P_1$	10 231.42		
				$^2P_2$	14 615.36	*19.55*	2.5603 ($^3P_0$)
$4s'\ ^4P_3$	−12 963.55	*45.86*	3.3352 ($^3P_2$)	$^2P_1$	14 634.91		
$^4P_2$	−12 917.69	*24.10*					
$^4P_1$	−12 893.59			$^4D_4$	14 886.36	*36.36*	2.5536 ($^3P_2$)
$5s'\ ^4P_3$	−29 159.0	*46.0*	4.3437 ($^3P_2$)	$^4D_3$	14 922.72	*25.02*	
$^4P_2$	*−29 113.0	*23.8*		$^4D_2$	14 947.74	*14.37*	
$^4P_1$	*−29 089.2			$^4D_1$	14 962.11		
				$^2D_3$	8 043.70	*33.82*	2.6943 ($^3P_2$)
$6s'\ ^4P_3$	*−37 081.9	*47.4*	5.3490 ($^3P_2$)	$^2D_2$	8 077.52		
$^4P_2$	*−37 034.5	*22.4*					
$^4P_1$	*−37 012.1			$4p'\ ^4S_2$	−19 109.00		3.6329 ($^3P_1$)

(Table 3, cont.)

Term symbol	Term value, cm^{-1}		n^*
$4p'\ {}^4\mathrm{P}_3$	−19 741.80	*20.98*	3.6645 ($^3\mathrm{P}_2$)
$^4\mathrm{P}_2$	−19 720.82	*16.75*	
$^4\mathrm{P}_1$	*−19 704.07		
$^2\mathrm{P}_2$	−17 771.18	*25.62*	3.5632 ($^3\mathrm{P}_0$)
$^2\mathrm{P}_1$	−17 745.56		
$^4\mathrm{D}_4$	−18 171.00	*34.50*	3.5798 ($^3\mathrm{P}_2$)
$^4\mathrm{D}_3$	−18 136.50	*22.43*	
$^4\mathrm{D}_2$	−18 114.07	*12.93*	
$^4\mathrm{D}_1$	−18 101.14		
$^2\mathrm{D}_3$	−20 268		3.6947 ($^3\mathrm{P}_2$)
$5p'\ {}^4\mathrm{S}_2$	*−31 998.07		4.6422 ($^3\mathrm{P}_1$)
$^4\mathrm{P}_3$	*−32 308.72	*20.5*	4.6714 ($^3\mathrm{P}_2$)
$^4\mathrm{P}_2$	*−32 288.2		
$^2\mathrm{P}_2$	−31 248.94	*26.50*	4.5616 ($^3\mathrm{P}_0$)
$^2\mathrm{P}_1$	*−31 222.44		
$^4\mathrm{D}_4$	*−31 588.20	*35.2*	4.5899 ($^3\mathrm{P}_2$)
$^4\mathrm{D}_3$	*−31 553.0	*19.9*	
$^4\mathrm{D}_2$	*−31 533.1	*13.3*	
$^4\mathrm{D}_1$	*−31 519.8		
$6p'\ {}^4\mathrm{P}_3$	*−38 795.4		5.6753 ($^3\mathrm{P}_2$)
$^4\mathrm{D}_4$	*−38 408.0	*36*	5.5963 ($^3\mathrm{P}_2$)
$^4\mathrm{D}_3$	*−38 372	*20*	
$^4\mathrm{D}_2$	*−38 352	*13*	
$^4\mathrm{D}_1$	*−38 339		
$3d'\ {}^4\mathrm{P}_3$	− 2 185.23	*−21.25*	2.9559 ($^3\mathrm{P}_2$)
$^4\mathrm{P}_2$	− 2 206.48	*−13.76*	
$^4\mathrm{P}_1$	− 2 220.24		
$^2\mathrm{P}_2$	− 5 521.08	*−24.67*	3.0592 ($^3\mathrm{P}_2$)
$^2\mathrm{P}_1$	− 5 545.75		
$^4\mathrm{D}_4$	76.81	*10.14*	2.8915 ($^3\mathrm{P}_2$)
$^4\mathrm{D}_3$	86.95	*8.41*	
$^4\mathrm{D}_2$	95.36	*5.54*	
$^4\mathrm{D}_1$	100.90		
$^2\mathrm{D}_3$	− 1 777.54	*10.88*	2.9456 ($^3\mathrm{P}_1$)
$^2\mathrm{D}_2$	− 1 766.66		
$^4\mathrm{F}_5$	845.11	*27.92*	2.8706 ($^3\mathrm{P}_2$)
$^4\mathrm{F}_4$	873.03	*19.89*	
$^4\mathrm{F}_3$	892.92	*13.27*	
$^4\mathrm{F}_2$	906.19		
$^2\mathrm{F}_4$	− 3 324.47	*41.83*	2.9900 ($^3\mathrm{P}_2$)
$^2\mathrm{F}_3$	− 3 282.64		
$4d'\ {}^4\mathrm{P}_3$	−24 152.92	*−20.46*	3.9404 ($^3\mathrm{P}_2$)
$^4\mathrm{P}_2$	−24 173.38	*−12.92*	
$^4\mathrm{P}_1$	−24 186.30		
$^2\mathrm{P}_2$	−25 600.0	*−26.9*	4.0453 ($^3\mathrm{P}_2$)
$^2\mathrm{P}_1$	−25 626.9		

Term symbol	Term value, cm^{-1}		n^*
$4d'\ {}^4\mathrm{D}_4$	−23 491.72	*11.08*	3.8951 ($^3\mathrm{P}_2$)
$^4\mathrm{D}_3$	−23 480.64	*8.55*	
$^4\mathrm{D}_2$	−23 472.09	*5.35*	
$^4\mathrm{D}_1$	*−23 466.74		
$^2\mathrm{D}_3$	−23 955.74	*12.98*	3.9306 ($^3\mathrm{P}_1$)
$^2\mathrm{D}_2$	−23 942.76		
$^4\mathrm{F}_5$	−22 961.11	*29.12*	3.8598 ($^3\mathrm{P}_2$)
$^4\mathrm{F}_4$	−22 931.99	*20.61*	
$^4\mathrm{F}_3$	−22 911.38	*13.61*	
$^4\mathrm{F}_2$	−22 897.77		
$^2\mathrm{F}_4$	−24 844.56	*42.45*	3.9895 ($^3\mathrm{P}_2$)
$^2\mathrm{F}_3$	*−24 802.11		
$5d'\ {}^4\mathrm{P}_3$	−34 394.1	*−18.8*	4.9342 ($^3\mathrm{P}_2$)
$^4\mathrm{P}_2$	*−34 412.9	*−14.9*	
$^4\mathrm{P}_1$	*−34 427.8		
$^4\mathrm{D}_4$	−34 116.1	*12.3*	4.8966 ($^3\mathrm{P}_2$)
$^4\mathrm{D}_3$	*−34 103.8	*7.5*	
$^4\mathrm{D}_2$	*−34 096.3		
$^4\mathrm{F}_5$	*−33 826.7	*28*	4.8583 ($^3\mathrm{P}_2$)
$^4\mathrm{F}_4$	* 33 799	*25*	
$^4\mathrm{F}_3$	*−33 774	*14*	
$^4\mathrm{F}_2$	*−33 760		
$6d'\ {}^4\mathrm{P}_3$	−39 948		5.9317 ($^3\mathrm{P}_2$)
$^4\mathrm{D}_4$	−39 787		5.8938 ($^3\mathrm{P}_2$)
$4f'\ {}^4\mathrm{D}_4$	−25 039.71	*−31.44*	4.0037 ($^3\mathrm{P}_2$)
$^4\mathrm{D}_3$	−25 071.15	*0.23*	
$^4\mathrm{D}_2$	−25 070.92	*−13.10*	
$^4\mathrm{D}_1$	*−25 084.02		
$^2\mathrm{D}_3$	−25 048.94	*−44.55*	4.0043 ($^3\mathrm{P}_2$)
$^2\mathrm{D}_2$	−25 093.49		
$^4\mathrm{F}_5$	−24 451.01	*4.05*	3.9613 ($^3\mathrm{P}_2$)
$^4\mathrm{F}_4$	−24 446.96	*6.62*	
$^4\mathrm{F}_3$	*−24 440.34	*5.16*	
$^4\mathrm{F}_2$	*−24 435.18		
$^2\mathrm{F}_4$	−24 439.15	*9.04*	3.9605 ($^3\mathrm{P}_2$)
$^2\mathrm{F}_3$	−24 430.11		
$^4\mathrm{G}_6$	−24 946.13	*29.29*	3.9968 ($^3\mathrm{P}_2$)
$^4\mathrm{G}_5$	−24 916.84	*21.62*	
$^4\mathrm{G}_4$	−24 895.22	*9.18*	
$^4\mathrm{G}_3$	−24 886.04		
$^2\mathrm{G}_5$	−24 966.95	*38.60*	3.9983 ($^3\mathrm{P}_2$)
$^2\mathrm{G}_4$	−24 928.35		
$5f'\ {}^4\mathrm{D}_4$	−34 865.10	*−27.3*	4.9999 ($^3\mathrm{P}_2$)
$^4\mathrm{D}_3$	*−34 892.4	*0*	
$^4\mathrm{D}_2$	*−34 892.4	*−16*	
$^4\mathrm{D}_1$	*−34 908		
$^2\mathrm{D}_3$	*−34 869.62	*−42.0*	5.0006 ($^3\mathrm{P}_2$)
$^2\mathrm{D}_2$	*−34 911.6		

(Table 3, cont.)

Term symbol	Term value, cm^{-1}		n^*	Term symbol	Term value, cm^{-1}		n^*
$5f'\ ^4F_5$	−34 569.90	*3.54*	4.9584 ($^3P_2$)	$6f'\ ^4D_4$	*−40 219.0		5.9972 ($^3P_2$)
$^4F_4$	*−34 566.36	*8.51*		$^4F_5$	*−40 049.3	*1*	5.9560 ($^3P_2$)
$^4F_3$	*−34 557.85	*3.6*		$^4F_4$	*−40 048	*9*	
$^4F_2$	*−34 554.3			$^4F_3$	*−40 039	*5*	
$^2F_4$	−34 558.43	*7.95*	4.9568 ($^3P_2$)	$^4F_2$	*−40 034		
$^2F_3$	*−34 550.48			$^2F_4$	*−40 044	*10*	5.9547 ($^3P_2$)
$^4G_6$	−34 843.5	*28.8*	4.9969 ($^3P_2$)	$^2F_3$	*−40 034		
$^4G_5$	*−34 814.7	*22.2*		$^4G_6$	*−40 222.4	*38.0*	5.9981 ($^3P_2$)
$^4G_4$	*−34 792.5	*13.6*		$^4G_5$	*−40 184.4	*19.9*	
$^4G_3$	*−34 778.9			$^4G_4$	*−40 164.5	*11*	
$^2G_5$	*−34 860.4	*38.5*	4.9993 ($^3P_2$)	$^4G_3$	*−40 154		
$^2G_4$	*−34 821.9			$^2G_5$	*−40 230.9	*33.1*	6.0001 ($^3P_2$)
				$^2G_4$	*−40 197.8		

Table 4

C II wavelengths in the vacuum ultraviolet.

Combination	ν_{calc} cm^{-1}	λ_{calc} A	λ *E* (10)	λ *BMR* (14, 15)	Remarks
$2p'\ ^2D_2 - 3p\ ^2P_1$	56791.7	1760.821	0.81 (3)	0.818*	weight 12
$^2D_2 -\ ^2P_2$	56802.8	1760 477			
$^2D_3 -\ ^2P_2$	56805.3	1760.399	0.40 (4)	0.412*	weight 12
$2p'\ ^2P_2 - 2p''\ ^2P_1$	58063.97	1722.238	2.21 (0)		
$^2P_2 -\ ^2P_2$	58082.74	1721.682	1.66 (2)		
$^2P_1 -\ ^2P_1$	58105.36	1721.012	0.99 (1)		
$^2P_1 -\ ^2P_2$	58124,13	1720.456	0.44 (0)		
$2p\ ^2P_2 - 2p'\ ^2D_3$	74866.6	1335.709	5.684 (14)	5.703*	weight 4
$^2P_2 -\ ^2D_2$	74869.1	1335.665			
$^2P_1 -\ ^2D_2$	74933.1	1334.524	4.515 (13)	4.534*	weight 4
$2p'\ ^2D_2 - 2p''\ ^2D_3$	75528.9	1323.997	3.916 (8)	3.94	
$^2D_3 -\ ^2D_3$	75531.4	1323.953			
$^2D_2 -\ ^2D_2$	75534.0	1323.907			
$^2D_3 -\ ^2D_2$	75536.5	1323.863			
$2p'\ ^2D_2 - 4p\ ^2P_1$	87585.2	1141.745	1.746 (2)	1.745*	weight 2
$^2D_2 -\ ^2P_2$	87591.9	1141.658			
$^2D_3 -\ ^2P_2$	87594.4	1141.625	1.630 (3)	1.623*	weight 6
$2p'\ ^2P_2 - 3d'\ ^2D_2$	87759.87	1139.473	9.49 (0)		
$^2P_2 -\ ^2D_3$	87770.75	1139.332	9.330 (3)	9.343	
$^2P_1 -\ ^2D_2$	87801.26	1138.936	8.936 (2)		
$2p'\ ^2P_2 - 3d'\ ^2P_2$	91514.29	1092.726	2.740 (2)		
$^2P_2\ \ ^2P_1$	91538.96	1092.431	2.422 (0)		
$^2P_1 -\ ^2P_2$	91555.68	1092.232	2.240 (0)		
$^2P_1 -\ ^2P_1$	91580.35	1091.937	1.930 (1)		

(Table 4, cont.)

Combination	ν_{calc} cm^{-1}	λ_{calc} A	λ *E* (10)	λ *BMR* (14, 15)	Remarks
$2p'\ ^2D_2 - 2p''\ ^2P_1$	93796.9	1066.133	6.121 (6)	6.138*	weight 4
$^2D_2 -\ ^2P_2$	93815.6	1065.921			
$^2D_3 -\ ^2P_2$	93818.1	1065.892	5.883 (7)	5.895*	weight 6
$2p'\ ^2D_2 - 4f\ ^2F_3$	94045.7	1063.313	3.30 (0d)		
$^2D_3 -\ ^2F_{4,3}$	94048.2	1063.285			
$2p\ ^2P_2 - 2p'\ ^2S_1$	96430.2	1037.020	7.017 (13)	7.020*	weight 4
$^2P_1 -\ ^2S_1$	96494.2	1036.332	6.330 (12)	6.332*	weight 2
$2p'\ ^4P_3 - 2p''\ ^4S_2$	98973.5	1010.371	0.369 (10+)*	0.374*	weight: E:2; BMR:2
$^4P_2 -\ ^4S_2$	99001.8	1010.083	0.074 (10)*	0.092*	E:2; BMR:2
$^4P_1 -\ ^4S_2$	99023.8	1009.858	9.854 (9)*	9.862*	E:2; BMR:2
$2p'\ ^2S_1 - 3d'\ ^2P_2$	105686.11	946.198	6.208 (2)		
$^2S_1 -\ ^2P_1$	105710.78	945.977	5.981 (1)		
$2p\ ^2P_2 - 2p'\ ^2P_1$	110560.6	904.481	4.468 (10)	4.482*	weight 2
$^2P_2 -\ ^2P_2$	110602.0	904.143	4.134 (12)	4.144*	weight 2
$^2P_1 -\ ^2P_1$	110624.6	903.958	3.950 (11)	3.952*	weight 2
$^2P_1 -\ ^2P_2$	110666.0	903.620	3.609 (10)	3.614*	weight 2
$2p\ ^2P_2 - 3s\ ^2S_1$	116474.1	858.560	8.561 (9)	8.559*	weight 1
$^2P_1 -\ ^2S_1$	116538.1	858.088	8.094 (8)	8.091*	weight 1
$2p'\ ^2D_2 - 3d'\ ^2D_2$	123492.8	809.764	9.770 (3+)		
$^2D_3 -\ ^2D_2$	123495.3	809.747			
$^2D_2 -\ ^2D_3$	123503.6	809.693	9.682 (4)		
$^2D_3 -\ ^2D_3$	123506.1	809.677			
$2p'\ ^4P_3 - 3s'\ ^4P_2$	123937.2	806.860	6.846 (6)		
$^4P_2 -\ ^4P_1$	123941.9	806.830			
$^4P_1 -\ ^4P_1$	123963.9	806.686	6.684 (4)		
$^4P_2 -\ ^4P_2$	123965.5	806.676			
$^4P_3 -\ ^4P_3$	123982.1	806.568	6.555 (7)		
$^4P_1 -\ ^4P_2$	123987.5	806.533			
$^4P_2 -\ ^4P_3$	124010.4	806.384	6.384 (5)*		weight 1
$2p'\ ^2D_2 - 3d'\ ^2F_3$	125008.7	799.944	9.947 (4)		
$^2D_3 -\ ^2F_3$	125011.2	799.928			
$^2D_3 -\ ^2F_4$	125053.1	799.660	9.664 (5−)		
$2p\ ^2P_2 - 3d\ ^2D_2$	145485.7	687.353			
$^2P_2 -\ ^2D_3$	145487.1	687.346	7.355 (11)		
$^2P_1 -\ ^2D_2$	145549.7	687.051	7.059 (10)		
$2p'\ ^2D_2 - 4d'\ ^2D_2$	145668.9	686.488	6.480 (2d)		
$^2D_3 -\ ^2D_3$	145684.3	686.416			
$2p'\ ^4P_3 - 3d'\ ^4D_3$	153518.2	651.389			
$^4P_3 -\ ^4D_4$	153528.4	651.345	1.342 (8)		
$^4P_2 -\ ^4D_2$	153538.1	651.304			
$^4P_2 -\ ^4D_3$	153546.5	651.269	1.262 (7)		
$^4P_1 -\ ^4D_1$	153554.6	651.234	1.216 (7−)		
$^4P_1 -\ ^4D_2$	153560.1	651.211			

(Table 4, cont.)

Combination	ν_{calc} cm^{-1}	λ_{calc} A	λ *E* (10)	λ *BMR* (14, 15)	Remarks
$2p'\,{}^4P_3 - 3d'\,{}^4P_3$	155790.4	641.888	1.875 (6 +)		
${}^4P_3 - {}^4P_2$	155811.7	641.800	1.772 (6)		
${}^4P_2 - {}^4P_3$	155818.7	641.771			
${}^4P_2 - {}^4P_1$	155853.7	641.627	1.591 (6)		
${}^4P_1 - {}^4P_2$	155862.0	641.593			
$2p\ {}^2P_2 - 4s\ {}^2S_1$	157170.5	636.252	6.247 (4)		
${}^2P_1 - S_1$	157234.5	635.993	5.988 (3)		
$2p'\,{}^4P_3 - 4s'\,{}^4P_2$	166522.9	600.518	0.532 (2)		
${}^4P_2 - {}^4P_1$	166527.1	600.503			
${}^4P_3 - {}^4P_3$	166568.8	600.353	0.369 (3)		
${}^4P_1 - {}^4P_2$	166573.2	600.337			
${}^4P_2 - {}^4P_3$	166597.1	600.251	0.265 (1)		
$2p\ {}^2P_2 - 4d\ {}^2D_2$	168060.2	595.025			
${}^2P_2 - {}^2D_3$	168060.9	595.022	5.032 (7d)		
${}^2P_1 - {}^2D_2$	168124.2	594.798	4.808 (6d)		
$2p\ {}^2P_2 - 5s\ {}^2S_1$	173284.3	577.086	7.108 (2)		Stark eff
${}^2P_1 - {}^2S_1$	173348.3	576.873	6.900 (1)		Stark eff
$2p'\,{}^4P_3 - 4d'\,{}^4D_3$	177085.8	564.698	4.645 (5bd)		
${}^4P_3 - {}^4D_4$	177096.9	564.663			
${}^4P_2 - {}^4D_2$	177105.6	564.635			
${}^4P_2 - {}^4D_3$	177114.1	564.608			
${}^4P_1 - {}^4D_1$	177122.2	564.582			
${}^4P_1 - {}^4D_2$	177127.6	564.565			
$2p'\,{}^4P_3 - 4d'\,{}^4P_3$	177758.1	562.562	2.577 (3 +)		
${}^4P_3 - {}^4P_2$	177778.6	562.497	2.498 (3)		
${}^4P_2 - {}^4P_3$	177786.4	562.473			
${}^4P_2 - {}^4P_1$	177819.8	562.367	2.355 (3)		
${}^4P_1 - {}^4P_2$	177828.9	562.338			
$2p\ {}^2P_2 - 5d\ {}^2D_2$	178431.5	560.439			
${}^2P_2 - {}^2D_3$	178432.1	560.437	0.443 (5d)		
${}^2P_1 - {}^2D_2$	178495.5	560.238	0.244 (4d)		
$2p\ {}^2P_2 - 6s\ {}^2S_1$	181200.7	551.874	1.894 (0)		Stark eff
$2p\ {}^2P_2 - 3p'\,{}^2P_1$	181960.3	549.570	9.568 (3)		
${}^2P_2 - {}^2P_2$	181979.8	549.512	9.507 (5)		
${}^2P_1 - {}^2P_1$	182024.3	549.377	9.375 (4)		
${}^2P_1 - {}^2P_2$	182043.8	549.318	9.317 (3)		
$2p'\,{}^4P_3 - 5s'\,{}^4P_2$	182718.2	547.291	7.288 (0)		
${}^4P_2 - {}^4P_1$	182722.7	547.277			
${}^4P_3 - {}^4P_3$	182764.2	547.153	7.169 (0 +)		
${}^4P_1 - {}^4P_2$	182768.5	547.140			
$2p\ {}^2P_2 - 6d\ {}^2D_2$	184011.0	543.446			
${}^2P_2 - {}^2D_3$	184011.7	543.444	3.475 (3d)		Stark eff
${}^2P_1 - {}^2D_2$	184075.0	543.257	3.291 (2d)		Stark eff
$2p'\,{}^4P_3 - 5d'\,{}^4D_4$	187721.3	532.705	2.716 (3d)		
${}^4P_2 - {}^4D_3$	187737.3	532.659			

(Table 4, cont.)

Combination	ν_{calc} cm^{-1}	λ_{calc} A	λE (10)	λBMR (14, 15)	Remarks
$2p'\,{}^4P_3 - 5d'\,{}^4P_3$	187999.3	531.917	1.917 (1d)		
${}^4P_2 - {}^4P_1$	188061.3	531.742	1.775 (0d)		
${}^4P_1 - {}^4P_2$	188068.4	531.721			
$2p\,{}^2P_2 - 3p'\,{}^2D_2$	188517.7	530.454			
${}^2P_2 - {}^2D_3$	188551.5	530.359	0.386 (4d)		Stark eff
${}^2P_1 - {}^2D_2$	188581.7	530.274	0.290 (3d)		Stark eff
$2p\,{}^2P_2 - 4p'\,{}^2P_1$	214340.8	466.547	6.536 (0)		
${}^2P_2 - {}^2P_2$	214366.4	466.491	6.492 (2)		
${}^2P_1 - {}^2P_1$	214404.8	466.407	6.404 (1)		
${}^2P_1 - {}^2P_2$	214430.4	466.352	6.358 (0)		
$2p\,{}^2P_2 - 5p'\,{}^2P_2$	227844.1	438.897	8.910 (1d)		
${}^2P_1 - {}^2P_1$	227881.6	438.824			

level with the highest J value in every term. In the (^3P) system the limit used in the calculation is indicated in the table. In those cases where less than three members of a series are known and, consequently, the limit cannot be decided from the trend of the series, the rule that levels with the same J value do not cross each other has been used for the assignment of limit component.

Vacuum ultraviolet wavelengths

Table 4 contains the C II lines observed by Edlén (10) below 1760 A, for which either the initial level or both the initial and final levels are established from lines in the long wavelength region. The wave-numbers and wavelengths calculated from the level values given in Table 3 are inserted in columns 2 and 3 of Table 4. The lines used to calculate the values of the low terms $2p\,^2P$, $2p'\,^4P$, $2p'\,^2D$ and $2p''\,^4S$ are marked with (*), and the weight assigned to each one of them is given in the last column. The notation "Stark eff." in this column indicates the lines whose initial level is sensitive to Stark effect. The wavelengths of these lines will be sensitive to the properties of the light source.

Acknowledgments. I am greatly indebted to Professor Bengt Edlén, Director of this Institute, for his invaluable advice and constant interest in this investigation. I wish also to thank Fil. Dr. Lennart Minnhagen for many valuable discussions. To Fil. Mag. Kjell Bockasten I should like to express my thanks for his great help in the experimental work.

The Physical Laboratory, University of Lund, June 1952.

REFERENCES

1. F. Paschen and J. S. Campbell, Ann. d. Phys. (5) *31*, 29, 1938.
2. K. Burns, K. B. Adams and J. Longwell, J. Opt. Soc. Am. *40*, 339, 1950.
3. W. F. Meggers and C. J. Humphreys, Bur. Stand. J. Research 13, 293, 1934.
4. K. Burns and F. M. Walters Jr, Publ. Allegheny Obs. *6*, 159, 1929; *8*, 39, 1931.

5. J. C. Dobbie, Ann. Solar Phys. Obs. *5*, Part I, 1938.
6. B. Edlén and P. Swings, Astrophys. J. *95*, 532, 1942.
7. L. Minnhagen, "The Stark Effect of Certain Multiplets", Diss. (Lund 1944), p. 56.
8. B. Edlén, Nova Acta Reg. Soc. Sci. Upsaliensis *9*, No. 6, 104, 1934.
9. J. W. Ryde, Proc. Roy. Soc. London A *117*, 164, 1927.
10. B. Edlén, Nova Acta Reg. Soc. Sci. Upsaliensis *9*, No. 6, 74, 1934.
11. ——, ZS. f. Phys. *98*, 561, 1936.
12. A. G. Shenstone and H. N. Russell, Phys. Rev. *39*, 415, 1932.
13. B. Edlén, Ark. Mat. Astr. Fys. Bd *29 A*, No. 21, 1943.
14. J. C. Boyce and C. A. Rieke, Phys. Rev. *47*, 653, 1935.
15. K. R. More and C. A. Rieke, Phys. Rev. *50*, 1054, 1936.

Added in proof

After the manuscript had been sent to the press some C II lines above 8 800 A were found and measured on plates taken by Bockasten using a modified vacuum spark and the stigmatic grating spectograph mentioned above. The result is given in the following supplement to Table 1:

Intensity	λ_{air}, *A*	ν_{obs}, cm^{-1}	ν_{calc}	Combination
4 w h	9 903.46	10 094.71	4.71	$4f\ ^2F_{3,4} - 5g\ ^2G_{4,5}$
2	9 882.71	10 115.91	5.94	$3p'\ ^4P_3 - 3d'\ ^4D_4$
1	9 870.86	10 128.05	8.13	$^4P_2 - {}^4D_3$
2 h	9 236.40	10 823.75	3.27	$4p\ ^2P_2 - 5s\ ^2S_1$
4 very w h	9 229.95	10 831.33	29.95	$^2P_1 - {}^2S_1$
			31.49	$4d\ ^2D_3 - 5f\ ^2F_4$
			32.20	$^2D_2 - {}^2F_3$

The value of the new term $5g\ ^2G_{5,4}$, 17 585.72 cm^{-1}, has been incorporated in Table 3. The series $ng\ ^2G$, thus completed, seems to indicate a slightly higher value for the series limit, corresponding to an increase in all values in Table 3, including the $^3P_{2,1,0}$-values, by 2 or 3 cm^{-1}.

Description of Plates I—II

Spectrograms obtained with a condensed hollow cathode discharge using a graphite tube as the cathode. (Magnification 2.6 times.)

I a, b: 21-foot concave grating spectrograph, 1st order; exposure 60 min.
c: Large glass prism spectrograph; exposure 90 min.

II a, b: 21-foot concave grating spectrograph, 2nd order; exposure 60 min.
c: Hilger E478 quartz spectrograph; exposure 30 min.

Tryckt den 5 maj 1953

Uppsala 1953. Almqvist & Wiksells Boktryckeri AB

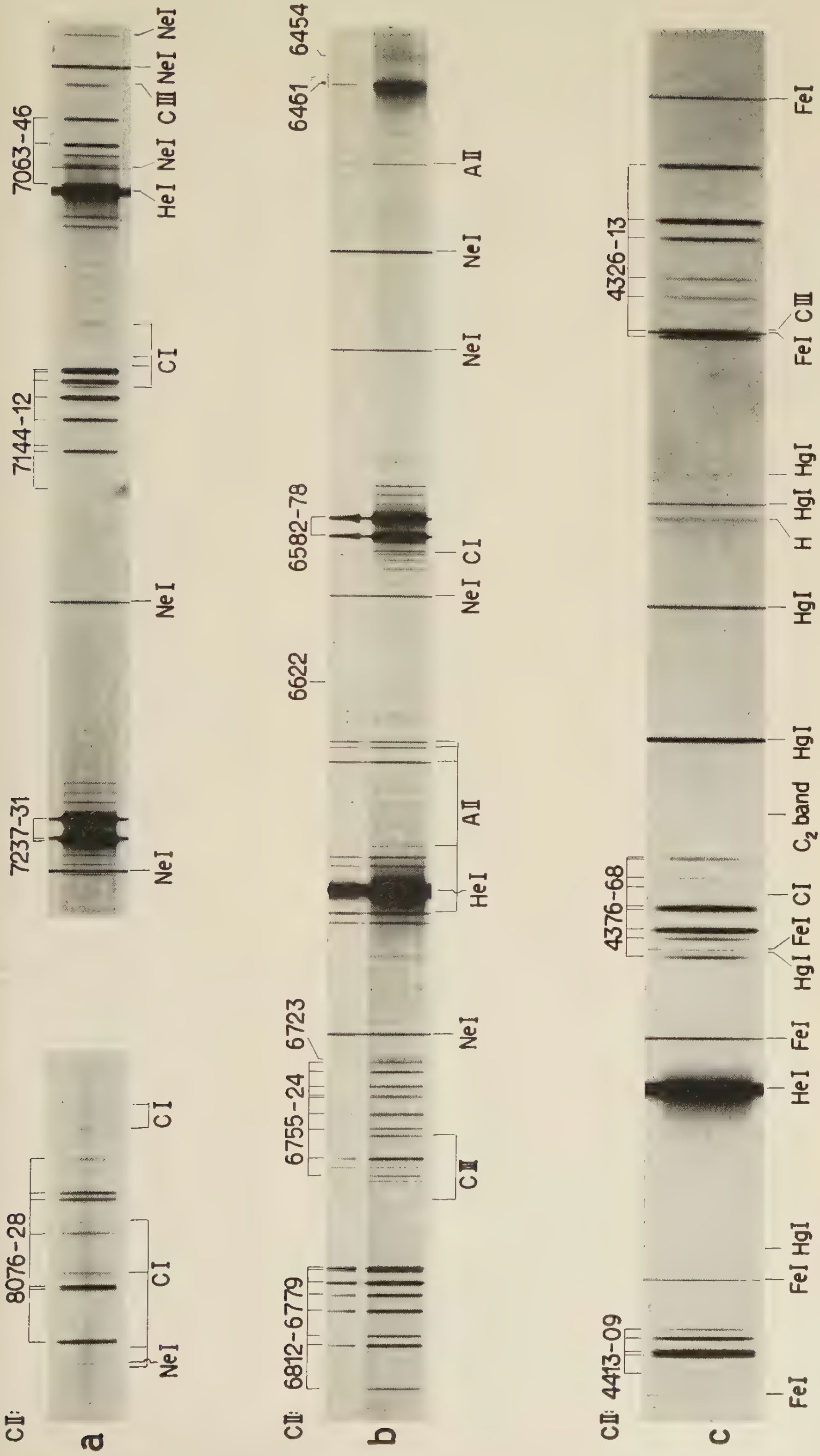
CII:
a
8076-28
7237-31
7144-12
7063-46
NeI
CI
CI
NeI
NeI
CI
HeI
NeI
NeI
CIII
NeI
NeI
CII:
b
6812-6779
6755-24
6723
6622
6582-78
6461
6454
CIII
NeI
HeI
AII
NeI
CI
NeI
NeI
AII
CII:
c
4413-09
4376-68
4326-13
FeI
FeI
HgI
FeI
HeI
FeI
HgI
FeI
CI
C$_2$ band
HgI
HgI
H
HgI
HgI
FeI
CIII
FeI

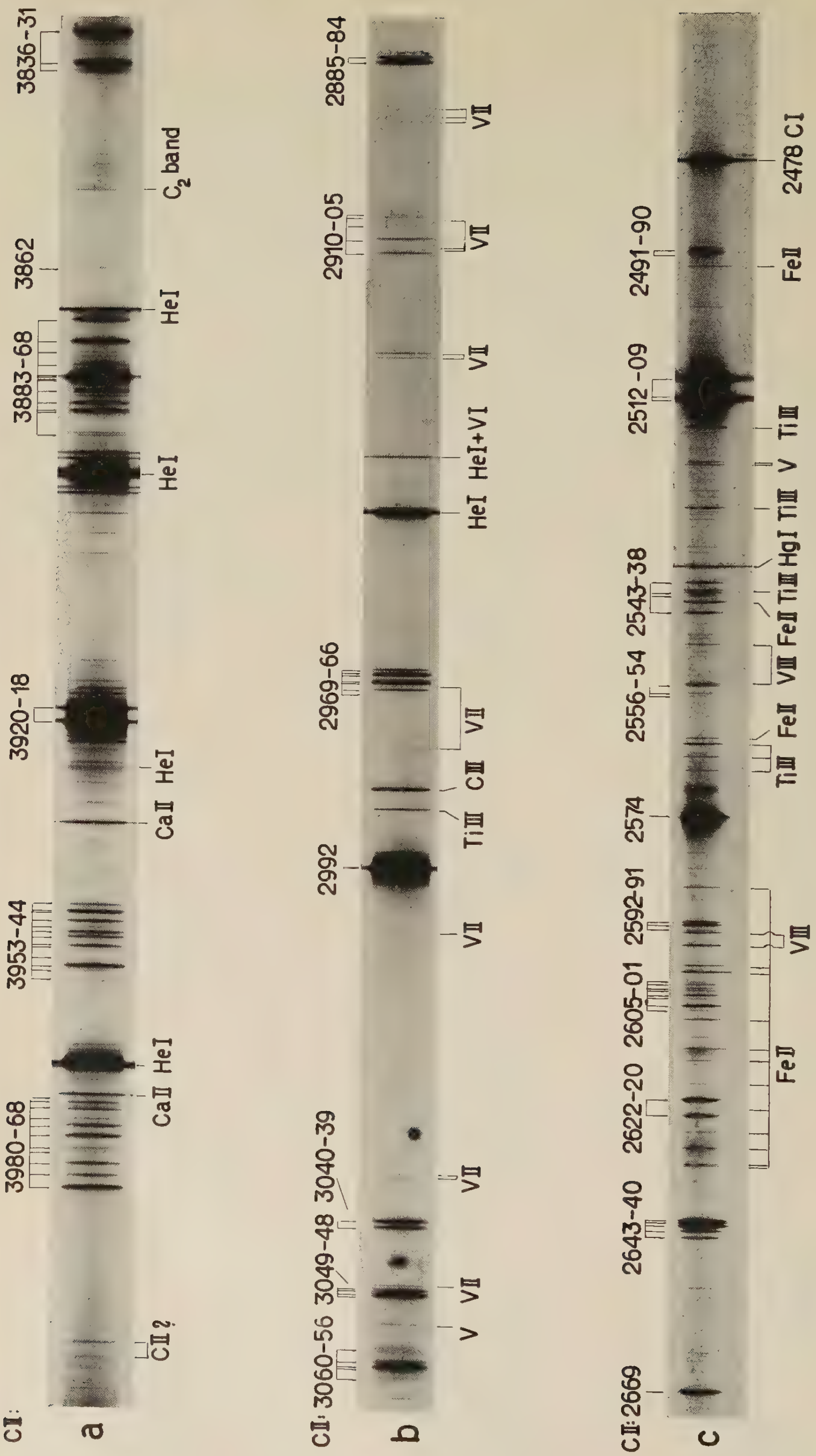
a
C II:
3836-31
C$_2$ band
3862
He I
3883-68
He I
3920-18
He I
Ca II
3953-44
He I
3980-68
Ca II
C II ?
b
C II: 3060-56
3049-48
3040-39
2992
2969-66
2910-05
2885-84
V II
V II
V II
He I + V I
He I
C III
Ti III
V II
V II
V II
V
c
C II: 2669
2643-40
2622-20
2605-01
2592-91
2574
2556-54
2543-38
2512-09
2491-90
2478 C I
Fe II
Ti III
V
Ti III
Hg I
Ti III
Fe II
V III
Fe II
Ti III
V III
Fe II

ARKIV FÖR FYSIK Band 7 nr 3

Communicated 11 March 1953 by ERIK HULTHÉN and G. BORELIUS

A nuclear spectrometer for heavy particles

Part II. Performance and focusing properties

By CURT MILEIKOWSKY

With 15 figures in the text

1. Introduction. Data of the pole pieces

The design and construction of a nuclear spectrometer of a versatile and general type has been described in Part I (1). In this paper the performance of the instrument is discussed. The focusing properties of the spectrometer have been investigated using a pair of pole pieces with conical surfaces. The cone angles were such that the field very closely approximated a $1/\sqrt{r}$ field to obtain the two-directional focusing introduced by SVARTHOLM and SIEGBAHN (2) in β-spectroscopy. The important advantage of such a field is the large solid angle of acceptance for a given resolution.

A radial section of the pole pieces is shown in Fig. 1. If we assume the permeability of the iron in the pole pieces to be infinite, the field obtained in the gap is, neglecting fringing effects and terms of second or higher order:

$$H_z(r) = H_z(r_0)\left[1 - n\frac{r-r_0}{r_0}\right] \tag{1}$$

where

$$n = \frac{r_0 \cdot \operatorname{tg}\alpha}{b}. \tag{2}$$

To a very good approximation we obtain a field which varies as $1/\sqrt{r}$, if $n = {}^1/_2$ and if b is much smaller than r_0.

In the actual case the pole pieces are made for a mean radius, r_0, of 400 mm and with a gap width of 52 mm at the mean radius. To obtain $n = {}^1/_2$, α was made 1°86.

2. The sector angle

To allow both source (i.e. target) and image to be placed outside the field in a fairly field-free space, the sector angle of the magnet is made smaller than $\pi\sqrt{2}$, namely π. Because of the fringing fields at the entrance and exit the effective sector angle is, however, somewhat larger than π.

Figure 2 shows the H_Z-component of the fringing field in the plane $z = 0$, approximately along the central path of particles from the target.

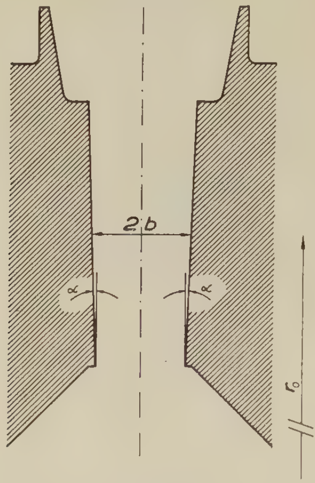

Fig. 1. Radial section of the pole pieces. r_0 = mean radius, 2 b – gap width, α – cone angle.

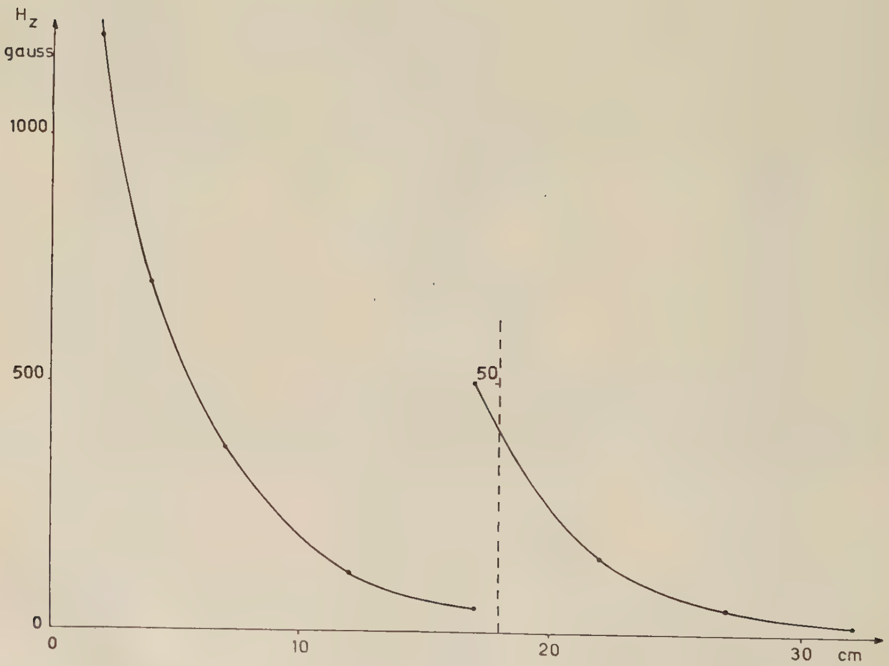

Fig. 2. Axial component of fringing field at magnet entrance in the central plane, $z = 0$.

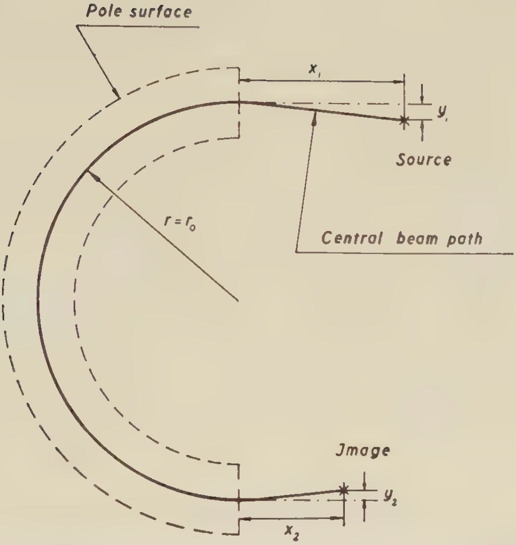

Fig. 3. Definition of source and image coordinates. The z-direction is perpendicular to the plane of the figure. The figure also shows the central beam trajectory.

The curve in Fig. 2 was used to calculate by a graphical method the path and final direction of a particle emerging from the field and having traveled along the circle $r = r_0$ inside the spectrometer.

The path obtained is given in Fig. 3. Along the first few centimeters the path still curves; it very soon becomes straight. This line forms an angle of about 5°7 to the direction the particle would have followed if there had been no stray field. The same argument is true about the entrance field; here the particle will travel in the opposite direction.

The sector angle of the magnet is 180°, and according to the preceding discussion we can conclude that the effective sector angle of the magnetic field is 180° + 2 × × 5°7 = 191°4. This conclusion was tested and verified in experimental investigations of the widths, described in later sections.

3. Stray field in the space of the bombarding beam

It is important for the successful use of the spectrometer that the stray field from the magnet be weak in the space of the bombarding beam, so weak that its influence on the bombarding particles is entirely negligible. The vertical component of this stray field was measured at spectrometer angle 90° with $H_z = 2\,200$ gauss inside the magnet at mean radius. The result is given in Fig. 4. It is evident that the field strength everywhere along the bombarding beam is very small. It would be even more reduced by screening with an iron tube. This has not hitherto been considered necessary. The increased field strength in the vicinity of the analyzing magnet is due to that latter magnet.

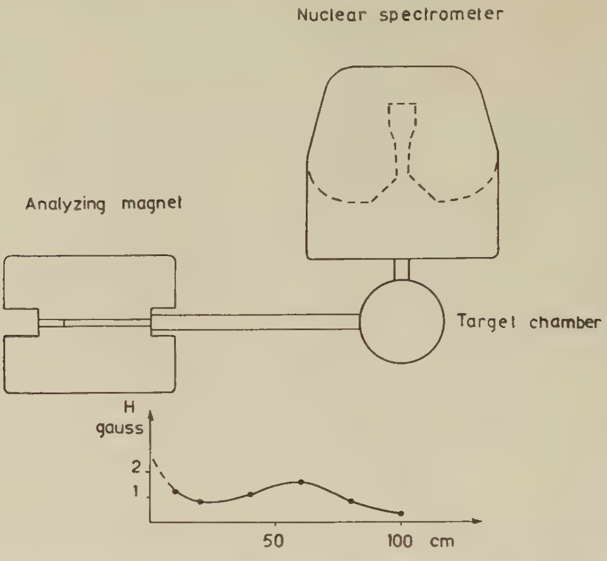

Fig. 4. Stray field (x-component) along the path of a bombarding proton beam at spectrometer field $H_z = 2200$ gauss and spectrometer angle $\theta = 90°$.

4. The stabilization and measurement of the spectrometer current

The spectrometer is equipped with an automatically current stabilizing electronic device which keeps the current constant to ± 0.1 %, as described in Part I.

The line width, on the other hand, due to aberrations and source dimensions, is 0.1–0.2 % in $H\varrho$. Therefore it was considered worthwhile to improve the current stabilization further.

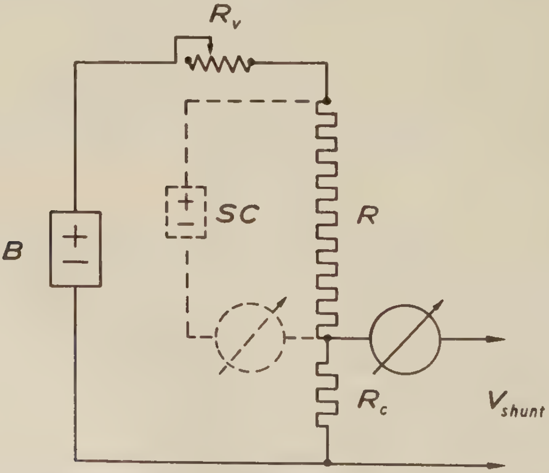

Fig. 5. Circuit diagram of the compensator for stabilizing and measuring the spectrometer current. B = battery, SC = standard cell, R_v = variable resistor, R = precision resistor, R_c = precision resistor, 200 Ω, variable in steps of 0.1 Ω.

The final stabilization is done by manually operating the fine control of the stabilizer, watching the light spot of a galvanometer in a compensator circuit and keeping the light spot at zero position at all times. The circuit diagram of the arrangement is given in Fig. 5.

The compensator, to go into more detail, consists of a battery cell, a variable resistor R_v, a precision resistor R of the order of 4000 ohms and a precision resistor R_c of a few hundred ohms variable in steps of 0.1 ohms, i.e. 1 in 2000, all coupled in series, as drawn in Fig. 5. The voltage drop over a precisely known part of the 4000 ohms is compared to the EMF of a standard cell via a light spot galvanometer. The variable resistor is changed till the galvanometer shows zero. The voltage drop over a shunt (ERMI, 60 mV) in the magnet current circuit, is compared to the voltage drop over R by means of the galvanometer.

The manual stabilizing, using the galvanometer spot as an indicator, allows the magnet current to be kept constant to ± 0.01 %. By varying the value of R_c in small, precisely known amounts and adjusting the magnet current to zero indication of the galvanometer, one varies the spectrometer current by small, precisely known amounts in an easy, practical way.

5. The electrical method for investigation of spectra

The electrical method for investigation of spectra uses a detector consisting of a slit in the image plane and an electric counter behind the slit. The field is varied and the spectrum is plotted as the number of counts per some unit of the source strength as a function of the field.

The α-counter used for the investigations described in this paper was a G.M.-tube operated in the proportional region. It was of the bell type with a thin end window. The field was varied in small steps by varying the magnet current as mentioned in sec. 4. This method is justified only to the extent that the field strength is proportional to the magnet current.

There are mainly four factors which might cause deviation from linear proportionality between current and field.

a) The permeability may not be constant over a large current range. This may be concluded from a consideration of the permeability curve Fig. 6.

b) Temperature variations may cause changes in gap dimensions or in the shunt used for measuring the current.

c) Saturation may cause changes in the field gradients.

d) Hysteresis may cause a non-unique dependence on field-current.

All these effects are small in our magnet and they are completely negligible in the narrow energy regions covered in the present investigation and in all Q-value measurements that have been done hitherto with this spectrometer. Long extrapolations are, of course, not allowed. For instance, Table I gives an idea of the

Table I

Calibration method	E keV	R_c ohms	$\sqrt{E}/R_c$
Ag (pp) Ag	855	76.1	0.384(2)
$N^{15}(p, \alpha)C^{12}$	3 940	162.8	0.385(6)
ThC α	6 058	199.9	0.389(4)

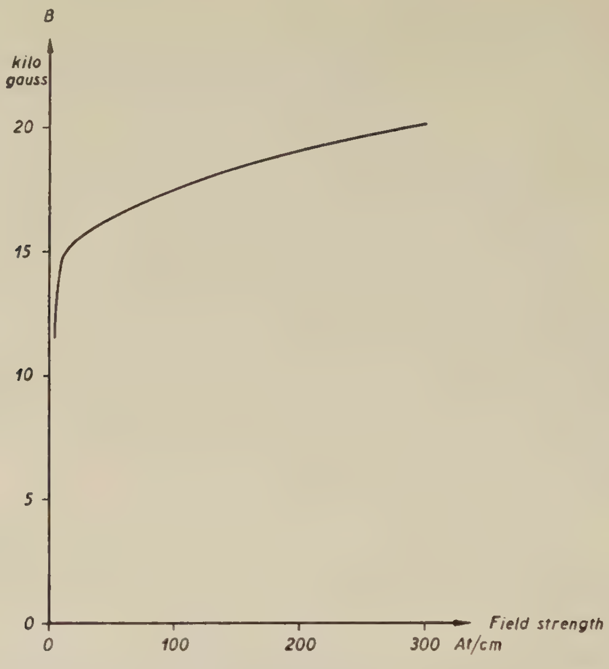

Fig. 6. Magnetic field in kilogauss as a function of ampère-turns per cm for the iron used in the magnet. (By courtesy of Surahammars Bruks AB.)

deviation from exact proportionality between magnet current and field strength over a large region.

In table I the first point was obtained by scattering protons calibrated with the fluorine resonance; the second point was obtained from the reaction $N^{15}(p, \alpha)C^{12}$ with $E_p = 873.5$ keV; the third point was taken from the ThC α-spectrum in Fig. 14.

6. Experimentally obtained line widths of radial and axial images for one source position

Fig. 7 shows the spectrum of the two α-lines from ThC at $E_a = 6.044$ MeV and $E_a = 6.084$ MeV. The abscissa is the resistor value R_c of the compensator and the ordinate is the number of α-counts per unit time. The figure gives the line width as 0.14 % in $H\varrho$.

In this work Th-sources having a diameter of 1.5 mm were used. They were produced in the common way, i.e. put on a positive electrode in a vessel containing Th-salts. The radioactive ions in the gas were collected by the electrode potential.

The source was always put at a distance $x_1 = 330$ mm from the entrance of the magnet. This is a convenient distance from the center of the target chamber to the magnet to be used in work on nuclear reactions. The source could be moved in the vertical direction, along the y_1-axis, to find optimum focusing conditions. The coordinate y_1 was measured from the horizontal line which would be the outside path corresponding to the internal path $r = r_0$; $z = 0$, i.e. the case of sector angle π and no

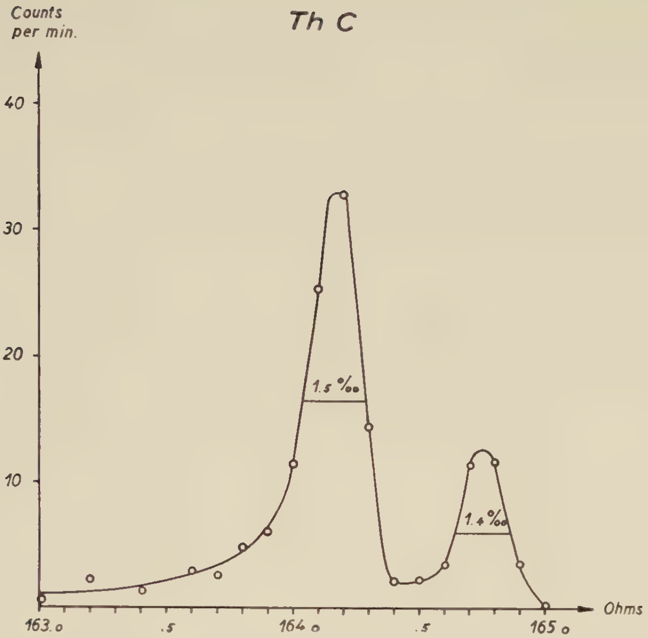

Fig. 7. Spectrum of ThC α-particles, electrically detected. $E\alpha = 6\,084$ and $6\,044$ MeV. $\Delta E\alpha$ is known to be 40.0 keV. Source diameter = 1.5 mm, detector slit = 1.5 mm. Along abscissa compensator resistor, R_c.

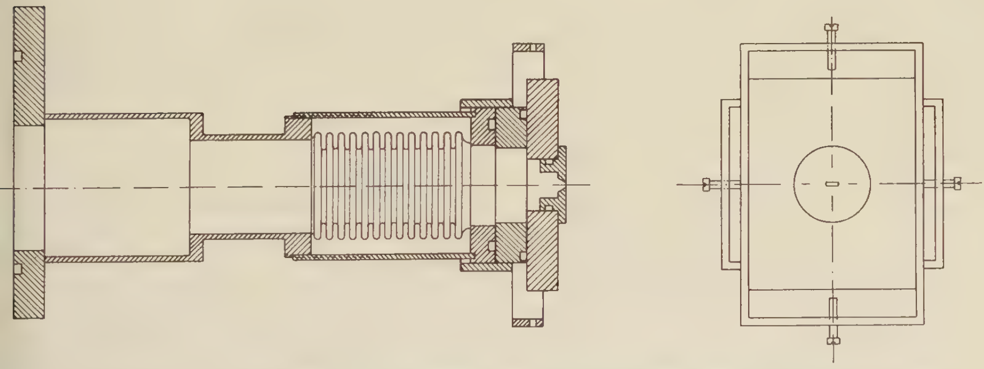

Fig. 8. Arrangement for the study of line shapes with the electrical method. The slit is movable under vacuum in the x-, y- and z-directions.

stray field. The coordinates of the detector slit are given in a similar way, as x_2 and y_2, as marked in Fig. 3.

To facilitate the search for the radial and axial images, the detector slit was also movable, as is shown in Fig. 8. Here the slit and window is mounted in a plate which can be moved vertically in a frame without breaking the vacuum. This frame can be moved horizontally in the z-direction in another frame. This second frame is connected to the vacuum chamber via a bellow and is steered and kept in position by a

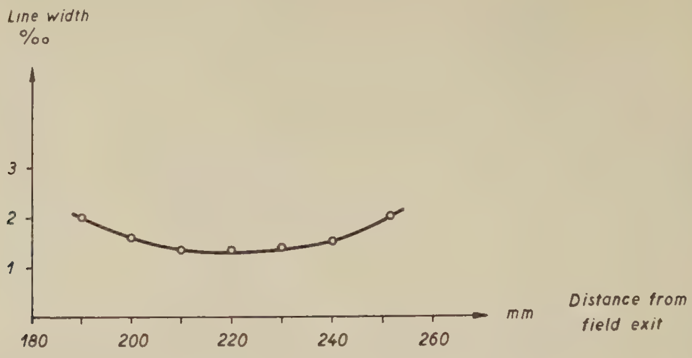

Fig. 9. The line width in parts per thousand as a function of the slit distance x_2 from the field exit. Source position: $x_1 = 330$ mm, $y_1 = 29$ mm.

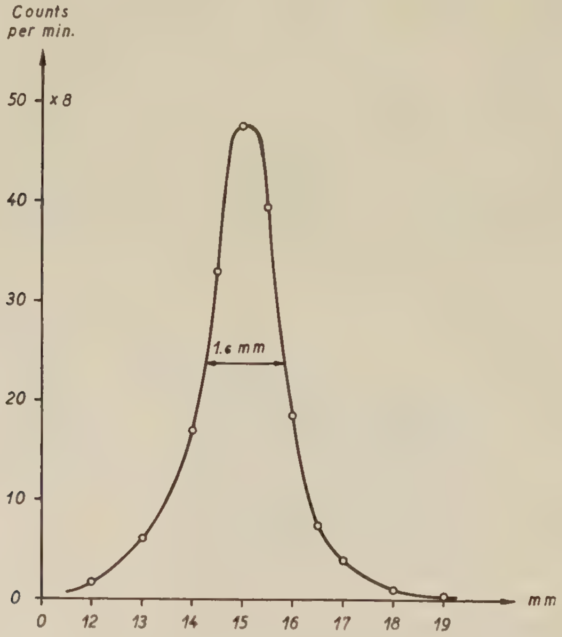

Fig. 10. Cross-section of the ThC α-spectrum at $x_2 = 220$ mm, i.e. number of particles as a function of z_2. Zero point of the z-scale along abscissa is arbitrary.

threaded tube that fits into a groove in the frame. Turning the threaded tube changes the distance x_2.

With fixed values of x_1 and y_1 ($x_1 = 220$ mm, $y_1 = 29$ mm) Th-spectra of the type shown in fig. 7 were taken for different values of x_2 and the line width was plotted as a function of x_2 (Fig. 9). Each half width is taken from a complete curve of the same statistics as the one in Fig. 7. It is clear that the narrowest line is obtained at $x_2 = 210$ mm, which is thus the place of the radial image.

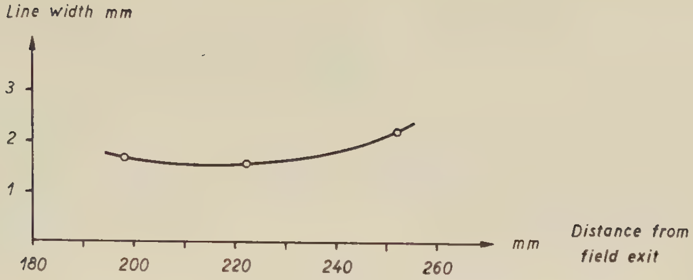

Fig. 11. Spectrum width in mm as a function of distance slit-field exit in mm.

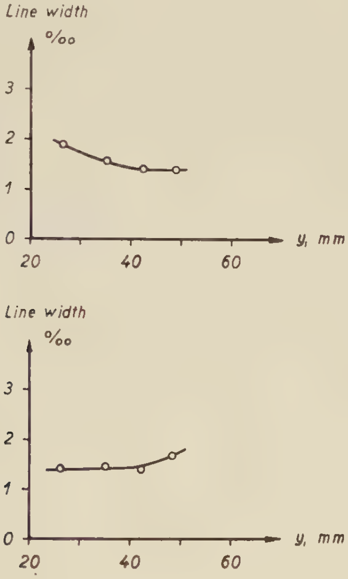

Fig. 12. Line width in parts per thousand as a function of source position y_1 at $x_1 = 330$ mm and $x_2 = 210$ mm for $y_2 = 11$ mm and $y_2 = 21$ mm.

The lines were also studied as to their dimensions in the z-direction. That is, the two-directional focusing was tested by moving a 1 mm hole as slit in the z-direction. The result for one value of x_2 appears in Fig. 10. The width of the line at half maximum is here 1.6 mm. Such curves were taken at various x_2-values. The half-width as a function of x_2 is plotted in Fig. 11. The minimum occurs near 210 mm, corresponding to the axial image. Radial and axial images thus coincide fairly well.

The dependence of the line width on the source position in the vertical direction was studied for two vertically different positions of the slit. In Fig. 12 the line width is plotted as a function of source position y_1 with $x_1 = 330$ at two values of y_2, namely $y_2 = 11$ mm and $y_2 = 21$ mm. The result shows that the line broadens if the vertical distance between the source and the detector slit is made larger or smaller than a distance which may be called the optimum distance. The line width is, however, less sensitive to an equal vertical displacement of both source and slit, i.e. when the optimum distance is kept.

7. The photographic method combined with a double-focusing field for investigating spectra

The photographic method for investigating spectra uses nuclear track plates for detecting the individual tracks. The magnetic field is kept constant, and the spectrum is obtained by reading in a microscope the number of tracks per strip of unit width along the plate. The plate holder used is drawn in Fig. 13. It can easily be taken out for changing the plate. The plate is mounted such that the particles strike at 45° to the surface, thus facilitating the reading of the tracks.

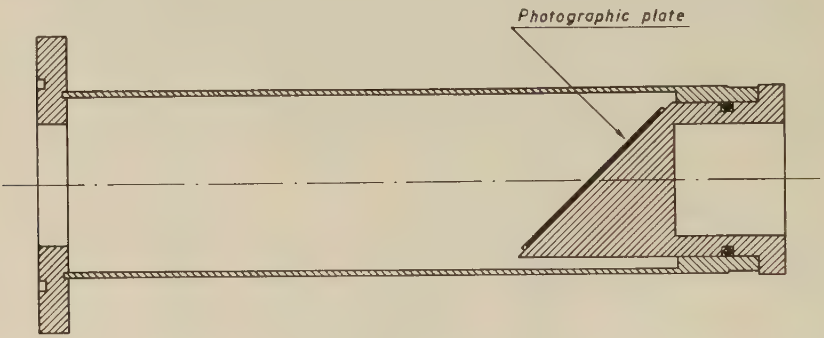

Fig. 13. Photographic plate holder.

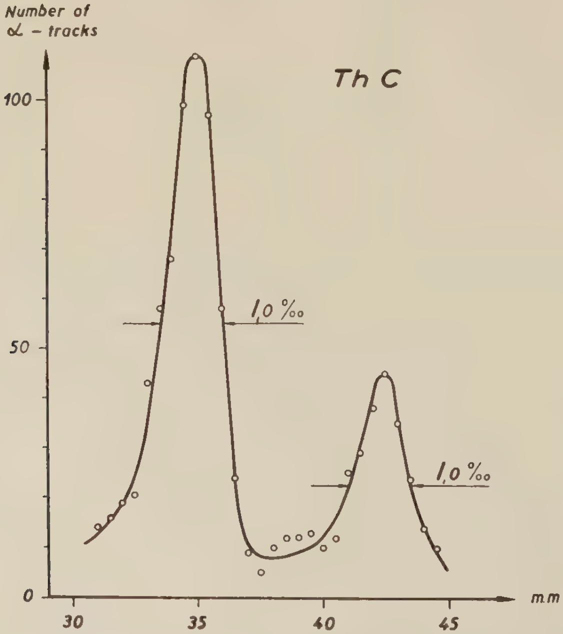

Fig. 14. Spectrum of ThC α-particles, detected in nuclear track emulsion. Source 0.3 × 3 mm². Distance between peaks = 7.4 mm in the plate.

The photographic method has several advantages over the electric method under certain conditions. There is no line broadening due to a slit width; the spectrum is obtained independently of intensity fluctuations of the source. The magnet current is kept constant and no consideration needs to be paid to permeability or hysteresis. The main point, however, is that the parts of the spectrum are obtained simultaneously, so that the exposure time required is much shorter than in the electrical method. Consequently, in work on low intensities the photographic method is often the only possible way.

As an example of the photographic method the Th-α-spectrum is given in Fig. 14. Ilford Nuclear Plates were used, $1'' \times 3''$, with an emulsion thickness of 100 μ.

8. Comparison with the ideal conical sector field

In the preceding sections experimentally obtained values were given for image position, line width, etc. It may be interesting to compare these empirical quantities with the corresponding quantities to be expected from an ideal conical sector field. The formulae for such a field have been given by SVARTHOLM (3) and by JUDD (4). Let us consider a field of sector angle $191\overset{\circ}{.}4$ with no fringing effects.

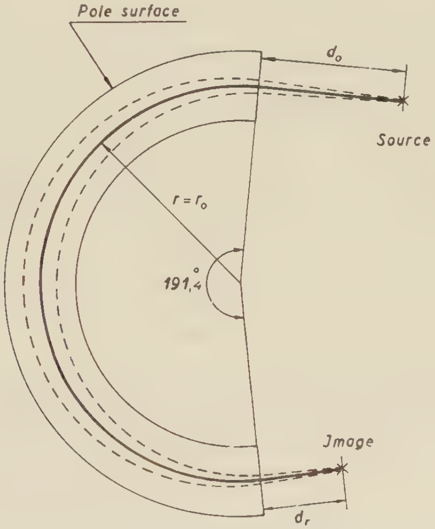

Fig. 15. Notations used in section 8 concerning the ideal conical sector field.

a. Position of radial image.

We use the following notation, also explained in Fig. 15.

d_0 = distance from source to field limit
d_r = distance from field limit to radial image
θ = sector angle.

Three angles, Φ_r, Φ_r' and θ_r, are defined as follows

$$\tan \Phi_r = \sqrt{1-n}\,\frac{d_0}{r_0} \qquad (3)$$

$$\tan \Phi_r' = \sqrt{1-n}\,\frac{d_r}{r_0} \qquad (4)$$

$$\theta_r = \sqrt{1-n}\,\theta \qquad (5)$$

When d_0 and θ are given, d_r is determined by the equation:

$$\Phi_r + \Phi_r' + \theta_r = \pi. \qquad (6)$$

Our values are: $d_0 = 330 - 0.1 \times 400 = 290$ mm
$\theta = 191^{\circ}\!.4$.

From the expressions (3)-(5) and equation (6) we get $d_r = 179$ mm. In the experiments we obtained $d_r = 210 - 0.1 \times 400 = 170$ mm. The accuracy of the empirical value is about 10 mm. Thus the spectrometer performance in this respect is close to the ideal case.

b. First order radial aberration.

SVARTHOLM (5) gives the first order aberration in the radial direction $\left(\text{where } \varrho = \frac{r-r_0}{r_0}\right)$ as

$$\varrho^{(1)} = -\frac{2}{3}(8\,m-1)\,\gamma_1^2 + \frac{2}{3}(8\,m-3)\,\gamma_2^2 . \qquad (7)$$

Here m is the coefficient for the ϱ^2 term in the expansion of the field:

$$H(r) = H(r_0)\left[1 - n\frac{r-r_0}{r_0} + m\left(\frac{r-r_0}{r_0}\right)^2 \cdots\right] \qquad (8)$$

γ_1 is the maximum initial inclination from the central path in the plane $z = 0$. It is determined by

$$\gamma_1 = \frac{h}{r_0\sqrt{2}} \qquad (9)$$

where h is half the maximum beam width in the radial direction. Thus, $2\,\gamma_1$ is the radial aperture angle. In a similar way, $2\,\gamma_2$ is the axial aperture angle.

In the present investigation we used a slit in the middle of the sector having the radial width $2\,h = 60$ mm and the axial width $2\,g = 40$ mm. The axial width corresponds to a $\gamma_2 = 2°$.

In the ideal conical case $m = 0.25$. As we use only the central part of the 140 mm broad field, the condition $m = 0.25$ is very closely fulfilled. Thus we get from formula (7) the maximum aberration width $\left|\frac{2}{3}\gamma_1^2 + \frac{2}{3}\gamma_2^2\right| = 2.7 \times 10^{-3}$, corresponding to 0.7 ‰ in momentum at the base of the line.

We can compare this with the actual line width at half height of 1.0 ‰ from Fig. 14, which was obtained with a very narrow source of size 0.3 × 3 mm². We must remember, however, that in a sector field the field entrance and field exit also contribute to the aberration. Formula (7) is not derived for a sector field and does not take these aberrations into account.

c. *Dispersion.*

The dispersion is defined as

$$D \equiv \frac{\delta s}{r_0} \Big/ \frac{\delta p}{p} \tag{10}$$

where $\delta s / r_0$ is the relative displacement perpendicular to the optic axis for the relative change of momentum $\delta p / p$. The dispersion is given by

$$D = \frac{1 + M_r}{1 - n} \tag{11}$$

where M_r is the radial magnification, which, according to JUDD, is given by

$$M_r = \frac{1}{\tan \Phi_r \sin \theta_r - \cos \theta_r} \tag{12}$$

Φ_r and θ_r are defined by expressions (3) and (4).

We now introduce the numerical values of our spectrometer given above and we find from (13) and (12)

$$M_r = 0.933$$

and the calculated dispersion

$$D = 3.87.$$

Let us now look at the ThC spectrum in Fig. 14. The distance between the two peaks, which is known to be 40.0 keV in energy, is 7.4 ± 0.3 mm in the plate, corresponding to 5.2 ± 0.2 mm perpendicular to the optic axis. Thus, according to the definition (11), the dispersion obtained is

$$D = 3.94 \pm 0.15.$$

Another feature is also important, namely the fact that the dispersion is very nearly constant over the energy region of about 6 %, which is covered by one plate in the arrangement of Fig. 13. This conclusion was obtained from a study of similar Th-α spectra at such fields, that the lines appeared near to the upper or lower end of the plate. Thus the whole region of the plate can be used for precision measurements.

It is evident, however, that a double-focusing spectrometer, used with photographic plates, has a relatively small energy region that can be covered at one exposure.

d. Solid angle.

The formula for the solid angle is approximately

$$\Omega \approx \frac{A}{\left(\frac{d_0}{r_0}\right) + 2} \text{ sterad} \tag{13}$$

if Ar_0^2 is defined as the maximum available cross-sectional area. The calculated value of Ω for a slit of 60×40 mm^2 is then $\Omega \approx 0.59 \times 10^{-2}$ sterad. Experimentally $\Omega = 0.43 \times 10^{-2}$ sterad was obtained.

9. Concluding remarks

The degree to which a spectrometer of the present type approximates the ideal field depends on such factors as dimensioning, materials, machining precision, cooling system etc., which were discussed in part I (1) of the description of the spectrometer. The experimental investigation, described in this paper, covering image position, line width, dispersion and solid angle, has shown that the instrument functions to a fairly good approximation as a conical sector field.

Acknowledgements

The author is indebted to Professor MANNE SIEGBAHN for his interest in this work and to Professor KAI SIEGBAHN and Docent NILS SVARTHOLM for valuable discussions on two-directional focusing.

Svenska Atómkommittén granted this work.

Nobel Institute of Physics, Stockholm 50, Sweden.

REFERENCES

1. MILEIKOWSKY, C., Ark. f. Fys. Bd 4, nr 16, 337 (1951).
2. SVARTHOLM, N., and SIEGBAHN, K., Ark. f. Fys. Bd. 33 A, nr 21 (1946).
3. SVARTHOLM, N., Ark. f. Fys. Bd 2, nr 14, 115 (1950).
4. JUDD, D. L., Rev. of Sci. Instr. Vol. 21, nr 3, 213 (1950).
5. SVARTHOLM, N., Ark. f. Fys. Bd 2, nr 20, 195 (1950).

Tryckt den 5 maj 1953

Uppsala 1953. Almqvist & Wiksells Boktryckeri AB

ARKIV FÖR FYSIK Band 7 nr 4

Communicated 11 March 1953 by AXEL E. LINDH and GUNNAR HÄGG

A determination of the Avogadro number

By GÖSTA BROGREN

If we know the atomic weights of certain elements, the density of some crystal composed of these elements, the wavelengths of a certain X-ray line, and the Bragg angle at which this line is reflected from particular atomic planes in the crystal, the structure of the crystal and the dimensions of the unit cell can be determined. The Avogadro number is then given by the expression

$$N = \frac{n \cdot M}{\varrho \cdot v}$$

where n is the number of molecules in the unit cell
M is the molecular weight[1]
ϱ is the density
v is the volume of the unit cell.

The most suitable crystals are those of the perfect type in which the crystallites are of rather large dimensions, so that a crystal used in an investigation consists of only a few crystallites. In such a case the density of the whole crystal should be the same as that of a single crystallite. As it has been shown that the calcite and the quartz crystals fulfil the above requirements (2, 3), we used these two crystals for our redetermination.

Calcite: Calcite belongs to the rhombohedral system. If the lattice constant d of the cleavage plane is known the volume v of the unit cell is obtained from the relation

$$v = d^3 \Phi,$$

where Φ is a geometric crystal factor that depends of the form of the unit cell. In earlier investigations a unit cell with its sides parallel to the cleavage surfaces and containing half a molecule of calcium carbonate has been used, and we use the same cell in order to simplify a comparison. For this we have

$$\Phi - \frac{(1 + \cos \beta)^2}{(1 + 2 \cos \beta) \sin \beta}$$

---

[1] The atomic and the molecular weights in this communication are given in the *chemical* scale, which means that the atomic weight of the natural mixture of the oxygen isotopes O^{16}, O^{17} and O^{18} is put equal to 16.0000. In the *physical* scale the mass of the isotope O^{16} is equal to 16.0000. The mean atomic mass of the natural oxygen mixture is in physical scale 16.0043_6 which gives the conversion ratio 1.000272 between the physical and the chemical scale (1).

β being the angle between the edges of the rhombohedron. β is obtained from the angle α between two cleavage surfaces by the relation

$$\cos\frac{\beta}{2} = \frac{1}{\sqrt{2\sin\frac{\alpha}{2}}}.$$

The β-values can be corrected to the desired temperature from the expression

$$\frac{d\beta}{dt} = 2\,\mathrm{tg}\,\frac{\beta}{2}\left(1-\frac{4}{3}\sin^2\frac{\beta}{2}\right)(\alpha_\perp - \alpha_{//})$$

by inserting $\alpha_\perp = -5.2 \cdot 10^{-6}$ degree^{-1} C

$\alpha_{//} = 25.3 \cdot 10^{-6}$ degree^{-1} C, (4)

which gives

$$\frac{d\beta}{dt} = -3.03 \cdot 10^{-6}.$$

As we found it difficult and uncertain to determine the angle between the cleavage surfaces by the common optical methods, we used an X-ray method. Two calcite crystals with the surfaces parallel to cleavage faces were mounted in a two-crystal spectrometer. The analyser crystal was 0.4 mm thick and aligned so that both the face and an internal cleavage direction were parallel to the spectrometer axis. The adjustments were controlled so that rocking curves of minimum width were obtained for external as well as internal reflection. Between the two peaks the analyser crystal had to be rotated through the angle α. This angle had to be corrected for the difference between the glancing angles in external and internal reflection.

Using this method, we obtained as mean value of five determinations

$$\beta_{20} = 101°\ 54'\ 8''$$

and

$$\Phi_{20} = 1.09596.$$

All β-values deviated less than 2″ from the mean value.

In Table 1 we give some earlier determinations of angle β.

Table 1. The rhombohedral angle β of calcite.

	$t°$ C	β_t	$\Delta\beta_t$	β_{20}
BEARDEN (5)	20°	101° 54′ 4″	0	101° 54′ 4″
TU (6)	23°.5	0.4″	+10.6″	11″
DU MOND and BOLLMAN (7)	18°	18″	−6.1″	12″
IEVINS and STRAUMANIS (8)	25°	5″	+15.2″	20″
			Mean	110° 54′ 12″

From the mean value we obtain

$$\Phi_{20} = 1.09598.$$

As appears from the Table 1, it is very difficult to make an accurate determina-ion of angle β, so that the geometric crystal factor Φ is liable to have a considerable rror, which in this case is due to the difficulty of aligning two lattice planes parallel o the spectrometer axis. If optical methods are employed, large crystals must be sed, and there is a greater risk that the two cleavage faces used do not belong to he same crystallite. In order to eliminate this uncertainty, we used another method f determining the volume of the unit cell. A rhombohedral crystal can always be eferred to a hexagonal system of axes. In the rhombohedral system the true unit cell ontains two molecules of calcium carbonate and the cleavage face has the index 211). In the corresponding hexagonal system the same surface is designated $(10\bar{1}4)$. The hexagonal "unit cell" contains 18 molecules and has the volume

$$v = \frac{3\,a^2 c \sqrt{3}}{2}$$

a and c can be determined with a tube spectrometer with the same accuracy as the spacing d of the cleavage planes used in the previous expression. This means that the uncertainty arising from the geometric crystal factor Φ is completely eliminated.

The density of calcite has been determined by De Foe and Compton (9), Bearden (5), and at the National Bureau of Standards (10). The mean of these measurements is

$$\varrho = 2.71029 \text{ g/cm}^3 \text{ at } 20^\circ \text{ C.}$$

The crystals used were all checked by means of X-rays. The spacing d agreed within the limits of error with the Siegbahn value $d_{18} = 3029.45$ X.U. for all specimens.

All molecular weights are computed from the mass spectrograph values of the atomic masses combined with the abundances of the isotopes. The chemical atomic weights were then obtained by dividing with the above conversion factor 1.000272. This method was used because the international chemical atomic weights are less accurate than the mass spectrograph values. Carbon consists of two isotopes, C^{12} (98.9 %) and C^{13} (1.1 %) (11). From the mass number 12.003842 (12) of C^{12} we obtain the chemical atomic weight 12.012. The international atomic weight is 12.010.

Calcium consists of six isotopes, viz. Ca^{40} (96.92 %), Ca^{42} (0.64 %), Ca^{43} (0.132 %), Ca^{44} (2.13 %), Ca^{46} (0.0032 %), and Ca^{48} (0.179 %) (13). From the isotopic masses, $m_{40} = 39.9755$, $m_{42} = 41.9722$, $m_{43} = 42.9725$, $m_{44} = 43.9692$, $m_{48} = 47.9678$ (12), we obtain the atomic weight 40.080 which is the same value as the international atomic weight 40.08, except that it contains one more figure.

The molecular weight of $CaCO_3$ is then $M = 100.092$.

It is well known that calcite always contains small amounts of impurities. Bearden (5) made a careful chemical analysis of all the crystal specimens he used for his density determination. Straumanis (14) also determined the percentage of impurities found in perfect calcite crystals. Their results are given in Table 2.

The agreement between the two analyses is good. The only significant difference is the abundance of $SrCO_3$ in Straumanis's results. Bearden does not say anything about this impurity, so it is possible that its presence was not taken into account. Except for SiO_2 all impurities involve bivalent metal ions, which replace calcium

Table 2. The percentage of impurities in calcite.

Bearden		Straumanis	
$CaCO_3$	99.98 %	$CaCO_3$	99.95 %
MnO	0.009 %	$MnCO_3$	0.011 %
FeO	0.006 %	$FeCO_3$	0.005 %
Al_2O_3	absent	$ZnCO_3$	0.001 %
MgO	absent	$SrCO_3$	0.01 %
SiO_2	0.0007 %[1]	$MgCO_3$	traces
		$BaCO_3$	traces

[1] Only in one specimen.

ions in the crystal lattice. As the replacing ions have about the same radii as the calcium ion, the substitution causes a very small change in the lattice spacing. No such ions will be placed between the ordinary lattice points and no holes will occour. The density, however, will not be the same as that for a crystal without impurities but will be directly proportional to the "effective" molecular weight of the crystal. The impurities in Table 2 are all heavier atoms than the original ones, so the molecular weight must be increased by 5 in the last figure to

$$M_{\text{eff}} = 100.097.$$

The axes lengths a and c in the hexagonal cell, as well as the spacing d for the cleavage plane, were determined by means of a tube spectrometer. We obtained at 18° C

$$a = 4980.02 \text{ X.U.} \pm 0.03 \text{ X.U.}$$
$$c = 17025.12 \text{ X.U.} \pm 0.10 \text{ X.U.}$$
$$d = 3029.45 \text{ X.U.} \pm 0.01 \text{ X.U.}$$

As conversion factor to the centimetre scale we used the relation established by The X-Ray Analysis Group of the American Institute of Physics and The American Society for X-Ray and Electron Diffraction (15, 16)

$$1 \text{ X.U.} = 1.00202 \cdot 10^{-3} \quad \text{Å} = 1.00202 \cdot 10^{-11} \text{ cm}.$$

The Avogadro number may now be obtained from both the rhombohedral unit cell, using the geometric crystal factor Φ, and from the hexagonal cell. We get

from the rhombohedral unit cell .... $N = 6.02329 \cdot 10^{23}$
from the hexagonal unit cell .... $N = 6.02327 \cdot 10^{23}$.

If we calculate N from the mean value of β in Table 1 we get

$$N = 6.02316 \cdot 10^{23}.$$

As mentioned above, the value obtained from the hexagonal cell is the most accurate, since no geometric crystal factor is involved. The agreement is better than was to be expected. The uncertainty in the adjustments of the crystal is such that an error of several seconds of arc may be introduced into the angle β.

Table 3. Abundance and masses of the silicium isotopes.

	Abundance in per cents					Isotopic mass
	William and Yuster	Ney and McQueen	White and Cameron	Ingram	Mean	
Si^{28}	92.27	92.24	92.16	92.28	92.24	27.98581
Si^{29}	4.68	4.69	4.71	4.67	4.69	28.98567
Si^{30}	3.05	3.07	3.13	3.05	3.07	29.98290

Quartz. Quartz is a hexagonal crystal and the volume of the unit cell is determined in the same way as that of the hexagonal calcite cell. It contains 9 molecules SiO_2. We have examined several different quartz crystals with a tube spectrometer to see if we could find any variation in the axis length but found non in spite of the fact that crystals of different origin were investigated. For the axes lengths at 18° C we obtained

$$a = 4902.88 \pm 0.02 \text{ X.U.}$$

$$c = 5393.62 \pm 0.02 \text{ X.U.}$$

The molecular weight is more difficult to determine. It is well known that the international chemical atomic weight of silicon is not determined with satisfying accuracy. The value, given in the atomic weight tables is 28.06. During recent years mass spectrograph investigations of the abundance (13, 17–19) and of the mass numbers (20–21) of the silicon isotopes have been carried out so it is possible to obtain a more reliable value.

The value of the chemical atomic weight calculated from the figures in Table 3, is 28.086, which is 0.026 higher than the international chemical value. The accuracy in the mass spectrograph determination is high, and as newer chemical determinations indicate a higher value than 28.06, we have accepted the above value, which gives the molecular weight 60.086.

The density has recently been determined by BATUECAS (29) as 2.65068 ± 0.00023 g/cm^3 at 0° C. Using BENOIT's (23) values of the linear expansion coefficients $\alpha_{//} = (7.161 + 0.0160\, t) \cdot 10^{-6}$ degree^{-1} and $\alpha_{\perp} = (13.255 + 0.0223\, t) \cdot 10^{-6}$ degree^{-1}, we obtain at 18° C

$$\varrho_{18} = 2.64905 \text{ g/cm}^3.$$

A calculation of the Avogadro number from these data gives

$$N = 6.02368 \cdot 10^{23}.$$

This value is not as accurate as those obtained from calcite. No chemical analysis of the abundance of impurities has been carried out. From the optical data and from the fact that no variation in the lattice constant could be observed we can draw the conclusion that the percentage of impurities must be very low. As quartz is a very nearly perfect crystal, it would be desirable to determine the lengths of the axes, the density and the percentages of impurities for the same crystal, but at present we have not the apparatus necessary.

In earlier calculations of the Avogadro number (24–25) — besides calcite — diamond, sodium chloride, potassium chloride and lithium fluoride have also been used. However, the results obtained from these crystals seem to be less reliable, for reasons reported below.

Diamond is a cubic crystal. Because of its hardness, and its flawlessness in good specimens, it seems most likely that diamond is a perfect crystal. Experiments do in fact show that good specimens reflect X-rays very nearly as perfect crystals should do (26–27). It has also been shown, however, that although some specimens are nearly perfect in their structure, others can be considered nearly mosaic (28).

The unit cell of diamond contains 8 carbon atoms. In the calculation referred to the following experimental data were used.

The length of the cube side at 18° C $a = 3559.67$ X.U. (6)
the density at 23.5° C $\varrho = 3.51536$ g/cm^3 (10)

and the linear expansion coefficient of diamond $\alpha = 1.18 \cdot 10^{-6}$ degree^{-1} C (29).

With the atomic weight of carbon 12.012, we get

$$N = 6.02363 \cdot 10^{23},$$

which is in good agreement with the calcite and the quartz values.

The spacing and the density were determined from different specimens, which seems to be especially incorrect in the case of diamond. The spacing has been determined by both TU and LONSDALE (30) for 2 and 4 diamonds respectively. They obtained the values:

TU	no. 1	3559.72 ± 0.05 X.U.
TU	no. 2	3559.62 ± 0.05 X.U.
LONSDALE	C3T	3560.00 ± 0.05 X.U.
	GS1	3559.84 ± 0.05 X.U.
	2π	3559.58 ± 0.05 X.U.
	C3U	3559.42 ± 0.10 X.U.

The value of the spacing varies far more than the experimental limits of error. The variation does not seem to be due to a variation in the percentage of impurities, since this is less than 0.01 by weight for clear diamonds.[1] It is most likely that the variation of the length of the edge line of the unit cell is accompanied by a variation of the density. For this reason it seems to be necessary to investigate the degree of perfection, the density and the spacing, and furthermore, to make a chemical analysis, of one and the same crystal in order to get an accurate value of the Avogadro number. It is also desirable to examine the isotopic ratio $\frac{C^{13}}{C^{12}}$ for the diamond, since this can vary about five per cent (11).

The other crystals used, NaCl, LiF and KCl, are all cubic and of NaCl-type.

NaCl has been investigated by RENNINGER (31) with a two-crystal spectrometer. He found that it is a mosaic crystal built up from small crystallites. The crystallites themselves are perfect. Between the crystallites there must be empty space, which makes the density of the whole crystal smaller than that of a single crystallite. An accurate determination of the lattice constant uses reflections from one single crystallite. When the Avogadro number is calculated from the data for mosaic crystals we therefore obtain values that must be too high.

---

[1] Private communication from Professor F. WICKMAN, Naturhistoriska Riksmuseet, Stockholm.

The mosaic structure makes a determination of the spacing very uncertain as it is very difficult to judge whether two different reflections are from the same crystallite. Siegbahn's value for the rock salt normal which was used in establishing the lattice constant of calcite, was at 18° C

$$2\,d = a = 5628.50 \text{ X.U.}$$

Tu (6) obtained for rock salt at the same temperature 5627.79 X.U., Ievins and Straumanis (32) got for rock salt $a = 5627.68$ X.U., and for chemically pure sodium chloride $a = 5627.37$ X.U., van Bergen (33) obtained for sodium chloride, which contained about 0.02 per cent impurities, $a = 5628.23$ X.U. Birge combined Tu's value of the spacing of *rock salt* with Hutchison's value of the density of chemically pure *sodium chloride* (34), when he calculated the Avogadro number. The above results show that this method is unreliable. Until further, more accurate measurements are carried out (where spacing, density and impurity analysis are determined for the same crystal, and its degree of perfection is checked with a two-crystal spectrometer), it is better not to use this crystal. The above objections are valid for the other mosaic crystals of NaCl-type.

In our own determinations, the accuracy of the calcite determinations is higher. If the quartz value is given half the weight, we get as mean

$$N = 6.02336 \cdot 10^{23}.$$

In the physical scale we have $N_{\text{phys}} = 6.02500 \cdot 10^{23}$.

If now the value of the faraday is known, we can determine the value of the electronic charge, since

$$e = \frac{F}{N}.$$

The faraday is defined as the quantity of electricity carried by the ions of one gram-equivalent of any atom or molecule. It was determined with precision by two different methods, using the silver voltameter and the iodine voltameter (35–36). Unfortunately, the results disagreed by an amount about four times the probable error. In order to obtain a more precise value, redeterminations have been carried out at the National Bureau of Standards, U.S.A. (37–41). The ratio of the cyclotron resonant frequency ν_c for the acceleration of protons to the nuclear resonance frequence ν_n in the same magnetic field has been measured using a new method (the omegatron method). The faraday is obtained form the relation

$$F = \gamma\, M_p \cdot \frac{\nu_c}{\nu_n}$$

where γ is the proton gyromagnetic ratio, and M_p is the proton isotopic weight. The result for $M_p = 1.007580$ was

$$F = 9652.03 \pm 0.3 \text{ e.m.u./g (physical scale) (38, 40).}$$

Another independent determination (39) used the method of anodically oxidizing sodium oxalate in sulphuric acid solution. As a preliminary mean from eleven determinations was obtained $F = 9651.93 \pm 0.26$ e.m.u./g (physical scale).

It was later pointed out (41) that when mass spectroscopic values reported since the publication of the above results are used, the omegatron result is raised 18 part pr million and the sodium oxalate result lowered by a still greater amount. The resultant disagreement of approximately one part in 10000 far exceeds the estimated probable errors of the two determinations. The atomic or isotopic weights are not given, so it is impossible to discuss the correct value.[1]

In order to determine the charge of the electron, we take as the mean faraday the value.

$$F = 9652.0 \text{ e.m.u./g. (physical scale)},$$

which seems to be reliable within $\pm$ 0.5 e.m.u. We then obtain, using $c = 2.9979 \cdot 10^{10}$ cm/sek (43, 46) and 1 int.coulomb = 0.999835 absolute coulomb (44),

$$\begin{aligned} e = \frac{F}{N} &= 1.6029 \cdot 10^{-20} \text{ e.m.u.} \\ &= 1.6029 \cdot 10^{-19} \text{ abs. coulomb} \\ &= 4.8027 \cdot 10^{-10} \text{ e.s.e.} \end{aligned}$$

As appears from the above, it seems to be necessary to determine the mass and abundance of the isotopes of the elements, that appear in the crystals and in the determinations of the faraday before more accurate values can be obtained. The investigations on the relative abundance of the isotopes of some light elements have shown that this varies. Hence the conversion factor between the physical and the chemical scale is no longer a constant. For this reason, it would be better to express all determinations in the physical scale. If precise values are to be obtained, every measurement using elements with more than one natural isotope should be combined with a determination of the relative abundance.

Institute of Physics, University of Uppsala, Sweden, December 1952.

REFERENCES

1. Landolt-Börnstein, Zahlenwerte und Funktionen. I. Band. 1. Teil. Berlin 1950.
2. A. H. Compton and S. K. Allison, X-rays in Theory and Experiments. Second edition. New York 1935.
3. G. Brogren, Arkiv för Fysik. *6*, 321, 1953.
4. H. L. Megans, Proc. Roy. Soc. A *142*, 198, 1933.
5. J. A. Bearden, Phys. Rev. *38*, 2089, 1931.
6. Y. Tu, Phys. Rev. *40*, 673, 1932.
7. J. W. W. Du Mond and V. L. Bollamn, Phys. Rev. *50*, 524, 1936.
8. A. Ievins and M. Straumanis, Zs. f. Phys. *116*, 194, 1940.

---

[1] In this connection it may be pointed out that the atomic weights of silver and iodine used in the original determinations of the faraday were 107.880 and 126.915 respectively. The actual values (13) of the abundances of the silver isotopes are 51.35 % for Ag^{107} and 48.65 % for Ag^{109}. The packing fraction is $- 4.95 \cdot 10^{-1}$ (42) which gives an atomic weight of 107.890. The present isotopic mass of iodine is 126.94515 (45) which gives an atomic weight of 126.907.

If these values are used, the silver faraday is increased from 9650.45 e.m.u. to 9651.32 e.m.u. (physical scale) and the iodine faraday decreased from 9652.21 to 9651.58 e.m.u.

9. O. K. De Foe and A. H. Compton, Phys. Rev. *25*, 618, 1925.
10. J. A. Bearden, Phys. Rev. *54*, 701, 1938.
11. A. O. Nier, Phys. Rev. *77*, 789, 1950.
12. T. L. Collins, A. O. Nier and W. H. Johnson, Phys. Rev. *84*, 717, 1951.
13. J. R. White and A. E. Cameron, Phys. Rev. *74*, 991, 1948.
14. M. Straumanis and A. Dravmiks, Zs. Anal. Chem. *120*, 168, 1940.
15. W. L. Bragg, J. Sci. Instr. *24*, 27, 1947.
16. E. Armstrong-Wood, Phys. Rev. *72*, 436, 1947.
17. E. P. Ney and J. H. McQueen, Phys. Rev. *69*, 41, 1946.
18. M. G. Ingram, Phys. Rev. *70*, 653, 1946.
19. D. Williams and P. Yuster, Phys. Rev. *69*, 556, 1946.
20. H. E. Ducksworth, R. S. Preston and K. S. Woodcock, Phys. Rev. *79*, 188, 1950.
21. H. E. Ducksworth and R. S. Preston, Phys. Rev. *79*, 402, 1950.
22. T. Batuecas, Nature *159*, 705, 1947.
23. J. R. Benoit, Trav. et Mém. d. Bur. Int. d. Poid. et Mes. *6*, 1, 1888.
24. R. T. Birge, Reports on Progress in Physics *8*, 94, 1941.
25. —— Am. J. Phys. *13*, 63, 1945.
26. W. H. Bragg, Proc. Phys. Soc. *33*, 304, 1921.
27. W. Ehrenburg and H. Mark, Zs. f. Phys. *42*, 807, 1927.
28. M. Renninger, Zs. f. techn. Phys. *16*, 440, 1935.
29. Int. Crit. Tables. Vol. III.
30. K. Lonsdale, Phil. Trans. Roy. Soc., London, *240 A*, 219, 1947.
31. M. Renninger, Zs. f. Krist. *89*, 344, 1934.
32. A. Ievins and M. Straumanis, Zs. f. Phys. *102*, 353, 1936.
33. H. van Bergen, Ann. d. Phys. *39*, 553, 1941.
34. C. A. Hutchison and H. L. Johnston, Phys. Rev. *62*, 32, 1943.
35. E. W. Washburn and S. J. Bates, J. Am. Chem. Soc. *34*, 1341 and 1515, 1912.
36. G. W. Vinal and S. J. Bates, Bull. Bur. Stand. *10*, 425, 1914.
37. J. A. Hipple, H. Sommer and H. A. Thomas, Phys. Rev. *76*, 1877, 1949.
38. H. Sommer, H. A. Thomas and J. A. Hipple, Phys. Rev. *80*, 487, 1950.
39. D. N. Craig and J. I. Hoffman, Phys. Rev. *80*, 487, 1950.
40. H. Sommer, H. A. Thomas and J. A. Hipple, Phys. Rev. *82*, 697, 1951.
41. H. Sommer, D. N. Craig, J. I. Hoffman and J. A. Hipple, Phys. Rev. *85*, 740, 1952.
42. A. J. Dempster, Phys. Rev. *53*, 64, 1938.
43. E. Bergstrand, Arkiv för Fysik *2*, 119, 1950.
44. J. W. W. Du Mond and E. R. Cohen, Rev. Mod. Phys. *20*, 82, 1948.
45. E. E. Hayes, P. I. Richards and S. A. Goudsmit, Phys. Rev. *84*, 824, 1951.
46. E. Bergstrand, Nature *165*, 405, 1950.

Tryckt den 30 maj 1953

Uppsala 1953. Almqvist & Wiksells Boktryckeri AB

ARKIV FÖR FYSIK Band 7 nr 5

Communicated 8 April 1953 by ARNE WESTGREN and G. BORELIUS

Astigmatic two-directional focusing in a nuclear spectrometer as a means of eliminating line broadening due to angular energy spread of transmutation particles

A nuclear spectrometer for heavy particles. Part. III

By CURT MILEIKOWSKY

With 7 figures in the text

1. Introduction

When high resolution and precision is desired in the measurement of nuclear reaction energies by means of magnetic analysis strict conditions have to be chosen, which considerably decrease the number of particles available for the measurement.

For good resolution in the spectrometer the target spot has to be restricted to mall dimensions, especially in the radial direction. As the current density of the bombarding beam is necessarily limited by several factors, among others the focusing ystem of the acceleration tube, the dimension restrictions impose a limitation on the number of primary particles per unit time which can take part in the experiment.

The number of target nuclei available for a precision experiment is thus determined by the mentioned target spot area and the target thickness. The maximal allowed target thickness depends on the resolution required; very often, however, other factors determine the actual thickness. For these reasons it is in many cases important r necessary to have a spectrometer with a large solid angle of acceptance. With large solid angle, however, aberrations etc. do follow which influence the resolution.

In an actual case where a solid angle of 4×10^{-3} sterad is used, the double focusing pectrometer for heavy particles (ref. 1) at the Nobel Institute the line width at half he peak is about 0.1 % as a result of aberrations and the source dimensions ($1 \times 5\,\mathrm{mm}^2$) sed in practice. This was found experimentally by means of the α-particles from ThC and ThC^1 (ref. 2).

In the study of particle groups from nuclear transmutations, however, the line widths are generally many times as large. This line broadening is sometimes due to arget thickness but sometimes entirely due to the energy spread of the particles aused by the motion of the center of mass during the reaction.

It is the purpose of this paper to present a focusing method for the study of Q-values f nuclear transmutation, for simplicity called Q-focusing, such that the large solid ngle of anastigmatic double focusing is preserved, but a line broadening due to the ngular energy spread is avoided.

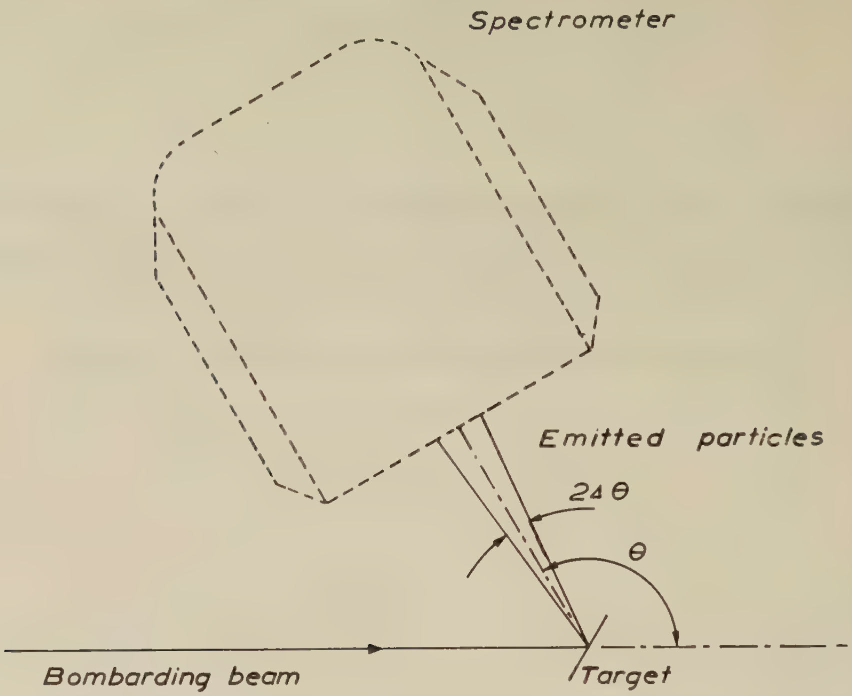

Fig. 1. Definition of angles θ and $2\,\Delta\,\theta$. θ is the angle between the direction of the bombarding beam and the emitted particles, $2\,\Delta\,\theta$ is the angle of acceptance of the spectrometer.

2. The angular energy spread

The expression for the angular energy spread is

$$\frac{\partial E_2}{\partial \theta} = -\frac{2\sqrt{M_1 M_2 E_1/E_2}}{M_2 + M_3 - \sqrt{M_1 M_2 E_1/E_2}\cos\theta} \cdot \sin\theta. \tag{1}$$

Here M_1, M_2 and M_3 are the masses of the bombarding particle, of the observed particle, and of the residual nucleus.

E_1 and E_2 are the energies of the bombarding particle and the observed particle.

θ is the angle between bombarding and observed particles, as shown in fig. 1.

The expression for $\frac{\partial E_2}{\partial \theta}$ shows that the angular energy spread is zero in the forward and backward directions, i.e. at $\theta = 0°$ and $180°$.

The forward direction may possibly be used but requires very thin target backings. This leads to several difficulties as to target cooling etc. The 180°-direction can hardly be used without severe influence from the spectrometer magnet upon the bombarding beam itself and its entrance angle. Besides, a straight backward direction presents many problems from the practical point of view. The main point, however, is that one wants to be able to use all values of θ for the purpose of identification of reactions and energy calibration.

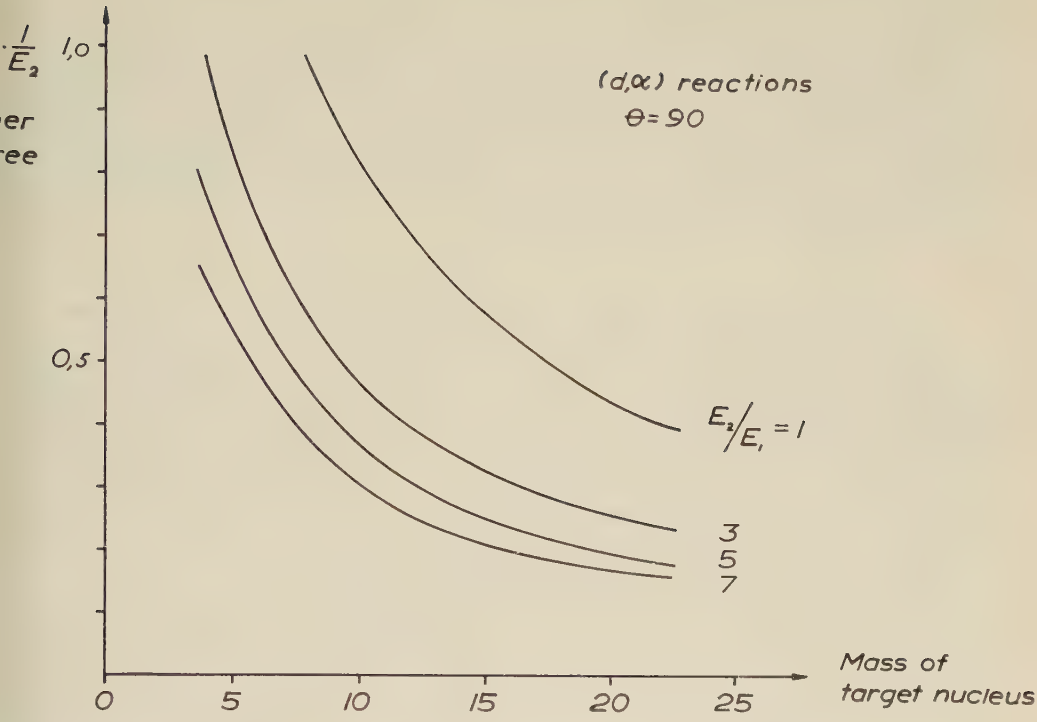

Fig. 2. Energy dependence of emitting angle for (d, α)-reactions. $\frac{\partial E_2}{\partial \theta}\cdot\frac{1}{E_2}$ is expressed in % per degree and given for $E_2/E_1 = 1, 3, 5$ and 7 at $\theta = 90°$.

$\frac{\partial E_2}{\partial \theta}$ has a maximum in the neighbourhood of $\theta = 90°$, and may here represent a considerable effect. At 90° we can write the expression (1) in the following form:

$$\frac{\partial E_2}{\partial \theta}\frac{1}{E_2} = -\frac{2\sqrt{M_1 M_2 E_1/E_2}}{M_2 + M_3}\cdot\frac{\pi}{180} \quad \text{(in \% per degree).} \tag{2}$$

The relative energy spread per degree given by formula (2) is shown in fig. 2 with some characteristic values of the parameters M_3 and E_1/E_2 for the reaction type (d; α).

From fig. 2 one easily gets the energy spread in per cent per degree also for (p, α)-reactions or (d, p)-reactions by dividing the ordinates by the factor $\sqrt{2}$ or the factor $2\,\frac{M_3+1}{M_3+4}$.

Now, returning to the actual spectrometer mentioned in the introduction, the solid angle there is 4×10^{-3} sterad. In the direction of the angular energy spread the aperture is 4°, i.e. $2\Delta\theta = 4°$, fig. 1. This means that the energy spread in the spectrometer is four times the numbers given as ordinates in fig. 2. It is clear that the lines are considerably broadened due to the energy spread, as compared to the line width of 0.1 % from other effects.

For instance, let us consider the reaction $O^{16}(d, \alpha)N^{14}$, where $M_3 = 14$ and suppose $E_2/E_1 \approx 3$. Fig. 2 gives an angular energy spread of 0.3 % per degree, i.e. 1.2 % in the spectrometer at $\theta = 90°$. One can work in the region $\theta = 45°—135°$. At 45° and 135° the energy spread is 0.9 %. At $\theta = 30°$, of course the spread is less, 0.6 %; here, however, target layers will be passed obliquely so that the effective layer thickness will be four times the actual layer thickness.

3. The principle of astigmatic two-directional focusing or *Q*-focusing

Whereas a homogeneous field has radial focusing only, a field which varies as $1/\sqrt{r}$ does focus in the radial direction and also in the axial direction. Such a field gives the famous double-focusing, which was introduced by SIEGBAHN and SVARTHOLM in β-spectroscopy (ref. 3, 4). By double-focusing we mean here the anastigmatic case, i.e. radial and axial foci coincide. This case is extremely convenient for radioactive sources, where no energy dependence on emitting angle occurs. When such a dependence is present, as in trasmutation work on light nuclei, a line broadening appears (section 2 of this paper) if a large solid angle is used.

To be able to use the large solid angle without the disadvantage of the line broadening, it is here proposed to introduce an astigmatism of convenient amount by choosing a somewhat different field gradient. Thus the radial and axial images will not coincide. Let us now imagine that we put a photographic plate in the radial image perpendicular to the optic axis, and let us study the picture we get of a point shaped source.

If the particles emitted by the source had the same energy in all directions, we would get a line in the plate parallel to the axis of the field, which we call the z-direction. That is the case $\frac{\partial E_2}{\partial \theta} = 0$. If however, $\frac{\partial E_2}{\partial \theta} \neq 0$, i.e. the energy of the emitted particles depends on the emitting angle, we get a line sloping by an angle ψ to the z-direction in the plate (fig. 3). This angle ψ depends on the numerical value of $\frac{\partial E_2}{\partial \theta}$ and on the dispersion of the system or the gradient $\frac{\partial H}{\partial r}$.

Suppose now that the source (= target) emits two particle groups due to the same nuclear reaction, the two groups being very close in energy. These particle groups will appear in the plate, both sloping by the angle ψ to the z-direction (fig. 3). The width of each line will be determined by the resolution of the field and not by the value of $\partial E_2/\partial \theta$ as in the anastigmatic case. The solid angle and resolving power of the field is still very nearly the same as in the anastigmatic case, the resolving power even slightly better for a certain range of field gradients.

For the practical application with a counter as detector one would use a slit, tilted by the angle ψ. In the practical application of the photographic detection method the plate would be mounted at an angle ν to the optic axis, where $\nu \neq 90°$. The actual slope of the line to the z-direction in the plate would be ψ_ν where

$$\operatorname{tg} \psi_\nu = \frac{\operatorname{tg} \psi}{\sin \nu}.$$

Although the desire to eliminate the line broadening due to $\partial E_2/\partial\theta$ is the main reason for considering the astigmatic case, it has some other advantages. One comes from the fact that ψ depends on $\partial E_2/\partial\theta$, thus on the mass of the target nucleus. ψ will therefore give some information about the target nucleus and hence help in the identification of the reaction that emitted that particular particle group. It is another advantage that the interpretation of the position of the line is independent of the angular distribution of intensity. That is not the case for the anastigmatic double focusing.

4. Choice of an appropriate field gradient

In the following quantitative discussion we will consider a sector field of sector angle $\theta < \pi\sqrt{2}$. We assume that source and image are outside the field, this being a practical case used in spectrometers for nuclear transmutation work. We restrict ourselves to a field which has only the first order term in $\frac{r-r_0}{r_0}$. This is quite sufficient for most practical purposes. A more general discussion would follow similar lines.

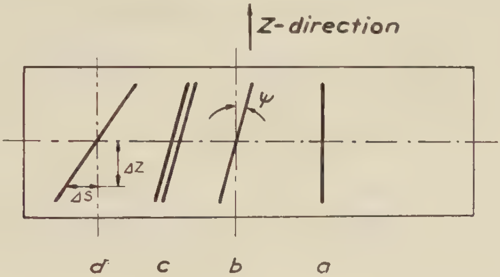

Fig. 3. Images of a point source as expected in a photographic plate mounted perpendicular to the optic axis. a is the case $\frac{\partial E_2}{\partial\theta} = 0$, b defines the tilting angle ψ when $\frac{\partial E_2}{\partial\theta} \neq 0$, c shows two resolved lines, d defines Δs and Δz, discussed in the text. If $2l$ is the length of a line, the line width in the anastigmatic case is $2l \cdot \sin\psi$.

We write the field as

$$H_2(r) \approx H_2(r_0)\left[1 - n\frac{r-r_0}{r_0}\right] \tag{3}$$

where H_z is the magnetic field in the z-direction (axial direction) and r_0 is the mean radius. For $n = \frac{1}{2}$ expression (3) approximates a $1/\sqrt{r}$-field.

We now want to choose a value of n, a little different from $n = 0.50$, such that an appropriate distance is obtained between the radial focus and the axial focus. This distance, d_r—d_z, should be such that for instance the length of a line in the photographic plate turns out conveniently, say about half the gap, that is 20–25 mm for the spectrometer of ref. 1. In the same spectrometer $2\Delta\theta$ is about 4°, thus $d_r - d_z$ should be about $\frac{20}{\operatorname{tg} 4^\circ} = 300$ mm or $\frac{3}{4}\,r_0$.

To get an idea of how much we must change n we use a formula given by JUDD (5) for the first order astigmatism

$$d_r - d_z \approx r_0 (2n-1) \left\{ \frac{d_2}{r_0} + \left(1 + \frac{d_2^2}{2r_0^2}\right) \left[\theta + \frac{d_0}{r_0} \frac{1}{1 + \frac{d_0^2}{2r_0^2}} \right] \right\}. \tag{4}$$

The quantities appearing in (4) are defined in fig. 4.

For $d_r \approx d_z \approx d_0$ this expression simplifies to

$$\frac{d_r - d_z}{r_0} \approx 5\,(2n-1). \tag{5}$$

Expression (5) shows that $d_r - d_z = 0.7\, r_0$ is obtained when $n = 0.57$ or $n = 0.43$.

5. The tilting angle ψ

We now proceed to compute an approximate expression for the angle ψ. We define Δs and Δz as is done in fig. 3 and get

$$\operatorname{tg} \psi = \frac{\Delta s}{\Delta z}. \tag{6}$$

An expression for Δs is obtained in the following way. Recalling that the dispersion D is defined as

$$D \equiv \frac{\delta_s}{r_0} \Big/ \frac{\delta p}{p} \tag{7}$$

and noting, that $\delta p/p = \frac{1}{2}\, \delta E/E$ we get

$$\frac{\Delta s}{r_0} = \frac{1}{2} D \frac{\Delta E_2}{E_2}. \tag{8}$$

We denote the emitting angle at the source which corresponds to the displacement in the plane of the radial image as $\Delta\theta$ (fig. 1). Then

$$\frac{\Delta E_2}{E_2} = \Delta\theta \cdot \frac{\partial E_2}{\partial \theta} \cdot \frac{1}{E_2} \tag{9}$$

and thus

$$\frac{\Delta s}{r_0} = \frac{1}{2} D\, \Delta\theta \cdot \frac{\partial E_2}{\partial \theta} \cdot \frac{1}{E_2} = \frac{1}{2} \cdot \frac{1 + M_r}{1 - n} \cdot \Delta\theta \cdot \frac{\partial E_2}{\partial \theta} \cdot \frac{1}{E_2}. \tag{10}$$

Now turning to $\Delta z/r_0$ we have

$$\frac{\Delta z}{r_0} = \frac{d_r - d_z}{r_0} \cdot \operatorname{tg}(\Delta\theta)_z \approx \frac{d_r - d_z}{r_0} \cdot (\Delta\theta)_z \tag{11}$$

where $(\Delta\theta)_z$ is the aperture in axial direction. We note that $\operatorname{tg}(\Delta\theta)_z \approx (\Delta\theta)_z$ and that $\Delta\theta/(\Delta\theta)_z = 1/M_z$ where M_z is the axial magnification.

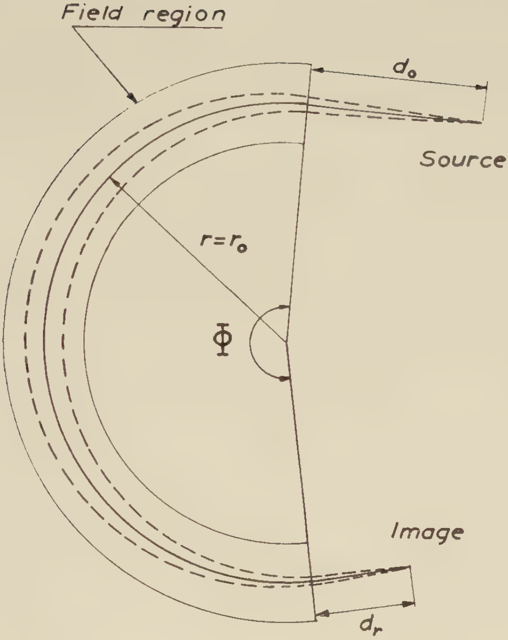

ig. 4. The sector angle Φ, the distance d_0 from source to field limit, and the distance d_r from field nit to radial image are shown in the fig. The distance from field limit to axial image is called d_z.

Thus

$$\operatorname{tg}\psi = \frac{1}{2}\,\frac{1+M_r}{1-n}\cdot\frac{1}{M_z}\cdot\frac{r_0}{d_r-d_z}\cdot\frac{\partial E_2}{\partial\theta}\cdot\frac{1}{E_2}\,. \tag{12}$$

For calculation of M_r, M_z, d_r and d_z one may use the formulae given in ref. 5, mely:

$$M_r = \frac{1}{\sqrt{1-n}\,\frac{d_0}{r_0}\cdot\sin\sqrt{1-n}\,\Phi-\cos\sqrt{1-n}\,\Phi} \tag{13}$$

$$M_z = -\frac{1}{\sqrt{n}\,\frac{d_0}{r_0}\cdot\sin\sqrt{n}\,\Phi-\cos\sqrt{n}\,\Phi} \tag{14}$$

$$\operatorname{arctg}\left(\sqrt{1-n}\,\frac{d_0}{r_0}\right)+\operatorname{arctg}\left(\sqrt{1-n}\,\frac{d_r}{r_0}\right)+\sqrt{1-n}\,\Phi=\pi \tag{15}$$

$$\operatorname{arctg}\left(\sqrt{n}\,\frac{d_0}{r_0}\right)+\operatorname{arctg}\left(\sqrt{n}\,\frac{d_z}{r_0}\right)+\sqrt{n}\,\Phi=\pi. \tag{16}$$

Here Φ is the sector angle of the field and d_0 is the distance from the source to e field limit (fig. 4).

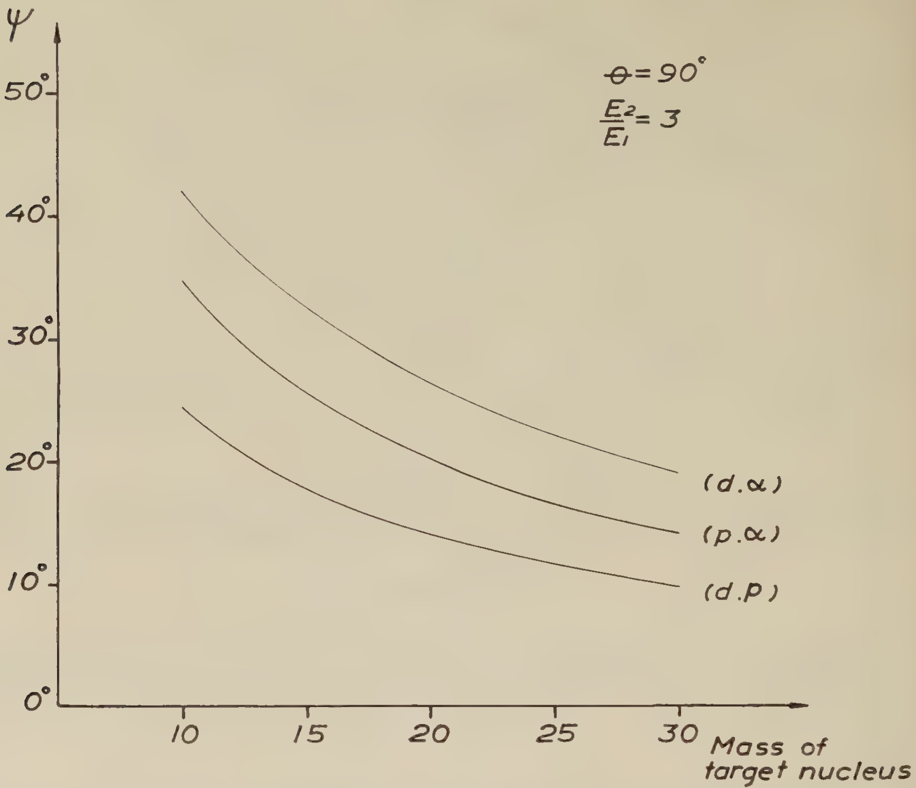

Fig. 5. Tilting angle ψ for (d, α), (p, α) and (d, p) reactions as a function of mass of target nucleus at $E_2/E_1 = 3$, $\theta = 90°$. ψ is calculated from the approximate expression.

To get an easier form of $\operatorname{tg} \psi$ we use, however, the following approximations:

$$\frac{d_r - d_z}{r_0} \approx 5\,(2\,n - 1) \tag{5}$$

$$\frac{\Delta\,\theta}{(\Delta\,\theta)_z} = \frac{1}{M_z} \approx 1 \qquad\qquad M_r \approx 1 \tag{17, 18}$$

$$\frac{\partial E_2}{\partial \theta} \cdot \frac{1}{E_2} \approx - \frac{2\sqrt{M_1\,M_2 \cdot E_1/E_2}}{M_2 + M_3} \cdot \sin\theta. \tag{2}$$

We obtain

$$\psi \approx \operatorname{arctg}\left[\frac{2}{5}\,\frac{1}{(1-n)\,(2\,n-1)} \cdot \frac{\sqrt{M_1\,M_2\,E_1/E_2}}{M_2 + M_3} \cdot \sin\,\theta\right]. \tag{19}$$

For example, choosing $n = 0.57$, we get for the reactions O^{16} (d, α) N^{14} assuming $E_2/E_1 = 3$ and $\theta = 90°$, a value of $\psi = 31°$. Fig. 5 shows ψ for (d, α), (p, α) and (d, p)-reactions as calculated by means of formula 19.

It would be of interest to know the accuracy of approximation (5). In fig. 6 d_r/r_0 and d_z/r_0 are given as calculated from JUDD's formulae for $n = 0.50 - 0.62$. The difference of these two curves is the dot-dashed curve, whereas the dotted curve corresponds to the approximation $(d_r - d_z)/r_0 = 5\,(2\,n-1)$. It is clear that the approximation in good to less than 5 % in the considered region of n.

6. The length of the line image

Assume that the length of the line image is $2l$ and the available gap clearance is $2\,g$. The component of l in the z-direction is l_z so that $l_z = l \cdot \cos\psi$.
We see that

$$\frac{l_z}{r_0} = \frac{d_r - d_z}{r_0} \cdot (\Delta\,\theta)_{z\,\max} = \frac{d_r - d_z}{r_0} \cdot M_z \cdot (\Delta\,\theta)_{\max} =$$

$$= \frac{d_r - d_z}{r_0} \cdot M_z \cdot \frac{g}{d_0} \cdot \frac{\sqrt{n}\,\frac{d_0}{r_0}}{\sqrt{1 + n\left(\frac{d_0}{r_0}\right)^2}} \approx 5\,(2\,n-1)\sqrt{n} \cdot \frac{g}{r_0} \cdot \frac{M_z}{\sqrt{1 + n\left(\frac{d_0}{r_0}\right)^2}}. \tag{20}$$

Example: For $n = 0.57$, $g/r_0 = 1/20$ and $d_0/r_0 = 0.72$ formula 20 gives $l_z = 19.6$ mm when $r_0 = 400$ mm.

7. Solid angle and resolution

Let us consider the expression for solid angle Ω and resolving power R (ref. 5)

$$\Omega/A = \frac{1}{\sqrt{\left(\frac{d_0}{r_0}\right)^4 + \frac{1 + \left(\frac{d_0}{r_0}\right)^2}{n\,(1-n)}}} \tag{21}$$

$$R = \frac{1 + 1/M_r}{\alpha\,s\,(1-n)}. \tag{22}$$

Here A is defined from $A\,r_0^2 =$ maximum available cross-sectional area, s is source vidth and α is a factor somewhat greater than unity depending on the aberrations.

It is clear that Ω changes very little with a small change of n from $n = 0.50$. The esolving power, on the other hand, is more sensitive to a change of n and increases vith larger n. The case $n = 0.60$ has in fact been considered by JUDD from the pure point of view of optimum compromise between solid angle and resolving power equirements.

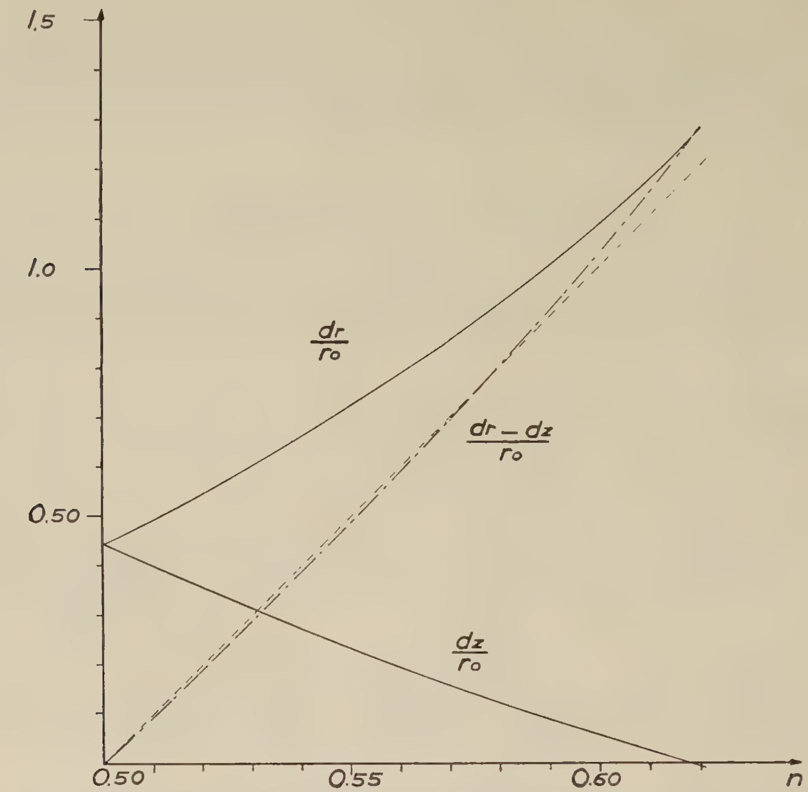

Fig. 6. d_r/r_0 and d_z/r_0 calculated with Judd's formulae. The dot-dashed curve shows the difference, $\frac{d_r - d_z}{r_0}$, and the dashed straight line gives the approximation $\frac{d_r - d_z}{r_0} = 5\ (2n-1)$.

8. Shape of pole pieces

The field

$$H(r) = H(r_0)\left[1 - n\frac{r - r_0}{r_0}\right] \tag{3}$$

can be obtained by means of pole pieces which have conical surfaces. The shape of conical pole pieces may be determined by the three parameters mean radius r_0, gap height $2b$, and angle of surface to symmetry plane α (fig. 7). If the iron has very high permeability, the field obtained between the pole surfaces is

$$H(r) = H(r_0)\left[1 - \frac{r_0 \operatorname{tg} \alpha}{b} \cdot \frac{r - r_0}{r_0}\right] \tag{23}$$

n is thus determined by the choice of r_0, b and α, obeying

$$n = \frac{r_0 \cdot \operatorname{tg} \alpha}{b}. \tag{24}$$

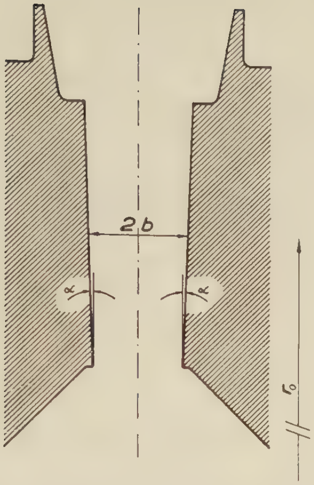

ig. 7. Radial section through pole-pieces with conical surfaces. The parameters are mean radius r_0, gap height 2 b and cone angle α.

The spectrometer described in ref. 1 and ref. 2 was made for anastigmatic double-
ocusing i.e. $n = 0.50$. The simplest way to adapt such an instument for the astig-
atic Q-focusing would be not to change α or r_0 but just to insert between each pole
iece and the yoke a thin plane sheet of iron. To obtain $n = 0.57$, for example, the
eet thickness should be 3.6 mm as the original gap was 52 mm.

9. Summary. Features of the proposed Q-focusing method

By means of a slightly astigmatic two-directional focusing system, particles
n be focused through a large solid angle to a tilted line image of definite length.
he line is not broadened by the variation of energy with emitting angle that is
used by the motion of the center of mass. The solid angle is very nearly the same
the solid angle of the anastigmatic case. If n is chosen larger than 0.50, the resolu-
on is somewhat more favourable than the anastigmatic resolution.

The line slope to the axial direction may facilitate to some extent the identification
the reaction that caused the particular particle group.

Also, the determination of the Q-value is independent of any assumption or
easurement on the angular distribution of intensity of the reaction.

REFERENCES

1. Mileikowsky, C., Ark. f. Fys. Bd 4, nr 16, 337 (1951).
2. ——, Ark. f. Fys. Bd 7, nr 3, 33 (1953).
3. Siegbahn, K. and Svartholm, N., Nature, Vol. 157, 872 (1946).
4 Svartholm, N. and Siegbahn, K., Ark. f. Fys. Bd 33 A, nr 21 (1946).
5. Judd, D. L., Rev. of. Sci. Instr., Vol. 21, nr 3, 213 (1950).
6. Svartholm, N., Ark. f. Fys. Bd 2, nr 20, 195 (1950).

Tryckt den 8 maj 1953

Uppsala 1953. Almqvist & Wiksells Boktryckeri AB

ARKIV FÖR FYSIK Band 7 nr 6

Communicated 28 January 1953 by Erik Hulthén

The angular correlation of Ni^{60}

By T. Wiedling

With 1 figure in the text

I. Introduction

The angular correlation of Ni^{60} has been measured by a number of investigators 1–7). The first successful experiments were performed by **Brady** and **Deutsch** with eiger-Müller counters and repeated later by them with scintillation-counters. After hat the correlation of Ni^{60} has been frequently measured and has been used when esting angular correlation apparatuses. Some time ago the Zürich group (8) has einvestigated the Ni^{60}-correlation in the light of their discovery of the influence 9) of the electron shell on the angular correlation. The value of $\frac{W(\pi)}{W\left(\frac{\pi}{2}\right)} - 1$ was, ccording to their experiment 0.148 ± 0.003 for different Co^{60}-sources. The difference etween the expected theoretical value 0.167 for an E2,E2 transition and the nisotropy found they explained in the following way: Either the assignment 4 E2)2(E2)0 is wrong or the directional correlation is influenced by the electron hell. The angular correlation was also found to be unchanged for magnetic field trengths up to 8000 Oersted.

II. Apparatus

The apparatus used in our experiment was the same as the one earlier (10) described vith the exception of replacing the scintillation counters consisting of 1P21 multipliers nd NaI(Tl)-crystals with E.M.I. 5311 multipliers and sodium-iodide crystals with diameter of 2.5 cm and a thickness of 1.2 cm.

III. Experimental

The Co^{60}-source used in this experiment consisted of solid $CoCl_2$ of high specific ctivity. The source-holder was made of aluminum with thin walls (<0.01 cm).

The energy-discriminating property of the scintillation counter was used in such manner that quantum-energies less than 0.51 MeV were discriminated. In this vay internal and external pair-creation with accompanied annihilation radiation n the source and source-holder were eliminated as were also Compton scattered

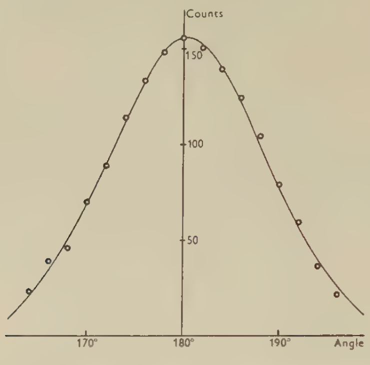

Fig. 1. Angular distribution of coincidences from annihilation radiation, experimental points, theoretical Gaussian distribution curve.

quanta. This was tested with the positron-emitter Na^{22}. According to these tests the calculated ratio between the number of real coincidences and the number of coincidences because of annihilation radiation or Compton-scattering between the counters was larger than 6000 : 1. The discrimination just mentioned was electronically made by a conventional discriminator stage.

Because of the finite angular resolution of the counters it is necessary to apply a correction to the anisotropy found. To get the value of this correction the angular resolution has been determined using annihilation radiation. From the halfwidth of the resolution-curve obtained the correction mentioned can be calculated (11) (12). The experimental points have been found to fit a Gaussian distribution quite well. (Fig. 1.)

Data were collected with the movable counter in the positions 90° and 180°.

The anisotropy found, after application of all corrections necessary except for the correction of the finite angular resolution of the counters, was

$$\frac{W(\pi)}{W\left(\frac{\pi}{2}\right)} - 1 = 0.147 \pm 0.007.$$

Using Church and Kraushaar's or Walter's correction formulas it is possible to calculate an expected experimental correlation coefficient from the angular resolution curve. Then we get

$$\frac{W(\pi)}{W\left(\frac{\pi}{2}\right)} - 1 = 0.155$$

and

$$\frac{W(\pi)}{W\left(\frac{\pi}{2}\right)} - 1 = 0.162$$

respectively.

IV. Discussion

The Ni^{60} nucleus is of the even-even type and is thus expected to have zero angular momentum in its ground-state. Other (13) measurements indicate that the spins of the first and second excited states are 2 and 4. From HAMILTON's (14) correlation formulas the anisotropy is then $\frac{W(\pi)}{W\left(\frac{\pi}{2}\right)}-1=0.167$.

The discrepancies between the values given above are too great to draw any definite conclusions concerning the states of Ni^{60}. One of the more accurate measurements earlier published with the exception of AEPPLI's is that of DARBY (7) who got an uncorrected value of 0.147. He performed his measurements on metallic cobalt. The angular correction given by him was $+0.006$.

At present it seems necessary to make new and even more accurate investigation, especially concerning the angular resolution problem.

January 1953. Physical Institute, University of Stockholm, Sweden.

REFERENCES

1. R. BERINGER, Phys. Rev. *63*, 23 (1943).
2. W. M. GOOD, Phys. Rev. *70*, 978 (1946).
3. E. L. BRADY and M. DEUTSCH, Phys. Rev. *72*, 870 (1947), *74*, 1541 (1948), *78*, 558 (1950).
4. A. H. WILLIAMS and M. L. WIEDENBECK, Phys. Rev. *78*, 822 (1950).
5. J. R. BEYSTER and M. L. WIEDENBECK, Phys. Rev. *79*, 411 (1950).
6. R. M. STEFFEN, Phys. Rev. *80*, 115 (1950).
7. E. K. DARBY, Can. J. Phys. *29*, 569 (1951).
8. H. AEPPLI, H. FRAUENFELDER, E. HEER, and R. RÜETSCHI, Phys. Rev. *87*, 379 (1952).
9. H. AEPPLI, A. S. BISHOP, H. FRAUENFELDER, M. WALTER, and W. ZÜNTI, Phys. Rev. *82*, 550 (1951).
10. T. WIEDLING, Arkiv för Fysik *6*, 39 (1952).
11. E. L. CHURCH and J. J. KRAUSHAAR, Phys. Rev. *88*, 419 (1952).
12. ERNST HEER, Private communication. The formula is deduced by M. WALTER.
13. D. ALBURGER, Private communication.
14. D. R. HAMILTON, Phys. Rev. *58*, 122 (1940).

Tryckt den 8 maj 1953

Uppsala 1953. Almqvist & Wiksells Boktryckeri AB

ARKIV FÖR FYSIK Band 7 nr 7

Read 14 January 1953

Reports from the Conference of the Swedish National Committee for Physics in 1952

By Gudmund Borelius and Erik Rudberg

The Swedish National Committee for Physics held its sixth general physics conerence in Stockholm on September 25–27, 1952. About 150 physicists from different esearch institutions in Sweden attended this meeting and enjoyed the hospitality of he Royal Institute of Technology, were all the different sessions were held. It was ortunate that, as regards time and place, this physics meeting could be planned to join p with the International Instruments and Measurements Conference and Exhibition 952. By agreement it was arranged that the members of the physics conference ould participate in the discussions of the instruments conference, whose members vere in their turn invited to two of the physics sessions, which were therefore conucted in the international languages adopted for the instruments conference. hrough this cooperation the physics conference also had the pleasure to welcome s Scandinavian guest lecturers Prof. E. Bak and Mr. J. R. Andersen of Copenagen, who spoke on microwave spectroscopy and special microwave measurements, rof. E. Laurila of Helsingfors, who gave a paper on measuring instruments emloying feed-back and Prof. S. Westin of Trondheim, who reported on a new electric alculating machine and discussed geotechnical measurements with strain gauges. – A number of other guest physicists from abroad also honoured the meeting by heir presence. Dr. Sven Benner, of the Radiophysics Laboratory at the King ustaf V Jubilee Clinic in Gothenburg, once again placed his valuable experience at isposal by accepting to serve as Secretary of the conference.

Short summaries of the papers presented at the physics conference in Stockholm 952 are published in the rest of this report.

engt Andersson, Department of Physics, Chalmers Institute of Technology, Gothenburg.

A curved-crystal focusing γ-ray spectrometer with scintillation detector

A γ-ray spectrometer of the Cauchois-Du Mond type has been constructed and as just been completed at Fysiska institutionen, Chalmers tekniska högskola, Göteorg. The spectrometer utilizes the (310) planes of quartz in a crystal plate of dimenons 10 × 20 × 1 mm effective volume, the plate having been bent into a cylinder of dius 1020 mm. The directly transmitted beam is absorbed by a 400 mm long, 20-slit on collimator with tapering partitions. This collimator transmits about 30 % of e diffracted beam. As a detector of γ-rays a NaI (Tl)-crystal is used together with an EMI 5311-photomultiplier tube, connected to a cathode follower, an amplifier, a single channel discriminator and either a scaler or a counting rate meter. In the present form the spectrometer covers a range down to about a 0.15 MeV. To give good stability, the moving instrument parts and the fixed collimator have been mounted on a rigid, U-shaped iron beam, 30 × 200 cm.

G. ANIANSSON, Department of Theoretical Chemistry, Royal Institute of Technology, Stockholm.

A new method for the measurement of the α-particle range and straggling in liquids

The alpha source is placed on a plane steel surface opposite a plane surface of a scintillation crystal. The liquid is placed between the two surfaces. A photomultiplier with counting equipment registers the light pulses which are generated in the scintillation crystal when the distance between source and crystal is less than the range. The number of counts per unit time versus the distance between source and crystal will be a straight line intersecting the distance axis at the alpha particle range. The straggling of the alpha-particles will give a minor distortion of the straight line.

If only the smallest light pulses up to a certain amplitude are counted, a number of counts per unit time $N(x)$ versus distance curve is obtained from which the straggling curve (a Gaussian distribution) can be derived by computing $N(x) - d \cdot \frac{dN(x)}{dx}$ (x = distance and N = counts per unit time.)

E. ARBMAN, The Gustaf Werner Institute for Nuclear Chemistry, Uppsala.

A new double-focusing beta-ray spectrometer

A beta-ray spectrometer of the double-focusing type has been constructed and its focusing properties studied. The magnet is designed for a maximum transmission of 6 %. A magnetic field of the desired form $H(r) = H(r_o) \cdot 2r_o/(r_o + r)$ is obtained by using conical pole surfaces. The field is nearly proportional to the current through the coils of the spectrometer. The resolution, as the measured width at half height of the line, is 0.4 % for a solid angle of 0.5 % of a sphere. For a solid angle of about 4 %, width af sample = 20 mm and width of the GM-slit = 16 mm a "half value width" of 2,8 % has been obtained.

SETH BERGLUND, Department of Physics, University of Uppsala.

Studies of secondary electron emission

A high yield of secondary electron emission is obtained with certain alloys after an activation process, consisting in heat treatment in vacuum. It has been believed that changes of structure in the alloy are of importance in this process, but results with copper-beryllium alloys indicate that the rise in yield can be attributed to a surface layer containing the oxides of Cu and Be.

The stability of such surfaces has been studied in tubes, constructed for this urpose. A decay of the secondary emission coefficient with time seems to be inevi- ble.

ÖSTA BROGREN, Department of Physics, University of Uppsala.

Concerning the suitability of quartz as X-ray gratings

In connection with an investigation of the possibilities of utilizing some atomic lanes in quartz with small spacings in X-ray spectroscopy, the qualities of these ratings have been investigated. The measurements were carried out by means of a ouble crystal spectrometer; the width of the rocking-curve, the integral reflection nd the percent reflection were determined. These qualities were also calculated nder the assumption that quartz was a perfect crystal. After removal of the very urface-layer by etching, the experimental results show a very good agreement ith the theoretical calculations, which proves that quartz may be considered to e a perfect crystal. In connection with the etchings a study of the influence of the eformed surface layer has been made.

.-Å. BRUNBERG, Department of Electronics, Royal Institute of Technology, Stockholm.

xperimental determination of electron orbits in the field of a magnetic dipole

The problem concerning the movement of charged particles in a magnetic dipole eld has been tackled mathematically by C. Störmer and others in connection with e theories of the aurora and the cosmic radiation. However, the calculations are ther complicated, and could only be carried out by a tedious numerical integra- on process. Some years ago an experimental method was developed by K. G. ALMFORS in order to find the solution of the problem. It was a model scale experi- ent, which made it possible to measure the deflection of charged particles in a agnetic dipole field as a function of their energy. This method has been further eveloped and higher energies have been measured. The intention is to give a general rvey of particle orbits in the energy interval $10^{10}-\infty$ eV and thereby measure e final direction of charged particles (electrons) far away from the dipole as a nction of the energy, the latitude and the direction, in which the electrons are nt out from the earth. There is some hope that the results of the experiment will lp to solve the problem of the origin of cosmic radiation.

. v. DARDEL, Department of Physics, Atomic Energy Laboratory, Stockholm.

Slowing down of neutrons in water

A preliminary account is given of an experimental and theoretical study of the owing down of neutrons in water. The experiment consists of a measurement of e mean energy of the neutrons emitted from a water moderator, as a function of e delay after the pulses of the pulsed neutron source. The energy determination is tained from the absorption in a boron absorber. The theoretical part is limited to the study of the slowing down process for certain simple models, each of which approximates the actual conditions in a limited energy region. The models studied are 1) free atoms at rest, 2) free atoms in a Maxwellian velocity distribution, 3) atoms bound to a plane by an elastic force.

G. v. DARDEL, Department of Physics, Atomic Energy Laboratory, Stockholm.

A 40-channel time analyzer

A 40-channel time analyzer has been constructed according to the principles of a previously described 20-channel version. The shortest resolving time is 2 μsec. A scale of 4 and a mechanical register are used in each channel, but an extension to a scale of 16 is possible for half the channels. The apparatus is provided with 8 separate input circuits so that it may be used either as one 40-channel analyzer or as up to 8 synchronized analyzers, each having a fraction of the total number of channels.

Planned applications for the new analyzer were discussed.

B. EDLÉN, Department of Physics, University of Lund.

Report from the meeting of the Joint Commission for Spectroscopy

GUNNAR ERLANDSSON, Department of Physics, University of Stockholm.

Microwave Spectrometry at Stockholms Högskola

A Stark-effect modulation microwave spectrometer has been built at Stockholms Högskola. The spectrometer, which is working in the region 16.3–25.7 kMc/s, has been tried on methyl alcohol and nitromethane. In methyl alcohol seven absorption lines have been found, which have not been reported previously. In nitromethane 94 lines have been measured, 15 of which have been reported previously. Frequency measurements have been made with a cavity wave meter with an accuracy of about ± 5 Mc/s. A short description of the apparatus was given in the lecture.

S. v. FRIESEN, Department of Physics, University of Lund.

Observations with nuclear emulsions

TOR RAGNAR GERHOLM, Department of Physics, Royal Institute of Technology, Stockholm.

Apparatus for measuring lifetimes of nuclear states in the region 10^{-8}—10^{-10} sec.

Very fast detectors for radioactive radiation can be made by combining organic scintillation crystals (anthracene, stilbene, diphenylacetylene) with photomultipliers (RCA 931A, 1P21, 5819). During the time these detectors were being developed oincidence circuits were also being designed with small time constants of the order f $5 \cdot 10^{-10} - 5 \cdot 10^{-9}$ sec., using as a non-linear element crystal diodes of the type eveloped during World War II for microwave radar detectors.

From the detectors the electric signals are led by means of coaxial cables (or wave guides) to the coincidence circuit. If the length of one of these cables is increased by Δl, the corresponding signal will have a time delay $\Delta t = \frac{\Delta l}{v}$, where v is the signal velocity in the cable. The coincidence counting rate plotted as a function of the variation in cable length Δl gives a curve similar to the gaussian distribution, the esolution curve. The half-width of this curve assuming that the radioactive source gives prompt coincidences, is a measure of the resolving time of the equipment.

With such an apparatus, which was built mainly according to a scheme proposed by R. E. Bell, a resolving time of $2.0 \cdot 10^{-9}$ sec. has been measured at the Department of Physics II, Royal Institute of Technology (stilbene crystals + selected 1P21 or 5819).

The apparatus is intended for measuring lifetimes of excited states. By analysis of the resolution curve, it is, within reasonable limits of error, possible to measure ifetimes, wich are much smaller than the resolving time of the apparatus. (Z. Bay, T. D. Newton and others).

A simple method to measure the rise times of the electric signals from the photomultipliers has been developed. Thus it has been possible to study the rapidity of he scintillation-crystals and the photomultipliers directly, and this rapidity limits he use of the coincidence method.

Sven Glad, Department of Physics, University of Lund.

The spectrum of singly-ionized carbon, C II

The C II spectrum in the region 8800–1987 A has been studied by means of a condensed hollow cathode discharge. The present wave-length material has been used o recalculate the term values of C II. From several intercombination-lines observed, an exact linking up of the doublet and quartet systems has been obtained. From the determinations of the series limits of the doublet terms built on $2s\ {}^1S$, and the quartets built on $2p\ {}^3P$, the distance between $2s\ {}^1S_0$ and $2p\ {}^3P_2$ has been established to be 52 423 ± 4 cm^{-1}.

E. Hellstrand and R. Persson, Department of Physics, Atomic Energy Laboratory, Stockholm.

Time-of-flight measurements of the neutron resonance absorption in uranium

With the time-of-flight method the resonance absorption of neutrons in natural uranium has been studied. The 7 MeV cyclotron of the Nobel Institute in Stockholm has been modulated to give a pulsed neutron source. The detecting equipment onsisted of three BF$_3$-chambers with amplifiers and a twenty-channel time-analyzer. The pulse length was 6 μs and the flight path 6.15 m. The samples were made of powdered UO$_3$.

The transmission of neutrons as a function of the energy shows at least three resonances, at 6, 6.20 and 38 eV. With the given resolution only the 6.6 eV resonance could be more carefully analyzed. For this resonance we get the following values of the resonance parameters:

$$\sigma_0 = 5400 \begin{matrix} +3500 \\ -2200 \end{matrix} \text{ barns}$$

$$\Gamma = 0.050 \pm 0.015 \text{ eV.}$$

As the natural width Γ is of the same order as the Doppler width Δ ($\Delta = 0.052$ eV for this resonance) the Doppler effect cannot be neglected. Considering this effect we get the following values:

$$\sigma_0 = 5000 \begin{matrix} +2000 \\ -1500 \end{matrix} \text{ barns}$$

$$\Gamma = 0.050 \pm 0.010 \text{ eV.}$$

B. HOLMBERG, Department of Theoretical Physics, University of Lund.

An attempt at a quantum-mechanical treatment of the three-body problem in scattering

ERIK HULTHÉN, Department of Physics, University of Stockholm.

A Fabry-Perot etalon with reflecting films of wedge-shaped thicknesses

A detailed analysis has been performed regarding the multiple beam interferences in Fabry-Perot etalons, assuming a linear increase of reflection along the plates as produced by silver depositions of wedge-shaped thicknesses. The Haidinger fringes observed when the wedges of the films are arranged oppositely indicate an increase of the contrast and the spectroscopic resolution, as compared with the fringes obtained with etalons which were coated with uniform depositions.

ERIK INGELSTAM, Department of Physics, Royal Institute of Technology, Stockholm.

Use of mechanical Fourier analysis for the treatment of problems in quantitative optical phase contrast

It is well possible to use the same methods and apparatus for harmonic analysis in physical optics as in mechanics and electricity thanks to the fact that the precision in some procedures (multiple-beam interferences, phase contrast devices combined with photoelectric intensity scanning) is of the same order as there, say of 1° of the period circle or less. The principle of the analysis is the fact that the object plane, with its possible amplitude and phase variations, (the x-plane) transfers to the Fraunhofer diffraction plane (u-plane), as a Fourier transform, and that a second Fourier transform transfers the latter to the phase contrast image plane (x'-plane), this transformation with change of phase and possibly amplitude at the borders of the phase plate or mirror.

These transformations are performed by means of a Mader Ott mechanical anal- er[1] with slight additions. Possible applications are the wave-front fine structure om optical gratings and from non-ideal optical polish, but in the first place the phase ntrast imagery of phase gradients. Extending the calculations made by LORD AYLEIGH[2] and DUFFIEUX *et al.*[3] to the phase contrast case, and combining them with echanical Fourier analysis of typical shapes of gradients, the necessary basis is hieved for evaluating decrements and central gradient values in phase boundaries. iis should make it possible to measure *e.g.* diffusion constants in some cases with precision up to that of the phase contrast refractometer.[4]

JONSSON, Department of Physics, Atomic Energy Laboratory, Stockholm.

Neutron flux measurements with fission chambers

A simple type of fission chamber, intended for strong neutron flux measurements, s been tested. The chamber is a cylindrical one with about 8 cm³ volume. Its outer ectrode consists of a metal foil with a thin layer of U_3O_8. The total weight of that aterial is about 20 mg. Theoretically, it has a sensitivity of $7.5 \times 10^{-6} \times M$ counts· m²/neutr., M being the total weight in mg of the U_3O_8 layer. The chamber is filled th argon to 1 at and is used at a tension of 300 V.

RIK KARLSON, Department of Mechanics and Mathematical Physics, University of ınd.

e^4-approximation of vacuum polarization

JOST and LUTTINGER[5] have calculated the e^4-approximation of vacuum polariza- on under the assumption that a regularization making the expression finite can ways be done. As the expression is then also gauge invariant, it will suffice to lculate the gauge invariant terms.

To see if such a regularization is possible, a complete calculation of the e^4-approxi- ation has been started. Up to the present only one of the two Feynman diagrams, at give contributions, has been treated. The method of regularization used is differentiate n times with respect to m^2, thus making the expression con- rgent for $n > n_0$, say, and then letting n go to zero by analytic continuation. The sult is that the linearly divergent terms are transformed into logarithmically vergent terms by the regularization. As it is only the sum of the expressions for e two Feynman diagrams, that must be finite, there is still the possibility left at the logarithmic divergencies from the two expressions will compensate each her, as is actually the case in the paper by JOST and LUTTINGER.

KELEN, Department of Physics, Royal Institute of Technology, Stockholm.

micromanipulator for electrical investigations of semiconducting materials

In studying the electrical properties of semiconducting materials, one often makes e of contacts between tiny metal points and the semiconductor. Since the location of the points, as well as the contact pressure applied to them, usually are of importance, there is a need of operating them with the aid of a micromanipulator which, of course, must be constructed on basis of other principles than the micromanipulators, commonly used in biological research.

---

[1] Math.-mech. Institut A. Ott, Kempten, Germany, Pamphlet Nr Ad. 341.

[2] LORD RAYLEIGH, Phil. Mag. (6) *33*, 161 (1917).

[3] M. DUFFIEUX, J. TIROUFLET, H. GUENOCHE and G. LANSRAUX, Annales de Physique *19*, 5, 1944. M. DUFFIEUX, L'intégrale de Fourier et ses applications à l'Optique. Rennes 1946.

[4] E. INGELSTAM, Arkiv för fysik *5*, Nr 42, 1952 (in print).

[5] JOST and LUTTINGER, Helv. Phys. Acta *23*, 201 (1950).

A micromanipulator was built, consisting of 5 operating units — one for each contact point — mounted on a common baseplate which also bears a supporting device for the semiconductor sample. Each operating unit makes possible independent displacement of a contact point in 3 perpendicular directions. Attention has been paid to the question of avoiding play. The location and displacements of the contact points are determined with the aid of a measuring microscope with horizontal axis. All parts of the apparatus are made of non-magnetic materials.

The micromanipulator was built at the Physical Institute, The Technical University of Norway at Trondheim.

O. KLEIN, Department of Theoretical Physics, University of Stockholm.

On the so-called cosmological problem

The ancient questions about the origin of the world and its structure at large have been the subject of much discussion in our days in connection with the enormous enlargement of the known part of the universe produced by the phantastic progress of astronomy. There is still a large gap, however, between the speculations concerning the mentioned cosmological questions and the more certain knowledge about the constitution and evolution of stars and stellar systems.

The cosmological speculations obtained a strong impulse through Einstein's general gravitation theory and soon afterwards, a more factual background through Hubble's discovery and interpretation of the redshift of spiral nebulae. In later years the strangely regular and largely universal abundance distribution of chemical elements has given rise to new attempts of limiting the ambiguity of the cosmological problem. In this connection also the radioactive determinations of the age of the earths crust and of the chemical elements have come to play a significant role. Still, the correlation of facts, in spite of a number of promising ideas, is not only ambiguous but even deficient.

One of the most interesting attempts to create a complete cosmology in harmony with the facts mentioned is that given by GAMOW, ALPHER and HERMAN in a theory, in which the formation of elements (through successive neutron capture) is brought into connection with the expansion of the universe. A fundamental difficulty of this theory, however, is the shortness of the time ($< 2 \cdot 10^9$ years) since the formation of elements in comparison with the age of the earth, which is connected with the extreme deviation of the beginning state in this theory from a state of equilibrium.

In the thermodynamical theory of the abundance distribution of chemical elements it is assumed that the present state of the world has developed from an earlier state of approximate equilibrium. On this theory and some well-known numerical relations — which since the days of Eddington were usually taken as an indication of a connection between macro- and microphysics outside the scope of our ordinary laws of nature — it seems to be possible to develop a program for the treatment of the cosmologigal problems without the introduction of new assumptions as to the laws of nature, whereby the problem would never comprise the universe as a whole but only stellar systems of increasing order.

A. KLEMM, Physikalisches Institut, Chalmers Technische Hochschule, Gothenburg.

Isotopieeffekte bei der electrolytischen Ionenwanderung in geschmolzenen Salzen

Unsere Messungen haben ergeben, dass die Isotopieeffekte der Kationenwanderung in bestimmter Weise vom Verhältnis der Kationen zur Anionenmasse abhängen. Aus dieser Abhängigkeit lässt sich folgern, dass für die Wanderungsgeschwindigkeit der Kationen gekoppelte Schwingungen von Bedeutung sind, in deren Frequenz die reduzierte Masse aus einem Kation und 2,1 Anionen eingeht. Insbesondere wird dieser Befund durch eine neue Messung gestützt, nach der der Isotopieeffekt für Zinkionen im Bromid um den erwarteten Betrag grösser ist als im Chlorid.

GUNNAR KÄLLÉN, Department of Mechanics and Matematical Physics, University of Lund.

On the magnitude of the renormalization constants in quantum electrodynamics

In a paper which has recently appeared in the Helvetica Physica Acta the author has given an implicit definition of the renormalization constants in quantum electrodynamics.[1] The mass- and charge-renormalizations are there described with the aid of two constants K and L which are expressed as integrals over finite functions ($\Pi(p^2)$ and $\Sigma(p^2)$) in momentum space. The question whether the renormalization method is consistent or not can then be formulated in terms of the behaviour of these functions for large, negative values of the argument — a formulation which is independent of perturbation theory. If the functions vanish for $-p^2 \to \infty$, the whole theory is consistent and the constants K and L (and a third constant N which is a normalization constant for the spinor-field) are finite. If this is not the case but if the expressions $\frac{\Pi(p^2)}{-p^2}$ and $\frac{\Sigma(p^2)}{-p^2}$ vanish for $-p^2 \to \infty$, the renormalized expressions are finite, but the renormalization constants themselves infinite. If $\frac{\Pi(p^2)}{-p^2}$ and $\frac{\Sigma(p^2)}{-p^2}$ do not vanish for large values of $-p^2$, the system of equations has no solution.

If we make the assumption that every expression appearing in the theory is finite (*e.g.* also K and L) we can make a formal argument with the result that the functions Π and Σ are everywhere larger than a given function which does not tend to zero as $-p^2 \to \infty$. This is in obvious contradiction to our assumption and would thus indicate that if a solution exists at all, the renormalization constants themselves are infinite quantities. It must be stressed that this statement is here made without reference to perturbation theory. The argument is, however, incomplete, because we have not given proper consideration to states with longitudinal and scalar photons. An investigation of this point has been started, but no definite result has been obtained.

---

[1] G. KÄLLÉN, Helv. Phys. Acta *25*, 417 (1952).

E. KRONQVIST and A. GIANSOLDATI, Department of Physics, Royal Institute of Technology, Stockholm.

The influence of cold-working on the magnetic susceptibility of some binary systems

The recovery of cold-working has been studied by mesuring the paramagnetic susceptibility for some binary alloy systems.

For the majority of the systems — Ag Mn, Au Mn, and Ag Pd as well as for Au Cr and Cu Mn, previously investigated — the magnetic susceptibility was diminished by cold-working. For the Au Fe alloys, however, cold-working produced an increase of the susceptibility.

A closer analysis of the results shows that for some systems, the changes caused by cold-working to a large extent originate from the electronic configurations of the transition-metal atoms in the alloys. The number of the $3d$ electrons ($4d$ electrons for the Pd atoms) must be changed. For other systems, *e.g.* Ag Mn, cold-working does not seem to change the electronic configuration appreciably.

Such an influence on the electronic configuration can explain that the electrical resistivity in some cases (Au Cr and Ag Cr) is decreased by cold-working.

A recent theory for the magnetism by ZENER, which assumes that electrons are moved between the atoms, is supported by the results of these measurements.

B. LEHNERT, Department of Electronics, Royal Institute of Technology, Stockholm.

Some experiments on magneto-hydrodynamic flow

The state of motion of an electrically conducting liquid is strongly modified by an external magnetic field. Thus the liquid becomes anisotropic in presence of the field, which can be shown *e.g.* in the following simple cases:

1. *Laminar motion.*

In the laminar case stationary motion in a homogeneous magnetic field tends to be two-dimensional with regard to the direction of the field. Thus the motion of a circular, conducting disc at the bottom of a cylindrical vessel is projected along the lines of an axially symmetric magnetic field.

2. *Turbulent motion.*

The turbulent state of motion may also be affected by an external magnetic field. Thus in the turbulent state the torque between an immovable outer cylinder and a rotating concentric inner cylinder in a conducting liquid is decreased by an axial magnetic field.

3. *Transition between laminar and turbulent motion.*

HARTMANN (1935) studied the flow of mercury in rectangular channels placed in a magnetic field. The results show that the critical velocity is a linear function of the strength of the field. A transformation of the fundamental magneto-hydrodynamic equations to dimensionless form gives three characteristic parameters

$$R_1 = \frac{V_K}{B_K} \cdot \sqrt{\mu \varrho} \qquad R_2 = \frac{V_K L_K}{1/\mu \sigma} \qquad R_3 = \frac{V_K L_K}{\nu}$$

here V_K, L_K and B_K are characteristic velocities, lengths and field-strengths, re-pectively (MKSA-units are used). For a given value of the quantity R_1, V_K is pro-ortional to B_K, which may explain the dependence found by Hartmann.

. Lidén and N. Starfelt, Department of Radiophysics, University of Lund.

Scintillation-spectrometer studies of β-bremsstrahlung

The spectral distibution of the bremsstrahlung emitted when the β-radiation from ^{32} and S^{35} is completely absorbed in Pb, Sn, Fe, Al and C, has been studied by ieans of a scintillation spectrometer fitted with a single-channel differential dis-riminator and an NaI (Tl) crystal. The internal bremsstrahlung in P^{32} and S^{35} as been studied separately and in this way the external bremsstrahlung could fterwards be estimated. Corrections were applied for the efficiency of the crystal, he secondary photo-absorption and the resolving power of the apparatus. The total iternal and external bremsstrahlung-energy per β-decay was obtained as well as he Z-dependence of the external radiation.

The experimentally observed spectral distribution of P^{32}'s external radiation has een compared with data calculated from Bethe and Heitler's theory of bremsstrah-ung and good agreement was obtained. On the other hand, data for the internal adiation of P^{32} calculated from Knipp-Uhlenbeck's theory show greater discrepan-ies with the experimental results which yield appreciably higher values than theory specially at energies greater than 200 kV.

The uncorrected experimental distribution for Pb has two maxima, one an ab-orption phenomenon and the other a K-radiation peak. A very intense K-peak obtained for Sn with β-radiation from S^{35}.

. Lundquist, Department of Electronics, Royal Institute of Technology, Stockholm.

Magnetic-hydrodynamic turbulence

In cosmic physics a knowledge of the properties of electrically conducting gases most important. Due to the large dimensions it seems probable that the normal tate of motion is turbulent. The electro-magnetic phenomena caused by turbulence re highly interesting. They have been studied by Batchelor who discusses the pontaneous growth of magnetic energy in a conducting liquid. Similar results have een reached by Chandrasekhar. The arguments are mainly kinematic. However, is possible to develop the theory in a different way without this limitation, starting om a transformation of the equations of motion into a remarkably symmetric rm.

er-Olov Löwdin, Department of Mechanics and Mathematical Physics, University of Uppsala.

Some actual problems in the theory of molecules and crystals

In order to coordinate the various efforts to improve the molecular theory, an ternational conference on "Quantum Mechanical Methods in Valence Theory" as held on Shelter Island, N. Y., U. S. A., in September 1951. One of the most important results of the conference was the statement about the insufficiency of the previously often used semi-empirical approaches and the necessity of carrying through more exact investigations even in cases when those are associated with rather laborious numerical computations of, for instance, many-centre integrals.[1] A summary is given of some investigations connected with the conference program, of which the following are of a principal nature: calculation of the cohesive energy of molecules and crystals[2], investigation of the perturbing influence of heteroatoms or substitution groups in aromatic molecules[3], critical treatment of the basis of the molecular orbital theory and the corresponding band theory for crystals, modification of the molecular orbital theory in order to obtain a correct asymptotic behaviour of the binding energy for separated atoms, discussion of the connection between the molecular orbital theory and the valence bond theory, and renewed calculation of the expression for the van der Waals energy for small distances. The following investigations are connected with problems concerning the numerical technique: evaluation of two-, three-, or four-centre integrals[4] together with a discussion of the various methods of computing such integrals, numerical integration of ordinary differential equations[5], and calculation of analytic atomic wave functions. The results are being published in a series of articles in Arkiv för Fysik and Journal of Chemical Physics.

K. G. MALMFORS, Nobel Institute for Physics, Stockholm.

Nuclear resonance scattering of γ-rays

Many attempts have been made to demonstrate the resonance exictation of nuclei by γ-rays. Due to the fact that the width of the energy levels is much smaller than the energy shift due to the recoil, it was not until recently that such experiments gave a positive result. (MOON, 1950.) The energy shift was compensated by utilizing a rotor, which moved the γ-source (Au^{198}) towards the scatterer (Hg^{198}) with the appropriate velocity.

In the experiments reported at the conference, the resonance conditions are obtained by heating the γ-source to such a high temperature (about 1000° C) that the Doppler-broadening of the γ-line is sufficiently large to cover the energy displacement associated with the recoil.

The width of the 411 keV level in Hg^{198} was found to be about $4 \cdot 10^{-5}$ eV and the mean life about $2 \cdot 10^{-11}$ sec. in good agreement with the results obtained by MOON.

L. MINNHAGEN, Department of Physics, University of Lund.

High-frequency excitation of the argon spectra A I, II and III

The spectra of argon I, II and III have been excited by means of a transmitter of 1 kW average power, which has been operated — both continuously and pulsed —

---

[1] Report of the Conference in Valence Theory on Shelter Island, 1951.

[2] P. O. LÖWDIN, J. Chem. Phys. *19*, 1570 and 1579 (1951).

[3] P. O. LÖWDIN, J. Chem. Phys. *19*, 1323 and 1396 (1951), *20* (1952) in press.

[4] S. O. LUNDQUIST–P. O. LÖWDIN, Arkiv för Fysik *3*, 147 (1951).

[5] P. O. LÖWDIN–A. SJÖLANDER, Arkiv för Fysik *3*, 155 (1951). P. O. LÖWDIN, Quarterly of Applied Math. *10*, 97 (1952).

t about 9 Mc/s. During pulse working it has been found possible to increase the anode oltage of the transmitting valve up to 9 kV which is three times its normal value. oth the length and the frequency of the pulses can be varied. The transmitter has een constructed by Dr. L. Stigmark.

As the pulse power increases, the intensity of the argon II spectrum rises relave to that of argon I, as does also the intensity of A III relative to that of A II. ecordings have been made with a grating in the region 1900–9900 A under diferent excitation conditions. Up to about 5000 A the recordings have been made in e second order (dispersion 2.5 A/mm).

Mr. K. B. Eriksson took part in the preliminary work.

ke Nilsson, Department of Physics, University of Uppsala.

The excitation potential of the Kα_1-lines of 26 Fe–29 Cu and a precision determination of Planck's constant

The X-ray intensity of the Kα_1-lines of 26 Fe 29 Cu has been recorded in the neighorhood of the excitation potential with an X-ray spectrograph with bent crystal nd Geiger counter. The obtained isochromates were compared with the K-absorpon edges of the same elements. These were determined with a double crystal specometer and a Geiger counter in 1939 by Beeman and Friedman.[1]

In our case the resolution is mainly determined by the voltage drop of the cathode nd the Maxwell distribution of the emitted electrons and was observed to be about third of a volt. The isochromates show a more detailed structure than the absorpon curves. Thus the main edge is very sharp and the elements Fe, Co and Ni have fine structure just in front of it. An almost horizontal level close to the main edge terminated by a sudden intensity increase, showing the position of the low-energy art of the $4s$ band.

If the transitions are merely dipole the mixture of the necessary p states in the $3d$ nd $4s$ bands cannot increase gradually towards the $4p$ band and as the absorption rves seem to indicate. The fine structure in the main edge probably corresponds to ansitions into the empty part of the $3d$ band, and the constant intensity some volts oove the main edge must be the result of a constant admixture of p function over e entire $4s$ band.

Whether the reason for the different behaivour of the absorption edges and the ochromates merely is the difference in the resolving powers of the two methods of cording, must be the subject of further investigations.

The exitation potential V and the frequency ν of the K-absorption edge are conected by the relation $h\nu = eV$. To get the correct value of V we have to add the ork function of the cathode to the measured voltage difference between the elecodes.[2] As a preliminary result of the determination of the constant h/e we get the llowing values:

26 Fe: $1.3794 \cdot 10^{-17}$ e.s.u.
27 Co: 1.3796
28 Ni: 1.3796
29 Cu: 1.3795
Mean: $1.3795 \cdot 10^{-17}$ e.s.u.

---

[1] W. W. Beeman and H. Friedman, Phys. Rev. *56*, 392 (1939).

[2] Å. Nilsson, Arkiv för Fysik *5*, 130 (1952).

Kai Siegbahn, Department of Physics, Royal Institute of Technology, Stockholm.

Precision measurements of gamma radiation

The development of high precision instruments for measuring nuclear radiation and the availability of strong radioactive sources have recently resulted in a substantial gain in accuracy in the field of nuclear spectroscopy. At present it is possible to measure internal conversion lines and photolines from secondary converters under certain conditions with an accuracy of about 1 or 2 parts in 10^4. A set of standard-lines for reference purpose in β-ray spectroscopy has been established extending from $H\varrho = 1388$ to $H\varrho = 10000$. Some of these have been measured in an absolute way; other lines have been directly related to these. A few further lines of somewhat less accuracy are also available for reference purposes. In order to increase the precision, an iron-free double focussing spectrometer has been designed. The spectrometer is equipped with an X-ray tube which will enable a detailed study of the binding energies of the different electron shells at various conditions. An elaborate high vacuum evaporation set up to form the appropriate thin films has been constructed.

N. G. Sjöstrand, Department of Physics, Atomic Energy Laboratory, Stockholm.

The influence of a cadmium sheet on the distribution of neutrons in graphite

A theoretical and experimental investigation has been made on the influence of a cadmium sheet on the distribution of neutrons in a rectangular block of graphite. Theoretically, the problem has been treated by "The Spherical Harmonic Method", and the experiments have been performed in a way similar to the diffusion length measurements reported by Carlbom at the conference last year.[1] Good agreement was found between theory and experiment.

Hilding Slätis, Nobel Institute for Physics, Stockholm.

A semicircular permanent magnet beta-ray spectrometer for photographic recording of conversion lines

The instrument was constructed in order to obtain a high resolving power for conversion lines in beta spectra from samples, where the specific activity is high enough to prevent broadening of the lines. The spectrometer consists of a rectangular iron yoke (80 × 42 × 40 cm), in the center of which the magnetic field is developed between two circular iron discs. The distance between these discs is 40 mm and the diameter 40 cm. The pole pieces are 30 mm in thickness and form the vertical walls of the circular vacuum chamber, in which the frame containing the source and the film or plate (19 × 270 mm) can be inserted. The magnetic induction is maintained by 240 pieces of so called "Fama 700", an aluminium-nickel-cobalt alloy from the Swedish firma Fagersta. The size of the pieces is 3 × 3 × 6 cm. The pieces are arranged in two layers, each between two iron discs of 20 mm thickness and 60 mm apart. The permanent magnet layers are inside the magnetization coils, which are used only when the remanence is to be changed. The spectrometer is kept inside a box equipped with a thermostat, which keeps the temperature constant (the decrease in remanence is 2.2 parts in 10000 for an increase of 1° C temperature). The field is

---

[1] L. Carlbom, Arkiv för Fysik, *5*, 122 (1952).

easured by reading the current in and weighing the force acting on a rectangular
il, the lower part of which hangs in the field to be measured, the upper part being
tside the yoke. The energy of the electrons belonging to a conversion line can be
easured with an accuracy of 0.1 %. The smallest half width of the conversion lines
easured in the beta spectrum of ThB is so far 1.2 parts in 10000. In agreement with
earlier observation by G. Lindström the half width of the F-line was found to
larger than that for the I-line. For this difference the present author found the
lue 3 parts in 10000. As is known, the F-line belongs to the K-shell and the I-line
the L_1 shell.

For the G- and H-lines, which also are K-lines, the author found a half width
ich was again 3 parts in 10000 larger than that for the I_a-line, which belongs to the
-shell. It therefore seems to be possible that for the ThB spectrum all K-con-
rsion lines are by the same amount broader than the L-conversion lines. It may
that a characteristic line width belongs to each shell, this line width being larger
r the inner shells.

Taylor, Department of Physics, Atomic Energy Laboratory, Stockholm.

The purification of boron trifluoride for use in neutron counters

Fractional condensation is used, the gas being streamed at a constant rate through
train of cold traps held at well-defined temperatures. The effects of different flow
tes and temperatures are described, and methods are given for holding these at
e required values. Starting with commercial cylinder gas, the process delivers up
1 liter (NTP) per hour of BF_3 having as low electron capture as the best produced
the Ca F_2 method.

. Westergaard, Department of Physics, Atomic Energy Laboratory, Stockholm.

eneral considerations on the design of control and measuring equipment for the Swedish nuclear reactor

An outline of the entire control system is given, together with considerations
the reliability of different types of equipment. Also some considerations upon
e problem: complexity of equipment versus performance and ease of maintenance.

orbjörn Westermark, Department of Theoretical Chemistry, Royal Institute of
Technology, Stockholm.

Production and properties of P^{33}

P^{33} amounting to 1.4 ± 0.2 % was found in P^{32} preparations from Harwell. It is
ost probably formed by the reaction S^{33} (n, p) P^{33} with a cross-section of 0.03
rns. This is in accordance with the findings of Jensen *et al.*[1] and of Sheline
al.[2] This reaction is exothermic, and irradiating with thermal neutrons should
eld pure P^{33}. Experiments have yielded 30 % P^{33} (the rest being P^{32}) after irradia-
on of sulphur near the reflector of the Harwell reactor. The cross-section for the

---

[1] E. W. Jensen *et. al.*, Phys. Rev. *85*, 112 (1952).

[2] R. K. Sheline *et. al.*, Phys. Rev. *83*, 919 (1951).

mentioned reaction was found to be $2.3 \cdot 10^{-3}$ barns for thermal neutrons. Chemical experiments strongly suggest that the activity is due to a P isotope and all physical evidence favours P^{33}. — The maximum beta energy was found to be 246 ± 5 keV. No gamma quanta were found, the experimental limit being that less than 3.5 % of the betas is present. The half-life of P^{33} has been found to be 25.4 ± 0.2 days and of P^{32} 14.25 ± 0.05 days, but these latter results are only preliminary. A more detailed publication[1] appears in Physical Review.

E. Åström, Department of Electronics, Royal Institute of Technology, Stockholm.

Electrodynamics in accelerated frames of reference

If it were possible to find a finite volume in which the gravitational potential were constant, the metric — according to current theory — would be flat in that region. It would then be possible to introduce orthogonal, Cartesian coordinates in a four-dimensional space. If we wish to introduce a new frame of reference, only those are of interest for which each point in the new frame corresponds to only one point in the four-dimensional orthogonal frame. In particular the orthogonal transformations, of which the Lorentz transformation is a special case, satisfy this condition. A frame corresponding to that, classically known as a "rotating frame of reference", is also of a certain interest. In that case we must require, in addition to the mentioned condition, that the difference between the classical and the present treatment shall vanish with vanishing distance to the "axis of rotation".

The latter frame is Euclidean. It is necessary, however, to distinguish between covariant and contravariant quantities. Since the special theory of relativity is defined in the orthogonal frame, our transformation enables us to define the corresponding quantities and equations in the new frame.

---

[1] T. Westermark, Phys. Rev. *88*, 573 (1952).

Tryckt den 12 maj 1953

Uppsala 1953. Almqvist & Wiksells Boktryckeri AB

ARKIV FÖR FYSIK Band 7 nr 8

Communicated 25 April 1953 by Erik Hulthén and Arne Westgren

Reaction energy of $O^{18}(p, \alpha)N^{15}$ and the atomic mass of oxygen 18

By Curt Mileikowsky

With 16 figures in the text

1. Introduction

In the present paper a measurement of the reaction energy of $O^{18}(p,\alpha)N^{15}$ by neans of magnetic analysis is described. The purpose of the measurement is not nly to obtain a nuclear transmutation value of the mass of oxygen 18, but also o get new information on the following nuclear cycle:

$$F^{19}(p,\alpha)O^{16},\ O^{16}(d,\alpha)N^{14},\ N^{14}(d,p)N^{15},\ O^{18}(p,\alpha)N^{15}$$
$$O^{18}(p,n)F^{18},\ Ne^{20}(d,\alpha)F^{18},\ Ne^{20}(d,p)Ne^{21},\ Ne^{21}(d,\alpha)F^{19}$$

This cycle is interesting for several reasons. It leads to the fundamental mass lifference $2H^2-He^4$ and presents the possibility of checking the consistency of diferent Q-measurements. In particular, it may be noted that the cycle connects the luorine and neon isotopes in two ways, directly by means of the reaction $Ne^{21}(d,\alpha)F^{19}$ nd indirectly by means of the other seven reactions.

The "gap" between neon and fluorine was recently closed by measurements of the eaction energy of $Ne^{21}(d,\alpha)F^{19}$ (ref. 1) and of $F^{20}(\beta^-)Ne^{20}$ (ref. 2, 3). Within the imits of error these measurements agree as to the mass differences between neon nd fluorine isotopes. As a large number of atomic masses in modern mass tables ref. 4, 5) depend on this mass difference any additional information on this subject s of interest. One way is to measure the reaction $Ne^{22}(d,\alpha)F^{20}$, which is now being lone in this laboratory, another way is to measure $O^{18}(p,\alpha)N^{15}$ as part of the cycle onsidered above.

The reaction energy of $O^{18}(p,\alpha)N^{15}$ has been measured earlier (ref. 6, 7) though nly with an accuracy of 40 keV. The Q-values corresponding to the ground state ransitions of the reactions forming the above mentioned cycle, except for $O^{18}(p,\alpha)N^{15}$ nd $Ne^{20}(d,\alpha)F^{18}$, have been measured by different groups using magnetic analysis, he probable error being 10 keV or less (ref. 1, 8–10). The reaction $Ne^{20}(d,\alpha)F^{18}$ has een measured with the photographic range method with an accuracy of 20 keV. ref. 11).

2. Experimental set-up

The measurements of the present investigation were made with the double-focusing pectrometer for heavy particles described in ref. 12, 13. The beam was obtained rom the high voltage set with analyzing magnet described in ref. 14. The general rrangement is shown in Fig. 1.

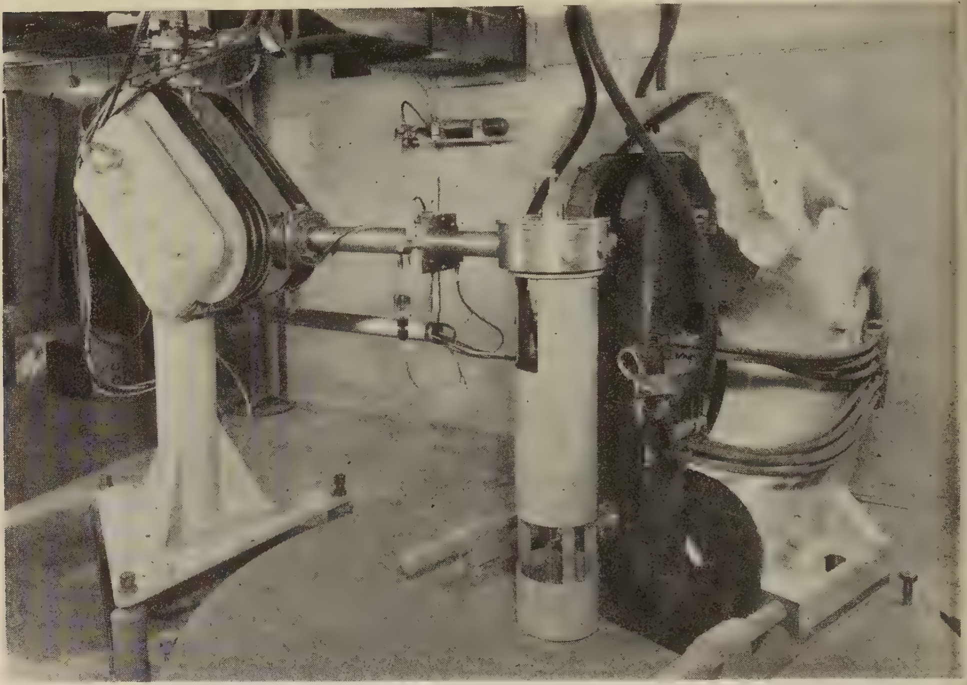

Fig. 1. General view of analyzing magnet, target chamber and spectrometer.

The spectrometer is mounted on a table, which can be rotated, such that particles emitted from the target can be accepted by the spectrometer at an arbitrary angle θ between beam and particle direction in the region $0-135°$. The vacuum chamber, however, allows values of θ only in intervals of 15°. The table, which carries the spectrometer, was made horizontal to an accuracy of better than 1 part in 1 000. The axis of the cone supporting the targets was adjusted to vertical direction and brought to coincide very accurately (0.1 mm) with the vertical axis of rotation of the spectrometer table.

The target surface was vertical and was always brought to coincide with the above mentioned cone axis. The target backing plates were circular, $\Phi = 14$ mm, 2 mm thick. Four targets were mounted on a cube at one time, as in Fig. 2. This cube was eccentrically mounted on the supporting cone and could be manoeuvred under vacuum, such that any of the four targets could be put into position without opening the system. For the target cube only four definite positions relative to the supporting cone were used, with intervals of 90 degrees. The angular position of the supporting cone on the other hand, was always chosen such that the angle of the target surface to the incident beam direction was half the angle between the direction of the emitted particles studied and the incident beam in the horizontal plane. This is clarified by Fig. 2 where these two angles are denoted by $1/2\ \varphi$ and φ.

The incident beam itself was adjusted in such a way that it came in horizontally, hitting the target surface at optimum height for the spectrometer.

The incident beam had to pass two slits, one before the analysing magnet and

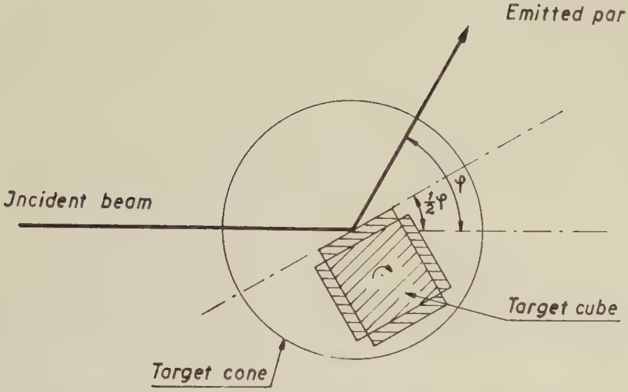

ig. 2. Target cube for four targets. The cube is rotatable and eccentrically mounted, such that any target can be turned into position without breaking the vacuum.

ne after this magnet. These slits could be adjusted by micrometer screws to desired ositions and widths (ref. 15).

The distance from the first slit to the entrance of the bending field in the analyser as $0.6\ r_0 = 24$ cm, the distance from the field exit to the last slit was $1.75\ r_0 = 70$ cm he ion optics of the incident beam was in principle such that the image of the ion ource came in the first slit and the image of the first slit fell in the second slit. This, owever, was only approximately the case. The beam from the accelerator was not lways focused exactly in the plane of the first slit, and the distance analyzer–second it was not exactly chosen according to the above-mentioned principle. This distance as chosen such that the slit house with micrometers would allow the spectrometer be turned to backward angles. It was found that these deviations, as expected, ad no detectable influence on beam direction or spot position at the target. It is nportant here that the second slit is rather close to the target (34 cm).

3. Experimental procedure

The measurement of nuclear reaction energies consists of four partial measurements oncerning the energy of the incident beam, the energy of the studied particles, the ngle between incident beam direction and particle direction, and the surface layers.

The analyzing magnet and the spectrometer both have to be calibrated and this etermines the general procedure adopted. Very convenient for the calibration of e analyzer or incident proton beam is the 873.5 keV resonance of the reaction $^{19}(p,\alpha,\gamma)$, being an international standard in nuclear energy measurements (ref. 16). he fluorine resonance has a fairly narrow line, $\Gamma = 5.2$ keV, and a very good cross- ction. The $O^{18}(p,\alpha)N^{15}$ reaction has a resonance close to the fluorine resonance.

The calibration of the spectrometer is more difficult. The emitted α-particles from e $O^{18}(p,\alpha)N^{15}$-reaction have an energy, which is less than 4 MeV in a useful region angles, if the bombarding energy is 873.5 keV. Consequently no radioactive α- nitting standards can be used. As energy extrapolations were not desired a well- nown nuclear reaction was preferred for the spectrometer calibration, $N^{15}(p,\alpha)C^{12}$. he Q-value of this reaction has been measured independently by the MIT-group and the Pasadena-group (and the Wisconsin-group), both getting within one keV the same value, $Q = 4.961 \pm 0.006$ MeV (ref. 4, 8). Both the O^{18} and N^{15} targets were produced in the same way by means of electromagnetic separation, which may be favourable for the measurement.

At a proton energy of 873.5 keV the α-particles from the reaction $N^{15}(p,\alpha)C^{12}$ have an energy at $\theta = 135°$ which is about the same as the energy of the α-particles from $O^{18}(p,\alpha)N^{15}$ at $\theta = 60°$. Therefore, the experimental procedure was chosen as follows.

First, the analyzing magnet was calibrated with the fluorine resonance. The current of the analyzing magnet was then kept constant to better than 1 part in 4000 during all the experiment. At the end of the experiment the fluorine resonance was taken again to obtain a check of the constancy of the analyzing field.

Second, the scattering edges were investigated with the spectrometer at $\theta = 60°$. The scattering was made at the proton energy 873.5 keV on four targets (fig. 2), namely the clean target backing (silver or beryllium), the fluorine target, the oxygen target and the nitrogen target. In this way the layers on the surfaces were obtained from the energy positions of the scattering edges. This method is sensitive at this angle since the target surface was at 30° to the incident beam, which had to penetrate twice the double thickness of the layer. Electrical detection was used for this phase of the work.

Third, the oxygen-18 target was bombarded at spectrometer angle $\theta = 60°$ with the same proton beam, and the α-group detected in a photographic plate. The spectrometer current was kept constant to better than 1 part in 3000 during this exposure and also during the fourth phase, without interruption.

Fourth, the nitrogen target was bombarded with spectrometer angle $\theta = 135°$ without any change in spectrometer current from the preceding bombardment, as was mentioned above, the α-particle-group again being registered in a photographic plate.

Fifth, the scattering was done again on the clean backing and on the oxygen, nitrogen and fluorine targets. This was done to check whether any carbon had been shot onto the targets during the bombardments. To keep the amount of carbon deposited at a minimum a liquid air cooling trap was used, mounted in the neighbourhood of the target, all through the experiment.

Sixth, the magnetic field of the analyzer was again checked by means of the fluorine resonance.

4. Production of targets

The oxygen-18 and nitrogen-15 targets were produced by electromagnetic separation in the Institute's separator (ref. 20,21). Two sets of targets were finally used, one set on silver as backing and one set on beryllium. For the N^{15}-targets the ion source was run with ordinary nitrogen and the mass-15 beam was collected in one beryllium and one silver plate. For the production of one of the O^{18}-targets the ion source was fed with ordinary water vapor and the mass 20 beam, partly consisting of H_2O^{18}, was collected in a silver plate. The other O^{18}-target was produced by using in the ion source water vapor, which was already enriched in O^{18} by a factor of 25 so that 5% of the oxygen was O^{18}. In this case the mass-20 beam was collected in a beryllium plate. This beam probably entirely consisted of H_2O^{18}.

Both oxygen targets — and also the nitrogen targets — were run in the separator to what was judged to be saturation. With the ordinary water vapor the mass-20 ent was 0.3 μA and the separation was carried on for 3 hours, i.e. 1 μA hour. he case of enriched water vapor the mass 20 current was 1.6 μA and the separation 1.5 hours, corresponding to 2.4 μA hours.

he number of O^{18}-nuclei per mm² in the two targets differed considerably, g 18 times larger in the beryllium target, as obtained from the number of α-icles from the $O^{18}(p,\alpha)N^{15}$ reaction. A discussion of the target properties will be n in a later section of this paper.

he enriched oxygen (5% O^{18} and 0.2% O^{17}) of the water used here was obtained 1 Atomic Energy Research Establishment, Harwell, England. The electromagnetic rations were made by lic. S. Thulin.

he fluorine targets were produced by evaporation of CaF_2 in an ordinary evapora- chamber, and the clean beryllium surface was made by evaporating beryllium beryllium plate.

hus, to sum up, we had the following targets:

clean machined plate of pure silver.
thin fluorine target evaporated on silver.
^{18} in silver, separated, from ordinary water vapor.
^{15} in silver, separated, from natural nitrogen.
clean beryllium surface, beryllium evaporated on beryllium.
thin fluorine target evaporated on beryllium.
^{18} in beryllium, separated, from enriched water vapor.
^{15} in beryllium, separated, from natural nitrogen.

5. Measurement of the angles

s $\partial Q/\partial \theta$ is 7.5 keV per degree for $O^{18}(p,\alpha)$ at $\theta = 60°$, according to the formulae ection 12, the measurement of the angle θ, which is the angle between the emitted icle direction and the incident beam, has to be accurate to a few tenths of a ree.

he angle θ in the present arrangement is actually obtained by measuring two les, φ and ν defined as shown in Fig. 3. φ is the angle between the incident beam

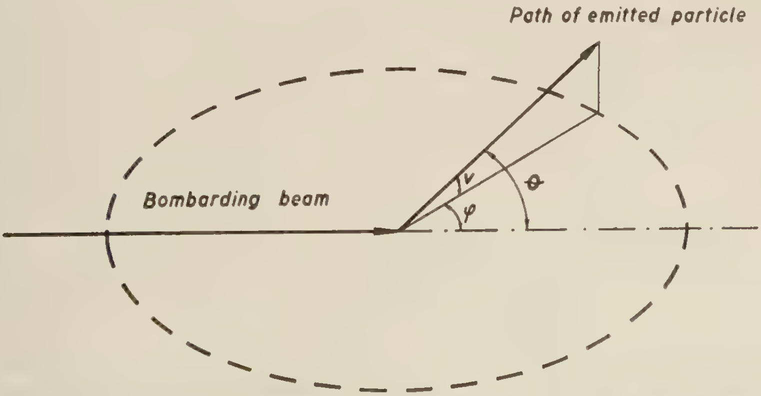

3. Schematic representation defining the angles φ and ν. φ is the angle in the horizontal plane, ν is the angle to the horisontal plane.

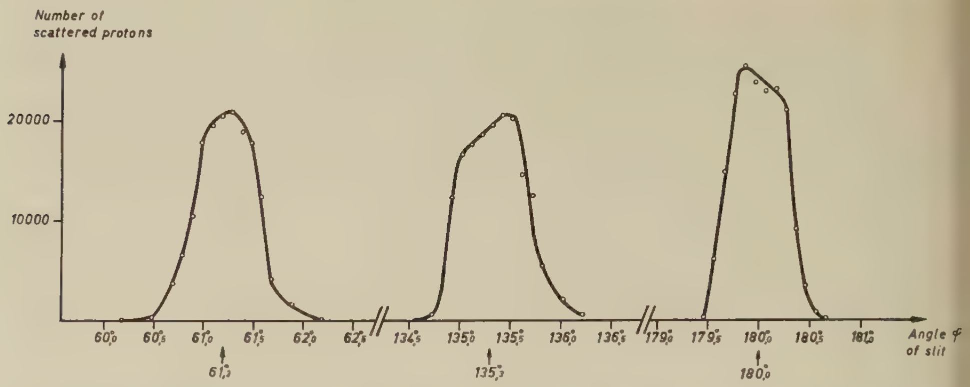

Fig. 4. Number of particles scattered into the spectrometer, per microcoulomb of incident beam as a function of angle φ. The peak at 180°0 represents the incident beam direction, the two peaks at 61°2 and 135°3 correspond to two positions of the spectrometer, which were used in the experiments.

and the projection on the horizontal plane of the central beam of the emitted particles accepted by the spectrometer. φ is the angle that is varied when the table carrying the spectrometer is rotated. ν is the angle between the horizontal plane and the central beam of the emitted particles accepted by the spectrometer (ref. 13). The angle ν is always the same independently of the value of φ. A consideration of Fig. 3 shows that θ is related to φ and ν according to the expression

$$\cos\theta = \cos\varphi \cdot \cos\nu. \tag{1}$$

The measurements of the angles φ and ν were made with scattered protons. The cone supporting the target was mounted concentrically in a second cone and the axis of the cones coincided accurately with the vertical central axis of the spectrometer table. The second cone carried an angular precision scale and a 20 cm long arm, which could be rotated in the horizontal plane around the vertical axis of the cones.

For the measurement of φ a narrow vertical slit was mounted on the end of the above-mentioned arm. The beam center hit the target surface at the vertical symmetry axis. The slit arm was now turned such that the slit came in the beam path. The number of protons scattered into the spectrometer was counted for several angle readings of the slit position. The number of scattered protons per microcoulomb of current passing the slit after the analyzing magnet is plotted in Fig. 4 as a function of the angle readings. Next, the slit arm was turned to the region of 135°, which was also the position of the spectrometer. The number of particles scattered into the spectrometer per microcoulomb of current hitting the target was counted for several slit arm positions, and plotted in Fig. 4. The same was again done at 60°. The mean angle values for the three directions are given in Fig. 4 as 180°0, 135°3 and 61°2. The two angle positions φ_2 and φ_1 of the spectrometer are thus 135°3 ± 0°2 and 61°2 ± 0°2.

The angle ν was measured in a similar way. Instead of the vertical slit the arm carried a tilted slit (60° to vertical direction) and between that slit and the spectrometer was a fixed, narrow vertical slit. Thus, turning the arm meant that the very small hole admitting particles to the spectrometer moved in the vertical direction,

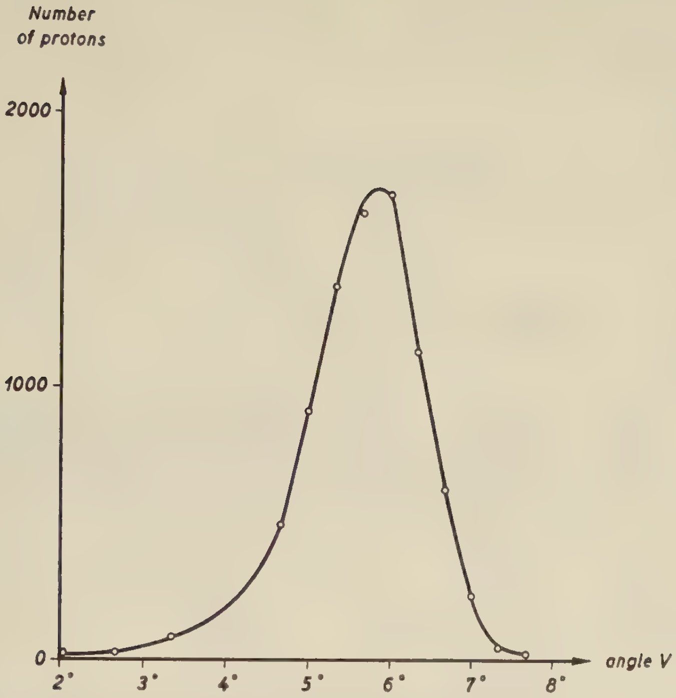

. 5. Number of particles scattered into the spectrometer, per microcoulomb of incident beam as a function of angle ν.

responding to a change of ν. The scattered particles were counted for different gles ν and the curve obtained as plotted in Fig. 5. The measurement gave a mean ue of $\nu = 5.^\circ7 \pm 0.^\circ2$.

Now, finally, we obtain the values θ_1 and θ_2 corresponding to the two spectrometer itions φ_1 and φ_2 from expression 1, with the obtained value of ν:

$$\theta_1 = 61.^\circ4 \pm 0.^\circ2 \quad \theta_2 = 135.^\circ0 \pm 0.^\circ2.$$

A check of the difference between the measured angles φ_1 and φ_2 was given by periferal distance between the two spectrometer positions. This distance was $\frac{8}{3}$ of the total circle periphery, which corresponds to $\varphi_2 - \varphi_1 = 74.^\circ4 \pm 0.^\circ2$ in eement with the measured value within the limits of errors.

6. Investigation of the target layers by scattering

ll the scattering curves were taken at a proton beam energy of 873.5 keV and $\theta = 61.^\circ4$. The scattering on clean silver and on the fluorine, oxygen-18 and rogen-15 targets on silver is shown in Figs. 6 and 7; the scattering on clean yllium, and on the fluorine, oxygen-18 and nitrogen-15 targets on beryllium ore the Q-measurement is shown in Fig. 8; a similar scattering on the same targets r the Q-measurement is shown in Fig. 9

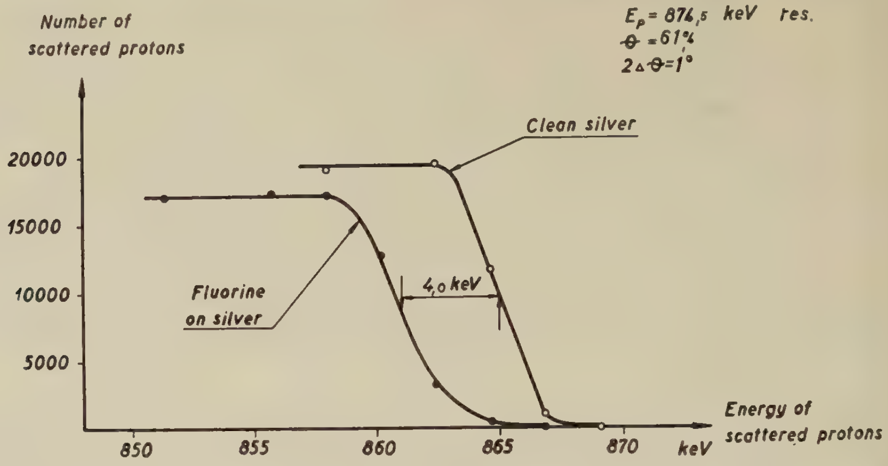

Fig. 6. Spectrum of protons scattered from clean silver and from the fluorine target on silver. Incident proton energy = 874.5 keV.

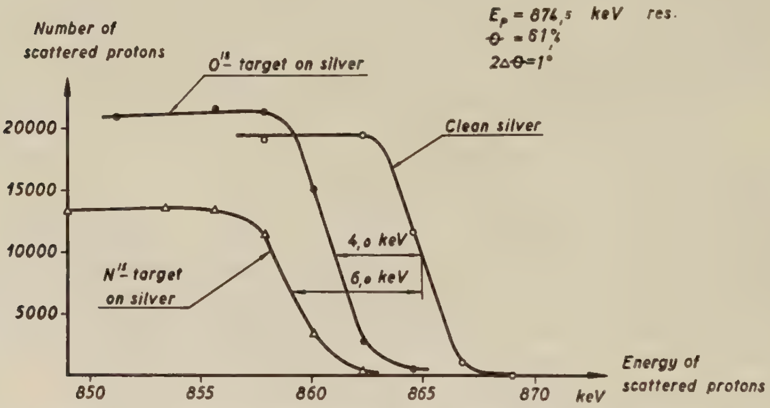

Fig. 7. Spectrum of protons scattered from clean silver, from the O^{18}-target on silver and from the N^{15}-target on silver. Incident proton energy = 874.5 keV.

The position of a scattering edge is taken as the energy where the intensity is half the maximum intensity, i.e. the midpoint of the edge.

It is to be noted, that at $\theta = 61\overset{\circ}{.}4$ the angle between beam and target surface was always kept about 30° in accordance with Fig. 2. Therefore, a surface layer of thickness t keV will slow down the proton beam by $2\,t$ keV and the protons scattered in the direction $\theta \approx 60^\circ$ will again lose $2\,t$ keV before leaving the surface. Thus, the measured edge displacements in Figs. 6–9 are actually four times the corresponding true layer thicknesses for protons of 873.5 keV.

Table I gives a summary of the observed edge displacements from Figs. 6–9 and the corresponding layer thicknesses.

The layer thicknesses of table I are for protons of energy 873.5 keV; for alpha particles of energy 4000 keV the layers are 3.7 times thicker. It should be noticed

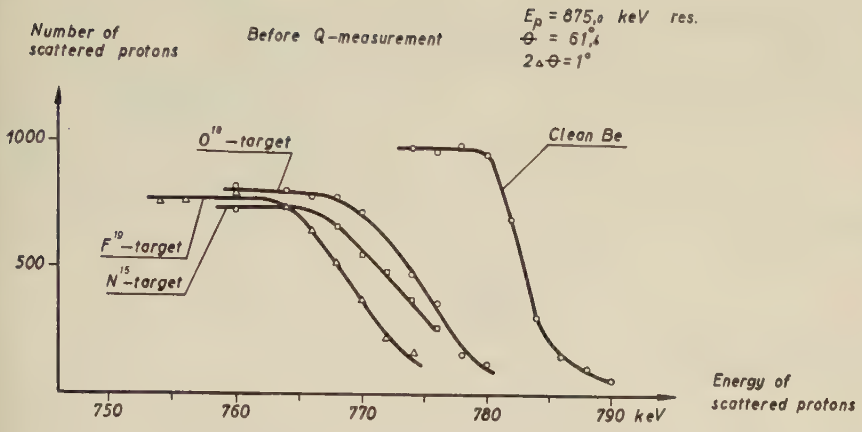

ig. 8. Spectrum of protons scattered from clean beryllium, from the O^{18}-target, the N^{15}-target d the F^{19}-target, all on beryllium, before Q-measurement. Incident proton energy = 875.0 keV.

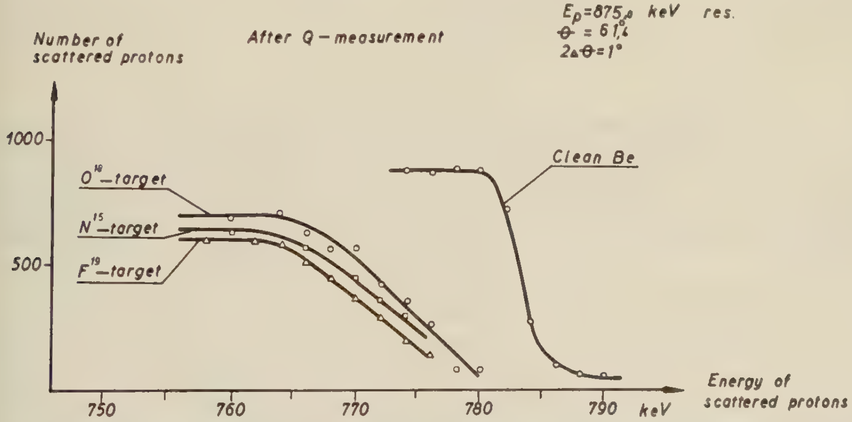

g. 9. Spectrum of protons, scattered from clean beryllium, from the O^{18}-target, the N^{15}-target d the F^{19}-target, all on beryllium, after Q-measurement. Incident proton energy = 875.0 keV.

at observing displacements of scattering edges of the backing material gives formation on the thickness of external layers, i.e. layers on the backing.

These layers very probably consist of carbon which was deposited during the paration. They are kept down to a keV or two by the use of a water cooled baffle tween the oil pump and the vacuum system of the separator and would probably further reduced if a liquid air cooling trap were used near the collector, as was ne in the target chamber during the Q-experiment. One gets an idea of the quantities matter entering into this discussion from the fact that 1 keV of carbon corresponds $\sim 4\ \mu g/cm^2$ having a thickness of ~ 150 A.

It should be pointed out here, that one should not try to draw conclusions from e height of the horizontal parts of the scattering curves; the efficiency of the unter was not constant enough for such conclusions to be valid.

Table I. Summary of edge displacements and external target thicknesses during Q-measurements of $O^{18}(p,\alpha)N^{15}$

	Target	Position of scattering edge keV	Displacement of scattering edge keV	Layer thickness keV
A. Silver backing				
	Clean silver	865	0	—
	O^{18}-target	861	4	1
	N^{15}-target	859	6	1.5
	F^{19}-target	861	4	1
B. Beryllium backing				
Before Q-measurement	Clean Be	783	0	—
	O^{18}-target	775	8	2
	N^{15}-target	774	9	2.2
	F^{19}-target	770	13.5	3.2
After Q-measurement	Clean Be	783	0	—
	O^{18}-target	774	9	2.2
	N^{15}-target	773	10	2.5
	F^{19}-target	772	11.5	2.7

7. Measurement of the bombarding energy

The current of the analyzing magnet was electronically stabilized to about 1 part in 1000 (ref. 14) and was further manually stabilized to 1 part in 4000 and measured by means of a compensator-galvanometer arrangement, similar to the one described in ref. 13.

The analyzing magnet with slits is primarily an energy selecting device. As the slit widths did not exceed 1 mm and the field was kept constant, the energy spread of the beam that had passed the second slit was necessarily within the maximum limits ± 3.5 keV. The edges of the second slit are insulated and serve as a part of the stabilizing system for the high voltage (ref. 15): If the beam hits one of the edges, this signal steers the high voltage back to a value, which sends the beam into the slit again. This stabilizing scheme serves two purposes: it maximizes the intensity of the beam reaching the target, the analyzer being regarded as a selector and furthermore it keeps the beam in the center of the second slit, thus diminishing the energy spread to considerably less than ± 3.5 keV.

The fluorine resonance, which was used for measuring the bombarding energy, was studied with a sodium iodide scintillation counter, mounted just above the target, outside the vacuum chamber. The number of γ-counts per microcoulomb of incident beam current is plotted against analyzer current in Fig. 10 for the fluorine target on silver, which was used in one of the Q-runs. By taking the same resonance also after the Q-run a check was obtained on the analyzer's constancy over the total time, which was found to be within 3 keV for the Q-measurement on the silver targets, and within 2 keV for the Q-run on the beryllium targets. The natural width at half height of the 873.5 keV resonance is 5.2 keV; the width in Fig. 10 is a little over 6 keV, which is due to the fluorine layer thickness of 2 keV in this case (surface angle 30°).

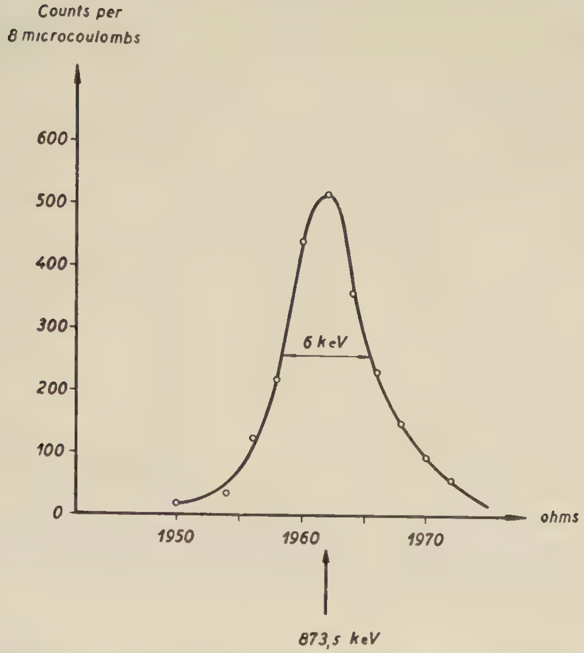

Fig. 10. Fluorine resonance at 873.5 keV used for calibration of analyzing magnet. The curve shows number of γ-counts per microcoulomb of incident beam plotted against current of magnetic analyzer, measured in terms of compensator resistance.

For the final evaluation of the proton energies in the silver and beryllium Q-runs a correction has to be made for the fluorine layer thickness. We therefore get

$$E_{P\,A_g} = 874.5 \pm 2 \text{ keV} \qquad E_{P\,Be} = 875.0 \pm 2 \text{ keV}.$$

8. The shape of the α-particle spectra

The α-spectra obtained from the reactions $O^{18}(p,\alpha)N^{15}$ and $N^{15}(p,\alpha)C^{12}$ at the same spectrometer field and at the same bombarding proton energy at the angles $= 61^{\circ}.4$ and $\theta = 135^{\circ}.0$ are given in Fig. 13 for the run on silver backings and in Fig. 14 for the run on beryllium backings. Fig. 15 shows the α-spectrum from $O^{18}(p,\alpha)N^{15}$ at $\theta = 135^{\circ}$.

As both reactions have a good yield at 873.5 keV it was not necessary to use the full solid angle of the spectrometer. A slit in the center of the gap reduced the total axial aperture $2\Delta\theta$ to 1°. For these reactions the angular energy spread of the mitted particles due to the center of mass motion, $\partial E_2/\partial\theta$, is about 6 keV per degree. Thus the energy spread of the α-particle groups due to this effect is not more than keV in the figures 11–13. The line width at half height due to target spot size, mperfections in the stabilization etc. would be expected to be about 12 keV (ref. 13). The actual line widths are larger than would be expected from these effects alone.

We see, however, that the α-lines taken in the 135°-direction are much narrower han those taken in the 60°-direction. This indicates that the line width is due to ayers. The beam-surface angle is 67°.5 for the 135°-direction and 30° for the 60°-

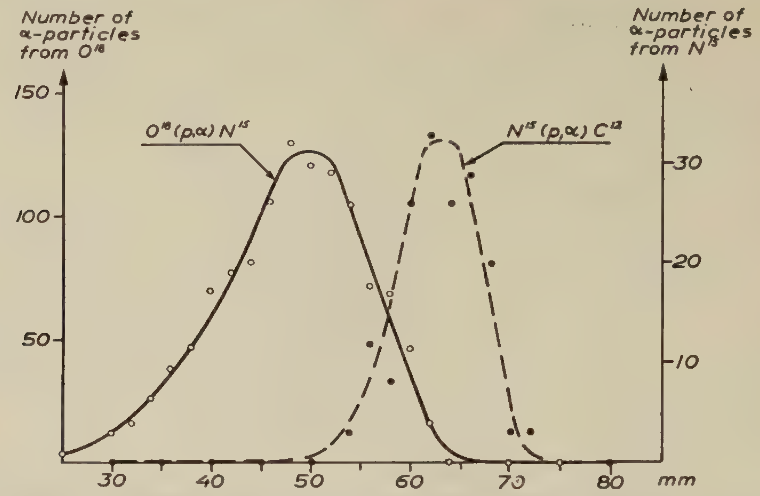

Fig. 11. Spectra of α-particles from the reaction $O^{18}(p,\alpha)N^{15}$ at $\theta = 61.^{\circ}4$ and the reaction $N^{15}(p,\alpha)C^{12}$ at $\theta = 135.^{\circ}0$. The spectrometer field and the incident proton energy, 874.5 keV, were the same for both spectra. Photographic detection. 10 mm of the photographic plate corresponds to 35.5 keV. Both targets on silver backing.

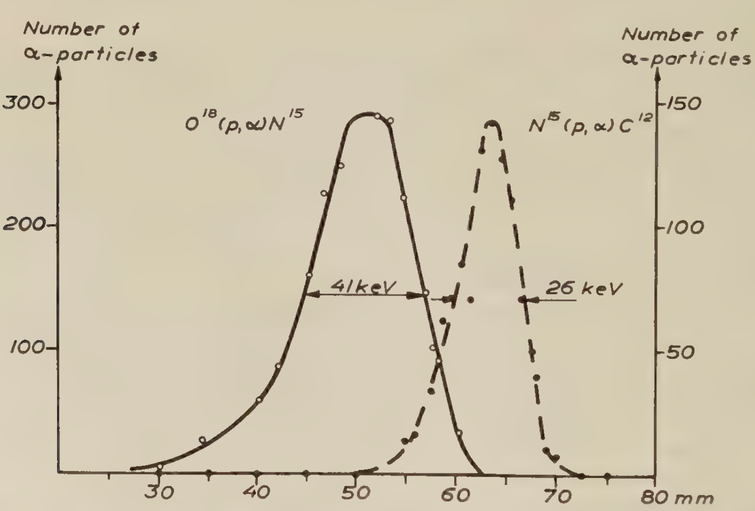

Fig. 12. Spectra of α-particles from the reaction $O^{18}(p,\alpha)N^{15}$ at $\theta = 61.^{\circ}4$ and the reaction $N^{15}(p,\alpha)C^{12}$ at $\theta = 135.^{\circ}0$. The spectrometer field and the incident proton energy, 875.0 keV, were the same for both spectra. Photographic detection. 10 mm of the photographic plate corresponds to 35.5 keV. Both targets on beryllium backing.

direction of the spectrometer (fig. 2). Thus, α-particles emitted in the 60°-direction will be slowed down by a certain layer twice as much as α-particles, emitted in the 135°-direction, by the same layer.

The widths at half height obtained for $O^{18}(p,\alpha)N^{15}$ and the two $N^{15}(p,\alpha)C^{12}$ peaks at 135° are 17 keV, 26 keV and 35 keV, and for $O^{18}(p,\alpha)N^{15}$ at 60° 41 keV in

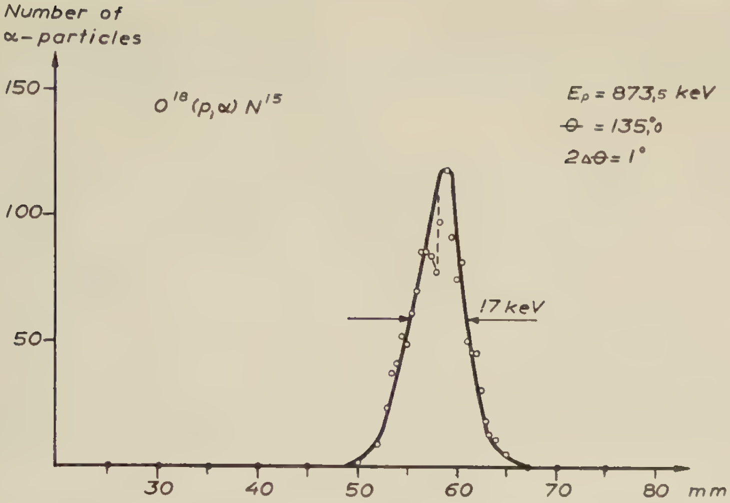

ig. 13. Spectrum of α-particles from the reaction $O^{18}(p,\alpha)N^{15}$ at $\theta = 135^\circ.0$. Incident proton nergy = 873.5 keV. Photographic detection. 10 mm of the photographic plate corresponds to 22.3 keV. Target on beryllium backing.

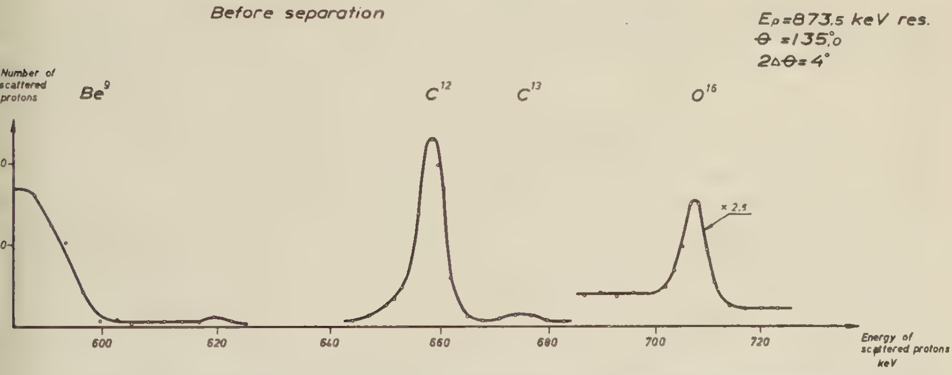

ig. 14. Spectrum of protons scattered from machined beryllium plate before separation. $\theta = 135^\circ.0$. ncident proton energy 873.5 keV. Bombardement 80 μC. Total aperture in θ-direction $2\Delta\theta = 4^\circ$. No cooling trap was used. Photographic detection.

he case of beryllium backing and 60 keV in the case of silver backing. As the stopping ower of a layer is 3.7 times larger for α-particles of 4000 keV than for protons of 73.5 keV the line widths due to layers are almost entirely caused by the slowing own of the α-particles.

Now, considering the 41 keV α-line in Be, this layer would slow down protons of 73.5 keV in the 60° direction by about 8 keV for one passage. At the same target ot the slowing down of 873.5 keV protons along the same direction due to the xternal layer on the beryllium was found to be 4 keV. We must therefore conclude at the oxygen 18 is, in the target considered, extended to a depth, in keV, which mounts to more than the external layer. It seems reasonable to assume that the xygen 18 is distributed in the external layer and to a certain depth in the beryllium acking, as the external layer was built up during the production of the target.

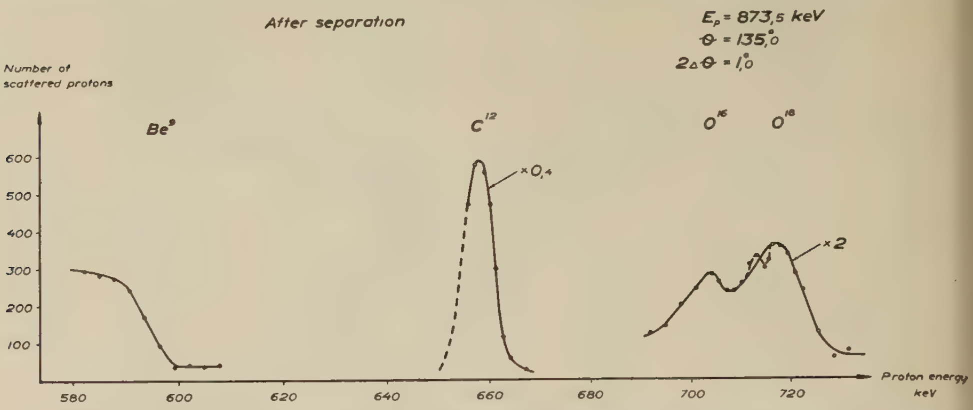

Fig. 15. Spectrum of protons scattered form separated O^{18}-target in beryllium. $\theta = 135°.0$. Incident proton energy 873.5 keV. Bombardment 80 μC. Total aperture in θ-direction, $2\Delta\theta = 1°$. Photographic detection.

9. Scattering picture of the oxygen 18 target

One would desire to get a picture of the target nuclei inside the backing material also from another approach. This is possible with scattering if the nuclei of the backing material are lighter than the target nuclei. It was actually for this reason that beryllium was chosen as a target backing. Protons scattered from beryllium will have lower energy than protons scattered from layers of heavier elements. Thus carbon and oxygen layers will cause proton peaks in an energy region where there is no background from the Be target backing.

The scattering picture was taken for two cases, from a clean, machined beryllium plate before separation and from the beryllium plate containing the separated O^{18}-target. The beam hits exactly the same spot that had been used in the measurement of the Q-value of $O^{18}(p,\alpha)N^{15}$. The proton spectra obtained with the photographic method are shown in Figs. 14 and 15. The total apertures in θ-direction were $2\Delta\theta = 4°$ and $2\Delta\theta = 1°$, and the incident proton energy 873.5 keV. In each spectrum we see the beryllium edge, the carbon-12 peak, the oxygen-16 peak and for the separated target also the oxygen-18 peak.

We will not try here to go into a very detailed interpretation of these scattering spectra but some main conclusions can be drawn. Although the oxygen-18 peak is not quite resolved from the oxygen-16 peak its width at half height is seen to be roughly 12–14 keV. This is definitely broader than the carbon peak which is about 7 keV broad. The width of the Be edge is about 5 keV. These lines are formed by protons passing the layers twice, thus the width of the O^{18} for one passage of 700 keV protons would be about 6–7 keV. This corresponds to a layer of 20 keV for α-particles of 4000 keV (ref. 19) still at $\theta = 135°$ and to 40 keV at $\theta = 60°$ (surface angle 30°). This is in agreement with the obtained line widths in the preceding section, 17 keV and 41 keV.

One curious thing may be mentioned here. In the scattering peak of oxygen 18 there is a small bump about 5 keV below the main peak, denoted by a dashed line in Fig. 15. The same structure is found in the α-peak of Fig. 13, where there is a bump 8 keV below the main peak. Taking into account the relative stopping cross ctions for protons and alphas of these energies and the twofold proton passage in e scattering we find that the bumps and their positions both are explained, if we ssume the target to be a double layer with a layer spacing of 2.5 keV for protons 700 keV.

The scattering picture also gives a rough estimation of the number of nuclei rming the layers. From the number of tracks in the carbon peak (75 000) of Fig. 15, om the number of microcoulombs (80) in the bombardment, from the solid angle nd the experimental cross section for proton scattering on carbon (ref. 20) the umber of carbon nuclei in the surface layer is calculated to 2.6 × 10^{17} C^{12} nuclei er cm². This corresponds to a stopping thickness of 2.5 keV for protons of 700 keV, hich is in agreement with the thickness of the external layer, discussed in section 6.

As to the number of O^{18}-nuclei in the target we can proceed in the same way. ere, however, we do not have any experimental value of the scattering cross ction, so we have to use the Rutherford scattering formula, which may be wrong y a factor of 2 or 3 because we are in the neighbourhood of a resonance. We obtain × 10^{17} O^{18} nuclei per cm².

From the total of α-tracks of the $O^{18}(p,\alpha)N^{15}$ reaction (Fig. 12), 16 000 tracks at 0 μC bombardment, and from the number of protons in the scattering peak (Fig.), 27 000 tracks at 80 μC bombardment, we obtain the ratio of the reaction cross ction at 60° to the scattering cross section at 135° as 0.049.

The number of tracks in the α-peak of Fig. 13 indicates a smaller cross section r the $O^{18}(p,\alpha)N^{15}$ reaction in the 135° direction, by a factor of 5, which might due to a strong angular distribution.

10. Evaluation of the α-spectra

In the evaluation of α-spectra from nuclear reactions there is a choice between fferent methods of reading the peaks. One may take the energy values from the sitions of the peak maxima or from some part of the high energy edge. What ethod to choose in a given case depends on which are the most important of the any factors contributing to the peak shape, such as source size, layer stopping, gular energy spread due to the motion of the center of mass, aberrations etc. hen the predominant factor determining the line width (say for instance the gular energy spread at full solid angle) is symmetric with respect to the correspond-g experimental parameter determining the line position (in this example θ) one ould prefer to use the peak maxima for defining the line positions, and make cessary corrections for other parameters (for instance layer corrections.).

In the present case the predominant cause for the line width is the target layer. ere we do not have the symmetry conditions and prefer to use the high energy ge of the lines, extrapolated as a straight line to zero. This seems to be justified the fact that we are interested in the difference of the position of two reaction groups. The angular energy spread is small in the present case, because we have stricted the axial aperture angle to 1°, and it is very nearly the same for both actions, namely 6.1 keV and 5.5 keV. The aberration width is also small and the me for the α-groups from both reactions. The layer thicknesses are about the me but cause different stopping because of the different angles of emission. Thus e important thing is to get rid of the layer effects; this is best done by a straight e extrapolation to zero. The statistics of the peaks in Figs. 11 and 12 is thought be sufficient for applying this method.

The position differences as measured in this way from the two independent runs on silver backings and beryllium backings in Figs. 11 and 12 are 8.0 ± 2 mm and 8.5 ± 1.5 mm, corresponding to the energy differences 27 ± 7 keV and 30 ± 5 keV. Here we have used the dispersion from ref. 13, which gives 10.0 mm in the plate = = 35.5 ± 2 keV at 3980 keV.

11. Calculation of the *Q*-value from the measured quantities

The Q-value of $O^{18}(p,\alpha)N^{15}$ is calculated in the following way: the energy of the α-particles from $N^{15}(p,\alpha)C^{12}$ is calculated; the energy difference obtained from the spectra is subtracted; the Q-value is calculated. This is done with the appropriate experimental corrections and with relativity corrections.

If M_0, M_1, M_2 and M_3 are the masses of the target nucleus, the bombarding particle, the emitted particle and the residual nucleus, respectively, if E_1 and E_2 are the energies of the bombarding particle and the emitted particle, and if θ is the angle between the directions of the incident particle and the emitted particle, non-relativistic expressions for $\sqrt{E_2}$ and Q can be written as (ref. 21)

$$\sqrt{E_2} = \frac{\sqrt{M_1 M_2}}{M_2+M_3}\cdot\sqrt{E_1}\cdot\cos\theta + \sqrt{\frac{M_3}{M_2+M_3}Q + \frac{M_3-M_1}{M_2+M_3}E_1 + \frac{M_1 M_2}{(M_2+M_3)^2}E_1\cos^2\theta} \qquad (2)$$

$$Q = \frac{M_3+M_2}{M_3}E_2 - \frac{M_3-M_1}{M_3}\cdot E_1 - 2\,\varepsilon\cos\theta \qquad (3)$$

where

$$\varepsilon = \frac{\sqrt{M_1 M_2 E_1 E_2}}{M_3} \qquad (4)$$

In these expressions the nuclear masses are to be used, not integer mass numbers.

Three different relativistic effects enter into an experiment of the present type, namely in the determination of the incident particle energy, in the determination of the observed emitted particle energy, and in the dynamics of the reaction. In the present investigation the first two effects do not appear in the calculations because of the calibration methods used. The third effect is taken into account by replacing the masses M by effective masses M_{eff} according to (ref. 21).

$$M_{\mathrm{eff}} = M + \frac{E}{2c^2}. \qquad (5)$$

In this way we obtain from the two independent runs the Q-value of the reaction $O^{18}(p,\alpha)N^{15}$

$Q = 3.963 \pm 0.011$ MeV $Q = 3.959 \pm 0.009$ MeV.

We adopt the mean value

$Q = 3.961 \pm 0.009$ MeV.

12. Probable errors.

he probable errors of the different measurements have been discussed in the ceding sections and are summarized in table II.

Table II

Source of error	Probable error	
	Silver run	Beryllium run
Proton energy	2 keV	2 keV
Statistical error of E_2	7 keV	5 keV
Angle of observation	$0\overset{\circ}{.}2$	$0\overset{\circ}{.}2$
Q-value of $N^{15}(p, \alpha) C^{12}$	6 keV	6 keV

o obtain the probable error in E_2 we reduce the errors to E_2 by means of the nulae

$$\frac{\partial E_2}{\partial E_1} = \frac{M_3 - M_1 + (M_3 \varepsilon / E_1) \cos \theta}{M_2 + M_3 - (M_3 \varepsilon / E_2) \cos \theta} = 0.48 \text{ for } N^{15}(p, \alpha) C^{12} \tag{6}$$

$$\frac{\partial E_2}{\partial \theta} = - \frac{2 M_3 \varepsilon \sin \theta}{M_2 + M_3 - (M_3 \varepsilon / E_2) \cos \theta} = 5.6 \text{ keV for } N^{15}(p, \alpha) C^{12} \tag{7}$$

$$\frac{\partial E_2}{\partial Q} = \frac{M_3}{M_2 + M_3 - (M_3 \varepsilon / E_2) \cos \theta} = 0.72 \tag{8}$$

Ve obtain a total error of E_2 for the α-particles from $N^{15}(p,\alpha)C^{12}$ which is 4.5 keV ore the statistical error is taken into account. The statistical error and the disper- error are accounted for in the error of $E_2(N^{15}) - E_2(O^{18})$. The total error of for $O^{18}(p,\alpha)N^{15}$ is thus 8.3 keV in the silver run and 6.7 keV in the beryllium . We now reduce these errors and the experimental errors of table II to Q to ain the total error in the Q-value of O^{18}. This is done by means of the formulae

$$\frac{\partial Q}{\partial E_1} = - \frac{M_3 - M_1}{M_3} - \frac{\varepsilon}{E_1} \cos \theta = -1.1 \text{ for } O^{18}(p, \alpha) N^{15} \tag{9}$$

$$\frac{\partial Q}{\partial E_2} = \frac{M_2 + M_3}{M_3} - \frac{\varepsilon}{E_2} \cdot \cos \theta = 1.3 \text{ for } O^{18}(p, \alpha) N^{15} \tag{10}$$

$$\frac{\partial Q}{\partial \theta} = 2 \varepsilon \sin \theta = 7.5 \text{ keV/degree for } O^{18}(p, \alpha) N^{15} \tag{11}$$

he total probable error ΔQ in the Q-values is now given by

$$\Delta Q = \sqrt{\left(\frac{\partial Q}{\partial E_1} \Delta E_1\right)^2 + \left(\frac{\partial Q}{\partial E_2} \cdot \Delta E_2\right)^2 + \left(\frac{\partial Q}{\partial \theta} \cdot \Delta \theta\right)^2}$$

re ΔE_1 and $\Delta \theta$ here are the experimental probable errors of E_1 and θ and ΔE_2 he total error in E_2, given above for the two cases. We obtain a total probable r of the Q-value of the reaction $O^{18}(p,\alpha)N^{15}$ of 11 keV and 9 keV for the two pendent runs.

13. The atomic mass of oxygen 18

From our Q-value of $O^{18}(p,\alpha)N^{15}$ we calculate the mass of O^{18} using the atomic masses of H^1, D^2 and N^{15} from nuclear data, namely (ref. 4):

$$\begin{aligned} H^1 &= 1.008142(\pm\ 3)\ \text{amu} \\ He^4 &= 4.003873(\pm 15)\ \text{amu} \\ N^{15} &= 15.004863(\pm 12)\ \text{amu} \end{aligned}$$

With 1 amu = 931.152 MeV we get the following value:
Atomic mass of O^{18} *= 18.004848 ± 0.000022 amu.*
The largest contribution to the probable error in this value comes from the uncertainty in our knowledge of the He^4 mass.

14. Discussion of results

The present Q-value is in agreement with earlier measurements in the Cavendish Laboratory, which gave $Q = 3.96 \pm 0.15$ MeV (ref. 22), $Q = 3.97 \pm 0.05$ MeV (ref. 6) and $Q = 3.96 \pm 0.04$ MeV (ref. 7). The atomic mass of O^{18} obtained from the present work is somewhat lower than Ewald's mass spectroscopic value 18.004875 ± 0.000013 (ref. 23) and Ogata's msp value 18.004883 ± 0.000020 (ref. 24). The difference between our mass of O^{18} and the msp values, 27 and 35 μMU resp., is perhaps not surprising in view of the fact that Ewald's and Ogata's msp values for N^{15} are considerably higher, 65 and 39 μMU resp., than the nuclear reaction value for N^{15}.

The nuclear reaction cycle connecting the neon and fluorine isotopes which was discussed in the introduction is schematically represented in Fig. 16. The reactions are:

(1)	$F^{19}(p,\alpha)O^{16}$	$Q_1 = 8.124 \pm 0.007$	adjusted (ref. 4)
(2)	$O^{16}(d,\alpha)N^{14}$	$Q_2 = 3.116 \pm 0.009$	»
(3)	$N^{14}(d,p)N^{15}$	$Q_3 = 8.608 \pm 0.007$	»
(4)	$O^{18}(p,\alpha)N^{15}$	$Q_4 = 3.961 \pm 0.009$	experimental
(5)	$O^{18}(p,n)F^{18}$	$Q_5 = 2.453 \pm 0.002$	»
(6)	$Ne^{20}(d,\alpha)F^{18}$	$Q_6 = 2.78\ \ \pm 0.02$	»
(7)	$Ne^{20}(d,p)Ne^{21}$	$Q_7 = 4.529 \pm 0.007$	»
(8)	$Ne^{21}(d,\alpha)F^{19}$	$Q_8 = 6.432 \pm 0.010$	»

We obtain the mass difference $2H^2 - He^4$ from the cycle by taking (1) + (2) + (3) − − (4) + (5) − (6) + (7) + (8):

$$2H^2 - He^4 = (n + H^1 - H^2) + (Q_1 + Q_2 + Q_3 + Q_5 + Q_7 + Q_8) - (Q_4 + Q_6).$$

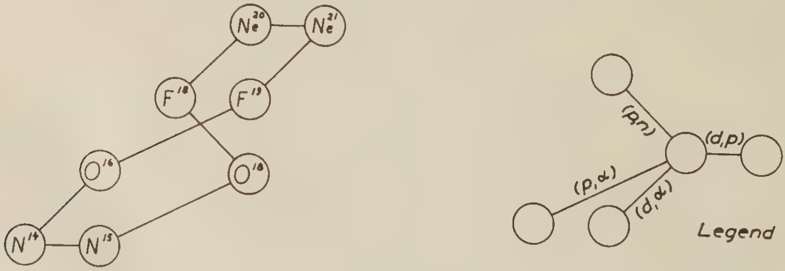

Fig. 16. Representation of nuclear reaction cycle containing $O^{18}(p,\alpha)N^{15}$.

ı $n + H^1 - H^2 = 2.225 \pm 0.002$ from ref. 4 we get

$$2H^2 - He^4 = 23.840 \pm 0.029 \text{ MeV.}$$

nis is in agreement with the weighted mean of $2H^2 - He^4 = 23.834 \pm 0.007$ MeV
is obtained from several nuclear cycles in the region of very light nuclei (ref. 4).
agreement shows the consistency of the Q-values entering into the cycle con-
red. It seems to be justified to use the cycle to get additional information on the
s differences between neon and fluorine isotopes. This is done by calculating
Q-value of $Ne^{21}(d,\alpha)F^{19}$ as expected from the Q-values of the reactions (1)–(7).
h $n + H^1 - H^2 = 2.225 \pm 0.002$ MeV and $2H^2 - He^4 = 23.834 \pm 0.007$ MeV from
4 we calculate $Q = 6.426 \pm 0.028$ MeV for $Ne^{21}(d,\alpha)F^{19}$, which is in agreement
the observed $Q = 6.432 \pm 0.010$ MeV of this reaction (ref. 1).

hus, the present Q-value of O^{18} (p,α) N^{15} confirms the mass differences between
and fluorine isotopes as obtained with the reaction Ne^{21} (d,α) F^{19} and the
ansitions F^{20} (β^-) Ne^{20}.

15. Acknowledgements.

he author is indebted to Professor MANNE SIEGBAHN for his interest in this
x, to Tekn. lic. S. THULIN for separating the targets, and to Tekn. lic. R. T.
LI and Civiling. K. AHNLUND for their help in the runs.

obel Institute of Physics, Stockholm 50, Sweden.

RÉFÉRENCES

Mileikowsky, C. and Whaling, W., Phys. Rev. 88, 1254 (1952).
Alburger, D. E., Phys. Rev. 88, 1257 (1952).
Wong, C., Bull. Am. Phys. Soc. 27, No 6, 7 (1952).
Li, C. W., Whaling, W., Fowler, W. A., and Lauritsen, C. C., Phys. Rev. 83, 512 (1951).
Li, C. W., Phys. Rev. 88, 1038 (1952).
Freeman, J. M., Proc. Phys. Soc. A 63, 688 (1950).
Seed, J., Phil. Mag. 42, 566 (1951).
Strait, E. N., van Patter, D. M., Buechner, W. W., and Sperduto, A., Phys. Rev. 81, 747 (1951).
Van Patter, D. M., Sperduto, A., Endt, P. M., Buechner, W. W., and Enge, H. A., Phys. Rev. 85, 142 (1952).
Richards, H. T., Smith, R. V., and Browne, C. P., Phys. Rev. 80, 524 (1950).
Middleton, R., and Tai, C. T., Proc. Phys. Soc. A 64, 801 (1951).
Mileikowsky, C., Ark. f. Fys. Bd 4, Nr 16, 337 (1952).
—— Ark. f. Fys. Bd 7, Nr 3, 33 (1953).
Mileikowsky, C., and Pauli, R. T., Ark. f. Fys. Bd 4, Nr 12, 287 (1952).
Pauli, R. T., Ark. f. Fys. (to be published).
Herb, R. G., Snowdon, S. C., and Sala, O., Phys. Rev. 75, 246 (1949).
Bergström, I., Thulin, S., Svartholm, S., and Siegbahn K., Ark. f. Fys. Bd 1, Nr 11, 281 (1949).
Mileikowsky, C. and Pauli, R. T., Ark. f. Fys. Bd 4, Nr 13, 299 (1952).
Livingston, M. S., and Bethe H. A., Rev. Mod. Phys. 9, 245 (1937).
Williamson, R. M., Browne, C. P., Craig, D. S., and Donahue, D. J., Phys. Rev. 84, 731 (1951).

21. Brown, A. B., Snyder, C. W., Fowler, W. A., and Lauritsen, C. C., Phys. Rev. 82, 159 (1951).
22. Burcham, W. E., and Smith, C. L., Nature 143, 795 (1939).
23. Ewald, H., Z. Naturforsch. 6 a, 293 (1951).
24. Ogata, K., and Matsuda, H., Phys. Rev. 89, 27 (1953).

Tryckt den 13 maj 1953

Uppsala 1953. Almqvist & Wiksells Boktryckeri AB

ARKIV FÖR FYSIK Band 7 nr 9

Communicated 27 May 1953 by MANNE SIEGBAHN and BENGT EDLÉN

Gamma-rays, X-rays and bremsstrahlung from Tm^{170} sources

By K. LIDÉN and N. STARFELT

With 5 figures in the text

Summary. The spectral distribution of the electromagnetic radiation from a thin m^{170} source placed between Tm radiators of various thickness has been investigated sing a scintillation spectrometer. The experimental results have been used in a alculation of the relative intensities of the γ-rays, the x-rays and the brems-trahlung from homogeneously activated Tm^{170} sources. The calculated distribution f the radiation from a Tm^{170} source, 1.0 g/cm^2, shows good agreement with experi-nents. With a Tm^{170} source, 150 mg/cm^2, the intensity of the continuous external remsstrahlung excited by the β-particles in the source, amounts to 29 % of the otal intensity. With 1.0 g/cm^2 the spectral composition is 10 % 84 keV γ-rays, 7 % Tm + Yb K x-rays, and 43 % bremsstrahlung.

1. Introduction

Under certain circumstances the bremsstrahlung from γ-sources and the x-rays rom absorption and ionisation processes within the source may be of special inter-st. This is especially the case for high β-energies, thick sources, and elements with igh atomic numbers. Furthermore, if only a small part of the decays are followed y emission of γ-quanta and internal conversion electrons, the above mentioned adiation may give an important contribution to the γ-radiation. Therefore, in at-empts to produce monochromatic γ-ray sources these facts may play an important ôle.

Previously it has been shown (LIDÉN STARFELT 1953 a) how, in addition to the ontinuous bremsstrahlung, β-rays excite K x-rays especially from elements of high tomic number. Recently the interest in monochromatic, soft γ-radiation for special edical and industrial applications has increased. MAYNEORD (1952) and WEST 1953) discuss in detail the possibilities of using Tm^{170} for such purposes. A possible isturbance by the bremsstrahlung is noticed but is not treated further from lack f experimental data.

2. The radiations from Tm^{170}

A detailed investigation of the disintegration of Tm^{170} has been performed by RAHAM *et al.* (1952). They also give a complete list of earlier measurements. Tm^{170} ecays with a half life of 127 days by β-emission. 76 % of the disintegrations proceed

Table 1. Wavelengths λ (X. U.) (LANDOLT-BÖRNSTEIN 1950) and quantum energies E (keV) of Tm and Yb K x-rays.

		α_2	α_1	β_3	β_1	β_2	K-edge
Tm	λ:	248.61	243.87	215.58	214.87	209.8	208.5
	E:	49.79	50.76	57.42	57.61	59.0	59.4
Yb	λ:	240.98	236.28	209.16	208.34	203.22	201.6
	E:	51.37	52.39	59.18	59.42	60.91	61.4

directly to the ground state of Yb^{170} with a β-ray energy of 968 keV. The other β-component with the energy 884 keV proceeds to the ground state of Yb^{170} via an excited state emitting 84.1 keV γ-rays or internal conversion electrons. The conversion coefficients are (GRAHAM *et al.*) $\alpha_K = 1.6$, $\alpha_L = 4.1$ and $\alpha_M = 1.2$. Thus 3.2 % of the disintegrations give 84 keV γ-rays, 5.1% Yb K x-rays (Table 1, mean energy K_α, K_β: 54.1 keV) and 17 % Yb L and M x-rays with energies less than 10 keV. Furthermore, there is a weak continuous γ-spectrum, the internal bremsstrahlung, the largest intensity of which is in the low energy part of the spectrum. Some observations of γ-lines with higher energies than 84 keV, not found by GRAHAM *et al.*, may be caused by the bremsstrahlung.

For a thick source, the composition of the emitted electromagnetic radiation is modified. Continuous bremsstrahlung is excited by the β-radiation. Photoelectric absorption in the source of bremsstrahlung quanta and of 84 keV γ-quanta result in emission of the K x-rays of Tm (Table 1, mean energy K_α, K_β: 52.9 KeV). K x-rays are also emitted by Tm atoms, ionized by the β-rays.

3. Apparatus and measurements

To predict more exactly the composition of the radiation from various Tm^{170} sources we have investigated the spectral distribution of the electromagnetic radiation from a thin Tm^{170} source sandwiched by two inactive Tm_2O_3 radiators, the thickness of which have been varied.

The investigations were performed with a scintillation spectrometer using a NaI (Tl) crystal 16 × 16 × 16 mm in conjunction with an E.M.I. 5311 photomultiplier and a single channel differential discriminator. The mounting of the thin Tm^{170} source between the Tm_2O_3 discs (area 0.50 cm^2), the collimator and the crystal are shown in Fig. 1. The spectrometer has been calibrated using the following γ- and x-ray lines: Hg^{203} 280 keV, Ce^{141} 145 keV, Tm^{170} 84 keV and Yb K x-rays 53.5 keV. The Yb K x-ray peak value has been calculated from the Gaussian distribution of K_{α_1}, K_{α_2}, $K_{\beta_{1,3}}$ and K_{β_2} lines using the relative intensities 100 : 50 : 35 : 15 and the actual resolving power. The measurements are corrected for crystal efficiency; the correction for the Compton electrons had no appreciable effect on the distribution. In Fig. 2 the total absorption, the theoretical and the effective photoelectric absorption in the actual crystal are represented. The latter has been determined by investigation of the photo- and Compton electron spectrum of the γ-lines Hg^{203} 280 keV, Au^{198} 412 keV, Cs^{137} 662 keV and Rb^{86} 1080 keV (LIDÉN-STARFELT 1953 b). Throughout the paper we have used absorption data from WHITE (1952).

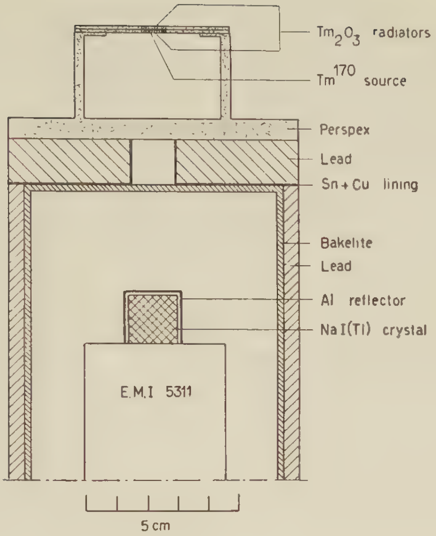

Fig. 1. Source and radiator mounting; detector part of the spectrometer.

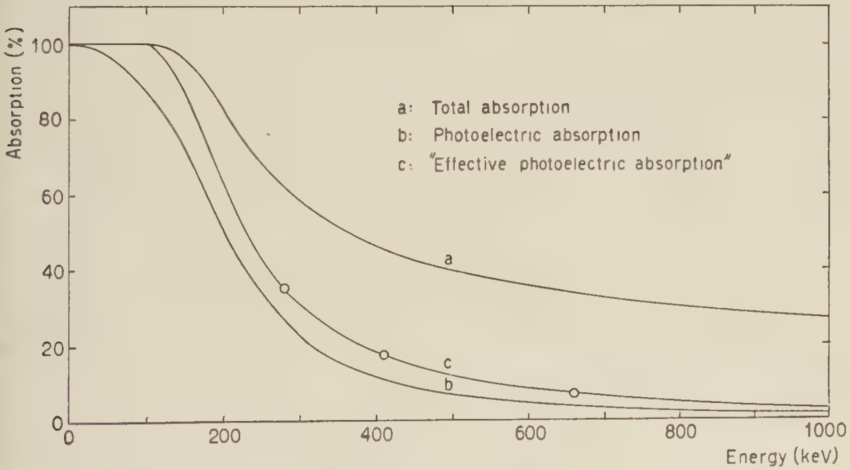

Fig. 2. Crystal efficiency.

4. Results

Fig. 3 (a) shows a plot of the spectrum from the thin Tm^{170} source without Tm_2O_3 radiators. Since one knows the K x-ray escape factor for the crystal, the K fluorescense yield of Yb and the Gaussian distribution of each single γ-ray and K x-ray line it is possible to calculate the K-conversion coefficient, α_K, of Tm^{170} 84 keV from the diagram, corrected for the internal bremsstrahlung. This radiation was measured

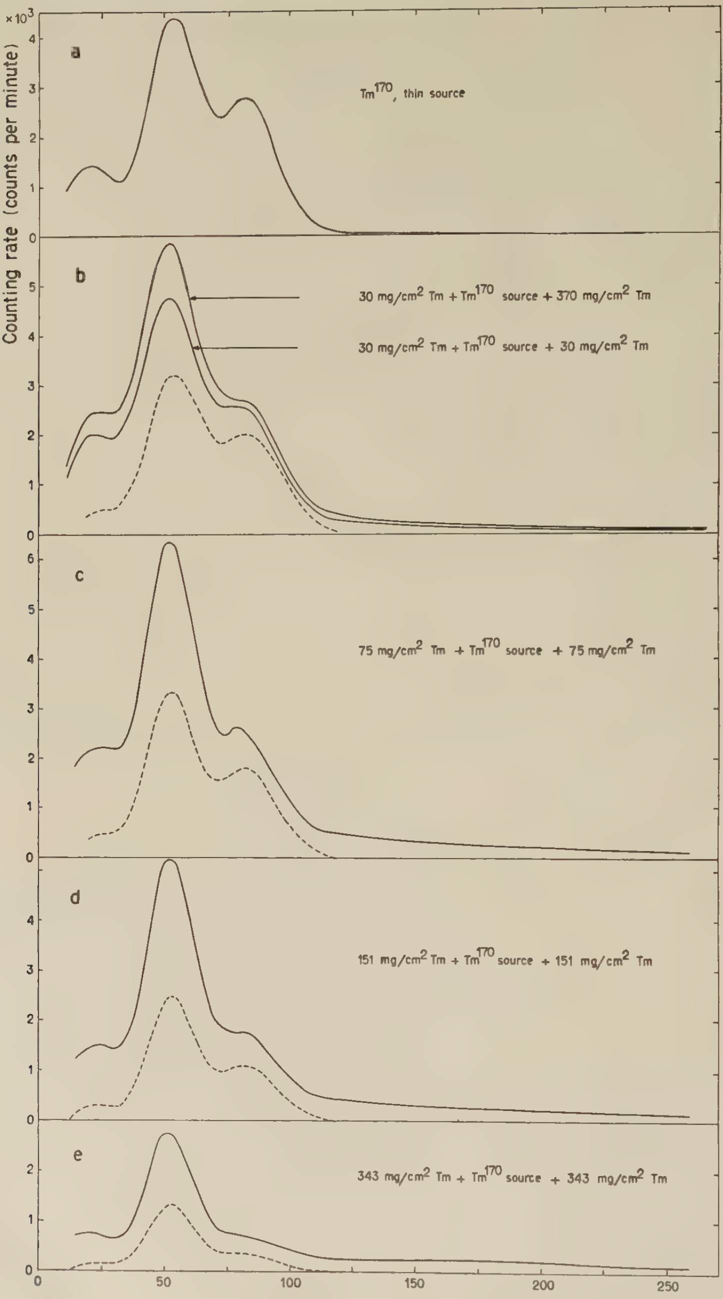

Fig. 3. The measured spectral distribution of the γ-rays, x-rays and bremsstrahlung from (a) a thin Tm^{170} source and (b)–(e) Tm^{170} surrounded by Tm_2O_3 radiators. Above 100 keV the curves are corrected for crystal efficiency. The dashed curves represent the radiation from the thin Tm^{170} source, attenuated in the radiator.

perimentally above 100 keV; the distribution obtained was extrapolated to lower ergies through comparison with the internal bremsstrahlung from Ra E (MADAN-Y, RASETTI 1951). Our result, $\alpha_K = 1.56 \pm 0.15$, agrees with that of GRAHAM *et al.*, $= 1.60 \pm 0.15$, and MCGOWAN (1952), $\alpha_K = 1.5 \pm 0.2$, obtained with thin sources. The other curves in Fig. 3 show measurements with 30, 75, 151, and 343 mg/cm^2 ı radiator, in the shape of Tm_2O_3 discs, placed on each side of the Tm^{170} source st mentioned. The dashed curves in Fig. 3 show the primary radiation from the ırce after attenuation in the respective radiators. (The absorption data of Tm ve been graphically interpolated from WHITE's data for Sn, I, W, Pt and Pb). *e difference between the two curves must consist of bremsstrahlung and K x-rays m Tm.*

From each diagram, the intensity of the bremsstrahlung with energy higher than keV and the intensity of the Tm K x-rays + the bremsstrahlung between 30 and keV are calculated. The radiation spectrum from a homogeneously activated ı^{170} source may be considered as consisting of the following four components: ı^{170} 84 keV γ-rays (A), Yb K x-rays (B), Tm K x-rays + bremsstrahlung 30–85 V (C), and bremsstrahlung above 85 keV (D). The mean quantum energy of the emsstrahlung above 85 keV, calculated from the measured spectral distributions 150–160 keV. This value is found to be almost independent of the source thickss.

If we assume a cylindrical source divided into thin layers, perpendicular to the is, the total radiation in the direction of the axis may be obtained by taking the n of the contributions from all the layers. To investigate as accurately as possible variation of this contribution with the position of the layer, the above menned measurements have been supplemented by measurements with a thin radiator the direction of the detector and a thick radiator on the other side of the Tm^{170} ırce. The intensities of the four components are then represented in Fig. 4, where ı^{170} 84 keV without radiator is put equal to 100, and the intensities of the other nponents are normalized on the basis of this value. On the curves (C) and (D) in ;. 4 the points at zero and 30 mg/cm^2 are measured with the radiator combinations ro + 370 mg/cm^2 and 30 + 370 mg/cm^2 respectively. The other points on these rves represent measurements with identical radiators on both sides of the Tm^{170} ırce. There are no experimental points in the region above 343 mg/cm^2. Here the ape of the curves is determined only by the absorption in the source and thus ey may easily be extrapolated from the experimentally determined parts of the rves.

From the diagram, the intensities of the different radiation components of a ck homogeneously activated source may be calculated by integrating the curves er the whole thickness of the source.

The curves (C) and (D) of the diagram are based on measurements of certain tinct radiator combinations, each of which corresponds to a certain homogeneous ı^{170} source. However, investigations have shown that the emission of the principal rt (> 90%) of the components (C) and (D) takes place within 75 mg/cm^2 from a Tm^{170} er. For instance, the radiator combinations 75 + 75 mg/cm^2 and 75 + 370 mg/cm^2 pectively give the same intensity within the experimental error both for (C) and (D). This fact shows also that the above mentioned extrapolation of the curves ainst larger source thickness is allowed. In calculating the intensities of the nponents (C) and (D) for a homogeneous Tm^{170} source thicker than 150 mg/cm^2 curves are valid without restrictions except in the back region of 75 mg/cm^2.

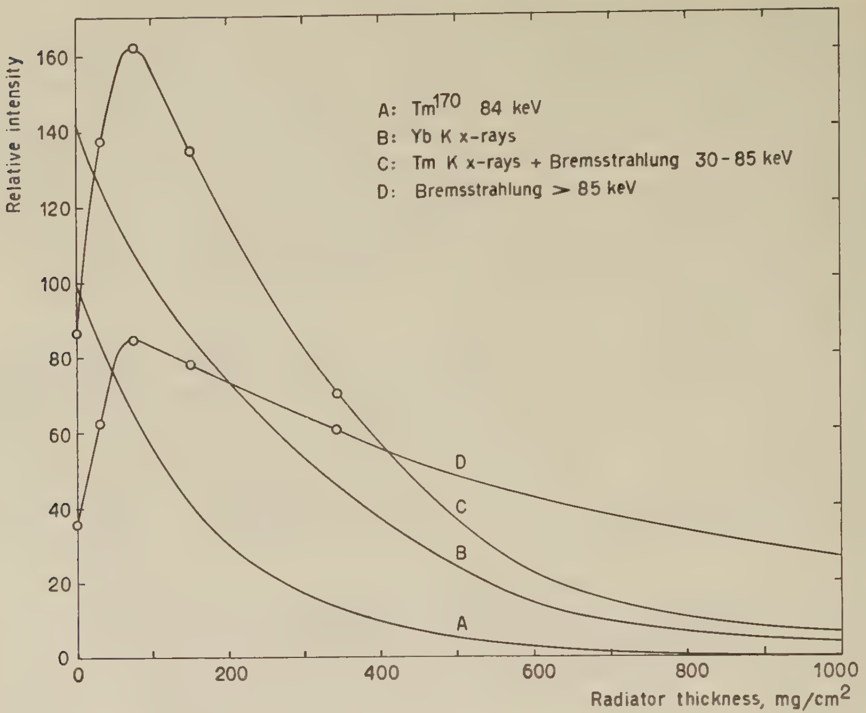

Fig. 4. The relative intensities of the radiation components, (A) 84 keV γ-rays, (B) Yb K x-rays, (C) Tm K x-rays + bremsstrahlung 30–85 keV and (D) bremsstrahlung above 85 keV, plotted against the radiator thickness.

For the end layer (75 mg/cm²) in the direction of the detector, (C) and (D) are valid because the points at zero, 30 and 75 mg/cm² are measured with a back radiator larger than 75 mg/cm². In using the curves (C) and (D) a small correction has to be made for the contribution from the end layer of 75 mg/cm² on the back of a thick source. At the back surface of the source half the intensity of the radiation, the β-rays as well as the γ-rays, x-rays and bremsstrahlung, escapes from the source. In this back surface layer considered as a radiation source, only half as much of the components (C) and (D) is created as in a radiating layer with more than 75 mg/cm² Tm on both sides. The correction of the curves (C) and (D) for the back 75 mg/cm² of a source with d mg/cm² total thickness is performed by taking the relative intensity at the thickness d equal to 59 % and 53 % of the value on the curve (C) and (D) respectively. From this point a curve is drawn which is fitted to the original curve at $(d-75)$ mg/cm².

In Table 2 the relative intensities of (A)-(D) are calculated for some different cylindrical sources with equal diameters and equal specific activity. As a comparison, the same components for a thin source are also given in Table 2. In this case (C) and (D) consist of internal bremsstrahlung. From the table it appears how rapidly the continuous bremsstrahlung above 85 keV (component (D)) increases with increasing source thickness, compared with the 84 keV γ-rays [component (A)]. From *ble 2.* Relative intensities of the radiation components A, B, C and D from homogeneously activated Tm^{170} sources, having the same specific activity.

Source-thickness mg/cm²	A	B	C	D
150	100	165	201	100
300	141	268	366	210
600	164	362	517	370
1 000	167	391	566	507
0	100	142	20	9

ble 3. Percentage contribution of the components I, II and III to the total radiation from Tm^{170} sources.

Source-thickness mg/cm²	I	II	III
150	18	53	29
300	14	52	34
600	12	50	38
1 000	10	47	43
0	37	52	11

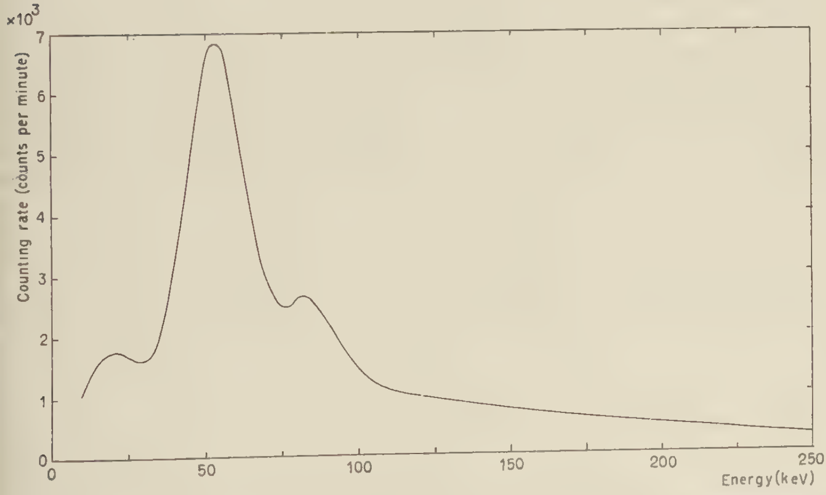

. 5. The experimental spectral distribution of the γ-rays, x-rays and bremsstrahlung from a nogeneously activated Tm^{170} source, 1.0 g/cm². (Above 100 keV the curve is corrected for crystal efficiency.)

a previous investigation of x-rays excited in lead by the β-radiation from P^{32} (Lidén-Starfelt 1953 a), the contribution of the Tm K x-rays to component (C) is estimated to be at least $^2/_3$. On this basis Table 3 has been calculated. Here the intensity of the 84 keV γ-ray (I), Yb + Tm K x-rays (II), and the continuous bremsstrahlung above 30 keV (III), respectively, are given in per cent of the total intensity.

As an illustration of the usefulness of the above given method of calculation, we have compared the measured spectral distribution (Fig. 5) from a homogeneously activated Tm^{170} source (1.0 g/cm^2, diameter 5 mm) with calculated values of the components (A), (B) + (C) and (D). Fig. 5 gives (11 ± 2) %, (58 ± 3) % and (31 ± 2) % for (A), (B) + (C) and (D) respectively, while the calculation from Fig. 4 gives 10 %, 59 %, and 31 %.

5. Conclusions

From this investigation it may be concluded:

a) With increasing source thickness the contribution to the total radiation intensity from the Tm^{170} γ-line, 84 keV, decreases rapidly. (Table 3.)

b) The simultaneous decrease of the intensity of the Yb K x-rays is compensated by the creation of Tm K x-rays (Table 3).

c) The continuous bremsstrahlung increases strongly with increasing source thickness. At 1000 mg/cm^2 it reaches an intensity which is almost as high as the intensity of the K x-rays from Yb + Tm. The mean quantum energy of the bremsstrahlung above 85 keV is about 150 keV, almost independent of the source thickness.

d) A similar distribution to that of Tm^{170}, 0.5–1.0 g/cm^2, for the K x-rays and the bremsstrahlung, may be obtained from a P^{32} (or Sr^{90}) + 500 mg/cm^2 Pb radiator (Lidén–Starfelt 1953 a).

Radiation Physics Department, University of Lund, Sweden. May 1953.

REFERENCES

Burhop, E. H. S., 1952, *The Auger Effect and Other Radiationless Transitions* (Cambridge: University Press).
Graham, R. L., Wolfson, J. L., and Bell, R. E., 1952, Canadian Journal of Physics *30*, 459.
Landolt–Börnstein, 1950, *Zahlenwerte und Funktionen, vol. I, 1* (Berlin: Springer).
Lidén, K., and Starfelt, N., 1953 a, Arkiv för Fysik, in the press; 1953 b, to be published in Arkiv för Fysik.
Madansky, L., and Rasetti, F., 1951, Phys. Rev. *83*, 187.
Mayneord, W. V., 1952, British Journal of Radiology *25*, 517.
McGowan, F. K., 1952, Phys. Rev. *85*, 151.
West, R., 1953, Nucleonics *11*, No 2, 20.
White, G. R., 1952, *X-ray Attenuation Coefficients from 10 keV to 100 MeV*. National Bureau of Standards Report 1003.

Tryckt den 12 september 1953

Uppsala 1953. Almqvist & Wiksells Boktryckeri AB

ARKIV FÖR FYSIK Band 7 nr 10

Communicated 13 May 1953 by M. Siegbahn and G. Borelius

Reaction energy of $Ne^{20}(d, \alpha) F^{18}$ by magnetic analysis

By Curt Mileikowsky

With 2 figures in the text

I. Introduction.

The reaction $Ne^{20}(d, \alpha) F^{18}$ is a member of the important nuclear reaction ycle (ref. 1, 2).

$$F^{19}(p, \alpha) O^{16},\ O^{16}(d, \alpha) N^{14},\ N^{14}(d, p) N^{15},\ O^{18}(p, \alpha) N^{15}$$
$$O^{18}(p, n) F^{18},\ Ne^{20}(d, \alpha) F^{18},\ Ne^{20}(d, p) Ne^{21},\ Ne^{21}(d, \alpha) F^{19}$$

All the other reactions in this cycle are measured accurately by magnetic nalysis or threshold experiments (ref. 2, 4, 5, 6, 7) and it was regarded desirable o measure also $Ne^{20}(d, \alpha) F^{18}$ by magnetic analysis. $Ne^{20}(d, \alpha) F^{18}$ has earlier een measured by Middleton and Tai with the range method (ref. 3).

2. Experimental set-up and procedure.

For this experiment the Cockcroft-Walton accelerator (ref. 8) of the Nobel nstitute was used together with the nuclear spectrometer for heavy particles ef. 9, 10). The experimental set-up utilized was described in ref. 2. Five dif- erent targets were mounted on the rotatable target carrier, namely

1. Thin fluorine on silver backing
2. Aluminum evaporated on aluminum backing
3. Beryllium evaporated on beryllium backing
4. Thin Ne^{20}-target electromagnetically separated on silver backing
5. Thin O^{16}-target oxydized on silver backing.

The calibration of the bombarding beam was made with the fluorine resonance or protons. Protons of 873.5 keV were then scattered from aluminum and the attering edge was taken with electric detection in the spectrometer. The ectrometer field was kept at the value corresponding to the Al (p, p) scattering lge. A deuteron beam was now scattered into the spectrometer from the be- yllium target and for the analyzing magnet a field was chosen such that the euterons from the $Be^9(d, d)$ edge could be detected in a photographic plate. hus the deuteron energy was known and this field of the analyzer was kept nstant during the experiment. After the experiment this calibrating procedure as repeated.

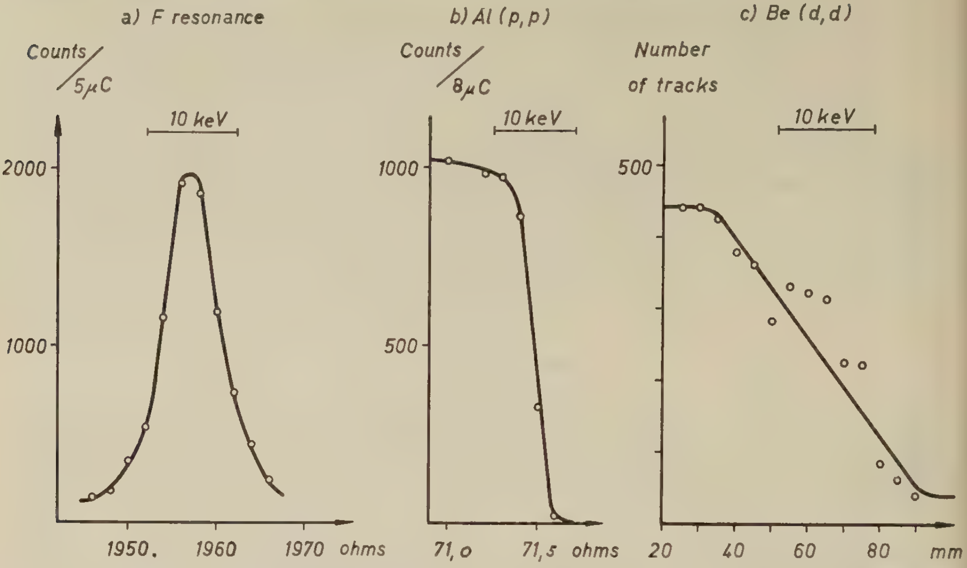

Fig. 1. Calibration of the deuteron beam. a) The fluorine resonance for protons at 873.5 keV. The curve shows the number of γ-counts per 5 μC of bombarding proton beam as a function of compensator reading of the analyzer field. b) Spectrum of scattered protons from Al. $E_p = 873.5$ keV. $\theta = 135.0°$. Electrical detection. c) Spectrum of scattered deuterons from Be. $\theta = 135.0°$. Photographic detection.

The different phases of one of these calibrations of the deuteron beam energy are illustrated in fig. 1. The calibration of the spectrometer field used in the measurement of the ground state α-group from $Ne^{20}(d, \alpha)F^{18}$ was performed by means of the proton group corresponding to the ground state transition of the reaction $O^{16}(d, p)O^{17}$. The proton group was taken at $\theta = 61.4°$ and the α-group at 135.0°. For details of the angle determination see ref. 2. Both groups were detected in Ilford photographic plates (50 μ thick, 1×3″) and the individual tracks were counted. The alpha and proton spectra are shown in fig. 2.

3. Results

Evaluating fig. 1 we use the mid-points of the fluorine resonance and of the aluminum and beryllium scattering edges. We find that the deuteron energy of the beam was 856 keV and we take the error as ±8 keV. If the error of the deuteron energy is ΔE_1, then the error in the Q-value ΔQ, caused by ΔE_1, is given by.

$$\Delta Q = \Delta E_1 \left[\left(\frac{\partial E_2}{\partial E_1}\right)_{O^{16}} \cdot \left(\frac{\partial Q}{\partial E_2}\right)_{Ne^{20}} - \left(\frac{\partial Q}{\partial E_1}\right)_{Ne^{20}} \right].$$

Thus the error in the Q-value due to the error ±8 keV in the beam energy is ±4 keV (ref. 11).

Evaluating fig. 2 we find that the peak positions have a distance of 2.5 mm corresponding to 6±4 keV. The error is ±5.5 keV referred to Q. The Q-value

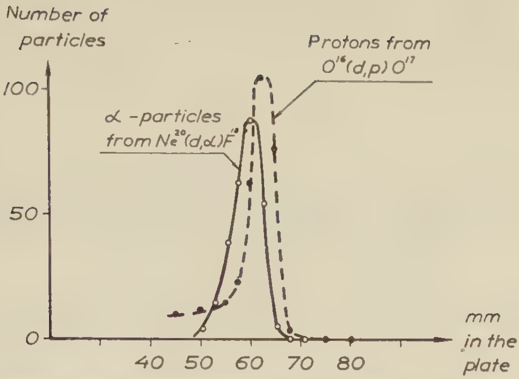

g. 2. Spectra of alphas from $Ne^{20}(d, \alpha) F^{18}$ at $\theta = 135.0°$ and protons fron $O^{16}(d, p) O^{17}$ at $\theta = 61.4°$. Deuteron energy 856 keV. 10.0 mm in the plate corresponds to 23.0 keV.

the calibrating reaction $O^{16}(d, p) O^{17}$ is known with a probable error of
5 keV. The angles are measured to ±0.2°.

Using nuclear masses and relativistic corrections (ref. 11) and taking into ac-
ount the difference between the proton and alpha energy scales, 6,9 ‰, we obtain

$$Q = 2.791 \pm 0.009 \text{ MeV}.$$

This value is in agreement with Middleton and Tai's photographic range
alue 2.78 ± 0.02 MeV. From the nuclear cycle mentioned in the introduction
e can calculate the fundamental mass difference $2\,H^2 - He^4$ using the accurately
nown Q-values and the known mass difference $n + H^1 - H^2 = 2.225 \pm 0.002$ MeV.
e obtain $2\,H^2 - He^4 = 23.829 \pm 0.022$ MeV in good agreement with the weighted
ean of $2\,H^2 - He^4 = 23.834 \pm 0.007$ MeV that is derived from several nuclear
cles in the region of very light nuclei (ref. 12). This demonstrates the con-
stency of the Q-values in this cycle.

REFERENCES

. Li, C. W., Phys. Rev. 88, 1038 (1952).
. Mileikowsky, C., Ark. f. Fys. Bd 7 Nr 8, 89 (1953).
. Middleton, R., and Tai, C. T., Proc. Phys. Soc. A 64, 801 (1951).
. Strait, E. N., Van Patter, D. M., Buechner, W. W., and Sperduto, A., Phys. Rev. 81, 747 (1951).
. Van Patter, D. M., Sperduto, A., Endt, P. M., Buechner, W. W., and Enge, H. A., Phys. Rev. 85, 142 (1952).
. Mileikowsky, C., and Whaling, W., Phys. Rev. 88, 1254 (1952).
. Richards, H. T., Smith, R. V., and Browne, C. P., Phys. Rev. 80, 524 (1950).
. Mileikowsky, C., and Pauli, R. T., Ark. f. Fys. Bd 4 Nr 12, 287 (1952).
. Mileikowsky, C., Ark. f. Fys. Bd 4 Nr 16, 337 (1952).
. ——, Ark. f. Fys. Bd 7 Nr 3, 33 (1953).
. Brown, A. B., Snyder, C. W., Fowler, W. A., and Lauritsen, C. C., Phys. Rev. 82, 159 (1951).
. Li, C. W., Whaling, W., Fowler, W. A., and Lauritsen, C. C., Phys. Rev. 83, 512, (1951).

Tryckt den 13 maj 1953

Uppsala 1953. Almqvist & Wiksells Boktryckeri AB

ARKIV FÖR FYSIK Band 7 nr 11

Read 23 April 1952

Some remarks on the rôle of overlapping in the X-ray scattering by crystals

By I. WALLER and S. O. LUNDQVIST

With 1 figure in the text

It has usually been assumed that the scattering of x-rays by crystals can calculated from the f-factors for free atoms. The results have in many cases een in agreement with the experimentally determined structure factors. Some viations from the theoretical results have however been reported by several iters.[1] The effect of bonding and overlapping was considered by EWALD d HÖNL[2] in an investigation of the "forbidden" x-ray reflections in diamond. e shall here consider the effect in a first approximation of the overlapping tween neighbouring atoms or ions in a crystal consisting of atoms or ions ving complete electron shells. Analogous calculations can be made in the case other types of binding.

The structure amplitude F_{hkl} is for sufficiently hard radiation given by the tegral[3]

$$F_{hkl}=\int e^{i\boldsymbol{\varkappa}\cdot\boldsymbol{r}}\varrho(\boldsymbol{r})\,d\boldsymbol{r}. \tag{1}$$

k, l are the Millerian indices of that crystal plane from which we observe e reflected radiation, $\varrho(\boldsymbol{r})$ is the charge density in units of the electron charge fined by (2) for a general Ψ, $\boldsymbol{\varkappa}=4\pi\frac{\sin\theta}{\lambda}\boldsymbol{n}$ where θ is the glancing angle, λ is e wavelength of the incident radiation and $\boldsymbol{n}$ denotes a unit vector normal the crystal plane $(h\,k\,l)$.

The wave function Ψ for the N electrons in a crystal consisting of atoms ions with complete electron shells is taken in this approximation as the ater-determinant of one-electron functions

$$\Psi=det\{\psi_\mu(x_i)\}$$

ere the $\psi_\mu(x)$ are suitable chosen atomic wave functions, e. g. solutions of e Hartree-Fock equations for free atoms or ions. The index μ then refers to an electron in a certain orbital μ' and in a definite spin-state j associated with an atom or ion at a certain lattice point G. The given atomic wave functions are written

---

[1] e. g. BRILL, HERMANN, PETERS (1939), JAMES, JOHNSON (1939), FRANKLIN (1950), BRILL 50).

[2] Ann. Phys. *25*, 281 (1936).

[3] I. WALLER, Zs. f. Phys. *51*, 213 (1928).

$$\psi_\mu(x) = \psi_{\mu'}^G(\boldsymbol{r})\,\delta_{j\zeta}.$$

The charge density is given by

$$\varrho(\boldsymbol{r}_1) = \frac{\sum_{\zeta_1} \int \Psi^* \Psi \, d\tau_2 \cdots d\tau_N}{\int \Psi^* \Psi \, d\tau_1 \cdots d\tau_N}, \tag{2}$$

the sign $\int d\tau_i$ implying summation over the spin coordinate ζ_i and integration over the space coordinates. Performing the integration in (2) and using well-known theorems about determinants we get the following expression for $\varrho(\boldsymbol{r})$:[1]

$$\varrho(\boldsymbol{r}) = \sum_\zeta \sum_{\mu\nu} T_{\mu\nu}\,\psi_\nu(x)\,\psi_\mu^*(x) \tag{3}$$

Here $T_{\mu\nu} = \frac{\Delta_{\mu\nu}}{\Delta}$, Δ is the determinant

$$\Delta = det\{S_{\mu\nu}\} \tag{4}$$

where $S_{\mu\nu}$ are the overlap integrals

$$S_{\mu\nu} = \int \psi_\mu^*(x)\,\psi_\nu(x)\,d\tau \tag{5}$$

and $\Delta_{\mu\nu}$ is the cofactor associated with the element (μ,ν) in Δ. After summation over the spin variable ζ we get

$$\varrho(\boldsymbol{r}) = \sum_{\mu\nu} T_{\mu\nu}\,\psi_\nu(\boldsymbol{r})\,\psi_\mu^*(\boldsymbol{r}) \tag{6}$$

where contributions are obtained only when μ and ν refer to electrons with the same spin. Inserting the expression for the charge density (6) into (1) we get

$$F_{hkl} = \sum_{\mu\nu} T_{\mu\nu} \int e^{i\varkappa\cdot\boldsymbol{r}}\,\psi_\nu(\boldsymbol{r})\,\psi_\mu^*(\boldsymbol{r})\,d\boldsymbol{r} \tag{7}$$

From (7) the structure factor referred to the unit cell can be obtained in the usual way by separating the phase factors of the different cells.

As an example of the effect of overlapping we have calculated F_{hkl}^{cell} for the lithium hydride crystal under the assumption of complete ionisation, that is, each ion is supposed to have two electrons each in an ls-state with opposite spins. As it is impossible to say to what extent this assumption is fulfilled, the results are only intended to give an estimate of the order of magnitude of the effect of the overlapping. Numerical calculations of the cohesive energy of LiH are in progress, and may yield some information about the state of ionisation. As atomic wave functions we have used the hydrogen-like ls-functions with an effective nuclear charge $Z' = Z - {}^5/_{16}$. The spherical average of the rge density with regard to each nucleus has been used in the calculations. e numerical values of the elements $T_{\mu\nu}$ used in our calculation are given ow.[1]

---

[1] Cf. P. O. Löwdin, Quarterly Progress Report, M.I.T. Solid-State and Molecular Theory Group, Jan. 15 (1952), p. 10, and paper to be published where the corresponding expression for the cohesive energy is derived.

$_{\mu} = 1.419$ μ associated with a H^--ion.
$_{\mu} = 1.021$ μ » » Li^+-ion.
$_{\nu} = 0$ $\mu \neq \nu$ μ and ν » » the same ion.
$_{\nu} = 0.052$ » » » nearest unlike neighbours.
$_{\nu} = 0.165$ » » » nearest negative neighbours.

e results are given in the following table together with the values obtained overlap effects are neglected and are compared with the experimental results ained by AHMED and ZINTL-HARDER.[2] In order to compare the theoretical ults with the experimental, which are only relative, we have given the values ative to that of the strongest reflexion F_{002}.

Table of F_{hkl}/F_{002}

theoretical values of F_{002} are 2.15 if overlap is included and 2.03 if overlap is neglected.

$h\,k\,l$	$\frac{\sin\theta}{\lambda}$	Theoretical overlap included	Theoretical overlap neglected	Experimental Ahmed	Experimental Zintl-Harder
1 1 1	0.212	0.498	0.626	0.484	0.516
0 0 2	0.245	1.000	1.000	1.000	1.000
2 2 0	0.346	0.758	0.773	0.916	0.847
1 1 3	0.406	0.540	0.586	0.567	0.619
2 2 2	0.424	0.623	0.645	0.707	0.809
0 0 4	0.490	0.530	0.552	0.688	0.712
3 3 1	0.534	0.433	0.463	0.484	0.530

The effect of overlapping is appreciable only at small glancing angles. For l even" reflections the values are higher than the corresponding values for e ions, for "all odd" reflections the values are lower, depending on the fact t the charge density is higher in the neighbourhood of the nuclei of the gative ions in the crystal than in free ions, whereas the charge density in vicinity of the positive ion is practically unchanged. The theoretical and erimental values agree rather well for the "all odd" reflections, for the l even" reflections the experimental values are somewhat higher than the oretical values. Because of the uncertainty in the temperature factors, the erimental values for the higher reflections are rather uncertain, the value F_{111}/F_{002} is probably the most reliable.

In this connection we should like to make some remarks about the conclu- n drawn by AHMED, that LiH has only about 25 per cent ionic character h limiting values 50 per cent ionic character or "complete covalency". In

---

The elements $T_{\mu\nu}$ were calculated by one of us (S. O. L.) in connexion with an investi- on of the cohesive energy of LiH (to be published).

M. S. AHMED, Phil. Mag. *42*, 997 (1951). E. ZINTL and A. HARDER, Z. Phys. Chemie B. 265, 1931, Ibid B. *15*, 416, 1932. The experimental values have been corrected for tem- ature scattering, using the temperature factors given by AHMED, which are, however, very ertain.

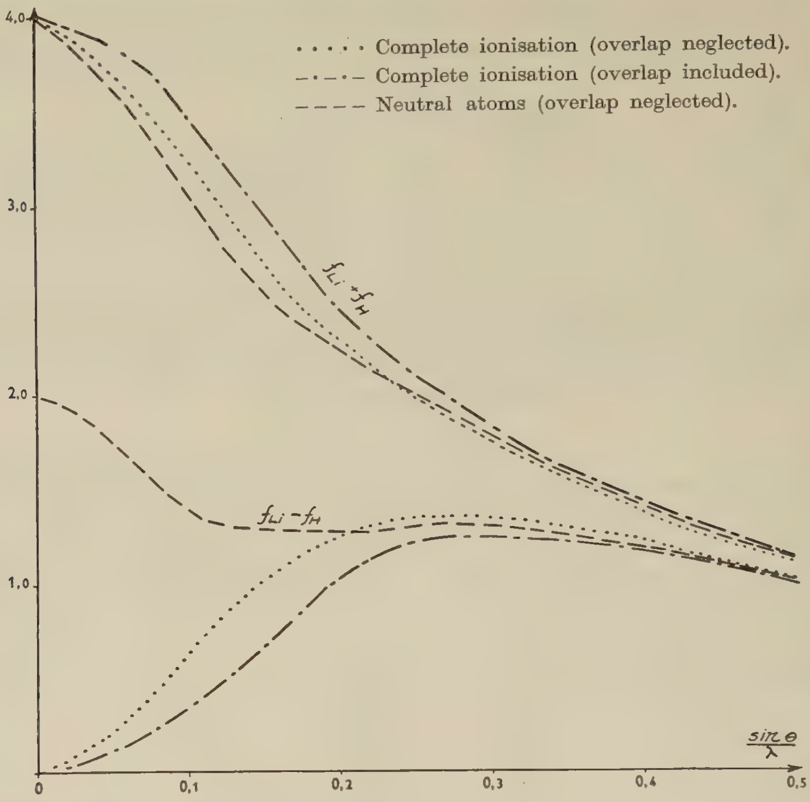

Fig. 1. The curves f_{Li} f_{H}.

Fig. 1 we have drawn the continuous curves ($f_{\mathrm{Li}} \pm f_{\mathrm{H}}$), where f_{Li} and f_{H} are atomic f-factors, in the two extreme cases of ionized atoms and neutral atoms, as well as the corresponding curves obtained if complete ionisation is assumed and overlap effects are included. On these curves, only those points for which the Bragg condition is fulfilled correspond to measurable quantities.

Ahmed's method of determining the state of ionisation consists in drawing curves connecting the points corresponding to "all even" and "all odd" reflections respectively, separating these into atomic f-curves, and extrapolating the f-curves to $\frac{\sin\theta}{\lambda}=0$. If we note that the first reflection occurs at $\frac{\sin\theta}{\lambda}=0.212$, it will be seen from the curves that the extrapolation to $\frac{\sin\theta}{\lambda}=0$ will unfortunately only give little information as regards the state of ionisation.

Institute of Mechanics and Mathematical Physics, University of Uppsala, Uppsala.

Tryckt den 30 juli 1953

Uppsala 1953. Almqvist & Wiksells Boktryckeri AB

ARKIV FÖR FYSIK Band 7 nr 12

Communicated 14 January 1953 by M. SIEGBAHN and E. HULTHÉN

On the band-spectrum of silver oxide

By ULLA UHLER

With 4 figures in the text

Abstract

The blue and ultra-violet band-systems of AgO have been made the subject of new investigation. The blue bands are degraded to the red and represent a $^2\Pi$ -$^2\Pi$ ansition. The upper state (A $^2\Pi$) is predissociated. The two systems have the lower ate in common (X $^2\Pi$). The upper state of the ultra-violet bands which shade off the violet, is also a $^2\Pi$ (B $^2\Pi$). These statements have been checked by rotaonal analysis. The vibrational constants are

		ω_e	$\omega_e x_e$
X	$^2\Pi_{3/2}$	490.6	2.9
	$^2\Pi_{1/2}$	490.2	3.1
A	$^2\Pi_{3/2}$	$\omega_e - 2\,\omega_e x_e = 241.0$	
	$^2\Pi_{1/2}$	$\omega_e - 2\,\omega_e x_e = 237.2$	
B	$^2\Pi_{3/2}$	539.1	6.2
	$^2\Pi_{1/2}$	535.7	6.3

The vibrational constants differ from those given by LOOMIS and WATSON, who rlier carried out a vibrational analysis.

The rotational analyses gave the following constants:

the isotope Ag^{107}

		B_v	D_{mean}	r_e
X	$^2\Pi_{3/2}$	$0.3035 - 0.0025_5\,(v+\frac{1}{2})$ cm^{-1}	$0.50 \cdot 10^{-6}$ cm^{-1}	$1.998 \cdot 10^{-8}$ cm
	$^2\Pi_{1/2}$	$0.3020 - 0.0025\,(v+\frac{1}{2})$	0.45	2.003
A	$^2\Pi_{3/2}$	$B_0 = 0.2816$	$D_0 = 1.71$	$r_0 = 2.074$
	$^2\Pi_{1/2}$	$B_0 = 0.2811$	$D_0 = 1.68$	$r_0 = 2.076$
B	$^2\Pi_{3/2}$	$B_0 = 0.3195$	$D_0 = 0.50$	$r_0 = 1.947$

the isotope Ag^{109}

		B_v	D_{mean}	r_e
X	$^2\Pi_{3/2}$	$0.3026 - 0.0024_5\,(v+\frac{1}{2})$ cm^{-1}	$0.50 \cdot 10^{-6}$ cm^{-1}	$1.998 \cdot 10^{-8}$ cm
	$^2\Pi_{1/2}$	$0.3014 - 0.0026\,(v+\frac{1}{2})$	0.43	2.002
A	$^2\Pi_{3/2}$	$B_0 = 0.2809$	$D_0 = 1.69$	$r_0 = 2.074$
	$^2\Pi_{1/2}$	$B_0 = 0.2804$	$D_0 = 1.67$	$r_0 = 2.076$
B	$^2\Pi_{3/2}$	$B_0 = 0.3188$	$D_0 = 0.52$	$r_0 = 1.947$

I. Introduction

Three band-systems, one in the far red, one in the blue region and the third one in the ultra-violet part of the spectrum, have been ascribed to silver oxide. In 1935, LOOMIS and WATSON (1) made vibrational analyses of the blue and ultra-violet systems. They state that the systems represent a $^2\Pi-^2\Sigma$ and a $^2\Sigma-^2\Sigma$ transition respectively with the lower state in common. The red bands were too faint to be measured.

The present investigation was undertaken in order to make a rotational analysis especially of the blue system, which shows a wider structure than the ultra-violet one. The bands of the blue system occur in pairs, nearly equal in intensity and with a constant doublet interval of roughly 170 cm^{-1}. Loomis and Watson assumed this to be the doublet interval of the upper $^2\Pi$-state and the lower state to be a $^2\Sigma$-state. The $^2\Pi$-state belongs with very good approximation to Hund's coupling case *a*. Hence the bands should show the appearance of a $^2\Pi$ (case *a*)$-^2\Sigma$ (case *b*) transition. However, the bands did not show the expected structure; no Q-branches could be found and the branches observed were of approximately equal intensity. Thus one was led to assume that the blue bands represented a $^2\Pi$ (case *a*)$-^2\Pi$ (case *a*) transition. The number of branches seems to agree well with this assumption. Rotational analyses have been carried out on the following bands: 0,0 , 0,1, and one of the two sub-bands of 0,2. The vibrational assignment has been changed, thus giving constants different from those obtained by Loomis and Watson.

To check these rotational analyses it seemed to be of interest to carry out an analysis of the ultra-violet band-system too, as the two systems probably have a state in common in view of the remarkable agreement between their lower vibrational constants. These bands are reported to be a $^2\Sigma-^2\Sigma$ transition. The new vibrational analysis and the rotational analysis show, however, that they represent a $^2\Pi-^2\Pi$ transition. Rotational analyses of the 0,0 and 0,1 bands have been given.

II. Experimental

The source of light used to obtain the bands was a vacuum arc. The electrodes were water-cooled silver rods of highest purity (99.7% silver, obtained from Kungl. Mynt och Justeringsverket). Fil. lic. Gunnar Almkvist has earlier constructed the vacuum arc and has found out the best experimental conditions. The arc was burning in a slow stream of oxygen at a pressure of about 20 mm Hg. A higher pressure increased the intensity of the bands but caused the arc to burn unsteadily. The fairly low pressure made the arc burn with remarkable steadiness. The current was 22–26 A from a 440 Volt D.C. output.

The spectrograms were taken with a Wood's 21 ft concave grating in the first order (165000 lines in all). The dispersion in the blue region is about 1.24 Å/mm and in the ultra-violet part of the spectrum 1.27 Å/mm. Owing to the dense structure of the bands very hard plates must be used to give as high a contrast as possible. Ilford Thin Film Half Tone plates were used.

On account of the low sensitivity of the plates rather long exposure times were necessary. The band-systems themselves seem to be rather weak. Good spectograms of both band-systems were obtained with an exposure time of 15 hours. The ultra-violet band-system is weaker than the blue one. The blue system was also photographed with an exposure of 4 hours, giving mainly the strong 0,0 bands, which were overexposed on the 15-hours plates. To obtain a general survey of the blue bands

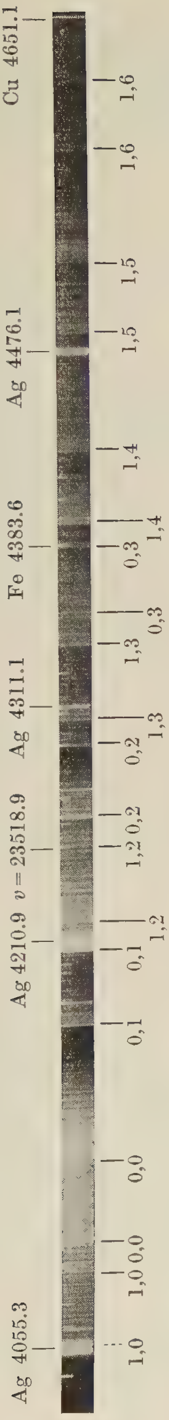

Fig. 1 a. The blue band-system.

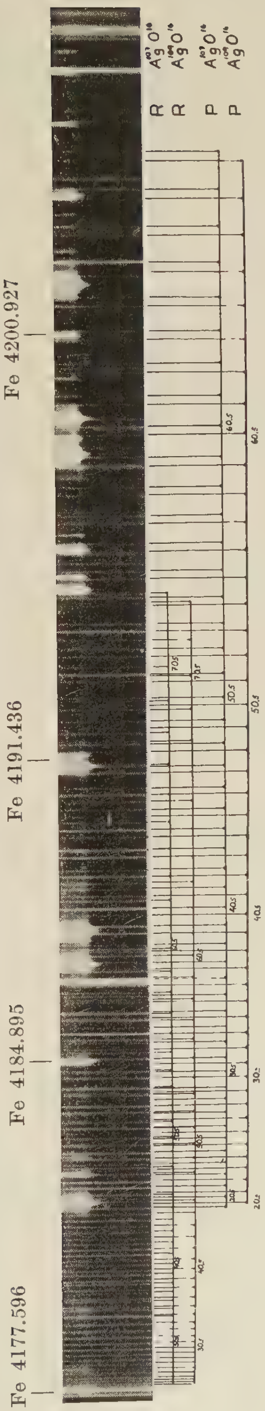

Fig. 1 b. The $(0,1)_{3/2}$ band.

(Fig. 1 a), these were photographed in a prism spectrograph with smaller dispersion (~6.3 Å/mm). The exposure time was 45 mins. In spite of the high temperature in the light source the spectrograms obtained show little continuum and seem to be rather free from disturbing impurities. This is certainly due to the high contrast plates and the intense light source. Iron lines taken from HARRISON's (2) tables were used for comparison.

III. The blue system

Vibrational analysis

The appearance of the blue system is shown in Fig. 1 a. The bands shade off to longer wave-lengths and occur in pairs of equal intensity, the bands of each pair being separated by a constant interval of 170 cm^{-1}.

The wavenumbers of the bands, measured by LOOMIS and WATSON (1) agree fairly well with my measurements. The strongest bands ($\nu = 24\,416.0$ cm^{-1} and $\nu = 24\,244.5$ cm^{-1}) are denoted 1,0 by Loomis and Watson, while their 0,0 bands are too weak to be seen. My plates do not show any heads at the expected places either. The rotational analysis give the B-values (and r-values) of the upper and lower states. Thus a quantum-mechanical calculation of the intensities of the bands could be made. The calculation was quite approximate (parabolas as potential functions) but showed distinctly that the 0,0 bands should be the strongest ones.

The strongest bands are assigned 0,0 in the present vibrational analysis and it explains also the bands in front of the 0,0 bands (further to the violet) and the head $\nu = 23\,518.9$ cm^{-1}. This head does not fit in the vibrational scheme given by LOOMIS and WATSON but was measured by them.

The blue band-system is predissociated and no band-heads containing the level $v' = 2$ have been observed.

The vibrational constants have been calculated from the band-heads instead of the band-origins. They have been recalculated with regard to the origins only for $X\,^2\Pi_{3/2}$ because rotational analyses has not been carried out for a sufficient number of bands. These values are given later. The band-heads measured are given in Tables 1 and 2. The approximate intensities are seen from Fig. 1 a.

The bands can be represented by the equations

$$\nu_{3/2} = 24\,539.9 + 241.0\,(v' + \tfrac{1}{2}) - [490.3\,(v'' + \tfrac{1}{2}) - 2.8_5\,(v'' + \tfrac{1}{2})^2]$$

$$\nu_{1/2} = 24\,370.5 + 237.2\,(v' + \tfrac{1}{2}) - [490.5\,(v'' + \tfrac{1}{2}) - 3.0_4\,(v'' + \tfrac{1}{2})^2].$$

The differences between calculated and observed values are given in brackets. The $(1,0)_{3/2}$ band-head is covered by the strong atomic line Ag 4055.264 Å.

The high dispersion plates did not allow of measurement of the 1,4, 1,5, and 1,6 bands measured by LOOMIS and WATSON, as these heads were too weak.

The vibrational analysis, suggested above, explains every strong head, that has been observed. However, the upper ω-value is abnormally low and the possibility, that the blue bands represent two systems both predissociated above $v' = 0$ and with the lower state in common, may not be excluded. In such a case, the two upper terms must have remarkably similar doublet splittings, which seems rather odd.

The structure of the bands

The rotational structure is not fully resolved and the lines overlap considerably in the vicinity of the heads. Thus no particular effort was made to obtain lines with low J-values. Apart from the regions in the neighbourhood of the heads, the rotational

Table 1

Bandheads of $^2\Pi_{3/2}-{}^2\Pi_{3/2}$

v' \ v''	0	1	2	3
0	24 416.0 (−0.1)	23 931.1 (+0.2)	23 452.4 (±0.0)	22 973.3 (uncertain)
1	atomic line	—	23 693.5 (−0.1)	23 220.0 (+0.2)

Table 2

Bandheads of $^2\Pi_{1/2}-{}^2\Pi_{1/2}$

v' \ v''	0	1	2	3
0	24 244.5 (+0.1)	23 760.3 (−0.1)	23 281.7 (+0.1)	22 811.0 (uncertain)
1	24 481.8 (0.0)	—	23 518.9 (+0.1)	23 046.7 (+0.1)

tructure is sufficiently resolved to permit of rotational analysis. The sub-bands ituated towards the violet, show the simplest structure. The appearance of the 0,1 and is shown in Fig. 1 b. The 0,0 and the 0,2 violet sub-bands show a similar structure.

If we assume the transition to be a $^2\Pi-{}^2\Sigma$, according to Loomis and Watson, e should expect two sub-bands $^2\Pi_{3/2}-{}^2\Sigma$ and $^2\Pi_{1/2}-{}^2\Sigma$. The $^2\Pi$-state belongs to Hund's ase *a* with good approximation, due to the large doublet interval 170 cm^{-1}. Thus a $^2\Pi$ (case *a*)–$^2\Sigma$ transition one should get, besides the main branches, satellite ranches of comparable intensity, giving six branches in every sub-band. Among hese the Q, ^RQ and ^PQ branches would have twice the intensity of the R, P, ^QR, P, ^OP and ^SR branches. The number of branches is reduced to four in each sub-band we assume the spin-doublet splitting in the $^2\Sigma$-state to be negligible. Thus in every ub-band we should have four branches with the relative intensities 1:3:3:1. etails on $^2\Pi$ (case *a*)–$^2\Sigma$ transitions have been given by Herzberg (3) and Mul-iken (4). In this case the number of branches will be doubled because of the isotope-olecule, i.e. one would expect twelve or possibly eight branches in each sub-band. owever, in the violet sub-bands only four branches could be found, each of aproximately the same intensity. Nor do the red sub-bands show any branches ronger than the others. As is seen from Fig. 1 b, all the lines in the region are sed in forming these branches.

The upper state is predissociated, and the reduced number of branches might be xplained by assuming that one of the Λ-doublet levels is predissociated earlier an the other. This assumption gives the right number of branches if the spin-oublet splitting in the $^2\Sigma$-state is neglected, but is contradicted by the intensity lations between the remaining branches. If either the + or − levels are cut off,

Table 3

Wavenumbers of the $(0,0)_{3/2}$ and $(0,1)_{3/2}$ bands

J	The $(0,0)_{3/2}$ band				The $(0,1)_{3/2}$ band			
	$Ag^{107}O^{16}$		$Ag^{109}O^{16}$		$Ag^{107}O^{16}$		$Ag^{109}O^{16}$	
	R_2	P_2	R_2	P_2	R_2	P_2	R_2	P_2
17,5		24 395.40*		24 395.40*				
18,5		94.01*		94.01*				
19,5	24 414.88*	92.54*	24 414.88*	92.54*		23 907.49*		23 908.30*
20,5	14.51*	91.06*	14.51*	91.06*		06.25		07.04
21,5	14.07*	89.43*	14.07*	89.43*		04.92*		05.64
22,5	13.63*	87.92	13.63*	88.02*		03.45		04.16*
23,5	13.14*	86.23*	13.14*	86.43*		01.98		02.70
24,5	12.62*	84.64	12.62*	84.83		00.50*		01.29*
25,5	11.94	82.98	12.04	83.14	23 927.82	898.87		899.65
26,5	11,28	81.19	11.44	81.36	27.30	97.34*	23 927.99	98.01
27,5	10.59	79.40	10.72	79.61	26.76*	95.58	27.41	96.33
28,5	09.85	77.54	10.00	77.84*	26.12*	93.84	26.76*	94.54*
29,5	08.95	75.65*	09.07	75.95*	25.44*	92.11	26.12*	92.85
30,5	08.14	73.65*	08.25	73.95	24.70*	90.33	25.44*	90.98*
31,5	07.22	71.65	07.39	71.89	23.91*	88.46	24.70*	89.21
32,5	06.33*	69.65	06.33*	69.93	23.16	86.54	23.91*	87.31
33,5	05.25	67.44	05.38	67.78	22.31	84.58	23.01	85.34*
34,5	04.15	65.33	04.30	65.70*	21.37	82.61	22.11	83.38
35,5	03.00	63.05*	03.10	63.38*	20.41	80.57	21.13	81.36
36,5	01.87*	60.83	01.87*	61.14	19.36	atomic line	20.07	79.26
37,5	00.53	58.47	00.70	58.81	18.29	76.27	19.02	77.10
38,5	399.14	56.09	399.27	56.35	17.12	74.07	17.85	74.93
39,5	97.83	53.63	97.97	53.89	15.97	71.84	16.70	72.62*
40,5	96.44	51.12*	96.62	51.41	14.65	69.52*	15.41	70.35
41,5	94.80	48.51	94.98	48.85	13.41	67.13	14.13	67.98
42,5	93.24	45.87	93.41	46.20	11.98	64.70	12.73	65.49*
43,5	91.58	43.20	91.76	43.50	10.57	62.23*	11.34	63.06*
44,5	89.87	40.40	90.05	40.74	09.04	59.61*	09.80	60.51
45,5	88.02*	37.52*	88.20	37.84*	07.49*	57.01	08.30*	57.90
46,5	86.23*	34.61*	86.43*	34.98	05.86	54.34	06.64	55.24*
47,5	84.25	31.67	84.54	32.04	04.16*	51.61	04.92*	52.49
48,5	82.22	28.62	82.47	29.03	02.37	48.80	03.14	49.71
49,5	80.10	25.52	80.42	25.94	00.50*	45.92	01.29*	46.84
50,5	77.84*	22.30	78.22	22.71	898.58	42.97	899.38	43.90
51,5	75.65*	19.05	75.95*	19.45	96.61	39.93	97.34*	40.90
52,5	73.32	15.71	73.65*	16.11	94.54*	36.84	95.29	37.78
53,5	70.94	12.22	71.21	12.64	92.34	33.66	93.18	34.60*
54,5	68.40	08.74	68.73	09.14	90.06	30.42	90.98*	31.40
55,5	65.70*	05.11	66.09	05.56	87.73	27.10	88.58	28.07
56,5	63.05*	01.44	63.38*	01.86	85.34*	23.70	86.12	24.65
57,5	60.21	297.67	60.57	298.10	82.78	20.18	83.67	21.21
58,5	57.36	93.77	57.67	94.22	80.14	16.58	81.03	17.60
59.5	54.29	89.80	54.68	90.26	77.44	12.88	78.31	13.88

ble 3 (cont.)

J	The $(0,0)_{3/2}$ band				The $(0,1)_{3/2}$ band			
	$Ag^{107}O^{16}$		$Ag^{109}O^{16}$		$Ag^{107}O^{16}$		$Ag^{109}O^{16}$	
	R_2	P_2	R_2	P_2	R_2	P_2	R_2	P_2
60,5	24 351.12*	24 285.70	24 351.48	24 286.24	23 874.58	23 909.10	23 875.49	23 810.14
61,5	47.96	81.51	48.37	82.09	71.69	05.21	72.62	06.29
62,5	44.56	77.18	45.05	77.72	68.60	01.23	69.52	02.32
63,5	41.07	72.80	41.49	73.36	65.49*	797.13	66.34	798.23
64,5	37.52*	68.28	37.84*	68.84	62.11*	92.92	63.06*	94.01
65,5	33.68	63.64	34.14	64.21	58.65	88.59	59.61	89.71
66,5	29.74	58.91	30.22	59.48	55.08	84.16	56.07	85.25
67,5	25.78	54.01	26.16	54.54	51.33	79.52	52.37	80.69
68,5	21.50	48.91	21.94	49.52	47.41	74.79	48.44	75.96
69,5	17.08	43.78*	17.59	44.27*	43.36	69.92	44.44	71.16
70,5	12.33	38.29*	13.01	38.96*	39.08	64.86	40.18	66.07
71,5	07.63	32.74	08.21	33.45	34.61*	59.71*	35.72	60.91
72,5	02.54	26.97	03.18	27.67	29.89	54.29*	31.03	55.47*
73,5		21.01*		21.70		48.67		49.90*
74,5		15.01*		15.62*		atomic line		44.11

Table 4

Wavenumbers of the $(0,2)_{3/2}$ band

	$Ag^{107}O^{16}$		$Ag^{109}O^{16}$		J	$Ag^{107}O^{16}$		$Ag^{109}O^{16}$	
	R_2	P_2	R_2	P_2		R_2	P_2	R_2	P_2
5		23 420.21			50,5	23 424.90	23 369.23	23 426.21	23 370.71
5		18.92*			51,5	23.15	66.48	24.57	67.98
5		17.40*		23 418.92*	52,5	21.34*	63.60	22.68	65.12
5		15.78*		17.40*	53,5	19.41	60.74	20.78	62.19
5	23 447.64*	14.20*		15.78*	54,5	17.40*	57.74	18.79	59.22
					55,5	15.38	54.69	16.72	56.23
5	46.99*	12.49		14.20*	56,5	13.21	51.54	14.57	53.08
5	46.44	10.91*	23 447.64*	12.34*	57,5	10.91*	48.31	12.34*	49.95
5	45.76	09.09	46.99*	10.45	58,5	08.63*	45.02	10.03	46.60
5	45.03	07.27	46.32	08.63*	59,5	06.15	41.60	07.58	43.21
5	44.27	05.48	45.58	06.83					
5	43.45	03.64*	44.75	05.05*	60,5	03.64*	38.16	05.05*	39.73
5	42.65	01.63	43.91	03.04	61,5	01.04*	34.56	02.42	36.20
5	41.77	399.67*	43.05	01.04	62,5	398.25	30.89	399.67*	32.50
5	40.83	97.70	42.10	399.07	63,5	95.38	27.12	96.86	28.70
5	39.76	95.59	41.10	97.00	64,5	92.38	23.24	93.86	24.87
					65,5	89.30	19.22	90.75	20.84
5	38.72	93.48	40.09	94.91	66,5	86.04	15.08	87.51	16.75
5	37.65	91.35	38.96	92.74	67,5	82.63	10.82	84.12	12.49
5	36.50*	89.12	37.72	90.57	68,5	79.03	06.43	80.57	08.11
5	35.29*	86.82	36.50*	88.23	69,5	75.33	01.88	76.88	03.60
5	33.95*	84.48	35.29*	85.91					
5	32.56	82.10	33.95*	83.50	70,5	71.40	297.22	73.03	298.96
5	31.10*	79.66	32.46	81.10	71,5	67,29	92.31	68.92	94.12
5	29.78	77.17	31.10*	78.61	72.5	62.96	87.32	64.58	89.09
5	28.18	74.55	29.47	76.00	73,5		82.07		83.88
5	26.55	72.00	27.92	73.41	74,5		76.59		78.44

Table 5

Wavenumbers of the $(0,0)_{1/2}$ band

J	$Ag^{107}O^{16}$				$Ag^{109}O^{16}$			
	R_{1c}	P_{1c}	R_{1d}	P_{1d}	R_{1c}	P_{1c}	R_{1d}	P_{1d}
28,5	24 239.01*							
29,5	38.33*	24 204.96		24 204.37*		24 205.28*		24 204.68*
30,5	37.59*	03.03*	24 236.66*	02.27*	24 237.74	03.34*	24 236.77*	02.48
31,5	36.79*	01.18	35.80*	00.25	36.87*	01.58	35.96*	00.57*
32,5	35.80*	199.19	34.83*	198.15*	35.96*	199.49*	35.06*	198.46*
33,5	34.83*	97.11*	33.82*	96.16	35.06*	97.44	34.04*	96.50
34,5	33.82*	95.06	32.80*	94.10	34.04*	95.38*	33.03*	94.31*
35,5	32.80*	92.87*	31.80*	91.85*	33.03*	93.19*	31.88*	92.15
36,5	31.72*	90.73	30.57*	89.68	31.88*	91.02	30.78	90.01*
37,5	30.57	88.49*	29.41*	87.43*	30.78*	88.83	29.55	87.76
38,5	29.28	86.15	28.16*	85.03	29.41*	86.44	28.32	85.41
39,5	27.98	83.70	26.74*	82.69*	28.16*	84.11*	27.03	83.00
40,5	26.57	81.32*	25.36*	80.17	26.74*	81.64	25.64	80.52
41,5	25.12	78.77	23.95	77.68*	25.36	79.12*	24.10	78.03*
42,5	23.75	76.27	22.38	75.09	23.82*	76.59	22.60	75.42
43,5	22.06	73.67	20.87	72.51	22.25	73.97	21.02	72.77
44,5	20.43	70.99	19.15	69.75	20.59	71.29*	19.30	70.08
45,5	18.68	68.21	17.35	66.97*	18.89	68.52*	17.64	67.30
46,5	16.86	65.39	15.62	64.07	17.00	65.70	15.80	64.47
47,5	14.99	62.50	13.66	61.21	15.24	62.81	13.90	61.56
48,5	12.99	59.40	11.70	58.20	13.27	59.90	11.94	58.61
49,5	10.94	56.43	09.70	55.11	11.29	56.83	09.89	55.49
50,5	08.83	53.31	07.50	51.94	09.18	53.68	07.81	52.37
51,5	06.73	50.09	05.28*	48.73	07.00	50.51	05.55	49.14
52,5	04.37*	46.81	03.03	45.49	04.68	47.24	03.34*	45.88
53,5	02.03	43.43	00.57*	42.05	02.27*	43.85	00.90	42.46
54,5	199.49*	39.99	198.15*	38.60	199.84	40.41	198.46*	39.03
55,5	96.90	36.43	95.48*	35.02	97.23*	36.86	95.83	35.44
56,5	94.31*	32.78	92.87*	31.38	94.56	33.25	93.19*	31.77
57,5	91.44	28.96	90.01*	27.59	91.85	29.45	90.35	28.04
58,5	88.49*	25.14	87.06	23.73	88.95*	25.61	87.43*	24.22
59,5	85.54	21.17	84.11*	19.77	85.91	21.69	84.47	20.24
60,5	82.39	17.09	80.76	15.68	82.76*	17.62	81.32*	16.19
61,5	79.12*	12.99	77.68*	11.50	79.47	13.46	78.03*	12.03
62,5	75.79	08.60	74.27	07.19	76.09	09.17	74.64	07.75
63,5	72.19	04.20	70.72	02.77	72.72*	04.77	71.29*	03.30
64,5	68.52*	099.67	66.97*	098.18	68.87	00.19	67.38	098.71
65,5	64.77	94.95	63.19	93.51	65.09	095.51	63.62	94.07
66,5		90.06		88.66		90.68		89.29
67,5		85.00		83.65		85.69		84.23

Q-branches or ^{R}Q and ^{P}Q branches will be left, all of which are stronger than the other branches. Thus the blue bands can not represent a $^2\Pi$–$^2\Sigma$ transition. A $^2\Pi$-state seems to be involved in view of the large doublet separation. A $^2\Pi$–$^2\Delta$ or $^2\Delta$–$^2\Pi$ transition is excluded, as these transitions also give rise to strong Q-branches. Conseuently, there remains only the possibility of a $^2\Pi$–$^2\Pi$ transition, divided into the ib-bands $^2\Pi_{3/2}$–$^2\Pi_{3/2}$ and $^2\Pi_{1/2}$–$^2\Pi_{1/2}$, with both $^2\Pi$-states belonging to Hund's case If one of the $^2\Pi$-states belonged to Hund's case b, both the sub-bands would iow a far more complicated appearance, with several satellite branches, as in a I–$^2\Sigma$ transition. HERZBERG (3) gives the outlines of a $^2\Pi$(case a)-$^2\Pi$(case a) transi- on. In each sub-band there will be a weak Q-branch and P and R branches of ap- roximately equal intensity. Each branch will split up into two components due to ie Λ-type doubling. Theoretically, in a $^2\Pi_{3/2}$-state the Λ-type doubling is propor- onal to $(J-\frac{1}{2})(J+\frac{1}{2})(J+{}^3/_2)$, and is usually too small to measure when the doublet ɛparation A is large. In a $^2\Pi_{1/2}$ (case a) state we have theoretically a Λ-type doubling roportional to $(J+\frac{1}{2})$ for not too large J-values, with the coefficient a approximately roportional to A (MULLIKEN (4); JEVONS (5)).

In the violet sub-bands four branches of equal intensity have been found, as ientioned above. They form one P and one R branch of each isotope-molecule. The -branches are too weak to be observed, especially as the first Q-lines, which might therwise be observed, are situated in a region where the lines overlap very much. o Λ-type doubling has been observed.

The red sub-bands show a different appearance. The Λ-type doubling is not neg- gible, and for this reason the bands contain eight branches, namely two R and two branches of every isotope-molecule, making eight branches in all. The lines here verlap very often, giving the whole band a more complicated appearance than iat of the other sub-band.

As the branches in respect of intensity and number agree with the expected ructure, the blue bands must represent a $^2\Pi$–$^2\Pi$ transition, where the violet sub- ands have $\Omega={}^3/_2$ and the red sub-bands $\Omega={}^1/_2$. The lower state is here denoted y $X\,^2\Pi$. The upper state is called $A\,^2\Pi$.

otational analysis

Tables 3–6 give the wave-numbers of the 0,0, 0,1, and 0,2 bands. The subscript 1 idicates the transition $^2\Pi_{1/2}$–$^2\Pi_{1/2}$, while the subscript 2 is used for the branches be- onging to $^2\Pi_{3/2}$–$^2\Pi_{3/2}$. The indices c and d distinguish the two Λ-type components. verlapping lines are marked with an asterisk. The errors in the measurements do ot as a rule exceed 0.05 cm^{-1}. Table 7 gives the combination differences of the pper level of the 0,0, 0,1, and 0,2 violet sub-bands. The agreement is good.

The rotational term-values of the components of doublet states have been calcu- ited by HILL and VAN VLECK (6) for any coupling case. They obtained

$$\begin{aligned} F_1(J) &= B\left[(J+\tfrac{1}{2})^2-\Lambda^2-\tfrac{1}{2}\sqrt{4(J+\tfrac{1}{2})^2+Y(Y-4)\Lambda^2}\right]-DJ^4 \\ F_2(J) &= B\left[(J+\tfrac{1}{2})^2-\Lambda^2+\tfrac{1}{2}\sqrt{4(J+\tfrac{1}{2})^2+Y(Y-4)\Lambda^2}\right)-D(J+1)^4, \end{aligned} \tag{1}$$

here $Y=\dfrac{A}{B}$. When A is large, i.e. Hund's case a, the formula may be replaced by

$$F(J)=B_{\mathrm{eff}}\,J(J+1)-DJ^2(J+1)^2.$$

Terms independent of J have been omitted. The rotational constant $\mathrm{B}_{\mathrm{eff}}$ is some- hat different for the two doublet components. To get the rotational constants B_v'' id D_v'', the graphic method was used, $\Delta_2 F''(J)/(J+\frac{1}{2})$ being plotted against $(J+\frac{1}{2})^2$. his gives $4\,B_v''$ as the intersection with the ordinate, and $8\,D_v''$ as the inclination of

Table 6

Wavenumbers of the $(0,1)_{1/2}$ band

J	$Ag^{107}O^{16}$				$Ag^{109}O^{16}$			
	R_{1c}	P_{1c}	R_{1d}	P_{1d}	R_{1c}	P_{1c}	R_{1d}	P_{1d}
25,5		23 729.06*		23 728.24*				23 729.06*
26,5		27.49*		26.66*		23 728.24*		27.49*
27,5		25.92*		25.03*		26.66*		25.92*
28,5		24.25*		23.44*		25.03*		24.25*
29,5		22.59*		21.76*		23.44*		22.59*
30,5	23 755.46*	20.90*	23 754.46*	20.05*	23 756.04	21.76*	23 755.10*	20.90*
31,5	54.70*	19.06*	53.71*	18.06*	55.46*	20.05*	54.46*	19.06*
32,5	53.89*	atomic line	52.86*	16.25*	54.70*	18.06*	53.71*	atomic line
33,5	53.06*	15.43*	52.06*	14.41*	53.89*	16.25*	52.86*	15.43*
34,5	52.06*	13.41*	51.35	12.50*	53.06*	14.41*	52.06*	13.41*
35,5	51.09*	11.35*	50.46	10.55	52.14*	12.41	51.09*	11.35*
36,5	50.17*	09.28*	49.45	08.50	51.09*	10.39	50.17*	09.28*
37,5	49.18*	07.23*	48.36*	06.40*	50.11*	08.25	49.08*	07.23*
38,5	48.36*	05.03*	47.25*	04.24	49.08	06.12	48.04*	05.03*
39,5	47.25*	03.00*	46.15*	02.04	48.04*	03.88	46.87*	02.88
40,5	46.15*	00.85*	44.89*	699.79	46.87*	01.73	45.64*	00.75
41,5	44.89*	698.64*	43.57*	97.45	45.64*	699.46*	44.43*	698.28
42,5	43.57*	96.25*	—	95.16*	44.36*	97.11*	43.08	95.90
43,5	—	93.87*	atomic line	92.61	42.97	94.68	—	93.55
44,5	atomic line	91.43	—	90.17	—	92.20	atomic line	91.03
45,5	—	88.81	38.00	87.61	atomic line	89.63	38.79	88.46
46,5	37.73	86.25	36.38	84.94	38.42	87.01	37.24	85.82
47,5	35.94	83.35	34.78	82.11	36.82	84.44	35.56	83.12
48,5	34.25	80.81	32.95	79.48	35.16	81.74	33.80	80.49
49,5	32.60	78.07	31.26	76.64	33.38	79.00	31.98	77.72
50,5	atomic line	75.12	29.49	73.85	31.40	75.99	atomic line	74.76
51,5	28.73	72.16	27.42	70.85	29.53	73.13	28.24*	71.87
52,5	26.66*	69.18	25.40*	67.77	27.49*	70.09	26.17	68.74
53,5	24.62	66.05	23.18*	64.69	25.40*	67.00	24.02	65.63
54,5	22.38	62.87	20.90*	61.48	23.18*	63.78	21.76*	62.36
55,5	20.05*	59.53	18.63*	58.16	20.90*	60.55	19.57	59.08
56,6	17.59	56.11	16.25*	54.79	18.63*	57.20	17.16*	55.78
57,5	15.15	52.72	13.77	51.39	15.99	53.68	14.52	52.26
58,5	12.50*	49.13	11.09	47.75	13.41*	50.18	12.05	48.80
59,5	09.81	45.44	08.36	44.07	10.62	46.49	09.28*	45.09
60,5	06.96	41.68	05.52	40.27	07.84*	42.73	06.40*	41.25
61,5	04.01	37.79	02.45	36.38	05.03*	38.97	03.48	37.43
62,5	00.85	33.81	699.46*	32.38	01.83*	34.94	00.41	33.48
63,5	697.70	29.73	96.25*	28.29	698.64*	30.79	697.11*	29.36
64,5	94.30	25.45	92.89	24.03	95.16*	26.47	93.87*	25.12
65,5	90.91	21.10	?	19.69	91.88	22.20	?	20.78
66,5		16.56		15.09		17.67		16.26
67,5		11.84		10.40		12.99		11.59

the line. This was done separately for the two sub-bands. For $^2\Pi_{1/2}$, B_{eff} is obtained as a mean value of the c and d levels. The uncertainty in the B-values is about 2 units in the last figure. The values obtained are

Table 7

e combination differences $\Delta_2 F(J)$ of the $A\ ^2\Pi_{3/2}$-state $v' = 0$. (The values given refer to $Ag^{107}O^{16}$)

J	From 0,0	From 0,1	From 0,2	J	From 0,0	From 0,1	From 0,2
19,5	22.34			46,5	51.62	51.52	51.44
				47,5	52.58	52.55	52.61
20,5	23.45			48,5	53.60	53.57	53.63
21,5	24.64			49,5	54.58	54.58	54.55
22,5	25.71						
23,5	26.91			50,5	55.54	55.61	55.67
24,5	27.98			51,5	56.60	56.68	56.67
25,5	28.96	28.95		52,5	57.61	57.70	57.74
26,5	30.09	29.96		53,5	58.72	58.68	58.67
27,5	31.19	31.18		54,5	59.66	59.64	59.66
28,5	32.31	32.28		55,5	60.59	60.63	60.69
29,5	33.30	33.33	33.44	56,5	61.61	61.64	61.67
				57,5	62.54	62.60	62.60
30,5	34.49	34.37	34.50	58,5	63.59	63.56	63.61
31,5	35.57	35.45	35.52	59,5	64.49	64.56	64.55
32,5	36.68	36.62	36.67				
33,5	37.81	37.73	37.76	60,5	65.42	65.48	65.48
34,5	38.82	38.76	38.79	61,5	66.44	66.48	66.48
35,5	39.95	39.84	39.81	62,5	67.38	67.37	67.36
36,5	41.04	—	41.02	63,5	68.27	68.36	68.26
37,5	42.06	42.02	42.10	64,5	69.24	69.19	69.14
38,5	43.05	43.05	43.13	65,5	70.04	70.06	70.08
39,5	44.20	44.13	44.17	66,5	70.83	70.92	70.96
				67,5	71.77	71.81	71.81
40,5	45.32	45.13	45.24	68,5	72.59	72.62	72.60
41,5	46.29	46.28	46.30	69,5	73.30	73.44	73.45
42,5	47.37	47.28	47.38				
43,5	48.38	48.34	48.48	70,5	74.04	74.22	74.18
44,5	49.47	49.43	49.47	71,5	74.89	74.90	74.98
45,5	50.50	50.48	50.46	72,5	75.57	75.60	75.64

II: $Ag^{107}O^{16}$ $Ag^{109}O^{16}$

$^3/_2$ $B_0'' = 0.3022\ \text{cm}^{-1}$ $D_0'' = 0.53 \cdot 10^{-6}\ \text{cm}^{-1}$ $B_0'' = 0.3013\ \text{cm}^{-1}$ $D_0'' = 0.49 \cdot 10^{-6}\ \text{cm}^{-1}$

$B_1'' = 0.2995$ $D_1'' = 0.48$ $B_1'' = 0.2989$ $D_1'' = 0.49$

$B_2'' = 0.2972$ $D_2'' = 0.49$ $B_2'' = 0.2965$ $D_2'' = 0.50$

$^1/_2$ $B_0'' = \frac{B_{0c} + B_{0d}}{2} = \frac{0.3008 + 0.3008_5}{2} = 0.3008$ $B_0'' = \frac{0.3001 + 0.3002}{2} = 0.3002$

$D_0'' = \frac{0.44 + 0.46}{2} = 0.45$ $D_0'' = \frac{0.45 + 0.44}{2} = 0.45$

$B_1'' = \frac{0.2984 + 0.2983}{2} = 0.2984$ $B_1'' = \frac{0.2975 + 0.2974}{2} = 0.2975$

$D_1'' = \frac{0.45 + 0.43}{2} = 0.44$ $D_1'' = \frac{0.42 + 0.40}{2} = 0.41.$

Unfortunately, only the upper level $v' = 0$ has been investigated. The plates were too weak to permit of rotational analysis of any band containing $v' = 1$. An attempt was made on the 1,3 band but it failed.

When $\Delta_2 F'(J)/(J + \frac{1}{2})$ was plotted against $(J + \frac{1}{2})^2$ the curves obtained were not straight lines as were the lower ones, but were bent downward at the end. This is probably due to the predissociation. It is therefore difficult to obtain correct values of B' and D'. It seemed more convenient to use another method. The following expression is formed

$$\frac{R(J-2) - R(J-1) + P(J) - P(J+1)}{4J} = B'' - B' + 6D' - 2J^2(D'' - D').$$

Plotting the left-hand-side expressions against J^2, one obtains ΔB as the intercept at $J = 0$. ΔD is obtained from the slope. These graphs were, of course, curved as well as the other ones, but here it was easier to neglect the last curved part of the diagram.

Thus, as ΔB and ΔD have been determined, B' and D' are easily computed, since B'' and D'' are already known.

The magnitude of the error for the B'-value is certainly larger than those for the B''-values. It is roughly $\pm$ 0.0005.

The constants derived are:

$A\,^2\Pi$:	$Ag^{107}O^{16}$	$Ag^{109}O^{16}$
$\Omega = {}^3/_2$	$B_0' = 0.2816$ cm^{-1} $D_0' = 1.71 \cdot 10^{-6}$ cm^{-1}	$B_0' = 0.2809$ cm^{-1} $D_0' = 1.69 \cdot 10^{-6}$ cm^{-1}
$\Omega = {}^1/_2$	$B_0' = \frac{B_{0c}' + B_{0d}'}{2} = \frac{0.2812 + 0.2811}{2} = 0.2812$	$B_0' = \frac{0.2804 + 0.2804}{2} = 0.2804$
	$D_0' = \frac{1.68 + 1.67}{2} = 1.68$	$D_0' = \frac{1.67 + 1.67}{2} = 1.67.$

The internuclear distances of $^2\Pi_{3/2}$ and $^2\Pi_{1/2}$ are 2.074 Å and 2.076 Å respectively equal for both isotope-molecules.

The isotopic effect

Silver has two isotopes with the atomic weights 107 and 109 and with a relative abundance of 1:1. The two isotope-molecules have slightly different vibration and rotation constants on account of their different reduced masses μ. If the subscript i refers to the heavier molecule we have

$$\varrho^2 = \frac{\mu}{\mu_i}$$

$$\varrho^2 = 0.9976 \qquad \varrho = 0.9988.$$

The vibrational isotopic displacement may be approximated to

$$\Delta\nu = \nu_v - \nu_v^i \sim (1-\varrho)\left[(v' + \tfrac{1}{2})\,\omega_v' - (v'' + \tfrac{1}{2})\,\omega_v''\right] \sim (1-\varrho) \cdot \nu_v.$$

Table 8

Band	$\Delta\nu_{\text{cal.}}$	$\Delta\nu_{\text{obs.}}$
0,0	−0.1	0.0
0,1	−0.7	−0.6
0,2	−1.3	−1.2

Table 8 gives the vibrational isotopic shift of some bands. The agreement is satisactory.

The rotational isotopic effect is of greater interest. Assuming $B_v^i = \varrho^2 \cdot B_v$, we btain experimental values of ϱ^2 from the B-values estimated above. The result is iven in Table 9.

Table 9

Level	$\varrho^2_{\text{obs.}}$
$X_{3/2}\,v''=0$	0.9970
$X_{1/2}\,v''=0$	0.9978
$X_{3/2}\,v''=1$	0.9980
$X_{1/2}\,v''=1$	0.9970
$X_{3/2}\,v''=2$	0.9976
$A_{3/2}\,v'=0$	0.9975
$A_{1/2}\,v'=0$	0.9973
Mean value	0.9975

he agreement between the observed and theoretical values of ϱ^2 is very good.

he **Λ**-type doubling

The Λ-type doubled lines of the $^2\Pi_{3/2}$–$^2\Pi_{3/2}$ transition are not resolved, quite in greement with the theory. As mentioned above, the magnitude of the splitting is mall, especially for large A-values, and no splitting has been observed in these ands, not even for the highest J-values.

In the sub-bands $^2\Pi_{1/2}$–$^2\Pi_{1/2}$, however, the Λ-type doubling is not negligible. Fig. 2 hows the Λ-type doubling in the 0,0 band. It is computed as $\varepsilon(J) = P_{1c}(J) - P_{1d}(J)$, nvolving the splitting of both the upper and lower states. For low J-values we have

$$\varepsilon(J) = 0.02_9\,(J + \tfrac{1}{2}).$$

t high J-values the Λ-type doubling remains constant at a value of 1.45 cm^{-1}. his is in accordance with the theory of the Λ-type doubling (Jevons (5)).

he coupling constants

The constant separation between the sub-bands is equal to the difference or the um of the doublet splittings of the two $^2\Pi$-states, according as the two states are f the same kind (both normal or both inverted) or of the opposite kind. Thus the oublet splittings of the $^2\Pi$-states cannot be determined directly. Very approximate alues of the coupling constants of the upper and lower levels may be obtained rom the slightly different B-values of the two sub-bands.

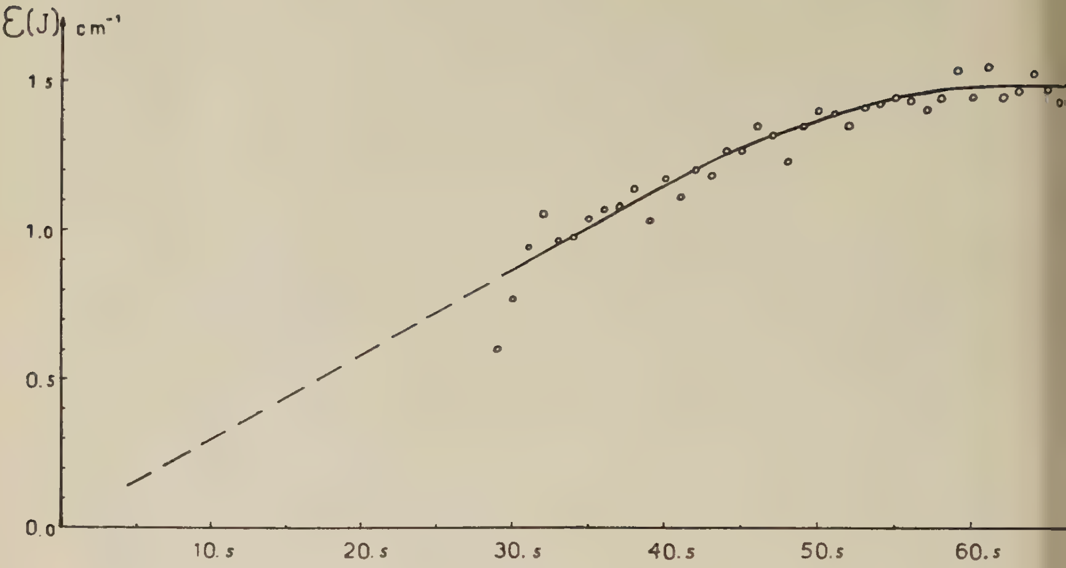

Fig. 2. The Λ-type doubling of the $(0,0)_{1/2}$ band.

Provided that A (or Y) is large, Eq. (1) can be written

$$F_{1,2}(J) \sim B\left[(J+\tfrac{1}{2})^2 - \Lambda^2 \mp \frac{1}{2}\, Y\cdot\Lambda\left(1+\frac{4\,(J+\frac{1}{2})^2}{Y^2\,\Lambda^2}\right)^{\frac{1}{2}}\right]$$

or

$$F_{1,2}(J) \sim B\left[(J+\tfrac{1}{2})^2 \mp \frac{Y\Lambda}{2} \mp \frac{1}{Y\Lambda}\,(J+\tfrac{1}{2})^2\right].$$

Consequently, B_{eff} is approximately

$$B_{\text{eff}} = B\left(1 \pm \frac{B}{A\Lambda}\right).$$

and the B-value difference gives a value of the coupling constant A. The values obtained are

$$X\,{}^2\Pi : A_1 \sim 140 \text{ cm}^{-1}$$

$$A\,{}^2\Pi : A_2 \sim 330 \text{ cm}^{-1}.$$

These values are very rough, as the errors in the B-values exert a great influence. Whether the states are regular or inverted will be discussed later.

The vibrational constants

More accurate values of the vibrational constants have been calculated from the bands 0,0, 0,1, and 0,2 of $X\,{}^2\Pi_{3/2}$. The method used has been given by LAGERQVIST (7).

Consider two bands with the same upper level but with different lower levels i and k).

$$[R(J-1)+P(J)]_{v',\,v_i''}=2\,\nu_0(v',v_i'')+2\,(B'-B_i'')\,J^2$$

$$[R(J-1)+P(J)]_{v',\,v_k''}=2\,\nu_0(v',v_k'')+2\,(B'-B_k'')\,J^2.$$

The difference between the equations (M) is plotted against J^2:

$$M=2\,[\nu_0(v',v_i'')-\nu_0(v',v_k'')]+2\,(B_k''-B_i'')\,J^2=2\,[G''(v_i'')-G''(v_k'')]+2\,(B_k''-B_i'')\,J^2.$$

This gives $2\,\alpha$ as the slope of the line and an accurate value of $\Delta\,G''$ as the intercept on the ordinate.

This method was used on the bands mentioned and gave the values

$$\omega_e''=490.9_1$$

$$\omega_e''\,x_e''=2.8_4.$$

he predissociation

In the level $v'=0$, a cut-off occurs in the rotational structure. In $^2\Pi_{1/2}$ no higher evel than $J=66.5$ has been found. In $^2\Pi_{3/2}$ there is a breaking-off in the level $J\sim 73.5$. The most simple explanation is that the upper level is predissociated. A ough calculation shows that the breaking-off on $v'=2$ would occur soon after the urn of the head. No band-heads involving the level $v'=2$ have been observed, owever. One would expect to see especially the 2,0 bands, which are not overlapped y other bands. Probab lythese bands are rather weak, so that the lines of $J\sim 20.5$–30.5 re faint and the intensity maximum lies at higher J-values where the bands are lready predissociated (assuming Boltzmann distribution).

IV. The ultra-violet system

ibrational analysis

The ultra-violet bands of AgO shade off to shorter wavelengths and form very narked non-overlapping sequences. The 0,0 sequence is the strongest one. The plates lso show the 0,1 and 1,0 sequences. A reproduction of the first bands of the 0,0,),1 and 1,0 sequences is given in Fig. 3.

The distance between the 0,0 and 0,1 sequences shows that the ultra-violet system as the lower state in common with the blue system. The analysis of the blue bands howed that the lower state is a $^2\Pi$-state. Thus the ultra-violet bands can not reresent a $^2\Sigma$–$^2\Sigma$, as was stated by LOOMIS and WATSON (1).

The only possible transitions are $^2\Sigma$–$^2\Pi$, $^2\Delta$–$^2\Pi$ and $^2\Pi$–$^2\Pi$. If either of the first wo alternatives is the right one, the bands would contain strong Q-branches and very sub-band would show a double-headed structure. The distance between the P and Q heads may be approximately calculated. Consider for example, the first and in the 0,0 sequence (see Fig. 3 b). If we plot the distances between consecutive ines of the strong branch (probably the P-branch) against J (a relative J-numbering s the absolute numbering is unknown), we obtain $2\,\Delta\,B$ as the inclination of the ine. The distance between the head and the origin is given by the formula

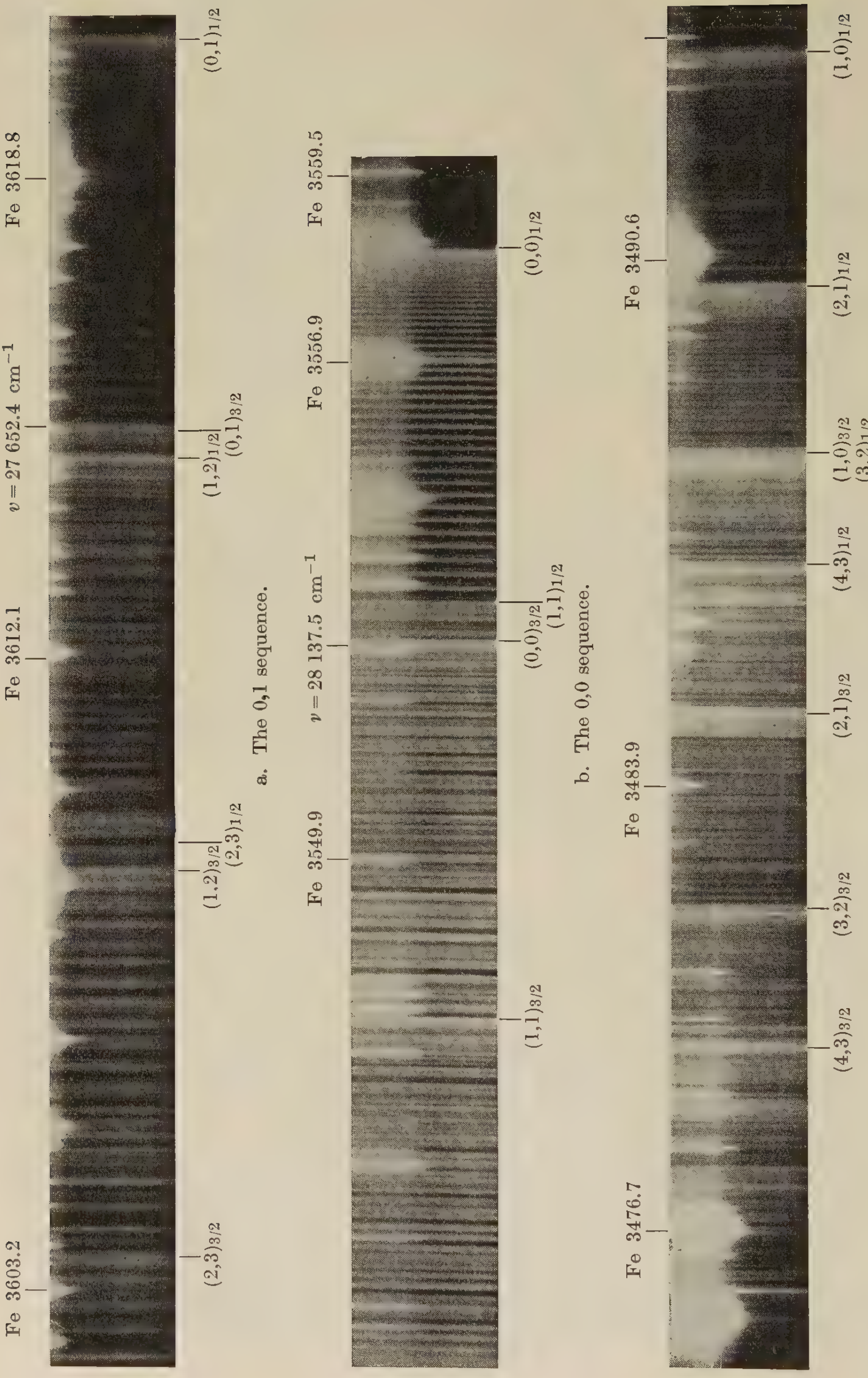

a. The 0,1 sequence.

b. The 0,0 sequence.

c. The 1,0 sequence.

Fig. 3. The ultra-violet band-system.

$$\nu_{\text{head}} - \nu_{\text{origin}} = -\frac{(B'+B'')^2}{4(B'-B'')},$$

as the B''-value is known.

These calculations give a value for the distance between the P and Q heads of 5–6 cm^{-1}. ($B'' \sim 0.30$ and $\Delta B \sim 0.017$.) No head at such a distance is to be observed in this or any other band. Thus these bands do not contain strong Q-branches, so the possibilities $^2\Sigma-^2\Pi$ and $^2\Delta-^2\Pi$ must be excluded. Consequently, the ultraviolet bands must represent a $^2\Pi-^2\Pi$ transition. The upper state is here denoted $B\ ^2\Pi$.

As the state $X\ ^2\Pi$ belongs to Hund's case a, the bands must show a doublet structure and occur in pairs of apparently equal intensity. No such doubling has been observed by Loomis and Watson. They give a list of the frequencies of the observed band-heads. The present measurement of the heads agrees well, on the whole, with these values except in one case. The head at $\nu = 28\,130.0$ cm^{-1} has not been found, but instead a strong head situated at $\nu = 28\,137.5$ cm^1 (see Fig. 3 b).

This head does not fit in the vibration-scheme nor does the strong head at $\nu = 27\,652.4$ cm^{-1}. In the new vibrational analysis the bands at 28 137.5 cm^{-1} and 27 652.4 cm^{-1} are assigned to 0,0 and 0,1 respectively, thus supplying the missing sub-bands of the bands 0,0 at 28 094.3 cm^{-1} and 0,1 at 27 610.6 cm^{-1}. The vibrational assignment of the heads measured is given in Tables 10 and 11. The band-heads may be represented by the following equations:

$$(1)\quad \nu_{3/2} = 28\,113.9 + [539.1\,(v'+\tfrac{1}{2}) - 6.1_5\,(v'+\tfrac{1}{2})^2] - [490.7\,(v''+\tfrac{1}{2}) - 2.8_7\,(v''+\tfrac{1}{2})^2]$$

$$(2)\quad \nu_{1/2} = 28\,072.1 + [535.7\,(v'+\tfrac{1}{2}) - 6.3_4\,(v'+\tfrac{1}{2})^2] - [489.9\,(v''+\tfrac{1}{2}) - 3.0_8\,(v''+\tfrac{1}{2})^2].$$

The agreement between the ω''-values of the blue and ultra-violet system is good.

The differences between the calculated and observed values are given in brackets in Tables 10 and 11. According to Eq. (2) the heads at 27 229.0 cm^{-1} and 28 716.2 cm^{-1} given by Loomis and Watson are the $(1,3)_{3/2}$ and $(3,2)_{3/2}$ bands respectively.

The vibrational constants of the upper level differ for the two sub-systems. This is the reason why the two doublet components do not show a constant separation. The separation changes systematically. It is of the same magnitude (~ 40 cm^{-1}) as the distance between two members of a sequence. These circumstances make it less obvious that also the ultra-violet bands show a doublet structure. Especially the 1,0 sequence looks very complicated. The vibrational assignment has been checked by rotational analysis.

Rotational analysis

Rotational analysis has been carried out mainly for the 0,0 bands. The ultra-violet system is weaker than the blue one and shows a very dense rotational structure. The bands overlap very much, as the distance between two consecutive heads is only ~ 40 cm^{-1}. Only the 0,0 sequence was well exposed and convenient for rotational analysis. The 0,1 bands have also been measured, though only as a check on the analysis. The lines are weak and slightly blurred, as may be seen in Fig. 3 a. The 1,0 sequence was not worth measuring, as the lines seemed to be too weak for analysis. The band constants have been derived entirely from the 0,0 bands.

The analysis is comparatively simple, as the lower combination differences are known. The sub-band situated towards the violet turned out to be the $^2\Pi_{3/2}-^2\Pi_{3/2}$ transition. No satellite branches have been observed. Consequently, also the $B\ ^2\Pi$ belongs to Hund's case a. Tables 12–14 give the wave-numbers of the 0,0 and 0,1

Table 10

Bandheads of $^2\Pi_{1/2}$—$^2\Pi_{1/2}$

v' \ v''	0	1	2	3
0	28 094.3 (−0.1)	27 610.6 (−0.2)		
1	28 617.0 (+0.2)	28 133.3 (+0.1)	27 655.6 (+0.3)	
2		28 643.9 (−0.1)		27 694.9 (−0.1)
3			28 664.3 (−0.4)	
4				28 677.0 (+0.4)

Table 11

Bandheads of $^2\Pi_{3/2}$—$^2\Pi_{3/2}$

v' \ v''	0	1	2	3
0	28 137.5 (+0.2)	27 652.5 (+0.3)		
1	28 664.3 (−0.2)	28 179.4 (−0.2)	27 700.1 (−0.2)	
2		28 693.7 (0.0)		27 741.0 (0.0)
3			28 716.8 (0.0)	
4				28 733.1 (0.0)

bands. The vibrational isotopic effect is negligible in the 0,0 sequence and the lines of the two isotope-molecules are badly resolved, as the rotational isotopic effect, too, is small. For the $(0,0)_{1/2}$ band no distinction between the isotopes has been made. The rotational constants have been derived graphically by the same method as was used for the lower state of the blue bands.

The constants derived are:

	$Ag^{107}O^{16}$	$Ag^{109}O^{16}$
$X\,^2\Pi$:		
$\Omega = ^3/_2$	$B_0 = 0.3024 \quad D_0 = 0.50 \cdot 10^{-6}$	$B_0 = 0.3015 \quad D_0 = 0.53 \cdot 10^{-6}$
$\Omega = ^1/_2$	$B_0 = 0.3006 \quad D_0 = 0.46 \cdot 10^{-6}$	
$B\,^2\Pi$:		
$\Omega = ^3/_2$	$B_0 = 0.3195 \quad D_0 = 0.50$	$B_0 = 0.3188 \quad D_0 = 0.52$
$\Omega = ^1/_2$	$B_0 = 0.3178 \quad D_0 = 0.51$	

The internuclear distance $r_0' = 1.947$ Å, equal for both isotopic molecules.

Table 12

Wavenumbers of the 0,0 band

J	$^2\Pi_{3/2}$–$^2\Pi_{3/2}$				$^2\Pi_{1/2}$–$^2\Pi_{1/2}$			
	$Ag^{107}O^{16}$		$Ag^{109}O^{16}$		Mean value of the isotopes			
	R_2	P_2	R_2	P_2	R_{1c}	P_{1c}	R_{1d}	P_{1d}
17,5	28 160.14*		28 160.14*		28 117.49*		28 117.09	
18,5	61.39*		61.39*		18.81*		18.39	
19,5	62.63*		62.63*		20.11*		19.61	
20,5	64.10*		64.10*		21.42*		20.97	
21,5	65.58*		65.58*		22.79*		22.30	
22,5	66.94*		66.94*		24.20*		23.70	
23,5	68.55*		68.55*		25.65*		25.08	
24,5	70.09*		70.09*		27.06*		26.60	
25,5	71.63*	28 138.56*	71.63*	28 138.56*	28.54*	28 095.38*	28.08	28 095.14
26,5	73.10*	38.78*	73.10*	38.78*	30.11*	95.67*	29.57	95.38*
27,5	74.72*	39.10*	74.72*	39.10*	31.70*	95.97*	31.14	95.67*
28,5	76.38*	39.43*	76.38*	39.43*	33.27*	96.35*	32.74	95.97*
29,5	78.03*	39.82*	78.03*	39.82*	34.93*	96.86*	34.37	96.35*
30,5	79.69*	40.30*	79.69*	40.30*	36.51*	97.26*	35.97	96.86*
31,5	81.47*	40.71*	81.47*	40.71*	38.26*	97.72*	37.74	97.26*
32,5	83.20*	41.19*	83.20*	41.19*	39.96	98.20*	39.43*	97.72*
33,5	84.96*	41.74*	84.96*	41.74*	41.74*	98.73*	41.19*	98.20*
34,5	86.70*	42.30*	86.70*	42.30*	43.50*	99.27*	42.87*	98.73*
35,5	88.52*	42.87*	88.52*	42.87*	45.47	99.86*	44.85*	99.27*
36,5	90.53*	43.50*	90.53*	43.50*	47.32	100.48*	46.77*	199.86*
37,5	92.46*	44.17*	92.46*	44.17*	49.20	01.15*	48.47*	100.48*
38,5	94.47*	44.85*	94.47*	44.85*	51.18	01.83*	50.36	01.15*
39,5	96.35*	45.57*	96.35*	45.57*	53.16	02.54*	52.44	01.83*
40,5	98.42*	46.34*	98.42*	46.34*	55.17	03.31*	54.31*	02.54*
41,5	200.59	47.20*	200.40	47.20*	57.09*	04.08*	56.37*	03.31*
42,5	02.64	48.03*	02.40	48.03*	59.30*	04.92*	58.41*	04.08*
43,5	04.79	48.81*	04.56	48.81*	61.39*	05.79*	60.53*	04.92*
44,5	07.03	49.75*	06.82	49.75*	63.56	06.71*	62.63*	05.79*
45,5	09.14	50.73*	08.91*	50.73*	65.76	07.59*	64.74*	06.71*
46,5	11.31	51.62*	11.05	51.62*	67.93	08.56*	66.94	07.59*
47,5	13.62	52.69*	13.41	52.69*	70.09*	09.57*	69.06*	08.56*
48,5	15.96*	53.69*	15.76	53.69*	72.47	10.57*	71.44	09.57*
49,5	18.26	54.76*	18.04	54.76*	74.72*	11.66*	73.65*	10.57*
50,5	20.62	55.86*	20.32*	55.86*	77.04	12.74*	75.89	11.66*
51,5	22.90	57.09*	22.71	57.09*	79.38	13.89*	78.37	12.74*
52,5	25.31	58.27*	24.94	58.27*	81.96*	15.03*	80.78	13.89*
53,5	27.86	59.29*	27.46*	59.29*	84.33	16.23*	83.20*	15.03*
54,5	30.40	60.53*	30.14	60.53*	86.70*	17.49*	85.58*	16.23*
55,5	32.91	62.02*	32.68	62.02*	89.20	18.81*	87.95	17.49*
56,5	35.42	63.38*	35.21	63.38*	91.84	20.11*	90.53*	18.81*
57,5	38.14	64.74*	37.84	64.74*	94.47	21.42*	93.07*	20.11*
58,5	40.70	66.16*	40.35	66.16*	97.08*	22.84*	95.69	21.42*
59,5	43.39	67.53*	43.09	67.53*	99.68	24.26*	98.42	22.84*

Table 12 (cont.)

J	$^2\Pi_{3/2}$–$^2\Pi_{3/2}$				$^2\Pi_{1/2}$–$^2\Pi_{1/2}$			
	$Ag^{107}O^{16}$		$Ag^{109}O^{16}$		Mean value of the isotopes			
	R_2	P_2	R_2	P_2	R_{1c}	P_{1c}	R_{1d}	P_{1d}
60.5	28 246.13	28 169.06*	28 245.81	28 169.06*	28 202.33	28 125.65*	28 201.08*	28 124.26*
61,5	48,82	70.56*	48.48	70.56*	05.05	27.06*	03.71	25.80
62,5	51.55	72.08*	51.29	72.08*	07.74*	28.54*	06.20	27.26
63,5	54.35	73.65*	54.05	73.65*	10.55	30.11*	08.91*	28.77
64,5	57.15	75.27*	56.77	75.27*	13.25	31.65*	11.70	30.30
65,5	60.07	76.85*	59.70	76.85*	15.96*	33.27*	14.50*	31.91
66,5	62.98	78.55*	62.62	78.55*	18.81	34.93*	17.31	33.48
67,5	65.87	80.23*	65.49	80.23*	21.57	36.51*	20.32*	35.16
68,5	68.84	81.96*	68.51	81.96*	24.56	38.26*	23.10	36.82
69,5	71,85	83.78*	71.53	83.78*	27.46	39.82*	26.15	38.56*
70,5	74.92	85.58*	74.57	85.58*		41.60		40.30*
71,5	77.99	87.45*	77.69	87.45*				
72,5	81.19	89.38*	80.70	89.38*				
73,5	84.27	91.25*	83.80	91.25*				
74,5	87.38	93.19*	86.98	93.19*				
75,5	90.55	95.15*	90.13	95.15*				
76,5	93.77	97.18*	93.35	97.18*				
77,5	96.99	99.24*	96.64	99.24*				
78,5	300.39	201.40*	99.95	201.40*				
79,5	03.68	03.51*	303.27	03.51*				
80,5	07.06	05.72*	06.57	05.72*				
81,5	10.47	07.85*	10.08	07.85*				
82,5	13.90	10.01*	13.42	10.01*				
83,5	17.30	12.31*	16.86	12.31*				
84,5	20.92	14.62*	20.37	14.62*				

The agreement between B''-values obtained from the ultraviolet and the blue systems is satisfactory. The B-values can be combined in the equations:

Isotope 107: $\Omega = {}^3/_2 \quad B_v = 0.3035 - 0.0025_5 \; (v + \tfrac{1}{2})$

$\Omega = {}^1/_2 \quad B_v = 0.3020 - 0.0025 \; (v + \tfrac{1}{2}).$

The internuclear distances of $^2\Pi_{3/2}$ and $^2\Pi_{1/2}$ are 1.998 Å and 2.003 Å respectively.

Isotope 109: $\Omega = {}^3/_2 \quad B_v = 0.3026 - 0.0024_5 \; (v + \tfrac{1}{2})$

$\Omega = {}^1/_2 \quad B_v = 0.3014 - 0.0026 \; (v + \tfrac{1}{2}).$

The internuclear distances are 1.998 Å and 2.002 Å, which agrees well with the values given above.

The isotopic effect

The vibrational isotopic effect is negligible in the 0,0 sequence and of the magnitude 0.5 cm^{-1} in the 0,1 sequence. Only for the $(0,0)_{3/2}$ band have different B-values of the two isotopes been obtained. The ϱ^2 values obtained are:

Table 13

Wavenumbers of the $(0,1)_{3/2}$ band

J	$Ag^{107}O^{16}$		$Ag^{109}O^{16}$		J	$Ag^{107}O^{16}$		$Ag^{109}O^{16}$	
	R_2	P_2	R_2	P_2		R_2	P_2	R_2	P_2
34,5	27 703.80		27 704.34		47,5	27 733.37	27 672.54*	27 733.84	27 672.91*
35,5	05.85		06.36	27 660.63*	48,5	35.94	73.76	36.35	74.30
36,5	07.96	27 661.09	08.41	61.48	49,5	38.53	75.17*	38.88	75.62
37,5	10.26	61.88*	10.71	62.46*					
38,5	12.36	62.72	12.83	63.37*	50,5	41.08	76.58*	41.45	77.02*
39,5	14.44	63.81*	14.88	64.15*	51,5	43.84	77.93	44.13	78.48*
					52,5	46.42	79.32*	46.83	79.76*
40,5	16.80	64.59*	17.14	64.99	53,5	49.28	80.73*	49.61	81.18*
41,5	18.98	65.70	19.40	66.13	54,5	52.06	82.34	52.36	82.71
42,5	21.24	66.75	21.67	67.14	55,5	55.00	83.96*	55.33	84.41*
43,5	23.61	67.92*	24.00	68.32*	56,5	57.87	85.48*	58.24	85.92*
44,5	25.99	69.01	26.39	69.55*	57,5	60.39	87.16	60.74	87.51
45,5	28.44	70.05*	28.83	70.60	58,5	63,41	88.92*	63.76	89.35*
46,5	30.90	71.41	31.30	71.73*	59,5		90.55*		90.95*

Level	ϱ^2
$X\,^2\Pi_{3/2}v''=0$	0.9970
$B\,^2\Pi_{3/2}v'=0$	0.9978.

The theoretical value of ϱ^2 is 0.9976.

The Λ-type doubling

The Λ-type doubling is quite analogous to the one observed for the blue system. No splitting has been found for the $^2\Pi_{3/2}$–$^2\Pi_{3/2}$ transition. A Λ-type doubling increasing linearly with $(J+\frac{1}{2})$ for small J-values and then having a constant value is obtained for $^2\Pi_{1/2}$-$^2\Pi_{1/2}$. It amounts to 1.4 cm^{-1} for high J-values, and for low J-values the equation $\varepsilon(J)=0.02_2\,(J+\frac{1}{2})$ is valid.

The coupling constants

The difference or the sum of the coupling constants of the two $^2\Pi$-states must be approximately equal to the doublet separation obtained from the v_{00} values for the sub-systems. Using the formulae derived in connection with the coupling constants of the blue system,

$$B_{\text{eff}}=B\left(1\pm\frac{B}{A\Lambda}\right),$$

we obtain

$$X\,^2\Pi \quad A_1\sim 130\ \text{cm}^{-1}$$
$$B\,^2\Pi \quad A_3\sim 150\ \text{cm}^{-1}.$$

The values of the blue system are

$$X\,^2\Pi \quad A_1\sim 140\ \text{cm}^{-1}$$
$$A\,^2\Pi \quad A_2\sim 330\ \text{cm}^{-1}.$$

These values are very uncertain, however.

Table 14

Wavenumbers of the $(0,1)_{1/2}$

J	$Ag^{107}O^{16}$				$Ag^{109}O^{16}$			
	R_{1c}	P_{1c}	R_{1d}	P_{1d}	R_{1c}	P_{1c}	R_{1d}	P_{1d}
14,5	27 629.93*		27 629.43*				27 629.93*	
15,5	31.05*		30.65*		27 631.54*		31.05*	
16,5	32.31*		31.90*		32.73*		32.31*	
17,5	33.64*		33.22*		34.06		33.64*	
18,5	35.00*		34.49		35.37		35.00*	
19,5	36.34*		35.94		36.77		36.34*	
20,5	37.81*		37.35		38.34		37.81*	
21,5	39.26*		38.85		39.78		39.26*	
22,5	40.83*		40.32		41.43		40.83*	
23,5	42.46*		42.00		42.89		42.46*	
24,5	43.90*	27 612.29*	43.42	27 611.88	44.51	27 612.69*	43.90*	27 612.29*
25.5	45.58*	12.69*	45.11	12.29*	46.21	13.10*	45.58*	12.69*
26,5	47.22*	13.10*	46.72	12.69*	47.73	13.55*	47.22*	13.10*
27,5	48.88*	13.55*	48.42	13.10*	49.48	14.03*	48.88*	13.55*
28,5	50.65*	14.03*	50.18	13.55*	51.26	14.52*	50.65*	14.03*
29,5	52.51*	14.52*	51.89	14.03*	53.09	15.12*	52.51*	14.52*
30,5	54.30*	15.12*	53.65	14.52*	54.84	15.69*	54.30*	15.12*
31,5	56.21*	15.69*	55.60	15.12*	56.79	16.30*	56.21*	15.69*
32,5	58.02*	16.30*	57.36	15.69*	58.61	17.01*	58.02*	16.30*
33,5	59.99*	17.01*	59.41	16.30*	60.63*	17.72*	59.99*	17.01*
34,5	61.99	17.80*	61.37	17.01*	62.56*	18.37*	61.88*	17.72*
35,5	64.13*	18.57*	63.37*	17.80*	64.59*	19.14*	63.81*	18.37*
36,5	66.22*	19.37*	65.42	18.57*	66.66*	19.90*	65.78*	19.14*
37,5	68.32*	20.23*	67.56*	19.37*	68.68	20.73*	67.92*	19.90*
38,5	70.49	21.11*	69.55*	20.23*	70.87	21.57*	70.05*	20.73*
39,5	72.54*	22.05*	71.73*	21.11*	72.91*	22.51*	72.18	21.57*
40,5	74.79	22.96*	73.89	22.05*	75.17*	23.42*	74.42	22.51*
41,5	77.02*	23.98*	76.16	22.96*	77.43	24.58*	76.58*	23.42*
42,5	79.32*	25.04*	78.48*	23.98*	79.76*	25.64*	78.88	24.58*
43,5	81.63	26.12	80.73*	25.04*	82.04	26.68*	81.18*	25.64*
44,5	83.96*	27.11	83.13	26.23	84.41*	27.69	83.50	26.68*
45,5	86.36	28.24	85.48*	27.37	86.79	28.80	85.92*	27.94
46,5	88.92*	29.43*	87.92	28.52	89.35*	29.93	88.39	29.04
47,5	91.35	30.65*	90.55*	29.82	91.70	31.05*	90.95*	30.21
48,5	93.81	31.90*	93.07	31.05*	94.20	32.31*	93.38	31.54*
49,5	96.33	33.22*	95.51	32.31*	96.77	33.64*	95.93	32.73*

From the equations

$$F_1(J) = B[(J+\tfrac{1}{2})^2 - \Lambda^2 - \tfrac{1}{2}\sqrt{4(J+\tfrac{1}{2})^2 + Y(Y-4)}] - DJ^4$$

$$F_2(J) = B[(J+\tfrac{1}{2})^2 - \Lambda^2 + \tfrac{1}{2}\sqrt{4(J+\tfrac{1}{2})^2 + Y(Y-4)}] - D(J+1)^4$$

we can see immediately that F_2 always lies above F_1 and that F_2 gives a greater effective B-value than F_1. $^2\Pi_{3/2}$ are $^2\Pi_{1/2}$ are distinguishable by the Λ-type doubling,

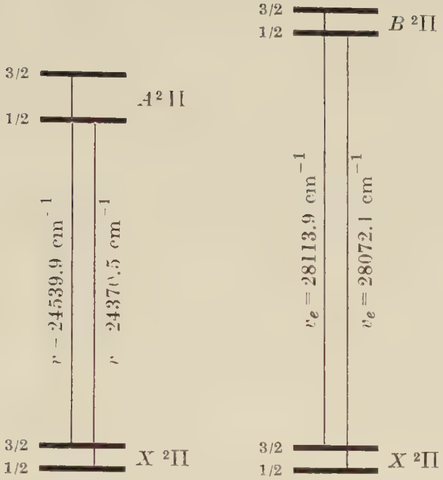
3/2
1/2
$B\ ^2\Pi$
3/2
1/2
$A\ ^2\Pi$
$\nu = 24539.9\ \mathrm{cm}^{-1}$
$\nu = 24370.5\ \mathrm{cm}^{-1}$
$\nu_e = 28113.9\ \mathrm{cm}^{-1}$
$\nu_e = 28072.1\ \mathrm{cm}^{-1}$
3/2
1/2
$X\ ^2\Pi$
3/2
1/2
$X\ ^2\Pi$

Fig. 4. The band-systems of AgO. The doublet splitting is greatly exaggerated.

apart from other facts. In the present case the B-values for $^2\Pi_{3/2}$ are greater than those for $^2\Pi_{1/2}$. This indicates that $^2\Pi_{3/2}$ lies above $^2\Pi_{1/2}$ and that all three doublets are regular (Fig. 4).

We have

$$|A_2 - A_1| \approx 169.4$$
$$|A_3 - A_1| \approx 41.8$$

but it is impossible to obtain accurate values of the coupling constants as no $^2\Pi$–$^2\Sigma$ transition is known.

My thanks are due to Professor ERIK HULTHÉN, Director of the Institute of Physics, for drawing my intention to this problem and for his keen interest with which he has followed my work throughout. I also wish to thank Docent ALBIN LAGERQVIST and Fil. Lic. BENGT KLEMAN for many helpful discussions. I am much indebted to Fil. lic. GUNNAR ALMKVIST for good advice and for his kindness in lending me his vacuum arc.

January 1953. Physics Department, University of Stockholm.

REFERENCES

1. F. W. LOOMIS and T. E. WATSON, Phys. Rev. *48*, 280, 1935.
2. G. R. HARRISON, Wavelength Tables, New York, 1939.
3. G. HERZBERG, Spectra of Diatomic Molecules, Van Nostrand Company, New York, 1950, 257 and 268.
4. R. S. MULLIKEN, Rev. Mod. Phys. *3*, 129 and 110, 1931.
5. W. JEVONS, Reports on Band-Spectra of Diatomic Molecules, Cambridge, 1932, 126.
6. E. L. HILL and J. H. VAN VLECK, Phys. Rev. *32*, 250, 1923.
7. M. HULTIN and A. LAGERQVIST, Ark. f. Fysik *45*, 471, 1951.

Tryckt den 8 augusti 1953

Uppsala 1953. Almqvist & Wiksells Boktryckeri AB

ARKIV FÖR FYSIK Band 7 nr 13

Communicated 3 June 1953 by MANNE SIEGBAHN and G. BORELIUS

Determination of the radiation hazards from a 1.5 MeV high voltage accelerator

By KATARINA AHNLUND

With 2 figures in the text

Introduction

The 1.5 MeV high voltage accelerator of the Nobel Institute (1) is used for acceleration of protons or deuterons for work in nuclear transmutation studies. The radiation intensities in the neighborhood of the machine have been measured, especially in such localities to which personnel has access. As there have been some inquiries from people planning accelerator buildings as to the expectable radiation from this type of machine, it has been found suitable to publish some experiences.

Mainly two kinds of penetrating radiation originate from the accelerator, electromagnetic radiation and fast neutrons. A large part of the beam hits the lenses and walls of the accelerating system. Then, in the first place, secondary electrons are emitted which move upwards and give rise to X-rays as they strike the inner surfaces of the tube. Secondly, by a deuteron beam, deuterium is stored on the walls and acts as target for additional incident deuterons. By the D + D reaction fast neutrons are produced. With a deuteron energy of 1 MeV the neutrons have energies of 1.7–4 MeV. The neutrons in turn can, by capture, produce γ-radiation.

Electromagnetic radiation

The X-radiation was measured with a calibrated GM-detector during the acceleration of a 0.88 MeV, 100 μA proton beam. This has been a normal running condition during the determinations of nuclear Q-values. Table 1 gives the exposures measured at the various positions indicated in the general view of the high tension hall in Fig. 1.

In no place in the target room was the exposure bigger than 1.5 mr/hour. The control room I is only used by start and occasional supervision of the machine. The door between the high tension hall and the workshop is shielded by 0.5 cm of lead, which is indicated in the figure. The carpenter's shop, which has no special shielding is not so extensively used. The high tension set is in use for about 30 hours a week. Then the safe level of exposure to this kind of radiation 300 mr/week will for no personnel be exceeded (2). Continuous detection of the electromagnetic radiation by pocket dosimeters has given similar results.

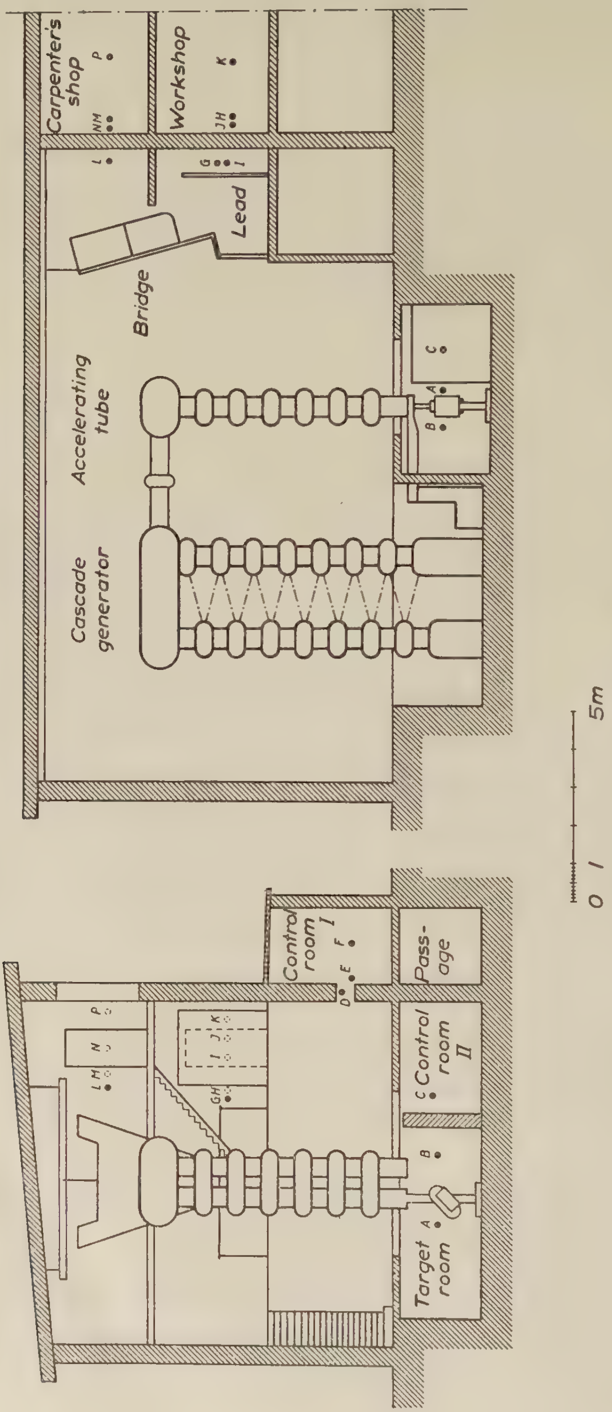

Fig. 1. Plan of the high tension hall with adjoining localities.

Table 1. Radiation level of electromagnetic radiation at $E_p = 0.88$ MeV, $I_p = 100$ μA.

Position in Fig. 1	X-ray Exposure mr/h
A	1.5
B	1.5
C	0.5
D	9
E	12
F	3
G	20
H	1
I	7
J	5
K	2.5
L	13
M	1
N	6
P	3.5

Maximum permissible exposure = 300 mr/week for total exposure to all kinds of radiation.

Neutron radiation

Most of the fast neutrons are produced in the lowest part of the acceleration tube and in the target system, where the beam hits several narrowing arrangements. Therefore the protection against this type of radiation is of significance mainly for the target room. On the other hand it has been found most practical to manage the machine from a place in the neighborhood of the target, from where all additional apparatus can be easily supervised. Then one must have at least some part of the target room well shielded against the fast neutrons. As these are best slowed down by light elements, especially hydrogen, a water-filled tank is introduced between the accelerator and the control equipment. See Fig. 2, where a plan of the target room is given. The water container has the dimensions $235 \times 235 \times 50$ cm³ and is welded of 0.5 cm iron plates.

A measurement of the neutron flux in the target room has been performed by means of a boron chamber surrounded by an inner layer of 5 cm of paraffin and a removable outer layer of 0.5 cm of cadmium. A 100 mC Ra Be-source was used to calibrate the chamber. The fluxes of fast and slow neutrons were measured on the places which are indicated in Fig. 2. Point 1 lies 1.8 m from the first narrowing part of the acceleration tube where most of the neutrons are generated. The source strength can be estimated to about 10 C.

The table shows that the wall reduces the fluxes by a factor of ten. The stipulated tolerance dosage for fast neutron exposure is 10–20 n/cm², sec during a 120 hours' working week (3). One finds that the water wall installation is quite necessary and that the actual wall thickness reduces the neutron exposure at the control panel to less than half the permissible neutron dosage in case the machine is run for 30 hours a week.

Table 2. Radiation level of neutrons at $E_d = 0.88$ MeV, $I_d = 50$ μA.

Position in Fig. 1	Fast neutron flux n/cm^2, sec.	Total neutron flux n/cm^2, sec.
1	190	210
2	110	120
3	17	20
4	19	22
5	20	24
6	75	85

Tolerance dosage = 10–20 fast n/cm^2, sec., during a 120 hours working week (3).

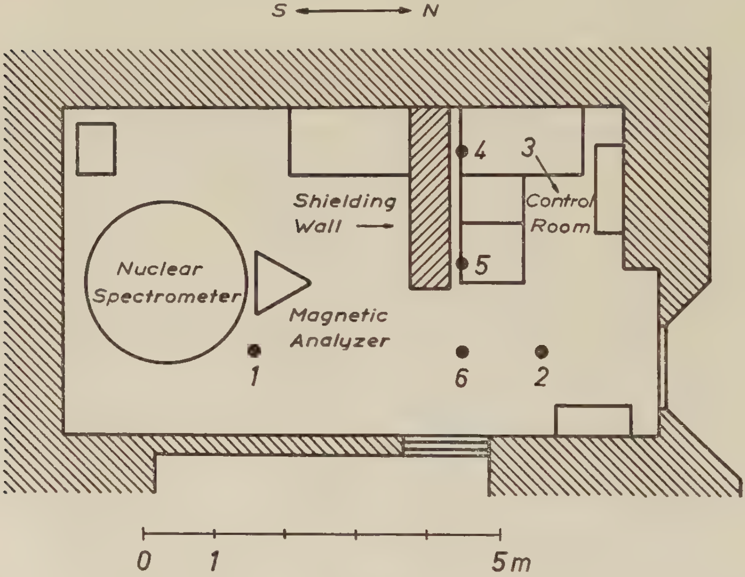

Fig. 2. Plan of the target room.

Concluding remarks

By adding the exposures of the different kinds of radiation one obtains the total dosage for personnel continuously working in the target room. During the present running conditions of the machine the permissible dosage is not exceeded. Later on, the question of further protective measures may be actualized.

By the construction of a high voltage accelerator one must consider how dangerous radiation is produced. It is important to give the acceleration tube a sufficiently transparent construction. This is of course also valuable in order to obtain good pumping speeds in the vacuum system. If a narrowing passage in the beam channel is placed after an energy selector the secondary electrons are hindered by the selector from moving upwards the tube and much less X-radiation will result than if the narrowing passage lies before the selector. In the upper parts of the tube one can use such materials in which X-rays are not easily produced. Stored deuterium from which neutrons originate can be made to gase away by heating.

The main protection against all kinds of radiation is of course distance. The importance of sufficiently spaced localities around the accelerator and target system is emphasized by this aspect as well as by others.

REFERENCES

1. MILEIKOWSKY, C., and PAULI, R. T., Ark. f. fys. Bd *4*, nr 12, 287, 1951.
2. Recommendations of the International Commission on Radiological Protection, Br. Journ. of Rad. 1950.
3. HUGHES, Pile Neutron Research, 1953.

Tryckt den 30 november 1953

Uppsala 1953. Almqvist & Wiksells Boktryckeri AB

ARKIV FÖR FYSIK Band 7 nr 14

Communicated 3 June 1953 by MANNE SIEGBAHN and G. BORELIUS

Proton groups from deuteron bombardment of Ne^{20} by magnetic analysis. Transitions to the ground state and first excited state of Ne^{21}

By KATARINA AHNLUND

With 8 figures in the text

Introduction

In the present investigation a magnetic analysis has been made of the two proton groups of longest range from the reaction $Ne^{20}(d,p)Ne^{21}$. (Fig. 1.)

The ground state transition is one part of the important nuclear reaction cycle linking the isotopes of fluorine and neon (ref. 1):

$$F^{19}(p,\alpha)O^{16},\ O^{16}(d,\alpha)N^{14},\ N^{14}(d,p)N^{15},\ O^{18}(p,\alpha)N^{15}$$
$$O^{18}(p,n)F^{18},\ Ne^{20}(d,\alpha)F^{18},\ Ne^{20}(d,p)Ne^{21},\ Ne^{21}(d,\alpha)F^{19}$$

VAN PATTER *et al.* (ref. 2) have made one precise measurement of the Q-value of $Ne^{20}(d,p)Ne^{21}$ by magnetic analysis of protons from a separated gas-target from

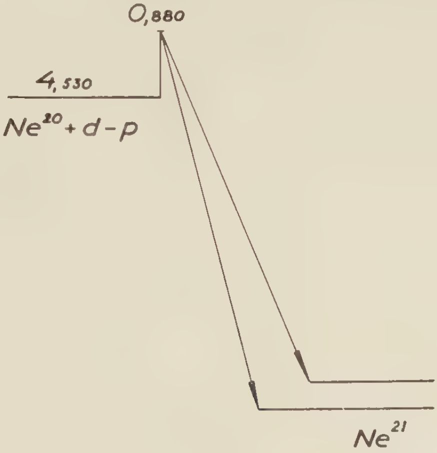

Fig. 1. Level scheme of the reaction $Ne^{20}(d,p)Ne^{21}$.

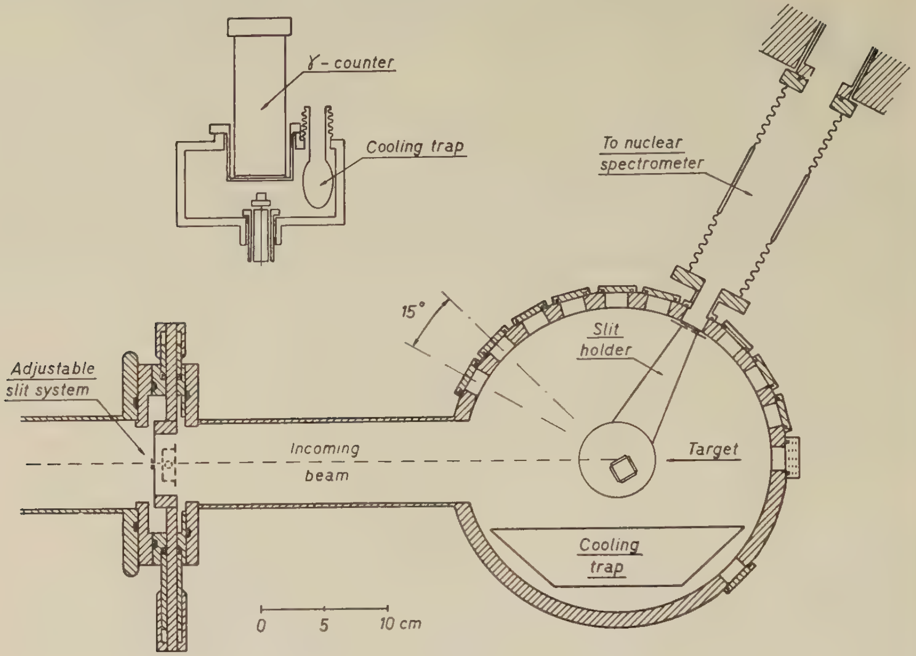

Fig. 2. Horizontal section of the target chamber.

the isotope separator of this institute. In view of the importance of the reaction cycle above it has been considered worth while to make a new determination with altered experimental conditions and on several Ne^{20}-targets.

MIDDLETON and TAI (ref. 3) have used a photographic range method for a systematic survey of the $Ne^{20}(d,p)Ne^{21}$ transitions obtainable with 7.8 MeV deuterons.

Experimental apparatus

The deuterons were obtained from the 1.4 MeV Cockroft-Walton accelerator of the Nobel Institute and bent by a 90° homogeneous field magnetic analyzer (ref. 4). Two adjustable slit systems placed before and after the magnet serve to focus a spot of adequate dimensions on the target. The second slit system is also a feeling medium for an electronic stabilization of the high tension (ref. 5). The target chamber is shown in fig. 2. The reaction products are analyzed by a heavy particle spectrometer (ref. 6, 7) which is connected to one of the openings in the target chamber wall placed at 15° intervals. Fig. 3 shows a sectional view of the target support consisting of three rotatable systems by means of which various operations can be performed without breaking the vacuum. In the cover of the chamber a scintillation γ-detector and a liquid air trap are sunk.

For detection of the particles which had passed the spectrometer two types of detectors were employed. In the case of proton scattering the great intensities allowed direct detection by means of a heavy-particle scintillation counter, which is shown in Fig. 4. For weaker intensities photographic detection by Ilford C 2 100 μg plates was used.

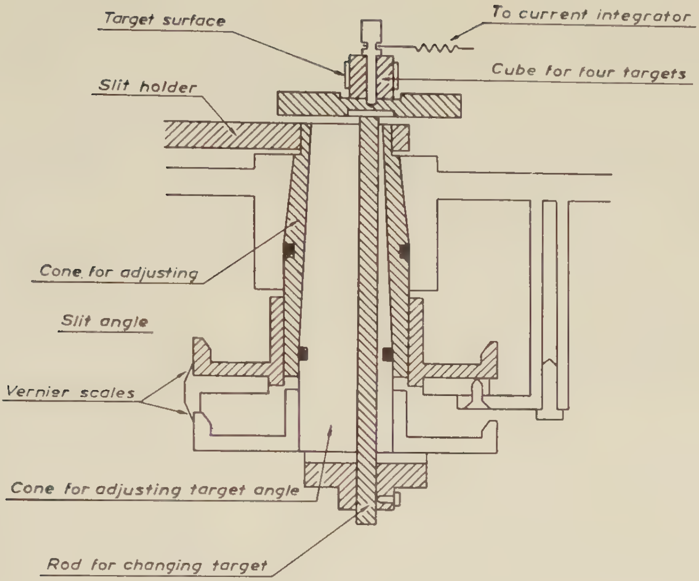

Fig. 3. Sectional view of the target system.

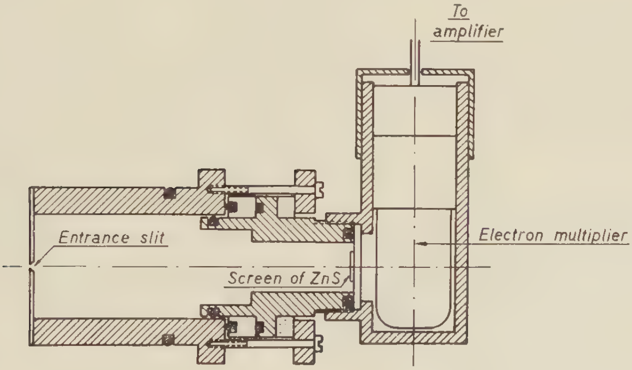

Fig. 4. Scintillation detector for heavy particles. The RCA 1P28 electron multiplier tube must be iron-shielded as the detector is placed in the stray field from the spectrometer.

Experimental procedure

The general procedure comprises the following main points:

a. Establishment of fixed geometrical conditions between incident beam, target and detecting apparatus.
b. Determination of the incident particle energy.
c. Determination of the energy of the reaction products.
d. Investigation of the target layers.

The adjusting procedure according to point a. has been reported in ref. 1. The incident beam direction is perpendicular to the target surface, which coincides with the vertical rotation axis of the nuclear spectrometer. This is valid to 1 part in 1000. The acceptance directions used for the spectrometer are known to $\pm 0\overset{\circ}{.}2$.

The analyzing magnet which determines the deuteron energy was first calibrated for protons with the 873.5 KeV $F^{19}(p,\alpha,\gamma)$ resonance and the calibration was referred to a deuteron beam of approximately equal energy by a method with successive elastic scatterings into the nuclear spectrometer (ref. 8). This procedure was performed before and after the Q-measurements. The incident beam energy is kept to better than ± 2 KeV by a combination of electronic and manual stabilization.

It is convenient to calibrate the spectrometer field by a nuclear reaction with accurately known Q-value. The two proton groups from $Ne^{20}(d,p)Ne^{21}$ which are measured in this investigation have energies of about 4.5 and 4.9 MeV in the $\Theta = 135^\circ$ direction. A suitable calibration reaction has been found in $Be^9(d,p)Be^{10}$, whose ground state protons in 90° and 135° have energies in the neighbourhood of the above-mentioned values. The Be^9-reaction has a good intensity and its Q-value is known to ± 6 keV. A further advantage is that one can use the accurately computable energy difference between the protons ejected in the two different angles to measure the deviation from linearity between spectrometer field and magnetizing current in the energy region used in this experiment.

A determination of the Q-values according to points b. and c. consists of the following partial measurements, which must be performed in one sequence.

$$\mathrm{A}\left\{\begin{array}{l} F^{19}(p,\alpha,\gamma) \\ Al(p,p)\ 135^\circ \\ Be(d,d)\ 135^\circ \end{array}\right. \qquad \mathrm{B}\left\{\begin{array}{ll} Be^9(d,p)Q_0 & 90^\circ \\ Ne^{20}(d,p)Q_0 & 135^\circ \\ Ne^{20}(d,p)Q_1 & 135^\circ \\ Be^9(d,p)Q_0 & 135^\circ \end{array}\right. \qquad \mathrm{C}\left\{\begin{array}{l} Be(d,d) \\ Al(p,p) \\ F^{19}(p,\alpha,\gamma) \end{array}\right.$$

Production of targets

The following six targets were used:

Thin F evaporated on silver backing.
Aluminium evaporated on aluminium backing.
Beryllium evaporated on beryllium backing.
Thin Ne^{20} separated in silver backing.
Thin Be evaporated on silver backing.
Clean machined silver.

All the backings were thick.

The first three targets were used for the calibration of the deuteron beam. Two complete series of targets were produced for two different determinations of the Q-values.

The target backings were machined with a clean and sharp tool just before they were put into the evaporation chamber or the isotope separator. One fluorine target was made of evaporated LiF, the other of CaF_2. The procedure of evaporating aluminium and beryllium on backings of the same metal was used in order to obtain optimally clean surfaces. The thicknesses of the layers on the silver plates have been determined by studying the positions of scattering edges for elastically scattered protons from these targets compared to protons from the clean silver plate.

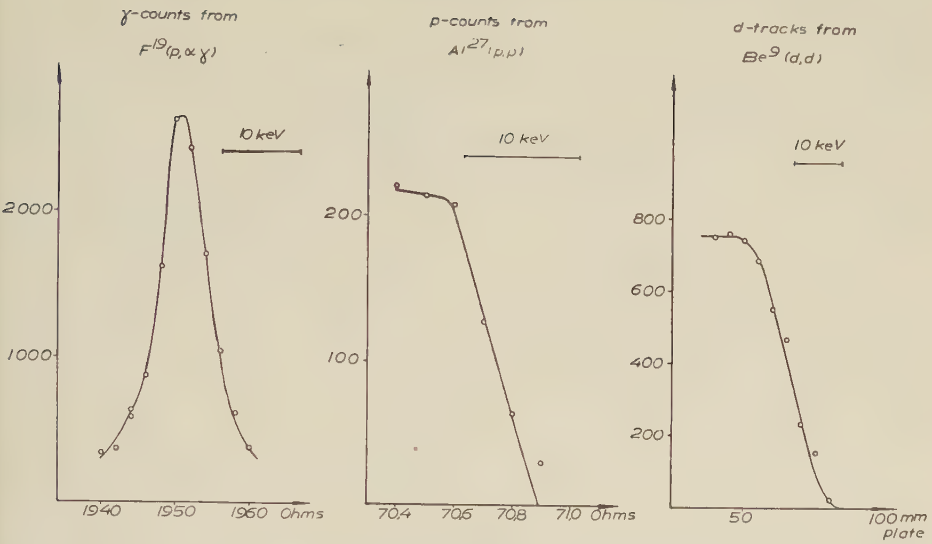

Fig. 5. Calibration of the deuteron beam. a) F^{19} (p, α, γ)-resonance at 873.5 keV. b) Spectrum of scattered protons from Al. $\Theta = 135.0°$ $E_p = 873.5$ keV. c) Spectrum of scattered deuterons from Be. $\Theta = 135.0°$. $E_d = 845.0$ keV.

Results

Fig. 5 shows a series of curves from one determination of the deuteron energy giving $E_1 = 874.5$ keV. The two determinations before and after a Q-value measurement have proved to coincide to better than 1 keV. We adopt an inaccuracy in the bombarding energy of ± 2 keV considering also temporary fluctuations in the high tension during the run.

The investigation of the external target layers by elastic scattering of protons gives curves of the type given in fig. 6. As the angle $\Theta = 61.4°$ to the incident beam has been used, the edge displacement between the target studied and the clean silver corresponds to an energy loss 4 times the actual layer thickness. The following thicknesses were obtained for 873 keV protons for the different thin targets used.

Run 1		Run 2	
Target	Layer keV	Target	Layer keV
LiF	2.3	CaF_2	3.8
Ne^{20}	0	Ne^{20}	0.7
Be^{9}	3.4	Be^{9}	1.3

For 875 keV deuterons the layers are 1.6 times thicker and for the ejected protons of 4.5–4.8 MeV 0.4 times the value given in the table.

The external layers partly consist of contaminants, especially carbon. One keeps down the growth of carbon layers during the runs by means of the liquid oxygen

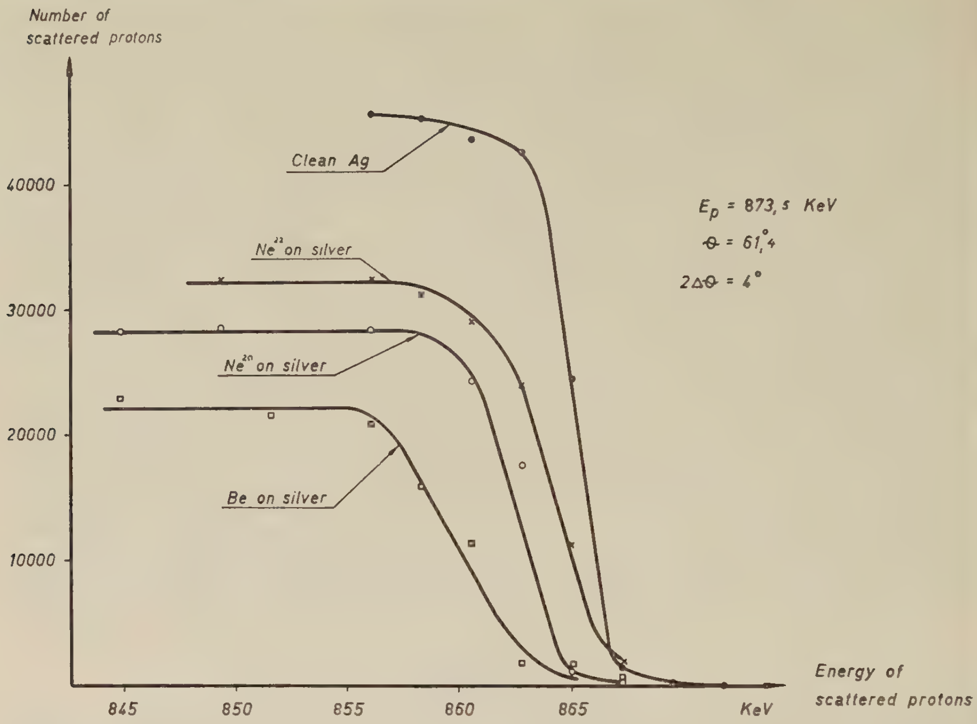

Fig. 6. Spectrum of protons, scattered from clean silver and from thin Be- and Ne^{20}-targets on silver. $\Theta = 61.4°$ $E_p = 873.5$ keV.

cooling trap in the target chamber. It has then been assumed that the evaporated target substances are spaced uniformly over the measured external layers. In the case of the separated Ne^{20}-targets the Ne is also distributed in the outer parts of the silver backings. Then the total Ne^{20}-thicknesses are not obtained by elastic scattering on silver. An estimation can however be made from the widths of the (d,p)-distributions. These have been shown to practically coincide with the widths due to angular energy spread of the outgoing protons. Thus it has been considered unnecessary to apply any correction in our Q-values for the depth of the internal Ne^{20}-layer.

The (d,p)-distributions for the two proton groups from $Ne^{20}(d,p)Ne^{21}$ and the corresponding calibration reactions $Be^9(d,p)Be^{10}$ are given in fig. 7 and 8. Due to the low intensity of the Ne-reactions the spectrometer acceptance angle 4° has been used. This involves the following line-widths: for $Be^9(d,p)Be^{10}$ 36 keV in $\Theta = 90°$ and 24 keV in 135° and for $Ne^{20}(d,p)Ne^{21}$ 13 keV in 135°. These values are widths at the bottom of the distributions.

The distance between the peaks has been determined from the maximum of each distribution. This has been judged as the most reliable method, as the bad statistics of the Ne^{20}-peaks — which totally consist of only a hundred tracks each — make an extrapolation to the high energy edge fairly inaccurate. The peak corresponds to the mean angle as the predominant broadening factor, the angular energy spread,

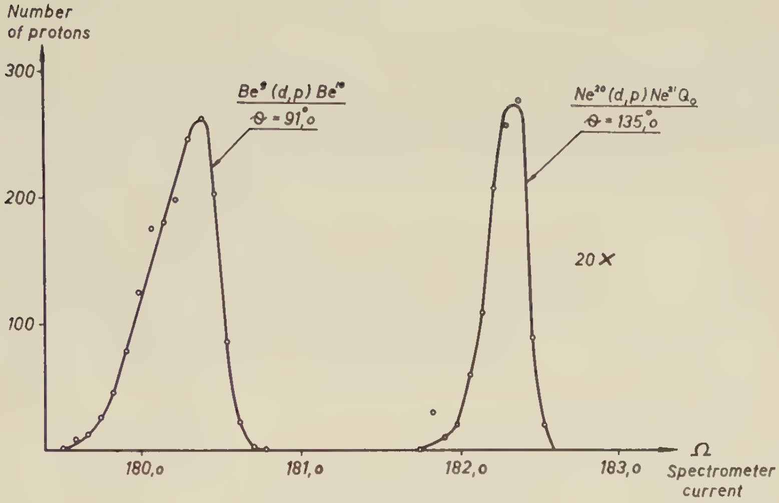

Fig. 7. Spectrum of protons from the reactions $Be^9(d, p)Be^{10}$ in $\Theta = 91.0°$ and $Ne^{20}(d, p)Ne^{21}$ Q_0 in $\Theta = 135.0°$. $E_d = 876.5$ keV. Photographic detection. 1 Ω = 51.7 keV. The asymmetry in the Be-distribution is caused by unequalness in the Be-layer.

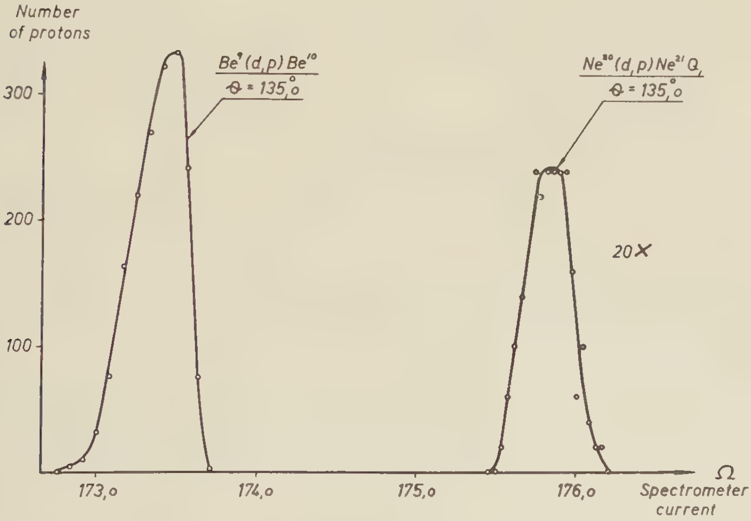

Fig. 8. Spectrum of protons from the reactions $Be^9(d, p)Be^{10}$ in $\Theta = 135.0°$ and $Ne^{20}(d, p)Ne^{21}$ Q_1 in $\Theta = 135.0°$. $E_d = 876.5$ keV. Photographic detection 1 Ω = 53.3 keV.

is symmetric with respect to this angle. In the calculations this peak position has been related to target nuclei half-way into the target layer.

From the known Q-value of the $Be^9(d,p)Be^{10}$ reaction $Q = 4.587 \pm 0.006$ (ref. 9) we calculate the Q-values of the Ne-reaction using nuclear masses and relativistic corrections (ref. 10) and taking into account the non-linearity of the spectrometer, as revealed by the distance between the two peaks from the Be-reaction. In this way we obtain from the two independent determinations of $Ne^{20}(d,p)Ne^{21}$:

	Run 1	Run 2
Q_0	4.524(4) ± 0.009 MeV	4.527(1) ± 0.009 MeV
Q_1	4.175(5) ± 0.009 MeV	4.177(5) ± 0.008 MeV
$Q_0 - Q_1$	0.348(9) ± 0.007 MeV	0.349(6) ± 0.006 MeV

We adopt the mean values:

$$Q_0 = 4.526 \pm 0.009 \text{ MeV}$$
$$Q_1 = 4.177 \pm 0.009 \text{ MeV}$$
$$Q_0 - Q_1 = 0.349 \pm 0.006 \text{ MeV}$$

$Q_0 - Q_1$ gives the first excited level of Ne^{21} (fig. 1). In the table below are listed the various sources of errors contributing to the probable errors in the results.

Source of error	Probable error
Q-value of $Be^9(d,p)Be^{10}$	6 keV
Deuteron energy	2 keV
Angle Θ	0.2°
Statistical error in each (d,p)-peak	3 keV
Dispersion between peaks	2 keV
Layer correction in one peak	1 keV

The various errors are reduced to errors in the Q-values (ref. 10) and give the net values: $\Delta Q_0 = 9$ keV, $\Delta Q_1 = 9$ keV, $\Delta(Q_0 - Q_1) = 6$ keV.

The probable error is smallest for the difference $Q_0 - Q_1$ since the uncertainty in the Be^9–Q-value cancels out.

The present Q-values are in agreement with the earlier measurements in the M.I.T. laboratory. Van PATTER *et al.* have obtained the ground state Q-value 4.529 ± 0.007 MeV (ref. 2) and the first excited level in Ne^{21} 0.352 ± 0.012 MeV (ref. 11). In the same laboratory a $Na^{23}(d,\alpha)Ne^{21}$-transition has given the position of the first level in Ne^{21} as 0.343 ± 0.010 MeV (ref. 11).

I am grateful to Tekn. lic. S. THULIN for preparing the Ne-targets and to Tekn. Dr. C. MILEIKOWSKY and Tekn. lic. R. PAULI for their help in the runs.

Nobel Institute of Physics, Stockholm 50, Sweden.

REFERENCES

1. MILEIKOWSKY, C., Ark. f. Fys., *7* nr 8, 89 (1953).
2. VAN PATTER, D. M., SPERDUTO, A., ENDT, P. M., BUECHNER, W. W., and ENGE, H. A., Phys. Rev. *85*, 142 (1952).
3. MIDDLETON, R., and TAI, C. T., Proc. Phys. Soc. 64 A, 801 (1951).
4. MILEIKOWSKY, C., and PAULI, R. T., Ark. f. Fys. *4*, nr 12, 287 (1952).
5. PAULI, R. T., Ark. f. Fys. (to be published).
6. MILEIKOWSKY, C., Ark. f. Fys., *4*, nr 16, 337 (1952).
7. —— Ark. f. Fys., *7*, nr 3, 33 (1953).
8. —— Ark. f. Fys., *7*, nr 10, 117 (1953).
9. VAN PATTER, D. M., M.I.T., Technical Report No. 57 (jan. 1952).
10. BROWN, A. B., SNYDER, C. W., FOWLER, W. A., and LAURITSEN, C. C., Phys. Rev. *82*, 159 (1951).
11. SPERDUTO, A., BUECHNER, W. W., and VAN PATTER, D. M., M.I.T. Progress Report (May 1951).

Tryckt den 30 november 1953

Uppsala 1953. Almqvist & Wiksells Boktryckeri AB

ARKIV FÖR FYSIK Band 7 nr 15

Communicated 22 April 1953 by Oskar Klein and Ivar Waller

Hybridization of atomic orbitals in formation of molecules

By Inga Fischer-Hjalmars

With 2 figures in the text

Summary

The condition of maximum penetration, previously suggested by the present author, has been generalized and studied in more detail. It has been shown that the composition of the bonding atomic orbital, found by this condition, is remarkably different from the bonding atomic orbital, found by the condition of maximum overlapping. The difference is substantially due to the fact that there is a considerable difference in orbital energies between the atomic $2s$ and $2p$ orbitals. It is suggested that this difference is important for the determination of the shape of the molecules NH_3 and H_2O.

1. Introduction

The purpose of most theoretical investigations of molecular structure is to calculate the energies of the electronic states and the corresponding wave functions. Strictly, this can only be obtained from a study of the complete system of electrons and nuclei of the molecule. For practical reasons, such a treatment is not possible for molecules in general, on account of the complexity of the systems. Therefore, it is inevitable to introduce approximations. It is, of course, desirable to make as small approximations as possible, but in some respects even a very crude calculation can give some valuable information. This is, for example, evident from the widespread application of the condition of maximum overlapping, introduced by Pauling [1]. He states that it should be expected "that of two orbitals in an atom the one which can overlap more with an orbital of another atom will form the stronger bond with that atom". Recently, Maccoll [2] has reinvestigated Pauling's condition and has given it a slightly changed formulation. He has also shown its applicability to bonds between equal atoms and has discussed its generalization to bonds between unequal atoms.

In some cases, however, it seems as if overlapping is not the only factor, determining the shape of the molecule. Hence, the present author has suggested an alternative condition, denoted *the condition of maximum penetration* [3]. The idea that led to this condition was as follows. According to the self-consistent field method, the "orbital energy" of an electron is determined by the potential field of all the nuclei of the molecule and by the average potential field of the other electrons. The terms, dominating the energy expression, originate from the kinetic energy and the potential of the nuclei. It was suggested that the bond-forming power of an atomic orbital should be roughly proportional to these terms, when modified so that the effective charges of the nuclei were substituted for the real charges. These terms, called the penetration terms, are in case of the two-atomic molecules, $a-b$, discussed in [3]:

$$P = \int \varphi_a^* \left(T - \frac{Z_{a\ \mathrm{eff}}}{r_a} - \frac{Z_{b\ \mathrm{eff}}}{r_b} \right) \varphi_a \, dV, \tag{1}$$

where T is the kinetic energy of the electron, and φ_a is a normalized atomic orbital of the nucleus a. φ_a is in general a linear combination of (ns), (np)... functions. The values of the coefficients in this expression are supposed to be found by minimizing P with regard to these coefficients.

In many cases, the condition of maximum penetration will yield the same result as the condition of maximum overlapping, *e.g.*, in molecules where the bond strength is substantially due to a high electron density between the joined nuclei. However, this should not be the case, when the hybridized atomic orbital is composed of atomic orbitals with widely different orbital energies. To investigate this point in some more detail, we have now applied the condition of maximum penetration in a generalized form to the hydrides of nitrogen, oxygen and fluorine. Moreover, an additional calculation for the previously treated lithium hydride has been made.

2. Derivation of the penetration condition

The molecules to be discussed here have the common formula AH_n, $n=1, 2, 3$. We assume that the atomic orbitals of the atom A are hybridized in such a way that in every A – H direction there is one hybridized orbital with its symmetry axis almost in the direction of the bond. Orbitals in different A – H directions should be *equivalent* in the sense of LENNARD-JONES [4], *i.e.*, the orbitals should be identical except for their orientation in ordinary space. It has been shown that such equivalent orbitals are almost perfectly localized [5]. We shall, accordingly, neglect any interaction between an equivalent orbital in one A – H direction and the other hydrogen atoms. Similarly, we shall neglect any interaction between the hydrogen atoms and the pair of electrons in non-bonding orbitals, commonly called "lone pairs".

Hence, to a certain extent, we can treat each bond separately. Let φ_a be that atomic orbital of the atom A which participates in the bond

$$A - H_a \; (a = 1, 2, \ldots, n)$$

and φ_h the $1s$ orbital of the atom H_a. According to the valence bond theory, the wave function for this particular bond is:

$$\Psi(1,2) = \frac{1}{2\sqrt{1+S^2}} \left\{ \begin{vmatrix} \varphi_a(1)\,\alpha(1) & \varphi_a(2)\,\alpha(2) \\ \varphi_h(1)\,\beta(1) & \varphi_h(2)\,\beta(2) \end{vmatrix} - \begin{vmatrix} \varphi_a(1)\,\beta(1) & \varphi_a(2)\,\beta(2) \\ \varphi_h(1)\,\alpha(1) & \varphi_h(2)\,\alpha(2) \end{vmatrix} \right\}, \tag{2}$$

where 1 and 2 represent the coordinates of the two electrons, α, β are eigenfunctions of the spin operator, and $S = \int \varphi_a^*(1)\,\varphi_h(1)\,dV_1$.

Let φ_a be an eigenfunction of the atomic hamiltonian operator $H_A = T + V_a$ ith the eigenvalue E_a. V_a is the sum of the COULOMB field of the nucleus nd the average field of all the other electrons at A. φ_h is an eigenfunction f the atomic operator $H_H = T - 1/r_H$ with the eigenvalue E_h. The hamiltonian of the two electrons of the bond between A and H_a is:

$$H = T_1 + T_2 - \frac{Z_A}{r_{A1}} - \frac{Z_A}{r_{A2}} - \frac{1}{r_{H1}} - \frac{1}{r_{H2}} + \frac{1}{r_{12}} + \frac{Z_A}{r_{AH}}, \tag{3}$$

here energy and length are expressed in atomic units (a.u.). The effective harge Z_A in (3) is defined as follows:

$$-Z_A \overline{\frac{1}{r_A}} = \overline{V_a}. \tag{4}$$

he averages of $1/r_A$ and V_a in (4) must be computed over that atomic orbital n which Z_A/r_A is operating. Thus, the effective charge will be different for ifferent atomic orbitals.

The energy of the two bonding electrons is:

$$E = \int \Psi^*(1,2)\, H\, \Psi(1,2)\, d\,V_1\, d\,V_2 = \frac{1}{1+S^2}\{(a\,h\,|\,H\,|\,a\,h) + (a\,h\,|\,H\,|\,h\,a)\}, \tag{5}$$

here

$$(a\,b\,|\,H\,|\,c\,d) = \int \varphi_a^*(1)\, \varphi_b^*(2)\, H\, \varphi_c(1)\, \varphi_d(2)\, d\,V_1\, d\,V_2.$$

fter insertion of (3) we obtain

$$(a\,h\,|\,H\,|\,a\,h) = E_a + E_h - \left(a\left|\frac{1}{r_H}\right|a\right) - \left(h\left|\frac{Z_A}{r_A}\right|h\right) + \left(a\,h\left|\frac{1}{r_{12}}\right|a\,h\right) + \frac{Z_A}{r_{AH}}, \tag{6}$$

$$h\,|\,H\,|\,h\,a) = S^2\left(E_a + E_h + \frac{Z_A}{r_{AH}}\right) - S\left\{\left(h\left|\frac{1}{r_H}\right|a\right) + \left(a\left|\frac{Z_A}{r_A}\right|h\right)\right\} + \left(a\,h\left|\frac{1}{r_{12}}\right|h\,a\right). \tag{7}$$

y comparing (6) and (7) we can infer that the following relation is approxiately valid:

$$(a\,h\,|\,H\,|\,h\,a) \approx S^2\,(a\,h\,|\,H\,|\,a\,h). \tag{8}$$

hen, from (5) and (8) it follows that

$$E \approx (a\,h\,|\,H\,|\,a\,h). \tag{9}$$

o obtain (8) we have made the following assumption with regard to the last erm of (7):

$$\left(a\,h\left|\frac{1}{r_{12}}\right|h\,a\right) \approx S^2\left(a\,h\left|\frac{1}{r_{12}}\right|a\,h\right). \tag{10}$$

(10) can be compared with the approximate formula suggested by MULLIKEN [6]. According to this formula we have

$$\left(a h \left| \frac{1}{r_{12}} \right| h a\right) \approx \frac{1}{4} S^2 \left\{ \left(a a \left| \frac{1}{r_{12}} \right| a a\right) + \left(h h \left| \frac{1}{r_{12}} \right| h h\right) + 2 \left(a h \left| \frac{1}{r_{12}} \right| a h\right) \right\}. \tag{11}$$

As one-center integrals are always larger than the corresponding two-center integrals, it is obvious that the right member of (10) will yield lower numerical values than the right member of (11). However, integrals of this type are comparatively small, so that the inexactitude of (10) cannot invalidate the results, obtained in the following parts. A more critical point of the derivation above is the following relation, implicit in (8):

$$\left(h \left| \frac{1}{r_H} \right| a\right) + \left(a \left| \frac{Z_A}{r_A} \right| h\right) \approx S \left\{ \left(a \left| \frac{1}{r_H} \right| a\right) + \left(h \left| \frac{Z_A}{r_A} \right| h\right) \right\}. \tag{12}$$

A more satisfactory approximation would have been:

$$\left(h \left| \frac{1}{r_H} \right| a\right) + \left(a \left| \frac{Z_A}{r_A} \right| h\right) \approx \frac{1}{2} S \left\{ \left(a \left| \frac{1}{r_H} \right| a\right) + \left(h \left| \frac{Z_A}{r_A} \right| h\right) + \left(h \left| \frac{1}{r_H} \right| h\right) + \left(a \left| \frac{Z_A}{r_A} \right| a\right) \right\}. \tag{13}$$

The relative inexactitude of (12) is about equal to that of (10), but the integrals of (12) are not small compared to the energy of the bond. Thus, the inaccuracy introduced by (12) is not negligible in comparison with the expression we wish to compute. However, the purpose of the present simplified calculation is not to find a correct value of the bond energy. This is, of course, only possible to obtain by the most accurate methods available. The purpose is only to study the hybridization of the atomic bonding orbitals φ_a, φ_b, . . . of the atom A. In this connexion (12) can be accepted, since the two members are similar functions of the hybridization parameter. It is only the derivative with respect to this parameter that will be of any importance in what follows.

Starting from (9) we can obtain a still simpler expression for an estimate of the hybridization parameter. All the terms of $(a h | H | a h)$ are not functions of this parameter. The last term in the right member of (6), Z_A / r_{AH}, is obviously a function of the interatomic distance only. The same is the case with the term $(h | Z_A / r_A | h)$. Moreover, E_h is a constant. Hence, we can confine ourselves to the three remaining terms, which we call P_a:

$$P_a = E_a - \left(a \left| \frac{1}{r_H} \right| a\right) + \left(a h \left| \frac{1}{r_{12}} \right| a h\right). \tag{14}$$

Let

$$V_h(1) = -\frac{1}{r_{H1}} + \int \varphi_h^*(2) \frac{1}{r_{12}} \varphi_h(2)\, d V_2. \tag{15}$$

Then, (14) can be put in the form

$$P_a = \int \varphi_a^* (T + V_a + V_h) \varphi_a \, d V. \tag{16}$$

It is seen that (16) is a slightly modified form of the expression (1).

When an atom is joined to more than one other atom, the bonding orbitals of the central atom cannot be treated separately. The penetration expression must be composed of the penetration terms of all the bonding electrons *and* of the corresponding terms of lone pair electrons. The penetration terms for the orbitals of the other A − H bonds of the molecule are similar to (16). The corresponding expression of the lone pair electrons differs from (16) in the omission of the term V_h. The sum of all the penetration terms of the molecule is

$$P=\sum_{b=1}^{n}P_b+\sum_{l=1}^{m}P_l=\sum_{b=1}^{n}\int\varphi_b^*(T+V_b+V_h)\varphi_b\,dV+\sum_{l=1}^{m}\int\varphi_l^*(T+V_l)\varphi_l\,dV. \quad (17)$$

Here the subscript b indicates a bonding orbital and the subscript l a lone pair orbital. As above, n is the number of electrons from the atom A participating in bond formation. m is the number of electrons forming lone pairs at A (twice the number of lone pairs).

The orbitals φ_b and φ_l must be consistent with the symmetry of the molecule. Moreover, they must be mutually orthogonal and normalized. These conditions restrict the possibilities considerably. In the case of methane, for instance, the hybridized orbitals are completely determined by these conditions. When there is any degree of freedom as to the composition of the orbitals, the corresponding parameter can be found from the condition that P in (17) must have a minimum value with respect to that parameter. This is the generalized formulation of the condition of maximum penetration.

3. Atomic orbitals

Various calculations on molecular problems have been carried out during the last twenty-five years. Almost all numerical computations have been based on comparatively simple, analytical wave functions. These functions have been supposed to be satisfactory approximations to the correct eigenfunctions of the atomic hamiltonians. The most important exceptions to this are the numerical computations of self-consistent field (SCF) atomic orbitals, made by Hartree, Fock, and coworkers (see *e.g.* the review [7]). A comparison of the SCF and the analytical orbitals indicates that only an inadequate estimate of the charge distribution can be obtained from simple, analytical functions. Only when these functions are composed of several exponentials, each fitting one part of the corresponding SCF function, one can hope to obtain an accurate result. Recently, Löwdin [8] has computed analytical expressions of several atomic orbitals, which are in satisfactory coincidence with the SCF orbitals over the whole range of the variable r. However, it turns out that these expressions are so complicated that one does not feel tempted to adopt them in actual computations of molecular structure. Therefore, we have made a compromise and have chosen to carry out the computations with analytical atomic orbitals, which coincide with the SCF orbitals within that part of space which seemed to be of principal significance to the present problem, *i.e.*, for values of r close to the equilibrium distance between the joined atoms. This can be obtained by using only one or two exponentials:

$$\psi_{2s} = \sqrt{\frac{\mu^5}{3\pi N}} \left(r\, e^{-\mu r} - \frac{3A}{\mu}\, e^{-\mu b r} \right) \tag{18}$$

$$\psi_{2p} = \sqrt{\frac{\nu^5}{\pi}}\, r \cos\theta\, e^{-\nu r}. \tag{19}$$

The forms of (18) and (19) are in accordance with the analytical expressions given by MORSE *et al.* [9], cf. also DUNCANSON and COULSON [10]. The values of A and b in (18) determine the node. As the position of the node is not very significant in the present connexion, we have used the relation: $A = (2b)^3/(1+b)^4$ instead of the more complicated expression given in [9]. Then, the normalizing factor is: $N = 1 - 192\, b^3/(1+b)^8$. The simple form (19) of the $2p$ orbital is not very satisfactory. However, the main point is that μ must be considerably different from ν, since the $2p$ orbital is much more extended than the $2s$ orbital, and the orbital energies are *not* the same. To fit (18) and (19) to the SCF functions within the desired range of r, the difference between μ and ν must be more pronounced than found from the variational treatment of [9] and [10]. This is also evident from the values of the orbital energies, computed by the self-consistent field method. The values of the parameters b, μ, and ν, which have been adopted in the present computation, are collected in Table 1.

Table 1. Values of the parameters in ψ_{2s} and ψ_{2p} of (18) and (19) and values of the effective charges, discussed in part 4.

Atom	b	μ	ν	Z_s	Z_p
Li	4.09	0.658	0.545	1.15	1.00
N	3.09	2.02	1.64	2.69	1.96
O	3.08	2.36	1.89	3.13	2.23
F	3.07	2.61	2.00	3.59	2.47

4. Effective charges

The effective charges, reproduced in Table 1, are defined by (4). According to this definition, Z_A does not depend on the rest of the molecule. The average values in (4) should be computed over definite atomic orbitals. Hence, Z_A will have different values for $2s$ and $2p$ orbitals. From computations of Z_A values of different atoms A, it was found that the screening of the nuclear charge for an electron in one atomic orbital, caused by an electron in another atomic orbital, was almost independent of the atomic number. We have, therefore, adopted the following screening constants:

Screening by $(1s)$ for $(2s)$ 0.91
" " $(2s)$ " $(2s)$ 0.65
" " $(2p)$ " $(2s)$ 0.60
" " $(1s)$ " $(2p)$ 1.00
" " $(2s)$ " $(2p)$ 0.79
" " $(2p)$ " $(2p)$ 0.73

As an example, we reproduce the computation of Z_s of the oxygen atom: $Z_s = 8 - 2\times 0.91 - 0.65 - 4\times 0.60 = 3.13$. The other Z values of Table 1 have been computed in a similar way.

5. Lithium hydride

In this molecule, LiH, there is only one electron in the valence shell of each atom. Accordingly, there is no lone pair to take into consideration, and (17) is in this case simply: $P = P_b$. The difference between the present computation and the computation made in [3] is that V_h in (15) has been substituted for the simple potential $-1/r_H$.

Let

$$\varphi_a = \alpha\,\psi_{2s} + \beta\,\psi_{2p},$$

where

$$\alpha^2 + \beta^2 = 1.$$

Then

$$P = \alpha^2 \{E_{2s} + (2s\,|\,V_h\,|\,2s)\} + \beta^2 \{E_{2p} + (2p\,|\,V_h\,|\,2p)\} + 2\alpha\beta\,(2s\,|\,V_h\,|\,2p). \quad (20)$$

According to the condition of maximum penetration, the best value of the parameter β/α should be that for which P becomes a minimum. The parameter values deduced by application of this condition to (20) are reproduced in Table 2. The values have been computed for the experimental interatomic distance, $r_{\mathrm{LiH}} = 1.6$ Å $= 3.02$ a.u., and for two other distances, also used in [3]. The evaluation of the integrals in (20) is discussed in the Appendix. For comparison, the values of β/α, which have been obtained from the most complete treatment given in [3] and from the condition of maximum overlapping are also reproduced in the table.

Table 2. LiH: The parameter β/α of the bonding orbital and the penetration terms.

r_{LiH} a.u.	Values of β/α obtained from			P in (20) a.u.	$P - E_{2s}$ a.u.
	maximum penetration	[3]	maximum overlapping		
2.64	0.36	0.52	0.99	−0.2090	−0.0225
3.02	0.32	0.41	1.09	−0.2049	−0.0185
3.40	0.28	0.54	1.16	−0.2007	−0.0142

As is seen from Table 2, the values of β/α obtained from the penetration condition are not far from the values yielded by a closer computation, although somewhat lower. The best parameter values lie between the values obtained from the penetration and the overlapping conditions, although closer to the former.

The last column of Table 2 shows the contribution to the total binding energy from the penetration terms. These values should be compared with the values of the binding energy from experiments: 0.0967 a.u., and from the most complete computation of [3]: 0.0671 a.u. As was pointed out in part 2, the penetration terms are not a satisfactory expression of the total energy and, consequently, they cannot be used for a computation of the bond energy.

A more detailed discussion of the result will be given in comparison with the results for the other molecules.

6. Hydrogen fluoride

This molecule, HF, belongs, as well as LiH, to the symmetry group $C_{\infty v}$ (*cf.* for example [11]). The experimental value of the interatomic distance is 0.9171 Å = 1.733 a.u. [12]. The different feature of HF is that there are three lone pairs at the fluorine nucleus. Two of the lone pair orbitals, $\psi_{2p,x}$ and $\psi_{2p,y}$, have node planes, containing the symmetry axis of the molecule. They are not modified by the presence of the hydrogen atom. The third lone pair orbital had originally spherical symmetry. In formation of the molecule it will assume cylindrical symmetry with the same symmetry axis as the molecule and, consequently, as the bonding orbital. This lone pair orbital must be modified so that it remains orthogonal to the bonding orbital, originally the orbital $\psi_{2p,z}$.

Let the bonding orbital be

$$\varphi_a = \alpha\,\psi_{2s} + \beta\,\psi_{2p},$$
$$\alpha^2 + \beta^2 = 1,$$

where we have omitted the subscript z. Then, the lone pair orbital is

$$\varphi_l = \beta\,\psi_{2p} - \alpha\,\psi_{2s}.$$

It is not necessary to include the penetration terms of the other two lone pair orbitals, as these are independent of the hybridization parameter. Hence, we find from (17):

$$P = P_a + 2P_l = (1+\beta^2)E_{2s} + (1+\alpha^2)E_{2p} + \alpha^2(2s\,|\,V_h\,|\,2s) + \beta^2(2p\,|\,V_h\,|\,2p) + 2\alpha\beta(2s\,|\,V_h\,|\,2p). \tag{21}$$

The minimum value of P with respect to β/α can be found without difficulty. The computed values are:

$$\beta/\alpha = 0.1865;\quad P = -2.5235 \text{ a.u.};\quad P - 2E_{2s} - E_{2p} = -0.1648 \text{ a.u.}$$

7. The water molecule

According to experiments [12], the water molecule, H_2O, has a triangular shape and belongs to the symmetry group C_{2v}. The O—H distance is 0.9584 Å = 1.811 a.u. and the angle H–O–H is 104° 27′. Let a coordinate system have the orientation, shown in Fig. 1, with the z-axis perpendicular to the plane of the molecule. We have $2\theta = 14°\,27'$. There are six valence electrons at the oxygen atom: two lone pairs and two bonding electrons. Let γ be the angle between the x-axis and the symmetry axis of the bonding orbital φ_a. γ is not necessarily equal to θ. As the $2p$ orbitals are transformed like vectors we get

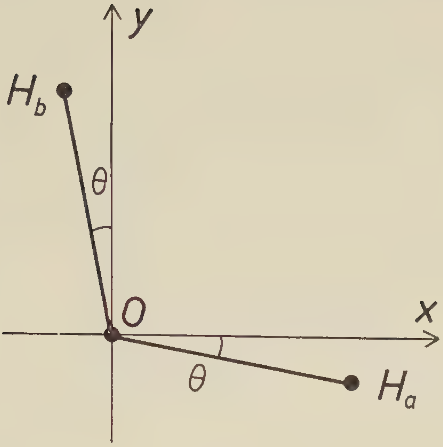

Fig. 1.

$$\psi_{2p,a} = \cos\gamma \cdot \psi_{2p,x} - \sin\gamma \cdot \psi_{2p,y}$$

$$\psi_{2p,b} = -\sin\gamma \cdot \psi_{2p,x} + \cos\gamma \cdot \psi_{2p,y}$$

or

$$\psi_{2p,a} = \cos(\theta-\gamma)\,\psi_{2p,h} + \sin(\theta-\gamma)\,\psi_{2p,h_\perp}. \tag{22}$$

Here the subscript h indicates a $2p$ orbital, the axis of which coincides with the direction of the bond O—H_a. $h_\perp$ indicates a $2p$ orbital with its axis perpendicular to this bond direction. The two ortho-normalized bonding orbitals are

$$\left.\begin{aligned}\varphi_a &= \alpha\,\psi_{2s} + \beta\,\psi_{2p,a},\\ \varphi_b &= \alpha\,\psi_{2s} + \beta\,\psi_{2p,b},\end{aligned}\right\} \tag{23}$$

where

$$\alpha = \sqrt{\frac{\sin 2\gamma}{1+\sin 2\gamma}}, \quad \beta = \sqrt{\frac{1}{1+\sin 2\gamma}}. \tag{24}$$

The two lone pair orbitals were in the free atom a $2s$ orbital and a $2p, z$ orbital. In the molecule the $2s$ orbital must be modified so that it remains orthogonal to the bonding orbitals. The modified $2s$ orbital and the $2p, z$ orbital can just as well be written as equivalent orbitals or as any other arbitrary transform, since the sum of the lone pair penetration terms is invariant to a unitary transformation. Let us put

$$\varphi_l = \frac{1}{\sqrt{2}}\{\delta\,\psi_{2s} - \varepsilon(\psi_{2p,x} + \psi_{2p,y}) + \psi_{2p,z}\},$$

$$\varphi_m = \frac{1}{\sqrt{2}}\{\delta\,\psi_{2s} - \varepsilon(\psi_{2p,x} + \psi_{2p,y}) - \psi_{2p,z}\},$$

where

$$\delta=\sqrt{\frac{1-\sin 2\gamma}{1+\sin 2\gamma}},\quad \varepsilon=\sqrt{\frac{\sin 2\gamma}{1+\sin 2\gamma}}. \tag{25}$$

Inserting (22) in (23) we obtain for the penetration terms of a bonding orbital:

$$P_a=\alpha^2\left[E_{2s}+(2s\,|\,V_h\,|\,2s)\right]+\beta^2\left[E_{2p}+\cos^2(\theta-\gamma)\,(2p,h\,|\,V_h\,|\,2p,h)+\right.$$
$$\left.+\sin^2(\theta-\gamma)\,(2p,h_\perp\,|\,V_h\,|\,2p,h_\perp)\right]+2\alpha\beta\cos(\theta-\gamma)\,(2s\,|\,V_h\,|\,2p,h).$$

The penetration terms of a lone pair orbital are:

$$P_l=\tfrac{1}{2}\{\delta^2 E_{2s}+(2\varepsilon^2+1)\,E_{2p}\}.$$

Finally, $P=P_a+P_b+2P_l+2P_m$, or, regarding (24) and (25):

$$P\left[\frac{1+\sin 2\gamma}{2}\right]=E_{2s}+(2+3\sin 2\gamma)\,E_{2p}+\sin 2\gamma\,(2s\,|\,V_h\,|\,2s)+$$
$$+\cos^2(\theta-\gamma)\,(2p,h\,|\,V_h\,|\,2p,h)+\sin^2(\theta-\gamma)\,(2p,h_\perp\,|\,V_h\,|\,2p,h_\perp)+ \tag{26}$$
$$+2\sqrt{\sin 2\gamma}\cos(\theta-\gamma)\,(2s\,|\,V_h\,|\,2p,h).$$

Now, γ should be computed from the penetration condition: $\frac{\partial P}{\partial \gamma}=0$. This condition implies a somewhat complicated relation between θ and γ. It is impracticable to express γ as an explicit function of θ. Instead, the minimizing value of γ has been found by interpolation in the plot of $\frac{\partial P}{\partial \gamma}$ against γ. The numerical results are as follows:

$$2\gamma=4^\circ 0';\quad P=-2.4675\text{ a.u.};\quad P-2E_{2s}-3E_{2p}=-0.3097\text{ a.u.};$$
$$\varphi_a=0.255\,\psi_{2s}+0.967\,\psi_{2p,a};$$
$$\varphi_l=\frac{1}{\sqrt{2}}\{0.928\,\psi_{2s}-0.255\,(\psi_{2p,x}+\psi_{2p,y})+\psi_{2p,z}\}.$$

8. The ammonia molecule

This molecule, NH_3, has pyramidal structure and belongs to the symmetry group C_{3v}. The N—H distance is 1.014 Å = 1.916 a.u. and the H-N-H angle ω is 106° 47′ [12]. Let the axes of a coordinate system have the orientation indicated in Fig. 2. The angle between any coordinate axis and the nearest N—H direction is θ. Let γ be the angle between a coordinate axis and the axis of the bonding orbital, directed towards the nearest hydrogen atom. Then we have

$$\psi_{2p,a}=\cos\gamma\,\psi_{2p,x}-\frac{1}{\sqrt{2}}\sin\gamma\,(\psi_{2p,y}+\psi_{2p,z}),$$

or

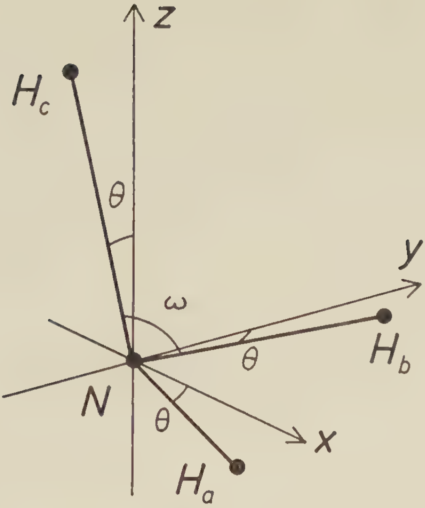

Fig. 2.

$$\psi_{2p,a} = \cos(\theta-\gamma)\,\psi_{2p,h} + \sin(\theta-\gamma)\,\psi_{2p,h_\perp}, \tag{27}$$

where the same notations are used as in (22). Let

$$\varphi_a = \frac{1}{N}(\alpha\psi_{2s} + \psi_{2p,a}) \tag{28}$$

and corresponding expressions of φ_b and φ_c. The coefficients N and α are determined by the condition of ortho-normalization:

$$N = \cos\gamma + \frac{1}{\sqrt{2}}\sin\gamma;$$

$$\alpha = [\sqrt{2}\sin\gamma\cos\gamma - \tfrac{1}{2}\sin^2\gamma]^{\frac{1}{2}} = \sqrt{-\cos\omega'}, \tag{29}$$

where ω' is the angle between the axes of any two bonding orbitals. It can be easily shown that

$$N^2 = 1 + \alpha^2 = 1 - \cos\omega'. \tag{30}$$

As nitrogen has five electrons in the valence shell, there is one pair of non-bonding electrons beside the three bonding electrons. The lone pair orbital was originally a $2s$ orbital. In the molecule it assumes cylindrical symmetry with the axis of the molecule as symmetry axis. According to the ortho-normalization conditions, the lone pair orbital must be

$$\varphi_l = \frac{1}{N}\{\beta\,\psi_{2s} - \alpha\,(\psi_{2p,x} + \psi_{2p,y} + \psi_{2p,z})\},$$

where N and α are the same constants as in (29) and

$$\beta = \cos\gamma - \sqrt{2}\sin\gamma, \quad \beta^2 = 1 + 2\cos\omega'. \tag{31}$$

The penetration terms of a bonding orbital are found by inserting (27) in (28):

$$P_a N^2 = \alpha^2 [E_{2s} + (2s\,|\,V_h\,|\,2s)] + E_{2p} + \cos^2(\theta-\gamma)(2p, h\,|\,V_h\,|\,2p, h) + \\ + \sin^2(\theta-\gamma)(2p, h_\perp\,|\,V_h\,|\,2p, h_\perp) + 2\alpha\cos(\theta-\gamma)(2s\,|\,V_h\,|\,2p, h).$$

Moreover,

$$P_l N^2 = \beta^2 E_{2s} + 3\alpha^2 E_{2p}.$$

As $P = P_a + P_b + P_c + 2P_l$, we have after inserting (29), (30), and (31):

$$P(1-\cos\omega') = (2+\cos\omega')E_{2s} + 3(1-2\cos\omega')E_{2p} - \\ -3\cos\omega'(2s\,|\,V_h\,|\,2s) + 3\cos^2(\theta-\gamma)(2p, h\,|\,V_h\,|\,2p, h) + \\ +3\sin^2(\theta-\gamma)(2p, h_\perp\,|\,V_h\,|\,2p, h_\perp) + 6\sqrt{-\cos\omega'}\cos(\theta-\gamma)(2s\,|\,V_h\,|\,2p, h). \tag{32}$$

P should be minimized with respect to γ. As ω' is a somewhat complicated function of γ, see (29), the minimum is found by interpolation in the plot of $\frac{\partial P}{\partial \gamma}$ against γ as in part 7. The numerical results are:

$$\gamma = 2^\circ\,55', \quad \text{or} \quad \omega' = 94^\circ\,2'; \quad P = -2.1362 \text{ a.u.};$$

$$P - 2E_{2s} - 3E_{2p} = -0.3970 \text{ a.u.};$$

$$\varphi_a = 0.256\,\psi_{2s} + 0.967\,\psi_{2p,a};$$

$$\varphi_l = 0.896\,\psi_{2s} - 0.256\,(\psi_{2p,x} + \psi_{2p,y} + \psi_{2p,z}).$$

9. Discussion

In the preceding parts we have computed the coefficients of the bonding orbitals and of the lone pair orbitals from the condition of maximum penetration. According to this condition, an atomic orbital should have the largest bonding power, when the orbital energy, computed in the field of the central atom and of the joined hydrogen atoms, has a minimum. To simplify the computation, only the most important terms of the energy expression have been considered. These terms have been called the penetration terms. When the central atom has more than one electron in the valence shell, the sum of the penetration terms for bonding electrons as well as lone pair electrons has been minimized, because the subsidiary conditions, ortho-normalization and symmetry conditions, are so many that there remains only one degree of freedom for all the atomic orbitals. taken as an entity. The final expression, P, to be minimized is given in (17).

It is interesting to compare the orbitals, computed from the penetration condition, with the orbitals, computed from the condition of maximum overlapping.

MACCOLL [2] has shown that, according to the latter condition, the bonding power decreases in the series $(sp) > (sp^2) > (sp^3)$. From this it follows that the diatomic molecules LiH and HF should have (sp) bonding orbitals of the form $\varphi = \frac{1}{\sqrt{2}}(\psi_{2s} + \psi_{2p})$. The same type of bonding orbitals should be formed at the oxygen atom and, consequently, the water molecule should be linear. In ammonia there are three hydrogen atoms, joined to the nitrogen atom. Hence, the bonding orbitals should be of the (sp^2) type, and ammonia should be a planar molecule.

The orbital coefficients, found from the penetration condition and from the overlapping condition, are reproduced in Table 3. To simplify the computation according to the overlapping condition, the parameters μ and ν of the $2s$ and the $2p$ orbitals (18) and (19) have been put equal, and the node of the $2s$ orbital has been neglected. These simplifications do not change the coefficients very much, as is seen from Table 2, where the complete expressions (18) and (19) have been used. In Table 3 $\psi_{2p,l}$ is the $2p$ orbital, obtained from putting $\alpha\psi_{2s} + \beta\psi_{2p,l}$ equal to the forms of φ_l given in parts 7 and 8.

Table 3. Coefficients of the bonding orbital φ_b and the lone pair orbital φ_l, obtained from the penetration and the overlapping conditions.

Molecule	Coeff. of $\varphi_b=\alpha\psi_{2s}+\beta\psi_{2p,b}$				Coeff. of $\varphi_l=\alpha\psi_{2s}+\beta\psi_{2p,l}$			
	Max. penetr.		Max. overlap.		Max. penetr.		Max. overlap.	
	α	β	α	β	α	β	α	β
LiH ($r_{\mathrm{LiH}}=3.02$) . . .	0.952	0.310	0.707	0.707	–	–	–	–
NH_3	0.256	0.967	0.577	0.816	0.896	0.444	0	1
H_2O	0.255	0.967	0.707	0.707	0.656	0.752	0	1
HF.	0.183	0.983	0.707	0.707	0.983	0.183	0.707	0.707

Table 3 shows that, according to the penetration condition, the orbitals of the free atom are only slightly modified by the formation of the molecule. The bonding orbitals are mainly the orbitals of the unpaired electrons of the free atom, and the lone pair orbitals are mainly the orbitals of the paired electrons of the free atom. The modifications are not at all so pronounced as according to the condition of maximum overlapping. This is due to the fact that *the $2s$ and the $2p$ orbitals have not the same orbital energy.* A hybridization means a change of the orbital energy of a lone pair. The energy required for this change must be supplied by the energy, liberated by bond formation. From experiments we know the magnitude of the bond energy. From the SCF calculations we know the difference in orbital energy between a $2s$ and a $2p$ orbital. On account of the energy balance, these figures show immediately that the hybridization, computed from the condition of maximum overlapping, is impossible in the molecules considered here. For these molecules the condition of maximum penetration seems to give a more correct picture of the real electron distribution.

In discussing the molecular shape of the molecules NH_3 and H_2O, it appears to be important to consider the difference in orbital energy between $2s$ and $2p$ orbitals. Let us consider H_2O in some detail. The discussion of NH_3 is quite similar. The two unpaired electrons of the free oxygen atom are assigned to $2p$ orbitals. These orbitals are modified in the formation of the molecule H_2O for the following reasons, discussed by POPLE [13]: repulsion of the hydrogen atoms, repulsion of electrons in different bonding orbitals or in different lone pair orbitals and repulsion between bonding orbitals and lone pair orbitals. POPLE suggests that repulsion of electrons from different lone pairs is the most important factor, prohibiting the molecule from assuming a linear shape. It appears to us that a more serious prohibition of the linear shape is the fact that a considerable amount of energy is required to transform the $2s$ lone pair orbital of the free atom into a pure $2p$ lone pair orbital, which is a necessary condition of the linear shape.

The orbitals, found from the penetration condition, are certainly not the best bonding orbitals obtainable in the "linear combination of atomic orbitals" approximation. This is due to the complete neglect of the exchange energy, as discussed in part 2. It may be useful to recall the figures of Table 2. It is shown that the best linear combination of atomic orbitals (column [3]) has values of the coefficients lying between the values found from the penetration condition and the overlapping condition.

It is interesting to compare the results of the present investigation with the calculation by POPLE [13] on the water molecule. He has carried out a numerical computation of the contribution to the total energy from the interaction between different parts of the molecule. The interaction energy is composed of proton repulsion, attraction of each bond orbital by the proton of the other, and the repulsion of the orbitals; attraction of the lone pairs by the protons and their repulsion by the bond electrons, and repulsion between the lone pairs. Only a part of this interaction energy is included in the penetration terms, *i.e.* the repulsion of the orbitals, concentrated at the central atom. This repulsion is represented in the penetration terms as a screening of the nuclear charge. The rest of the interaction energy is composed of attractive and repulsive parts. It is very plausible that these parts will almost cancel. On account of this, the inclusion of the complete interaction energy should probably only modify the present results slightly. Therefore, it appears to us to be sensible that the minimum of the total energy should correspond to a hybridization angle in the neighbourhood of the angles minimizing the penetration terms and the interaction energy separately. POPLE has found the minimum of the interaction energy at an angle, which with the present notation is: $2\gamma = 15°$. Here, we have found $2\gamma = 4°$. As the computation on LiH showed that the penetration condition yields somewhat too small values of the hybridization parameter, it is very plausible that the best value of 2γ should lie betyeen $4°$ and $15°$. We note that POPLE has carried out his computations, using the simplified orbitals mentioned above in connexion with the computation according to the overlapping condition. However, neither the overlap integrals nor the terms computed by POPLE are very sensitive to the parameters of (18) and (19).

In Table 4 we have collected the energy values computed from the penetration condition and compared them to the experimental values of the energy of the bonds.

Table 4. Energy values in kcal/mole.

Molecule	P	$P-nE_{2s}-mE_{2p}$	Exptl bond energy
LiH	129	1×12	60.6
NH_3	1340	3×83	92.2
H_2O	1346	2×97	109.4
HF	1583	1×103	141

The coefficients n and m in column 3 of Table 4 are the numbers of $2s$ and $2p$ electrons respectively in the free atom. It is certainly merely accidental that the values of column 3 are comparatively close to the experimental bond energy values. In column 3 both repulsive terms (part of the interaction energy) and attractive terms (the exchange energy) are neglected.

10. Dipole moments

Previously, it has been suggested that the dipole moment of a molecule should be the vector sum of the dipole moments of the bonds of the molecule. Accordingly, bond moments computed from the dipole moments of simple molecules have been used to calculate the dipole moments of complicated molecules. Discrepancies between calculated values and values obtained directly from experiments have been interpreted as due to exceptional structures of the molecules. It has, however, been pointed out recently that beside the bonds the lone pairs will also contribute to the total molecular dipole moment [5], [13], [14].

The present investigation indicates that the hybridization is not so pronounced as has been believed previously on account of the condition of maximum overlapping. It may be interesting to compute the dipole moments of the lone pair orbitals obtained from the condition of maximum penetration, to see whether these lone pair orbitals contribute negligibly or not to the molecular dipole moment.

The computation of the dipole moment of a lone pair orbital is quite straightforward. We assume the lone pair orbital to be

$$\varphi_l=\alpha\,\psi_{2s}+\beta\,\psi_{2p,\,l},$$

as in part 9. Then, the moment in the z-direction is

$$\mu_z=\int\varphi_l^*\,z\,\varphi_l\,dV=2\alpha\beta\,(2s\,|\,z\,|\,2p,\,l)=2\alpha\beta\,\bar{z}_{sp}. \tag{33}$$

The expressions of μ_x and μ_y are similar to (33). The total dipole moment, derived from the two electrons of the lone pair, is

$$\mu_l=2\,(\mu_x^2+\mu_y^2+\mu_z^2)^{\frac{1}{2}}. \tag{34}$$

When applying (34) to the molecules discussed below, we obtain, in units of ea_0:

$$\mathrm{HF}: \quad \mu_l = -4\alpha\beta\bar{z}_{s\,p}; \tag{35}$$

$$\mathrm{H_2O}: \quad \mu_l + \mu_m = -4\sqrt{2}\,\delta\varepsilon\,\bar{x}_{s\,p}; \tag{36}$$

$$\mathrm{NH_3}: \quad \mu_l = -\frac{1}{N^2}\,4\sqrt{3}\,\alpha\beta\,\bar{x}_{s\,p}. \tag{37}$$

The values computed for the lone pair moments are reproduced in Table 5. The μ-values of the table are the experimental values of the total molecular dipole moments. The difference $\mu - \mu_l$ can be divided into components in the directions of the bonds. The components of $\mu - \mu_l$ in these directions are called μ_b in the table. All values are given in Debye units:

$$1\,D = 10^{-18}\,e.\,s.\,u. = 0.3935\,ea_0.$$

Table 5. Total dipole moment μ, lone pair dipole moment μ_l and component μ_b of $\mu - \mu_l$ in the direction of a bond. All values are in Debye units.

Molecule	μ	μ_l	$\mu - \mu_l$	μ_b
NH_3	−1.48	−4.66	+3.18	+2.82
H_2O	−1.84	−3.30	+1.46	+1.20
HF	−1.98	−1.65	−0.33	−0.33

As is seen from Table 5 the lone pair moments are considerable, although the hybridization parameters (Table 3) are not very large. When the hybridization angles are small, we find from (25), (29), and (31) that the right members of (36) and (37) are proportional to $\sqrt{-\cos(90^\circ + 2\gamma)}$ and $\sqrt{-\cos\omega'}$ respectively. Hence, μ_l can never be negligible in comparison to μ when the hybridization angle 2γ is about 1°, or more.

In Table 5, it has arbitrarily been assumed that μ has the same direction as μ_l. If they had opposite directions, all the differences $\mu - \mu_l$ would have larger absolute values than μ and μ_l separately. This would imply a charge distribution, where the negative charge is localized at two or several points far removed from the central atom. Since such a distribution is very improbable, the difference $\mu - \mu_l$ of Table 5 must be equal to the partial moment derived from the bonds. We note, that μ_b is defined as a partial moment in the bond direction, which is not necessarily equal to the direction of the symmetry axis of the bonding orbital.

Assuming the μ_b-values of Table 5 to be of the right order of magnitude, we have made use of these values in a computation of the coefficient of molecular orbitals of the form

$$\chi_a = a\varphi_a + h\varphi_h. \tag{38}$$

As above, φ_a is a bonding orbital of the central atom, and φ_h is a $1s$ orbital of the corresponding hydrogen atom. Let the x-axis have the same direction as the A—H bond. Then the dipole moment of χ_a is:

$$\mu_\chi = a^2(a\,|\,x\,|\,a) + 2ah(a\,|\,x\,|\,h) + h^2(h\,|\,x\,|\,h). \tag{39}$$

ince φ_h has spherical symmetry, and H lies on the x-axis, the integral $h \mid x \mid h) = 0$. Let

$$\varphi_a = \alpha\, \psi_{2s} + \beta\, \psi_{2p,\,a},$$

nd let the symmetry axis of φ_a make an angle $\theta - \gamma$ with the x-direction. Then

$$(a \mid x \mid a) = 2\,\alpha\beta \cos(\theta-\gamma)\,(2\,s \mid x \mid 2\,p,\, x)$$

$$(a \mid x \mid h) = \alpha\,(2\,s \mid x \mid h) + \beta \cos(\theta-\gamma)\,(2\,p,\, x \mid x \mid h).$$

he normalization condition of (38) is

$$a^2 + 2\,a\,h\,S(a,\, h) + h^2 = 1, \tag{40}$$

here

$$S(a,\, h) = \alpha \int \varphi_h^* \,\psi_{2s}\, d\,V + \beta \cos(\theta-\gamma) \int \varphi_h^* \,\psi_{2p,\,x}\, d\,V.$$

he dipole moment of the bond, μ_b, is related to μ_χ in the following way:

$$\mu_b = 2\left(\mu_\chi - \frac{r_{A\,H}}{2}\right) \tag{41}$$

xpressed in $e a_0$ units. An estimate of μ_b has been given in Table 5. The tegrals of (39) and (40) can be computed easily. Hence, the two coefficients f (38) can be determined from (39), (40), and (41). We have computed the oefficients a and h in this way for the different hydrides. The results are ollected in Table 6.

Table 6. Coefficients of the molecular orbitals $\chi_a = a\,\varphi_a + h\,\varphi_h$.

Molecule	a	h	$\frac{h}{a}$
NH_3	0.49	0.63	1.29
H_2O	0.66	0.47	0.71
HF	0.80	0.33	0.41

Obviously, the values of Table 6 only indicate the order of magnitude of e coefficients. According to the table, the A—H bonds are essentially coalent, at least in NH_3 and H_2O. The comparatively large values of μ_b of Table 5 re understood, when we remember that the atomic orbitals φ_a of the atom A re much more extended than the orbitals φ_h of the hydrogen atom. Accordgly, there will be a resultant negative charge at the hydrogen atom also when e coefficient of φ_h is somewhat smaller than the coefficient of φ_a, as in H_2O. HF, where the coefficient of φ_a is twice as large as the coefficient of φ_h, e dipole moment of the bond is, nevertheless, almost zero.

This last part of the present calculations appears to confirm the importance the contribution from the lone pairs to the resulting dipole moment of the olecule.

The present investigation was made possible by a grant from *Statens Natur vetenskapliga Forskningsråd*. I am much indebted to Professor O. KLEIN fo his kind interest and for all the facilities he has put at my disposal at th institute. I am also indebted to Dr. P.-O. LÖWDIN, Uppsala, for informatio relating to some of his unpublished calculations on atomic wave functions.

Appendix. Evaluation of integrals

A. One-electron integrals. The evaluation of these integrals is quite straight forward, when carried out in spherical or elliptical coordinates, depending o whether they are one-center or two-center integrals. The numerical values ar listed in Table 7 and 8. All the integrals of these tables and of Table 9 ar expressed in atomic units; 1 a.u. = 27.205 electron volts.

Table 7. One-center integrals.

$$(a\,|\,P\,|\,b) = \int \varphi_a^* P \varphi_b \, d\,V$$

Integral	Li	N	O	F
$(2s\,|\,T\,|\,2s)$	0.220	2.609	3.570	4.381
$(2p\,|\,T\,|\,2p)$	0.149	1.345	1.786	2.000
$(2s\,|\,1/r_A\,|\,2s)$	0.353	1.147	1.340	1.484
$(2p\,|\,1/r_A\,|\,2p)$	0.273	0.820	0.945	1.000
$(2s\,|\,x\,|\,2p, x)$	—	1.151	0.970	0.898

Table 8. Two-center integrals

$$S(a, h) = \int \varphi_a^* \varphi_h \, d\,V; \quad (a\,|\,x\,|\,h) = \int \varphi_a^* x \varphi_h \, d\,V$$

Integral	NH_3	H_2O	HF
$S(2s, h)$	0.528	0.492	0.470
$S(2p, h)$	0.477	0.429	0.412
$(2s\,|\,x\,|\,h)$	0.406	0.311	0.259
$(2p, x\,|\,x\,|\,h)$	0.943	0.797	0.747

B. Two-electron integrals. The two-electron integrals arise from the potentia V_h in (15). All the two-electron integrals are thus of the COULOMB type:

$$\left(a; h\left|\frac{1}{r_{12}}\right|b; h\right) = \int \varphi_a^*(1)\,\varphi_h^*(2)\,\frac{1}{r_{12}}\,\varphi_b(1)\,\varphi_h(2)\,d\,V_1\,d\,V_2,$$

where φ_a and φ_b are atomic orbitals, concentrated around the nucleus A. Inte grals of this type are easily evaluated. The potential $1/r_{12}$ should be expresse in spherical coordinates of the two electrons, the coordinates being centred a the hydrogen atom. Then, the integration over the coordinates of the secon electron is simple. The remaining integral is an ordinary one-electron, two-center integral, most easily evaluated after introduction of elliptical coordinates. The numerical values of the integrals are listed in Table 9.

Table 9. Two-electron, two-center integrals.

$$(a \mid V_h \mid b) = \int \varphi_a^*(1)\, V_h(1,2)\, \varphi_b(1)\, d V_1\, d V_2$$

Integral	LiH : r_{LiH} =			NH_3	H_2O	HF
	2.64	3.02	3.40			
$(2s \mid V_h \mid 2s)$	0.015	0.013	0.011	0.056	0.064	0.071
$(2p, h \mid V_h \mid 2p, h)$	0.028	0.025	0.022	0.119	0.132	0.145
$(2p, h_\perp \mid V_h \mid 2p, h_\perp)$	–	–	–	0.028	0.036	0.042
$(2s \mid V_h \mid 2p, h)$	0.020	0.018	0.015	0.070	0.094	0.107

Institute of Mathematical Physics, University of Stockholm, April 1953.

REFERENCES

1. L. Pauling, The Nature of the Chemical Bond, 2nd ed. Ithaca (1948) p. 76.
2. A. Maccoll, Trans. Faraday Soc. *46* (1950) 369.
3. I. Fischer, Ark. Fys. *5* (1952) 349.
4. J. Lennard-Jones, Proc. Roy. Soc. A *198* (1949) 1, 16.
5. J. Lennard-Jones and J. A. Pople, Proc. Roy. Soc. A *202* (1950) 166.
6. R. S. Mulliken, J. chim. phys. *46* (1949) 497.
7. D. R. Hartree, Rep. Phys. Soc. Progr. Phys. *11* (1946–47) 113.
8. P.-O. Löwdin, private communication.
9. P. M. Morse, L. A. Young, and E. S. Haurwitz, Phys. Rev. *48* (1935) 948.
10. W. E. Duncanson and C. A. Coulson. Proc. Roy. Soc. Edinb. A *62* (1943) 37.
11. H. Eyring, J. Walter, and G. E. Kimball, Quantum Chemistry, New York (1944) p. 376.
12. G. Herzberg, Infrared and Raman Spectra of Polyatomic Molecules, New York (1945).
13. J. A. Pople, Proc. Roy. Soc. A *202* (1950) 323.
14. C. A. Coulson, U. Danielsson, and H. H. Greenwood, unpublished calculations.

Tryckt den 30 november 1953

Uppsala 1953. Almqvist & Wiksells Boktryckeri AB

ARKIV FÖR FYSIK Band 7 nr 16

Communicated 27 May 1953 by MANNE SIEGBAHN

The strong surface coupling nuclear model and hindered alpha decay

By J. O. RASMUSSEN, Jr.[1]

With 1 figure in the text

A. BOHR (1, 2) has discussed in considerable detail the problem of the coupling of individual nucleon motion to deformations of the nuclear surface and has treated theoretically the strong coupling approximation (2) for strong interaction between the single particle and the nuclear surface deformations. In this case the precession of the angular momentum vector j of the particle about the symmetry axis of the spheroidal nucleus is so rapid that the projection Ω of j on the nuclear symmetry axis becomes approximately a constant of motion. For ground states of odd mass nuclei possessing appreciable spheroidal distortion, in the strong coupling approximation it is possible to have nuclear spin $I = |\Omega|$ with $|\Omega|$ taking any half-integral values less than or equal to j. DAVIDSON and FEENBERG and also FORD have recently published calculations (3) based on A. Bohr's model.

In the present note it is suggested that nuclei whose magnetic moments lie near the opposite Schmidt limit from ordinary shell model predictions and which lie in regions of generally large nuclear spheroidal distortion (i.e., distant from closed shell neutron or proton numbers) may have predominantly strong-coupling configurations in the ground state with $I < j$. Eu^{153} with $I = 5/2$, $\mu = +1.6$ appears to have a $j = l - 1/2$ state for the odd proton. The odd proton should then be in a $5\,g_{7/2}$ orbital with projection 5/2 along the symmetry axis. Similarly, Yb^{173} with $I = 5/2$, $\mu = -0.65$ appears to have its odd neutron in a $j = l + 1/2$ state. The odd neutron might thus be either in a $5\,f_{7/2}$ or a $7\,i_{13/2}$ state with projection of 5/2. The quadrupole moments of both the above nuclei are fairly large, indicating the large spheroidal distortion essential to the validity of the strong coupling approximation.

In the strong surface coupling approximation odd nucleon nuclei situated in the same nucleon shell and having the same spin may have the odd nucleons in single particle orbitals of different nature, and this fact may have an important bearing on the alpha decay rate problem for odd nucleon types.

Am^{241} and Np^{237} have like spins (4, 5), $I = 5/2$, yet the ground state alpha transition from Am^{241} to Np^{237} is highly hindered (6), (nearly a factor of 1000). Likewise, Pa^{231} and Ac^{227} have like spins (5, 7) $I = 3/2$, yet again the ground state alpha transition between them is hindered (8) (factor of about 500).

---

[1] On leave from University of California Radiation Laboratory, Berkeley, California.

There is presently no adequate theory giving quantitative explanation of the hindrance factors commonly found in alpha decay of odd nucleon types, although it seems likely, as PERLMAN, GHIORSO, and SEABORG (9) have stressed, that the hindrance is largely associated with a nuclear effect (alpha particle formation probability), rather than an extra-nuclear or barrier effect resulting from non-zero angular momentum of alpha emission. Going a step further, it seems a plausible assumption that an alpha transition which leaves the odd nucleon in the same particle state should proceed relatively unhindered and that the more hindered alpha decay groups should correspond to changes in the state of the odd nucleon. If this assumption is valid, the hindrance of the ground state alpha transitions in Am^{241} and in Pa^{231} is not in agreement with the simple shell model concept that the spin 3/2 must correspond only to a $p_{3/2}$ proton and 5/2 to an $f_{5/2}$ proton. The strong surface coupling model, on the other hand, opens the possibility that the odd protons, though giving rise to the same nuclear spin in different nuclei, may have quite different wave functions. To be consistent with the above assumption about alpha decay hindrance, the odd protons in Am^{241} and in Np^{237} must be in different orbitals, as must also those in Pa^{231} and Ac^{227}. The difference might show up, though not necessarily so, by the nuclear magnetic moments of one or more of the above nuclei lying near the opposite Schmidt limit from simple shell model predictions.

The strong coupling theory also seems to offer hope for the interpretation of the closely spaced excited levels often observed near the gound state of heavy element nuclei. A. BOHR and MOTTELSON (10) have interpreted low-lying first excited states of some even-even nuclei as having rotational character. From A. Bohr's equation (95) (ref. 2) it is seen that a nuclear level with no rotational excitation in an odd nucleon nucleus will also have nuclear rotational excited states corresponding to the same particle state and lying above it with spins successively I_0+1, I_0+2, I_0+3, etc. (where I_0 is the spin of the state without rotational excitation). The relative energies for such a nuclear rotational "band" may be determined from A. Bohr's Eqn. (95) (assuming spheroidal symmetry) as

$$E_I = W + \frac{\hbar^2}{2\mathcal{J}} I(I+1) \tag{1}$$

where $\hbar^2/2\mathcal{J}$ is the rotational energy quantum, I is the total spin of the nuclear state, and W is a constant for a given band. Eqn. (1) is not valid if $\Omega = 1/2$ and $K = 1/2$ (see ref. 3).

It is interesting with the aid of eqn. (1) to seek for possible rotational bands in Np^{237}, although it should be borne in mind that insofar as the strong coupling representation is an approximation the relationship (eqn. 1) will not be exact, and level positions may be perturbed by neighboring levels of the same spin and parity.

If it be assumed that the 71 kev, the 114 kev, and the 170 kev levels in Np^{237} constitute a rotational band (the spin of the 71 kev base level being designated I_0), one can substitute in eqn. (1) and solve simultaneous equations for I_0 and $\hbar^2/2\mathcal{J}$, obtaining the result $\hbar^2/2\mathcal{J} = 6.5$ kev and $I_0 = 2.3 \approx 5/2$. The rotational quantum is comparable to that of 7.4 kev found for nearby even-even nuclides from the energies of their first excited states. A spin of 5/2 for the 71 kev state, to which unhindered alpha decay (see Fig. 1) from Am^{241} occurs, would accord with a further assumption that the odd proton in the 71 kev state of Np^{237} has the same particle state as the odd proton in the ground state of Am^{241}.

The 11 kev difference between ground and first excited states of Np^{237} is so small as to preclude their constituting a rotational band with the rotational quantum near 6.5 kev. An obvious interpretation of the 43 kev state is as the first rotational excited state corresponding to the ground state. As such, the 43 kev state would possess a spin $I = 7/2$. From numerical agreement alone an equally good assignment would set the 43 kev state as the first rotational excited state corresponding to the 11 kev state, with a spin sequence of 3/2 and 5/2. The latter interpretation would seem favored by the fact that the 71 kev state decays by electric dipole transitions to the 43 kev and 11 kev states [10] but not to the ground state. The possibility that alpha decay occurs to two unresolved levels near 43 kev is not unlikely.

The parity of the nuclear state is determined solely by the odd or even character of the l value of the particle state (12). Hence, levels of a given rotational band will be of the same parity.

The above suggestions are summarized in Fig. 1.

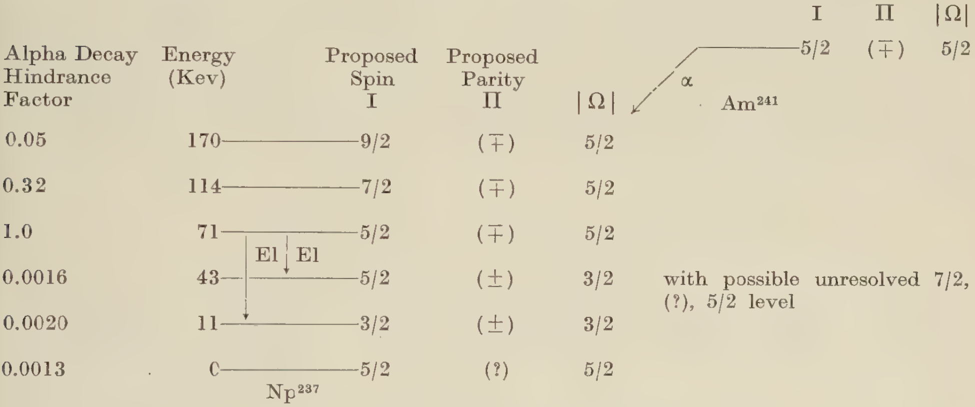

Fig. 1. Possible Nuclear Level Assignments.

The El transitions from the 71 kev state are slower (11) by a factor of $\sim 4 \times 10^5$ than predicted by Weisskopf's lifetime formula (13). These transitions must thus be of a quite special nature. The only even parity orbital in the 82–126 shell is the $7\,i_{13/2}$, so either the 71 kev or the 11 kev state must have the odd proton in a $7\,i_{13/2}$ orbital in view of the fact that the El transition connecting these states requires a parity change. If, then the other state involved an odd proton in a $5\,f$ or $4\,p$ orbital, there would be a difference in l for the 59 kev transition of 3 or 5 units, a possible explanation for the large hindrance in the electromagnetic transition.

The experimental information in the heavy region concerning nuclear energy levels and their associated spins and parities does not seem complete enough at this time to provide a real test of the validity of strong coupling interpretations like the one above. Additional experimental work can provide the answers regarding the ultimate value of the surface coupling modifications of the nuclear shell model for the analysis of nuclear data in the region of large spheroidal distortion.

I wish to express appreciation to Dr Aage Bohr for helpful comments.

Nobel Institute of the Swedish Royal Academy of Sience, Department for Physics, Stockholm, Sweden.

REFERENCES

1. A. Bohr, Phys. Rev. *81*, 134 (1950).
2. ——, Kgl. Danske Videnskab. Selskab, Mat. fys. Medd. *26*, no 14 (1952), p. 28.
3. K. W. Ford, Phys. Rev. *90*, 29 (1953). J. P. Davidson and E. Feenberg, Phys. Rev. *89*, 856 (1953).
4. M. Fred and F. S. Tomkins, Phys. Rev. *89*, 318 (1953).
5. J. E. Mack, Rev. Mod. Phys. *22*, 64 (1950).
6. F. Asaro, F. L. Reynolds, and I. Perlman, Phys. Rev. *87*, 277 (1952).
7. F. S. Tomkins, M. Fred, and W. F. Meggers, Phys. Rev. *84*, 168 (1951).
8. E. Cotton, Ann. phys. *6*, 481 (1951).
9. I. Perlman, A. Ghiorso, and G. T. Seaborg, Phys. Rev. *77*, 26 (1950).
10. A. Bohr and B. R. Mottelson, Phys. Rev., *89*, 316 (1953).
11. J. K. Beling, J. O. Newton, and B. Rose, Phys. Rev. *87*, 670 (1952), Phys. Rev. *86*, 797 (1952).
12. A. Bohr (private communication).
13. V. F. Weisskopf, Phys. Rev. *83*, 1073 (1951).

Tryckt den 30 november 1953

Uppsala 1953. Almqvist & Wiksells Boktryckeri AB

ARKIV FÖR FYSIK Band 7 nr 17

Communicated 3 June 1953 by Erik Hulthén

Microwave spectrum and molecular structure of fluorobenzene

By Gunnar Erlandsson

Some preliminary results on the microwave spectrum of fluorobenzene have been reported in a previous paper (1). A more detailed analysis has now been carried out resulting in the identification of a number of lines as arising from rotational transitions, having $\Delta J = 0$ and J-values up to 48. The calculations have shown that the constants given in (1) must be altered slightly to fit the Q-branch lines. They have also revealed a numerical error in the calculation of the bond distances.

Experimental technique and results

The Stark-effect modulation spectrometer used has been shortly described elsewhere (2). The frequency-region investigated is $17.7 - 26.7$ kMc/s. Frequency measurements are accurate to about ± 5 Mc/s. For resolution of Stark-effect components a DC-field of up to 2 000 volts/cm has been used with a small square-wave voltage superimposed.

The frequency values obtained are presented in Table I together with estimated relative intensities and rotational assignments. In addition to these lines there is a number of weaker satellite lines around some of the stronger ones in the table. These satellites are believed to be due to excited vibrational states. Their frequencies have not been measured because they could not be satisfactorily observed on the oscilloscope screen but only displayed by the Brown recorder.

Stark effect resolution has been tried on some of the lines assigned as arising from the transitions $J = 4 - 5$ and $J = 5 - 6$. Complete resolution has not been obtained in any case owing to weakness and broadening of the components and to mixing of the Stark-effect patterns with neighbouring unresolved lines. The experiments have shown, however, that the number of components is low in all cases tried. The splitting is unsymmetrical with the inner components stronger and more closely spaced than the outer ones. From the formulas of Golden and Wilson (3) it may therefore be concluded that these lines have $|\Delta J| = 1$. The best results have been obtained with the lines at 21 388 and 23 388 Mc/s. Both of these give four distinct components the succesive distances of which indicate that their m-values are $1 - 4$. The component $m = 0$ would then be unresolved from $m = 1$.

Attempts to resolve some of the unidentified lines and those involving higher $J =$ values have met with no success.

Table I

Transition	Calculated frequency Mc/s	Observed frequency Mc/s	Estimated relative intensity
–	–	17724	W
–	–	18370	M
$3_{2.1}-4_{2.2}$	18424	18420	M
$3_{1.2}-4_{1.3}$	18634	18633	M
$(57_{18.40}-57_{18.39})$	–	18806	M
$4_{1.4}-5_{1.5}$	19216	19217	W
–	–	19238	W
–	–	19429	W
$17_{5.13}-17_{5.12}$	19530	19529	W
$4_{0.5}-5_{0.5}$	19674	19674	W
–	–	20063	M
$(54_{17.38}-54_{17.37})$	–	20219	W
$20_{6.15}-20_{6.14}$	20274	20275	W
$29_{9.21}-29_{9.20}$	20508	20508	W
$23_{7.17}-23_{7.16}$	20655	20657	W
$26_{8.19}-26_{8.18}$	20719	20718	M
–	–	20882	W
$4_{2.3}-5_{2.4}$	21385	21388	S
–	–	21551	M
$(51_{16.36}-51_{16.35})$	–	21608	M
$12_{3.11}-12_{3.10}$	21845	21848	W
–	–	21889	M
$4_{4.1}-5_{4.2}$	21992	21991	W
$4_{4.0}-5_{4.1}$	22003	22001	W
$4_{3.2}-5_{3.3}$	22025	22028	W
$4_{3.1}-5_{3.2}$	22317	22321	W
$5_{1.5}-6_{1.6}$	22858	22862	M
$4_{1.3}-5_{1.4}$	22937	22939	M
$48_{15.34}-48_{15.33}$	22980	22943	M
$5_{0.5}-6_{0.6}$	23130	23132	M
$4_{2.2}-5_{2.3}$	23389	23388	S
–	–	23642	M
–	–	23941	W
$15_{4.12}-15_{4.11}$	23974	23973	M
$45_{14.32}-45_{14.31}$	24215	24185	S
–	–	24895	M
$42_{13.30}-42_{13.29}$	25332	25312	M
–	–	25403	M
$5_{2.4}-6_{2.5}$	25423	25425	S
$18_{5.14}-18_{5.13}$	25592	25589	W
–	–	25758	W
–	–	26174	W
$39_{12.28}-39_{12.27}$	26294	26280	M
$5_{5.1}-6_{5.2}$	26373	26374	M
$5_{5.0}-6_{5.1}$	26374		
$5_{3.3}-6_{3.4}$	26440	26441	M
$6_{1.6}-7_{1.7}$	26458	26457	W
$5_{4.2}-6_{4.3}$	26478	26479	M
$5_{4.1}-6_{4.2}$	26524	26526	S
$6_{0.6}-7_{0.7}$	26600	26603	S
$21_{6.16}-21_{6.15}$	26751	26758	S

Molecular structure

The fluorobenzene molecule has been investigated by electron diffraction methods by FINBAK and HASSEL (4) and by OOSAKA (5). Their investigations have shown that the regular hexagonal structure of the benzene molecule is fairly undisturbed by the fluorine substitution. According to (4) the bond distances are

$$d_{\mathrm{C-C}} = 1.40 \pm 0.01 \text{ Å}; \ d_{\mathrm{C-H}} = 1.04 \pm 0.05 \text{ Å}; \ d_{\mathrm{C-F}} = 1.31 \pm 0.03 \text{ Å}.$$

These values were used to calculate approximate values of the rotational constants of the molecule. The lower rotational energy levels were then obtained using the methods and tables of KING, HAINER and CROSS (6). It was found that all lines arising from the transition $J = 4 - 5$ and some lines arising from $J = 3 - 4$, $5 - 6$ and $6 - 7$ should be expected to fall in the frequency region investigated. Comparison of the expected spectrum and the experimental results showed that these could be brought practically to coincidence by slightly altering the values of the rotational constants. (Some missing lines were found afterwards at their expected frequencies.) The results up to this point were published in (1).

A closer inspection of the results obtained, showed that the limits of error in the rotational constants were fairly wide. Also the Q-branch lines calculated from these constants did not agree with the experimental results. Since the frequencies of these lines are more sensitive functions of the rotational constants than are the above mentioned R-branch lines, they offer a possibility of obtaining better values for these constants as far as centrifugal distortion can be disregarded.

Since no guidance to the identification of the Q-branch lines was obtained from their Stark-effects, a trial process was employed involving the calculation of expected spectra for different values of the excentricity parameter $\varkappa = (2\,\mathrm{B} - \mathrm{A} - \mathrm{C})/(\mathrm{A} - \mathrm{C})$ in the vicinity of the value $\varkappa = -0.590 \pm 0.003$ obtained from the R-branch lines. These calculations were carried out by means of the continued fraction method of KING, HAINER and CROSS (6). Comparing these spectra with the experimental results it was found that $\varkappa = -0.5880$ and $\frac{1}{2}(\mathrm{A} - \mathrm{C}) = 1.94839$ kMc/s gave a good agreement up to $J = 29$. Returning to the R-branch lines it was found that $\frac{1}{2}(\mathrm{A} + \mathrm{C}) = 3.71593$ kMc/s gave an agreement between calculated and observed frequencies, which was even better than before. Some Q-branch lines with $J > 29$ have also been calculated. These show a systematic deviation towards lower frequencies. Since this discrepancy could not be satisfactorily removed by ajusting the parameters, it may be concluded that it is due to centrifugal distortion. The results thus obtained are:

$$\mathrm{A} = 5.6643 \pm 0.0002 \text{ kMc/s}; \quad \mathrm{B} = 2.5703 \pm 0.0002 \text{ kMc/s}; \quad \mathrm{C} = 1.7675 \pm 0.0002 \text{ kMc/s}$$

or in cm^{-1}

$$\mathrm{A} = 0.188950 \text{ cm}^{-1}; \quad \mathrm{B} = 0.085739 \text{ cm}^{-1}; \quad \mathrm{C} = 0.058962 \text{ cm}^{-1}.$$

These constants may be used for calculation of the interatomic distances. Since the molecule except for zero-point vibrations is a plane structure, however, only two parameters may be evaluated. The accuracy of the values thus obtainable is limited by zero-point vibrations, which influence the result in two ways:

(i) the structure is not exactly plane due to vibrations normal to the plane.
(ii) the moments of inertia obtained by inversion of the rotational constants are effective values $\frac{1}{I_{\text{eff}}} = \overline{\left(\frac{1}{I}\right)} \neq \frac{1}{\bar{I}}$ where the bars denote average values.

The equilibrium values of the rotational constants would satisfy the relation $I_{a,e} + I_{b,e} = I_{c,e}$, whereas the average values due to (i) would give $I_{a,av} + I_{b,av} > I_{c,av}$. For the effective values this inequality may also be reversed. In the actual case one obtains:

$$I_a + I_b = 89.230 + 196.642 = 285.872 \pm 0.030 < I_c = 285.949 \pm 0.050.$$

The deviation is larger than the inaccuracy due to the measurements. The limits of error in the rotational constants have therefore tentatively been increased by a factor 10 in the calculation of bond distances.

Assuming a regular hexagonal structure of the molecule, except for the fluorine substitution, and assuming the C–H distance to be known. the C–C and C–F distances may be calculated. Since the axis of smallest moment of inertia passes through the fluorine atom, the C–C distance is obtained from I_a. The C–F distance may then be obtained from I_b or I_c. Using $d_{\text{CH}} = 1.05$ Å $+ \Delta d_{\text{CH}}$ the following results were obtained

$$d_{\text{CC}} = 1.4043 \pm 0.0003 \text{ Å} - 0.13\,\Delta d_{\text{CH}};\ d_{\text{CF}} = 1.294 \pm 0.010 \text{ Å} - 0.47\,\Delta d_{\text{CH}}.$$

Comparing these results to the values given by FINBAK and HASSEL (4) i.e. $d_{\text{CC}} = 1.40 \pm 0.01$, $d_{\text{CH}} = 1.04 \pm 0.05$ and $d_{\text{CF}} = 1.31 \pm 0.03$ it is found that the agreement is satisfactory.

Acknowledgement

I wish to express my thanks to Professor ERIK HULTHÉN for his interest in this work and for helpful discussions and to Statens Naturvetenskapliga Forskningsråd for economical support.

Stockholm, June 8, 1953.
Department of Physics, University of Stockholm.

REFERENCES

1. G. ERLANDSSON, Arkiv för Fysik, *6*, nr. 45 (1953).
2. ——, Arkiv för Fysik, *6*, nr. 47 (1953).
3. S. GOLDEN and E. B. WILSON jr., Journ. Chem. Phys. *16*, 669 (1948).
4. CHR. FINBAK and O. HASSEL, Arch. Math. Naturvidenskab *45*, 45 (1941).
5. H. OOSAKA, Bull. Chem. Soc. Japan *15*, 31 (1940).
6. G. KING, R. M. HAINER and P. C. CROSS, Journ. Chem. Phys. *11*, 27 (1943).

Tryckt den 2 december 1953.

Uppsala 1953. Almqvist & Wiksells Boktryckeri AB

ARKIV FÖR FYSIK Band 7 nr 18

Communicated 3 June 1953 by BENGT EDLÉN

Characteristic X-rays from thick β-ray sources

By K. LIDÉN and N. STARFELT

With 2 figures in the text

During a scintillation spectrometer study of the internal and external bremsstrahlung of P^{32} and S^{35}* we observed, in special cases, an intense emission of X-rays characteristic of the external bremsstrahlung radiator. Such X-rays have been photographed by EDWARDS and POOL (1946); they also studied the X-rays from P^{32} on different radiators by absorption measurements with an ionization chamber. SIEGBAHN and SLÄTIS (1948) investigated the faint X-radiation from P^{32} and RaE with a β-spectrometer using a Pb converter; they observed characteristic X-rays from Pb. EDWARDS and POOL pointed out the experimental difficulties of making accurate intensity measurements. However, in the present investigation we have been able to study with greater precision the intensity of characteristic X-rays excited by β-particles.

The investigations were performed with a scintillation spectrometer using a NaI(Tl) crystal $10 \times 10 \times 10$ mm in conjunction with an EMI 5311 photomultiplier and a single channel differential discriminator. The mounting of the carrier free β-sources (190 μC of P^{32}, $E_{\max}$ 1.7 MeV; 520 μC of S^{35}, $E_{\max}$ 0.17 MeV) between the radiator sheets, the collimator and the crystal are shown in Fig. 1. The results of the bremsstrahlung measurements from P^{32} + Pb radiator, P^{32} + Sn radiator and S^{35} + Sn radiator are given in Fig. 2. In Fig. 2(*b*) the P^{32} + Sn radiator curve is normalized to the peak of S^{35} + 37 mg/cm² Sn. Experiments showed that the internal bremsstrahlung from P^{32} and S^{35} and the external bremsstrahlung from the perspex absorber (8 mm for P^{32}, none for S^{35}) were negligible. Corrections due to crystal efficiency, escape, Compton background, and absorption, had no appreciable effect on the shape of the distribution in the region of interest.

In order to find, in the Pb and Sn peaks, the intensity ratio of the K-radiation to that of the continuous bremsstrahlung below the K-absorption edge, the bremsstrahlung from P^{32} + Al radiator and from S^{35} + Al radiator respectively was studied experimentally and the transparency of the Pb and Sn radiators for this radiation was calculated; throughout the paper we have used the absorption data from WHITE (1952). The spectral distribution of the external bremsstrahlung from an Al radiator has mainly the same shape as the respective external bremsstrahlung from P^{32} + Pb and S^{35} + Sn would have had, assuming no γ-absorption in the radiator. We found that the K X-radiation part of the peak for P^{32} + 220 and 560 mg/cm² Pb radiator

---

* A preliminary report of this investigation was given at the sixth meeting of *the Swedish National Committee for Physics*, held in Stockholm on Sept. 25–27, 1952.

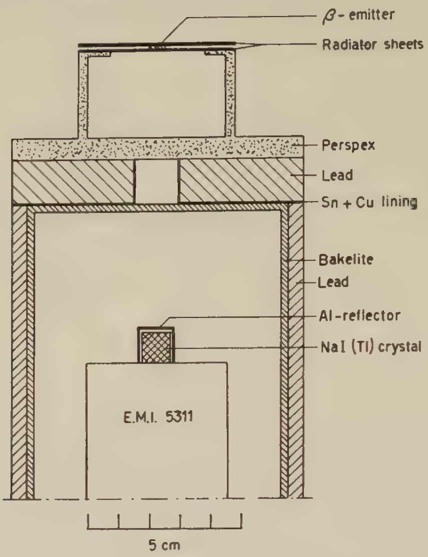

Fig. 1. Source and radiator mounting; detector part of the spectrometer.

was 70% and 75% respectively. For S^{35} + 37 and 74 mg/cm² Sn radiator we obtained 50% and 60% respectively.

It appears from fig. 2(*a*) that the intensity of the P^{32} + Pb radiator peak is largest at 230 mg/cm². The total area of the peak corresponds to a yield of 0.11 quanta per β-particle, i.e. this radiator emits 8% of K-quanta per P^{32}-disintegration. S^{35} + 37 mg/cm² Sn gives 0.003 quanta per β-particle within the peak, i.e. 0.15% of K-quanta per S^{35}-disintegration.

It may be mentioned that we have observed an L X-ray peak but no K X-radiation from S^{35} + 37 mg/cm² Pb radiator.

Using the above mentioned spectrum of the bremsstrahlung of P^{32} + Al radiator and WHITE's lead absorption data, the number of lead atoms ionized in the K-shell by photoelectric absorption of bremsstrahlung quanta is calculated. After correction for the fluorescens yield (BURHOP 1952), the intensity of the K X-rays excited by the bremsstrahlung is obtained. The remaining part of the observed K X-rays is excited by β-particle ionization of the K-shell. The calculated ratio of the contribution of these two processes to the K X-radiation is about 1:4 for P^{32} + 230 mg/cm² Pb and 1:2 for P^{32} + 590 mg/cm² Pb.

With increasing β-energies the intensity of the K X-ray peak increases, but at the same time the intensity of the high energy bremsstrahlung increases; compare S^{35} + Sn and P^{32} + Sn of Fig. 2(*b*). In this case the true peak intensity ratio for equal activity of S^{35} and P^{32} is 1:12. Further, as the fluorescence yield ω_K decreases with decreasing atomic number Z($\omega_K = 0.50$ at Z = 33 and $\omega_K = 0.10$ at Z = 18 [BURHOP 1952]), the yield of K X-rays is lower for small Z.

It follows that every β-emitting isotope also emits its own characteristic X-rays with an intensity depending on the β-energy and the thickness of the source. This emission is very small for a pure isotope of low activity, i.e. thin sources. However, the K X-ray emission from thick sources may be fairly important — a fact which

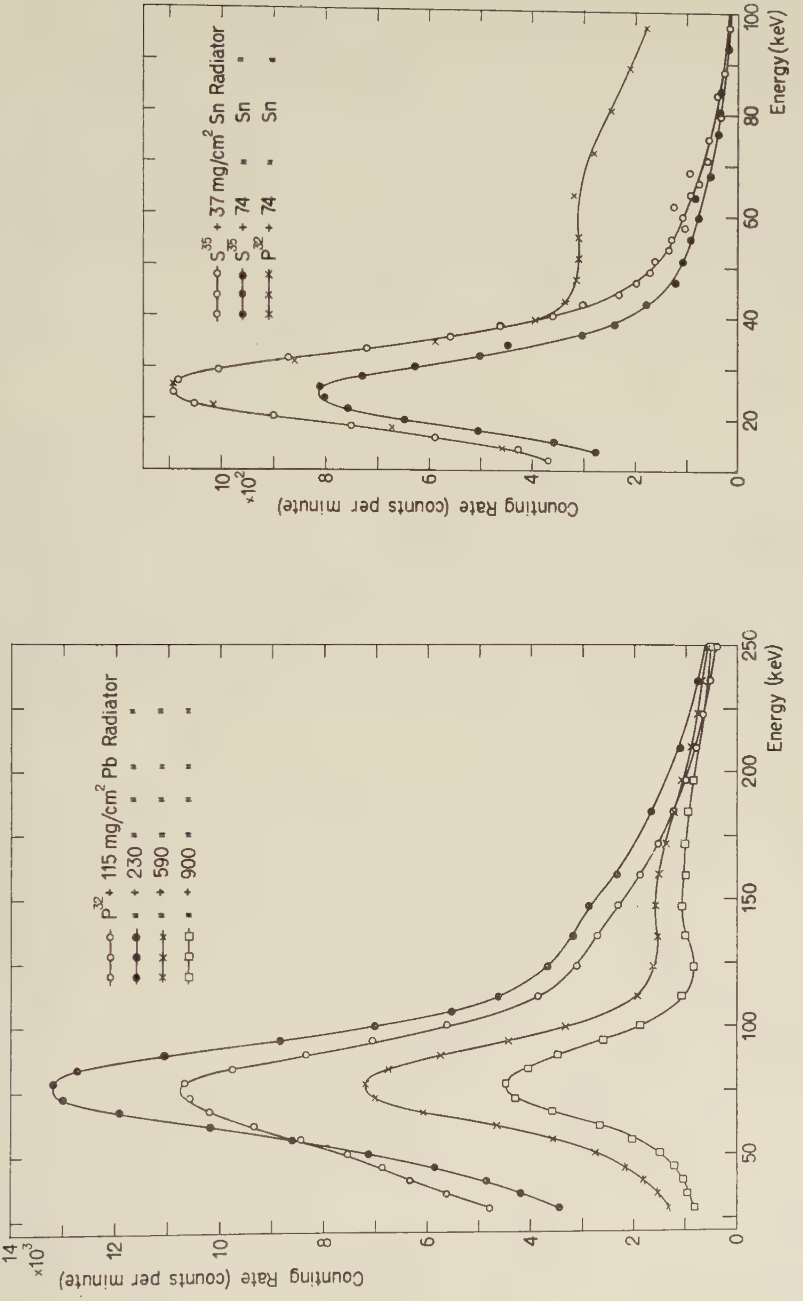

a   *b*

Fig. 2. The energy distribution of the external bremsstrahlung from (*a*) Pb radiators, (*b*) Sn radiators.

must be considered when investigating internal conversion coefficients of γ-rays, K-capture branching ratios of β-emitters, etc.

The Kβ X-rays of the above mentioned K X-radiation can be critically absorbed. This gives rise to a more monochromatic peak. 200 mg/cm^2 of Pt and 50 mg/cm^2 of Ag are convenient absorbers for the Kβ X-rays of Pb and Sn respectively.

Using separated long-lived β-emitters, e.g. $Sr^{90} + Y^{90}$, constant and practically monochromatic X-ray sources can be prepared. Such sources with a β-activity of 0.1–10 mC may be suitable for energy calibration of scintillation spectrometers, etc. Sources with 0.1–100 Curies might be used as monochromatic X-ray sources for industrial thickness measurements and for medical and industrial radiography. It may be assumed that an X-ray source of this type will be an alternative to the use of soft γ-ray sources such as Tm^{170} (MAYNEORD 1952, WEST 1953). Measurements have shown that the radiation from strong sources of Tm^{170} is mainly due to the K X-rays from both Tm and Yb and to the bremsstrahlung (LIDÉN-STARFELT, 1953).

Radiation Physics Department, University of Lund, Sweden. May 1953.

REFERENCES

BURHOP, E. H. S., 1952, *The Auger Effect and Other Radiationsless Transitions.* (Cambridge: University Press).

EDWARDS, J. E., and POOL, M. L., 1946, *Phys. Rev. 69,* 549.

LIDÉN, K., and STARFELT, N., 1953 *Arkiv för Fysik* (in the press).

MAYNEORD, W. V., 1952, *British Journal of Radiology 25,* 517.

SIEGBAHN, K., and SLÄTIS, H., 1948, *Arkiv för Matematik, Astronomi och Fysik, 34 A,* No. 6.

WEST, R., 1953, *Nucleonics 11,* No. 2, 20.

WHITE, G. R., 1952, *X Ray Attenuation Coefficients from 10 KeV to 100 MeV.* National Bureau of Standards Report 1003.

Tryckt den 11 september 1953

Uppsala 1953. Almqvist & Wiksells Boktryckeri AB

ARKIV FÖR FYSIK Band 7 nr 19

Communicated 3 June 1953 by Axel E. Lindh and G. Hägg

The X-ray diffraction from quartz

By Öved Adell, Gösta Brogren and Lars-Erik Haeggblom

With 6 figures in the text

Introduction

The original theory for X-ray diffraction developed by Darwin (1) was based on the assumption of a perfect crystal. The predictions given by this theory did not exactly fit the experimental results for any crystal and the discrepancy was accounted for the mosaic structure present in real crystals. Prins (2) (1930) modified the above theory by introducing the effect of absorption of X-rays in the crystals. A series of experiments were carried out with calcite, which at that time was most extensively used in X-ray spectrometers. It was shown that for certain specimens of calcite the agreement between the theoretical predictions and the experimental results was excellent and that there was no evidence of mosaic structure (3–5). The use of focusing spectrometers brought other crystals to the fore as X-ray gratings, and among these quartz has been widely used. This crystal has good elastic qualities.

Table 1. The constants, used in the calculations.

Emission line	Wave-length	$\frac{\mu}{\varrho_{Si}}$	$\frac{\mu}{\varrho_0}$	$\delta_{Si} \cdot 10^6$	$\beta_{Si} \cdot 10^6$	$\delta_0 \cdot 10^6$	$\beta_0 \cdot 10^6$	$\delta \cdot 10^6$	$\beta \cdot 10^6$	$\frac{\beta}{\delta}$
Ag $K\alpha_1$	558	3.7	0.7	0.54	0.0020	0.61	0.0005	1.15	0.0025	0.0022
Mo $K\alpha_1$	708	6.4	1.2	0.87	0.0044	0.96	0.0010	1.80	0.0054	0.0030
U $L\alpha_1$	909	11.1	2.4	1.41	0.0100	1.62	0.0025	3.03	0.0125	0.0041
Au $L\beta_1$	1080	22	4.0	1.96	0.0234	2.24	0.0049	4.20	0.0283	0.0066
Tl $L\alpha_1$	1205	31	5.1	2.44	0.0392	2.79	0.0077	5.23	0.0469	0.0088
W $L\beta_1$	1242	33	5.7	2.64	0.0416	3.02	0.0088	5.66	0.0499	0.0090
Au $L\alpha_1$	1274	35	6.3	2.73	0.044	3.13	0.0091	5.86	0.053	0.0092
Cu $K\alpha_1$	1537	60	11.1	3.99	0.093	4.60	0.011	8.60	0.104	0.0121
Co $K\alpha_1$	1785	90	20	5.38	0.157	6.20	0.040	11.58	0.197	0.0170
Fe $K\alpha_1$	1932	111	22	6.27	0.212	7.27	0.047	13.54	0.259	0.0193
Cr $K\alpha_1$	2285	180	36	8.77	0.405	10.03	0.094	18.80	0.499	0.0265
V $K\alpha_1$	2498	225	45	10.62	0.554	12.15	0.128	22.77	0.682	0.0299
Ti $K\alpha_1$	2743	310	64	12.71	0.840	15.20	0.191	27.91	1.031	0.0369
Ca $K\alpha_1$	3352	555	115	19.01	1.840	22.04	0.431	41.05	2.271	0.0553
U $M\beta$	3708	717	153	23.26	2.635	26.96	0.635	50.22	3.270	0.0651
U $M\alpha_1$	3902	830	179	25.80	3.200	29.84	0.785	55.64	3.985	0.0716
Ag $L\alpha_1$	4146	975	212	29.04	4.000	33.69	0.990	62.73	4.99	0.0795
Rh La_1	4588	1270	275	35.64	5.750	41.35	1.420	76.99	7.17	0.0931

Several different atomic planes have a good reflecting power, so that it is possible to employ lattices with different spacings. A knowledge of the X-ray diffraction pattern is of fundamental importance for the spectroscopist. As no information about this was available, we have applied the Darwin-Ewald-Prins dynamic theory for the diffraction in a perfect absorbing crystal to some atomic planes in quartz, and calculated the width of the rocking curve in a two-crystal spectrometer as well as the percent reflection and the double crystal coefficient of reflection. These quantities have also been determined experimentally. The investigations were carried out in the region 560–2500 X. U. The results show that quartz can be considered a perfect crystal in this region, at least for certain specimens. Some of the results have already been published (6).

Theoretical calculations

The Darwin-Ewald-Prins expression for the diffraction pattern from a perfect absorbing crystal is

$$F(l)=\tfrac{1}{2}\left[\frac{\dfrac{A+jB}{\delta}}{l-j\dfrac{\beta}{\delta}\pm\sqrt{\left(l-j\dfrac{\beta}{\delta}\right)^2-\left(\dfrac{A+jB}{\delta}\right)^2}}\right]^2+\tfrac{1}{2}\left[\frac{\dfrac{A+jB}{\delta}\cos 2\vartheta_0}{l-j\dfrac{\beta}{\delta}\pm\sqrt{\left(l-j\dfrac{\beta}{\delta}\right)^2-\left(\dfrac{A+jB}{\delta}\right)^2\cos^2 2\vartheta_0}}\right]^2.$$

The percent reflection, the coefficient of reflection and the form of the rocking curve can be calculated from $F(l)$ by tedious graphic integrations. The constants are obtained as indicated in the earlier report (6). The structure factors are calculated on the assumption that the binding is purely covalent. In reality the binding is partly of ionic character, but the above assumption has little effect on the value of the structure factor. The atomic scattering factors are taken from JAMES and BRINDLEY (7). The β values are calculated from experimental values of the absorption coefficients. Where no such values were available, they were calculated from the formulas given by JÖNSSON (8).

Experimental parts

The two-crystal spectrometer and the methods of measurements have been described earlier (6, 9). The heights of the two horisontal slits were one mm, which corresponds to a horisontal divergence ϕ_m of the X-ray beam of $\frac{1}{300}$ radians. All quartz crystals were etched with 40% hydrofluoric acid until the spectroscopic measurements were no longer affected by the etching. The investigation of each atomic plane was completed by repeating the measurements with the first emission line used. In doing so we always obtained results that agreed with the first recordings within the experimental limits of error.

Results and discussions

The present investigation comprises the results from planes $(10\bar{1}0)$, $(20\bar{2}3)$, $(22\bar{4}3)$ and $(11\bar{2}0)$. Some results for the last plane have been reported earlier. When it came to our notice that a paper published by PARRATT (10) gave some experimental values in the region 560 X.U.–4600 X.U. we used these results and carried out calculations of the corresponding theoretical values. As the K-absorption edge of silicon has the wave-length 6300 X.U., it was necessary to apply a correction for the anomalous contribution to the scattering power from the K-electrons of silicon. The correction was calculated from the formulas developed by HÖNL (11–12).

The effect of the surface treatment appears from Tables 2–4. For planes $(10\bar{1}0)$ and $(22\bar{4}3)$ the coefficient of reflection remains nearly constant during the etching. The width of the rocking curve on the other hand decreases 10 to 20%, which means that the resolving power increases. The decrease in the width is compensated by

Table 2. Influence of surface treatment on plane $10\bar{1}0$. Measurements with Cu Kα_1.

Time of etching in min.	Width of the rocking curve in sec. of arc.	Percent reflection · 10^2	Coefficient of reflection in radians
0	5.6	54	$1.86 \cdot 10^{-5}$
4	5.2	60	$1.82 \cdot 10^{-5}$
10	5.0	63	$1.81 \cdot 10^{-5}$
15	5.0	63	$1.81 \cdot 10^{-5}$

Table 3. Influence of surface treatment on plane $20\bar{2}3$. Measurements with Cu Kα_1.

Time of etching in min.	Width of the rocking curve in sec. of arc.	Percent reflection · 10^2	Coefficient of reflection in radians
0	2.9	42	$0.84 \cdot 10^{-5}$
1	2.4	53	$0.79 \cdot 10^{-5}$
2	2.2	55	$0.74 \cdot 10^{-5}$
4	2.0	58	$0.69 \cdot 10^{-5}$
6	2.0	58	$0.69 \cdot 10^{-5}$

Table 4. Influence of surface treatment on plane $22\bar{4}3$. Measurements with Au Lα_1.

Time of etching in min.	Width of the rocking curve in sec. of arc.	Percent reflection · 10^2	Coefficient of reflection in radians
0	1.7	44	$0.46 \cdot 10^{-5}$
2	1.4	55	$0.44 \cdot 10^{-5}$
5	1.3	58	$0.45 \cdot 10^{-5}$
10	1.3	58	$0.45 \cdot 10^{-5}$

Table 5. Theoretical and experimental values of the full width w of the rocking curve, the percent reflection P, and the coefficient of reflection R.

Atomic plane	Line	Wave-length in X.U.	Glancing angle ϑ	l		$A \cdot 10^6$	$B \cdot 10^6$	w sec. of arc.		$P \cdot 10^2$		$R \cdot 10^5$ radians	
				Radians · 10^5	sec. of arc.			exp.	theory	exp.	theory	exp.	theory
$10\bar{1}0$	Mo Kα_1	708	4°47′	2.2	4.5	0.306	0.0012	2.7	2.1	71	77	1.04	0.95
	Au Lβ_1	1080	7°18′	3.2	6.6	0.714	0.0061	3.6	3.1	72	76	1.37	1.25
	Au Lα_1	1274	8°38′	3.9	8.1	0.996	0.0116	4.2	3.8	67	69	1.64	1.55
	Cu Kα_1	1537	10°26′	4.8	10.0	1.46	0.0236	5.0	4.9	63	64	1.81	1.82
	Fe Kα_1	1932	13° 9′	6.1	12.5	2.28	0.0563	6.2	5.9	57	57	2.13	2.06
	Cr Kα_1	2285	15°27′	7.3	15.0	3.20	0.1087	7.2	6.9	51	51	2.25	2.21
$20\bar{2}\bar{3}$	Ag Kα_1	558	11°44′	0.58	1.2	0.204	0.0009	1.0	0.6	56	78	0.31	0.26
	Mo Kα_1	708	14°57′	0.73	1.5	0.316	0.0021	1.0	0.7	63	76	0.37	0.31
	Au Lβ_1	1080	23°11′	1.2	2.4	0.738	0.0112	1.3	1.1	62	70	0.49	0.43
	Au Lα_1	1274	27°35′	1.5	3.0	1.03	0.0211	1.6	1.3	60	65	0.54	0.49
	Cu Kα_1	1537	34° 4′	1.8	3.8	1.50	0.0455	2.0	1.6	57	61	0.69	0.66
	Co Kα_1	1785	40°35′	2.4	4.9	2.02	0.0784	2.8	2.4	52	57	0.91	0.85
$22\bar{4}\bar{3}$	Ag Kα_1	558	15°59′	0.44	0.9	0.195	0.0281	0.5	0.4	61	65	0.19	0.16
	Mo Kα_1	708	20°27′	0.55	2.1	0.303	0.0449	0.7	0.5	60	65	0.23	0.19
	Au Lβ_1	1080	32°13′	0.93	1.9	0.706	0.1096	0.9	0.7	60	64	0.32	0.29
	Au Lα_1	1274	38°58′	1.19	2.5	0.985	0.1573	1.1	0.9	58	60	0.45	0.40

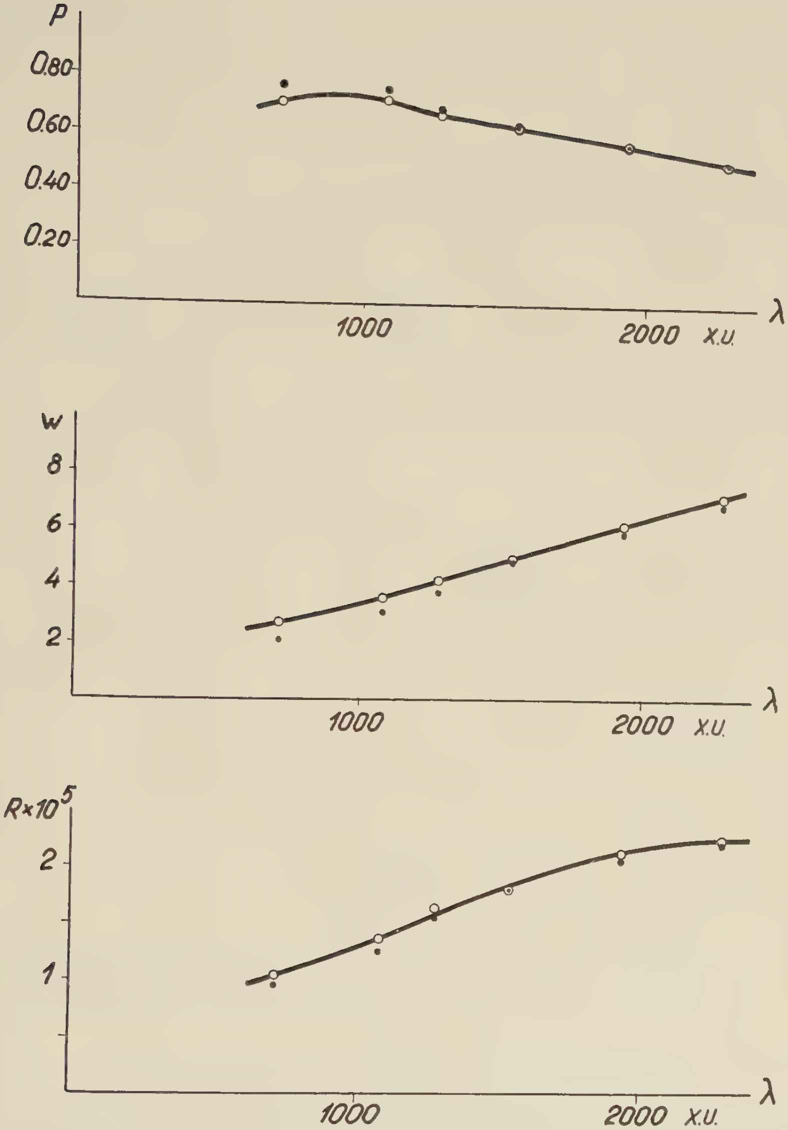

Fig. 1. The percent reflection P, the full width w of the rocking curve and the coefficient of reflection R as a function of wave-length for plane $(10\bar{1}0)$. In Figs. 1–5 the open circles are the experimental values, the filled circles are the calculated ones.

an increase in the percent reflection so that the coefficient of reflection remains nearly constant. The variations are much greater for plane $(20\bar{2}\bar{3})$, probably due to inferior grinding and polishing. The observations confirm the earlier conclusion that a crystal must be etched before it is used as an X-ray grating if maximum resolving power is to be attained.

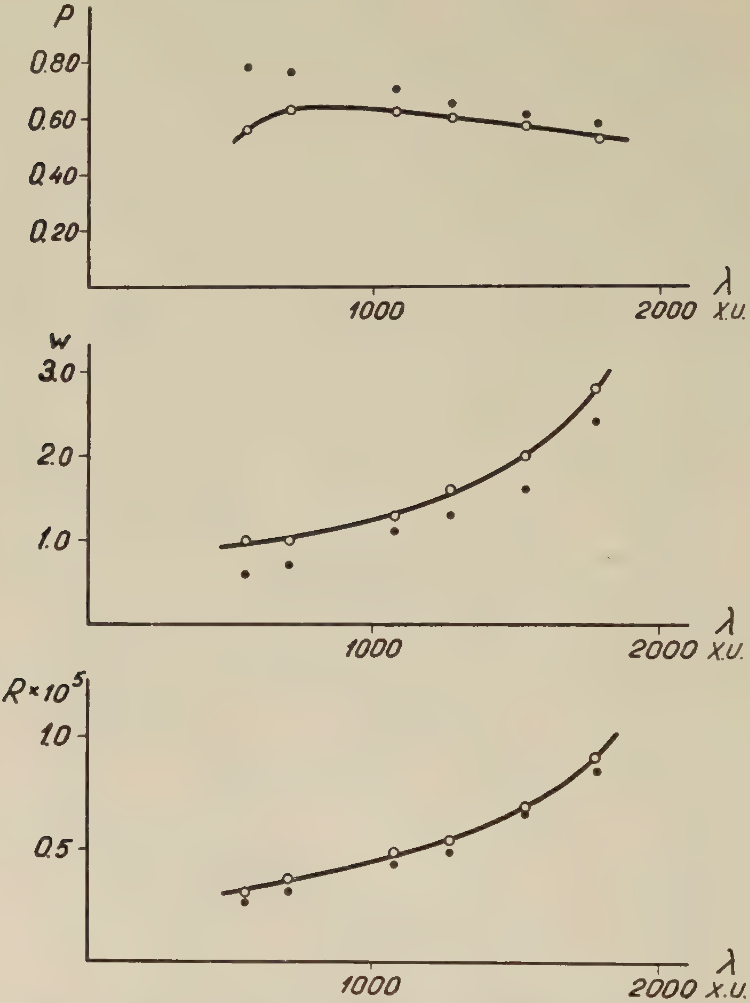

Fig. 2. The percent reflection P, the full width w of the rocking curve and the coefficient of reflection R as a function of wave-length for plane $(20\bar{2}\bar{3})$.

Our new values for the coefficient of reflection R, the percent reflection P and the full width w of the rocking curve at half maximum intensity as a function of wave-length appear from Table 5 and Figures 1–3. The agreement between theory and experiment is very good, especially for the coefficient of reflection. When the wave-length diminishes the discrepancy increases. This must be due to the fact that the crystal is a conglomeration of rather large crystallites. Each individual crystallite is large enough and perfect enough for dynamical reflection to take place in it but the different crystallites are inclined to one another. A truly ideal crystal reflects in accordance with the requirements of the dynamical theory for every wave-length, but a crystal that is a conglomerate of ideally reflecting crystallites will have reflecting

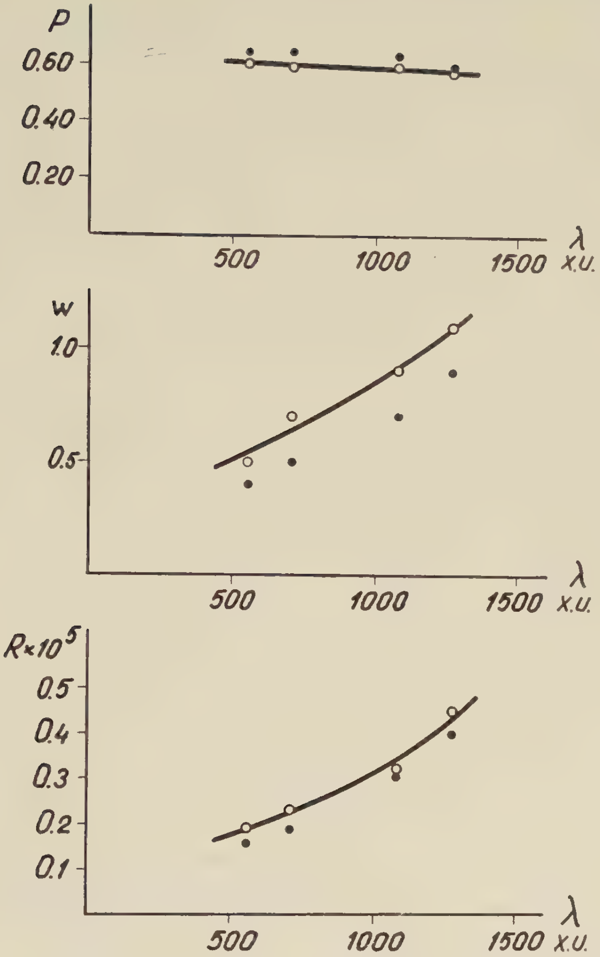

Fig. 3. The percent reflection P, the full width w of the rocking curve and the coefficient of reflection R as a function of wave-length for plane $(22\bar{4}\bar{3})$.

properties, which depend on the wave-length. If the crystallites are so large that the incident radiation is reflected by only one, the crystal will reflect like an ideal crystal. When the incident radiation falls on several surface crystallites, but penetrates so slightly that it does not strike any crystallite under the surface, the coefficient of reflection will agree with the dynamical theory. On the same time, different orientations of the crystallites give rise to a broadening of the rocking curve and the percent reflection is consequently lowered. If the absorption decreases, as it does when the wave-length of the incident radiation decreases, some radiation can pass through the crystallites in the surface to be reflected from others inside the crystal, inclined to those in the surface layer, the coefficient of reflection must increase as well as the width of the rocking curve. The percent reflection is lowered here, too. The better the agreement between theory and experiments, the larger must the

Table 6. Quartz 11$\bar{2}$0. Theoretical and experimental values of the full width w of the rocking curve, the percent reflection P and the coefficient of reflection R.

Emission line	Wave-length X.U.	Glancing angle ϑ	l		$A \cdot 10^6$	$B \cdot 10^6$	w sec. of arc.			$P \cdot 10^2$			$R \cdot 10^5$ radians		
			radians · 10^5	sec. of arc.			theory	BROGREN	PARRATT	theory	B.	P.	theory	B.	P.
Ag Kα_1	558	6°32′	1.0	2.1	−0.203	0.026	1.0	2.3	2.5	68	39	38	.41	.55	.60
Mo Kα_1	708	8°18′	1.3	2.6	−0.319	0.039	1.3	2.3	2.5	68	48	42	.52	.58	.68
U Lα_1	909	10°41′	1.6	3.4	−0.540	0.065	1.7		2.5	67		48	.67		.76
Tl Lα_1	1205	14°14′	2.2	4.5	−0.934	0.109	2.3	2.7		67	54		.84	.88	
W Lβ_1	1242	14°40′	2.3	4.8	−1.01	0.117	2.4		2.9	67		50	.88		.90
Cu Kα_1	1537	18°16′	2.9	6.0	−1.53	0.165	3.0	3.4	3.4	66	55	49	1.08	1.10	1.10
Fe Kα_1	1932	23°10′	3.7	7.7	−2.42	0.252	3.6	4.0	4.1	59	53	47	1.24	1.26	1.24
Cr Kα_1	2285	27°47′	4.6	9.4	−3.40	0.325	4.7	5.2		51	45		1.41	1.48	
V Kα_1	2498	30°38′	5.2	10.7	−4.28	0.373	5.4	6.3	6.4	47	39	39	1.59	1.60	1.59
Ti Kα_1	2743	34° 1′	6.0	12.4	−5.07	0.383	6.6		7.6	41		36	1.69		1.73
Ca Kα_1	3352	43° 8′	8.3	17.0	−7.58	0.406	10.2		11.3	36		31	2.32		2.20
U Mβ	3708	49° 9′	10.2	21.0	−9.33	0.398	12.8		13.3	31		25	2.61		2.36
U Mα_1	3902	52°44′	11.5	23.8	−10.38	0.376	15.0		15.4	27		24	2.71		2.45
Ag Lα_1	4146	57°44′	13.9	28.7	−11.77	0.307	17.2		18.1	24		21	2.88		2.75
Rh Lα_1	4588	69°21′	23.2	48.1	−14.57	0.155	30.0		27.5	21		17	4.46		3.24

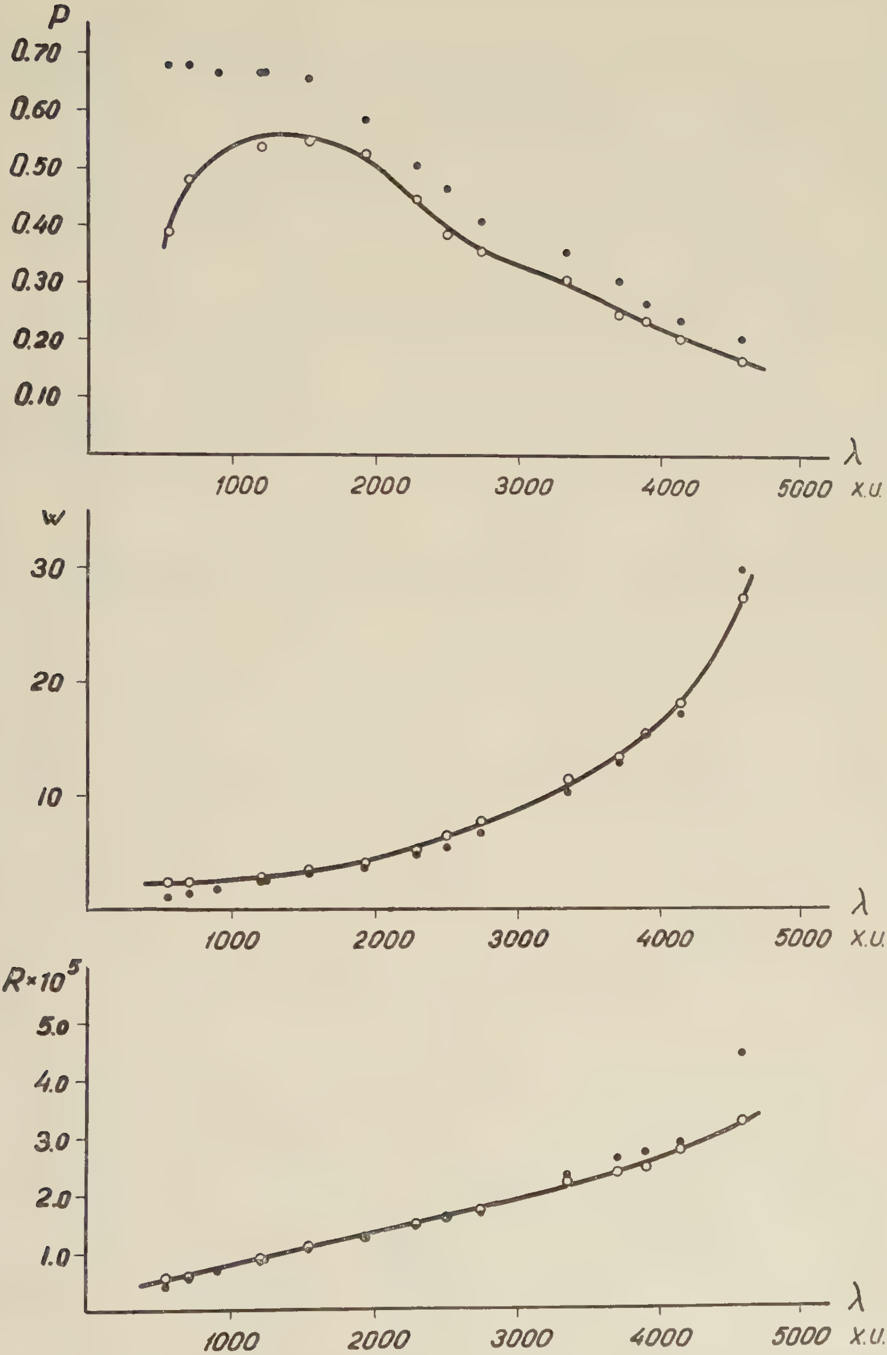

Fig. 4. The percent reflection P, the full width w of the rocking curve and the coefficient of reflection R as a function of wave-length for plane $(11\bar{2}0)$.

Table 7. The reflectivities for some emission lines obtained with plane $10\bar{1}0$ in quartz. w is the full width of the rocking curve at half maximum intensity, P the percent reflection, and R the coefficient of reflection. $S = \lambda/d\lambda = \frac{2 \operatorname{tg} \vartheta}{w}$ is the resolving power of these crystals with the double spectrometer in (1 + 1) position. Parratt's values are indicated by P, ours B and the calculated values T.

Line	Wave-length X.U.	Glancing angle ϑ	w sec. of arc.			$P \cdot 10^2$			$R \cdot 10^5$ radians			$\lambda/d\lambda$	
			W_P	W_B	W_T	P_P	P_B	P_T	R_P	R_B	R_T	S_P	S_B
Mo Kα_1	708	4°47′	9.3	2.7	2.1	13	71	77	0.72	1.04	0.95	3720	12 500
Au Lα_1	1274	8°38′	10.3	4.2	3.8	19	67	69	1.25	1.64	1.55	6100	14 900
Cu Kα_1	1537	10°26′	10.7	5.0	4.9	23	63	64	1.52	1.81	1.82	7100	15 100
Fe Kα_1	1932	13° 9′	11.8	6.2	5.9	25	57	57	1.80	2.13	2.06	8300	15 900

Table 8. Quartz $10\bar{1}\bar{1}$. Experimental values of the full width w of the rocking curve at half maximum intensity, the percent reflection P and the coefficient of reflection R.

Line	Wave-length	Glancing angle ϑ	w sec. of arc.	$P \cdot 10^2$	$R \cdot 10^5$ radians	$\lambda/d\lambda$
Ag Kα_1	558	4°98′	3.9	77	1.60	8 900
Mo Kα_1	708	6° 5′	4.4	79	2.11	10 000
Au Lα_1	1274	11° 1′	7.9	79	3.45	10 200
Cu Kα_1	1537	13°19′	8.8	78	3.90	11 100
Fe Kα_1	1932	16°50′	11.5	72	4.57	10 900
Cr Kα_1	2285	20° 2′	13.5	69	5.06	11 200
Mo Kα_1	Second order		1.0	72	0.50	89 000
Cu Kα_1	» »		2.3	66	1,00	95 000

crystallites be. One might also say that if the agreement is very good, the individual crystallites build up a crystal where the deviations from regularity are extremely small.

Fig. 4 and Table 6 give the values for plane ($11\bar{2}0$). In the region 560–2500 X.U. our measurements agree with Parratt's within the experimental limits of error. The comparison with the calculated values gives the same results as for the other planes. It should be noted, however, that the theoretical values of the coefficient of reflection exceed the experimental ones in the wave-length region above 3000 X.U. Except for the last value in Table 6, the differences are smaller than the uncertainty in calculations and experiments. For the longest wave-length used, 4588 X.U. (the Rh Lα_1-line) the calculated values of w and R are much larger than the experimental ones. As the factor $\frac{2\delta}{\sin 2\vartheta_0}$ is included in both the coefficient of reflection and the width of the rocking curve, and as this factor here gets a large value, this seems to be the reason for the deviation. The agreement between theory and experiment

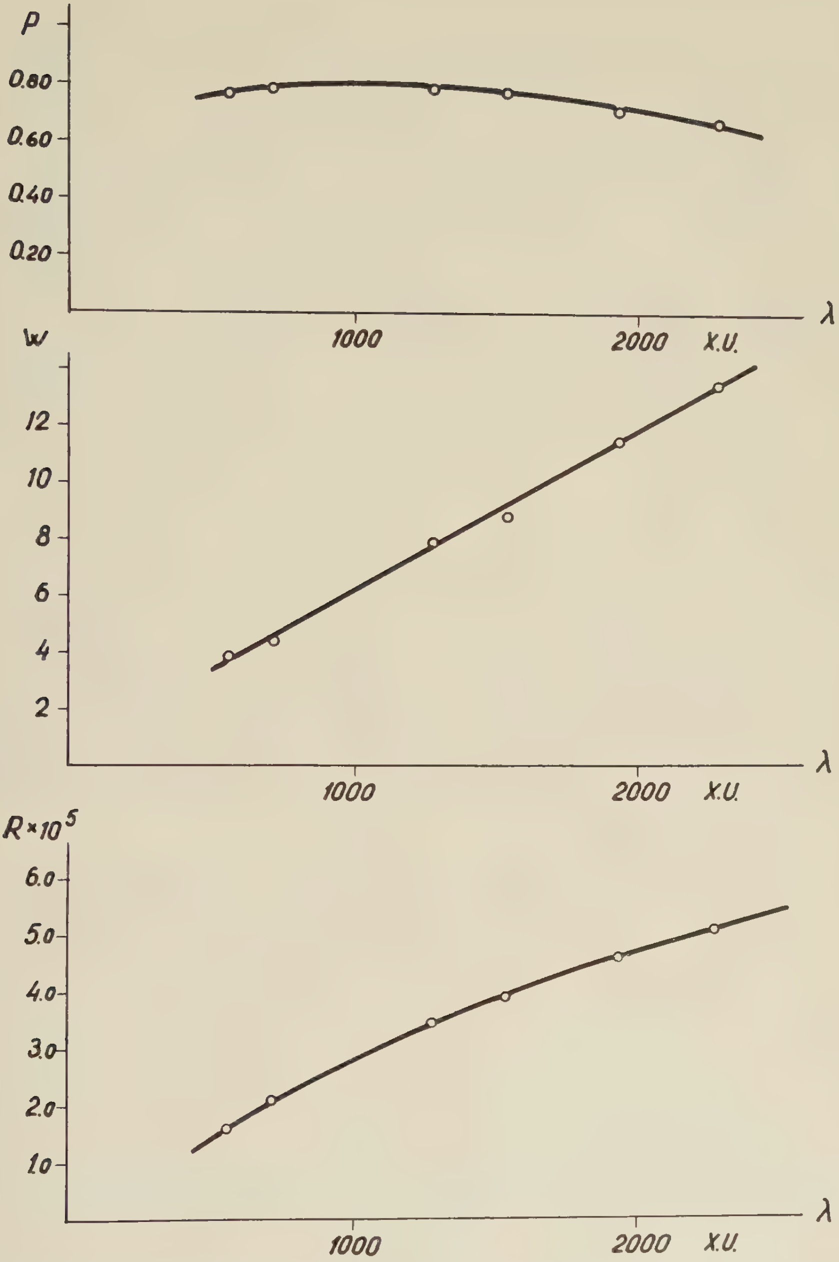

Fig. 5. The percent reflection P, the full width w of the rocking curve and the coefficient of reflection R as a function of wave-length for plane $(10\bar{1}1)$.

Table 9. The reflecting properties of calcite 211 after ALLISON (14), PARRATT (4) and PARATT-MILLER (5).

Line	Wave-length X.U.	Glancing angle ϑ	w sec. of arc.			$P \cdot 10^2$			$R \cdot 10^5$ radians			$\lambda/d\lambda$	
			A	A	P–M	A	P_1	P–M	ALLISON	P_1	P–M	ALLISON	PARRATT
W Kα_1	209	1°59′	4.6			35			1.17			3 100	
Ag Kα_1	558	5°18′	4.4			59			1.53			8 700	
Mo Kα_1	708	6°43′	5.2		5.2	63		66	1.86		2.40	9 300	9 300
Ir Lβ_1	1155	11° 0′	8.3			64			2.95			9 800	
Cu Kα_1	1537	14°42′	9.8	10.0	10.0	62	61	65	3.46	3.80	3.90	11 000	10 800
Fe Kα_1	1932	18°36′	12.9			58			4.18			11 100	
Cr Kα	2285	22°10′	14.2			55			4.68			11 800	
U M	2299	22°12′		15.0			51			4.81			11 200

must be considered very good, especially if we take into consideration the uncertainty in many of the constants that must be used in the calculations. This is a further proof that quartz is very nearly a perfect crystal. It is worthy of note that the agreement between theory and experiment is better than is obtained with calcite, which indicates that good specimens of quartz reflect more nearly in accordance with the dynamical theory than those of calcite. It would be very interesting to extend the investigations above 4600 X.U. With plane $10\bar{1}0$ it is possible to reach about 8000 X.U. when working in vacuum. As the K absorption edge of silicon occurs at 6730 X.U., such an investigation would include the very interesting region of anomalous scattering and dispersion around the K absorption edge. At the same time valuable information could be obtained about the reflecting and resolving power in the region where the crystal is extensively used in focusing X-ray spectrographs.

Plane $10\bar{1}0$ was also investigated by PARRATT (13). The reflectivities for the lines used by Parratt and here are given in Table 7. There is a considerable discrepancy between the two series of values. Paratt's values for the full width of the rocking curve are 2–3 times larger than ours, and his values for the percent reflection are very much smaller. His values for the coefficient of reflection are lower than both ours and the calculated ones with a maximum difference of about thirty per cent. The probable reason to the difference is that his quartz crystals were not perfect enough to give dynamic reflections. The calculations assume a perfect ideal crystal. If we instead consider a crystal composed of rather small crystallites, the rocking curves are broadened and the percent reflection decreases. The changes should be most pronounced at short wave-lengths. Most quartz crystals seem to give such rocking curves. In our preliminary work with plane $10\bar{1}0$, we got a full width of 8″ for Cu Kα_1. The quartz specimens, used by PARRATT, must have been of a similar type.

Earlier (6) the possible effect of thermal lattice vibrations was discussed. If the characteristic temperature of quartz is low, this would influence the atomic scattering factors so that the intensity of the diffracted radiation would decrease. This would lower the experimental values relative to the calculated ones. The amount of this discrepancy should increase with $\frac{\sin \vartheta}{\lambda}$. No such discrepancy is ob-

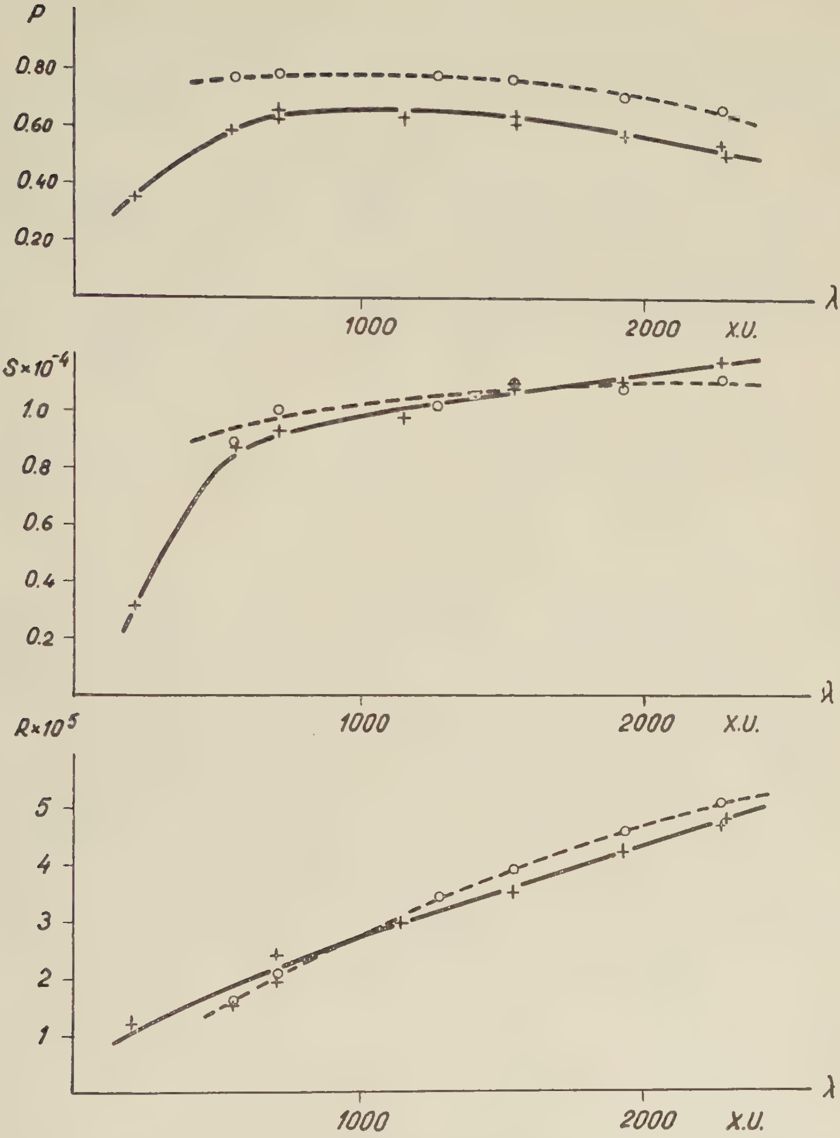

Fig. 6. A comparison between the reflectivities of calcite (211) and quartz (10$\bar{1}\bar{1}$). P is the percent reflection, R the coefficient of reflection and $S = \lambda/d\lambda$ the resolving power of the double spectrometer in position (1 + 1). Open circles indicate quartz values, crosses calcite ones.

served. Even for plane (22$\bar{4}$3), which has the smallest spacing, the experimental values are higher. Consequently the characteristic temperature is so high that no correction is necessary.

The last experiments were carried out with plane 10$\bar{1}\bar{1}$. As the comparisons for plane 11$\bar{2}$0 had been extended over a larger wave-length range than could be in-

Table 10. The reflecting properties for Cu Kα_1- and Mo Kα_1-radiation.

Radiation	Crystal	Atomic plane	Spacing X.U.	ϑ	w''	$R \cdot 10^5$ radians	$S = \frac{2 \operatorname{tg} \vartheta}{w}$
Cu Kα_1	Quartz	$10\bar{1}0$	4246.0	10°26′	5.0	1.81	$1.50 \cdot 10^4$
	»	$10\bar{1}\bar{1}$	3336.3	13°19′	8.8	3.90	$1.11 \cdot 10^4$
	»	$11\bar{2}0$	2451.4	18°16′	3.4	1.10	$4.00 \cdot 10^4$
	»	$20\bar{2}\bar{3}$	1372.0	34° 4′	2.0	0.69	$1.40 \cdot 10^5$
	Calcite	211	3029.5	14°42′	10.0	3.90	$1.08 \cdot 10^4$
Mo Kα_1	Quartz	$10\bar{1}0$	4246.0	4°47′	2.7	1.04	$1.25 \cdot 10^4$
	»	$10\bar{1}\bar{1}$	3336.3	6° 6′	4.5	2.11	$0.98 \cdot 10^4$
	»	$11\bar{2}0$	2451.4	8°18′	2.3	0.58	$2.61 \cdot 10^4$
	»	$20\bar{2}\bar{3}$	1372.0	14°57′	1.0	0.37	$1.10 \cdot 10^5$
	»	$22\bar{4}\bar{3}$	1012.8	20°27′	0.7	0.23	$2.20 \cdot 10^5$
	Calcite	211	3029.5	6 43′	5.2	2.31	$0.89 \cdot 10^4$
	»	310	1522.3	13°27′	1.5	0.47	$6.56 \cdot 10^4$
	»	655	1033.1	20° 2′	1.0	0.33	$1.51 \cdot 10^5$

vestigated with our double spectrometer and as the results there verified the assumption that quartz is a perfect crystal, only a rough calculation of the coefficient of reflection for the Mo Kα_1 and Cu Kα_1 lines was made for plane ($10\bar{1}\bar{1}$). This calculated value agreed satisfactorily with the experimental results, indicating that the crystal specimens could be considered perfect as regards this plane too. The spacing of the plane is 3336.3 X.U., which is somewhat larger than that of calcite 211 ($d_{211} = 3029.5$ X.U.). The structure factor is higher than for any other plane in quartz and the reflection power should be about the same as for calcite 211. Table 8 gives the values of the reflectivities of quartz $10\bar{1}\bar{1}$, Table 9 those of calcite 211. A comparison between these shows that the coefficient of reflection is nearly the same, but the rocking curves are narrower in the quartz case, which compensates for the larger spacing, so that the resolving power is nearly the same. At short wave-lengths the resolving power decreases more rapidly for calcite. The percent reflection is always higher for the quartz plane, which is due to its smaller absorption coefficient and probably to a more perfect structure as well. The latter point is borne out by the fact that the decrease in percent reflection at short wave-lengths – where the absorption is small and the decrease due to deviations from the perfect crystal structure – is larger in the calcite case. The reflectivities for plane $10\bar{1}\bar{1}$ are thus as good as or superior to those of calcite in the wave-length region investigated. This is probably also true for longer wave-lengths, where this plane is especially suitable. Plane $10\bar{1}\bar{1}$ can replace calcite 211 even in the double spectrometer without loss in intensity or resolving power. In focusing spectrometers it is much superior, owing to its excellent elastic properties. It is very surprising that, as far as we know, this plane has not been used outside this laboratory.

The values of the reflectivities for the Cu Kα_1 and Mo Kα_1 lines for our quartz planes are given in Table 10. It should be pointed out that the resolving power is very high in some cases, but the corresponding coefficient of reflection is lower. In many cases it is necessary to work with first order reflections and use planes with small spacings. As is to be seen, there are several suitable planes that may be used. Some of them will give more intense reflection than the most intensely reflecting calcite planes with the same spacings. Besides $10\bar{1}\bar{1}$, this is the case with planes $(20\bar{2}\bar{3})$ and $(30\bar{3}\bar{1})$, which both have a spacing of 1 370 X.U. and a structure factor of nearly 30, and with plane $50\bar{5}2$ (spacing 810 X.U.). Several other planes can be used. Some offer the advantage that the structure factors of higher orders are small, compared with the first order ones. This makes it possible to work with X-ray tube voltages far in excess of the double threshold voltage.

A comparison between calcite and quartz data shows that quartz seems to be the more perfect crystal as the experimental data are in better conformity with the theoretical predictions. The characteristic temperature of quartz seems to be so high that the effect of thermal vibrations on the diffraction can be neglected. Furthermore, its hardness and inertness to chemical reagents renders a quartz crystal very durable and constant in its diffraction properties. This is all evidence that the more intensely reflecting quartz planes can be used more extensively in X-ray spectroscopy than they customarily are.

The investigation received financial support from the Swedish Natural Science Research Council, which is gratefully acknowledged.

Institute of Physics, University of Uppsala, Sweden, March 1953.

REFERENCES

1. C. G. Darwin, Phil. Mag. *27*, 325 and 675, 1914.
2. J. A. Prins, Zs. f. Phys. *63*, 477, 1930.
3. S. K. Allison, Phys. Rev. *41*, 1, 1932.
4. L. G. Parratt, Phys. Rev. 41, 561, 1932.
5. L. G. Parratt, and F. Miller jr., Phys. Rev. *49*, 280, 1936.
6. G. Brogren, Arkiv för Fysik *6*, 321, 1953.
7. R. W. James and G. W. Brindley, Phil. Mag. *12*, 81, 1931.
8. E. Jönsson, Dissertation. Uppsala 1928.
9. G. Brogren, Arkiv för Fysik *3*, 507, 1951.
10. L. G. Parratt, Rev. Sci. Instr. *5*, 395, 1934.
11. H. Hönl, Zs. f. Phys. *84*, 1, 1933.
12. —— Ann. der Phys *18*, 625, 1933.
13. L. G. Parratt, Rev. Sci. Instr. *6*, 113, 1935.
14. S. K. Allison, Phys. Rev. *41*, 13 and 688, 1932.

Tryckt den 29 oktober 1953

Uppsala 1953. Almqvist & Wiksells Boktryckeri AB

ARKIV FÖR FYSIK Band 7 nr 20

Communicated 3 June 1953 by E. HULTHÉN and G. BORELIUS

Studies of the heterocharges of electrets

By S. WIKSTRÖM

With 5 figures in the text

1. Introduction

Electret is the name given by FARADAY to a permanently polarized dielectric body. This body has a resulting dipole moment and shows electric charges of opposite polarity on two of its sides. The first person to make an electret was EGUCHI (1), who let a molten mixture of carnauba wax and rosin solidify in the shape of a disc under the influence of an electric d.c. field. EGUCHI found that immediately after the removal of the electrodes the surfaces of the disc carried charges of opposite sign to those of the adjacent electrodes. Following GEMANT's (2) terminology these charges are called heterocharges, while charges with the same sign as the adjacent electrodes are called homocharges.

EGUCHI found further that the heterocharges under certain circumstances might decrease to zero during the first days after the short-circuit and that a homocharge was then built up which showed no decrease in five years provided that the disc was kept short-circuited. EGUCHI's results have been verified by GEMANT (2), THIESSEN (3), GROSS (4) (5) (6), BINDER (7) and the author himself among others. A resumé of the most important papers on the subject is given by GUTMAN (8).

Thanks, in the first place to the works of GROSS the veil of mysticism over this subject has been lifted and the fundamental properties of electrets have been made known. Thus a coexistence of heterocharge and homocharge has been established, the former being due to ionic space charges and dipole orientation and the latter to breakdown discharges in the interface between the electrode and the dielectric surface. Further, homocharges can only appear when the polarizing field has reached a certain threshold value of the field strength, which is approximately 10 kV/cm (3). A recombination between the two types of charges is not possible and, since neither of them sets up an electric field within the dielectric when the latter is short-circuited, they can be kept constant for very long times. Thus the half life for the heterocharge is in the order of hundreds of thousands of years (5). The customary method of estimating the properties of an electret is to measure the surface charge density by an electro-phorus method. GROSS (6) and BINDER (7) have measured simultaneously the surface charge and the current in the charging (or discharging) circuit and have hereby shown that a breakdown occurs in the interface between the electrode and the dielectric. As these authors have made their measurements below the melting point of the material used, their current–time curves are continuous and show the amount of electricity that is stored up in the electret. Studies of the liberation of electricity on reheating of electrets have been made by FREI and GROETZINGER (9), but, as they heated the electret above the melting point, they could only regain a rather small part of the "frozen in" charge. This agrees with the experience of the author.

The present paper deals only with the heterocharge, and in order to evaluate this the author has reheated the electrets and measured the liberated amount of electricity $\int i\,d\tau$ instead of measuring the surface charge density. The measurement of $\int i\,d\tau$ takes a comparatively long time, but the result shows the size of the heterocharge better than a measurement of the surface charge density will do, the latter being dependent on the breakdown field strength of the surrounding air.

First, a study has been made of the relation between charging and discharging rate, temperature and "frozen in" charge, and in connection with this the ratio between the ionic and the dipole part of the heterocharge has been estimated. It has also been investigated how an electric d.c. field at room temperature will affect an already prepared electret, and how the presence of an increased pressure will affect the charging and discharging of an electret. Finally consideration has been given to the question of how the capacitance and loss angle $\mathrm{tg}\,\delta$ vary with frequency when the electret is polarized and unpolarized.

2. Experimental technique

The electrets used in this investigation are made of a mixture of 80% light yellow carnauba wax and 20% beeswax in the shape of discs with a diameter of 65 mm and a thickness of 1.2 mm. The mixture, which has a softening point of about 72° C, is poured into a bowl of diameter about 100 mm and depth about 30 mm to solidify. After solidification the piece of wax is set up in a lathe and the desired disc turned with the utmost accuracy. After cautious polishing, both sides are silvered chemically.

Polarization and depolarization of the electrets was always done in the same container and without touching the electret between a polarization and the following depolarization. The container has a cover in which highly insulated ceramic bushings for the electret terminals are mounted. Inside the container one of these terminals is shaped as a horizontal supporting electrode for the electret, while the other rests with a light spring pressure against the upper side of the electret. At the bottom of the container a drying agent is placed. A high precision thermometer is mounted in a rubber stopcock passing through a hole in the cover of the container. The container is put into an oil bath which is heated by an electric element, and circulation in the oil bath is accomplished by means of an electrically driven propeller. The temperature is regulated by a contact thermometer, and the cooling of the bath is done with a watercooled copper-tube coil.

Polarization of a disc was arranged in the following way. The disc was placed in the container and short-circuited, after which the system was heated to the polarization temperature. When the temperature had remained constant for at least 1 hour, the short-circuit was broken and the polarizing voltage connected during the predetermined polarizing period. With the polarizing voltage still connected, the system was then cooled down to 20° C, after which the polarizing voltage was broken and the disc short-circuited.

The polarizing voltage was taken from a rectifier with a highly effective filter and was measured with a Simpson Universal Instrument. As the purpose of the experiments was to study the heterocharge, the polarizing voltage chosen was 500 volts, which is sufficiently high to get a strong heterocharge with the discs used, but also low enough to avoid the forming of homocharges (3) (6) (7). The polarization temperature has in many cases been 65° C and the polarization period 2 hours. This time is sufficiently long for the electret to become fully charged at 65° C (6). The cooling period was of the same length in all experiments (40 minutes). The time was measured with a normal chronometer giving an accuracy of 0.1 second.

During depolarization the electret was connected to a circuit, which is indicated in Fig. 1, where R is a special Welwyn resistor with the resistance 1.3×10^{10} ohms and S is a string electrometer with a voltage range from 15 V down to 0.05 V, the deflection of which was studied through a microscope. E is the electret. The discharge current is consequently determined by measuring the voltage over a high-ohmic discharge resistor. The reheating rate during depolarization was the same in all experiments.

When not used for experiments the electrets were always kept over a drying agent in a desiccator.

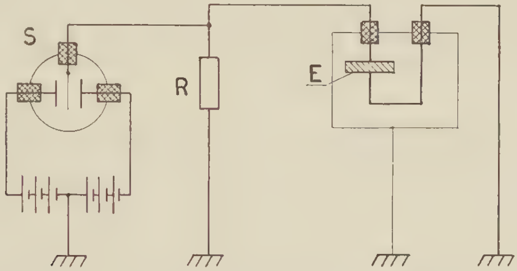

Fig. 1. Circuit when measuring the discharge current while reheating. S is an astaticized string electrometer, E the electret, and R a highohmic resistor with the resistance 1.3×10^{10} ohms.

3. Results

3.1. *Study of the charging and discharging rate.* It is of interest to find out how the obtainable degree of polarization varies with the polarizing temperature. Consequently experiments have been conducted with constant polarization time (2 hours) and constant voltage (500 V) but at different temperatures, these being 30°, 40°, 50°, 55°, 60°, and 65° C. The cooling period was 40 minutes in each experiment, and the same reheating rate during depolarization and end temperature (65° C) were applied throughout. Two series of experiments were made, one in which the disc was depolarized after 48 hours' short-circuit, and one in which it was depolarized immediately after cooling to 20° C. In Fig. 2 the discharge currents during depolarization are shown for the first series. The curves for the second series are similar, but differ from those in Fig. 2 in so far that an initial discharge current is flowing at time 0 ($t = 25°$ C). The liberated amount of electricity has been determined through integrating the surfaces under the curves in Fig. 2 up to 60 000 seconds, after which the current was zero within the limit of experimental errors ($< 0.01 \cdot 10^{-10}$ A). This integration has been made for both series and the result is plotted as curves in Fig. 3. It is apparent from these curves that the degree of polarization that can be obtained with a constant field during a given time is highly

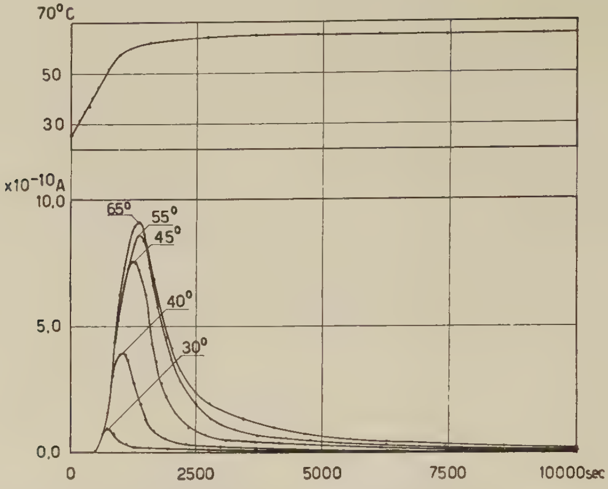

Fig. 2. Discharge current curves for a disc polarized with 500 volts for 2 h at the temperatures: 30° C, 40° C, 50° C, 55° C and 65° C. Reheating rate the same in each case and shown at top of diagram.

dependent on the temperature during polarization. This is also expressed by GROSS (5) (6), who has suggested that the charging and discharging rates are very much dependent on temperature, and that the discharge current is solely dependent on temperature.

In addition to the curves shown in Fig. 3 ln Q has been drawn against $1/T$, the points then being found to lie on a straight line up to 60° C. Consequently the growth of the heterocharge with temperature follows a law of the well-known type $Q = Q_0 \cdot e^{-\frac{W}{RT}}$ and the energy of activation has been calculated as $W \approx 16\,000$ cal/mol from the slope of this straight line.

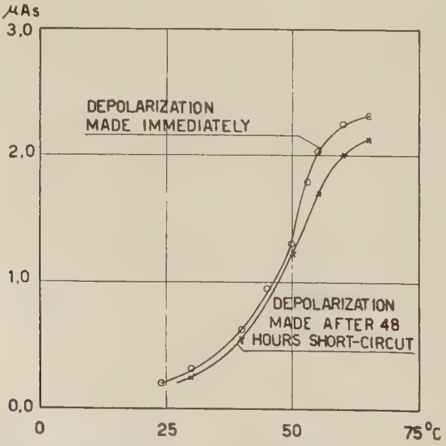

Fig. 3. The regained amount of electricity as a function of polarization temperature when polarizing for 2 h with 500 volts. End temperature at depolarization 65° C in each case.

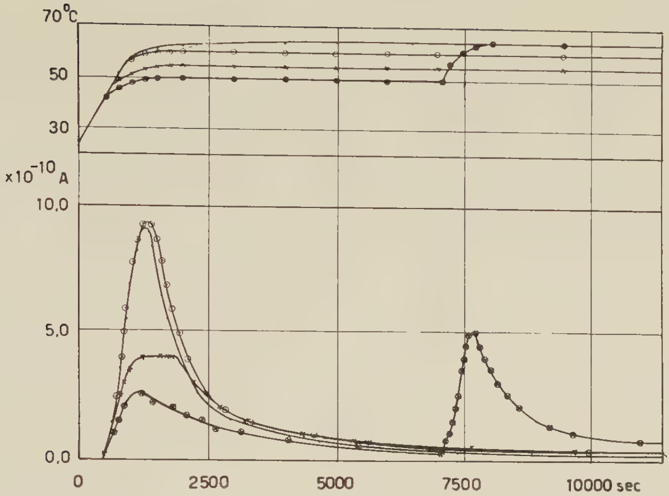

Fig. 4. Discharge current curves for different depolarization temperatures. Polarization the same in each case; 500 V, 2 h, 65° C. Corresponding temperatures shown at top of diagram.

There is a noticeable difference between the two curves in Fig. 3 which shows that a certain quantity of the polarization disappears during the first 48 hours' short-circuit and that this quantity tends to be greater at higher temperatures. This quantity is most probably due to the displacement of ions within the disc (3) (5) and has, according to Fig. 3, a value of about 0.19 μAs when the disc is polarized at 65° C.

From the curves in Fig. 2 it is evident that, as long as the residual polarization is comparatively great, the current is independent of the residual polarization and greatly dependent on the temperature, but when a sufficient discharge has occurred the current becomes dependent on both temperature and residual polarization. Further, the current passes its maximum when the temperature is around 61° C and a rather long time before the end temperature 65° C is reached. This indicates that the maximum discharge rate probably lies in the neighbourhood of 61° C.

In order to confirm this, the disc was polarized in the ordinary way (65° C; 2 hours; 500 V), and after 48 hours' short-circuit at 20° C was depolarized with the end temperature 61° C. After this, two further experiments were made with end temperatures during depolarization of 55° C and 50° C respectively. The corresponding discharge currents are shown in Fig. 4.

It can be seen there that the discharge is more rapid at 61° C than at 65° C. From the curve it can be calculated that the amount of electricity dischargeable during the first 10 000 seconds at 61° C is 1.72 μAs. For a discharge at 65° C the corresponding figure is 1.47 μAs. When the time of measurement was prolonged, it was noted that the discharge current fell to zero ($<0.01 \cdot 10^{-10}$ A) after a total depolarization time of approx. 30 000 seconds in the first case and approx. 60 000 seconds in the second case. The value of the totally discharged amount of electricity is 2.12 μAs in each case.

It is also noticeable from the curves in Fig. 4 that the discharge rate is much lower at 55° C than at 61° C, and that at 50° C it is so low that after a comparatively

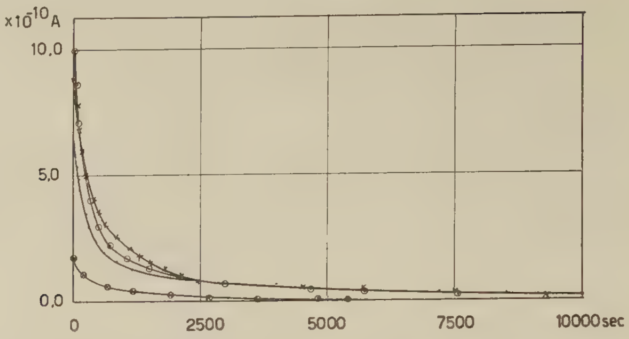

Fig. 5. Discharge current curves for the same disc polarized with 500 volts for 2 h at different temperatures and then immediately depolarized at the same temperature.

× Polarization and depolarization temperature 55° C
⊙ » » » » 61° C
· » » » » 65° C
⊗ » » » » 69.8° C

small discharge the current decreases and almost falls to zero. When the temperature is increased from 50° C to 65° C, a second discharge follows which is stronger than the first one. It is also interesting that i seems to be dependent on $\frac{dT}{d\tau}$. Comparing the values at $\tau = 600$ sec in Fig. 4, the temperature and the residual polarization are almost the same for the four curves. The current, however, as also $\frac{dT}{d\tau}$, is apparently smaller on the "50° C-curve", in spite of the fact that not more than one per cent of the total charge has been liberated. Further, the current maxima for all curves occur when $\frac{dT}{d\tau}$ approaches zero. This applies likewise to the "50° C-curve", where the electret has more than 90 per cent of its charge left when the current passes its maximum. In other words, the curves indicate that the current follows a law of the type $i = f\left(Q,\ T,\ \frac{dT}{d\tau}\right)$. This result may be used as basis for further investigations.

The interesting circumstance, described above, that the discharge rate is dependent on the temperature, has been further confirmed in another way. The disc was heated to a certain temperature, 55° C, 61° C, 65° C, and 69.8° C, at which it was polarized for two hours with 500 V. Immediately after this, depolarisation was started. Fig. 5 shows the discharge current for the four selected temperatures. It is apparent that the discharge current and the total regained amount of electricity is smaller, when the experiment is carried out at 65° C and 69.8° C than when it is carried out at the lower temperatures. The total regained heterocharge has been determined as 1.01 μAs at 55° C, 1.02 μAs at 61° C, 0.87 μAs at 65° C and 0.21 μAs at 69.8° C. The last value is of the same magnitude as the earlier determined ionic charge. These values are much smaller than those obtained when the usual treatment is employed, and indicate that the molecular mechanism, during the cooling in the field, is not fully explained.

3.2. *Effect of a d.c. field on an already prepared electret.* A series of experiments was made in the container mentioned in paragraph 2 as follows.

The disc was polarized at 65° C with 500 V for 2 hours, after which it was cooled to 20° C with the field remaining. The cooling period was 40 min. in each experiment. Immediately after cooling the electret was exposed to a second d.c. field, of opposite or same direction as the polarizing field, for a period of 24 hours and at a temperature of 21° C, after which it was depolarized. This second field had a voltage of 500 V or 1000 V. After this the same disc was completely depolarized and then repolarized at 21° C for 24 hours with 500 V or 1000 V, whereupon depolarization followed immediately. It was also polarized and then depolarized in the same way after a short-circuit period of 18.5 hours. Finally the disc was polarized in the normal way, i.e. 500 V, 65° C, 2 hours, and was then exposed to a second d.c. field of opposite direction to the polarizing field for 24 hours at 21° C and with the voltages 500 V or 1000 V .Depolarization was started after a short-circuit period of 18.5 hours in both cases.

The discharge current curves corresponding to the above described experiments indicate that polarization at 65° C and 21° C can be superposed, so that a current reversal can occur during depolarization. A part of the polarization obtained at 65° C will recombine with the polarization obtained at 21° C, if the disc is kept short-circuited 18.5 hours before depolarizing. By comparing the surfaces under the curves, the less permanent part of the heterocharge can be calculated to lie between 0.14–0.29 μAs, which is in agreement with the result in 3.1.

3.3. *Search for an effect of increased pressure on the charging and discharging of an electret.* These experiments have been carried out in a container of the same type as described in paragraph 2, but capable of withstanding pressures up to 20 atm.

It has been suggested by GEMANT (2) that electrets can to some extent be characterized as piezoelectric and thus be affected by pressure. In order to test this, two series of rather laborious experiments were made. First the disc was polarized and depolarized at atmospheric pressure, then it was polarized at 5.0 atm and depolarized at atmospheric pressure, and finally it was polarized and depolarized at 5.0 atm. Polarization data were 500 V at 65° C for 2 hours. The discharge was measured up to 60 000 seconds after which the current was zero within the limits of experimental errors. A difference between the results from the three experiments could be found neither in $\int i\,d\tau$ nor in the shape of the current time curves. This series was repeated once with the same result.

Another series of experiments was made to find out whether an increased pressure can influence the degree of polarization. For this purpose the disc was polarized for 2 hours at 65° C. Then the pressure was increased, the polarizing voltage broken, the disc short-circuited, and cooling commenced. The disc was left short-circuited for 24 hours before being depolarized. Experiments were made when cooling at atmospheric pressure and at the pressures 2.5, 5.0, 10.0, and 15.0 atm. In these experiments, too, the discharge was measured up to 60 000 seconds. The result of this series of experiments was that $\int i\,d\tau$ was about one fifth of the magnitude obtained in the former series, and also that $\int i\,d\tau$ was independent of the magnitude of pressure during cooling. Also this series was recapitulated once with the same result.

3.4. *Effect of polarization on capacitance and* $tg\,\partial$. Capacitance and $tg\,\partial$ versus frequency were measured at 21° C for a non-polarized wax disc as described in paragraph 2 with a Q-meter from Boonton Radio Corporation, after which the disc was polarized for two hours with 500 V at a temperature of 65° C, then cooled to 20° C with the field remaining. Immediately after this treatment the capacitance and $\operatorname{tg}\partial$ versus frequency were measured again, and the values obtained indicate that the capacitance is unaffected by polarization but that $\operatorname{tg}\partial$ will increase slightly after the disc has been polarized. The measurements were made from 0.1 to 20.0 Mp/sec with intervals of 0.1 Mp/sec. The reproducibility of the effect was checked by repeated experiments.

It is interesting to note that this result agrees with those obtained by SHEPARD ROBERTS (10) with ferro-electrics. Thus ROBERTS found that the remanent polarization in $BaTiO_3$ will cause an increase in $\operatorname{tg}\partial$. Moreover he found special resonance frequencies, where $\operatorname{tg}\partial$ will increase to several times its normal value, if the dielectric was subjected to a d.c. field during the measurement. No corresponding effect appears with the type of heterocharged electrets studied here.

SUMMARY

Heterocharged electrets of carnauba wax have been studied from the following points of view: The dependence of the charging and discharging rate on temperature. Influence of a d.c. field at room temperature on a prepared electret. Influence of pressure during charging and discharging. Influence of polarization on the a.c. capacitance and loss angle.

Finally the author wishes to express his thanks to Professor G. BORELIUS and Doc. J. O. LINDE at the Royal Institute of Technology at Stockholm for stimulating discussions and helpful suggestions, and also to the Rifa Company which has given him free use of their laboratories and special materials for the experiments.

REFERENCES

1. M. EGUCHI, Phil. Mag. *49* (1925) 178.
2. A. GEMANT, Phil. Mag. *20* (1935) 929.
3. P. A. THIESSEN, A. WINKEL, K. HERRMAN, Phys. ZS *37* (1936) 511.
4. B. GROSS, Phys. Rev. *66* (1944) 26.
5. B. GROSS, F. DENARD, Phys. Rev. *67* (1945) 253.
6. B. GROSS, Journ. Chem. Phys. *17* (1948) 866.
7. F. BINDER, ZS Naturforsch. *6a* (1951) 714.
8. F. GUTMAN, (42 ref.) Rev. mod. Phys. *20* (1948) 457.
9. H. FREI, G. GROETZINGER, Phys. ZS *37* (1930) 720.
10. SHEPARD ROBERTS, Mass. Inst. of Technology (1946).

Tryckt den 30 november 1953

Uppsala 1953. Almqvist & Wiksells Boktryckeri AB

ARKIV FÖR FYSIK Band 7 nr 21

Communicated 8 April 1953 by OSKAR KLEIN and IVAR WALLER

On regularization by means of analytic continuation

By ERIK KARLSON

With 1 figure in the text

Summary. A modified form of the method of regularization with the aid of analytic continuation suggested by KÄLLÉN can also be applied to the e^4-approximation of the vacuum polarization. The result is that only gauge invariant terms will appear. All computations are carried out on convergent expressions.

I. Introduction

It is a well-known fact that the direct computation of the vacuum expectation value of the current operator in an external electromagnetic field by expansion of the operators in powers of the coupling constant and the external field gives rise, not only to a gauge invariant part, which after mass- and charge-renormalization contains only finite, observable terms, but also to terms, which are not gauge invariant. As has been pointed out by several authors[1] these latter terms will vanish in the e^2-approximation if the expressions are made finite by means of a suitable regularization procedure. It might be of interest to investigate if such a regularization would have the same effect on the e^4-approximation, especially as the e^4-approximation of the charge-renormalization has been calculated under the assumption that the terms, which are not gauge invariant can be made to vanish by regularization.[2]

To enable us to state our invariant regularization procedure we introduce the momentum space kernel $K_{\lambda\nu}(q)$ to the vacuum expectation value of the current operator in a very weak external field by the equations:

$$\langle 0 \,|\, j_\lambda(x) \,|\, 0 \rangle = \int dx' \cdot A_\nu^{\mathrm{ext}}(x')\, K_{\lambda\nu}(x-x') \tag{1}$$

$$K_{\lambda\nu}(x) = \frac{1}{(2\pi)^4} \int dq \cdot e^{iqx}\, K_{\lambda\nu}(q). \tag{2}$$

---

[1] W. PAULI–F. VILLARS, Rev. Mod. Phys. *21*, 434 (1949). Cf. also R. P. FEYNMAN, Phys. Rev. *74*, 1439 (1948). E. C. G. STUECKELBERG–D. RIVIER, Phys. Rev. *74*, 218 (1948). J. SCHWINGER, Phys. Rev. *76*, 790 (1949).

[2] R. JOST–J. M. LUTTINGER, Helv. Phys. Acta *23*, 201 (1950).

By reason of invariance we have

$$K_{\lambda\nu}(q)=(q_\lambda q_\nu-\delta_{\lambda\nu}q^2)\cdot A(q^2)+\delta_{\lambda\nu}B(q^2). \tag{3}$$

If our result is to be gauge invariant, we must have $B(q^2)=0$, but a direct computation leads to an indeterminate expression for $B(q^2)$, which must therefore be defined by a regularization procedure. For the invariant regularization we use a modification of the analytic continuation method suggested by KÄLLÉN.[1] In modified form the procedure can be stated as follows: The regularized momentum space kernel $K^{\text{reg}}_{\lambda\nu}(q)$ is defined as

$$K^{\text{reg}}_{\lambda\nu}(q)=\underset{\substack{n_1\to 0\\ n_2\to 0}}{\text{cont}}\,\frac{\partial^{n_1}}{\partial(m^2)^{n_1}}\,\frac{\partial^{n_2}}{\partial(\mu^2)^{n_2}}K_{\lambda\nu}(q) \tag{4}$$

where μ is the photon mass, introduced to avoid infrared divergencies. The analytic function is to be understood e.g. in the sense of a Riemann-Liouville integral.[2]

It will be shown later, that for n_1 and n_2 sufficiently large, all the integrals in the e^2- and e^4-approximations become convergent and well-defined.

It is convenient to compute not $K_{\lambda\nu}(q)$ itself but the following two expressions:

$$i\,q_\lambda K_{\lambda\nu}(q)=i\,q_\nu B(q^2) \tag{5}$$

and

$$K_{\nu\nu}(q)=-3\,q^2A(q^2)+4\,B(q^2). \tag{6}$$

These two expressions give us $A(q^2)$ and $B(q^2)$, and hence $K_{\lambda\nu}(q)$.

II. Regularization in the e^2-approximation

If we restrict ourselves to the case, where no real processes can take place, we get in the e^2-approximation (see the papers by KÄLLÉN[3] for notations and the general expression for the current operator):

$$K^{(2)}_{\lambda\nu}(q)=-\frac{1}{2}\,\frac{1}{(2\pi)^3}\int d\,p\cdot Sp\,[\gamma_\lambda(i\gamma(p+q)-m)\gamma_\nu(i\gamma p-m)]\cdot \\ \cdot\left\{\frac{\delta(p^2+m^2)}{(p+q)^2+m^2}+\frac{\delta((p+q)^2+m^2)}{p^2+m^2}\right\}. \tag{7}$$

---

[1] G. KÄLLÉN, Arkiv för fysik *5*, 131 (1952).

[2] The method of analytic continuation for solving wave equations was first introduced by RIESZ, and applied by him and FREMBERG to problems of classical physics. Quantum mechanical applications have been given by GUSTAFSON, NILSSON, and others. *Cf.* e.g. M. RIESZ, Conf. à la Réunion internat. des Math. Paris 1937, 153 (1938). M. RIESZ, Acta Math. *81*, 1 (1949). N. E. FREMBERG, Proc. Roy. Soc. *188*, 18 (1946). N. E. FREMBERG, Medd. Lunds Univ. Mat. Sem. *7*, 1 (1946). T. GUSTAFSON, Arkiv Mat. Astr. Fys. 34 A, No 2, 1 (1946). S. B. NILSSON, Arkiv för fysik *1*, 369 (1949).

[3] G. KÄLLÉN, Arkiv för fysik *2*, 187, 371 (1950), hereafter referred to as K I, K II, respectively.

From (5), (7) and the relation $i\gamma q = i\gamma(p+q) + m - (i\gamma p + m)$ we get

$$i q_\nu B^{(2)}(q^2) = \frac{1}{2}\frac{1}{(2\pi)^3}\int dp\cdot Sp\,[\gamma_\nu(i\gamma p - m)]\cdot\delta(p^2+m^2) - \\ - \frac{1}{2}\frac{1}{(2\pi)^3}\int dp\cdot Sp\,[(i\gamma(p+q)-m)\gamma_\nu]\cdot\delta((p+q)^2+m^2)$$

or

$$i q_\nu B^{(2)}(q^2) = \frac{2i}{(2\pi)^3}\int dp\cdot p_\nu\cdot\delta(p^2+m^2) - \frac{2i}{(2\pi)^3}\int dp\,(p+q)_\nu\cdot\delta((p+q)^2+m^2). \tag{8}$$

As this expression does not involve μ^2, we regularize it by differentiating n_1 times with respect to m^2.

$$\frac{\partial^{n_1}}{\partial(m^2)^{n_1}} i q_\nu B^{(2)}(q^2) = \frac{2i}{(2\pi)^3}\int dp\cdot p_\nu\cdot\delta^{(n_1)}(p^2+m^2) - \\ - \frac{2i}{(2\pi)^3}\int dp\,(p+q)_\nu\cdot\delta^{(n_1)}((p+q)^2+m^2). \tag{9}$$

For $n_1 \geqq 2$ these integrals are convergent, and by reason of symmetry they are both equal to zero. Thus

$$B^{(2)\,\mathrm{reg}}(q^2) = 0. \tag{10}$$

By taking the trace of (7) we get

$$K^{(2)}_{\nu\nu}(q) = -\frac{1}{2}\frac{1}{(2\pi)^3}\int dp\cdot Sp\,[\gamma_\nu(i\gamma(p+q)-m)\gamma_\nu(i\gamma p - m)]\cdot \\ \cdot\left\{\frac{\delta(p^2+m^2)}{(p+q)^2+m^2} + \frac{\delta((p+q)^2+m^2)}{p^2+m^2}\right\}. \tag{11}$$

We use the formula given by SCHWINGER[1]

$$\frac{\delta(p^2+m^2)}{(p+q)^2+m^2} + \frac{\delta((p+q)^2+m^2)}{p^2+m^2} = -\int_0^1 d\alpha\cdot\delta'(p^2+2(pq)\alpha+q^2\alpha+m^2) \tag{12}$$

and evaluate the trace

$$Sp\,[\gamma_\nu(i\gamma(p+q)-m)\gamma_\nu(i\gamma p - m)] = 8\,[(p(p+q)) + 2m^2]. \tag{13}$$

Thus

$$K^{(2)}_{\nu\nu}(q) = \frac{4}{(2\pi)^3}\int_0^1 d\alpha\int dp\cdot[(p(p+q)) + 2m^2]\cdot\delta'(p^2+2(pq)\alpha+q^2\alpha+m^2). \tag{14}$$

---

[1] J. SCHWINGER, op. cit.

By regularization we get

$$\frac{\partial^{n_1}}{\partial (m^2)^{n_1}} K_{\nu\nu}^{(2)}(q) =$$

$$= \frac{4}{(2\pi)^3}\int_0^1 d\alpha \int dp\,[(p\,(p+q)) + 2\,m^2]\cdot\delta^{(n_1+1)}(p^2 + 2\,(pq)\,\alpha + q^2\alpha + m^2) +$$

$$+ \frac{8\,n_1}{(2\pi)^3}\int_0^1 d\alpha \int dp\cdot\delta^{(n_1)}(p^2 + 2\,(pq)\,\alpha + q^2\alpha + m^2). \tag{15}$$

For $n_1 \geqq 2$, the integrals are both convergent. If we now put $p = p' - \alpha q$ we obtain

$$\frac{\partial^{n_1}}{\partial (m^2)^{n_1}} K_{\nu\nu}^{(2)}(q) =$$

$$= \frac{4}{(2\pi)^3}\int_0^1 d\alpha \int dp'\,[p'^2 + (1-2\alpha)\,(p'q) - \alpha\,(1-\alpha)\,q^2 + 2\,m^2]\cdot$$

$$\cdot\,\delta^{(n_1+1)}(p'^2 + q^2\alpha\,(1-\alpha) + m^2) +$$

$$+ \frac{8\,n_1}{(2\pi)^3}\int_0^1 d\alpha \int dp'\cdot\delta^{(n_1)}(p'^2 + q^2\alpha\,(1-\alpha) + m^2). \tag{16}$$

This can be written

$$\frac{\partial^{n_1}}{\partial (m^2)^{n_1}} K_{\nu\nu}^{(2)}(q) =$$

$$= \frac{8}{(2\pi)^3}\int_0^1 d\alpha \int dp'\,[\tfrac{1}{2}\,p'^2 + q^2\alpha\,(1-\alpha) + m^2]\cdot\delta^{(n_1+1)}(p'^2 + q^2\alpha\,(1-\alpha) + m^2) +$$

$$+ \frac{8\,n_1}{(2\pi)^3}\int_0^1 d\alpha \int dp'\cdot\delta^{(n_1)}(p'^2 + q^2\alpha\,(1-\alpha) + m^2) +$$

$$+ \frac{4}{(2\pi)^3}\int_0^1 d\alpha\,(1-2\alpha)\int dp'\,(p'q)\cdot\delta^{(n_1+1)}(p'^2 + q^2\alpha\,(1-\alpha) + m^2) +$$

$$+ \frac{12}{(2\pi)^3}\int_0^1 d\alpha\cdot\alpha\,(1-\alpha)\,q^2\int dp'\cdot\delta^{(n_1+1)}(p'^2 + q^2\alpha\,(1-\alpha) + m^2). \tag{17}$$

Here the first two integrals cancel each other exactly[1], and the third one is equal to zero by reason of symmetry.

---

[1] G. KÄLLÉN, Arkiv för fysik 5, 131 (1952).

Thus

$$\frac{\partial^{n_1}}{\partial (m^2)^{n_1}} K^{(2)}_{\nu\nu}(q) = \frac{12}{(2\pi)^3} \int_0^1 d\alpha \cdot \alpha (1-\alpha) q^2 \cdot \int d p' \cdot \delta^{(n_1+1)} (p'^2 + q^2 \alpha (1-\alpha) + m^2). \tag{18}$$

By carrying out the p'-integration we obtain

$$\frac{\partial^{n_1}}{\partial (m^2)^{n_1}} K^{(2)}_{\nu\nu}(q) = \frac{6(-1)^{n_1-1}(n_1-1)!\, q^2}{(2\pi)^2} \int_0^1 d\alpha \cdot \alpha (1-\alpha) \cdot \frac{1}{[q^2 \alpha (1-\alpha) + m^2]^{n_1}}. \tag{19}$$

From (6), (10), and (19) we get

$$\frac{\partial^{n_1}}{\partial (m^2)^{n_1}} A^{(2)}(q^2) = \frac{-2(-1)^{n_1-1}(n_1-1)!}{(2\pi)^2} \int_0^1 d\alpha \cdot \alpha (1-\alpha) \cdot \frac{1}{[q^2 \alpha (1-\alpha) + m^2]^{n_1}}. \tag{20}$$

The renormalized expression then becomes

$$\frac{\partial^{n_1}}{\partial (m^2)^{n_1}} [A(q^2) - A(0)] =$$

$$= \frac{(-2)(-1)^{n_1-1}(n_1-1)!}{(2\pi)^2} \int_0^1 d\alpha \cdot \alpha (1-\alpha) \cdot \left[\frac{1}{[q^2 \alpha (1-\alpha) + m^2]^{n_1}} - \frac{1}{(m^2)^{n_1}} \right]. \tag{21}$$

Thus we have

$$A^{\text{reg}}(q^2) - A^{\text{reg}}(0) =$$

$$= \underset{n_1 \to 0}{\text{cont}} \frac{2 \cdot e^{i n_1 \pi} \cdot \Gamma(n_1+1)}{(2\pi)^2} \int_0^1 d\alpha \cdot \frac{\alpha (1-\alpha)}{n_1} \cdot \left[\frac{1}{[q^2 \alpha (1-\alpha) + m^2]^{n_1}} - \frac{1}{(m^2)^{n_1}} \right] =$$

$$= \frac{-2}{(2\pi)^2} \int_0^1 d\alpha \cdot \alpha (1-\alpha) \cdot \log \left[1 + \frac{q^2}{m^2} \alpha (1-\alpha) \right] \tag{22}$$

and for $q^2 \ll m^2$ we get

$$A^{\text{reg}}(q^2) - A^{\text{reg}}(0) = \frac{-2}{(2\pi)^2} \int_0^1 d\alpha \cdot \alpha^2 (1-\alpha)^2 \cdot \frac{q^2}{m^2} =$$

$$= -\frac{1}{15} \frac{1}{(2\pi)^2} \frac{q^2}{m^2} \tag{23}$$

which is the well-known Uehling term.

III. Regularization in the e^4-approximation

In the e^4-approximation we get contributions from the following three Feynman diagrams (two of which are equal).

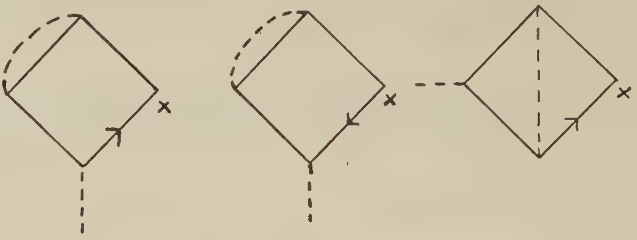

Fig. 1.

Thus

$$K_{\lambda\nu}^{(4)}(q) = 2\, U_{\lambda\nu}(q) + V_{\lambda\nu}(q) \tag{24}$$

where

$$U_{\lambda\nu}(q) = \frac{1}{4}\,\frac{1}{(2\pi)^6}\int\!\!\int d\,p_1\,d\,p_2\,\cdot$$

$$\cdot\, Sp\,[\gamma_\lambda\,(i\gamma\,(p_1+q)-m)\,\gamma_\nu\,(i\gamma\,p_1-m)\,\gamma_\sigma\,(i\gamma\,p_2-m)\,\gamma_\sigma\,(i\gamma\,p_1-m)]\times$$

$$\times\left\{\frac{\delta\,((p_1+q)^2+m^2)\,\delta\,(p_2^2+m^2)}{(p_1^2+m^2)^2\,((p_2-p_1)^2+\mu^2)}+\frac{\delta\,((p_1+q)^2+m^2)\,\delta\,((p_2-p_1)^2+\mu^2)}{(p_1^2+m^2)^2\,(p_2^2+m^2)}+\right.$$

$$+\,2\,\frac{\delta\,(p_1^2+m^2)\,\delta\,(p_2^2+m^2)}{(p_1^2+m^2)\,((p_1+q)^2+m^2)\,((p_2-p_1)^2+\mu^2)}+2\,\frac{\delta\,(p_1^2+m^2)\,\delta\,((p_2-p_1)^2+\mu^2)}{(p_1^2+m^2)\,((p_1+q)^2+m^2)\,(p_2^2+m^2)}+$$

$$\left.+\,\frac{\delta\,(p_2^2+m^2)\,\delta\,((p_2-p_1)^2+\mu^2)\,(1+\varepsilon\,(p_2)\,\varepsilon\,(p_2-p_1))}{(p_1^2+m^2)^2\,((p_1+q)^2+m^2)}\right\}. \tag{25}$$

$$V_{\lambda\nu}(q) = \frac{1}{4}\,\frac{1}{(2\pi)^6}\int\!\!\int d\,p_1\,d\,p_2\,\cdot$$

$$\cdot\, Sp\,[\gamma_\lambda\,(i\gamma\,(p_1+q)-m)\,\gamma_\sigma\,(i\gamma\,(p_2+q)-m)\,\gamma_\nu\,(i\gamma\,p_2-m)\,\gamma_\sigma\,(i\gamma\,p_1-m)]\times$$

$$\times\left\{\frac{\delta\,((p_1+q)^2+m^2)\,\delta\,((p_2+q)^2+m^2)}{(p_1^2+m^2)\,(p_2^2+m^2)\,((p_2-p_1)^2+\mu^2)}+\frac{\delta\,((p_1+q)^2+m^2)\,\delta\,(p_2^2+m^2)}{(p_1^2+m^2)\,((p_2+q)^2+m^2)\,((p_2-p_1)^2+\mu^2)}+\right.$$

$$+\,\frac{\delta\,((p_1+q)^2+m^2)\,\delta\,((p_2-p_1)^2+\mu^2)}{(p_1^2+m^2)\,(p_2^2+m^2)\,((p_2+q)^2+m^2)}+\frac{\delta\,(p_1^2+m^2)\,\delta\,((p_2+q)^2+m^2)}{((p_1+q)^2+m^2)\,(p_2^2+m^2)\,((p_2-p_1)^2+\mu^2)}+$$

$$+\,\frac{\delta\,(p_1^2+m^2)\,\delta\,(p_2^2+m^2)}{((p_1+q)^2+m^2)\,((p_2+q)^2+m^2)\,((p_2-p_1)^2+\mu^2)}+$$

$$+\,\frac{\delta\,(p_1^2+m^2)\,\delta\,((p_2-p_1)^2+\mu^2)}{((p_1+q)^2+m^2)\,(p_2^2+m^2)\,((p_2+q)^2+m^2)}+$$

$$+\frac{\delta\left((p_2+q)^2+m^2\right)\delta\left((p_2-p_1)^2+\mu^2\right)\left(1+\varepsilon(p_2+q)\,\varepsilon(p_2-p_1)\right)}{(p_1^2+m^2)\left((p_1+q)^2+m^2\right)(p_2^2+m^2)}+$$

$$+\left.\frac{\delta(p_2^2+m^2)\,\delta\left((p_2-p_1)^2+\mu^2\right)\left(1+\varepsilon(p_2)\,\varepsilon(p_2-p_1)\right)}{(p_1^2+m^2)\left((p_1+q)^2+m^2\right)\left((p_2+q)^2+m^2\right)}\right\}. \tag{26}$$

Multiplying (25) by $i\,q_\lambda$ and using the same decomposition as after equation (7) we obtain[1]

$$i\,q_\lambda\,U_{\lambda\nu}(q)=$$

$$=\frac{1}{4}\,\frac{1}{(2\pi)^6}\int\!\!\int d\,p_1\,d\,p_2\cdot S\,p\left[\gamma_\sigma(i\,\gamma\,p_2-m)\,\gamma_\sigma(i\,\gamma\,(p_1+q)-m)\,\gamma_\nu(i\,\gamma\,p_1-m)\right]\times$$

$$\times\left\{\frac{\delta\left((p_1+q)^2+m^2\right)\delta(p_2^2+m^2)}{(p_1^2+m^2)\left((p_2-p_1)^2+\mu^2\right)}+\frac{\delta\left((p_1+q)^2+m^2\right)\delta\left((p_2-p_1)^2+\mu^2\right)}{(p_1^2+m^2)(p_2^2+m^2)}+\right.$$

$$+\frac{\delta(p_1^2+m^2)\,\delta(p_2^2+m^2)}{\left((p_1+q)^2+m^2\right)\left((p_2-p_1)^2+\mu^2\right)}+\frac{\delta(p_1^2+m^2)\,\delta\left((p_2-p_1)^2+\mu^2\right)}{\left((p_1+q)^2+m^2\right)(p_2^2+m^2)}+$$

$$+\left.\frac{\delta(p_2^2+m^2)\,\delta\left((p_2-p_1)^2+\mu^2\right)\left(1+\varepsilon(p_2)\,\varepsilon(p_2-p_1)\right)}{(p_1^2+m^2)\left((p_1+q)^2+m^2\right)}\right\}-$$

$$-\frac{1}{4}\,\frac{1}{(2\pi)^6}\int\!\!\int d\,p_1\,d\,p_2\cdot S\,p\left[\gamma_\sigma(i\,\gamma\,p_2-m)\,\gamma_\sigma(i\,\gamma\,p_1-m)\,\gamma_\nu(i\,\gamma\,p_1-m)\right]\times$$

$$\times\left\{2\,\frac{\delta(p_1^2+m^2)\,\delta(p_2^2+m^2)}{(p_1^2+m^2)\left((p_2-p_1)^2+\mu^2\right)}+2\,\frac{\delta(p_1^2+m^2)\,\delta\left((p_2-p_1)^2+\mu^2\right)}{(p_1^2+m^2)(p_2^2+m^2)}+\right.$$

$$+\left.\frac{\delta(p_2^2+m^2)\,\delta\left((p_2-p_1)^2+\mu^2\right)\left(1+\varepsilon(p_2)\,\varepsilon(p_2-p_1)\right)}{(p_1^2+m^2)^2}\right\}. \tag{27}$$

We treat only the first of the two terms of $i\,q_\lambda\,U_{\lambda\nu}(q)$ in some detail, as the treatment of the other terms in $i\,q_\lambda\,U_{\lambda\nu}(q)$ and the terms of $i\,q_\lambda\,V_{\lambda\nu}(q)$ is rather similar

$$i\,q_\lambda\,U^{(1)}_{\lambda\nu}(q)=$$

$$=\frac{1}{4}\,\frac{1}{(2\pi)^6}\int\!\!\int d\,p_1\,d\,p_2\cdot S\,p\left[\gamma_\sigma(i\,\gamma\,p_2-m)\,\gamma_\sigma(i\,\gamma\,(p_1+q)-m)\,\gamma_\nu(i\,\gamma\,p_1-m)\right]\times$$

$$\times\left\{\left[\frac{\delta\left((p_1+q)^2+m^2\right)}{p_1^2+m^2}+\frac{\delta(p_1^2+m^2)}{(p_1+q)^2+m^2}\right]\times\left[\frac{\delta(p_2^2+m^2)}{(p_2-p_1)^2+\mu^2}+\frac{\delta\left((p_2-p_1)^2+\mu^2\right)}{p_2^2+m^2}\right]+\right.$$

$$+\left.\frac{\delta(p_2^2+m^2)\,\delta\left((p_2-p_1)^2+\mu^2\right)\left(1+\varepsilon(p_2)\,\varepsilon(p_2-p_1)\right)}{(p_1^2+m^2)\left((p_1+q)^2+m^2\right)}\right\}. \tag{28}$$

---

[1] The indeterminate expressions $\frac{\delta(p^2+m^2)}{p^2+m^2}$ are most simply given a well-defined meaning with the aid of an adiabatic switching off of the charge at minus infinity. It then appears that e.g. the expression $(p^2+m^2)\cdot 2\,\frac{\delta(p^2+m^2)}{p^2+m^2}$ has to be understood as $\lim\limits_{\varepsilon\to 0} 2\left[\bar{p}^2-(p_0+\varepsilon)^2+m^2\right]\times\frac{\delta(p^2+m^2)}{\bar{p}^2-(p_0+2\varepsilon)^2+m^2}=\delta(p^2+m^2)$. *Cf.* e.g. F. J. Dyson, Phys. Rev. *82*, 428 (1951). This has been used in eq. (27).

In order to combine the terms of (28) the following formula will be used

$$\int d\,p_2 \cdot \delta\,(p_2^2 + m^2)\,\delta\,((p_2 - p_1)^2 + \mu^2)\,(1 + \varepsilon\,(p_2)\,\varepsilon\,(p_2 - p_1)) =$$

$$= \frac{1}{\pi^2}\int d\,p_2 \int_0^1 d\,\alpha\,\frac{1}{[p_2^2 - 2\,\alpha\,(p_2\,p_1) + \alpha\,p_1^2 + (1-\alpha)\,m^2 + \alpha\,\mu^2]^2}\,. \tag{29}$$

To derive (29) we observe that by K II (116), (117) we have

$$\int d\,p_2 \cdot \delta\,(p_2^2 + m^2)\,\delta\,((p_2 - p_1)^2 + \mu^2)\,\varepsilon\,(p_2)\,\varepsilon\,(p_2 - p_1) =$$

$$= \frac{1}{\pi^2}\,P\int \frac{d\,p_2}{(p_2^2 + m^2)\,((p_2 - p_1)^2 + \mu^2)}\,. \tag{30}$$

We thus have an expression of the form

$$\delta\,(a)\,\delta\,(b) - \frac{1}{\pi^2}\,P\,\frac{1}{a\,b}\,.$$

Using the well-known integral representations

$$\delta\,(a) = \frac{1}{2\,\pi}\int d\,w \cdot e^{i\,w\,a} \tag{31}$$

and

$$P\,\frac{1}{a} = \frac{1}{2\,i}\int d\,w \cdot e^{i\,w\,a}\,\frac{w}{|\,w\,|} \tag{32}$$

we have

$$\delta\,(a)\,\delta\,(b) - \frac{1}{\pi^2}\,P\,\frac{1}{a\,b} = \frac{1}{4\,\pi^2}\int\!\!\int d\,w_1\,d\,w_2 \cdot e^{i\,w_1\,a + i\,w_2\,b}\,.\left[1 + \frac{w_1\,w_2}{|\,w_1\,w_2\,|}\right] =$$

$$= \frac{1}{2\,\pi^2}\int d\,w \int_0^1 d\,\alpha \cdot e^{i\,w\,[\alpha\,a + (1-\alpha)\,b]}\,.\,|\,w\,| =$$

$$= -\,\frac{1}{\pi^2}\int_0^1 d\,\alpha\,\frac{1}{[\alpha\,a + (1-\alpha)\,b]^2}\,. \tag{33}$$

Use has been made of the transformation

$$\begin{aligned} w_1 &= w\,\alpha \\ w_2 &= w\,(1-\alpha). \end{aligned} \tag{34}$$

From (30) and (33) we can immediately derive (29).

Using (29) and (12) in the form

$$\frac{\delta\,(p_2^2+m^2)}{((p_2-p_1)^2+\mu^2)}+\frac{\delta\,((p_2-p_1)^2+\mu^2)}{p_2^2+m^2}=$$

$$=-\int_0^1 d\alpha\cdot\delta'\,(p_2^2-2\alpha\,(p_2\,p_1)+\alpha\,p_1^2+(1-\alpha)\,m^2+\alpha\,\mu^2)$$

and the relation

$$\gamma_\sigma\,(i\gamma\,p_2-m)\,\gamma_\sigma=-2\,(i\gamma\,p_2+2\,m)$$

we obtain

$$i\,q_\lambda\,U_{\lambda\nu}^{(1)}(q)=\frac{1}{2}\,\frac{1}{(2\pi)^6}\int\!\!\int d\,p_1\,d\,p_2\cdot Sp\,[(i\gamma\,p_2+2\,m)\,(i\gamma\,(p_1+q)-m)\,\gamma_\nu\,(i\gamma\,p_1-m)]\times$$

$$\times\int_0^1 d\alpha\cdot\Bigg\{\left[\frac{\delta\,((p_1+q)^2+m^2)}{p_1^2+m^2}+\frac{\delta\,(p_1^2+m^2)}{(p_1+q)^2+m^2}\right]\cdot\delta'\,(p_2^2-2\alpha\,(p_2\,p_1)+$$
$$+\alpha\,p_1^2+(1-\alpha)\,m^2+\alpha\,\mu^2)+$$

$$+\frac{1}{\pi^2}\,\frac{1}{(p_1^2+m^2)\,((p_1+q)^2+m^2)\,(p_2^2-2\alpha\,(p_2\,p_1)+\alpha\,p_1^2+(1-\alpha)\,m^2+\alpha\,\mu^2)^2}\Bigg\}.\qquad(35)$$

The p_2-integration cannot be performed, as the integral is divergent. If, however, we differentiate the expression n_2 times with respect to μ^2 $(n_2\geqq 1)$, it will become convergent

$$\frac{\partial^{n_2}}{\partial\,(\mu^2)^{n_2}}\,i\,q_\lambda\,U_{\lambda\nu}^{(1)}(q)=$$

$$=\frac{1}{2}\,\frac{1}{(2\pi)^6}\int\!\!\int d\,p_1\,d\,p_2\int_0^1 d\alpha\cdot\alpha^{n_2}\cdot Sp\,[(i\gamma\,p_2+2\,m)\,(i\gamma\,(p_1+q)-m)\,\gamma_\nu\,(i\gamma\,p_1-m)]\times$$

$$\times\Bigg\{\left[\frac{\delta\,((p_1+q)^2+m^2}{p_1^2+m^2}+\frac{\delta\,(p_1^2+m^2)}{(p_1+q)^2+m^2}\right]\cdot\delta^{(n_2+1)}\,(p_2^2-2\alpha\,(p_2\,p_1)+\alpha\,p_1^2+$$
$$+(1-\alpha)\,m^2+\alpha\,\mu^2)+$$

$$+\frac{1}{\pi^2}\,\frac{(-1)^{n_2}\,(n_2+1)\,!}{(p_1^2+m^2)\,((p_1+q)^2+m^2)\,(p_2^2-2\alpha\,(p_2\,p_1)+\alpha\,p_1^2+(1-\alpha)\,m^2+\alpha\,\mu^2)^{n_2+2}}\Bigg\}.\qquad(36)$$

By the transformation $p_2=p+\alpha\,p_1$ we get

$$i\gamma\,p_2+2\,m=i\gamma\,p+\alpha\,(i\gamma\,p_1+m)+(2-\alpha)\,m.\qquad(37)$$

As the p-integration is convergent for $n_2\geqq 1$ the term linear in p can be put equal to zero by reason of symmetry. Thus

$$\frac{\partial^{n_2}}{\partial(\mu^2)^{n_2}}\, i q_\lambda\, U^{(1)}_{\lambda\nu}(q) = \frac{\partial^{n_2}}{\partial(\mu^2)^{n_2}}\, i q_\lambda\, U^{(1a)}_{\lambda\nu}(q) + \frac{\partial^{n_2}}{\partial(\mu^2)^{n_2}}\, i q_\lambda\, U^{(1b)}_{\lambda\nu}(q) \tag{38}$$

where

$$\begin{aligned}\frac{\partial^{n_2}}{\partial(\mu^2)^{n_2}}\, i q_\lambda\, U^{(1a)}_{\lambda\nu}(q) = &-\frac{1}{2}\,\frac{1}{(2\pi)^6}\int d p_1 \int_0^1 d\alpha\cdot\alpha^{n_2+1}\cdot Sp\,[(i\gamma(p_1+q)-m)\gamma_\nu]\times\\ &\times\int d p\cdot\Big\{\delta((p_1+q)^2+m^2)\cdot\delta^{(n_2+1)}(p^2+\alpha(1-\alpha)p_1^2+(1-\alpha)m^2+\alpha\mu^2)+\\ &+\frac{1}{\pi^2}\,\frac{(-1)^{n_2}(n_2+1)!}{((p_1+q)^2+m^2)(p^2+\alpha(1-\alpha)p_1^2+(1-\alpha)m^2+\alpha\mu^2)^{n_2+2}}\Big\}.\end{aligned} \tag{39}$$

$$\begin{aligned}&\frac{\partial^{n_2}}{\partial(\mu^2)^{n_2}}\, i q_\lambda\, U^{(1b)}_{\lambda\nu}(q) =\\ &=\frac{1}{2}\,\frac{m}{(2\pi)^6}\int\!\!\int d p_1\, d p\int_0^1 d\alpha\cdot\alpha^{n_2}(2-\alpha)\cdot Sp\,[(i\gamma(p_1+q)-m)\gamma_\nu(i\gamma p_1-m)]\times\\ &\times\Big\{\Big[\frac{\delta((p_1+q)^2+m^2)}{p_1^2+m^2}+\frac{\delta(p_1^2+m^2)}{(p_1+q)^2+m^2}\Big]\cdot\delta^{(n_2+1)}(p^2+\alpha(1-\alpha)p_1^2+(1-\alpha)m^2+\alpha\mu^2)+\\ &+\frac{1}{\pi^2}\,\frac{(-1)^{n_2}(n_2+1)!}{(p_1^2+m^2)((p_1+q)^2+m^2)(p^2+\alpha(1-\alpha)p_1^2+(1-\alpha)m^2+\alpha\mu^2)^{n_2+2}}\Big\}.\end{aligned} \tag{40}$$

The p-integration can now be performed

$$\begin{aligned}\int d p\cdot\delta^{(n_2+1)}(p^2+A) &= \frac{1}{2\pi}\int d p\int d w\cdot e^{iw(p^2+A)}\cdot(iw)^{n_2+1} =\\ &= \frac{i\pi^2}{2\pi}\int d w\cdot e^{iwA}\cdot(iw)^{n_2+1}\cdot\frac{1}{w\,|w|} =\\ &= -\frac{i\pi}{2}\int d w\cdot e^{iwA}\,(iw)^{n_2-1}\,\frac{w}{|w|} =\\ &= \frac{\pi(-1)^{n_2-1}(n_2-1)!}{A^{n_2}}\end{aligned} \tag{41}$$

and in the same way

$$\frac{(-1)^{n_2}(n_2+1)!}{\pi^2}\int d p\,\frac{1}{(p^2+A)^{n_2+2}} = \pi\cdot\delta^{(n_2-1)}(A). \tag{42}$$

From (39), (41), and (42) we now have

$$\frac{\partial^{n_2}}{\partial(\mu^2)^{n_2}}\, i\, q_\lambda\, U^{(1\,a)}_{\lambda\nu}(q) = -\frac{\pi}{2}\,\frac{1}{(2\pi)^6}\int d\,p_1\int_0^1 d\,\alpha\cdot\alpha^{n_2+1}\cdot S\,p\,[(i\,\gamma\,(p_1+q)-m)\,\gamma_\nu]\times$$
$$\times\left\{\frac{\delta\,((p_1+q)^2+m^2)\,(-1)^{n_2-1}\,(n_2-1)\,!}{(p_1^2\,\alpha\,(1-\alpha)+m^2\,(1-\alpha)+\mu^2\,\alpha)^{n_2}}+\right.$$
$$\left.+\frac{\delta^{(n_2-1)}\,(p_1^2\,\alpha\,(1-\alpha)+m^2\,(1-\alpha)+\mu^2\,\alpha)}{(p_1+q)^2+m^2}\right\}. \tag{43}$$

The trace is easily evaluated and gives

$$S\,p\,[(i\,\gamma\,(p_1+q)-m)\,\gamma_\nu] = 4\,i\,(p_1+q)_\nu. \tag{44}$$

By writing (12) in the form

$$\frac{\delta\,(a)}{b}+\frac{\delta\,(b)}{a} = -\int_0^1 d\,\beta\cdot\delta'\,(\beta\,a+(1-\beta)\,b) \tag{45}$$

and differentiating it n_2-1 times with respect to b we get

$$\frac{\delta\,(a)\,(-1)^{n_2-1}\,(n_2-1)\,!}{b^{n_2}}+\frac{\delta^{(n_2-1)}\,(b)}{a} = -\int_0^1 d\,\beta\,(1-\beta)^{n_2-1}\cdot\delta^{(n_2)}\,(\beta\,a+(1-\beta)\,b). \tag{46}$$

Thus

$$\frac{\delta\,((p_1+q)^2+m^2)\,(-1)^{n_2-1}\,(n_2-1)\,!}{(p_1^2\,\alpha\,(1-\alpha)+m^2\,(1-\alpha)+\mu^2\,\alpha)^{n_2}}+\frac{\delta^{(n_2-1)}\,(p_1^2\,\alpha\,(1-\alpha)+m^2\,(1-\alpha)+\mu^2\,\alpha)}{(p_1+q)^2+m^2} =$$
$$= -\frac{1}{[\alpha\,(1-\alpha)]^{n_2}}\int_0^1 d\,\beta\,(1-\beta)^{n_2-1}\cdot$$
$$\cdot\,\delta^{(n_2)}\left(\beta\,((p_1+q)^2+m^2)+(1-\beta)\left(p_1^2+\frac{m^2}{\alpha}+\frac{\mu^2}{1-\alpha}\right)\right). \tag{47}$$

From (43), (44), and (47) we obtain

$$\frac{\partial^{n_2}}{\partial(\mu^2)^{n_2}}\, i\, q_\lambda\, U^{(1\,a)}_{\lambda\nu}(q) = \frac{i}{(2\pi)^5}\int_0^1 d\,\alpha\cdot\frac{\alpha}{(1-\alpha)^{n_2}}\int_0^1 d\,\beta\,(1-\beta)^{n_2-1}\cdot\int d\,p_1\,(p_1+q)_\nu\times$$
$$\times\,\delta^{(n_2)}\left(p_1^2+2\,\beta\,(p_1\,q)+\beta\,q^2+m^2\left(\beta+\frac{1-\beta}{\alpha}\right)+\mu^2\,\frac{1-\beta}{1-\alpha}\right). \tag{48}$$

By differentiating n_1 times with respect to m^2 we have

$$\frac{\partial^{n_1}}{\partial (m^2)^{n_1}}\,\frac{\partial^{n_2}}{\partial (\mu^2)^{n_2}}\, i\, q_\lambda\, U^{(1a)}_{\lambda\nu}(q) =$$

$$= \frac{i}{(2\pi)^5}\int_0^1 d\alpha \frac{\alpha}{(1-\alpha)^{n_2}} \int_0^1 d\beta\,(1-\beta)^{n_2-1}\left(\beta+\frac{1-\beta}{\alpha}\right)^{n_1}\cdot \int d p_1\,(p_1+q)_\nu \times$$

$$\times\ \delta^{(n_1+n_2)}\left(p_1^2+2\beta\,(p_1 q)+\beta\, q^2+m^2\left(\beta+\frac{1-\beta}{\alpha}\right)+\mu^2\,\frac{1-\beta}{1-\alpha}\right). \tag{49}$$

Putting $p_1 = p-\beta q$ and again equating the terms linear in p to zero in the (convergent) p-integral we get

$$\frac{\partial^{n_1}\partial^{n_2}}{\partial (m^2)^{n_1}\partial (\mu^2)^{n_2}}\, i\, q_\lambda\, U^{(1a)}_{\lambda\nu}(q) = \frac{i\, q_\nu}{(2\pi)^5}\int_0^1 d\alpha\,\frac{\alpha}{(1-\alpha)^{n_2}}\int_0^1 d\beta\,(1-\beta)^{n_2}\left(\beta+\frac{1-\beta}{\alpha}\right)^{n_1}\times$$

$$\times \int d p\cdot \delta^{(n_1+n_2)}\left(p^2+q^2\beta\,(1-\beta)+m^2\left(\beta+\frac{1-\beta}{\alpha}\right)+\mu^2\,\frac{1-\beta}{1-\alpha}\right) =$$

$$= \frac{i\, q_\nu}{(2\pi)^5}\int_0^1 d\alpha\cdot\alpha^{n_2}(1-\alpha)^{n_1-1}\int_0^1 d\beta\,(1-\beta)^{n_2}(\alpha\beta+1-\beta)^{n_1}\times$$

$$\times \int d p\cdot\delta^{(n_1+n_2)}\left(p^2+q^2\beta\,(1-\beta)\,\alpha\,(1-\alpha)+m^2\,(\alpha\beta+1-\beta)\,(1-\alpha)+\mu^2\,(1-\beta)\,\alpha\right). \tag{50}$$

As the computation of the other terms of $i\, q_\lambda\, U_{\lambda\nu}(q)$ follows the same lines, we give only the result:

$$\frac{\partial^{n_1}\partial^{n_2}}{\partial (m^2)^{n_1}\partial (\mu^2)^{n_2}}\, i\, q_\lambda\, U_{\lambda\nu}(q) =$$

$$= \frac{i\, q_\nu}{(2\pi)^5}\int_0^1 d\alpha\cdot\alpha^{n_2}(1-\alpha)^{n_1-1}\int_0^1 d\beta\,(1-\beta)^{n_2}(\alpha\beta+1-\beta)^{n_1}\int d p\cdot\delta^{(n_1+n_2)}(p^2+A) -$$

$$-\frac{i\, m^2 q_\nu}{(2\pi)^5}\int_0^1 d\alpha\cdot\alpha^{n_2}(1-\alpha)^{n_1}(2-\alpha)\int_0^1 d\beta_1\,(1-\beta_1)^{n_2-1}(\alpha\beta_1+1-\beta_1)^{n_1}\int_0^{\beta_1} d\beta_2\,(1-2\beta_2)\cdot$$

$$\cdot\int d p\cdot\delta^{(n_1+n_2+1)}(p^2+B) -$$

$$-\frac{i\, n_1 q_\nu}{(2\pi)^5}\int_0^1 d\alpha\cdot\alpha^{n_2}(1-\alpha)^{n_1-1}(2-\alpha)\int_0^1 d\beta_1\,(1-\beta_1)^{n_2-1}(\alpha\beta_1+1-\beta_1)^{n_1-1}\cdot$$

$$\cdot\int_0^{\beta_1} d\beta_2\,(1-2\beta_2)\cdot\int d p\cdot\delta^{(n_1+n_2)}(p^2+B) \tag{51}$$

where

$$A = q^2 \beta (1-\beta) \alpha (1-\alpha) + m^2 (\alpha\beta + 1 - \beta)(1-\alpha) + \mu^2 (1-\beta)\alpha. \tag{52}$$

$$B = q^2 \beta_2 (1-\beta_2) \alpha (1-\alpha) + m^2 (\alpha\beta_1 + 1 - \beta_1)(1-\alpha) + \mu^2 (1-\beta_1)\alpha. \tag{53}$$

In the same way we find

$$\frac{\partial^{n_1}}{\partial (m^2)^{n_1}} \frac{\partial^{n_2}}{\partial (\mu^2)^{n_2}} i q_\lambda V_{\lambda\nu}(q) =$$

$$\begin{aligned}
= - \frac{2 i q_\nu}{(2\pi)^5} \int_0^1 d\alpha \cdot \alpha^{n_2} (1-\alpha)^{n_1 - 1} \int_0^1 d\beta (1-\beta)^{n_2} (\alpha\beta + 1 - \beta)^{n_1} \cdot \int dp \cdot \delta^{(n_1+n_2)}(p^2 + A) + \\
+ \frac{2 i m^2 q_\nu}{(2\pi)^5} \int_0^1 d\alpha \cdot \alpha^{n_2} (1-\alpha)^{n_1} (2-\alpha) \int_0^1 d\beta_1 (1-\beta_1)^{n_2 - 1} (\alpha\beta_1 + 1 - \beta_1)^{n_1} \cdot \\
\cdot \int_0^{\beta_1} d\beta_2 (1 - 2\beta_2) \int dp \cdot \delta^{(n_1+n_2+1)}(p^2 + B) + \\
+ \frac{2 i n_1 q_\nu}{(2\pi)^5} \int_0^1 d\alpha \cdot \alpha^{n_2} (1-\alpha)^{n_1 - 1} (2-\alpha) \int_0^1 d\beta_1 (1-\beta_1)^{n_2 - 1} (\alpha\beta_1 + 1 - \beta_1)^{n_1 - 1} \cdot \\
\cdot \int_0^{\beta_1} d\beta_2 (1 - 2\beta_2) \int dp \cdot \delta^{(n_1+n_2)}(p^2 + B).
\end{aligned} \tag{54}$$

It is obvious from (51) and (54) that $\frac{\partial^{n_1}}{\partial (m^2)^{n_1}} \frac{\partial^{n_2}}{\partial (\mu^2)^{n_2}} i q_\lambda K^{(4)}_{\lambda\nu}(q)$ is convergent for $n_1 \geqq 1$, $n_2 \geqq 1$ and that

$$\frac{\partial^{n_1}}{\partial (m^2)^{n_1}} \frac{\partial^{n_2}}{\partial (\mu^2)^{n_2}} i q_\lambda K^{(4)}_{\lambda\nu}(q) = \frac{\partial^{n_1}}{\partial (m^2)^{n_1}} \frac{\partial^{n_2}}{\partial (\mu^2)^{n_2}} (i q_\lambda V_{\lambda\nu}(q) + 2 i q_\lambda U_{\lambda\nu}(q)) = 0 \tag{55}$$

and from (5) that

$$i q_\lambda B^{(4)\,\mathrm{reg}}(q^2) = 0. \tag{56}$$

We will now show that the integrals in $\frac{\partial^{n_1}}{\partial (m^2)^{n_1}} \frac{\partial^{n_2}}{\partial (\mu^2)^{n_2}} K^{(4)}_{\nu\nu}(q)$ are also convergent for n_1 and n_2 sufficiently large. As the treatment of $K^{(4)}_{\nu\nu}(q)$ is analogous to the one for $i q_\lambda U_{\lambda\nu}(q)$ given in (28) to (51) we do not give the details here. The result is

$$\frac{\partial^{n_1}}{\partial (m^2)^{n_1}} \frac{\partial^{n_2}}{\partial (\mu^2)^{n_2}} U_{\nu\nu}(q) =$$

$$= \frac{2}{(2\pi)^5} \int_0^1 d\alpha \cdot \alpha^{n_2} (1-\alpha)^{n_1-1} \int_0^1 d\beta (1-\beta)^{n_2-1} (\alpha\beta + 1 - \beta)^{n_1} \int dp\, \delta^{(n_1+n_2)}(p^2+A) -$$

$$- \frac{2}{(2\pi)^5} \int_0^1 d\alpha \cdot \alpha^{n_2+1} (1-\alpha)^{n_1} \int_0^1 d\beta_1 (1-\beta_1)^{n_2-1} (\alpha\beta_1 + 1 - \beta_1)^{n_1} \cdot$$

$$\cdot \int_0^{\beta_1} d\beta_2 (m^2 - \beta_2 q^2) \int dp \cdot \delta^{(n_1+n_2+1)}(p^2+B) -$$

$$- \frac{2 n_1}{(2\pi)^5} \int_0^1 d\alpha \cdot \alpha^{n_2+1} (1-\alpha)^{n_1-1} \int_0^1 d\beta_1 (1-\beta_1)^{n_2-1} (\alpha\beta_1 + 1 - \beta_1)^{n_1-1} \cdot$$

$$\cdot \int_0^{\beta_1} d\beta_2 \int dp \cdot \delta^{(n_1+n_2)}(p^2+B) -$$

$$- \frac{4 (m^2)^2}{(2\pi)^5} \int_0^1 d\alpha \cdot \alpha^{n_2+1} (1-\alpha)^{n_1+1} (2-\alpha) \int_0^1 d\beta_1 (1-\beta_1)^{n_2-1} (\alpha\beta_1 + 1 - \beta_1)^{n_1} \cdot$$

$$\cdot \int_0^{\beta_1} d\beta_2 (\beta_1 - \beta_2) \int dp \cdot \delta^{(n_1+n_2+2)}(p^2+B) -$$

$$- \frac{8 n_1 m^2}{(2\pi)^5} \int_0^1 d\alpha \cdot \alpha^{n_2+1} (1-\alpha)^{n_1} (2-\alpha) \int_0^1 d\beta_1 (1-\beta_1)^{n_2-1} (\alpha\beta_1 + 1 - \beta_1)^{n_1-1} \cdot$$

$$\cdot \int_0^{\beta_1} d\beta_2 (\beta_1 - \beta_2) \int dp \cdot \delta^{(n_1+n_2+1)}(p^2+B) -$$

$$- \frac{4 n_1 (n_1-1)}{(2\pi)^5} \int_0^1 d\alpha \cdot \alpha^{n_2+1} (1-\alpha)^{n_1-1} (2-\alpha) \int_0^1 d\beta_1 (1-\beta_1)^{n_2-1} (\alpha\beta_1 + 1 - \beta_1)^{n_1-2} \cdot$$

$$\cdot \int_0^{\beta_1} d\beta_2 (\beta_1 - \beta_2) \int dp \cdot \delta^{(n_1+n_2)}(p^2+B) +$$

$$+\frac{4\,m^2 q^2}{(2\,\pi)^5}\int\limits_0^1 d\,\alpha\cdot\alpha^{n_2+1}\,(1-\alpha)^{n_1+1}\,(2-\alpha)\int\limits_0^1 d\,\beta_1\,(1-\beta_1)^{n_2-1}\,(\alpha\,\beta_1+1-\beta_1)^{n_1}\cdot$$

$$\cdot\int\limits_0^{\beta_1} d\,\beta_2\,(\beta_1-\beta_2)\,\beta_2\int d\,p\cdot\delta^{(n_1+n_2+2)}\,(p^2+B)+$$

$$+\frac{4\,n_1\,q^2}{(2\,\pi)^5}\int\limits_0^1 d\,\alpha\cdot\alpha^{n_2+1}\,(1-\alpha)^{n_1}\,(2-\alpha)\int\limits_0^1 d\,\beta_1\,(1-\beta_1)^{n_2-1}\,(\alpha\,\beta_1+1-\beta_1)^{n_1-1}\cdot$$

$$\cdot\int\limits_0^{\beta_1} d\,\beta_2\,(\beta_1-\beta_2)\,\beta_2\int d\,p\cdot\delta^{(n_1+n_2+1)}\,(p^2+B).\quad(57)$$

$$\frac{\partial^{n_1}}{\partial\,(m^2)^{n_1}}\,\frac{\partial^{n_2}}{\partial\,(\mu^2)^{n_2}}\,V_{\nu\,\nu}\,(q)=$$

$$=-\frac{2}{(2\,\pi)^5}\int\limits_0^1 d\,\alpha_1\int\limits_0^{\alpha_1} d\,\alpha_2\cdot\alpha_2^{n_2-1}\,(1-\alpha_2)^{n_1-1}\int\limits_0^1 d\,\beta\,(1-\beta)^{n_2-1}\,(\alpha_2\,\beta+1-\beta)^{n_1}\cdot$$

$$\cdot\int d\,p\cdot\delta^{(n_1+n_2)}\,(p^2+C)-$$

$$-\frac{2\,m^2}{(2\,\pi)^5}\int\limits_0^1 d\,\alpha_1\int\limits_0^{\alpha_1} d\,\alpha_2\cdot\alpha_2^{n_2}\,(1-\alpha_2)^{n_1}\int\limits_0^1 d\,\beta_1\int\limits_0^{\beta_1} d\,\beta_2\,(1-\beta_1)^{n_2-1}\,(\alpha_2\,\beta_1+1-\beta_1)^{n_1}\cdot$$

$$\cdot\int d\,p\cdot\delta^{(n_1+n_2+1)}\,(p^2+D)-$$

$$-\frac{2\,n_1}{(2\,\pi)^5}\int\limits_0^1 d\,\alpha_1\int\limits_0^{\alpha_1} d\,\alpha_2\cdot\alpha_2^{n_2}\,(1-\alpha_2)^{n_1-1}\int\limits_0^1 d\,\beta_1\int\limits_0^{\beta_1} d\,\beta_2\,(1-\beta_1)^{n_2-1}\,(\alpha_2\beta_1+1-\beta_1)^{n_1-1}\cdot$$

$$\cdot\int d\,p\cdot\delta^{(n_1+n_2)}\,(p^2+D)-$$

$$-\frac{24}{(2\,\pi)^5}\int\limits_0^1 d\,\alpha_1\int\limits_0^{\alpha_1} d\,\alpha_2\cdot\alpha_2^{n_2}\,(1-\alpha_2)^{n_1-2}\int\limits_0^1 d\,\beta_1\int\limits_0^{\beta_1} d\,\beta_2\,(1-\beta_1)^{n_2}\,(\alpha_2\,\beta_1+1-\beta_1)^{n_1}\cdot$$

$$\cdot\int d\,p\cdot\delta^{(n_1+n_2)}\,(p^2+D)+$$

$$+\frac{4}{(2\,\pi)^5}\int\limits_0^1 d\,\alpha_1\int\limits_0^{\alpha_1} d\,\alpha_2\cdot\alpha_2^{n_2-1}\,(1-\alpha_2)^{n_1}\;{}^{1}\int\limits_0^1 d\,\beta_1\int\limits_0^{\beta_1} d\,\beta_2\,(1-\beta_1)^{n_2}\,(\alpha_2\,\beta_1+1-\beta_1)^{n_1}\cdot$$

$$\cdot\,[\xi_1\,q^2+\xi_2\,m^2]\cdot\int d\,p\cdot\delta^{(n_1+n_2+1)}\,(p^2+D)+$$

$$+\frac{4n_1}{(2\pi)^5}\int_0^1 d\alpha_1\int_0^{\alpha_1} d\alpha_2\cdot\alpha_2^{n_2-1}(1-\alpha_2)^{n_1-2}\int_0^1 d\beta_1\int_0^{\beta_1} d\beta_2\,(1-\beta_1)^{n_2}(\alpha_2\beta_1+1-\beta_1)^{n_1-1}\cdot$$

$$\cdot\,\xi_2\cdot\int dp\cdot\delta^{(n_1+n_2)}(p^2+D)-$$

$$-\frac{2}{(2\pi)^5}\int_0^1 d\alpha_1\int_0^{\alpha_1} d\alpha_2\cdot\alpha_2^{n_2}(1-\alpha_2)^{n_1}\int_0^1 d\beta_1\int_0^{\beta_1} d\beta_2\,(1-\beta_1)^{n_2}(\alpha_2\beta_1+1-\beta_1)^{n_1}\cdot$$

$$\cdot\,[\eta_1(q^2)^2+\eta_2 m^2 q^2+2(m^2)^2]\times\int dp\cdot\delta^{(n_1+n_2+2)}(p^2+D)-$$

$$-\frac{2n_1}{(2\pi)^5}\int_0^1 d\alpha_1\int_0^{\alpha_1} d\alpha_2\cdot\alpha_2^{n_2}(1-\alpha_2)^{n_1-1}\int_0^1 d\beta_1\int_0^{\beta_1} d\beta_2\,(1-\beta_1)^{n_2}(\alpha_2\beta_1+1-\beta_1)^{n_1-1}\cdot$$

$$\cdot\,[\eta_2 q^2+4m^2]\cdot\int dp\cdot\delta^{(n_1+n_2+1)}(p^2+D)-$$

$$-\frac{4n_1(n_1-1)}{(2\pi)^5}\int_0^1 d\alpha_1\int_0^{\alpha_1} d\alpha_2\cdot\alpha_2^{n_2}(1-\alpha_2)^{n_1-2}\int_0^1 d\beta_1\int_0^{\beta_1} d\beta_2\,(1-\beta_1)^{n_2}\cdot$$

$$\cdot\,(\alpha_2\beta_1+1-\beta_1)^{n_1-2}\cdot\int dp\cdot\delta^{(n_1+n_2)}(p^2+D). \tag{58}$$

Here A and B are given by (52) and (53),

$$C=q^2\left[\beta+\frac{(1-\beta)\,\alpha_1(1-\alpha_1)}{\alpha_2(1-\alpha_2)}-\left(\beta+\frac{(1-\beta)(1-\alpha_1)}{1-\alpha_2}\right)^2\right]+$$

$$+\,m^2(\alpha_2\beta+1-\beta)(1-\alpha_2)+\mu^2(1-\beta)\,\alpha_2 \tag{59}$$

$$D=q^2\left[\beta_2+\frac{(1-\beta_1)\,\alpha_1(1-\alpha_1)}{\alpha_2(1-\alpha_2)}-\left(\beta_2+\frac{(1-\beta_1)(1-\alpha_1)}{1-\alpha_2}\right)^2\right]+$$

$$+\,m^2(\alpha_2\beta_1+1-\beta_1)(1-\alpha_2)+\mu^2(1-\beta_1)\,\alpha_2 \tag{60}$$

$$\xi_1=6\,\alpha_2^2\left(\beta_2+\frac{(1-\beta_1)(1-\alpha_1)}{1-\alpha_2}\right)^2-\tfrac{3}{2}\,(2\alpha_2-4\alpha_2(1-\alpha_1))\left(\beta_2+\frac{(1-\beta_1)(1-\alpha_1)}{1-\alpha_2}\right)+$$

$$+\,\tfrac{1}{4}\,(2(1-\alpha_1)^2-2(1-\alpha_1)+\alpha_2) \tag{61}$$

$$\xi_2=2+4\,\alpha_2 \tag{62}$$

$$\eta_1 = 2\,\alpha_2^2 \left(\beta_2 + \frac{(1-\beta_1)(1-\alpha_1)}{1-\alpha_2}\right)^4 - (2\,\alpha_2 - 4\,\alpha_2 (1-\alpha_1)) \left(\beta_2 + \frac{(1-\beta_1)(1-\alpha_1)}{1-\alpha_2}\right)^3 +$$

$$+ (2\,(1-\alpha_1)^2 - 2\,(1-\alpha_1) + \alpha_2) \times \left(\beta_2 + \frac{(1-\beta_1)(1-\alpha_1)}{1-\alpha_2}\right)^2 +$$

$$+ (1-\alpha_1) \left(\beta_2 + \frac{(1-\beta_1)(1-\alpha_1)}{1-\alpha_2}\right) \qquad (63)$$

$$\eta_2 = (2 + 4\,\alpha_2) \left(\beta_2 + \frac{(1-\beta_1)(1-\alpha_1)}{1-\alpha_2}\right)^2 -$$

$$- (6 - 4\,(1-\alpha_1)) \left(\beta_2 + \frac{(1-\beta_1)(1-\alpha_1)}{1-\alpha_2}\right) + 1. \qquad (64)$$

All the integrals in (57) and (58) are convergent for $n_1 \geqq 1$, $n_2 \geqq 1$. Thus the mass- and charge-renormalizations consist of subtracting finite terms from (57) and (58). If we make these renormalizations, the remaining terms will be the observable part of the vacuum expectation value of the current operator.

During the completion of the manuscript, the result of a computation of the contribution to the Lamb-shift from fourth order vacuum polarization was published by BARANGER, DYSON, and SALPETER.[1] As the method of regularization, which we have used here, might be of interest, and as the calculations on the vacuum polarization were started mainly to see, how this method works on the e^4-approximation, it seemed worth while to publish these calculations. On the other hand it is of little interest to make the somewhat tedious integrations in order to get a numerical value for the observable terms.

I wish to express my gratitude to Professor T. GUSTAFSON for the kind interest he has shown in this work. My thanks are further due to Dr. G. KÄLLÉN, who suggested this investigation, for many valuable discussions and good advice. Finally, I thank the Swedish Atomic Committee for financial support

Department of Mechanics and Mathematical Physics, University of Lund.

---

[1] M. BARANGER–F. J. DYSON–E. E. SALPETER, Phys. Rev. *88*, 680 (1952).

Tryckt den 4 december 1953

Uppsala 1953. Almqvist & Wiksells Boktryckeri AB

ARKIV FÖR FYSIK Band 7 nr 22

Communicated 10 September 1952 by MANNE SIEGBAHN and ERIK HULTHÉN

Measurements of conversion coefficients with a scintillation spectrometer

A series of 8 papers by I. BERGSTRÖM, K. NYBÖ[1], S. THULIN, A. H. WAPSTRA[2], and B. ÅSTRÖM

For the determination of conversion coefficients β-spectrometrical methods have been most commonly used. These methods, however, fail just in the interesting case of isomers not following an intense branch in β-decay or K capture, or in cases where the conversion coefficient is high. In these cases comparison of γ-intensities is inevitable. For this type of measurement we have used a scintillation spectrometer built at this institute.

The construction of the spectrometer is described in I, and its calibration in II. In III and IV measurements of some internal conversion coefficients are reported. The next paper, V, describes an additional measurement on Xe^{129} necessary for the interpretation of its decay discussed in III. VI, VII, and VIII describe some measurements on isotopes which were found to be useful for the calibration of the instrument and were therefore included in this series.

Two of us (K. NYBÖ and A. H. WAPSTRA) are greatly indebted to Professor MANNE SIEGBAHN for giving us the opportunity of working at the Nobel Institute of Physics. One of us (A.H.W.) has also to thank the Nobel Institute and the Netherlands Foundation for Fundamental Research (F.O.M.) for grants.

This series consists of the following papers:

I. A scintillation spectrometer, by B. ÅSTRÖM 241
II. Calibration of a scintillation spectrometer for comparison of γ- and X-ray intensities, by B. ÅSTRÖM, A. H. WAPSTRA, S. THULIN, and I. BERGSTRÖM 247
III. *K*-conversion coefficients of γ-transitions in the decay of Kr^{85m}, Xe^{129m}, Xe^{131m}, Xe^{133}, and Xe^{133m}, by I. BERGSTRÖM, S. THULIN, A. H. WAPSTRA, and B. ÅSTRÖM 255
IV. *K*-conversion coefficient of the isomeric γ-ray in Ag^{109}, by A. H. WAPSTRA 265
V. The decay of Xe^{129m}, by S. THULIN 269
VI. Conversion coefficients of the isomeric γ-ray in the decay of Ba^{137}, by A. H. WAPSTRA 275
VII. The decay of Bi^{207}, by A. H. WAPSTRA 279
VIII. On the decay of Hg^{203}, by S. THULIN and K. NYBÖ 289

---

[1] On leave from the University of Bergen, Norway.
[2] On leave from the "Instituut voor Kernphysisch Onderzoek", Amsterdam.

ARKIV FÖR FYSIK. Bd 7 nr 22

A scintillation spectrometer

By Björn Åström

The design and performance of a scintillation spectrometer using NaI (Tl) crystals is described. A method of improving the overload characteristics of a linear amplifier and the circuit of a simple one-channel differential discriminator is given.

Introduction. The great usefulness of NaI (Tl) crystals for the measurement of the energy of particles and quanta emitted in nuclear transitions has been described in several publications (see for instance 1, 2). The purpose of this paper is to give a description of a scintillation spectrometer using NaI (Tl) crystals which has been used in this laboratory.

As a scintillator for spectrometric measurements, NaI (Tl) has proved to be superior to any other material so far known. The use of only one type of scintillating material giving light pulses of a certain well defined shape also made possible some simplifications in the electronic part of the instrument.

The working principle of a scintillation spectrometer can be summarized as follows. A γ-quantum being absorbed in the crystal causes a light flash which is "seen" by a photomultiplier. This generates an electrical pulse which is amplified in a linear amplifier. Pulses with different amplitudes are sorted in an amplitude selective device — the differential discriminator — and counted separately by a scaler. All processes involved are linear, and a curve showing the number of pulses of a certain amplitude versus the amplitude gives information about the energy spectrum of the absorbed radiation.

A block diagram of the instrument is shown in Fig. 1 and a description of the various parts will be given in the following sections.

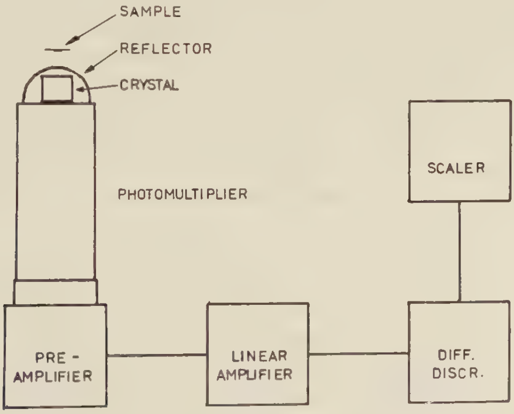

Fig. 1. Block diagram of the scintillation spectrometer.

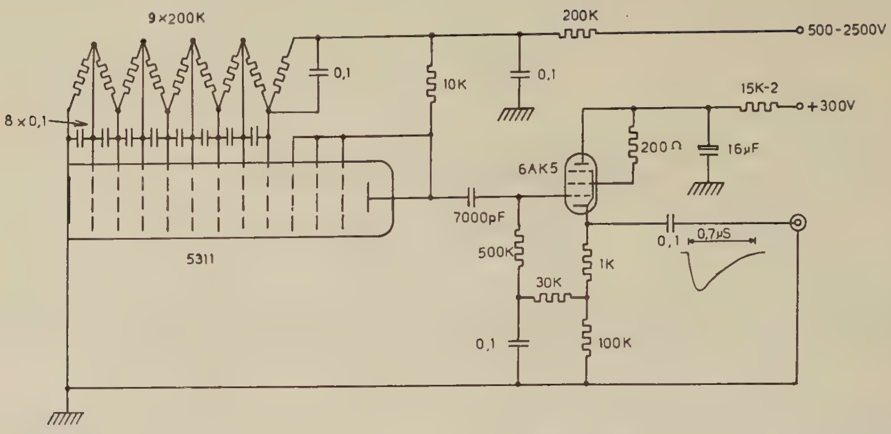

Fig. 2. Circuit of the photomultiplier and preamplifier. The multiplier is mounted directly on the case containing the preamplifier.

1. Crystal arrangement

A clear crystal and an efficient light collecting system are essential for good spectral resolution in a scintillation spectrometer. A general-purpose arrangement is indicated in Fig. 1. A 10 mm cubic crystal of NaI (Tl) which has just been cleaved from a larger piece of material is dipped in paraffin oil and placed directly on the top of the photomultiplier. Crystals that have absorbed humidity on their surfaces can be used again after washing in ethyl methyl ketone. Light leaving the crystal through the outer surfaces is reflected towards the photocathode by a highly polished aluminium cap, which at the same time keeps out humidity. Other crystal arrangements are used for special measurements, see (3).

2. Photomultiplier

The photomultiplier used was of type EMI 5311. The circuit of the multiplier and the preamplifier connected to it is given in Fig. 2. Here the shape of the pulses generated is also indicated.

Because of a saturating effect resulting in nonlinearity it is not possible to utilize the full amplification of the photomultiplier. The amplification can be decreased either by lowering the voltage between the dynodes or by connecting the last three dynodes to the collector, thus decreasing the number of amplifying stages. The last method was preferred, because a high voltage between multiplying dynodes improves the focusing of the electrons and thus favours good statistics in the multiplier.

The amplification in the photomultiplier is a very sensitive function of the total voltage between cathode and collector. In a certain measurement this voltage was 900 volts, and a change of 2 volts caused the amplitude of the pulses to change by about 1 %. When the AC line was connected to the scintillation spectrometer through a constant voltage transformer this degree of stability was achieved over long periods with the high voltage stabilizer described in (4).

3. Linear amplifier

If one wishes to measure low energy γ-rays or X-rays in the presence of high energy γ-rays, it is necessary that the amplifier used should have good overload characteristics. This means that the overshoot pulse following a large pulse that has saturated the amplifier should be as small as possible.

In the spectrometer described a model 500 amplifier (5) was used. The overload characteristics of that amplifier were improved by inserting two germanium diodes, one in series with the coupling condenser between the two first tubes and the other in parallel with the grid leak of the 6AC7 tube preceding the 6AG7. After this modification the overshoot was about 3 % of the overloading pulse causing it. This means that in the presence of 1 MeV γ-rays it was possible to measure down to 30 keV.

The amplifier is adjusted for best response to the NaI (Tl) pulses by varying the trimmer condensers in the feed-back loops. A clipping time of 5μs is used.

4. Differential discriminator

The sorting of pulses of different heights is done with a single-channel discriminator, the circuit of which is shown in Fig. 3.

Two Schmitt trigger circuits D_1 and D_2 are biased from the common potentiometer P_3. A small voltage can be added to the bias of D_2 by varying P_4. Pulses with an amplitude between the two levels thus obtained will therefore trigger D_1 but not D_2, and an anticoincidence arrangement connected to the output of the two trigger circuits will only record pulses within that amplitude channel. Potentiometers P_1 and P_2 are used to set zero discriminator level and channel width respectively. Small pulses also appear at the output of the anticoincidence circuit when both D_1 and D_2 are triggered, and the sensitivity of the scaler connected to the output should be adjusted so that only real anticoincidence pulses are counted.

In measurements where γ-ray intensities are compared (3) it is essential that the channel width should be constant over the whole discriminator range. This can be checked by measuring the area of a well-defined photopeak at different positions (using different amplifications) on the discriminator scale. A constancy better than $^1/_2$ % was achieved, with selected 6AC7 tubes. The range of the discriminator is 100 volts and the channel width most often used was 2 volts. The number of pulses larger than the dark-current pulses that can be handled by the instrument without serious piling up effects is about 100 000/min.

Measurements

The spectrometer described has been used for several measurements of γ- and X-ray energies, usually in cases where the activities were too low to be measured in a β-spectrometer (6, 7). The weakest sample measured was $\sim 10^{-5}$ mc (Xe^{129}) and the lowest energy 12.5 keV (Kr^{83}). The instrument has also been used for the measurement of γ- and X-ray intensities and the determination of conversion coefficients (3). Two spectrometers in a coincidence arrangement with 0.25 μs resolving time have been used in order to investigate cascade relations in decay schemes (8).

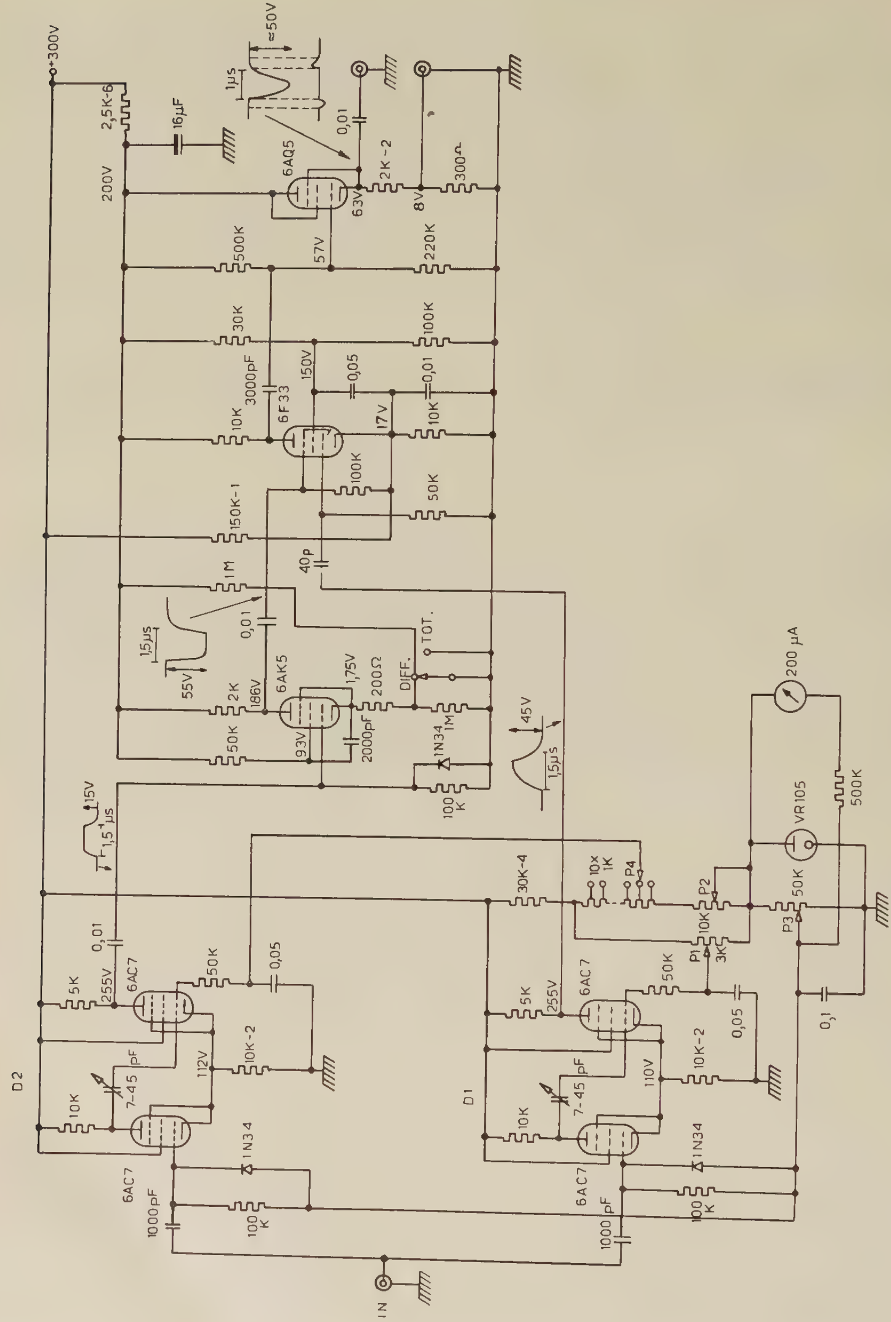

Fig. 3. Circuit of the single-channel discriminator.

Acknowledgement

The author is very much indebted to Mr. R. Backström for highly skilled technical assistance during the design and construction of the scintillation spectrometer.

Nobel Institute of Physics, Stockholm 50, Sweden.

REFERENCES

1. A. E. Johansson, Ark. f. fysik, *2*, 171 (1950).
2. R. Hofstadter and J. A. McIntyre, Nucleonics 7, Sept., 32 (1950).
3. B. Åström, A. H. Wapstra, S. Thulin, and I. Bergström, Ark. f. fysik, *7*, 247 (1953).
4. B. Åström, Rev. Scient. Instr., *21*, 323 (1950).
5. Elmore and Sands, Electronics Experimental Techniques, McGraw-Hill Book Company, 1949.
6. I. Bergström, Ark. f. fysik, Bd *5*, 191 (1951).
7. E. Kondaiah, Ark. f. fysik, Bd *4*, 81 (1951).
8. H. Slätis and L. Zappa, Ark. f. fysik, *6*, 81 (1952).

ARKIV FÖR FYSIK. Bd 7 nr 22

Calibration of a scintillation spectrometer for the comparison of γ- and X-ray intensities

By B. Åström, A. H. Wapstra[1], S. Thulin, and I. Bergström

The efficiency of a NaI (Tl) scintillation spectrometer for detecting electromagnetic radiations of different energies is determined by absorption methods, and by measuring isotopes with simple decay schemes and known internal conversion coefficients.

Introduction. The purpose of this investigation was to calibrate a scintillation spectrometer (1) for the comparison of γ- and X-ray intensities. As it is difficult to separate Compton continua belonging to γ-rays of different energies in the same sample, it was decided to use the area of the photopeak in the scintillation spectrum as a measure of the intensity of the absorbed radiation. For intensity comparison it is then necessary to know the efficiency, defined as the ratio $N_{\text{ph}}/N_{\text{tot}}$. Here N_{ph} means the number of pulses under the photopeak, and N_{tot} is the total number of quanta of corresponding energy entering the crystal.

It should be possible (2, 11) to compute the efficiency for different energies from theoretical absorption coefficients for the photo and Compton effects. As it is necessary to include second order effects – e.g. Compton effects followed by absorption in the crystal of the scattered γ-quantum, resulting in an increase of the photopeak – this computation would be rather difficult and probably not very precise. Only in the region where the Compton effect is relatively unimportant is such a computation feasible. It is then however advisable to use experimentally determined absorption coefficients (see section 4.1).

For higher γ-energies the efficiency can best be determined experimentally by measuring isotopes with simple well-known decay schemes (see section 4.2).

1. Experimental arrangement

The experimental arrangement is shown in fig. 1. An aluminum ring with polished inside surface was cemented with Glyptal to the top of the EMI 5311 photomultiplier. A 12 mm thick NaI (Tl) crystal with cross section 14×16 mm^2 was placed in this ring, and the remaining space filled with paraffin oil. A 2.4 mg/cm^2 Al-foil was placed on top of the whole assembly. This arrangement proved to be satisfactory in preventing detoriation of the crystal due to humidity.

From the optical point of view the arrangement was usable. It was found that the relative half-width $W_{\frac{1}{2}}$ of several photopeaks corresponded fairly well to the formula $W_{\frac{1}{2}}^2 = 0.010 + 0.0085/E$ (E in MeV). The first part will be mostly due to the inhomogenities in the photocathode. This might be improved by using a spacer between photocathode and counting crystal. The last part indicates that the absorption in the crystal of a γ-quantum of energy 1 MeV liberates 870 electrons at the photocathode.

---

[1] On leave from the "Instituut voor Kernphysisch Onderzoek", Amsterdam.

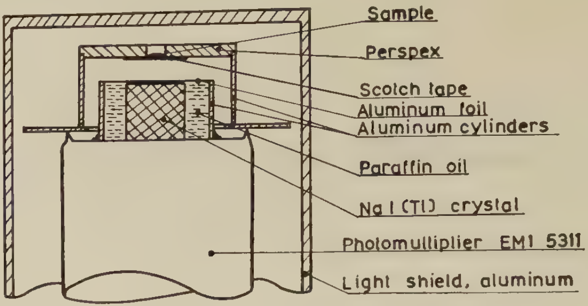

Fig. 1. Arrangement of the counting crystal.

As sample holders, disks of perspex were used, which could be placed on another aluminum ring. When necessary, electrons were absorbed by inserting 3 mm of beryllium between the sample and the crystal.

The distance between sample and crystal was only about 5 mm in order to obtain a large solid angle and make it possible to measure weak samples. This arrangement has the disadvantage that the computation of the γ-efficiency from absorption measurements becomes rather complicated (see section 4). The relative efficiency for different γ-energies is also a rather sensitive function of this distance.

In cases where weak samples were measured a 1 mm thick lead cylinder was put over the aluminum light shield in order to diminish the background.

The electronic part of the spectrometer has been described in (1).

2. Properties of the scintillation spectrometer

Scintillation spectra were obtained by measuring the pulse size distribution with a differential discriminator. This means that the number of pulses within a narrow amplitude band or channel were counted as a function of the setting of this channel in the pulse height scale. The correct way of plotting the spectrum would be to divide the number of pulses found at each setting of the channel by the actual channel width. The measurement of one well-defined peak at different positions in the pulse height scale (by changing the amplification) showed, however, that the channel width was constant to within 0.5 % over the whole range of the discriminator scale. It is of course necessary that the channel width be only a fraction of the whole discriminator scale; we generally used a 2 volt channel and a total range of 100 volts. For precise measurements we also measured the photolines to be compared at the same position on the discriminator scale.

The energy scale was not quite linear and the discriminator setting corresponding to zero γ-energy was at −1.6 V. In order not to spoil the constancy of the channel width, however, we did not try to eliminate these defects, which were unimportant in our investigation.

3. Discussion of the line shapes

As already discussed in the introduction, the photolines are used for the comparison of intensities. However, for some energies the photolines show satellites. The question then arises whether these satellite lines should be included in the photoline or not. For this reason the line shape as a function of energy is discussed.

For energies below 33 keV (this energy being the K-absorption limit in iodine), the absorption is mostly due to the photoeffect in the iodine L-shells. As the very weak L X-rays are to a great extent absorbed in the crystal, one gets a peak at the total energy of the absorbed X- or γ-ray.

Just above 33 keV the absorption in the crystal is high, due to K-shell photoeffect in the iodine, and all rays are absorbed as soon as they enter the crystal. Many of the iodine K X-rays generated have therefore a large chance of escaping from the crystal. Two peaks are thus found: one at the energy of the γ-ray and one at about 30 keV lower energy (the so called "escape peak", see for instance fig. 5). With increasing energy the γ-rays penetrate deeper into the crystal, and the escape peak therefore diminishes. Moreover the relative distance between the two peaks decreases and the two peaks are not separated. This process is almost finished at 80 keV, where only a slight broadening at the low energy side remains. For intensity measurements the escape peak is included in the photopeak.

For γ-rays in the neighbourhood of 150 keV (Kr^{85}, Xe^{131}) (3), a satellite line at about 50 keV lower energy is found. This peak is certainly not due to secondary processes in the crystal, since in absorption experiments it was found to be absorbed faster than the primary γ-rays. It was therefore not included in the photopeak area for γ-intensity comparisons. This peak is rather small, however, so the uncertainty introduced into the results is not large.

For higher energy γ-rays a Compton continuum appears. The shape of this continuum is important as in some cases it must be subtracted as a background (see next section). It consists of a rather broad "Compton peak", followed by a low energy tail that does not go to zero for zero energy, due to the fact that the resolution is proportional to the inverse square root of the energy.

In scintillation spectra of γ-rays with energies of about 0.5 MeV (annihilation radiation, Cs^{137}, Zr^{95}) a peak (a in fig. 4) is found at about 0.2 MeV. This peak is due to Compton scattering of the γ-rays before reaching the crystal (2). Probably the same explanation holds also for the satellite lines of 150 keV γ-rays discussed above.

4. Determination of crystal efficiency

4.1 Absorption measurements. In the energy region where every γ-ray absorbed in the counting crystal gives a light pulse only due to photoabsorption, the efficiency of the NaI (Tl) crystal for a collimated beam of γ-rays can be determined in the following way. The scintillation spectrum is measured with and without an absorbing NaI (Tl) crystal placed between the γ-source and the counting crystal; the ratio of the photopeak areas in these two cases is

$$\frac{S_a}{S} = \exp(-\lambda d),$$

in which λ is the absorption coefficient and d the thickness of the absorbing crystal. The efficiency e of the counting crystal (thickness D) is then

$$e = 1 - \exp(-\lambda D) = 1 - \left(\frac{S_a}{S}\right)^{D/d}.$$

The situation is somewhat more complicated if a collimated beam is not used. We give the computation for a cylindrical counting crystal having radius R and thick-

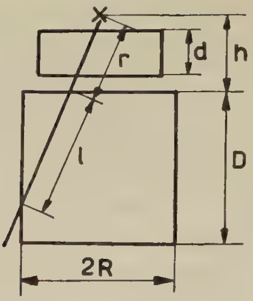

Fig. 2. Symbols used in the calculation of γ-ray paths in absorbing and counting crystals.

ness D, with a point source of γ-rays situated on the axis at a distance h from the surface of the counting crystal (fig. 2). If then the distance to a certain point on this surface is r, the length l of the path of the γ-ray in the absorbing crystal becomes rd/h, and in the counting crystal

$$l = rD/h \qquad \text{for} \quad r < h\sqrt{1+R^2/(h+D)^2} = r'$$

$$l = r\left(R/\sqrt{r^2-h^2}-1\right) \quad \text{for} \quad r' < r < \sqrt{h^2+R^2}.$$

The photopeak area with absorbing crystal interposed then becomes:

$$S_a = cI(\lambda, d),$$

where

$$I(\lambda, d) = \int_h^{\sqrt{h^2+R^2}} \frac{1-\exp(-\lambda l)}{r^2} \exp\left(-\lambda \frac{d}{h} r\right) dr.$$

Without absorber we obtain $S = cI(\lambda, o)$. The efficiency is 1 if all γ-rays incident on the crystal are absorbed:

$$S_0 = cI(\infty, 0).$$

For other cases, using the definition $S = eS_0$, we therefore have

$$e = \frac{I(\lambda, 0)}{I(\infty, 0)}.$$

In order to obtain this efficiency from the experimental results, $S_a/S = I(\lambda, d)/I(\lambda, o)$ and e are computed numerically and plotted as a function of λ. From the first plot, and the experimental value of S/S_a, λ is obtained, and e is then found from the second plot.

In the actual case of an extended source and a counting crystal in the shape of a rectangular parallelepiped the computation becomes more complicated. We therefore still used the formulas above for the computation, taking πR^2 equal to the actual upper surface of the counting crystal. The errors introduced by this approximation are mainly errors in $1-e$; in the case of large absorption coefficients (the first two cases in Table I) the errors in e are therefore small (estimated error 1 %). In the other two cases the error in e is estimated to be about 10 % of its value.

Table I

Efficiencies computed from absorption measurements.

Nuclide	E keV	e
Xe^{133}	30	0.968
Xe^{133}	81	0.916
Kr^{85m}	150	0.60
Xe^{131m}	164	0.55

4.2 Comparison of X- and γ-ray intensities. At higher energies the method discussed above is not convenient, because of low absorption and the uncertainties introduced by the Compton continuum. In this case we have therefore used another method.

If $S_{\gamma 1}$ and $S_{\gamma 2}$ are the areas of two photopeaks in a scintillation spectrum we obtain

$$\frac{S_{\gamma 1}}{S_{\gamma 2}} = \frac{e_{\gamma 1}}{e_{\gamma 2}} \cdot \frac{\gamma_1}{\gamma_2}.$$

Here γ_1 and γ_2 are the intensities of the two radiations, and $e_{\gamma 1}$ and $e_{\gamma 2}$ the crystal efficiencies. In the special case where $\gamma_2 = \gamma$ is a γ-ray and $\gamma_1 = X$ is the corresponding K X-ray, the ratio between the intensities becomes

$$\frac{X}{\gamma} = \alpha_K (1 - W_K)$$

where α_K is the K-conversion coefficient and W_K the Auger conversion probability e.g. the fluorescence yield of the K X-rays.

The ratio of the areas of the photopeaks is then

$$\frac{S_X}{S_\gamma} = \frac{e_X}{e_\gamma} \cdot \alpha_K (1 - W_K)$$

This formula can be used to compute e_γ if α_K and W_K are known and if e_X is determined with method 4.1 described above.

The results obtained for some nuclides are given in Table II.

Table II

Efficiencies determined from scintillation spectra of nuclides with one converted γ-ray.

Nuclide	E keV	α_K	$1-W_K$	S_X/S_γ	e_γ
Xe^{135}	250	0.054 ± 0.005 (4)	0.84 (4)	0.180 ± 0.010	0.245 ± 0.024
Hg^{203}	279	0.154 ± 0.015 (5)	0.95	0.63 ± 0.06	0.220 ± 0.030
Au^{198}	411	0.030 ± 0.002 (6)	0.95	0.30 ± 0.03	0.089 ± 0.013
Cs^{137}	612	0.095 ± 0.005 (7)	0.85	1.46 ± 0.10	0.055 ± 0.005

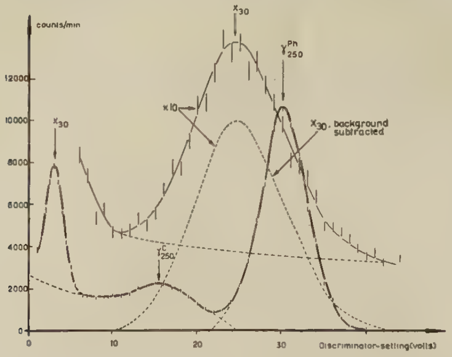

Fig. 3. Scintillation spectrum of Xe^{135}. γ^{Ph}_{250} = photopeak of the 250 keV γ-ray. γ^{C}_{250} = Compton distribution of the 250 keV γ-ray. X_{30} = photopeak of the 30 keV Cs X-ray, measured with two different pulse amplifications.

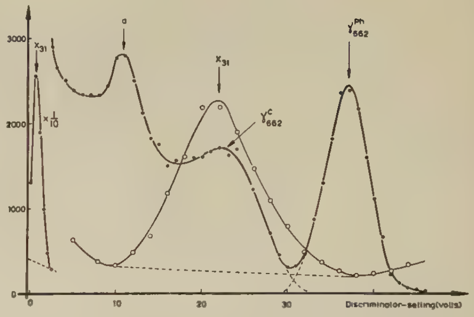

Fig. 4. Scintillation spectrum of Cs^{137} a = satellite peak discussed in section 3.

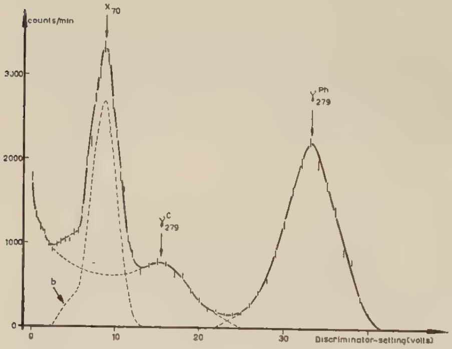

Fig. 5. Scintillation spectrum of Hg^{203} b = escape peak.

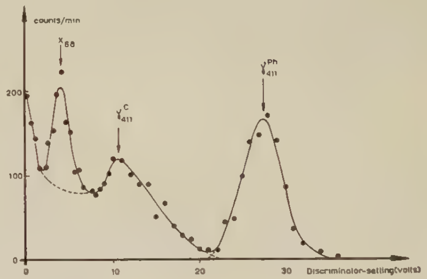

Fig. 6. Scintillation spectrum of Au^{198}.

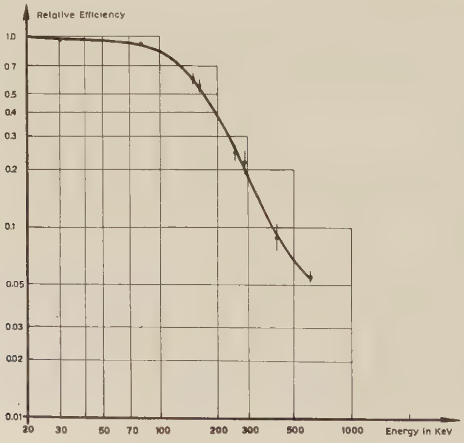

Fig. 7. Crystal efficiency as a function of γ-ray energy.

In these determinations the precision is partially limited by the difficulty of separating the X-ray peak from the Compton distribution of the γ-ray. In the cases of Xe^{135} (fig. 3) and Cs^{137} (fig. 4) this could be done rather precisely, as the shape of the X-ray peak was known fairly accurately from a study of the nuclide Cs^{131}, which emits only X-rays. The result also gave an indication of how the Compton background should be drawn in the scintillation spectra of the other two cases studied (Hg^{203}, fig. 5, and Au^{198}, fig. 6).

Fig. 7 shows the efficiency curve obtained with the two methods described above. This curve might be improved by a more complete study of the Compton background and by using nuclides with better known conversion coefficients. The spectrometer calibrated in this way has been used in order to classify several γ-transitions (3, 7, 8, 9, 10).

Nobel Institute of Physics, Stockholm 50, Sweden.

REFERENCES

1. B. Åström, Ark. f. Fysik, *7*, 241 (1953).
2. R. Hofstadter and J. A. McIntyre, Nucleonics *7*, No. 3, 32 (1950).
3. I. Bergström, S. Thulin, A. H. Wapstra, and B. Åström, Ark. f. Fysik, *7*, 255 (1953).
4. I. Bergström, Ark. f. Fysik, *5*, 191 (1952).
5. S. Thulin and K. Nybö, Ark. f. Fysik, *7*, 289 (1953).
6. G. J. Nijgh and A. H. Wapstra, unpublished work.
7. A. H. Wapstra, Ark. f. Fysik, *7*, 275 (1953).
8. —— Ark. f. Fysik, *7*, 265 (1953).
9. —— Ark. f. Fysik, *7*, 279 (1953).
10. S. Thulin, Ark. f. Fysik, *7*, 269 (1953).

K-conversion coefficients of γ-transitions occurring in the decay of Kr^{85m}, Xe^{129m}, Xe^{131m}, Xe^{133}, and Xe^{133m}

By I. Bergström, S. Thulin, A. H. Wapstra[1], and B. Åström

The *K*-conversion coefficients of γ-rays in the decays of Kr^{85m}, Xe^{129m}, Xe^{131m}, Xe^{133}, and Xe^{133m} have been measured by a combination of β-spectrometer and scintillation methods. The empirical K/L curve of Goldhaber and Sunyar for M4 transitions has been slightly corrected.

Introduction. In a previous paper by one of us (1) a β-spectrometrical study was made on mass-separated samples of the isomers of krypton and xenon. It was, however, not possible to determine from these studies the *K*-conversion coefficients of the isomeric transitions, which is still the best way to determine the multipole order and thus classify the isomers. We have therefore tried to determine the internal conversion coefficients by using a scintillation spectrometer. Its construction and calibration have been described earlier (2, 3).

Determination of internal conversion coefficients with the scintillation spectrometer

For determination of the *K*-conversion coefficients two methods, A and B, have been used.

Method A: In cases where only one γ-ray is emitted the *K* internal conversion coefficient α_K can easily be found, by comparing the γ- and X-ray intensities in a scintillation spectrum, as follows:

$$\alpha_K = \frac{K}{\gamma} = \frac{X}{\gamma F} = \frac{S_X/e_X}{S_\gamma/e_\gamma \cdot (1-W_K)} \qquad (1)$$

where K = intensity of *K*-conversion electrons
X = K X-ray intensity
γ = γ-ray intensity
S_X/S_γ = measured ratio of the areas under the X and γ-photolines in the scintillation spectrum
F = fluorescence yield
$W_K = 1 - F$ = internal conversion probability of K X-rays
e_X and e_γ = X- and γ-ray efficiencies[2] in the scintillation crystal. (These values are obtained from (3) fig. 7.)

---

[1] On leave from the "Instituut voor Kernphysisch Onderzoek", Amsterdam.

[2] The efficiency is defined as the ratio $e = N_{ph}/N_{tot}$. Here N_{ph} is the number of pulses under the photopeak in the scintillation spectrum and N_{tot} is the total number of quanta of the corresponding energy entering the crystal.

This formula is applicable to Xe^{131m} and Xe^{133}. We checked this method with the 81 keV γ-ray following the β-decay in Xe^{133}, the conversion coefficient of which was already known from β-spectrometer measurements. The agreement between the values determined with the two different methods was satisfying. It turned out, however, that in this case the value of the conversion coefficient determined with the scintillation method was far more precise than the β-spectrometer value. This is due to two circumstances:

1. The β-spectrometer value follows from the formula

$$\alpha_K = \frac{K}{\beta - K - L - M \dots} \tag{2}$$

In the case of large conversion coefficients the sum of the intensities of the conversion electrons $K+L+M+\dots$ is comparable with the intensity β of the β-spectrum, so the relative error in their difference becomes very large.

2. For low energy (for example 81 keV) γ-lines, as well as for the X-lines, the efficiencies e_γ and e_X are very nearly 1, so they can be determined with fair precision by an absorption method (3).

Method B: In some cases it is not possible to measure the X-ray intensity accurately. The X-ray line may be partly obscured by dark current pulses (low X-ray energy), or a γ-line may overlap the X-line, making a measurement of the X-ray intensity difficult. In these cases, however, the K internal conversion coefficient α_K of a γ-ray can be obtained from a combination of scintillation and β-spectrometer measurements, as shown in formula (3) below. This method can be used when there are two (or more) γ-rays in the same sample, the photolines of which can be resolved with the scintillation spectrometer. If the K-internal conversion coefficient α_{K_1} of one γ-ray is known we then obtain:

$$\alpha_{K_2} = \frac{K_2}{K_1}\,\frac{\gamma_1}{\gamma_2}\cdot\alpha_{K_1} = \frac{K_2}{K_1}\cdot\frac{S_{\gamma_1}/e_{\gamma_1}}{S_{\gamma_2}/e_{\gamma_2}}\cdot\alpha_{K_1}. \tag{3}$$

Here K_2/K_1 is the ratio of the intensity of the K conversion electrons, a value which can be obtained by β-spectrometer measurements. $S_{\gamma_1}/S_{\gamma_2}$ is the ratio of the area under the γ_1 and γ_2 photolines in the scintillation spectrum. e_{γ_1} and e_{γ_2} are the efficiencies of the γ_1 and γ_2 rays in the scintillation crystal. These values are obtained from (3). In this case it is thus not necessary to know the X-ray intensity.

The internal conversion coefficients of the isomeric transitions in Kr^{85m} and Xe^{133m} were obtained with method B.

The same method was also used for Xe^{129m}. In this case, however, there was a slight complication due to the presence of a γ-line with an energy near the energy of the X-line.

Measurements

Kr^{85m}. Kr^{85m} decays partly by a 305 keV isomeric transition to the ground state of Kr^{85} and partly by a β-transition to a 150 keV excited state in Rb^{85} (1). We have redetermined the conversion coefficient α_{K_1} of the 150 keV γ-ray and the ratio of the conversion lines $(K_2+L_2+\cdots)/(K_1+L_1+\cdots)$ with the intermediate image β-spectrometer (4). In correcting for the presence of L- and M-conversion

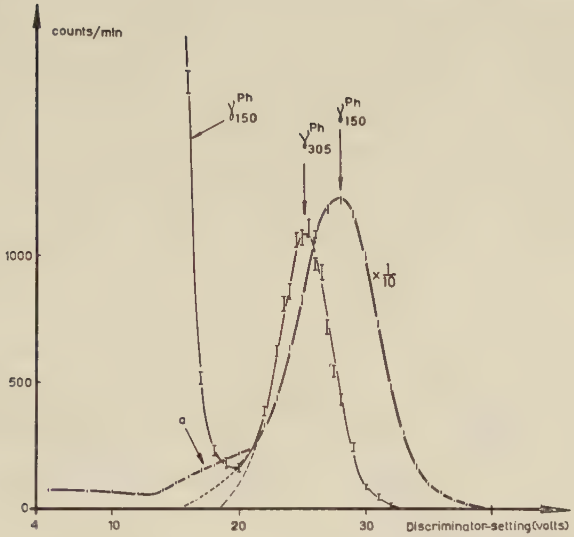

Fig. 1. Scintillation spectrum of Kr^{85m}. a = satellite line discussed in text. γ^{Ph}_{150} = photopeak of 150 keV γ-ray. γ^{Ph}_{305} = photopeak of 305 keV γ-ray, measured with a lower pulse amplification.

lines which were not separated from the K-lines we used for the 305 keV transition $K/(L+M) = 7$ (1); the same ratio for the 150 keV transition we assumed to be ~10(1). We then find

$$\begin{aligned} \alpha_{K_1} &= 0.040 \pm 0.003 \\ \frac{K_2}{K_1} &= 1.8 \pm 0.1. \end{aligned} \tag{4}$$

The scintillation spectrum is shown in figure 1. It clearly shows a satellite line (a), at about 100 keV, belonging to the 150 keV γ-ray (3). The efficiency of our counting crystal for the 150 keV γ-ray was determined by absorption experiments as described in (3). The efficiency for the 305 keV γ-ray was taken from the efficiency curve (3, fig. 7). With these values the ratio of the γ-intensities becomes

$$\gamma_1/\gamma_2 = 5.7 \pm 0.7. \tag{5}$$

Here the largest contribution to the uncertainty is due to the errors in the efficiencies. Using these data in formula (3) the K-conversion coefficient of the isomeric transition becomes

$$\alpha_{K_2} = 0.41 \pm 0.06. \tag{6}$$

From the data of Rose *et al.* (5) we find $\alpha_K = 0.48$ for a pure M4 and 0.85 for a pure E5 transition. Our value thus indicates an M4 transition, since the K-internal conversion coefficients for E4 and M3 radiations are much lower than 0.41.

Xe^{129m}. As earlier supposed by one of us (1) the 196 keV isomeric transition in this isomer is followed by a second γ-transition. Another paper (6) in this series

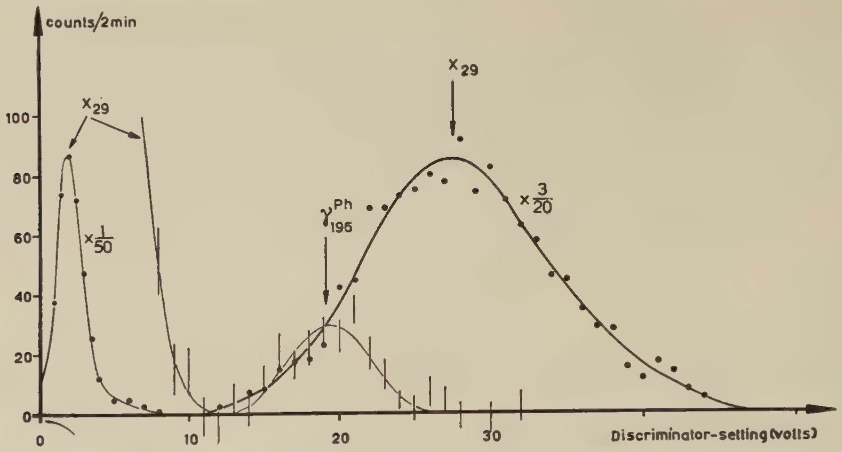

Fig. 2. Scintillation spectrum of Xe^{129m}. X_{29} = photopeak of 29 keV Xe X-ray, measured with two different pulse amplifications.

describes the discovery of this transition, which proved to have an energy of 40 keV. This means that the low energy γ-ray cannot be separated from the 29.2 keV X-line in our scintillation spectrometer. The ratio R of the intensities of the $X+\gamma_1$ and γ_2 peak in the scintillation spectrum thus becomes:

$$R=\frac{X+\gamma_1}{\gamma_2}=\frac{K_1+K_2-A+\gamma_1}{\gamma_2} \tag{7}$$

in which K_1 and K_2 are the intensities of K-conversion electrons corresponding to the γ-rays γ_1 (40 keV) and γ_2 (196 keV), and A the intensity of the K Auger electrons. We eliminate K_1 using the cascade relation

$$K_1+L_1+\gamma_1=K_2+L_2+\gamma_2. \tag{8}$$

Here L_1 and L_2 include the M, N . . . conversion electrons. We then find:

$$R=1+\alpha_{K_2}\left(2+L_2/K_2-\frac{A+L_1}{K_2}\right). \tag{9}$$

The ratios L_2/K_2 and $(A+L_1)/K_2$ are determined with the β-spectrometer. Thus the overlapping of the A and L_1 lines does not influence the intensity relation above (cf 6). Using the values given in (6), Table 1 we find:

$$\alpha_{K_2}=\frac{R-1}{1.76\pm0.07}. \tag{10}$$

Xe^{129m} was difficult to prepare in sufficient intensity in the isotope separator, due to the saturation effect caused by the large abundance of stable Xe^{129} (6) and to the fact that the unconverted γ_2 ray is rather weak.

Fig. 2 shows one of the two scintillation spectra that were measured. The con-

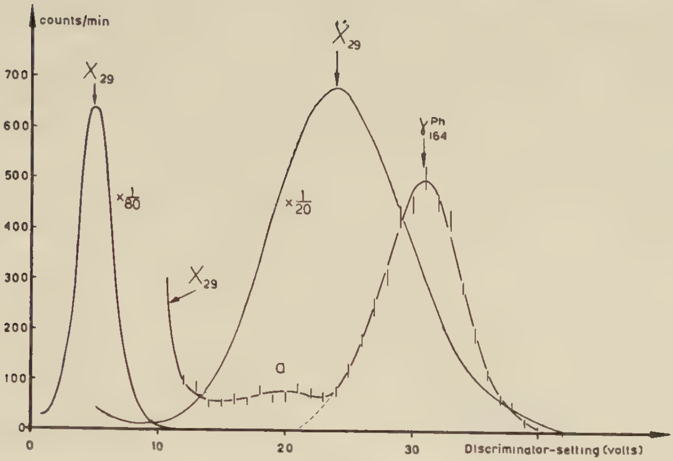

Fig. 3. Scintillation spectrum of Xe^{131m}. a = satellite line discussed in text.

version electrons were absorbed with 2 mm Be. From these spectra and using the efficiencies determined in (3), we find $R = 20$ and therefore[1]

$$\alpha_{K_2} = 11 \pm 3. \tag{11}$$

The tables of Rose *et al.* (5) give $\alpha_K - 14$ for M4 transitions and $\alpha_K = 9$ for E5 transitions. Our value would thus indicate a mixture of M4 and E5 radiations. This, however, is in disagreement with the intensity ratio $K/L = 2.76$, which indicates pure M4 transition (fig. 6). (According to Goldhaber and Sunyar (7) K/L should be less than 1 for E5 transitions). The isomeric transition in Xe^{129m} is thus most probably due to a pure M4 transition, and the K-internal conversion coefficient of the isomeric γ-ray in Xe^{129m} determined with the scintillation method is therefore probably somewhat too low.

Xe^{131m}. This isomer decays by the emission of only one γ-ray, of energy 164 keV. Fig. 3 gives one of the several scintillation spectra that were measured. At about 107 keV it shows the satellite a of the 164 keV line discussed in (3). In this case we were able to show that this peak was not directly due to the 164 keV γ-line. In absorption experiments (by placing a thin NaI crystal between the sample and the counting crystal) this satellite was more absorbed than the γ-line itself. From these spectra, using the value 0.16 ± 0.02 for the internal conversion probability W_K and the previously determined efficiencies (3) of our crystal for the 164 keV γ- and the 29 keV X-rays, we find according to Eq. 1

$$\alpha_K = 29 \pm 4. \tag{12}$$

Here the error is almost entirely due to the uncertainty in the 164 keV γ-efficiency. The value is to be compared with the theoretical values 34 for M4 and 21 for E5 transitions (15); it is in better agreement with the M4 value. This result agrees with the former assignment based on the K/L ratio.

---

[1] For the $X + \gamma_1$ peak we used the efficiency for the X-peak alone, as the admixture of γ_1 rays is only of a low intensity and the efficiency of their detection is only slightly different.

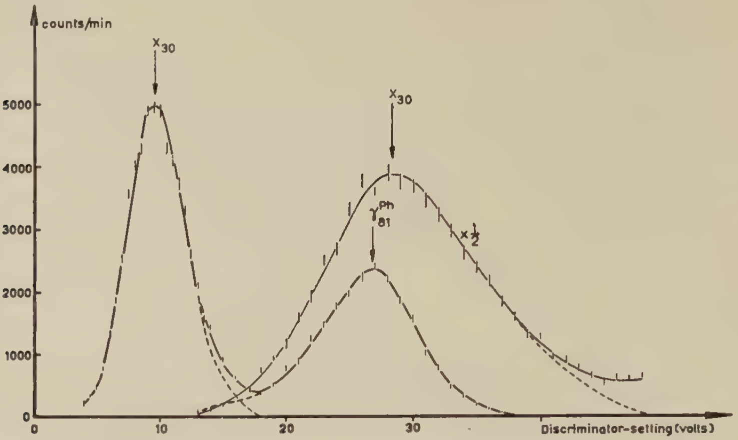

Fig. 4. Scintillation spectrum of Xe^{133}.

Xe^{133}. If the Xe^{133} is separated from fission gases the activity of the 5.3 day ground state is much stronger than that of the 2.3 day isomeric state (1). After some weeks it is thus possible to get almost pure 5.3 day Xe^{133} samples.

Fig. 4 gives a scintillation spectrum of such a Xe^{133} sample. The 81 keV γ-line (following the β-decay) and the K X-rays due to its K-conversion are not quite separated, partly due to the low energy tail of the 81 keV photoline (escape peak, see (3)). This is a pity, as the high precision with which the efficiencies can be determined in this case (see (3)) would allow a very good determination of the conversion coefficient if an analysis of the lines could be made accurately. We therefore tried to determine a "window curve" for the 30.2 keV X-line. For this purpose a sample of Cs^{131} was used. This is a K-capturing nucleus emitting only X-rays, of which the K_a X-rays have the energy 29.1 keV. The K X-ray peak of Cs^{131} was shifted by computation to the position of the 30.2 keV Cs K X-ray in Xe^{133} and used as window curve. It is estimated that the systematic errors introduced by this method are of the order of 1% or less, the random errors being of the same order. Three different scintillation spectra measured and computed by different observers gave intensity ratios X/γ agreeing within 1%. Again using the K internal conversion probability 0.16 ± 0.02 (1), and the crystal efficiencies determined by absorption, we find using Eq. 1.

$$\alpha_K = 1.47 \pm 0.05. \tag{13}$$

In this case the greater part of the error is due to the uncertainty in W_K. This new value is in agreement with the value

$$\alpha_K = 1.50 \pm 0.15 \tag{14}$$

which was β-spectrometrically determined as discussed previously (1). It indicates a pure M1-transition (cf. Table 1).

Xe^{133m}. This isotope decays by the emission of a 232 keV γ-ray to the ground state of Xe^{133}, which by β-emission decays to a level in Cs^{133} from which an 81 keV γ-ray is emitted.

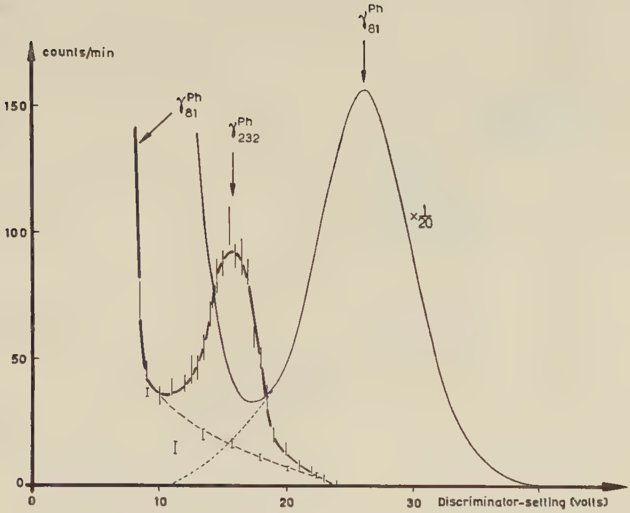

Fig. 5. Scintillation spectrum of Xe^{133m}.

From the β-spectrum of $Xe^{133m} + Xe^{133}$ the intensity ratio K_1/K_2 of the K-conversion lines corresponding to the 81 and 232 keV γ-rays can be calculated. After decay correction to the time when the scintillation spectrum was measured we obtain:

$$K_1/K_2 = 8 \pm 2. \tag{15}$$

The scintillation spectrum is shown in fig. 5. In order to separate the 81 keV and the 232 keV peaks the spectrum was remeasured nine days later. At this time the Xe^{133m} had decayed far more than the Xe^{133}, so after multiplying the second spectrum by the decay factor for Xe^{133} the difference of the two spectra should give a good idea of the shape and intensity of the 232 keV photo-line. The initial ratio of the two γ-peaks, using the crystal counting efficiencies derived from (3), then becomes

$$\gamma_1/\gamma_2 = 24 \pm 5. \tag{16}$$

Using now the conversion coefficient of the Xe^{133} 81 keV γ-ray (Eq. 13), we find, from Eq. 3,

$$a_{K_2} = 4.4 \pm 1.4. \tag{17}$$

This value should be compared with the theoretical values 6.6 for M4 and 4.1 for E5 transitions (15). So our value might indicate admixture of E5-radiation. This explanation is at variance with the experimentally found K/L ratio 2.9 (1), which classifies (7) the isomeric transition in Xe^{133m} as an M4-transition. (A pure E5 transition would according to GOLDHABER and SUNYAR require a value of $K/L - 1.0$.) This disagreement may however at least partially be explained by the difficulties in this measurement due to the low intensity of the 232 keV line in both β-spectrum and scintillation spectrum.

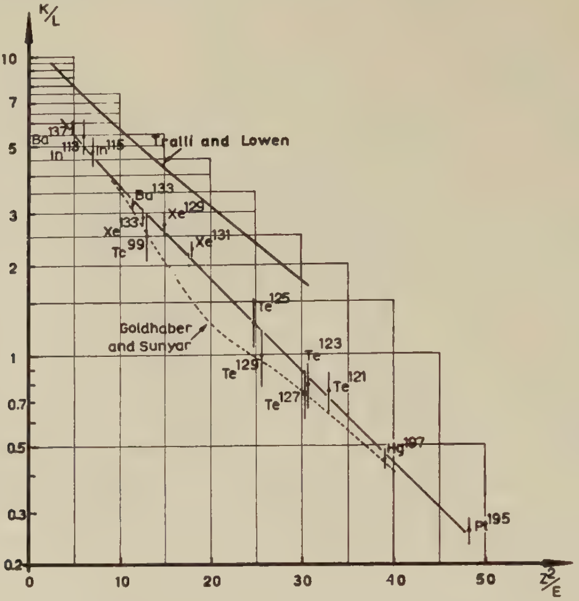

Fig. 6. K/L ratios for M4 transitions.

Conclusions

The results of our measurements are collected in the table below:

Table I

Nuclide	γ-energy	α_K	Theoretical values	
Kr^{85m}	305 keV	0.41 ± 0.06	0.48 (M4)	0.85 (E5)
Xe^{129m}	196	11 ± 4	14 (M4)	9 (E5)
Xe^{131m}	164	29 ± 4	34 (M4)	21 (E5)
Xe^{133}	81	1.47 ± 0.04	1.4 (M1)	2.6 (E2)
Xe^{133m}	232	4.4 ± 1.4	6.6 (M4)	4.1 (E5)

In this table we find that the results are in good agreement with the spin-orbit coupling theory, which suggests M4 or (and) E5 transitions in the isomers of Kr^{85m}, Xe^{129m}, Xe^{131m}, and Xe^{133m}. However, the interesting question whether these transitions are due to pure M4 or a mixture of M4 and E5 transitions cannot be answered unambigously for Xe^{129m} and Xe^{133m} by measurements with the rather weak samples available to us. The semi-empirical K/L curves for magnetic transitions given by GOLDHABER and SUNYAR (7) might therefore in these two cases give a more unambiguous classification. The ratios of the intensities of the K and L conversion lines in Xe^{129m} and Xe^{131m} found by one of us (1) were, however, considerably higher than those given in the plot for M4 K/L ratios in the paper of GOLDHABER and SUNYAR (7). As our values were considered to be rather accurate we rechecked the papers mentioned by GOLDHABER and SUNYAR. It turned out that many of the ratios included by them were $K/(L+M)$ ratios. In Fig. 6 we give therefore another plot including only values for which it is reasonably sure that they are K/L and not $K/(L+M)$ ratios. We have also included Ba^{137m} (8) and Pt^{195m} (9). The errors indicated are estimated by us if not mentioned in the original papers. From fig. 6 it is clear that the shape of the experimental plot is now in better agreement with the theoretical one computed by TRALLI and LOWEN (10), though their values certainly are too high.

Nobel Institute of Physics, Stockholm 50, Sweden.

REFERENCES

1. I. BERGSTRÖM, Ark. f. Fysik. Bd 5, Nr 14, 191 (1953).
2. B. ÅSTRÖM, Ark. f. Fysik, *7*, 241 (1953).
3. B. ÅSTRÖM, A. H. WAPSTRA, S. THULIN, and I. BERGSTRÖM, Ark. f. Fysik *7*, 247 (1953).
4. H. SLÄTIS and K. SIEGBAHN, Ark. f. Fysik, *1*, 339, 1950.
5. M. E. ROSE, G. H. GOERTZEL, B. J. SPINRAD, J. HARR, and P. STRONG, privately circulated tables.
6. S. THULIN, Ark. f. Fysik *7*, 269 (1953).
7. M. GOLDHABER and A. W. SUNYAR, Phys. Rev. *83*, 906, 1951.
8. A. H. WAPSTRA, Ark. f. Fysik. *7*, 275 (1953).
9. Private communication of O. HUBER.
10. TRALLI and LOWEN, Phys. Rev. *76*, 1541, 1941.

K-conversion coefficient of the isomeric γ-ray in Ag^{109}

By A. H. WAPSTRA[1]

By scintillation spectrometer measurements the *K*-conversion coefficient of the 40 sec. Ag^{109m} isomeric transition is found to be 9.5 ± 1 (E3 transition).

Introduction. The 40 sec. isomer Ag^{109m} is produced both by the 13 hr β-transition in Pd^{109} (1) and by the 470 days electron capture in Cd^{109} (2). In both cases it is difficult to determine the conversion coefficients from β-spectrometer measurements, for reasons similar to those mentioned in the case of Xe^{133} (15). We therefore planned to measure this conversion coefficient using scintillation spectrometry. In this determination we need to know the internal conversion $K/(L+M)$ ratio. Since the reported values were controversial (1.3 (1) and 0.86 ± 0.07 (2)) we also redetermined this ratio. Published values of the *K*-conversion coefficient are $\gtrsim 6.6$ (1) and 8.8 ± 1.5 (2).

The $K/(L+M)$ ratio

In order to determine this ratio we used an intermediate-image β-spectrometer (4) with a resolution of 5 %. The sample was Cd^{109} prepared by a (d, 2n) reaction on silver, using the 28 MeV deuterons of the Philips Synchro-cyclotron in the "Instituut voor Kernphysisch Onderzoek" in Amsterdam. It was used in the form of CdO spread on an 0.15 mg/cm² Al backing. The quality of the sample can be judged from the *K* and $L+M$ conversion lines shown in fig. 1 and from the fact that the Auger lines (18 and 22 keV) were almost separated. The intensity of the conversion lines was not influenced by absorption in the Geiger window as its cut-off was only 9 keV. The ratio of the intensities of the conversion lines in two runs with different samples agreed well and gave a value $K/(L+M) = 0.80 \pm 0.04$. The energy of the K-conversion electrons was 62.0 keV, and of the *L* electrons 84.2 keV, yielding values of 87.5 and 88.0 keV for the energy, using the calibration discussed in another paper (5). The last value is of course influenced by the unknown admixture of *M* converted electrons. Our best value 87.5 ± 0.8 keV is in agreement with former values 89 keV (2), 87 keV (1) and 87.5 keV (6).

The *K*-conversion coefficient

The scintillation spectrum of Cd^{109} is shown in Fig. 2. It shows a strong *K* X-line and a much weaker 87 keV γ-ray. The low energy side of the *K* X-line does not go back to zero, as may be seen more clearly in a spectrum taken with higher amplification (inset in fig. 2). There appears to be a line at about 6.5 keV, the origin of which is unknown. (It should be noticed that zero energy corresponds to -1.6 V

---

[1] On leave from the "Instituut voor Kernphysisch Onderzoek".

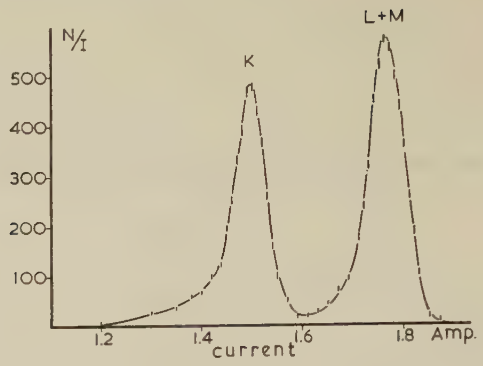

Fig. 1. Conversion lines of the isomeric γ-ray in Ag^{109m}.

on the discriminator scale (14). We assumed that this is a real line, so that there is not a continuously rising background below the K line; we therefore extrapolated the low energy end of the K line as shown in fig. 2. The ratio X_K/γ of the intensities of the X-rays and the 87 keV γ-rays, using the crystal efficiencies determined before (14) is then 33.8 ± 2.5.

In order to compute the conversion coefficient we assume that all electron capture processes in Cd^{109} lead to the isomeric state (2). If now a fraction X of these transitions are K-captures (the rest being L, M . . . captures) the number of K-vacancies per decay is

$$K_v = X + \frac{\alpha_K}{1 + \alpha_K (1 + L_I/K)} \cdot$$

The second term in this expression is due to K-conversion of the isomeric transition (L_1 means $L + M + \ldots$). The number of γ-rays per decay is

$$\gamma = \frac{1}{1 + \alpha_K (1 + L_I/K)}$$

so from the ratio $R = K_v/\gamma$ we can compute α_K. We find

$$\alpha_K = \frac{R - X}{X (1 + L_I/K) + 1} \cdot$$

Theoretical reasoning (see appendix) gives a value 0.78 for X. R is related to the ratio X_K/γ determined above and the internal conversion probability W_K of the Ag K X-rays by the formula $R = \frac{1}{1 - W_K} \cdot \frac{X_K}{\gamma}$. For W_K HUBER *et al.* (3) measured a value 0.17 ± 0.02, rather lower than the theoretical value 0.22. This should, however, be compared with the agreement between the theoretical value 0.15 and the experimental value 0.16 ± 0.02 for Xe (7). We therefore assumed a value 0.20 ± 0.03 for Ag; R then becomes 27.1 ± 2. With the values mentioned the K-conversion coefficient of the 87 keV isomeric transition in Ag^{109} becomes

$$\alpha_K = 9.5 \pm 1.0.$$

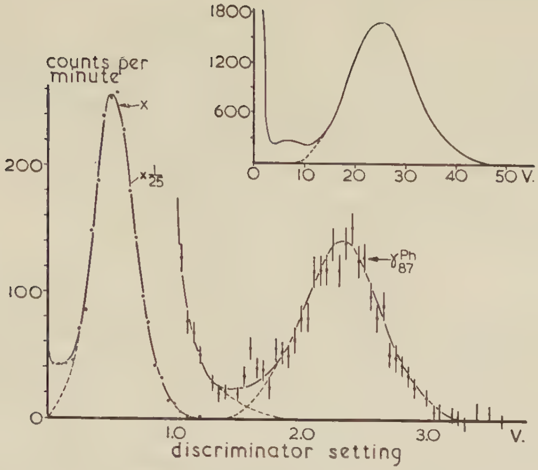

Fig. 2. Scintillation spectrum of Cd^{109}. The inset shows the K X-line taken with higher amplification.

This value is only in agreement with the theoretical value 11.0 for an E3 transition (13). It should be compared with the value 8.8 ± 1.5 (2), which value is, however, not corrected for the presence of L-capture, as is also the case in a very recent paper (3) of the same group (after such a correction it comes out to be 9.5).

Appendix. Computation of the relative number of *K*-captures

Apart from K-capture only L_I-capture is important for allowed transitions. The ratio between these is given (7) (see also 16) by the formula

$$\frac{L_I}{K}=\frac{1}{8}\left(\frac{Z-4.15}{Z-0.40}\right)^3\left(\frac{\Delta-B_L}{\Delta-B_K}\right)^2$$

in which Δ is the decay energy, B_L and B_K the binding energy of the L- and K-electrons, $(Z-4.15)$ the effective nuclear charge for the L_1-electrons, and $(Z-0.40)$ that for the K-electrons. We first tried to obtain Δ by plotting the difference in binding energies of the Cd-Ag isobaric pairs for the mass numbers 107 (8), 111 (9), 113 and 115 (10). We thus found a decay energy of only 95 keV for the $Cd^{109}-Ag^{109m}$ decay. Since for such low energies the L/K capture ratio is rather sensitive to small alterations in Δ we also tried to determine Δ by comparing the K-capture half-life with that of the similar transition in the 6.7 hour Cd^{107}. The decay energy of this transition is known to be 1340 keV from the β^+ transition between the same states (8); the above formula yields $L/K=0.101$ for this transition. As the intensities from transitions to other levels, and also from the β^+ transition, are very low (8), the partial half-life for K-capture becomes 7.4 h. The half-life of Cd^{109} is 470 days (11), so the partial half-life for K-capture is 470/X days. Now the K-capture half-life is proportional to the inverse square of the energy of the outgoing neutrino $(\Delta-B_K)^2$ (12), so using the values $B_K=25.5$ keV ($B_L=3.8$ keV) and $\Delta_{107}=1340$ keV it follows that

$$\Delta_{109} - B_K = 33.6 \sqrt{X}.$$

Inserting this result in the above formula and using the relation $L/K = (1 - X)/X$ we compute $X = 0.78$. With this value Δ becomes 56 keV, which is indeed somewhat lower than the value 95 keV derived above; from the latter value follows $X = 0.86$. We consider the first value to be far more reliable.

Nobel Institute of Physics, Stockholm 50, Sweden.

REFERENCES

1. K. Siegbahn, E. Kondaiah, and S. Johansson, Nature, *164*, 405 (1949).
2. H. Bradt, P. C. Gugelot, O. Huber, H. Medicus, P. Preiswerk, P. Scherrer, and R. Steffen, Helv. Phys. Acta *20*, 153 (1947).
3. O. Huber, F. Humbel, H. Schneider, and A. de Shalit, Helv. Phys. Acta *25*, 1 (1952).
4. H. Slätis and K. Siegbahn, Ark. f. Fysik *1*, 339 (1950).
5. A. H. Wapstra, Ark. f. Fysik *6*, 263 (1953).
6. J. M. Cork, W. C. Rutledge, A. E. Stoddard, C. E. Branyan, and J. LeBlanc, Phys. Rev. *79*, 238A (1950).
7. R. E. Marshak, Phys. Rev. *61*, 431 (1942).
8. H. Bradt, P. C. Gugelot, O. Huber, H. Medicus, P. Preiswerk, and H. Scherrer, Helv. Phys. Acta *18*, 351 (1945).
9. C. L. McGinnis, Phys. Rev. *81*, 734 (1951).
10. R. B. Duffield and J. D. Knight, Phys. Rev. *75*, 1613 (1949).
11. J. R. Gum and M. C. Pool, Phys. Rev. *80*, 315 (1950).
12. E. J. Konopinski, Rev. Mod. Phys. *15*, 209 (1943).
13. M. Goldhaber and A. W. Sunyar, Phys. Rev. *83*, 906 (1951).
14. B. Åström, A. H. Wapstra, S. Thulin, and I. Bergström, Ark. f. Fysik *7*, 247 (1953).
15. I. Bergström, S. Thulin, A. H. Wapstra, and B. Åström, Ark. f. Fysik *7*, 255 (1953).
16. M. E. Rose and J. L. Jackson, Phys. Rev. 76, 1540 (1949).

ARKIV FÖR FYSIK. Bd 7 nr 22

The decay of Xe^{129m}

By Sigvard Thulin

A second γ-transition in the decay of Xe^{129m} has been found. The energy of the corresponding γ-ray is 40.0 ± 0.5 keV, and the $K/L+M$ ratio 4.3 ± 0.7. A decay scheme is presented.

Introduction. The 8.0 d isomer of Xe^{129} was discovered in 1951 by Bergström (1). The technique of electromagnetic isotope separation was used to prepare a β-sample of the isotope from pile-irradiated Xe. β-spectrometer measurements showed the presence of K and $(L+M)$-electrons of a 196 keV γ-ray. The $K/(L+M)$ ratio (2.1) indicated that the γ-ray was probably due to an M4 transition. In terms of the strong spin-orbit coupling model (2) this would mean a transition between a $h_{11/2}$ and a $d_{3/2}$ state. The ground state of Xe^{129}, however, is known to have the spin $^1/_2$ $(s_{1/2})$. In order to obtain agreement with the j-j model it was therefore plausible to postulate a second γ-ray in the Xe^{129m} decay, corresponding to a $d_{3/2}-s_{1/2}$ transition. Experimental support for this prediction was also found in an investigation of Borkowsky and Brosi (3), who have reported a 39 keV γ-ray in the decay of I^{129}, which might be emitted from a low-lying state in Xe^{129}. The presence of γ-cascades of the type $h_{11/2}-d_{3/2}-s_{1/2}$ in various Te and Sn isomers also favoured the assumption of a second γ-ray in the Xe^{129m} decay. The plot published by Hill (4), showing the changes of the relative energies of the $h_{11/2}$, $d_{3/2}$ and $s_{1/2}$ states as a function of neutron number for several isomers, indicated that the $d_{3/2}-s_{1/2}$ transition in Xe^{129} should be of low energy. Our measurements indeed showed the presence of a 40 keV γ-ray (5, preliminar report), in addition to the earlier known 196 keV γ-ray.

β-spectrometer sample

The β-sample of Xe^{129m} was prepared by means of electromagnetic isotope separation. The obtainable activity is seriously limited by the presence of the stable Xe^{129} isotope, which has an abundance of 26.2 %. Experiments have shown that saturation effects occur when amounts of the order of 2 $\mu g/cm^2$ of a rare gas are collected on an aluminium disc. The maximum obtainable Xe^{129} activity is therefore determined by the specific activity of the Xe sample and is limited by saturation of stable Xe^{129} in the target. This phenomenon explains the rather weak activity of the β-sample used.

Due to the presence of Xe^{129} it was also impossible to use very thin collector foils, which would have been burnt. We therefore used a 70 mg/cm^2 aluminium foil as a backing for the β-sample.

β-spectrometer measurements

The electron spectrum was measured in the intermediate image spectrometer with a resolution of ~5 %. The GM-counter was provided with a nylon window having a cut-

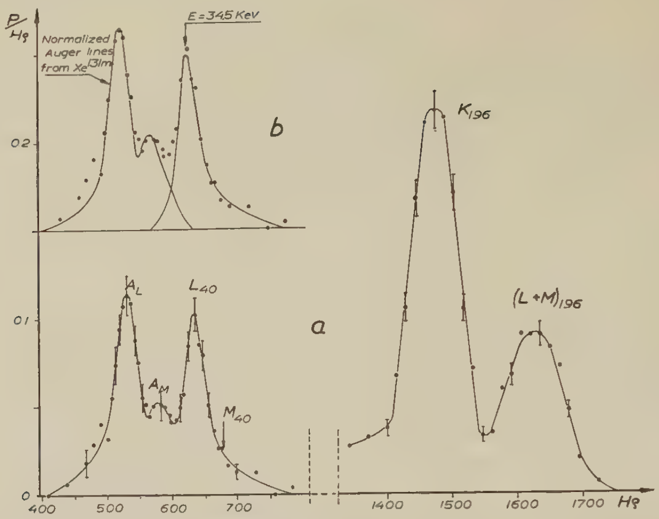

Fig. 1. a) Electron spectrum of Xe^{129m}. b) The components of the low-energy line group, as obtained when using the normalized Auger lines of a similar Xe^{131m} β-sample for the analysis.

off[1] of 9 keV. The electron lines of Xe^{129m} are shown in Fig. 1 a. In addition to the Auger lines A_L of energy $E_K - E_L - E'_L$, and A_M of energy $E_K - E_L - E'_M$, and the earlier reported K and $(L+M)$ conversion lines of a 196 keV γ-ray, there is an electron line at the energy 34.5 keV. This line is interpreted as an $(L+M)$ line, mainly on the grounds of the Auger line intensity. The K X-ray conversion probability (1 − fluorescence yield) for Xe is known to be 0.16. This value has been experimentally obtained by measuring the intensity ratio of the Auger lines and the K_{163} conversion line of Xe^{131m}, (thin GM-window, no Auger line absorption) (6). The Auger line intensity of Xe^{129m}, however, is ~ 0.4 times the K_{196} line intensity. This means that a considerable part of the Auger electrons are due to K conversion electrons of another γ-ray. The intensity of the corresponding K-line should be 7 times higher than the intensity of the 34.5 keV electron line. The 34.5 keV line is therefore most probably the L-line of a 40 keV γ-ray. Moreover, the tail on the high energy side of the 34.5 keV line indicates the presence of an M-line. The corresponding K-line has an energy of 5.4 keV and could not be detected with the GM-window used.

The presence of Auger lines close to the low energy conversion line (cf. Fig. 1) can be used for the energy determination of the corresponding γ-ray. The uncertainties due to remanence in the magnetic lens are eliminated by using the A_L line as a calibration line. From X-ray data and theoretical calculations of the relative intensities of the different Auger line components (7) the energy of the A_L peak is expected to be 24.4 keV (6). Using this line for calibration, we obtain the energies 34.5, 34.5 and 34.6 keV for the L_{40} line, measured in three different runs. In order to compute the energy of the corresponding γ-ray, it is essential to know the relative intensities of the L_I, L_{II} and L_{III} conversion electrons. According to the curves of Tralli and Lowen (8) the ratio of the magnetic internal conversion coefficient for the L_{III} shell to that for the L_I shell is ~ 0.03 and the corresponding ratio for the L_{II} to the L_I shell is ~ 0.05. These values are valid for M1 transitions and $Z = 35$, but may be considered as a justification for using the L_I binding energy in the calculation of the γ-ray energy from the 34.5 keV L line. We then obtain $E_\gamma = 40.0$ keV with a maximum error of ± 0.5 keV.

---

[1] The cut-off is here defined as the energy at which the linearly extrapolated plot of the low-energy part of the Co^{60} β-spectrum cuts the energy axis.

$K/L+M$ ratio of the 40 keV γ-ray

The $K/(L+M)$ ratio of the 40 keV γ-ray can in principle be determined by two different methods. In this case method II below is the most reliable.

Method I. The total intensity of the K conversion lines can be calculated from the relation

$$K_{40} + K_{196} = \frac{A_L + A_M + \cdots}{W_K}$$

where K_{40}, K_{196}, A_L, and A_M denote the intensities of the corresponding lines, and $W_K = 0.16$ is the conversion probability of K X-rays. Dividing by the intensity $(L+M)_{40}$ and rearranging, we obtain

$$\frac{K_{40}}{(L+M)_{40}} = \frac{A_L + A_M}{W_K\,(L+M)_{40}} - \frac{K_{196}}{(L+M)_{40}}. \tag{1}$$

The intensity ratios on the right-hand side of Eq. (1) are obtained by comparing the areas of the corresponding electron lines. This demands an analysis of the low energy line group and an estimate of the GM-window absorption. For this purpose the electron spectrum of Xe^{131} was measured under the same conditions as for Xe^{129}. The Auger lines of Xe^{131m} are then normalized to the A_L peak of Xe^{129m}, as shown in Fig. 1 b. The absorption of Auger lines in the GM counter window was obtained by comparing the intensities of the Auger lines and the K_{133} line in Xe^{131m}. This ratio should be 0.16, as mentioned above. The discrepancy obtained indicated an Auger line absorption of 20 %, which was corrected for in the area comparisons. The GM window absorption of the L_{40} line was probably less than 5 % and has been neglected.

Table 1 shows measured intensity ratios from three different β-spectrometer measurements on Xe^{129}, and calculated $K_{40}/(L+M)_{40}$ ratios.

Table 1

Intensity ratios of the electron lines of Xe^{129m}.

Run	Measured			Calculated
	$(A_L + A_M)/K_{196}$	$K_{196}/(L+M)_{196}$	$(L+M)_{40}/K_{196}$	$K_{40}/(L+M)_{40}$
1	0.462	2.04	0.276	6.9
2	0.442	2.17	0.259	6.8
3	0.455	2.00	0.262	7.1
M. V.	0.45 ± 0.06	2.1 ± 0.1	0.27 ± 0.03	6.9 ± 2.4

The consistency in the data from different runs does not indicate the real accuracy. Due to the statistical errors there are uncertainties in the shapes of the Auger line group and the $(L+M)_{40}$ line. In Table 1 we have given maximum errors. Though this method for the determination of $K/(L+M)$ ratios does not give accurate results in this case, it should in principle be usable. It illustrates another use of the appearance of Auger lines in β-spectrometer work.

Method II. The $K_{40}/(L+M)_{40}$ ratio can also be calculated from the cascade relation

$$K_{40}+L_{40}+M_{40}+\cdots\gamma_{40}=K_{196}+L_{196}+M_{196}+\cdots\gamma_{196} \tag{2}$$

where $K, L, M \ldots \gamma$ denote the relative intensities of the corresponding radiation. From (2) we find

$$\frac{K_{40}}{(L+M)_{40}}=\frac{\dfrac{K_{196}}{(L+M)_{40}}\left(1+\dfrac{(L+M)_{196}}{K_{196}}+\dfrac{1}{\alpha_{K196}}\right)-1}{1+\dfrac{1}{\alpha_{K40}}} \tag{3}$$

where $\alpha_K=K/\gamma$. The relative line intensities on the right side of (3) are obtained from Table 1.

By the scintillation spectrometer method $\alpha_{K_{196}}$ has been found to 11 (9). For $\alpha_{K_{40}}$ we have used a theoretical value, the computation of which demands an assumption on the radiation type of the 40 keV γ-ray. According to the nuclear shell model (2) this transition should be of M1 (or M1+E2) type. Using the curves of AXEL and GOODRICH (10) and the formula of DANCOFF and MORRISON, as presented by FLÜGGE (11), we obtain for M1 ratiation $\alpha_{K_{40}}=7.8$[1] which, inserted in Eq. (3), gives

$$\frac{K_{40}}{(L+M)_{40}}=4.3\pm0.7.$$

It is to be noticed that the result above is not very sensitive to different assumptions regarding the radiation type of the 40 keV γ-ray. In the case of total conversion of this γ-ray, for example, we obtain the largest possible value $K_{40}/(L+M)_{40}=4.8\pm0.7$. Thus we conclude that the value 6.9 obtained by method I is too high.

Classification of the γ-transitions. Decay scheme

The internal conversion coefficient of the 196 keV γ-ray, determined by the scintillation spectrometer method (9), indicates that the isomeric transition is of the M4+E5 type. An independent classification of this transition can be obtained from the empirical curve of the K/L ratio for M4 transitions given in (9). The experimental $K_{196}/(L+M)_{196}$ ratio is 2.1. The L/M ratio for the M4 transitions in Xe^{131m} and Xe^{133m} is 0.30 (6). Using the same L/M ratio for Xe^{129m} we obtain $K_{196}/L_{196}=2.7$. This value fits well to the K/L curve for pure M4 transitions. We therefore conclude that the isomeric transition in Xe^{129m} is essentially of the M4 type. The value $\alpha_K=11\pm3$ obtained in the scintillation spectrometer measurements (9) is probably somewhat low.

---

[1] A rough estimate of the K-conversion coefficient made by BORKOWSKI and BROSI (3) gave the value $\alpha_{K_{40}}=6$.

An indication of the multipole order of the 40 keV γ-radiation in Xe^{129m} can be obtained from a comparison with the 81 keV γ-ray in the decay of Xe^{133}. This γ-transition is of M1 type, from the measurements of $\alpha_{K_{81}}$ (9). The $K/(L+M)$ ratio is 4.9. Our value for the $K/(L+M)$ ratio of the 40 KeV γ in Xe^{129m} is 4.3 ± 0.7. Remembering that the K/L ratio increases slowly with energy for M1 transitions (8, 12) we conclude that the 40 keV γ-radiation in the decay of Xe^{129m} should also be of M1 type. The possibility of a mixture of M1 and E2 radiations cannot be excluded.

The decay of Xe^{129m} is thus in agreement with predictions of the nuclear shell model (2). The level scheme is shown in Fig. 2.

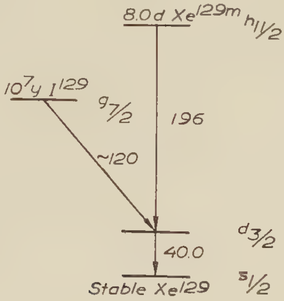

Fig. 2. Decay scheme of $Xe^{129}{}_m$ and I^{129}.

The 39 keV γ-ray reported in the decay of I^{129} (3) is certainly identical with the 40 keV γ-ray found by us. The maximum energy of the β-particles of I^{129} is reported to be 120 keV (3). The level scheme of I^{129} is therefore probably related to that of Xe^{129} as shown in Fig. 2.

It should be noticed that K-capture transition from Xe^{129m} to I^{129} would be energetically possible, according to the decay scheme of Fig. 2. Xe^{129m} would then be able to reach its ground state in two ways. The high Auger line intensity in our measurements might indicate the occurrence of K-capture. However, the probability of K-capture should be extremely small compared to that of γ-radiation.

Nobel Institute of Physics, Stockholm 50, Sweden.

REFERENCES

1. I. Bergström, Nature *167*, 634 (1951).
2. M. G. Mayer, Phys. Rev. *78*, 16 (1950).
   O. Haxel, J. H. D. Jensen, and H. F. Suess, Z. Phys. *128*, 295 (1950).
3. C. T. Borkowski and A. R. Brosi, ORNL 607, 52.
4. R. D. Hill, Phys. Rev. 79, 1021 (1949), Phys. Rev. *80*, 906 (1950).
5. S. Thulin and I. Bergström, Phys. Rev. 85, 1055 (1952).
6. I. Bergström, Ark. f. Fysik, *Bd 5*, nr 14, 191 (1952).
7. E. H. S. Burhop, Proc. Roy. Soc. *A 148*, 272 (1935).
8. N. Tralli and I. S. Lowen, Phys. Rev. *76*, 1541 (1949).
9. I. Bergström, S. Thulin, A. H. Wapstra, and B. Åström, Ark. f. Fysik. 7, 255 (1953).
10. P. Axel and R. F. Goodrich, ONR N6 ori -70 T. O. 1.
11. S. Flügge, Physik. Zeitschr. *42*, 221 (1941).
12. M. Goldhaber and A. W. Sunyar, Phys. Rev. *83*, 906 (1951).

ARKIV FÖR FYSIK. Bd 7 nr 22

Conversion Coefficients of the isomeric γ-ray in the decay of Ba^{137}

By A. H. WAPSTRA[1]

From β-spectrometer measurements on Cs^{137} the K-conversion coefficient of the 662 keV transition in Ba^{137m} was found to be 0.093 ± 0.006 (M4 transition) and the K/L ratio 5.8 ± 0.3. The Kurie plot is straight down to 75 keV if a special correction factor is used.

Introduction. For calibrating the scintillation spectrometer (11) the 662 keV γ-ray (1) in the 157 s isomer Ba^{137m} following the decay of 35 year Cs^{137} would be very useful, if the K-conversion coefficient were accurately known. Moreover the K/L ratio would give an improvement in the plot of K/L conversion coefficient for M4 transitions (10) in the region of low Z^2/E. As we had at our disposal a carrier-free sample of Cs^{137}, prepared for a precision determination of its γ-energy, the opportunity was taken of remeasuring both these values.

Older measurements had yielded the following values for the K-conversion coefficients: 0.10 (after correcting the total conversion coefficients given in this paper with the $K/(L+M)$ ratios discussed below), 0.118 (3), 0.081 (4) and 0.097 ± 0.003 (5) (the last reference came to our attention after we had completed our measurements). The older determinations of the ratios of the intensities of the conversion lines were all measurements of $K/(L+M)$; the reported values were 4.8 ± 0.3 (5) and 5.0 (4).

The K/L ratio

In order to separate the L- and M-peaks we had to use a spectrometer with a high resolving power. For this purpose the double focusing spectrometer of this Institute (6) (7) is almost ideally suited.

Fig. 1 shows the L and $M+N$ conversion lines of the 662 keV transition, using

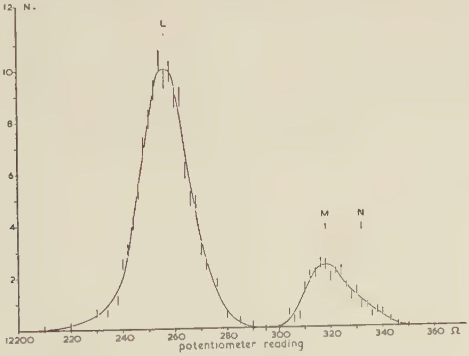

Fig. 1. L, M and N conversion electrons of the γ-line in Cs^{137}.

---

[1] On leave from the "Instituut voor Kernphysisch Onderzoek", Amsterdam.

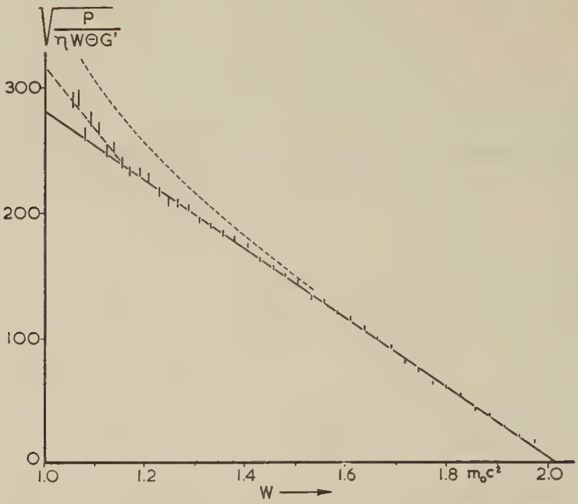

Fig. 2. Fermi-Kurie plot of the β-spectrum of Cs^{137}. The dashed line shows the Kurie plot with the usual correction factor G.

the same sample that was used for its energy determination (1). From this β-spectrum (the K-conversion line, situated at about 11840 Ω, is not shown) we derive a K/L ratio 5.8 ± 0.3. As the relative distance between the lines is rather small the fact that the transmission of the instrument varies somewhat with the energy is of almost no importance. The ratio of the intensities of the L and the $M+N$-conversion lines is 4.5 ± 0.5. With this value we derive from the $K/(L+M)$ ratios mentioned in the introduction the values 5.9 ± 0.4 and 6.1 for the K/L ratio, in sufficient agreement with our value.

The β-spectrum and the conversion coefficient

In order to determine the K-conversion coefficient we measured the β-spectrum in an intermediate image spectrometer (8) with a resolution of 5 %. Our active sample was prepared from the same carrier-free Cs^{137} used for determining the γ-energy, spread with insulin on an 0.15 mg/cm² Al backing.

Fig. 2 shows the (forbidden) Kurie plot, made with the improved correction factor $G' = (W_0 - W)^2 + A(W^2 - 1)$ defined by OSOBA (4). The factor A was taken from fig. 2 in Osaba's paper. (It should be mentioned that there appears to be an error in this plot, as is immediately clear from the fact that $G = (W_0^2 - 1) = 1.04$ for $W = 1$; this error, however, seems only to be a constant factor.) The dashed line in our fig. 2 shows the Kurie plot that would result if the usual correction factor G were used ($A = 1$); it is seen that the use of G' instead of G gives an enormous improvement: the plot is now quite straight, down to 75 keV. The deviation below 75 keV is partly due to straggled electrons, but also to the presense of Auger electrons. The cut-off of the Geiger window (defined as the low-energy extrapolated end-point of the Co^{60} spectrum) was 9 keV, so absorption was not serious for the Auger lines. The maximum energy found from this Kurie plot is 519 ± 5 keV.

In order to find the total intensity of the β-spectrum we recomputed the low energy part from the Kurie-plot. The total conversion factor then comes out to be 0.110 ± 0.005. With the ratios of the intensities of the conversion lines found above we derive a K-conversion coefficient $\alpha_K = 0.090 \pm 0.006$. As it is not sure that the correction factor G′ is valid for low momentum electrons we also recomputed the spectrum from the broken line through the experimental points in fig. 2. The difference of the two plots will certainly be a strong overestimation of any deviation, because of the influence of straggled and Auger electrons. With this recomputed spectrum the K-conversion coefficient comes out only 0.004 less, so we probably need not correct for such an effect. Another fact that may influence the result is the presence of a higher energy β-transition directly to the ground state of Ba^{137}. From our measurements we estimate the high energy spectrum to have an intensity of about 3 %, in approximate agreement with the former values 5 % (3) and ≤ 5 % (4), but in disagreement with the 8 % found by LANGER and MOFFAT (9). The ratio between counting rates at the conversion line and at the end-point of the main spectrum is only about half as large in our measurements as in figure 1 of Langer and Moffat's paper, in spite of their better resolution. This may be due to scattering of conversion electrons in their rather thick sources. With our value for the branching ratio the low-energy spectrum becomes about 2 % lower, so our final value for the K-conversion coefficient becomes

$$\alpha_K = 0.092 \pm 0.006.$$

This should be compared with the value 0.097 ± 0.003 determined by WAGGONER (5), and the theoretical value for a M4 transition, 0.094.

Nobel Institute of Physics, Stockholm 50, Sweden.

REFERENCES

1. G. LINDSTRÖM, K. SIEGBAHN, and A. H. WAPSTRA, Proc. phys. Soc. 66 B, 54 (1953).
2. J. TOWNSEND, G. E. OWEN, M. CLELAND, and A. L. HUGHES, Phys. Rev. *74*, 99, 1948.
3. A. C. G. MITCHELL and C. L. PEACOCK, Phys. Rev. *75*, 197, 1949; *76*, 186 A, 1949.
4. J. S. OSOBA, Phys. Rev. *76*, 345, 1950.
5. M. A. WAGGONER, Phys. Rev. *80*, 489, 1950.
6. A. HEDGRAN, K. SIEGBAHN, and N. SVARTHOLM, Proc. Phys. Soc. *63A*, 960, 1950.
7. A. HEDGRAN, Ark. f. Fysik, *5*, 1 (1952).
8. H. SLÄTIS and K. SIEGBAHN, Ark. f. Fysik, *1*, 339, 1950.
9. L. M. LANGER and R. D. J. MOFFAT, Phys. Rev. *82*, 635, 1951.
10. I. BERGSTRÖM, S. THULIN, A. H. WAPSTRA, and B. ÅSTRÖM, Ark. f. Fysik, *7*, 255 (1953).
11. B. ÅSTRÖM, A. H. WAPSTRA, I. BERGSTRÖM, and S. THULIN, Ark. f. Fysik, *7*, 247 (1953).

ARKIV FÖR FYSIK. Bd 7 nr 22

The decay of Bi^{207}

By A. H. WAPSTRA[1]

Bi^{207} decays by electron capture, 80 % of the decays leading to a 0.9 sec. isomeric state in Pb^{207} which deexcites by the successive emission of a 1060 keV and a 565 keV γ-ray, and 20 % to the 565 keV level. The total decay energy is 2050 keV. The Auger conversion probability for lead is 0.043 ± 0.015.

0. Introduction. A 50 y Bi K-capturing isotope was discovered and studied by NEUMANN and PERLMAN (1), and was assigned by them to Bi^{207}. A 565 keV and a 1063 keV γ-ray were found. These γ-rays were also found by GRACE and PRESCOTT (2), who proved them to be in cascade. These γ-rays are probably identical with the 0.5 and 1.0 MeV γ-rays found in the decay of a 0.9 seconds Pb isomer by CAMPBELL and GOODRICH (3).

NEUMANN and PERLMAN (1) also report four γ-rays with an energy >2 MeV. This is in disagreement with our former estimate 1.7 MeV (4) for the decay energy of Bi^{207}. Though admittedly this value is somewhat low, the difference from the minimum decay energy 2.5 MeV following from Neumann and Perlman's result seemed difficult to explain. Therefore we thought it useful to reinvestigate this isotope.

1. β-spectrometer investigation

An active Bi-sample was prepared by bombarding lead with 180 μA hr of 27 MeV deuterons in the Philips' synchro-cyclotron at the "Instituut voor Kernphysisch Onderzoek", Amsterdam. Bi was separated from this sample by a chemical procedure similar to that mentioned by GILE *et al.* (5). A rather thick sample (designated I) was prepared on a 4 mg/cm² Glasan paper backing. A much thinner sample (II) was prepared later by electroplating on a gold foil of about 4 mg/cm². The energy values of the lines discussed are derived from measurements with this sample. Both samples were measured in the intermediate image β-spectrometer described by SLÄTIS and SIEGBAHN (6), in the order shown in Table I (which also mentions the scintillation measurements described in section 2).

The most important result of the present investigation is that in the region above the K- and L-conversion lines of the 1060 keV γ-ray only a 1685 keV electron line was found, as shown in fig. 1.[2]

---

[1] On leave from the "Instituut voor Kernphysisch Onderzoek", Amsterdam.

[2] In this figure the counting rate is plotted against the current on a logarithmical scale. This method, used earlier e.g. by VERSTER *et al.* (7) has for line spectra definitive advantages over the normal method of plotting N/I against I on a linear scale:
1. the line form and the line width is the same for all currents;
2. for single lines the line height itself is proportional to its intensity;
3. it is not necessary to subtract the counter background in the drawing as it is now constant.
With both methods the line area is proportional to its intensity, which is important for unresolved lines.

Table I

Survey of Bi^{207}-measurements.

No.	Sample	Time after bombardment	Type of measurement
1	III	84 days	sc
2	III	118	sc
3	I	139	β
4	I	153	β
5	I	164	β
6	I	166	β
7	III	173	sc
8	II	175	β

The expected positions and intensities of the 6 lines with energy > 1.1 MeV found by NEUMANN and PERLMAN are indicated; all of them are here found to be at least 10 times less intense than reported by them. The 1685 keV line decayed, as shown in fig. 1, so it does not belong to the very long-lived Bi^{207}. Its origin is discussed in section 5.

The 6 lower energy lines reported by Neumann and Perlman were also found in this investigation (fig. 2, 3, 4; same logarithmic current scale); they are collected in Table II, which also gives their relative intensities (top counting rates) as measured with the thinner sample. The low energy lines are found at a somewhat higher energy than indicated by Neumann and Perlman. Our energy values agree with an interpretation as Auger lines ($KLL = 56$ keV, $KLM = 68$ keV). The disagreement with Neumann and Perlman's values is not due to remanent magnetism in our case, which a separate investigation (8) showed to be unimportant. The difference between the relative intensities of the Auger lines in Neumann and Perlman's work and those found in the present experiments is probably due to absorption, as even in our thin sample (fig. 2) the Auger lines were much broadened. The relative intensities of the 477, 554, and 968 keV lines in both our samples agree very well; the 1050 keV line appears somewhat higher in the thick sample measurements, but this is probably due to the somewhat better resolution obtained with the thinner sample.

Table II

Bi^{207} electron lines.

Present investigation		Neumann and Perlman	
Energy	Intensity	Energy	Intensity
57 keV	40	49	110
69 keV	23	62	50
477 keV	75	477	70
554 keV	25	551	8
972 keV	340	975	370
1054 keV	100	1050	80

Other weak lines found in the β-spectrum decayed with a half-life that indicates that they belong to 14.5 day Bi^{205}.

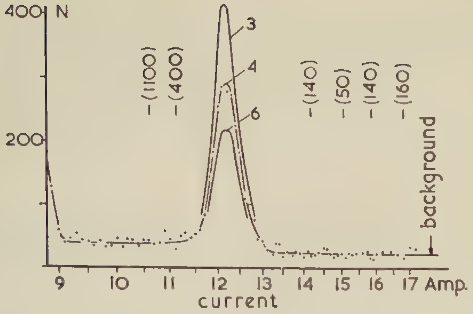

Fig. 1. High energy part of the β-spectrum. The positions and intensities of the electron lines found by Neumann and Perlman are indicated. The 1685 keV line decayed, as is clear from its intensities at different times (3, 4 and 6 table I).

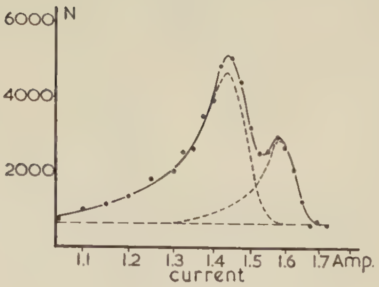

Fig. 2. Lead Auger lines in the Bi^{207} β-spectrum.

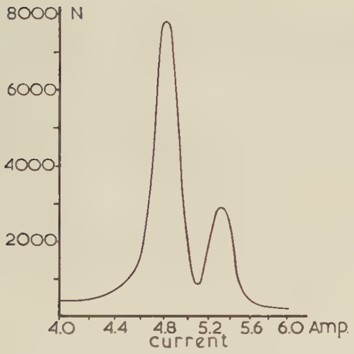

Fig. 3. Conversion lines of the Bi^{207} 565 keV γ-ray.

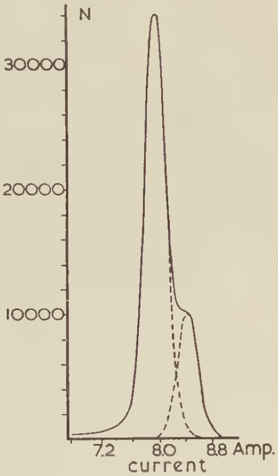

Fig. 4. Conversion lines of the Bi^{207} 1060 keV γ-ray.

2. Scintillation spectrum

We also measured a Bi^{207} sample in the scintillation spectrometer. The first measurement (1 Table I) did not show clear lines, probably due to the fact that Bi^{206} and Bi^{205} were still stronger than Bi^{207}.

Table III

Intensities of photolines.

Measurement	*K* X-rays	565 keV	1060 keV	1800 keV
2 (Table I)..........	9050 (9730)	258 (4200)	98 (4450)	27.4 (2900)
7 (Table I)..........	3470 (3730)	258 (4200)	68 (3100)	5.5 (580)

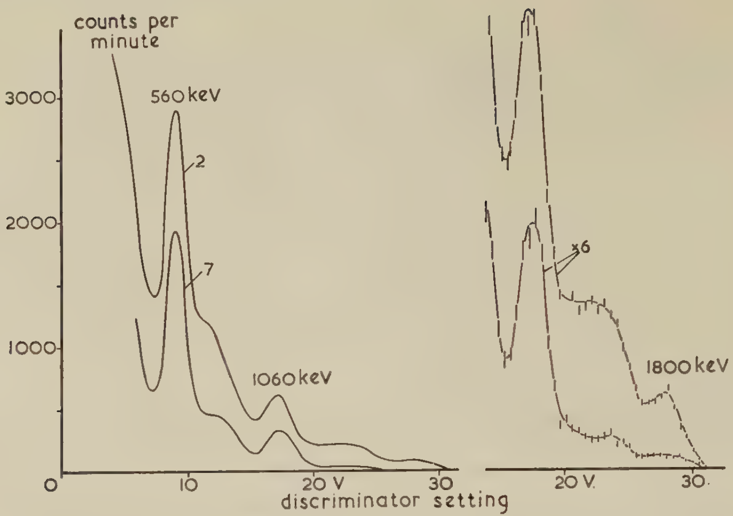

Fig. 5. Scintillation spectrum of Bi^{207}, measured on two data (2 and 7 table I). The right hand part gives the high energy part of the spectrum six times amplified.

Later measurements, however, (2 and 7 Table I), see fig. 5, clearly showed photolines of the K X-rays, and of γ-rays of 560, 1060, and 1800 keV. Their intensities in the two above measurements are collected in Table III.

The figures in brackets give the relative intensities of the γ-rays, as computed with the help of the efficiency curve for the scintillation spectrometer (20). The decay of the 1060 keV line may be due to an admixture of 6.4 day Bi^{206} at the time of our first measurement: γ-rays of 1020 keV and 1097 keV are known in the decay of this isotope (9). This, together with the presence of 14.5 day Bi^{205}, may also explain the decay of the K X-rays. Accepting this explanation the intensity of the 1060 keV photoline in measurement 7 (Table I) should be due wholly to Bi^{207}.

3. Assignment of the Pb^{207m} γ-rays

From the definition of conversion coefficients it follows that

$$\alpha_A : \alpha_{K_1} : \alpha_{K_2} = A_K/X_K : K_1/\gamma_1 : K_2/\gamma_2$$

in which A_K, K_1 and K_2 are the relative intensities of the K Auger electrons and the conversion electrons, and X_K, γ_1 and γ_2 are the relative intensities of the K X-rays and the γ-rays (The conversion coefficient α_A of the Auger electrons is connected with the more commonly used conversion probability W_K by $\alpha_A = W_K/(1-W_K)$.

It is rather difficult to find a good value for the intensities of the Auger lines. The peak counting rates listed in Table II are certainly an underestimation, as their shapes indicate a strong absorption in the sample. The total area of the lines may give a somewhat better estimate: comparing this with the area of the 477 keV line we find a total intensity of about 130 in the scale of Table II (derived from the measurement with the thin sample). This is to be compared with a value 160 derived from Neumann and Perlman's measurement. In our measurement there was still a certain amount of another activity (see section 5). The same is true for Neumann and Perlman's measurement, as indicated by the presence of the lines not found by us.

These lines may, however, be due to activities with lower atomic number, and which therefore make no contribution to the Auger lines. We will therefore accept an intensity 150, with a rather large estimated error (say 30 %).

We then get for the ratios mentioned above,

$$\alpha_A : \alpha_{K_1} : \alpha_{K_2} = 0.042 : 0.018 : 0.110.$$

From these ratios we can obtain the conversion coefficients of the two γ-lines, using the Auger conversion coefficient. For the conversion probability of these lines in lead we find a theoretical value $W_K = 0.045$ (11); this gives a conversion coefficient 0.043. The conversion coefficients found in this way are compared in Table IV with the theoretical values (12).

Table IV

K-conversion coefficients.

γ-line	Experimental	Theoretical
565 keV	0.018	0.0063 (E1) 0.0169 (E2) 0.042 (E3)
1060 keV	0.113	0.040 (E5) 0.065 (M3) 0.110 (M4) 0.185 (M5)

The estimated error of the experimental values is rather larger (35 %) due to the uncertainty in the intensity of the Auger electrons (The ratio of the two values is thought to be good within 15 %). Our values thus indicate that the 565 keV line is an E2 transition and the 1060 keV γ-ray an M4 transition. This is in agreement with the predicted assignments (13) of the levels found in the decay of the 0.9 sec. isomeric state (3) in Pb^{207}, which is illustrated in fig. 6. The same conclusion was reached by GRACE and PRESCOTT (2).

We can check the assignments of the γ-transitions with the ratios of the intensities of their conversion lines (see Table V).

Table V

Intensity ratios of conversion lines.

γ-line	Experimental $K/(L+M)$	Semi-theoretical K/L (13) (21)			
565 keV	3.0	4.1 (E2)	2.8 (E3)	6 (M3)	3.1 (M4)
1060 keV	3.4	4.5 (E3)	3.1 (E4)	8 (M3)	5.2 (M4)

This confirms that the 565 keV line is an E2 transition. The 1060 keV γ-ray could also be an E3 transition, but then the half-life of Pb^{207m} should be much less than 0.9 sec. Moreover our $K/(L+M)$ ratio for this transition is probably somewhat low because of the insufficient resolution of these electron lines.

It should be remarked that the only experimental value for the Auger conversion probability in this region of the periodic table gave a value 0.107 ± 0.006 for W_K in At (14), which is much higher than the theoretical value 0.045. We think that our measurements are a strong indication for a value much nearer to the theoretical value. If we consider the assignment of the Pb^{207} levels to be already certain, because of:

a. nuclear shell theory considerations;
b. the ratio of the conversion coefficients of the two γ-rays; and
c. the K/L ratios,

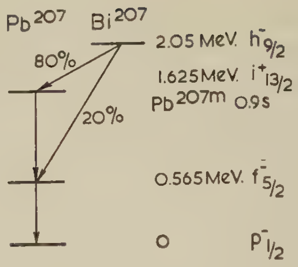

Fig. 6. Decay scheme of Bi^{207}.

we may consider our measurements as a determination of W_K; we then deduce a value $W_K = 0.043 \pm 0.015$, the main error being due to the uncertainty in the relative intensities of the Auger electrons. The deviating value found by GERMAIN (14) may be due to the presence of low-energy conversion electrons in the At^{211}—Po^{211} decay. The very recent value $W_K = 0.054 \pm 0.008$ for Hg (22) agrees with our result.

4. The decay scheme of Bi^{207}

From the approximately equal intensities of the 565 and 1060 keV γ-rays it is clear that the larger part of the capture processes in Bi^{207} lead to the 1625 keV 0.9 sec. isomeric state in Pb^{207}. Part of the difference in the intensities may be explained by the larger conversion coefficient of the 1060 keV ray. Assuming the theoretical conversion coefficients mentioned in section 3, we find that the relative intensity of the 565 keV γ-ray following the 1060 keV transition should be 3470, as compared to the 4200 given in Table III. Thus from the scintillation measurements we find that 17 ± 13 % of the transitions go directly to the 565 keV level (assuming no capture processes to the ground state). Analogous considerations of the intensities of the K-converted lines in the β-spectrum (Table II) give a value 23 ± 16 %, the mean value being 20 ± 11 %.

The fact that electron capture to the 565 keV level occurs, but is less intense than the decay to the 1625 keV state, fixes the state of the Bi^{207} ground level. The spin is 9/2, otherwise the transition to the 565 keV level should be at least 3 times forbidden and therefore would not be found. Now for both transition discussed the spin difference is 2, and, as the transition to the 1625 keV state is found to be less forbidden than to the other, this should be a ($\Delta I = 2$, yes) transition. So we find the Bi^{207} ground state to be an h 9/2 state, in agreement with the prediction of the nuclear shell model, and with the fact that the similar nucleus of Bi^{209} is also in an h 9/2 state. The decay scheme deduced in this way (fig. 6) allows very few electron capture transitions directly to the ground state, as we assumed above.

5. Impurities in our sample

In the next section we will try to estimate the decay energy of Bi^{207} from the ratio of L to K capture. For this reason it is necessary to discuss how much of the K X-rays in Table III belongs to Bi^{207}. An indication of the presence of other activities than the Bi^{205} already mentioned, is found only in the 1685 keV line in the β-spectrum. From the three β-spectrometer measurements it seems to decay with a half-life of 28 days; from the two scintillation measurements, however, we find a

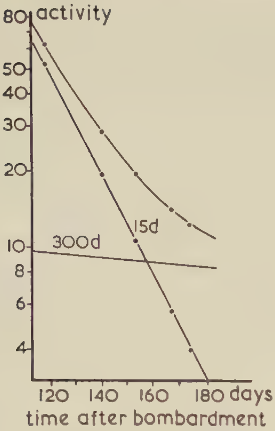

Fig. 7. Decay curve of the 1685 keV e⁻ line (and 1.77 MeV γ-line).

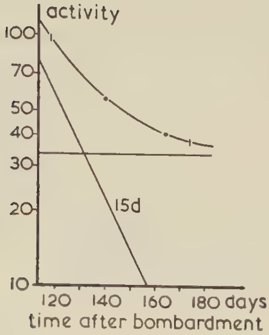

Fig. 8. Decay curve of the *K* X-radiations.

shorter half-life. This indicates that the decay is complex. It is rather obvious that this line is partly due to 14.5 day Bi^{205}. The corresponding γ-ray energy will then be 1.77 MeV, in approximate agreement with the value 1.84 MeV found before (10). Later measurements (18) indicate that some of the activity comes from a much longer-lived nuclide ($\geq$ 300 days), With the help of this assumption we constructed the decay curve shown in fig. 7.[1]

In the same way we constructed a decay curve of the *K* X-rays, or what should be the same, the Auger lines (fig. 8), assuming that the activity is the sum of a long-lived part and a part with half-life 14.5 days. Comparing the intensities of the 14.5 day components in fig. 7 and fig. 8, and assuming that about one *K*-quantum will be emitted per Bi^{205} decay, it is found that the 1.77 MeV γ-ray then occurs in 37% of the decays.

The long-lived part of the *K* X-rays has an intensity 3350 (in the intensity scale of Table III). It is an open question whether part of these *K* quanta belongs to the long-lived nuclide. The almost exact coincidence of the 1685 keV electron lines suggests that this nuclide may be an isomer of Bi^{205}. In that case it should give an addition of about 450 to the *K* X-peak if the γ-ray occurs to 100 % in its decay. We therefore assume that the intensity of the *K* X-rays of Bi^{207} is 2900^{+600}_{-900}; the upper error is thought to be large enough to include the possibility that the long-lived activity does not emit Pb *K* X-rays‘ and the lower error allows that the 1.77 γ-ray may only occur in 30 % of its decays.

---

[1] In a recent scintillation measurement by PRESCOTT, a 1.76 MeV gamma ray was found with an intensity agreeing with the long lived part of the 1.76 MeV gamma ray found by us. It is in coincidence with the 570 keV gamma ray, which indicates strongly that it belongs to Bi^{207} (we had assumed that it did not belong to Bi^{207} as it was not found by NEUMANN and PERLMAN); it appears to be only 7 % in coincidence with K X-rays, suggesting that this branch is preceded for the greater part by L-capture. Then the ratio of K- to L-capture in the branch to the isomeric state of Pb^{207} is higher than assumed in section 6 and therefore the decay energy is also higher. This is also indicated by the existence of a 2.47 MeV gamma ray, reported by PRESCOTT, with an intensity that is not excluded by our results presented in fig. 1. We thank Dr. PRESCOTT for permission to mention his results.

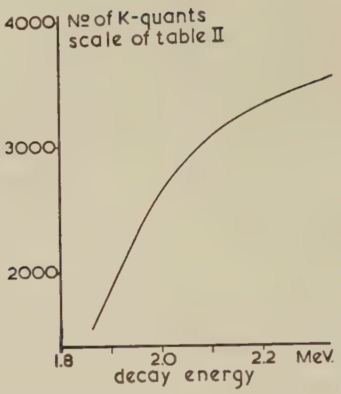

Fig. 9. Intensity of K X-rays (intensity scale of Table III) as a function of the decay energy.

6. The decay energy of Bi^{207}

Fom a paper of MARSHAK (15) we derive the following formula for the ratio of L to K capture:

$$\frac{L}{K} = \left(\frac{\Delta - B_L}{\Delta - B_K}\right)^{2n+2} \left\{\frac{g^2_{L_{\rm I}}}{g^2_K} + \frac{f^2_{L_{\rm II}}}{g^2_K} + H_n \left(\frac{mc^2}{\Delta - B_L}\right)^2 \frac{2\, g^2_{L_{\rm III}}}{R^2 g^2_K}\right\} \qquad 6.1$$

in which n indicates the degree of forbiddenness, Δ the transition energy of the decay in question, and B_L and B_K the binding energies of the L and K electrons (and therefore $\Delta - B$ is the energy of the outgoing neutrino). H_n is 0, 9, 30, and 63 for 0, 1, 2, and 3 times forbidden transitions. According to ROSE and JACKSON (16), $g^2_{L_I}/g^2_K$ is 0.150 in lead; from the values mentioned in table IV in Marshak's paper we find by extrapolation that the second term $f^2_{L_{II}}/g^2_K$ is small and that $2\, g^2_{L_{III}}/R^2 g^2_K$ is about 0.008. Now in our case we have a two times forbidden transition (to the 565 keV state) and a ($\Delta I = 2$, yes) transition. The transition probabilities in the latter, once forbidden special case are obtained by multiplying the transition probabilities for normal once forbidden transitions by the square of the energy of the outgoing neutrino, so that the formula becomes the same for both cases except for the factor H_n:

$$\frac{L}{K} = \left(\frac{\Delta - 16}{\Delta - 88}\right)^6 \{0.150 + 2\,000\, H_n/(\Delta - 16)^2\}. \qquad 6.2$$

(Strictly speaking this is only true for low Z-values; but the same is true for formula 6.1 itself. However, the experimental data are so rough that this probably does not matter).

With the help of formula 6.2 and the decay scheme discussed above we computed the intensity of the K X-rays as a function of the total decay energy (fig. 9, intensity scale of Table II). From this plot, and the experimental intensity of the K X-rays discussed in a former section, we deduce a decay energy $2.05^{+0.25}_{-0.15}$ MeV.[1] This corresponds to a L/K capture ratio 0.79 in the main transition and 0.24 in the transition to the 565 keV state.

From the data given above we may compute the fT values for the two transitions. For the transition to the 565 keV state we find (with help of the graphs given by

---

[1] See however the footnote on page 285.

Moszkowski (17)) log $fT = 11.8$, in approximate agreement with its assignment as a second forbidden transition. For the main transition we find log $q^2 ft = 9.6$. (The factor q^2, the square of the neutrino energy, is the equivalent of the factor $(W_0^2 - 1)$ for electron emission decays in the $\Delta I = 2$, yes, class). Up till now no fT values have been reported for electron captures of this kind; moreover Moszkowski pointed out that in our case the error in the fT value would be somewhat larger than 0.2 in an unstated direction. It is still probably significant that the value given above lies within the range of values found for β-transitions of this kind. If anything, both fT values are somewhat low, indicating a somewhat higher decay energy.

A last check on the Bi^{207} decay energy is the fT value for the K-capture decay of At^{211}. Its decay energy can be computed from the α-energies of At^{211} and Po^{211} and the decay energy of Bi^{207}; it is found to be 0.5 MeV. Log fT is then 5.6. This value is in agreement with other fT values for first forbidden transitions in this region of atomic masses (19).

Nobel Institute of Physics, Stockholm 50, Sweden.

REFERENCES

1. H. M. Neumann and I. Perlman, Phys. Rev. *81*, 958 (1951).
2. M. A. Grace and J. R. Prescott, Phys. Rev. *84*, 1059 (1951).
3. E. C. Campbell and M. Goodrich, Phys. Rev. *78*, 640 (1950).
4. A. H. Wapstra, Physica *17*, 628 (1951).
5. J. D. Gile, W. M. Garrison, and J. G. Hamilton, J. Chem. Phys. *19*, 256 (1951).
6. H. Slätis and K. Siegbahn, Ark. f. Fysik, *1*, 339 (1950).
7. N. F. Verster, G. Nijgh, R. van Lieshout, and C. J. Bakker, Phys. *17*, 637 (1950) (fig. 7).
8. A. H. Wapstra, Ark. f. Fysik *6*, 263 (1953).
9. D. E. Alburger and G. Friedlander, Phys. Rev. *81*, 523 (1951).
10. D. G. Karraker and D. H. Templeton, Phys. Rev. *81*, 510 (1951).
11. I. Bergström, Ark. f. Fysik, Bd 5, nr 14, 307 (1952).
12. M. E. Rose, G. H. Goertzel, B. I. Spinrad, J. Harr, and P. Strong, privately circulated tables.
13. M. Goldhaber and A. W. Sunyar, Phys. Rev. *83*, 906 (1951).
14. L. S. Germain, Phys. Rev. *80*, 937 (1950).
15. R. E. Marshak, Phys. Rev. *61*, 431 (1942).
16. M. E. Rose and L. L. Jackson, Phys. Rev. *74*, 1540 (1949).
17. S. A. Moszkowski, Phys. Rev. *82*, 35 (1951).
18. S. Thulin and A. H. Wapstra, unpublished measurements.
19. M. G. Mayer, S. A. Moszkowski, and L. W. Nordheim, Rev. Mod. Phys. *23*, 315 (1951).
20. B. Åström, A. H. Wapstra, I. Bergström, and S. Thulin, Ark. f. Fysik, *7*, 247 (1953).
21. I. Bergström, S. Thulin, A. H. Wapstra, and B. Åström, Ark. f. Fysik, *7*, 255 (1953).
22. C. D. Broyles, Nucl. Sci. Abstr. *6*, 5912 (1952).

ARKIV FÖR FYSIK. Bd 7 nr 22

On the decay of Hg^{203}

By SIGVARD THULIN and KARL NYBÖ[1]

The maximum energy of the Hg^{203} β-continuum is found to be 210 ± 2 keV. The K internal conversion coefficient of the 279 keV γ-ray is 0.154 ± 0.015 and the $K/(L+M)$ ratio is 2.8 ± 0.2.

Introduction. For measurements of internal conversion coefficients α_K with the scintillation spectrometer (1) it is necessary to know the efficiency of the NaI crystal arrangement for γ-quanta of various energies. In this investigation (1) an efficiency curve was obtained from measurements of α_K for several γ-rays for which α_K has been β-spectrometrically determined. One of the γ-rays chosen for this purpose was the 279 keV γ-transition in Tl^{203}. As α_K for this γ-ray was not earlier determined with sufficient accuracy the β-spectrum of Hg^{203} was remeasured. The results of this investigation will be reported below.

The 43.4 d Hg^{203} is known to decay with β-particles of maximum energy $E_{\max} \sim 210$ keV to an excited level in Tl^{203}, which reaches the ground state by emission of a γ-ray of energy 279 keV (2). The determination of $E_{\max}$ from the Fermi plot of the β-continuum normally gives uncertain results, for two reasons. Firstly, the low specific activity of the activated mercury makes it necessary to use thick samples. The large back-scattering and straggling effects in such samples cause a serious distortion of the β-continuum. Secondly, the K conversion line of the 279 keV γ-ray hides the β-continuum near its end point. SLÄTIS and SIEGBAHN (2) avoided this difficulty by using a coincidence method for the determination of $E_{\max}$. They obtained the value 208 keV. SAXON (3) has reported the value $E_{\max} = 205$ keV. This agreement is probably fortuitous, since Saxon used a very thick β-source (~ 2.4 mg/cm^2, GM-window 0.05 mg/cm^2). His Fermi plot is a straight line down to 40 keV, but this is most probably due to an accidental balancing of back-scattering and absorption effects.

The technique of electromagnetic isotope separation offers a simple method of preparing carrier-free β-samples of Hg^{203}, deposited on thin backing foils. Our measurements were performed with such a sample, prepared from pile-irradiated mercury (Harwell). Mercury vapour was fed to the ion source of the isotope separator and the ions of mass number 203 were collected on an Al foil of thickness 0.15 mg/cm^2.

β-spectrometer measurements

The β-spectrum of the separated Hg^{203} was repeatedly measured with a magnetic lens spectrometer (resolution $\sim 5\%$). A Fermi plot of the β-continuum is shown in Fig. 1. The deviation from the straight line begins at $\sim$80 keV. It is partly due to the presence of Auger lines. According to earlier measurements (4) the Fermi plot of a β-spectrum measured with β-samples of this type gives a deviation from the

---

[1] On leave from the University of Bergen, Norway.

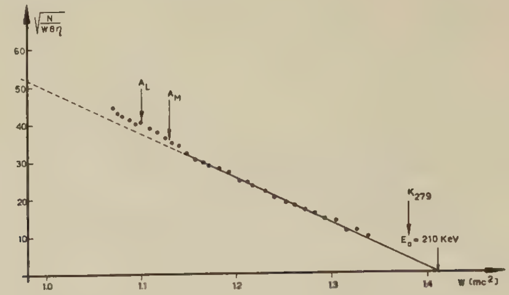

Fig. 1. Fermi plot of the Hg^{203} β-spectrum.

straight line at an energy of ~50 keV. From four different Fermi plots we obtain the values $E_{\max} = 209.5$, 210.0, 210.0 and 212.0 keV respectively.

The Fermi plot was used for a computation of the low-energy part of the β-continuum. By comparison of the areas under the β-continuum and under the conversion lines K_{279} and $(L+M)_{279}$, we obtain the K-conversion coefficient by the formula

$$\alpha_K = \frac{K}{\gamma} = \frac{K}{\beta - K - L - M \ldots}$$

where β, γ, K, L, M . . . denote the intensities of the β-particles, the γ-quanta and the K, L . . . conversion electrons respectively.

Table 1 gives the values of $K/(L+M)$ and α_K for two different runs.

Table I

Run	$\frac{K}{L+M}$	α_K
1	2.85	0.157
2	2.71	0.151
M. V.	2.78 ± 0.20*	0.154 ± 0.015*

* Maximum error.

As pointed out by GOLDHABER and SUNYAR (5), the 279 keV γ-ray in Tl^{203} is one of the few experimentally known cases where a γ-transition between a low-lying excited state and the ground state appears to correspond to a mixture of M1 and E2 radiations, the reported value of the experimental K conversion coefficient lying between the theoretical values (6) for M1 ($\beta^1_K = 0.49$) and E2 ($\alpha_K = 0.073$) transitions. Our experimental value $\alpha_K = 0.154 \pm 0.015$ is somewhat lower than that earlier reported (3), but the above reasoning is still valid. A computation of the proportion of M1 and E2 radiations from our value of α_K gives 20 % M1 and 80 % E2 quanta. The simultaneous existence of M1 and E2 quanta may indicate that the γ-ray is due to a transition between a $d_{3/2}$ and a $s_{1/2}$ state (7), since the ground state of Tl^{203} is known to have the spin $^1/_2$.

Nobel Institute of Physics, Stockholm 50, Sweden.

REFERENCES

1. I. Bergström, S. Thulin, A. H. Wapstra, and B. Åström, Ark. f. Fysik *7*, 255 (1953).
2. H. Slätis and K. Siegbahn, Ark. f. Mat. Astr. o. Fysik *36*, nr 21 (1949).
3. D. Saxon, Phys. Rev. *74*, 849 (1948).
4. I. Bergström and S. Thulin, Phys. Rev. *79*, 537 (1950).
5. M. Goldhaber and A. W. Sunyar, Phys. Rev. *83*, 906 (1951).
6. N. E. Rose, G. Goertzel, B. Spinrad, J. Harr, and P. Strong, Phys. Rev. *83*, 79 (1951).
7. M. G. Mayer, Phys. Rev. *78*, 16 (1950).
8. O. Haxel, J. H. D. Jensen, and H. F. Suess, Z. Phys. *128*, 295 (1950).

Tryckt den 3 december 1953

Uppsala 1953. Almqvist & Wiksells Boktryckeri AB

ARKIV FÖR FYSIK Band 7 nr 23

Communicated 8 April 1953 by G. BORELIUS and O. H. FAXÉN

Some aspects of the change between laminar and turbulent flow of liquids in cylindrical tubes

By E. RUNE LINDGREN

With 12 figures in the text

The purpose of this paper is to give a preliminary interpretation of some experimental observations on the stability of axi-symmetric Poiseuille flow. The conclusions suggested by these experiments are rather remarkable, though it is clear that the experiments should be repeated and extended under stricter conditions of accuracy and control. If, however, such new experiments should confirm the statements in this report, it would be stated that *laminar flow in smooth, cylindrical tubes never has given any experimental evidence of instability.*

The experiments here described show a general need for both experimental and theoretical investigations of some striking properties of fluid motions that do not seem to have been taken into consideration earlier. It is also doubtful that the Reynolds number alone determines the state of motion of liquids in pipes, as is currently believed.

Introduction

Theoretical investigations of the instability of viscous fluid motions, especially the plane Poiseuille and Blasius flows, have been carried on very extensively in recent years, climaxing in the works by C. C. LIN [1], C. L. PEKERIS [2] and L. H. THOMAS [3]. The paper by LIN also contains a valuable summary of earlier works together with the references necessary to give a general idea of the theoretical investigations in this field.

LIN's results indicate instability of plane Poiseuille flow under certain disturbances at various Reynolds numbers. His results are questioned by PEKERIS who uses another technique in determining constants of stability. He finds stability at the Reynolds numbers where, according to LIN, instability should occur. THOMAS later performed the calculations by the aid of an electronic computer and has shown that instability occurs at a lowest possible critical Reynolds number of

$$R=\frac{U\cdot d}{\nu}\simeq 5\,750=R_k \tag{1}$$

in agreement with LIN's result $R_k \gtrsim 5\,300$ (U = mean velocity of the flow, d = distance between the two fixed, parallel walls and ν = kinematic viscosity).

However, experimental verification must be obtained before this problem can be considered finally solved.

For several reasons it is doubtful that the stability conditions of the plane Poiseuille flow can be transformed and applied to the same axi-symmetric flow. J. PRETSCH, 1941 [4], directly attacked the axi-symmetric Poiseuille flow theoretically and found this type of fluid motion always to be stable. As the experimental results commonly seem to be considered to prove instability of this type of laminar flow, the works by PRETSCH and other authors[1] that indicate stability have been neglected[2].

Earlier experiments

The existence of two different types of flow in tubes has been mentioned already by PONCELET and ST. VENANT. The first experiments to obtain quantitative knowledge in this subject were undertaken by G. HAGEN, 1854 [5]. However, the first systematically performed experiments were published in 1883 by O. REYNOLDS [6]. He introduced dimensional analysis so as to obtain the smallest possible number of independent variables to specify the character of the flow and thus indicate when the change between laminar and turbulent motion should occur under different circumstances, provided one case was known experimentally. With a slight modification of his original formula, REYNOLDS found that the flow in a cylindrical pipe can be described by the value of the dimensionless expression (1), where in this case d is the diameter of the tube.

REYNOLDS obtained two different values of the critical Reynolds number R_k where the laminar flow changed to turbulent

$$1)\ R_k = 12000$$

$$2)\ R_k = 3800.$$[3]

The first value was obtained with water running through a rather short, smooth circular glass pipe, with care being taken to prevent any disturbances from appearing. The second value was obtained when a 5 m long smooth lead pipe was directly connected to the tap-water system. In the first case the occurrence of turbulence was observed by aid of coloured bands of fluid[4], in the second by pressure measurements.

After REYNOLDS, a number of followers tried to improve the experimental technique and verify the results of REYNOLDS. However, the phenomena only seemed to become more and more a mystery as almost every experiment gave different values of the "critical" Reynolds number, which at last came to cover a range of 200–51000. The latter result is due to V. W. EKMAN [7] who worked with water in REYNOLDS original apparatus (glass pipe). EKMAN concluded that there is no critical REYNOLDS number, if all disturbances are prevented carefully enough.

In 1921 L. SCHILLER [8] presented a paper describing systematically performed experiments by which he was able to give plausible reasons for the discrepancies of most earlier works within a certain limit. SCHILLER accepted EKMAN's idea of no upper limit of the critical number and introduced a lower limit of R_k, which is defined as the value of R where laminar flow remains laminar, independent of how great disturbances are introduced with the flow at the entrance of the tube. This lower limit is the currently accepted definition of the critical Reynolds number R_k.

---

[1] For references see ref. [1].

[2] Professor O. H. FAXÉN points out that A. VAN HECKE [20] has concluded from known experiments in the literature that the laminar flow in smooth, cylindrical tubes is stable at finite Reynolds numbers.

[3] This is the original value. SCHILLER [9] states that this rather should be 2100.

[4] For explanation of this technique see ref. [6] and [7].

SCHILLER introduced maximal disturbances by a plate at the entrance of the tube. When the plate was moved nearer the tube entrance, the "critical" Reynolds number decreased until a certain limit was reached. If the plate was then moved still nearer the opening no further change of R_k could be observed (see Fig. 12). SCHILLER supposed that he thus had introduced the limit of the maximal disturbances necessary to secure the lowest possible R_k. Also he found that a certain "distance of onset" (entry length) (~130 d) is necessary in order to obtain a sharply defined value of R_k. In addition it was shown that the smoothness of the tube walls is not significant as regards this lower R_k.

In this way SCHILLER (by pressure measurements) obtained a sharply defined "critical" value

$$R_k = 2320.$$

Later, SCHILLER [9] published an excellent review with a summary of earlier experimental methods and their results. Here he was able to give reasons for the earlier experimental discrepancies and thus could verify that his own measurements were correct and single-valued.

Among research workers in hydrodynamics this problem now seemed to be considered as settled experimentally, although WO. OSTWALD [10] in later experiments with water and glycerine believed he had obtained a single-valued "critical" number of about 250.

In 1934 SCHILLER published another paper [11] giving connections between the wave lengths of the disturbances and a modified Reynolds number. However, no papers by SCHILLER give any information towards a clarification of the initiating of turbulence.

It appears that a most valuable experimental investigation regarding the instability of the Poiseuille flow has been done in recent years by A. M. BINNIE 1945 [12], who visually observed the flow of a double-refringent weak suspension of (0.25%) benzopurpin in water between crossed nichols. These experiments certainly fulfilled the critical requirements due to SCHILLER, except perhaps that the entrance disturbances possibly can have been less intense than what is claimed by SCHILLER.

According to SCHILLER the pressure measurements show that, with too short a distance of onset, there is a continuous transition between laminar and fully developed turbulence. If the distance of onset is long enough, the onset of turbulence occurs instantaneously without a transition zone. It seems probable that this transition zone could be regarded as caused by the "turbulent flashes"[1] reported by REYNOLDS. Evidently SCHILLER made such an interpretation of his observations. However, BINNIE stated that the transition between laminar and turbulent flow occurred continuously although the distance of onset was clearly long enough. With increasing velocity, turbulent flashes occurred more and more frequently until fully developed turbulence was established. Flashes appeared at a Reynolds number of $R = 1960$ and complete turbulence was established when R attained a value of 2900. At still higher velocities the intensity of the turbulence was continually increased.

---

[1] These can be described as short lengths of turbulent motion in the fluid moving with the otherwise purely laminar flow. See ref [6].

BINNIE concluded from his experiments that he had in the main verified SCHILLER's results, but, as will be shown later, other conclusions may be drawn.

Experimental procedure

The following experimental investigation of the change between laminar and turbulent flow in a cylindrical pipe has been carried out along lines similar to those followed by both SCHILLER and BINNIE.

Double-refringent suspensions of White Hector bentonite in distilled water as well as pure distilled water have been used in the experiments. The bentonite suspensions have been of concentrations from 0.08% to 1% in weight (up to 2.5% in rare cases). White Hector bentonite was used because the clay particles of this type of bentonite are known to be specially small. Indeed, no individual particles could be observed in examining samples in an electron-microscope with a magnification of 30000 diameters. It could be observed that when the bentonite concentration exceeded about 2% the suspension behaved like a thixotropic gel. Likewise even the more diluted suspensions cannot be expected to behave exactly like pure Newtonian fluids. These anomalous properties of the suspensions (see, for instance, R. HOUWINK [13] on this subject) must of course be considered in connection with the experimental evaluation of the fluid motions.

The suspensions were prepared several months before the experiments were started and no aging effects have been observed during the measurements. These were in each case performed after first agitating the suspension by circulating it through the apparatus for a while. The viscosities were measured, after vigourous shaking of the samples, both by means of an Ostwald capillary viscometer and a Hoeppler viscometer and were finally checked by the free fall of a glass ball in larger samples of the suspensions. No systematic difference between the results from the three methods of measuring the viscosities has been observed.

The arrangement of the apparatus (which was placed vertically, thus differing from most earlier experiments) is shown in Fig. 1. Plexiglass tubes of three different diameters (20, 10 and 6 mm) but of the same length were used. Pressure measurements were performed only in the 10 mm tube, with the manometer holes situated as marked in the figure. Unless otherwise expressedly stated, the visual observations of the flow through the crossed nichols always were done in the position shown in Fig. 1. The quarter-wave length plates for Na-light were built in together with the nichols, but serve no purpose in these experiments.

The necessary inflow disturbances, in accordance with Schiller's statements, were secured by a plexiglass plate at a distance of 0.5 mm from the tube entrance.

The pressure holes in the middle tube were made after all other measurements were completed. A close visual inspection through the nichols along the tube showed that the flow was not at all disturbed by the holes, provided the levels in the manometer tubes were constant.

The fluid motions have also been pictured by means of cine-cameras. Arrangements can be seen in Fig. 2.

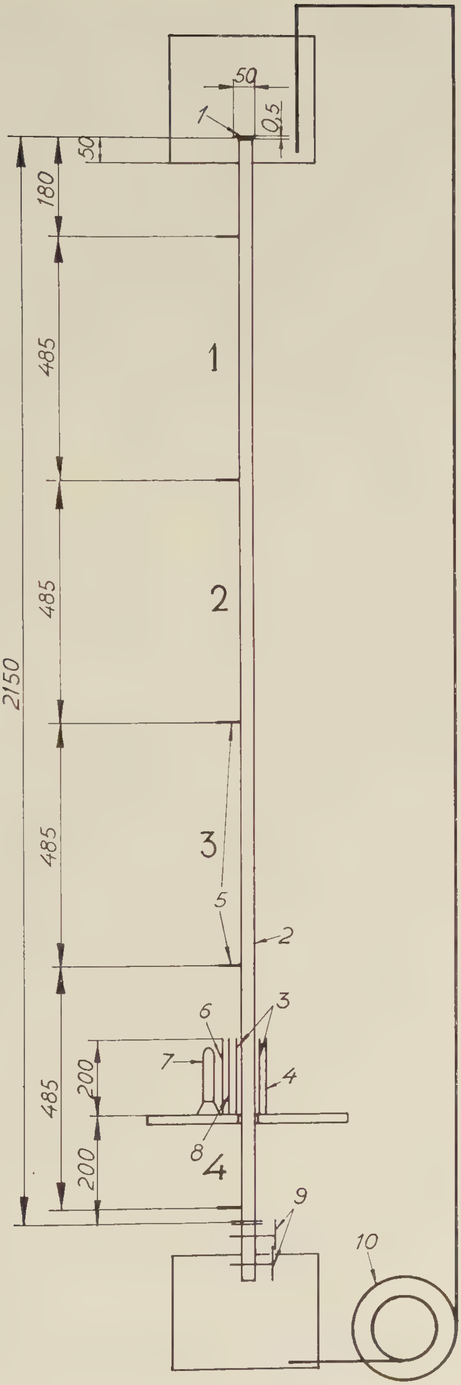

Fig. 1. Experimental equipment. 1. Disturbance plate. 2. Measuring tube. 3. $^{1}/_{4}$-wavelength plates. 4. Analyzer. 5. Manometer holes. 6. Opaque glass plate. 7. Na-lamp. 8. Polarizer. 9. Cocks. 10. Pump.

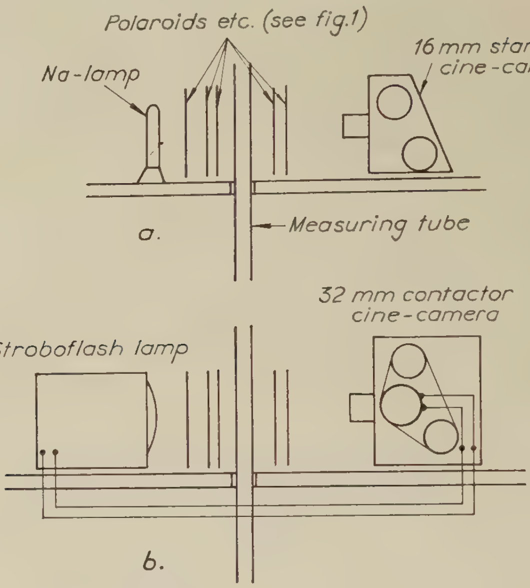
Polaroids etc. (see fig.1)
Na-lamp
16 mm standard cine-camera
a.
Measuring tube
32 mm contactor cine-camera
Stroboflash lamp
b.

Fig. 2. Arrangement of the photographic equipment.

Observations

Schiller states that there is an instantaneous change between laminar and turbulent flow at a "critical" Reynolds number, when the crucial conditions are fulfilled as in these experiments. However, this was never to be seen in the visual observations. Binnie's observations on the other hand were confirmed in every respect, that laminar flow continuously changes to turbulent by an increasing number of turbulent flashes with increasing velocity, until fully developed turbulence is established. With still increasing velocity the "turbulency" continuously increases.

The development of the fluid motion with increasing velocity is illustrated by Fig. 3. (These pictures have been taken with arrangements as indicated in Fig. 2 a.)

To avoid any misunderstanding it should be mentioned that no streamlines can be visualized by the method used. Instead it should be understood that the brightness at every point in the flow is approximately proportional to the corresponding shear forces. "Absolute darkness" means zero shearing force. Although the cylindrical form of the tube complicates the interpretation of the pictures, it can be seen that the laminar flow has something like a Poiseuille velocity distribution. This is important as the pictured flow (0.25% bentonite concentration) could be expected to show non-Newtonian behaviour.

Corresponding pictures taken with synchronized cine-camera and strobo-flash lamp (see Fig. 2b) are shown in Fig. 4 (only one picture of laminar flow). From the last pictures it can be seen that the vorticity is very much concentrated near the tube walls.

Owing to a misunderstanding, no pictures of complete turbulent flashes can be shown. They always appeared, however, in the form drawn in Fig. 5. The striking

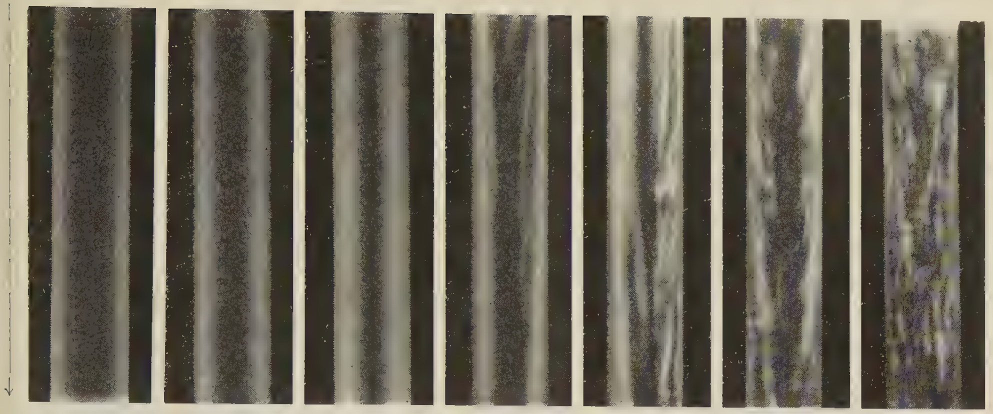

Fig. 3. The appearance of the flow of $^1/_4\%$ bentonite suspension at different velocities in the 20 mm tube under maximal entrance disturbances. Increasing velocity from left to right. The arrow indicates the direction of flow. These pictures are taken with the equipment shown in Fig. 2 a.

feature of the turbulent flashes was their arrow-like shape. The disturbances first appeared in the middle of the tube. They dissipated to the walls and disappeared. After that laminar flow was re-established.

The visual observations of the transition from laminar to turbulent flow can be summarized thus: At rest all the fluid is dark. With beginning low velocity the outer parts of the fluid begin to brighten with continuous transition to darker parts in the centre of the flow. With increasing velocity the dark area gradually diminishes to a thin black line in the middle of the flow. At a certain velocity it can be observed how this line begins to make slow oscillatory motions indicating a tendency to instability. A small increase of this velocity induces rare turbulent flashes. With increasing velocity an increasing number of turbulent flashes occur until complete turbulence is established. Still higher velocities continuously increase the "turbulency" (vorticity).

The described observations are valid for flows of all the used suspensions, if turbulence occurred at all (at 2.5% bentonite concentration in the 10 mm. tube, the velocity could not be raised so high that any instability could be observed).

In the first series of quantitative observations the flow of fluid (volume per time unit) has been measured for the different suspensions just as complete turbulence visually was established (this point was thought to correspond to the momentary change between laminar and turbulent flow in accordance to SCHILLER's measurements of the pressure fall). If these "critical" flows are plotted against the corresponding bentonite concentrations of the fluids, the graphs of Fig. 6 are obtained. These values divided by the respective tube diameters give approximatively straight lines for the "critical data" as functions of the bentonite concentration (at low concentrations). This is shown in Fig. 7. If, instead, the "critical" Reynolds numbers are plotted in the same way, the curves become more complicated as can be seen in Fig. 8.

Evidently the experiments show (Fig. 8) that with increasing bentonite concentration, turbulency occurs at increasing Reynolds numbers until a maximum is reached, whereafter still higher concentrations cause a decrease of the "critical" Reynolds

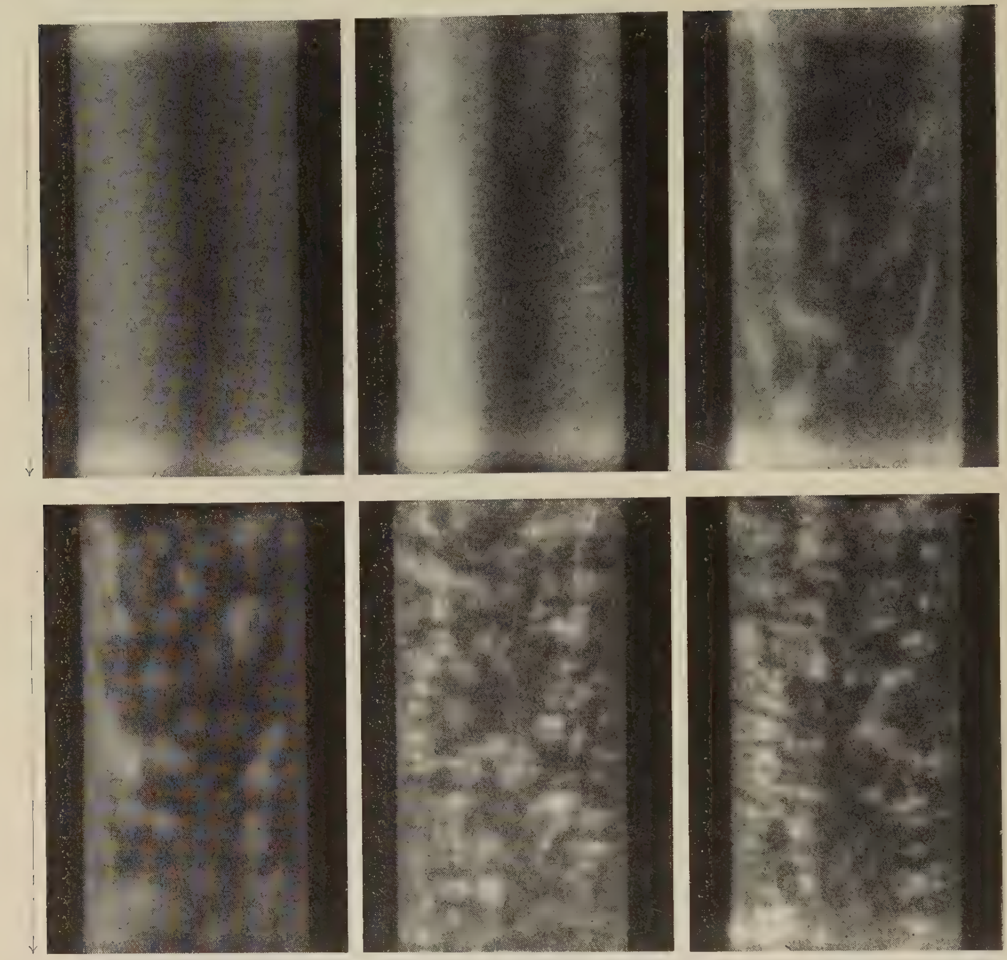

Fig. 4. The same flow as in Fig. 3, but pictured with the equipment shown in Fig. 2 b. Increasing velocity from upper left to lower right.

number. At the present state it is impossible to decide whether these effects depend on structural properties of the bentonite suspensions or if the variation of the viscosity alone can induce such behaviour. According to the hitherto general opinion the latter possibility is absurd, but, really, earlier investigations do not contradict even such an assumption. The further discussion will make this more believable. However, new experiments are urgently needed.

From Fig. 8 it can be seen that the wider the tube is, the lower is the "critical datum" obtained for the same fluid ($<1\%$ conc.). Extrapolation of the graphs in Fig. 8 would give very vague results. Instead, the straight lines in Fig. 7 are drawn out to intersect the ordinate-axis and the values thus obtained are divided by the actual value of the kinematic viscosity for aqua distillata. So calculated, the "critical" Reynolds numbers for pure water will be about 3 300, 3 000 and 2 500 for the tubes

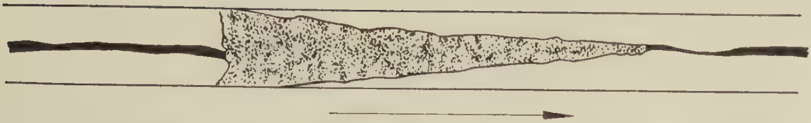

Fig. 5. Typical appearance of a turbulent flash. The arrow indicates the direction of flow. The flash moves with the flow and disappears gradually downstream.

of 6, 10 and 20 mm diameter respectively. The "critical" Reynolds numbers are considerably higher than the values according to SCHILLER except for the widest tube. However, the onset distance for this tube is only about 90d instead of 130d as claimed by SCHILLER. The fact that the "critical" Reynolds number increases with decreasing tube diameter can be explained either as a direct dependency on the diameter or as depending on the distance of onset.

Of course there are fewer points of observation than is desirable. However, the tendencies are so very distinct that no objections can be raised against the general conclusions derived from the experiments (every point in the graphs, of course, is the mean value of several measurements).

Both BINNIE's and the present measurements show continuous transition between laminar and turbulent flow. As demonstrated above, the present measurements also show some striking discrepancies from general accepted ideas due to SCHILLER. Thus the next natural step is to repeat SCHILLER's measurements. For this purpose simultaneous visual and pressure observations have been performed on flows in the 10 mm tube. Distilled water and bentonite suspensions of 0.1 and 0.6% concentration were used in these measurements. The remarkable results can be studied in Figs. 9, 10 and 11.

The measurements for pure water (Fig. 9) of part 3 (the number refers to the part of the tube as numbered in Fig. 1), which has an onset distance of about 110 diameters, are in good agreement with SCHILLER's results. Part 4, with an onset distance of about 160d, has a higher "critical" Reynolds number. Corresponding statements can be made for the measurements with the bentonite suspensions (see Figs. 10 and

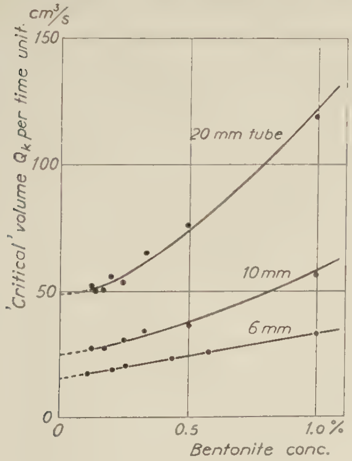

Fig. 6.

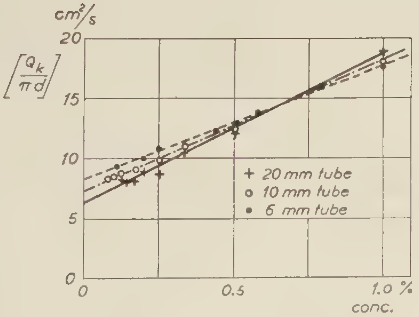

Fig. 7.

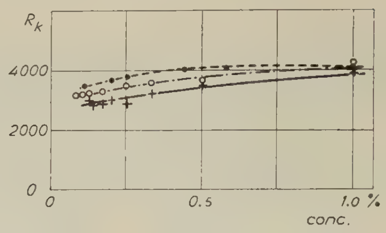

Fig. 8.

(When the bentonite concentration increases to 2 %, the Rk for the flow in the 20 mm tube decreases to a value of about 3300).

11). By this the earlier results of this report are verified, and it can be considered as proved that *the "critical" Reynolds number increases with increasing distance of onset.*

It can be mentioned that if the measurements are carried out on the two parts 3 and 4 together as one "measuring distance", the "critical" Reynolds number thus obtained has a value between the "critical" numbers of the parts 3 and 4 respectively (slightly higher than for part 3). This means that not only the distance of onset but also *the length of the measuring distance affects the value of the "critical" Reynolds number.* It should also be noticed that the pressure discontinuity is sharply defined only for the parts 3 and 4 in full agreement with SCHILLER's statements (Fig. 9).

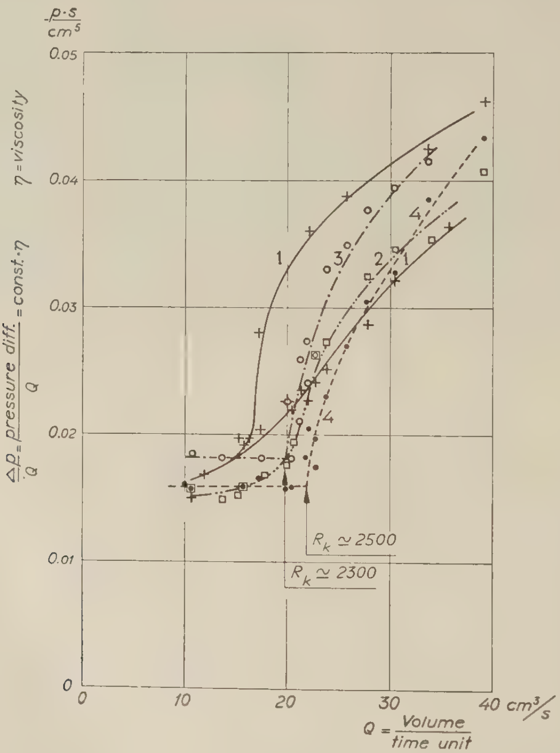

Fig. 9. The onset of turbulence for flow of pure water as indicated by pressure measurements.

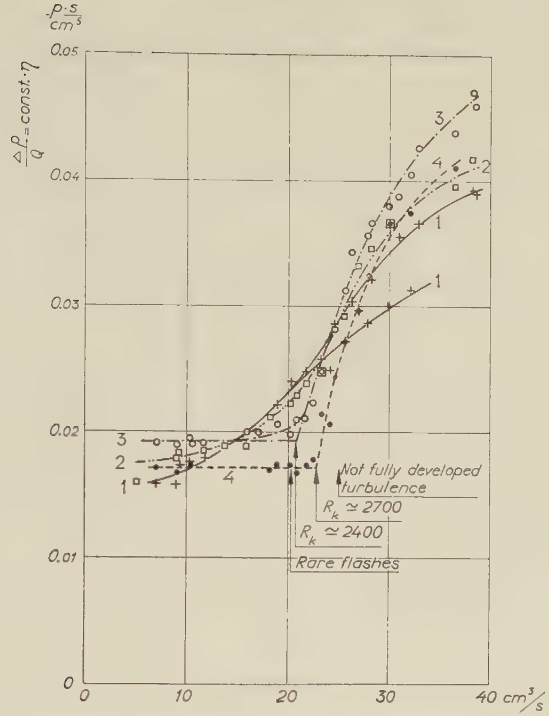

Fig. 10. The onset of turbulence for flow of 0.1 % bentonite suspension as indicated by pressure measurements and visual observations.

The Figs. 10 and 11 give some very interesting information. The most important fact is that *the pressure discontinuity does not seem to signify a sharp transition between laminar and turbulent flow* as has been the general opinion ever since REYNOLDS performed his experiments. Instead, this discontinuity occurs somewhere in the continuous transition zone when the turbulent flashes appear with a certain frequency depending on the velocity. Of course, it can be questioned if pure water does have the same transition character as even weak gel-forming colloids. However, the similarity of the graphs in Figs. 9 and 10 definitely verifies such an assumption.

In Fig. 10 it can be seen that curve 3 does not give a sharply defined pressure discontinuity as was the case in Fig. 9. This must depend on the higher velocity necessary to create turbulence as compared to pure water. This is quite natural. A higher velocity should require a longer distance of onset to create a similar type of flow than a lower velocity.

The characteristic differences between Figs. 9 and 10 are still more pronounced in Fig. 11. Here no sharp discontinuities occur at all. The curves are rounded and seem to have changed their character completely. To what extent these changes depend on the high velocities necessary to create turbulence or perhaps on the non-Newtonian properties of the fluid, cannot be judged from these preliminary experiments. This the more, as it is not known whether the increase of the "critical" Reynolds number with the bentonite concentration is an effect of structural changes of the fluid [14] or perhaps only an effect of the increase of the viscosity. As already mentioned,

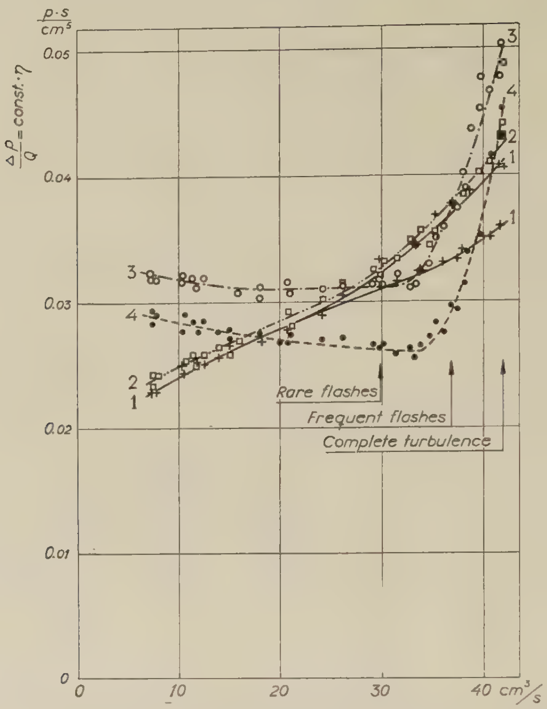

Fig. 11. Pressure measurements and visual observations of the onset of turbulence for flow of 0.6 % bentonite suspension.

especially here must new experiments be undertaken. The changed character of the curves *can* however be understood as only the lower parts of the corresponding curves in Figs. 9 and 10.

The double branches of the curves 1 show that there possibly exist two different states of motion for the entrance flow. Such double branches also could be traced for the curves 2, but so few points were obtained that no curve could be drawn. These points have been omitted in the graphs. It is also puzzling that the viscosity as indicated by curve 3 always has a higher value than the corresponding value indicated by curve 4. None of these phenomena can yet be explained, but this does not change the validity of the other observations reported. However, more accurate measurements are necessary.

As a final investigation, the flow of the 0.6 % bentonite suspension was closely examined visually along the whole length of the tube at different velocities. It was found that *the vorticity* (*turbulency*) *continually decreased with the distance travelled.* This was the case at all velocities where any change of the turbulency possibly could be observed as limited by the relatively short length of the tube. One typical case will be described: Fully developed turbulent flow entered into part 1 and frequent flashes were observed in part 2. Only a few flashes occurred in part 3 while no flashes at all could be observed in part 4. All degrees of such behaviour were observed at different velocities.

The preceding examination of the experimental results evidently shows that *the pressure discontinuity is not any crucial quantity indicating an instantaneous transition between different states of fluid motion.* Instead it has been shown that the change between laminar and turbulent fluid motions proceeds continuously and that this change occurs at higher velocities with increasing distance of onset. Finally, direct visual observations show that the vorticity decreases with the distance travelled.

The statements above are in agreement with a work by R. HERMANN [15] who has performed measurements on flows in a circular pipe with an entry length of up to 225 diameters at Reynolds numbers up to 1900000. He stated that the resistance (vorticity) slightly decreased with the entry length up to the value mentioned. Measurements with still longer inlet lengths have not been found in the literature.

However, in experiments with *undisturbed* entrance conditions, SCHILLER[1] and others [16] have found that in this case the "critical" Reynolds number decreases with increasing distance of onset and reaches a lower limit of about the same order (though always higher than) the commonly accepted value of R_k. These observations are in close accordance with measurements made by MOEBIUS [17]. From his measurements it has been concluded that with undisturbed entrance conditions at high Reynolds numbers, the specific flow resistance increases with increasing inlet length and finally reaches about the same values as obtained by HERMANN. These results cannot yet be discussed in connection with the observations reported by HERMANN and in this paper.[2] Extended measurements are needed.

Also it should be mentioned that observations of flows with maximal entrance disturbances reported by R. R. ROTHFUS and R. S. PRENGLE [18], definitely could be considered to contradict the experimental results presented in this paper. In order to clarify this state of affairs, the experiments by R. and P. have been repeated by inserting a thin metal rod through one of the manometer holes into the 10 mm tube. The flow then was observed visually by using 0.60 % bentonite suspension. In this way it could be shown that the observations reported by R. and P. are due to disturbances caused by the rod. Thus the position of the transition point between laminar and turbulent flow, which was questioned by R. and P., is identical with the position of the inserted measuring device in their experiments.

Some final remarks

SCHILLER, who performed his measurements with great care, already has mentioned some of the statements in this paper. However, as pressure measurements evidently seem to verify instability of the Poiseuille flow, SCHILLER explained the observed deviations[3] in his experiments as accidental occurrences instead of examining these phenomena more closely by extended measurements.

Further, Fig. 12 (which is taken from SCHILLER's work[4]) suggests some interesting subjects for closer investigation. For instance, which mechanism induces the in-

---

[1] See ref. [9], p. 583.

[2] Here, also the paper by VAN HECKE [20] should be noted.

[3] See ref [8], p. 441, rows 23–32.

[4] Ref. [8], p. 443.

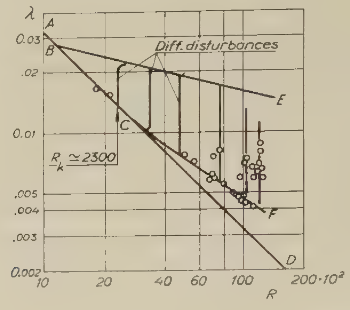

Fig. 12. The onset of turbulence in circular pipes for different entrance disturbances according to SCHILLER. λ = specific flow resistance. o = measuring points under undisturbed entrance conditions. Other points are very well concentrated on their respective lines.

stantaneous change of flow resistance (pressure fall) when the appearance of turbulent flashes reaches a certain frequency? Can this be explained by the principle of extreme values, and are statistical methods applicable to this problem? The significance of point B is another problem, and why does the line CF for laminar flow deviate from the Poiseuille line CD? According to SCHILLER this depends on the onset distance necessary to establish a fully developed parabolic velocity profile, due to a theory by ED. HAGENBACH [19]. Good agreement between theory and experiments has been obtained. With respect to the present investigation this could just as well be an effect of the kinetic energy of the flow at the tube entrance in general.

SUMMARY

The discussion of the results from the experimental investigations described in this paper makes it probable that:

a. The transition between laminar and turbulent flow in smooth, circular pipes proceeds continuously (at least up to Reynolds numbers of 3 300),

b. The pressure discontinuity (resistance increase) at certain Reynolds numbers does not mean an instantaneous onset of turbulence,

c. The vorticity of flows with high entrance disturbances in smooth, circular pipes decreases with the distance travelled (to some extent this has been observed at Reynolds numbers up to 1 900 000),

d. The Reynolds number by no means is a crucial variable that alone determines whether the flow shall be laminar or turbulent,

e. The classical experiments in determining the lower "critical" Reynolds number have been misinterpreted and that there does not exist a critical Reynolds number of the value $R_k \sim 2\,300$,

f. In defining the state of motion of flows in smooth, cylindrical tubes, the Reynolds number may be replaced by an expression in the form $F\left(\frac{U \cdot d}{\nu}, \frac{d}{l}\right)$, where l = distance travelled,

g. As the tendency to create turbulency depends on the bentonite concentration, a secondary conclusion is, that in running model tests with bentonite suspensions (and surely also with other gel-forming double-refringent colloids) care must be taken so that no false predictions are made as regards the flow of the original liquid. Model tests should not be performed with higher bentonite concentrations than 0.1–0.2%.

Acknowledgements

I should like to take this opportunity to express my gratitude to my teacher and friend, Professor O. H. FAXÉN, who has taken an active interest in the performance of the experiments. It has been most stimulating to work in Professor FAXÉN's department, which has also borne the expenses for the experimental equipment.

I am also indebted to other members of the staff of the Institute; Prof. H. BAECKSTROEM put parts of his laboratory at my disposal for a long period, Messrs. R. EKLUND and G. GRAN prepared the bentonite lump, Mr. L. EVERS took an active interest in the photographic work, Docent J. O. LINDE informed about non-Newtonian behaviour of fluids, Mr. S. LUNDIN performed the analysis in the electron microscope and Dr. H. SCHUH informed about important papers dealing with the stability of flows.

Also should be mentioned the firms R. SCHOENANDER Ltd, who kindly presented film material, and the BAROID SALES DIVISION, NATIONAL LEAD COMPANY, L.A., California, from whom was sent 2.5 kgs White Hector Bentonite free of charge all the way to Sweden. This was most obliging.

Much of the construction work of the apparatus, most of the photographic work and some of the first measurements have been performed by Mr. Y. DAGEL as a final work for obtaining the B.Sc. degree.

Professor FAXÉN also has read the original manuscript and has devoted invaluable work to the paper before printing.

Div. of Mechanics I, Royal Institute of Technology, Stockholm.

REFERENCES

[1]. LIN, C. C. On the Stability of Two-dimensional Parallel Flows. Part I. General Theory. Quart. Appl. Math., v. 3, 1945, p. 117. II. Stability in an Inviscid Fluid. Ibid, p. 218. III. Stability in a Viscous Fluid. Ibid, p. 277.

[2]. PEKERIS, C. L. Stability of the Laminar Parabolic Flow of Viscous Fluid between Parallel Fixed Walls. Phys. Rev. II, v. 74, 1948, p. 191.

[3]. THOMAS, L. H. The Stability of Plane Poiseuille Flow. Phys. Rev. II, v. 86, 1952, p. 812.

[4]. PRETSCH, J. Ueber die Stabilitaet einer Laminarstroemung in einem geraden Rohr mit kreisfoermigem Querschnitt. ZAMM, v. 21, 1941, p. 204.

[5]. HAGEN, G. Ueber den Einfluss der Temperatur auf die Bewegung des Wassers in Roehren. Math. Abh. Akad. d. Wiss., Berlin, 1855, p. 17.

[6]. REYNOLDS, O. An Experimental Investigation of the Circumstances which Determine whether the Motion of Water shall be Direct or Sinous, and the Law of Resistance in Parallel Channels. Phil. Trans. Roy. Soc., London, v. 174, 1883, p. 935.

[7]. EKMAN, V. W. On the Change from Steady to Turbulent Motion of Liquids. Ark. Mat., Astr. och Fys., vol. 6, nr 12, 1911.

[8]. SCHILLER, L. Experimentelle Untersuchungen zum Turbulenzproblem. ZAMM, v. 1, 1921, p. 436.

[9]. —— Das Turbulenzproblem und verwandte Fragen. Phys. Z., v. 26, 1925, p. 566.

[10]. OSTWALD, Wo., and AUERBACH, R. Ueber die Viskositaet kolloider Loesungen im Struktur-, Laminar- und Turbulenzgebiet. Koll. Z., v. 38, 1926, p. 261.

[11]. SCHILLER, L. Neue quantitative Versuche zur Turbulenzentstehung. ZAMM, v. 14, 1934, p. 36.
[12]. BINNIE, A. M. A Double-Refraction Method of Detecting Turbulence in Liquids. Proc. Phys. Soc., v. 57, 1945, p. 390.
[13]. HOUWINK, R. Elasticity, Plasticity and Structure of Matter. Cambridge University Press, 1937.
[14]. FORSLIND, E. The Clay-Water System. I and II. Swed. Cem. and Concr. Res. Inst. at the Roy. Inst. of Techn., Stockholm. Proc. nos. 16 and 17, 1952.
[15]. HERMANN, R. Experimentelle Untersuchung zum Widerstandsgesetz des Kreisrohres bei hohen Reynolds'schen Zahlen und grossen Anlauflaengen Inaug.-Diss., Hoh. Phil. Fak. Univ. Leipzig, 1930.
[16]. NAUMANN, A. Experimentelle Untersuchungen ueber die Entstehung der turbulenten Rohrstroemung. Forsch. auf d. Gebiete d. Ingenieurwesens, v. 2, 1931, p. 85.
[17]. Handbuch der Experimentalphysik, IV: 4, Leipzig 1932, pp. 91–92.
[18]. ROTHFUS, R. R. and PRENGLE, R. S. Laminar-Turbulent Transition in Smooth Tubes. Ind. and Eng. Chem., v. 44, 1952, p. 1683.
[19]. HAGENBACH, Ed. Ueber die Bestimmung der Zaehigkeit einer Fluessigkeit durch den Ausfluss aus Roehren. Pogg. Ann., v. 109, 1860, p. 385.
[20]. VAN HECKE, A. Théorie du mouvement des fluides (Première partie). Union des Ingenieurs sortis des Écoles speciales de l'Université catholique de Louvain, Bulletin Technique, no 3, 1952, Série technique 16.

Tryckt den 28 oktober 1953

Uppsala 1953. Almqvist & Wiksells Boktryckeri AB

ARKIV FÖR FYSIK Band 7 nr 24

Communicated 27 May 1953 by MANNE SIEGBAHN and ERIK HULTHÉN

An optical uncertainty principle and its application to the amount of information obtainable from multiple-beam interferences

By ERIK INGELSTAM

With 9 figures in the text

1. The one-dimensional optical uncertainty formula

In modern physics, great importance is attached to the uncertainty principle of Heisenberg, as it clearly expresses the limit which the wave structure of matter sets to the conceptions of classical mechanics. Its most usual formulation as

$$\Delta x \cdot \Delta p_x \sim h \tag{1}$$

deals with the degree of precision with which a length coordinate x and that of the component of linear momentum p in the same direction can be defined. The Δ signs have no rigorous meaning, giving only the order of magnitude of the uncertainties, depending on how they are defined in any special case; thus the amount at the right of the sign may vary by a factor of say 2 or 2π. It is also well known that the two variables can be changed in many ways, being for example energy W and time t, or any canonically related pair, as is discussed by HEISENBERG [1] and in most textbooks, but these modified formulations still express the same law of nature.

It has often been realized but is sometimes forgotten that HEISENBERG's principle corresponds to still more obvious principles in the propagation of waves of any kind. This connection was first made clear by BOHR [2], who related the new concepts to the wave-theoretical laws so significantly expressed by LORD RAYLEIGH in the field of optics.[1] In the present state of physical optics, it is of great interest to examine classes of uncertainty relations which can be deduced from the same fundamental arguments, with the wavelength of monochromatic radiation. The writer will return to these more general questions in later sections of this article.

As a parallel case to that considered in equation (1), let us imagine a plane wave front containing certain parallel borders dividing up the field. As indicated in Fig. 1, the xy plane is taken parallel to the wave fronts, with the borders, such as P_m and P_{m+1}, determining the y direction. This means that in all the following arguments no variation is assumed in the y direction, everything being thus one-dimensional and occurring as a function of x. The character of the borders P_m and P_{m+1} can be quite different: the domain P_mP_{m+1} may be a slit and the rest of the

---

[1] The writer is indebted to Prof. O. KLEIN for his kind interest in the present questions and his advice concerning references to the early literature.

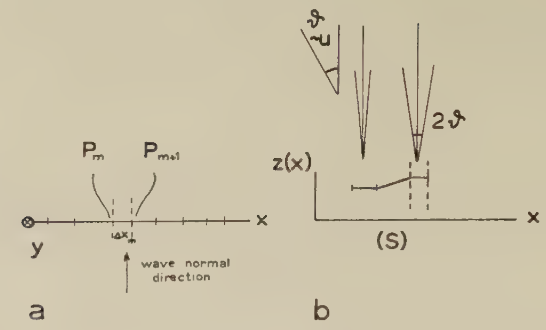

Fig. 1 a and b. Notations and coordinate relations of formulas (2) and (3).

screen opaque: the contrary may be the case, or $P_m P_{m+1}$ may introduce a phase shift with or without an amplitude attenuation with respect to the rest of the field. The first-mentioned disturbance is the most often considered and the one to which equation (1) is most directly applicable.

Let the front, of width X, be divided into zones with, generally, the widths of Δx_m. Within them, the complex amplitude distribution $F_m(x)$ may be constant, as indicated just now, or, a case we will consider more generally, having the modulus constant, the phase being variable. As is well known, the wave front is diffracted, and the distribution of amplitudes with the angle of the incident wave normal is the Fourier transform of the functions $F_m(x)$:

$$G(\sin\vartheta) \equiv G(u) = \sum_m \int_x^{x+\Delta x_m} F_m(x)\, e^{i\frac{2\pi}{\lambda} x u}\, dx \equiv \sum_m \int_x^{x+\Delta x_m} F_m(x)\, e^{i 2\pi x k_x}\, dx\,. \tag{2}$$

In the last member, the x component of the wave number vector k has been introduced for convenience, this vector having the modulus $1/\lambda$ and the direction of the wave front normal, $k_x = k u = u/\lambda$.

For the zones within which $F_m(x) = \text{constant}$, this constant is taken out of the integral sign, and the corresponding function is the well-known Airy curve, having its central lobe within the total angle 2ϑ where $\sin\vartheta = \lambda/\Delta x_m$. The same is the case for a strip where a continuous and linear phase change occurs, but where the centre of the fan is inclined as demanded by geometrical optics. According to equation (2) and the schematic figure 1 b, where part of a wave front is also indicated, the diffraction angles are greater the narrower are Δx_m; they have all been assumed to be only a few wavelengths wide, as this is the interesting case.

Information as to what has happened to the wave front at the xy plane is now contained in the diffracted fans, and the only physical method of studying them is by means of the energy distribution. Intensity measurements can be performed at the distant plane where the Fraunhofer condition is valid, or at the focal plane of a lens giving a linear scale of $f \cdot u$, where f is its focal length. The intensity is however always spread out, regularly for the zones with uniform phase, and irregularly for the others. The intensity distribution is the function GG^*, and the measurements are most often made on its maximum value. The treatment according to wave mechanical methods deals with the domains of variables within which they can be varied in order to give GG^* a not-negligible value. The formulation of this uncertainty principle which is most convenient for our purposes is [2]

$$\Delta x \cdot \Delta k_x \equiv \Delta x \cdot \frac{1}{\lambda} \Delta u \sim 1, \tag{3'}$$

which, in optics with monochromatic waves, to which field we have limited ourselves in assuming a constant λ, is best known as

$$\Delta x \cdot \Delta u \equiv \Delta x \cdot \Delta (\sin \vartheta) \sim \lambda. \tag{3}$$

In the most simple case just mentioned, this means that the main lobe of the diffraction figure corresponding to Δx_m is considered, the side lobes being neglected.

This uncertainty principle states that a narrow pencil or slit of light is always undetermined as regards the angle. Attention should in this connection be drawn to the fact that (3) is an illuminating formulation of the well-known Abbe condition for optical systems. Equation (3) also involves the theory of the resolving power of the microscope, as the aperture of the microscope, $\sin \vartheta$ or more generally $n \sin \vartheta$, must be large enough to include the angles of the fan of rays just mentioned, giving the well-known expression for the resolving power $\lambda/2n \sin \vartheta$.

If, in (3), the wave length associated with a particle is substituted, $\lambda = h/mv$, and it is observed that $p_x = mv \sin \vartheta$, the Heisenberg relation (1) is obtained. Eq. (3) then gives the relation for the diffraction of particle waves in a slit, and everything that has been said above applies to them.

2. Principles of the obtaining of phase information by means of multiple-beam interferences

The diffraction angles entering in equations (2) and (3) are closely connected to the phase distribution in the wave front. It is therefore of interest to examine closer the modifications possible in the uncertainty principle when very accurate information of phases is aimed at. In particular, two recently developed principles or techniques in optics are of great importance in this respect, namely phase contrast and improved interference methods, especially the utilization of multiple-beam interferences.

This last-mentioned technique will be considered in some detail in this paper, under as general assumptions as possible. In order to illustrate the general principle, it is most convenient to take Fizeau fringes (of equal thickness), either in transmission or reflexion. Thanks to great improvements in the technique of applying highly-reflecting coatings, made possible by means of evaporation in vacuo, the interference fringes appearing say in a wedge-shaped space between highly-reflecting surfaces can be characterized as real topography mapping lines closely following the variations in the optical path difference z, i.e. double the distance between the surfaces, and in this way the path difference can be measured with a precision of $\lambda/1000$, or, which is the same, the phase may be found to within $1/1000$ of a revolution. Fig. 2 shows an example of an interferogram of this kind. The problem we set ourselves in this paper is: how truly does the z-coordinate of the intensity centre of the fringe express the real thickness variation of the film in the x direction?

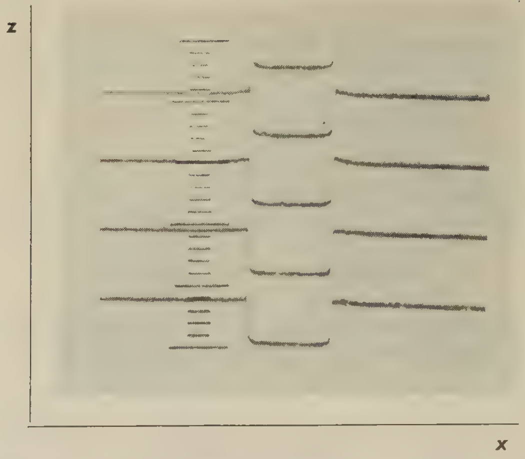

Fig. 2. Multiple-beam interferogram in reflexion, mercury line 5461 Å. The object is an optical flat coated with aluminium evaporated in vacuo, except for the central band. The whole plate is then coated with silver. The z coordinate scale, determined by the distance between the fringes, is 450 times larger than that of the x coordinate.

We make the following assumptions using the notation of Fig. 3. The monochromatic light entering the interference space AB is exactly collimated, and thus the entrance pupil at the focus of the collimating lens is of negligible diameter. The surfaces A and B are both semi-transparent, their amplitude transmitivity and reflectivity, equal at all points, being t and r respectively. This means an intensity reflexion factor of $R = r^2$ and a transmission factor of $T = t^2$, the absorption, which has no influence here, being $= 1 - R - T$. The interference space is viewed by means of an ideal lens L, its aperture assumed as large as to comprise all the diffraction angles from the space AB, no other associated stops being present. The lens is focused so as to image at the plane P′ a plane P in or near the space AB; often, P′ is the focal plane of a microscope, L being its objective, or, the film plane of the photographic objective L. We further should draw attention to the focal plane F of the lens L, as in this plane the Fraunhofer diffraction spectrum of the wave fronts appears. If u is the sine of any diffraction angle, the linear coordinate along that plane is $f \cdot u$.

An interference fringe is far from being an optical image in the ordinary sense. Moreover, it has not been of any particular interest to relate it to any coordinates of the interference space at all, except for its "center of gravity", which, as is well known, gives a topography, i.e. a phase information. For our purpose, however, it is of use to treat the problem as closely as possible by ordinary image theory. Referring to Fig. 4, we assume the amplitude of the incoming rays constant over the whole field, and so we can denote the x-independent amplitude of the first member taking part in the interference by A_0 (which is t^2 times a phase factor of the original amplitude). The next member is reflected twice and has undergone a phase delay on account of the distance between the reflecting surfaces, the next has undergone this effect twice, etc.:

$$F_0 = A_0; \quad F_1 = A_0 r^2 e^{-i\varphi(x)}; \quad F_2 = A_0 r^4 e^{-i2\varphi(x)}; \quad F_n = A_0 r^{2n} e^{-in\varphi(x)}.$$

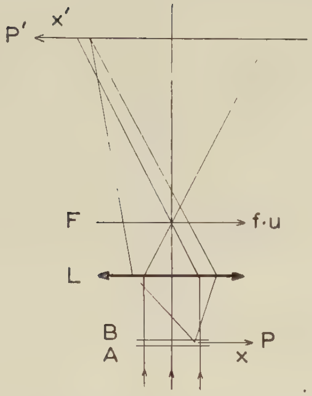

Fig. 3. Imaging of a plane P in the Fizeau interference space AB, by means of an ideal and infinitely extended lens L with its rear focal plane at F. The diffraction spectrum of the modulated wave front occurs in this plane, and an integration from it to the image plane P′ gives the intensity distribution of the interferogram.

The phase variation is wholly due to difference in optical path, so we can write, introducing the optical path coordinate z:

$$-\varphi(x)=\frac{2\pi}{\lambda}z(x);\quad F_n=A_0 r^{2n}\,\boldsymbol{e}^{in\frac{2\pi}{\lambda}z(x)}. \tag{4}$$

We can assume that all the path difference is due to topography of the surface A, which, while it sets no limitation to the generality in our conclusions, makes the proof more graphic in certain sense. A thickness variation of Δe, a topographic height, is of course doubled in the wave-front, $\Delta z=2\Delta e$.

One of the wavefronts, giving rise to components as just outlined, has a diffraction spectrum as a function of u according to the usual treatment

$$G(u)=\int_0^X F_n\,\boldsymbol{e}^{i\frac{2\pi}{\lambda}xu}\,dx,$$

and no intensity variation at all is seen in P′, as the second integration from F to P′ only results in the constant amplitude $A_0 r^{2n}$.

What happens in the interferometric combination of the components is a more or less strong modulation of the undulations, in space or in phase, so that an extreme concentration of energy is achieved in maxima at x near which $z(x)$ equals $N\lambda$ if r is so large as to make many components take part. The resulting spectrum originates from the ordinary summation, and is

$$G_\Sigma(u)=\int_0^X\sum_{n=0}^{\infty}A_0 r^{2n}\,\boldsymbol{e}^{in\frac{2\pi}{\lambda}z(x)}\cdot\boldsymbol{e}^{i\frac{2\pi}{\lambda}xu}\,dx. \tag{5}$$

In this case, the resulting amplitude at the P' plane is not constant, but under the given assumptions (x' transferred to x scale by the magnification factor g):

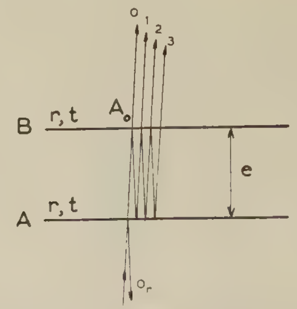

Fig. 4. Successive rays interfering in transmission.

$$F'(x) = \int_{-\infty}^{+\infty} G_{\Sigma}(u)\, e^{-i\frac{2\pi}{\lambda} g x u}\, du. \tag{6}$$

The most usual way to let the phases appear is to tilt B in respect to A around an axis parallel to the x axis, whereby to the topography to be examined is added a linear function $z = \alpha y$; α being the small tilt angle. This only means that the amplitudes are spaced in a plane which can be denoted as an $(x'z)$ plane, the last-mentioned coordinate z having the scale factor $\lambda/\alpha y$, corresponding to the spacing between consecutive fringes. The angle α is so small as not to introduce any falsifications in intensity distribution compared to that of the parallel interferometer. The fringes give the two-dimensional energy distribution due to $F(x, z(x))$. See Fig. 2. In the general case, neither $G_{\Sigma}(u)$ nor $F'(x)$ can represent $z(x)$ in an explicit way. In the analysis of the fringes shape, the intensity maximum (or, in rare cases, another characteristic point on the intensity-curve, such as a steep slope on one side) is sought and accepted as the $z(x)$ curve of the interferogram.

The intensity maxima are characterized as the maxima of $F'F'^*$.

3. The uncertainty principle containing path length

It is quite evident on account of the formulas (5) and (6) that the building up of the intensity of the fringe is intimately dependent on the diffraction angles u, as in the first factor of equation (5), the infinite sum, the argument is still increasing, while to this argument is added that of the diffraction factor. In the last integration, formula (6), all the u directions have been summed, but in the integrand the infinite number of terms combine with the x coordinate. Of course, our assumption that the lens comprises all angles u puts a limit to the slopes accessible by this method, a fact very well known to the experimenter. The only case when diffraction has no evident influence is when, for distinct portions of the x region, $z(x) = \text{constant}$, and in that case the interference fringes are exactly straight and the difference between the constant z values can be measured with theoretically unlimited precision. The sideways displacement of intensity for non-constant $z(x)$ portions can be demonstrated in many graphic ways. Thus, an inclined part as S in Fig. 1 b gives a Feussner surface for each member of the waves still more inclined, and so the image at

P' is definitely out-of-focus for such a portion. Still simpler cases are dealt with in the next section.

We now consider the relations between the measuring coordinates in this case. In the combined equations (5) and (6), u has been eliminated, and z has appeared, bearing its information. Physically speaking, the interference modulation condition (5) for the intensity maxima selects close domains of the angular spectrum u. The variation of the wave number vector x component, which was $\Delta k_x = (1/\lambda)\,\Delta u$, is, in the Nth order of interference in the interferometer, $\Delta k_x = (1/\lambda)\,\Delta\,(z/N\lambda)$. Geometrically, the variation $(z/N\lambda)$ is interpreted as the sine of the total variation of the wave number vector direction in the Δx region of the wave field of the interferometer.

The intensity distribution $F'F'^*$ has, thus, a variation domain of

$$\Delta x \cdot \Delta k_x \equiv \Delta x \cdot \frac{1}{\lambda}\Delta\left(\frac{z}{N\lambda}\right) \equiv \Delta x \cdot \frac{1}{N\lambda^2}\Delta z \sim 1, \tag{7'}$$

and the uncertainty relation valid for an interference fringe is then

$$\Delta x \cdot \Delta z \sim N\lambda^2. \tag{7}$$

This means that, the more we try to reduce the limit of error in locating and measuring the optical path values, Δz, the more undetermined it will be to which portions of the interference space these path values really belong. Δz is reduced by means of increasing the reflectivity r in formula (5), but the light then spreads more on account of diffraction in the x direction. In a well-dimensioned set-up, N will only be a few units, so it could be omitted when an ideal apparatus is being considered.

4. Treatment of some simple cases

When approaching the problem of identifying the multiple-beam interferences practically, it should first be kept in mind that (7) only gives the order of magnitude within which the information is uncertain. A closer treatment of the probability functions in wave mechanics gives in Heisenberg's relation a value reduced by 2π, i.e. corresponding to one radian in argument variation instead of one revolution. In the case of (7') and (7), a more reasonable value than λ would be $\lambda/2$, as is taken in other applications of information theory in optics [16]. When considering the practical consequences of (7) to the technique of precision measurement, it is advisable to take the narrower values just mentioned, and further, we pass over to the topography coordinate e instead of z, which is twice as great. Further, we include a factor we call α, increasing with N, which is intended to represent both technical imperfections and the influence of an increased number of the interference order. In this practical version we have thus

$$\Delta x \cdot \Delta e \sim \alpha \cdot \frac{\lambda^2}{8} \cdot \tag{8}$$

Fig. 5 shows very simply the meaning of Eq. (8). The multiple-beam interference technique, when properly exploited, is an extremely important way for obtaining

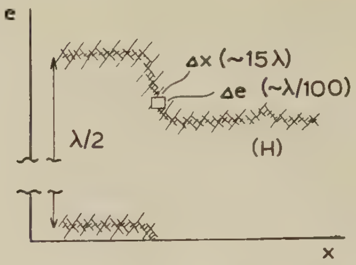

Fig. 5. A schematic outline of part of an interference fringe. The uncertainty rectangle is shown.

information about depth variations, and instruments are also available for industrial purposes ("Multimi" of C. E. Johansson, Eskilstuna, Sweden). The method is especially useful for measuring steps between planes and the uniformity of sheet thicknesses, etc. But we find from Eq. (8) that, when we try to reach very great sensitivity in depth information, we cannot also attain an unlimited sensitivity in the sideways representation of the contour by following the fringe. The interferogram as taken with a lower-power microscope indicates this itself, by providing a much coarser scale for the x coordinate (see Figs. 2 and 5), and in this case the uncertainty is automatically taken into consideration in the practical evaluation of the interferogram. It is obvious that small raised regions, ridges etc. (see Fig. 5 at H) must be invisible or falsely represented when they have a Δx less than that corresponding to the smallest Δz which the fineness of the fringe allows to be detected. The phenomenon has often from a practical point of view been pointed out by TOLANSKY [3, 4] and collaborators, and NOMARSKI [5] has shown, by means of a semi-quantitative diffraction treatment, that small microscopical particles remain invisible in multiple-beam interferences. In particular, topographical diagrams showing very clearly depth structure must be interpreted with care regarding Δx, if they are obtained when A and B are practically parallel and thus with a widely-spread intensity distribution. Here of course the assumption of one-dimensional variation is not valid, and intensity revealing z is a function of the x, y region imaged. The grainy structure often observed reveals crystallite topography, but does not image it. Nothing is gained in increasing the magnification of the microscope: even if the aperture is quite able to include even the extreme angles of diffracted light, the magnification is "empty" as regards the fringes. Of course a magnification chosen in order that the fringe may appear clearly to the eye or the photographic plate is of value, say of 10 up to 200 in linear measure, according to the topographies to be examined. Here the practical problem of constructing an objective with special corrections becomes of primary importance.

Although several authors, as BROSSEL [6] and FAUST [7], who have worked with multiple interferences, have pointed out that diffraction is a limiting condition for this technique, none has, to the writer's knowledge, formulated the uncertainty principle (7) or (8). This may be due to the overwhelming mathematical difficulties of an exact treatment of this diffraction problem even in simple cases. None of the ordinary simplifications introduced in diffraction calculations are valid here, and the uncertainty principle indicates the reason why this is so.

From the practical point of view, it may be of some interest to give some evidence for (8) by considering the method itself. Its theory is well-known. Assuming uniform

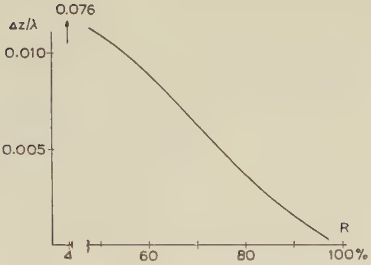

Fig. 6. Accuracy with which the centre of a multiple-interference fringe can be located, as a function of the reflectivity R of the interference plates.

flat surfaces, and thus neglecting diffraction, the summation of the terms of (4), writing $z(x) = \text{const.} = 2e$, gives the resulting amplitude

$$A = \sum_{n=0}^{\infty} F_n = \frac{A_0}{1 - r^2 \exp(i \cdot 2\pi \cdot 2e/\lambda)}$$

and the corresponding intensity AA^* is easily expressed, putting $r^2 = R$, as

$$I = \frac{A_0^2}{(1-R)^2 + 4R \sin^2 \frac{2\pi}{\lambda} e}.$$

The maxima of intensity I are sharp insofar as $m = 4R/(1-R)^2$, FABRY's sharpness coefficient, is large. The half-width of the intensity peaks is, expressed in z units, $z_1 = \lambda/\pi\sqrt{m}$. Practical experience indicates that a fringe can be located to one tenth of the half-width, and thus the practical Δz is given by

$$\Delta z = z_1/10 = (1-R)\lambda/20\pi\sqrt{R}.$$

This assumption, to which spectroscopists and interferometrists would agree, is conservative, as the contrast difference included in it, if calculated from the slope of the curve, is about 5 times as large as the threshold for visual contrast perception, often taken as a rule-of-thumb to be 2 per cent. Fig. 6 is a curve calculated from this formula, the abscissa being the reflectivity R within the limits ordinarily used in practice.

On the other hand, let us calculate by a semi-quantitative procedure the broadening of the interference fringe in the x direction, also as a function of the practical parameter the reflectivity R. In the general diffraction treatment, equations (3)–(7), we have considered the imaging of the interference fringe, and have thus performed an analysis of the intensity actually obtained in a certain plane. Of course, for a more rough treatment of the interference, we can consider the interference space itself, especially an average plane in it, say midway between A and B.

For this more obvious proof of the uncertainty relation (8) we may consider a small Δx portion, say of width a, which is a few wave-lengths. It may differ from the rest of the field as regards z (or e), i.e. be a ridge.

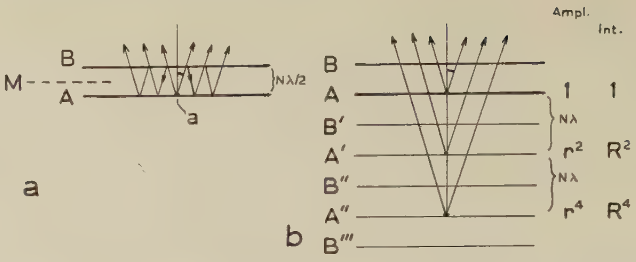

Fig. 7. Successive widening of the signal from a part a in a topography, on account of diffraction in the successive interfering rays; see the text.

In this case, the central diffraction lobe has the half-angle ϑ, assumed small and thus being $\vartheta = \lambda/a$. We take this measure as characteristic for the angular widening of the "signal" indicating a, and if we like, the amplitude can be considered constant within this fan. In fact, for phase distributions within a other than the constant value here assumed, the amplitudes have another distribution, but the maxima always lie within this fan, as may be shown by a special study of phase gradients.

When now $\Delta z/\lambda$ is diminished by increasing the reflectivity R following the technical procedure, the sideways distribution is widened as more multiple waves take part in the interference. Being approximately in phase with each other, they add in amplitude, and the intensity is built up from their square. Fig. 7 gives a pictorial representation of these widened diffractions, Fig. 7 a showing the space AB itself, while in Fig. 7 b the rays are separated as if they emerged from successive mirror images of A and B, etc. Amplitude and intensity reflexion factors giving the relative value of the successive signals from A, A′, A″, etc. are r^2, and R^2 respectively. Taking into account that the fan spreads more and more for the successive reflexions, Fig. 8 gives the diffraction broadening for three different R chosen within the region covered by Fig. 6. They are to be considered as zones of probability for the intensity distribution due to the presence of a, and when they are used to characterize width of the possible extension in the x direction, when as indicated the fringe is localized at the intermediate surface M of Fig. 7 a, only values of the function so large that they are well over visual contrast perception need be considered. The block diagrams shown in Fig. 8 should of course, in the vertical direction, be normalized to the total area unity when comparing them, but this is of no interest here, as we only think of the sideways distribution. The absolute value of the broadening for a given value of a is obviously the abscissa values of Fig. 8 multiplied with $\frac{1}{2}\cdot N\lambda/2$. The values of Fig. 8 thus represent $4\,\Delta x/N\lambda$, and we find by comparing the corresponding values of Fig. 6 with those of Fig. 8, that

$$\left(\frac{\Delta z}{\lambda}\right)\cdot\left(\frac{4\,\Delta x}{N\,\lambda}\right)\sim\text{constant}$$

thus confirming the validity of the product relation independently of m or R, and thus of the degree of multiplicity chosen for the interference. The absolute values are reliable, and conform to experience. The present treatment indicates that α of equation (8) should be proportional to N; as we deal with probability blocks the function of N is in fact less dependent on this order of interference. This is specially

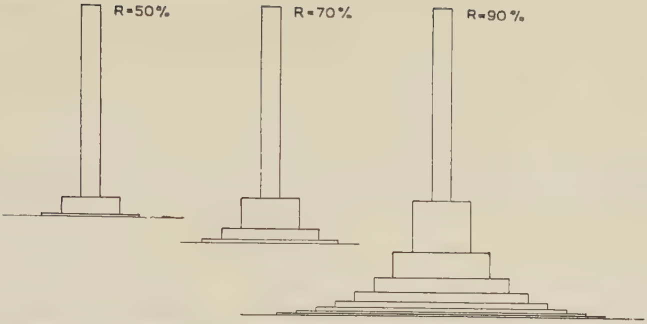

Fig. 8. Blocks showing the widening indicated in Fig. 7: the heights are relative intensities, comparable only within the same diagram; the widths are those of the fans in Fig. 7 b.

the case for the small N most often used, where the approximations involved in the Fraunhofer assumption for this treatment are very rough.

A very evident explanation of the relation is also that, in order to maintain the demanded accurate phase equality, or equality in optical path, for different diffraction angles, the rays must spread out on the border between one detail and the others, in order to find a hill or a crest with an equal optical path for the successive angles.

In conclusion, two remarks should be made concerning the applicability of formulas (7) and (8) to multiple-beam arrangements. The cases of transmission and reflexion are in this respect identical. It has been remarked by several authors that in the case of reflexion the presence of a term (first reflexion, ray o_r of Fig. 4) not included in the series (4) would cause a difference: the corresponding ray does not, however, improve the uncertainty condition, but only changes the intensity distribution. Further, it is also applicable to Fizeau mountings and to fringes of equal chromatic order, as, according to the arguments presented above, the fact is of fundamental nature. It goes without saying that all other more or less serious technical difficulties increase the value of α in (8), as in all practical applications of the Heisenberg relation in diffraction experiments etc. Of course, the principle applies to two-beam interferences (two members instead of an infinite series), but is there of less practical interest as the two factors are more equal in magnitude.

5. Disturbances of the simple x, z information by intersections

It is instructive to consider a wave as the means of transferring communication, as is now often done in other technical signalling methods. This has, for the domain of optics, been pointed out by TORALDO DI FRANCIA [8]. The wave cannot, on account of its nature, carry more than a certain amount of information, and the relation (7) should be an expression of this limiting condition. In a brief communication (unpublished) at the Paris Symposium on Phase Contrast (1951) TORALDO pointed out that it is not surprising that one can measure depth differences of even $\lambda/1000$. The wave nature of light sets a limitation only on the total number of informations avilable. We can get any degree of detail in the depth information, provided we give up some other information.[1] This is ex-

---

[1] I should like to express my cordial thanks to Prof. TORALDO for stimulating talks and correspondance on these questions.

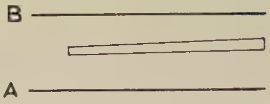

Fig. 9. A schematic case of superposition interference fringes: the interposed sheet differs from the surrounding space in refractive index, and therefore reflects at both its sides. It may be wedge-shaped, as here, and randomly inclined, both of which factors will influence the shape of the "anamalous fringes".

pressed by Eq. (7). For multiple interferences, the special modulation has been forced upon the wave by dividing it up as the result of the summation of partial waves as given in Eq. (4), so that it should give an exact information of phase, or of z or of e.

From this point of view, it is quite clear that any other stress on the same wave to give additional information will result in a modification of degree of information according to (7). The most striking example is the intersection of the multiple-interference space by reflecting layers tilted in respect to the surfaces A and B, as when introducing for example a glass or a mica sheet as shown in Fig. 9, which gives an intersection in one plane. The partial reflection at the two new borders gives new modulations to the same wave and the result is that the curves run in zigzags with quite definite amplitudes and spacings between the dents, depending on the new disturbance. The phenomenon, which is easily observed, was published [9, 10], but it was not considered as in principle correctly explained before an article of HUNTER and NABARRO [11]. Earlier, POLSTER [12] had however drawn attention to the same phenomenon in principle, and treated it briefly.

By analyzing the zigzags a lot of interesting information can be obtained concerning the tilting angle, the reflectivities, the thickness, and the birefringence, of the interposed sheet. This is all new information about phases, i.e. of the detailed structure of z. The total optical path, in this paper denoted by z, is still available as the average curve of the zigzag [13], in most cases without any correction. What is practically lost is the detailed x information concerning either of the surfaces.

With techniques specially suited to the quality of information required in a special case, e.g. refractive index differences, or roughness of interposed surfaces, these so-called superposed multiple-beam fringes are also of great value. But it is important to realize that the fringes obtained in such cases cannot be interpreted as simple (z, x)-curves. Special attention may be drawn to high-resolution interferences microscopes, where unknown structures must be deduced from interference contrast. It is possible that details visible during adjustments or at certain settings of the important interference microscope of DYSON are of this type [13, 14]. Mr. DYSON has, after correspondence with the writer, examined this possibility and found that the large zigzag contours visible with mica sheets are not due to this effect. He also considers that for biological specimens the reflectivity of bordering surfaces are moreover too small to disturb the main interference appreciably.

When new techniques open new fields of investigation, there is always the possibility that the new information will be obtained at the expense of information obtainable by classical methods. This is the case when both information variables are connected physically, as here. The experiments must be judiciously planned within the laws of uncertainty in order that just the information required may be obtained.

6. Connections to other branches of information theory

The formal information theory introduced by SHANNON, WIENER and others, and applied to signals, has also aroused interest in its application to optics and, more generally, to waves. Thus, BLANC-LAPIERRE and PERROT [16] have drawn attention to the fact that DUFFIEUX's treatment [17] of the incoherent imaging through a lens system can be considered as an information problem. The wave trains travelling through an aperture carry an information quantity equal to its surface divided by $\lambda^2/4$, corresponding to the finite resolving power of the system in both dimensions x and y. It is here only a question of amplitude information. The ideas have a close connection with the new concepts of transmission or contrast reduction curves for establishing true values of "resolving power".

The two-dimensional arguments presented in this paper deal with another question, namely position and phase in one space dimension, and if the uncertainty relations comprise the two space dimensions x and y, and include the phase function in every point, they should be considered as three-dimensional. DUFFIEUX [17] has, ingeniously but only in a verbal discussion, pointed out many consequences of the interrelationships between position and phase in the optics of coherent waves. TORALDO DI FRANCIA [8], and possibly others concerned with the actual techniques of microwaves, have brought the discussions further. One striking fact, often neglected on account of thinking formally after Abbe's formula, is that there exists no theoretical limit to the location by means of waves of two close points, and calculations have also been made recently of selective aperture screening causing an improvement of "resolving power" far above the classical value — while other information, namely the energy distribution in adjacent parts of the field, is reduced [18, 19, 20].

7. Application to phase contrast

The diffraction conditions in phase contrast imaging can be summarized by an uncertainty principle extending that in (7). A difference lies in the fact that the phase contrast involves interceptions in the u function, which makes the uncertainty product dependent on the x entensions, while still valid when averaged, as is required by the method, over the whole coherent wave field. This will be dealt with elsewhere.

Optics Laboratory, Royal Institute of Technology, Stockholm 70, May 1953.

REFERENCES

1. W. HEISENBERG, Die physikalischen Prinzipien der Quantentheorie. Leipzig 1930.
2. N. BOHR, Naturwiss. *16*, 245, 1928; cf. W. HEISENBERG, Naturwiss. *17*, 490, 1929.
3. S. TOLANSKY, Multiple-Beam Interferometry of Surfaces and Films. Oxford 1948.
4. S. TOLANSKY, Monograph Nr. 13, The Institute of Metals, London 1952, and other papers between 1948 and 1952.
5. G. NOMARSKI, Contraste de phase et contraste par interférences, page 65. Paris 1952.
6. J. BROSSEL, Proc. Phys. Soc. *59*, 224, 1947.
7. R. C. FAUST, Proc. Roy. Soc. A *211*, 240, 1952.
8. G. TORALDO DI FRANCIA, Atti della Fondazione Giorgio Ronchi *6*, 73, 1951.
9. S. TOLANSKY, Contraste de phase et contraste par interférences, page 163. Paris 1952.
10. A. M. GLAUERT, Nature *168*, 861, 1951.
11. S. C. HUNTER and F. R. N. NABARRO, Phil. Mag. (7) *43*, 538, 1952.

12. H. P. Polster, J. O. S. A. *39*, 1038, 1949.
13. P. J. Lindberg, Rep. Optics Lab. Roy. Inst. Techn. Stockholm, Nr 23, 1952.
14. J. Dyson, Proc. Roy. Soc. A *204*, 170, 1950.
15. J. Dyson, Contraste de phase et contraste par interférences, page 35, Paris 1952.
16. A. Blanc-Lapierre and M. Perrot, Comptes rendus (Paris) *231*, 539, 1950.
17. P.-M. Duffieux, L'Intégrale de Fourier et ses applications à l'optique. Rennes 1946.
18. G. Toraldo di Francia, Proceedings of the Symposium on Optics and Microwaves (Milano, 1952), Suppl. Nr. 3, Nuovo Cimento *9*, 426, 1952.
19. G. Toraldo di Francia, Atti della Fondazione Giorgio Ronchi, *7*, 366, 1952.
20. M. Françon and A. Saez, paper read before the Real Soc. Española de Fisica y Quimica, April 1953; and verbal communication.

Tryckt den 29 oktober 1953

Uppsala 1953. Almqvist & Wiksells Boktryckeri AB

ARKIV FÖR FYSIK Band 7 nr 25

Communicated 3 June 1953 by ARNE WESTGREN and LISE MEITNER

A critical comparison between some methods for measuring the strength of a Ra-Be neutron source absolutely

By KARL-ERIK LARSSON

With 8 figures in the text

Abstract. The neutron yield of a 250 mg Ra-α-Be source has been determined using two different methods, firstly by integrating the neutron density in a boric acid solution with a small BF_3-chamber and secondly by integration of the neutron density in pure water, using gold foils and subsequent absolute counting of the induced activity. The values found for the yield are $(2.57 \pm 0.12) \cdot 10^6$ neutrons/sec. with the BF_3 chamber method, and $(2.62 \pm 0.08) \cdot 10^6$ neutrons/sec. with the gold foil method. The neutron yield of this source has also been directly compared with the yield of a Harwell standard source, the result of the comparison being $(2.64 \pm 0.13) \cdot 10^6$ neutrons/sec., and indirectly with a Los Alamos source, giving the result $(2.55 \pm 0.21) \cdot 10^6$ neutrons/sec.

I. General

During the recent rapid development of neutron physics it has become increasingly clear that inaccuracy in the measurement of fast neutron fluxes (in the MeV region) has set a limit of about 10% to the accuracy with which absolute cross sections can be determined for reactions between fast neutrons and nuclei, or for processes in which the reaction of a charged particle with a nucleus results in the production of neutrons. For those purposes it is in general sufficient to use methods giving the absolute intensity of a mono-energetic neutron flux, which is easier to measure than a poly-energetic flux, since the methods of measurement available are energy-sensitive [1]. Although it is not often necessary to measure a poly-energetic flux, it is of some interest to measure the flux from a natural source, such as a RaBe source. This can then serve as a standard for the calibration of any other point source, by means of an energy-independent method such as the activation of a $MnSO_4$ solution.

II. Principle of the method

The neutrons from a RaBe source have a complicated and only partly known spectrum [2, 3, 4], and it is therefore hardly possible to measure the flux directly by a recoil method, since these methods are energy-sensitive. The simplest solution is to slow down the neutrons to thermal energies in a moderator, which must be large in extent compared to the distribution of thermal neutrons round the source. If the moderator contains a material which absorbs neutrons, the problem is then to measure the rate of capture, which must be equal to the rate of production by the source. If the source emits Q neutrons per second, and their mean life in the moderator is τ seconds, we have:

$$Q = \frac{4\pi}{\tau} \int_0^\infty \varrho(r)\, r^2\, dr, \tag{1}$$

where $\varrho(r)$ is the neutron density at a distance r from the source. Measurements of this type were first described by AMALDI and FERMI [5], and have since been used by several others [6, 7, 8]. The results have however varied greatly with the details of the methods used, and it is therefore worth while making a comparison between them. The measurements reported below were made using two different methods to determine the flux from the same RaBe source.

III. Measurements

A. Integration of the neutron flux in a H_3BO_3 solution, using a small BF_3 chamber.

1. Method

As follows from equation (1), the problem reduces to an integration of the neutron density over the whole of the volume occupied by the moderator. The neutron mean life is however given by

$$\tau = \frac{1}{v_{\mathrm{th}} \sum N_k\, \sigma_{k\mathrm{th}}} \tag{2}$$

where N_k is the density in the moderator of nuclei of type k, having thermal absorption cross section $\sigma_{k\mathrm{th}}$, assumed to follow the $1/v$ law, and v_{th} is the average neutron velocity at thermal energies. The result therefore depends directly on the value of σ_k for the moderator, which is a serious disadvantage, since the cross section is in general not known to better than a few percent. This difficulty can however be avoided in the following way.

We shall assume that the moderator contains absorbing nuclei of type A_i and cross section $\sigma_i(v)$, and that the detector used to integrate the neutron density is an ionisation chamber containing nuclei of the same sort as the absorber. If, when it absorbs a neutron, this sort of nuclei emits a charged particle which can be counted electrically, it may be shown that the dependence on cross section can be eliminated, provided that the nucleous A_i has a cross section considerably larger than the other types of nuclei making up the moderator. The number I of nuclear reactions occurring per unit time in an ionisation chamber containing n_i nuclei of type A_i is given by:

$$I = n_i \int_0^\infty \varrho(r, v)\, \sigma_i(v)\, v\, dv, \tag{3}$$

where $\varrho\,(r, v)\,dv$ is the velocity distribution at a distance r from the source. If the cross section $\sigma_i\,(v)$ obeys the $1/v$ law, it follows that

$$I = \varrho\,(r)\, v_{\text{th}}\, \sigma_{i\text{th}}\, n_i. \tag{3'}$$

Combining (1), (2), and (3′) we get:

$$Q = 4\pi \frac{N_i}{n_i}\left(1 + \frac{\sum\limits_{k \neq i} N_k\, \sigma_{k\text{th}}}{N_i\, \sigma_{i\text{th}}}\right) \int\limits_0^\infty I\, r^2\, dr. \tag{4}$$

If now $N_i\,\sigma_{i\text{th}} \gg N_k\,\sigma_{k\text{th}}$, the cross sections enter only in as small correction terms. This simple result is valid only if all the cross sections follow the $1/v$ law.

The above requirements are fulfilled by boron, which in the form BF_3 is often used as a filling gas for ionisation chambers. If the neutron density in a water solution of boric acid is measured with a small BF_3 chamber, the source strength is given by the equation:

$$Q = 4\pi \frac{N_{\text{B}}}{V \cdot N'_{\text{B}}}\left(1 + \frac{\sigma_{\text{H}}\, N_{\text{H}}}{\sigma_{\text{B}}\, N_{\text{B}}}\right) \int\limits_0^\infty I\, r^2\, dr, \tag{5}$$

where N_{B} and N'_{B} are the number of boron nuclei per cc in the BF_3 chamber and H_3BO_3 solution respectively, N_{H} the number of hydrogen nuclei per cc in the H_3BO_3 solution, σ_{B} and σ_{H} are the absorption cross sections for boron and hydrogen, and V is the active volume of the chamber.

The term $N_{\text{H}}\sigma_{\text{H}}/N_{\text{B}}\sigma_{\text{B}}$ cannot be made negligibly small, since the amount of boron present in the moderator is limited by the low solubility of boric acid in water, and by the need to maintain a reasonable counting rate. A relatively low concentration is therefore used, and the term $\sigma_{\text{B}}/\sigma_{\text{H}}$ is determined. This may be found integrating the neutron density in pure water and comparing the result with that for the boric acid solution. Then we have:

$$\frac{\sigma_{\text{B}}}{\sigma_{\text{H}}} = \frac{N_{\text{H}}}{N_{\text{B}}}\left(\frac{S_{\text{H}}}{S_{\text{H+B}}} - 1\right), \tag{6}$$

where S_{H} and $S_{\text{H+B}}$ are the values of $\int I\, r^2\, dr$ for water and for the boric acid solution, respectively. From equations (5) and (6) we can then find Q, by measuring the density integrals S both in water and in a boric acid solution, using the same BF_3 chamber. This method was first used and described by BAUER *et al.* [9].

2. Apparatus

The apparatus is shown in Fig. 1. A 250 mg RaBe source is mounted with aluminium clips on one end of a slender plexiglas rod, and suspended at the centre of a cylindrical tank 1 m in diameter and 1 m high, which is filled with the moderator liquid. The other end of the rod is fastened to a sliding carriage which can move along two parallel horizontal rails fastened to the upper edge of the tank. These rails also support another carriage, to which is attached a 5 mm brass tube 55 cm

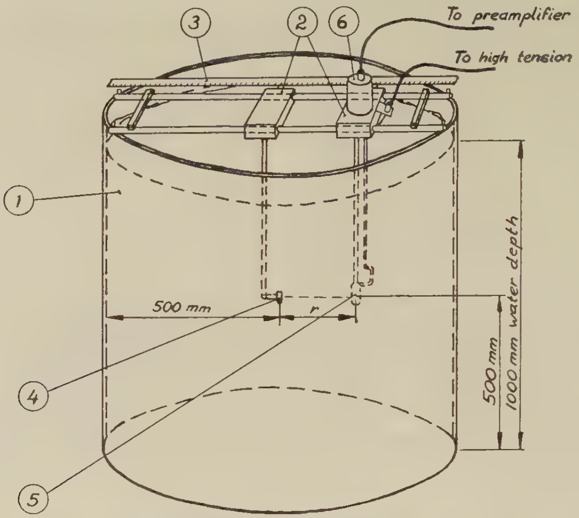

Fig. 1. Experimental arrangement. 1. Water tank with steel rails. 2. Carriages. 3. Steel scale. 4. Ra-Be-source. 5. BF_3-chamber. 6. Housing for first amplification stage.

long, at the lower end of which a small BF_3 chamber is mounted. The collector electrode of the BF_3 chamber is connected to a pre-amplifier on the carriage by means of a 0.02 mm tungsten wire, which is stretched down the centre of the brass tube and held in position with paraffin wax. A 2 mm glass tube running parallel to the brass tube carries a fine copper wire connecting the high voltage to the cathode of the chamber. The pre-amplifier is connected by a cable 1 meter long to the main amplifier, which is followed by a discriminator, scalar, and numerator. The movable carriage supporting the BF_3 chamber is fitted with a pointer running over a millimeter scale, so that the distance r between the centres of the BF_3 chamber and source can be read directly. The high voltage to the chamber is supplied by a stabilised 2 KV supply.

The most important part of the apparatus is the BF_3 chamber and its input circuits, which have both been described in detail in a previous article [10]. It is sufficient to point out here that the geometry and gas filling of the BF_3 chamber must be chosen so that the integral bias curve of the pulse distribution has a plateau at the low-amplitude end, in spite of wall effects in the chamber. If this is achieved, there are very few pulses too small to be detected, and one can assume that 100 % of the nuclear reactions occurring inside the chamber are detected. This means in practice that the chamber must not be too small, and a compromise must be made, since the chamber should be as small as possible in order not to disturb the neutron distribution.

3. Measurements

Four different series of measurements were made. The neutron density was measured over the range $3 < r < 40$ cm, in pure water, and in water containing the following percentages of boric acid: 0.549, 0.946, and 1.390. The concentrations of boric acid were found by titration. The neutron distributions are shown in Fig. 2, where

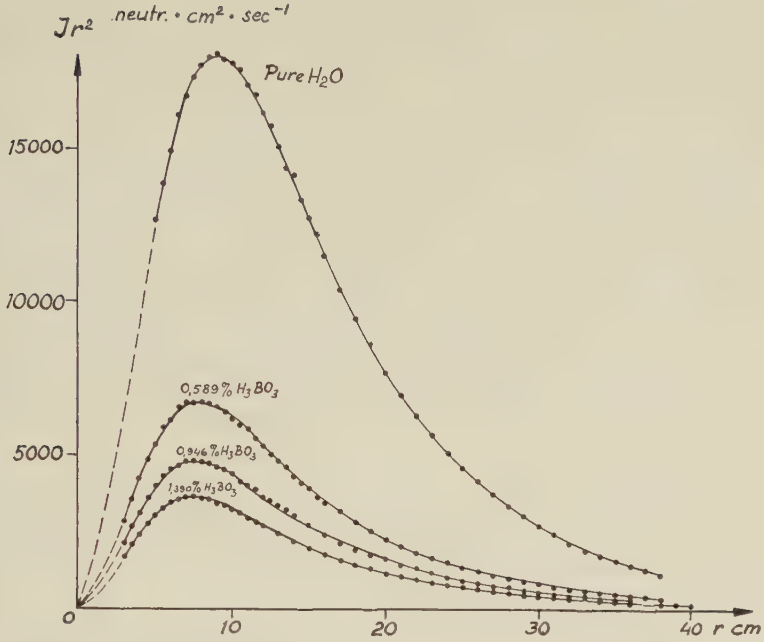

Fig. 2. Neutron density distributions in water and boric acid solutions.

Table I

oncen- ration of $_3BO_3$ (%)	Area S (neutrons · cm³ · sec.⁻¹)									
	Region (calculated)	Area	% of total area	Region (measured)	Area	% of total area	Region (calculated)	Area	% of total area	Total area S
0	$0<r<5.3$	39 970	12.3	$5.3<r<38.3$	275 300	84.4	$38.3<r<\infty$	10 750	3.3	326 000
0.589	$0<r<3.3$	7 110	6.4	$3.3<r<35.3$	98 900	89.2	$35.3<r<\infty$	4 890	4.4	110 900
0.946	$0<r<3.3$	5 560	7.0	$3.3<r<34.3$	69 700	88.4	$34.3<r<\infty$	3 660	4.6	78 900
1.390	$0<r<3.3$	3 920	6.7	$3.3<r<40.3$	53 100	90.7	$40.3<r<\infty$	1 550	2.6	58 600

$I r^2$ is given as a function of r. Before the intensity integrals can be evaluated it is necessary to estimate the intensities in two regions where they cannot be measured directly with the BF_3 chamber: close to the source ($0 < r < 3$ cm), and far away from it ($r > 35$ cm). In the region near the source the dimensions of the chamber are too large, and the cylindrical form of the source will give a neutron distribution which is not strictly spherical. The curves have therefore been extrapolated to zero assuming a gaussian distribution near the source [11], the curve being fitted to the first experimental points on the curve $I(r) = f(r)$. Far from the source ($r > 35$ cm), the intensity becomes too low for accurate measurement, but the curves $I r^2 = \varphi(r)$ fall off exponentially beyond $r = 20$ cm[12] (see Fig. 10 in reference 12), and an extrapolation may therefore easily be made. Table I lists the values found for the areas S under the curves, the contributions of the measured and calculated parts being shown separately. In each case the measured part constitutes some 90% of the total, and small errors in the extrapolations will have little effect on the final values.

Before the yield Q of the source can be calculated there are several corrections which must be considered:

1. Absorption of neutrons in the walls of the chamber.
2. Depression of the neutron density due to the finite size and absorption of the chamber.
3. Absorption of neutrons in the source.

The first of these corrections was determined directly by measuring the absorption in the silvered glass walls of the chamber. A glass tube closed at one end was prepared, using glass of the same sort and thickness as that used for the chamber, silvered in the same way. The transmission through this tube was found using a BF_3 chamber small enough to go inside it. The measurements were made in water, at various distances from the source. The ratio of the counting rates without and with this absorber was found to be 1.015 and the values for S were therefore multiplied by this factor.

The other corrections are difficult to measure. The depression effect can however be estimated theoretically, using the calculations of DRAPER [13] for the efficiency of a BF_3 chamber in a block of paraffin. The calculations show that the depression in the neutron density is 1.5–2 % in the four cases considered here, and the S-values have therefore been multiplied by a further factor 1.017.

The third correction must also be estimated. The total absorption cross section of the source, calculated from a knowledge of its construction, is $\sum = 1.6$ cm². The neutron flux at $r = 1$ may be calculated using equation 3 and assuming a gaussian density distribution. The result is $\varrho \cdot v \sim 2 \cdot 10^4$ neutrons $\text{cm}^{-2}\text{sec}^{-1}$. The absorbing material in the source is now imagined to be uniformly distributed throughout a sphere of radius 1 cm. The number of neutrons absorbed per second is then $0.03 \cdot 10^6$. Since the total yield of the source is $\sim 2.5 \cdot 10^6$ n.sec^{-1}, the correction for self absorption in the source is about 1%. The S-values have therefore been further multiplied by a factor 1.01.

The ratio σ_B/σ_H may now be calculated. The results are collected in Table II.

Table II

% H_3BO_3	$\frac{\sigma_B}{\sigma_H}$
0.589	2270
0.946	2280
1.390	2260
Mean value	2270

If the determination of S, excluding the corrections, is correct to 1 %, and the concentration of H_3BO_3 is known to 0,5 %, the error in the ratio σ_B/σ_H is $\pm$ 2 %.

The result is thus:

$$\frac{\sigma_B}{\sigma_H} = 2270 \pm 45.$$

The values found for this ratio by other workers lie between 1940 and 2380 [14] (see reference 14, p. 294).

Using this value for $\frac{\sigma_B}{\sigma_H}$ we can now calculate the yield Q of the source from equation (5). The number of boron nuclei per cc in the chamber can be found from the pressure in the chamber, $p = 439$ mm Hg at 17° C, and its volume, 3.34 cc, which was found by filling the chamber with water and weighing. The three values found in this way for Q are given in table III.

Table III

Concentration H_3BO_3 (weight %)	Q neutrons/sec.
0.589	$2.56 \cdot 10^6$
0.946	$2.57 \cdot 10^6$
1.390	$2.59 \cdot 10^6$
Mean value	$2.57 \cdot 10^6$

4. Discussion of the sources of error

The greatest source of inaccuracy in this measurement is due to an uncertainty about the cross section of boron. Mass-spectroscopic measurements by THODE *et al.* [15] have shown that the isotope ratio $B_{10}:B_{11}$ in different samples of natural boron may vary by as much as 3.5 %. It is also possible that the method [16] used to purify the BF_3 filling gas may have led to a small shift in the isotope ratio. Thus the cross section of the boron in the chamber may not be the same as that in the boric acid solution, as was assumed above, and this would influence the result directly, as may be seen at once if equation (5) is rewritten:

$$Q = \frac{4\pi N_B}{V \cdot N'_B} \cdot \frac{\sigma_B}{\sigma'_B} \cdot \left(1 + \frac{N_H \sigma_H}{N_B \sigma_B}\right) S. \tag{5'}$$

Q is then proportional to σ_B/σ'_B, where

σ_B = cross section for boron in the boric acid, and
σ'_B = cross section for the boron in the BF_3 counter gas.

The uncertainty in the result due to this effect may be taken to be 4 %.

Other factors appearing in the expression for Q are the uncertainty of 0.5 % in N_B caused by the errors in the determination of the concentration of boric acid, and the uncertainty of 0.3 % in N'_B emanating from errors in the measurement of the pressure in the BF_3 chamber.

The area S, excluding the correction terms is known with good accuracy, the greatest uncertainty coming from the extrapolation of the curve $I(r) = f(r)$ to $r = 0$. As this calculated part of the area constitutes ≤ 10 % of the total area, and the error made in the extrapolation should not exceed 10 %, the uncertainty in S from this cause should be ≤ 1%. Of the three correction factors, the correction for the absorption of the chamber walls is known to an accuracy of about 10 %, which gives a vanishingly small error in the correction factor 1.015. The correction for the self-absorption of the source is based on the knowledge of the total absorption cross section, 1.6 cm², of the source. As will be mentioned below, this cross section was measured at Harwell with the pile oscillator, the result being 1.4 cm², in reasonable agreement with the calculated value. The error in the correction factor 1.01 is therefore believed to be very small. The most uncertain correction is made for the depression in the neutron density made by the chamber. Draper's calculation was made assuming a constant neutron density, while the actual density distribution shows a gradient. The correction factor 1.017 for the depression effect should be regarded as an estimate, and the uncertainty is assumed to be 1%. The total error in S, including the uncertainty in the correction factors, is therefore taken to be 2%. There is finally a slight chance that the sensitive volume of the chamber is not equal to its geometrical volume: we may allow an error here of 0.5 %. Summing all these errors we find a total estimated error of 4.6%, and the absolute neutron yield of the source is

$$Q = (2.57 \pm 0.12) \cdot 10^6 \text{ neutron/sec.}$$

B. Integration of the neutron flux using gold foils in water

1. Method

Instead of using an ionisation chamber as neutron detector, one may make use of the radioactivity which is often induced in nuclei by neutron capture. The detector may consist of a thin foil. Let the foil be made of a material with thermal neutron absorption cross section σ_{th} and atomic weight M, the total weight of the foil being m grams. The source strength as found by integrating the neutron density in water (compare with equations (1) and (3) is then:

$$Q = 4\pi \frac{\sigma_{\text{Hth}}}{\sigma_{\text{th}}} \cdot \frac{M}{M_{\frac{1}{2}\text{H}_2\text{O}}} \cdot \int_0^\infty C(r)\, r^2\, dr. \tag{7}$$

The quantity to be measured in this case is the specific activity $C(r) = n/m$, where n is the absolute rate of capture in foils placed at different distances from the source; n may be found by an absolute determination of the induced radioactivity.

One of the most reliable ways of measuring low activities absolutely [17, 18] is the coincidence method. If uncertain corrections are to be avoided, this method requires that:

a. the deacy scheme for the detector element must be simple, preferably a single β-decay followed immediately by one or more γ-quanta, and
b. the internal conversion of the γ-ray must be slight.

Other requirements which the foil material must satisfy are that

c. the absorption cross section for thermal neutrons must be large, because of the low neutron flux to be measured,
d. the absorption cross section must follow the $1/v$ law, which was assumed in setting up equation 7,

e. the half-life must be suitable,
f. it must be possible to prepare the element in the form of thin foils, which must be chemically neutral, so that no changes occur in them in the course of activations in water lasting for a considerable time.

Gold (Au^{197}) fullfils these conditions sufficiently well. Its most serious disadvantage is that its $1/v$ region is short, the first resonance occurring at 4.95 eV[19]. The effect of the activity induced by resonance neutrons is allowed for as follows. The absolute activity n of the foil may be written:

$$n(r) = A \int_0^\infty \varrho(r, v)\, \sigma(v)\, v\, dv, \tag{8}$$

where A is the number of nuclei in the foil. Now

$$n_{\mathrm{tot}}(r) = A\, \sigma_{\mathrm{th}}\, v_{\mathrm{th}} \int_0^{v_{\mathrm{Cd}}} \varrho(r v)\, dv + A \int_{v_{\mathrm{Cd}}}^\infty \varrho(r, v)\, \sigma(v)\, v\, dv = n_{\mathrm{th}}(r) + n_{\mathrm{res}}(r). \tag{9}$$

It has here been assumed that the cross section follows the $1/v$ law up to at least the absorption cut-off of cadmium, v_{Cd}. Of the two contributions to the total activity n_{tot}, we are here interested only in that due to thermal neutrons, n_{th}. This is given by

$$n_{\mathrm{th}}(r) = n_{\mathrm{tot}}(r) \cdot (1 - 1/R(r)), \tag{10}$$

where $R(r) = n_{\mathrm{tot}}/n_{\mathrm{res}}$ is the "cadmium ratio".

Cadmium difference measurements must therefore be made. In spite of this the method is simple, and should give an accuracy comparable to that of the BF_3 chamber method.

2. Experimental procedure and apparatus

a. **Experimental procedure.** The application of the coincidence method to the measurement of weak sources has been described in detail by several authors [17]. When the activity of the source decreases markedly during the course of the measurements, it can be shown that the activity, N_0, of the source at the beginning of the measurements is given by:

$$N_0 = \frac{N_\beta N_\gamma}{N_{\beta\gamma}} \cdot \frac{\lambda}{1 - e^{-\lambda T}}, \tag{11}$$

where N_β, N_γ, and $N_{\beta\gamma}$ are the total numbers of pulses recorded in time T in the β, γ, and coincidence channels, and λ is the decay constant. These quantities must be corrected for background effects, and allowance must be made in N_β for any γ-quanta which may be counted by the β-counter. In the case in question here the foils are activated for a certain time t in the water tank be neutron irradiation from the Ra-Be source, and their activity at the end of the irradiation period is given by

$$N_0 = n(1 - e^{-\lambda t}), \tag{12}$$

where n is the activity of the foil after an infinitely long activation period. Equations (11) and (12) give:

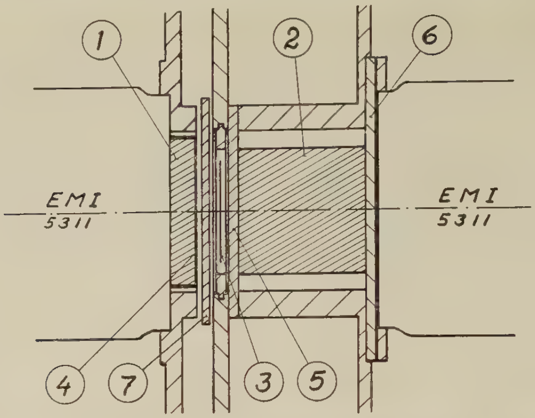

Fig. 3. Counter arrangement. 1. Stilbene crystal. 2. NaJ crystal. 3. Au foil. 4. Al reflector (0.15 mg/cm²). 5. Al absorber and reflector. 6. Perspex window. 7. Removable Al absorber.

$$n = \frac{N_\beta N_\gamma}{N_{\beta\lambda}} \frac{\lambda}{(1-e^{-\lambda T})(1-e^{-\lambda t})}. \tag{13}$$

This is the absolute rate of capture in the foil, which is the term inside the integral sign of equation (7).

b. **Apparatus.** Since the RaBe source gives a relatively low flux, the activity induced in thin gold foils is low, and it is therefore necessary to choose the counters and counter geometry so that the efficiency for both β and γ-counting is high. For this reason scintillation detectors were used. The experimental arrangement is shown in Fig. 3.

Two photomultipliers of type EMI 5311 were mounted with their cathodes facing each other in a light-tight box. The scintillator crystals, which were mounted directly against the cathodes, were in one case a stilbene crystal 30 × 30 × 5 mm, and in the other a NaI crystal 25 × 25 × 25 mm. The NaI crystal was clamped between two small springs in an aluminium housing filled with paraffin oil. The housing had a perspex window on the side facing the cathode, while its opposite side consisted of a 2.5 mm aluminium plate, which served both as an optical reflector and as a screen to absorb the β-rays emitted by the gold foil. The stilbene crystal was enclosed on five sides by thin aluminium reflectors (0.15 mg/cm²), cemented to the crystal with Canada balsam, the free side of the crystal being cemented, also with Canada balsam, to the cathode surface of the photomultiplier. The foil was mounted in a holder between the two crystals, as may be seen in Fig. 3, and provision was made to insert a 2.0 mm aluminium absorber between the foil and the stilbene crystal. The foils which were 20 × 20 × 0.01 mm, were mounted in small perspex frames by means of steel wires of diameter 0.05 mm (Fig. 4), in order not to disturb the neutron distribution in the moderator more than was necessary. The crystals were placed as close to the foil as was mechanically possible, to increase the detection solid angle: the space between the foil and the crystal surfaces was about 4 mm.

The factors governing the choice of the crystal types were the following. For γ-counting the crystal should consist of elements of high atomic weight, to give a

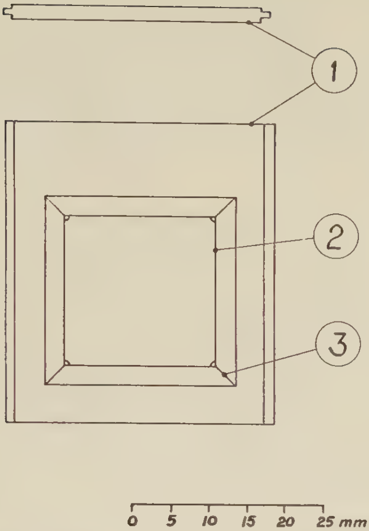

Fig 4 Foil mounting. 1. Perspex frame. 2. Au foil. 3. 0.05 mm steel wires fixed to the foil with araldite wax.

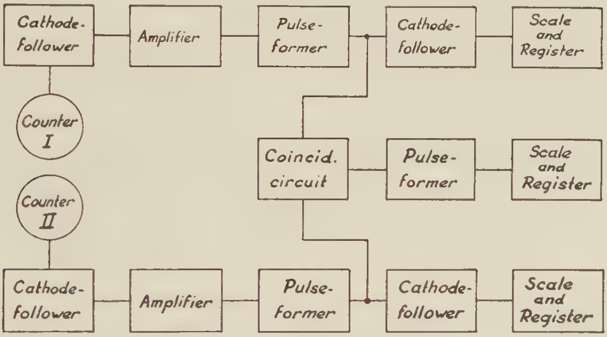

Fig. 5. Block diagram of circuit.

high efficiency: it is simplest to use NaI. With the arrangement used the total γ-efficiency was about 8 %. For the β-crystal, on the other hand, the γ-efficiency should be as low as possible, since the γ-counts in this channel must be found by an absorption method and subtracted from the β-counts. A thin stilbene crystal is suitable, giving in this case a β-efficiency of 30–35 %, while the γ-efficiency was only 1 or 2 %, for the selected crystal. To reduce background effects the whole arrangement was screened by 5 cm of lead.

A block diagram of the apparatus is given in Fig. 5. The pulses from the photomultipliers were fed through cathode-followers to low-gain feed-back amplifiers, and then to a pulseforming circuit. From here they were fed out through cathode-followers to two scalars, and also to a coincidence circuit of the usual Rossi type, after which they were again shaped, and fed to a third scalar. By simultaneously registering the counts from the β, γ, and coincidence channels, the effects of drifts in the electronic circuits were eliminated.

The minimum resolving time which could be used without loss of true coincidences was 0.4 μs, as determined by screening the counters from each other and irradiating them with two small radium sources. The resolving time used during the experiment was 0.6 μs.

3. Measurements

a. Activations. The foils were activated four at a time. They were suspended by means of fine steel wires stretched across a cubical frame-work of side 95 cm, at various well-defined distances from the neutron source, which was suspended in the same manner at the centre of the frame. The spacings between foils and source were measured with a cathetometer. The whole frame assembly was then immersed in water in the same tank as was used for the BF_3 chamber measurements. Each foil, which was weighed before mounting, was irradiated for 10 days, and its activity then measured. The measurement procedure always began with a background measurement, followed by a two-hours measurement of the activity (N_β, N_γ, $N_{\beta\gamma}$), a two-hours measurement of the β-activity with the 2.5 mm aluminium absorber inserted, and finally another background measurement. At least two such series were taken for each foil. Eight foils were activated, at distances r between 4, 70, and 13.12 cm.

The foils were subsequently wrapped in 1 mm cadmium sheet and reactivated, so that the correction could be made for resonance capture at 4.95 eV. Seven foils were activated in this way, for distances r between 4.74 and 11.69 cm. It was not practicable to measure at greater distances from the source, because of the extremely low activities of the foils (only 7 decays/sec at $r = 11.69$ cm). Instead of measuring the whole neutron distribution in the tank, one can make use of the very accurate results of the BF_3 chamber measurement described above. We need to find $S_{Au} = \int_0^\infty C_{th} r^2 \, d r$ where $C_{th} = n/m$. From the BF_3 chamber measurements we know $S_{BF_3} = \int_0^\infty I_{BF_3} r^2 \, d r$, accurate to 1% not including corrections. The neutron distribution is of course independent of the detector used, and thus the ratio C_{th}/I_{BF_3} should be constant and independent of r. This constant $F = C_{th}/I_{BF_3}$ was found, from eight measured values of C_{tot} and we therefore have:

$$S_{Au} = F \cdot S_{BF_3}. \tag{14}$$

b. Effects of decay scheme and internal conversion. The use of the coincidence method for the measurement of absolute decay rates assumes that the decay scheme of the detector element is simple, and that the internal conversion of the gamma radiation is negligible. These two conditions are however not strictly fulfilled by Au^{198}, since the currently accepted decay scheme [20, 21, 22] is shown in Fig. 6, and the experimentally measured [22] internal conversion coefficient is about 0.05. It can be shown [17] that the correction for the complex decay scheme is very small, since only about 1% of the decays do not

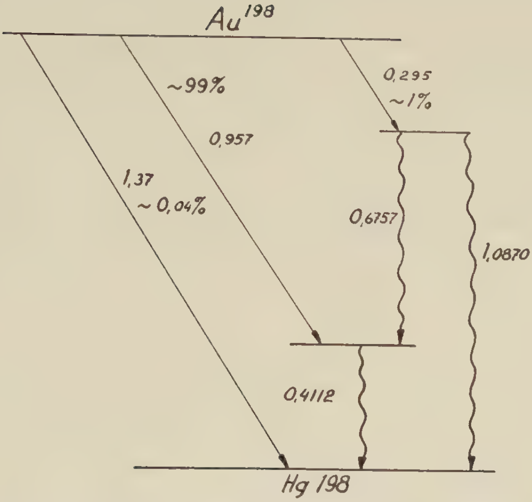

Fig. 6. Decay scheme of Au^{198}.

follow the simple main branch, but the correction for the internal conversion effect is more important. If the internal conversion coefficient is α, one finds that

$$\frac{N_\beta N_\gamma}{N_{\beta\gamma}} = N\left(1 + \alpha\frac{E_2}{E_1} - \alpha E_2\right) = n \qquad (15)$$

where N is the true decay rate, and E_1 and E_2 are mean values for the counting efficiencies of the direct and converted β-rays respectively. Since E_1 and E_2 are not precisely known, the correction cannot be calculated. One may however vary E_2 by making a series of measurements with different absorbers, which will give different values for n, the true value being that corresponding to $E_2 = 0$.

In order to investigate these two effects, a gold foil was irradiated to high activity in the reactor JEEP at Kjeller, Norway, and the absolute activity determined, with aluminium absorbers of various thicknesses between the foil and the β-crystal. The results of the measurements are shown in Fig. 7. There is no change in n for absorber thicknesses up to 54 mg/cm², but between this value and 81 mg/cm² there is a reduction of 4%. For thicker absorbers the value is independent of the absorber thickness. This is what one might expect if E_2 falls to zero between 54 and 81 mg/cm², which corresponds to an energy interval of 0.2–0.3 MeV. If $E_2 \approx E_1 \approx 0.2$, equation 15 gives a correction factor 1.04 for $\alpha = 0.05$. The experimental values for n have been divided by this factor.

c. **Results.** The results of the two series, with bare gold foils, and with the foils wrapped in cadmium, are given in Table IV, which also shows the corrections due to resonance absorption. The half-life of Au^{198} has been taken to be 2.69 days [23], for the purpose of calculating the saturation activity using Equation (13).

The following method has been used in making the correction for resonance absorption. If the values found for C_{tot}, given in column 3 of Table IV, are plotted on semi-logarithmic paper as a function of r, they are found to lie on a straight line.

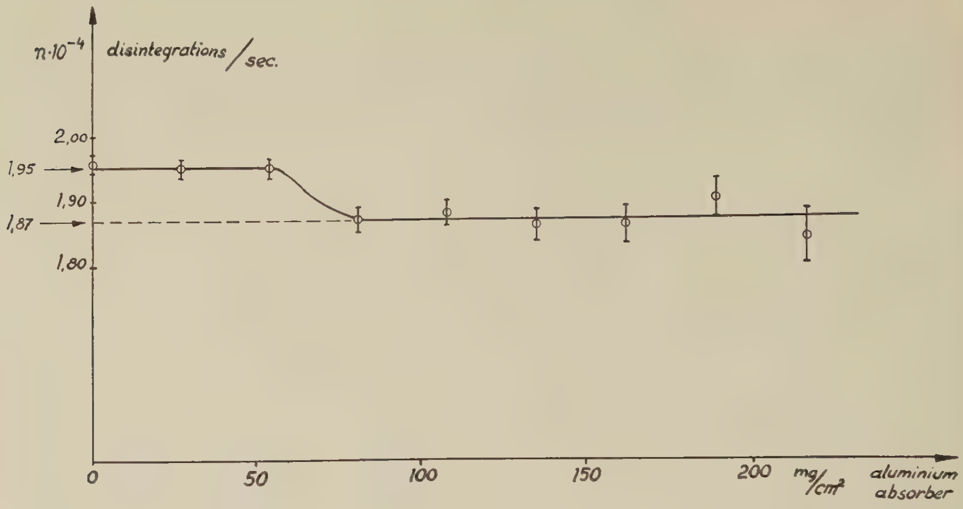

Fig. 7. Absorption curve showing the efect of internal conversion.

Table IV

Bare Au foils			Au foils wrapped in 1 mm Cd sheet					Correction of C_{tot} for resonance absorption		
r cm	foil weight (g)	C_{tot} pulses sec.$^{-1}$ g^{-1}	r cm	foil weight (g)	C_{res} pulses sec.$^{-1}$ g^{-1}	Calculated value of C_{tot}	$R = \frac{C_{tot}}{C_{res}}$	r cm	R read from curve	$C_{tot} = \left(1 - \frac{1}{R}\right) = C_{th}$
4.70	0.05312	5470	4.74	0.05658	1049	5500	5.24	4.70	5.17	4410
5.64	0.05641	4460	5.72	0.05751	850	4410	5.19	5.64	5.30	3620
6.93	0.05647	3360	6.66	0.05416	633	3570	5.64	6.93	5.68	2770
9.40	0.05408	1990	8.13	0.05488	413	2560	6.20	9.40	6.90	1700
10.05	0.05140	1680	9.39	0.05641	278	1930	6.94	10.05	7.30	1450
10.99	0.05470	1340	10.62	0.05540	192	1460	7.60	10.99	7.88	1170
12.15	0.05382	1045	11.69	0.05140	144	1150	7.99	12.15	8.55	923
13.12	0.05454	811						13.12	9.13	722

The empirical equation of this line is: $\ln C_{tot} = -0.225\, r + 9.678$. Using this relation, C_{tot} (column 7) is then calculated for those values of r for which C_{res} has been measured (column 6). The cadmium ratio $C_{tot}/C_{res} = R(r)$ (column 8) is then found: this ratio is shown as a function of r in Fig. 8. From this curve we take R (column 10) for those r-values for which C_{tot} has been measured. The specific activity C_{th} (column 11) then follows from the relation (10). Column 11 of Table IV thus gives the final result.

Since it is a consequence of this method that neutrons with velocities greater than v_{Cd} (the cadmium limit) are not counted, it may appear that C_{th} is too low. Measurements made with a BF_3 chamber screened with cadmium showed, how-

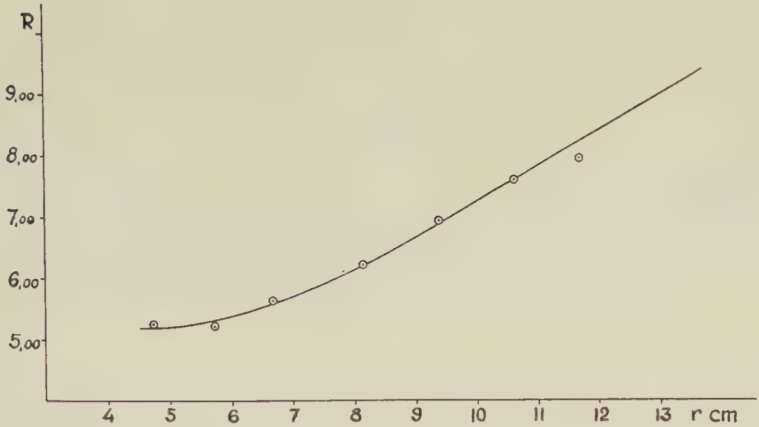

Fig. 8. Cadimum ratio in water for gold foils as a function of distance from the Ra-Be-neutron source.

ever, that the density of neutrons having energies above the cadmium limit is less than 0.5% of the total density, and may therefore be neglected.

Before the ratio $C_{\text{th}}/I_{\text{BF}_3}$ can be calculated, it is necessary to consider how great is the depression made in the neutron distribution by the gold foils. This would be very difficult to measure, so the theoretical results of SKYRME [24], who calculated the depression due to a circular foil, have been used. As is shown by Skyrme, the deviation of the absolute capture rate of a foil from the ideal, $\varrho v A \sigma$ (see Equ. 9), depends mainly on the self-screening of the foil and on the depression in the neutron density in its immediate neighbourhood. The result of the somewhat involved calculations (Equ. A 23 in Skyrme's article) shows that the disturbed capture rate (n) of the foil is given by

$$n = \varrho v A \sigma \left\{1 - \frac{t}{\lambda}\left(\frac{1}{2} E\left(\frac{t}{\lambda}\right) + A\left(\frac{a}{\lambda}\right) + D_1 - D_1'\right)\right\} \tag{16}$$

where t = the foil thickness,
λ = the total mean free path of neutrons in the foil,
a = the foil radius.

The function $\frac{1}{2} E\left(\frac{t}{\lambda}\right) + A\left(\frac{a}{\lambda}\right)$ is given in Skyrme's article for a series of values of the parameters. $D_1 - D_1'$ is a function of the foil radius a, and of the transport parameters of the moderator, namely the diffusion length L, the mean free paths λ_a for absorption and λ_s for scattering. The function D_1 is also calculated in Skyrme's article for a series of values of the actual parameters. D_1' is small compared to D_1 and may be neglected.

For the calculation of the correction factor, the following values are used for the various parameters:

1. The foil thickness $t = 0.001$ cm.
2. The total mean free path, λ, of neutrons in gold is calculated from the total cross section at thermal energy, which is ~ 100 barns [25].

   This gives $\lambda = 0.17$ cm.

3. The foil radius is chosen so that the area of the imagined circular foil is equal to the area of the actual square foil, which gives $a = 1.1$ cm.

   These variables determine the function $\frac{1}{2} E\left(\frac{t}{\lambda}\right) + A\left(\frac{a}{\lambda}\right)$, which then has the value 2.77.
4. For the diffusion length L of thermal neutrons in water the value 2.80 has been taken [26, 27, 12].
5. The mean free path, λ, of neutrons in water is determined from the value 0.325 barns for the absorption cross section of hydrogen [28] for thermal neutrons combined with the value adopted for L and is found to be 0.51 cm.

These values of L, λ and a completely determine the function D_1 the value of which is then 2.15.

The final expression for the absolute capture rate of the gold foil in water is thus

$$n = \varrho v A \sigma (1 - 0.03). \tag{17}$$

The values found for C_{th} must therefore be multiplied by 1.03. The calculation of the ratio F is shown in Table V, where column 2 gives the values corrected for the depression effect, and column 3 gives the corresponding BF_3 counting rates taken from the curve $I_{BF_3} = f(r)$, which was measured very accurately. The values for the ratio C_{th}/I_{BF_3} in column 4 are the same within the limits of statistical accuracy.

The neutron yield of the source may now be calculated from equations (7) and (14), the value for S_{BF_3}, $3.26 \cdot 10^5$, being taken from Table I.

If $\sigma_H = 0.325$ and $\sigma_{Au} = 95$ barns [25, 28], we find for the yield:

$$Q = 2.62 \cdot 10^6 \text{ neutrons/sec.}$$

This value has been corrected for self-absorption in the source by multiplication with the factor 1.01, as was done in the BF_3 chamber measurement.

Table V

r cm	$C_{\text{th}} \cdot 1.03 = C'_{\text{th}}$ pulses sec.$^{-1}$ g^{-1}	I_{BF_3} pulses/sec.	$\frac{C'_{\text{th}}}{I_{BF_3}} = F$
4.70	4 540	535	8.49
5.64	3 730	444	8.40
6.93	2 850	337	8.46
9.40	1 750	205	8.54
10.05	1 490	177	8.42
10.99	1 210	144	8.40
12.15	951	111	8.57
13.12	744	89.3	8.33
		Mean value	8.45

4. Sources of error

The cross sections σ_H and σ_{Au} entering the calculations both seem to be known with good accuracy. Many determinations of σ_H have been made, the mean value of which is 0.328 ± 0.005 barns (see reference 14, p. 294). In a measurement not yet published by B. HAMERMESH, G. R. RINGO and S. WEXLER at Argonne National Laboratory[1], a value of $\sigma_H = 0.329 \pm 0.004$ barns has been found. Further measurements at present being made by VON DARDEL and A. W. WALTNER at AB Atomenergi, Stockholm [28], have given a preliminary value of 0.325 barns, with a possible correction of $\leq 1\%$, so that their final value will probably fall within the limits $0.320 < \sigma_H < 0.325$ barns, with an error $< 1\%$. It therefore seems reasonable to take a value of $\sigma_H = 0.325$ barns $\pm 1\%$. According to POMMERANCE who has given a review of existing data concerning the cross section of gold (Au^{197}) the most probable value is at present $\sigma_{Au} = 95 \pm 1$ barns [25]. The most important source of error is to be found in the factor $F = \frac{C'_{th}}{I_{BF_3}}$. In particular, the estimation of the depression effect due to the foil is uncertain, as this correction is dependent on the values of the transport parameters of neutron diffusion in water, and because Skyrme's calculations are valid for a foil shape different from that actually used. An uncertainty of 1.5 % in C_{th} has therefore been assumed, which corresponds to an uncertainty of 50 % in the theoretical estimation of the factor 0.03. Further, the error in the correction factor 1.04 for the internal conversion is about 1%. Compared to this possible error of 2.5 % in C'_{th} the uncertainty in I_{BF_3} is very small, so that the total error in F is given as 2.5 %. The area S_{BF_3}, not including any corrections in this case, is — as discussed above — determined to an accuracy of $\sim 1\%$. In this measurement, as in the measurements with the BF_3 chamber, the loss of neutrons through the walls of the tank is completely negligible, since the distance from the source to the walls is 50 cm, which is some 6 migration lengths [12, 29] for RaBe neutrons. Summing the errors considered above, the estimated error of the determination of Q is ± 3 %, and the final result of the measurement is

$$Q = (2.62 \pm 0.08) \cdot 10^6 \text{ neutrons/sec.}$$

This result agrees well with that found using the BF_3 chamber.

C. Comparison between the 250 mC source and a standard Harwell source

By the kind cooperation of the reactor group at Harwell, and in particular of Dr. D. J. LITTLER, it has been possible to arrange for a comparison between this Swedish neutron source, and the Harwell standard, which is a 1290 mg RaBe source. This has been calibrated by Dr. LITTLER, using the Graphite Low Energy Experimental Pile [30]. The comparison between the 250 mg source and the Harwell standard was made by a pile method similar to that used by LITTLER to measure the spontaneous fission rate of uranium [31]. The method has been described in a Harwell report [32]. The comparison gave the result:

$$\frac{Q_{\text{Swedish}}}{Q_{\text{Harwell}}} = 0.273 \pm 2\ \%.$$

Since the yield of the Harwell source was $9.66 \cdot 10^6$ n/sec. $\pm$ 4.5 %, we have

$$Q_{\text{Swedish}} = (2.64 \pm 0.13) \cdot 10^6 \text{ n/sec.}$$

---

[1] Now published in Phys. Rev. *90*, 603, 1953.

The "absolute" part of the method used by Littler to calibrate the Harwell source lies in the absolute measurement of the β-activity induced in Na^{23} and P^{32} by pile irradiation. It is worth mentioning that the total cross section for the Swedish Ra-Be source as measured by Littler with the GLEEP pile oscillator was 1.4 cm^2, which may be compared with the value 1.6 cm^2 calculated previously and used in the calculation of the self-absorption of the source.

The Harwell source has also been compared with an American standard [33], the Los Alamos source No. 40. This had previously been compared with the American source No. 44, the yield of which has been measured absolutely by FRISCH and WALKER using integration of the neutron density in a water bath [6]. The comparison between the Los Alamos source No. 40 and the Harwell source gave the result:

$$\frac{Q_{\text{Los Alamos}}}{Q_{\text{Harwell}}} = 0.636 \pm 3\ \%.$$

From this ratio and that given above for the Swedish and Harwell sources, we find

$$\frac{Q_{\text{Swedish}}}{Q_{\text{Los Alamos}}} = 0.429 \pm 3.6\ \%.$$

Using the American value for the strength of source No. 40, $5.95 \cdot 10^6 \pm 7.5\%$ n/sec., we have then

$$Q_{\text{Swedish}} = (2.55 \pm 0.21) \cdot 10^6 \text{ n/sec.}$$

Considering the totally different methods used for the absolute calibrations, the agreement is very satisfactory.[1]

IV. Discussion of the results

Attempts to make absolute measurements of fast neutron fluxes have in general given poor accuracy, the best being about ± 6 %, even if the object was to measure mono-energetic neutrons [34]. Of those methods at present available for the determination of poly-energetic fluxes, the most accurate should be those which entail the slowing-down of the neutrons and their subsequent measurement at thermal energies, since one can then be certain that the detector is independent of energy. By such methods the total source strength can always be found, whatever the primary energy of the neutrons. The simplest way of finding the total source strength is by comparison with an accurately calibrated natural source.

The measurements described above gave results falling within a range of 3.5 %: this scatter is surprisingly small, considering that different methods were used, and that the errors estimated for the various measurements were relatively large. A general review of the sources of error in measurements of the diffusion type shows that two types of error are of primary importance: error in correcting for the depression caused by the foil or other detector, and, when an absolute measurement is based on the counting of the number of boron disintegrations, error in the boron cross section. The depression effect, studied in the work of Draper and Skyrme cited above, has also been treated by other authors, for example BOTHE [35] and TITTLE [27]. All these investigations, when applied to the foils and probes used in the present measurements, lead to corrections of the same order of magnitude. The uncertainty in the results due to these corrections is between 1 and 2 %. The absorption cross section of boron depends on the isotope ratio B_{10}/B_{11}, and the only way to avoid error from this cause would be to investigate the boron in the detector chamber and in the moderator solution, using the mass spectrometer.

---

[1] By the kind cooperation of Professor P. HUBER of Basel the Swedish source has also been compared with a Swiss source [8]. The comparison was made both at Basel by the activation of a Mn-solution, and at Stockholm by the integration of the neutron densities from the two sources in water with a small BF_3 chamber. The Swiss source has also been compared with the Harwell source at Harwell, by several different methods. The results, however, do not agree at all, showing variations up to 30 %. This is probably due to an unconsolidated mixture of Ra salt and Be powder in the Swiss source, causing the neutron yield to change when the source is shaken.

In view of these considerations it seems reasonable to assume an error of ± 3 % in the mean value of the measurements described above, which leads to the combined result

$$Q = (2.60 \pm 0.08) \cdot 10^6 \text{ neutrons/sec.}$$

There are two possible causes of change in a Ra-Be neutron standard of the sort used here: the mechanically mixed Ra salt and Be powder may be shaken into a new configuration; and there may be a slow increase in the yield, due to the growth of polonium in the disintegration series following radium. The first of these effects was tested experimentally by tapping the source sharply and then measuring its yield: there was no observable change. The increase in yield due to the growth of polonium cannot be calculated exactly, as it depends on the age of the radium in the source. This must however be at least eight years, which is the age of the source, and calculation shows that the maximum increase due to this cause is 0.5 % per year. The total increase in yield when equilibrium is reached, which would require more than a hundred years, is 25 %.

AB Atomenergi, Department of Physics, Stockholm.

REFERENCES

1. H. H. BARSCHALL, L. ROSEN and R. T. TASCHEK: Rev. Mod. Phys. *24*, 1, 1952.
2. D. L. HILL: AECD-1945, 1947.
3. M. TEUCHER: ZS. f. Phys. 126, 410, 1949.
4. P. DEMERS: Canadian Decl. Report, MP-204, 1945.
5. E. AMALDI, and E. FERMI: Phys. Rev. *50*, 899, 1936.
6. R. L. WALKER: MDDC-414, 1946.
7. J. ROTHBLAT: British Decl. Report, Br–224, 1943.
8. F. ALDER, P. HUBER: Helv. Phys. Acta, Bd XXII, 368, 1949.
9. S. G. BAUER, H. F. FREUNDLICH, L. KOWARSKI, A. N. MAY, H. SELIGMAN: British Decl. Report, Br-134, 1943.
10. K.-E. LARSSON and C. TAYLOR: Arkiv f. Fysik, Bd 3, 131, 1951.
11. R. E. MARSHAK: Rev. Mod. Phys. *19*, 185, 1947.
12. K.-E. LARSSON: Arkiv f. Fysik, Bd 2, 47, 1950.
13. J. E. DRAPER: Nucleonics, *6*, nr 3, 32, 1950.
14. W. F. HORNYAK, T. LAURITSEN, P. MORRISON, and W. A. FOWLER: Rev. Mod. Phys. *22*, 291, 1950.
15. H. G. THODE, J. MACNAMARA, F. P. LOSSING and C. B. COLLINS: J. Amer. Chem. Soc. *70*, 3008, 1948.

16. J. A. Bistline: Rev. Sci. Inst. *19*, 842, 1948.
17. J. L. Putman: Brit. J. Rad. *23*, 46, 1950.
18. R. Cohen: Ann. de Phys. *7*, 185, 1952.
19. R. K. Adair: Rev. Mod. Phys. *22*, 249, 1950.
20. L. G. Elliot, and J. L. Wolfson: Phys. Rev. *82*, 333, 1951.
21. P. E. Cavanagh: Phys. Rev. *82*, 791, 1951.
22. P. Hubert: Comptes Rendus, *232*, 2201, 1951.
23. L. M. Silver: Can. J. Phys. A, *29*, 59, 1951.
24. T. H. R. Skyrme: Canadian Decl. Report, MS-91.
25. H. Pommerance: Phys. Rev. *83*, 641, 1951.
26. F. J. Sisk, E. C. Campbell: Phys. Rev. *82*, 345, 1951.
27. C. W. Tittle: Phys. Rev. *80*, 756, 1950.
28. Guy von Dardel, A. W. Waltner, Phys. Rev. (to be published).
29. P. R. Wallace, and J. Le Caine: Canadian Report MT-12.
30. D. J. Littler: Proc. Phys. Soc., LXIV, 638, 1951.
31. —— Proc. Phys. Soc., LXV, 203, 1952.
32. D. J. Littler, and E. E. Lockett: Harwell Report, AERE, R/R 1035, 1952.
33. D. J. Littler, E. E. Lockett, A. D. McRonald, P. W. Mummery, P. R. Tunnicliffe: Harwell Report AERE, R/R 776, 1951.
34. K. W. Allen, D. L. Livesey, and D. H. Wilkinson: Proc. Cambridge Phil. Soc. *46*, 339, 1950.
35. W. Bothe, ZS. f. Phys. *120*, 437, 1942.

Tryckt den 30 november 1953

Uppsala 1953. Almqvist & Wiksells Boktryckeri AB

ARKIV FÖR FYSIK Band 7 nr 26

Communicated 3 June 1953 by E. HULTHÉN and G. BORELIUS

Paramagnetic susceptibility measurements on AgMn and AuMn alloys

By EBBE KRONQVIST and ALDO GIANSOLDATI

With 6 figures in the text

Introduction

At the Physical Department of the Royal Institute of Technology a number of investigations have been made on the paramagnetic susceptibility of binary alloys. In most cases the main component was one of the diamagnetic metals Au, Ag, or Cu, and the second component a transition metal. Alloys of such a constitution usually have a strong paramagnetic susceptibility which approximately follows Curie-Weiss' law. One of the most interesting results of measurements of this kind is the value of the atomic magnetic moment of the dissolved transition metal. Previously such determinations of the magnetic moment of the Mn atom, dissolved in diamagnetic metals, have been made by NÉEL (1) and GUSTAFSSON (2). Gustafsson's investigation was made on dilute AgMn and CuMn alloys from room temperature to about 400° C. Further information was considered to be of great interest, especially on the AgMn alloys, as the measurements on this system by NÉEL and GUSTAFSSON did not agree (2). Therefore a redetermination was made as the first part of this work.

In the second part of this investigation, the influence of cold-working on the paramagnetic susceptibilities of these alloys has been determined. It is, as a matter of fact, not quite clear, how cold-working changes the metal structure. It has been verified that cold-working causes appreciable disturbances of the lattice. Many investigations in this field, however, have given results which indicate a change in the atoms, a deformation of the outer electronic shells. Measurements of the paramagnetic susceptibility ought to be one of the best methods of checking the existence of such alterations. Such measurements have moreover been performed by one of the present authors on two alloy systems, AuCr and CuMn (3). In these cases there was an appreciable difference in the average magnetic atomic moment in the cold-worked and the annealed state. This result is not only an interesting contribution to our knowledge of the magnetic cold-working effects, but has also been used by LINDE to interpret some of the resistivity irregularities of the transition metals (4). In the present work the investigation of the effects of cold-working has been extended to AgMn and AuMn alloys.

The measurements

Four AgMn alloys in the concentration interval from 7.5 to 20 at% Mn were investigated. More dilute alloys were either not very much influenced by cold-working or recovered rapidly to a great extent at room temperature. In the AuMn system, the convenient concentration interval was even more limited. Also in this system, cold-working did not change the magnetic properties of dilute alloys appreciably at room temperature, and in alloys with a sufficiently high percentage of Mn an order process influences the magnetic susceptibility in such a way that it is difficult to determine the effects of cold-working. For this reason only two AuMn alloys with about 10 and 15 at% Mn were investigated.

The alloys were made of pure metals, Ag and Mn from Johnson, Matthey & Co., spectrographically standardized, and Au from Ädelmetall AB (mint gold). The components were weighed to 0.1 mg, put into a graphite crucible, enclosed in evacuated quartz tubes, and melted together in a tube furnace, the temperature of which was just above the melting points of the alloys. After some hours at this temperature, the alloys were melted once more in a high-frequency furnace. After that the weights of the samples (about 2 grams) were checked, and then they were rolled out to a length of about one or two cm. After homogenization during 24 hours at temperatures just below the solidus line, the samples were drawn to a quadratic section of about one sq.mm and a length of about 12 cm.

The measurements of the paramagnetic susceptibilities were carried out with an apparatus described by GUSTAFSSON (1).

First the paramagnetic susceptibility of the alloys was measured in the cold-worked state (after a decrease of the cross-section of 70–85%) from about 90° C to room temperature. It was not possible to extend this range upwards, because at higher temperatures the specimens recovered during the time necessary for the measurements. After being annealed at 200° C in an oil bath for a suitable time, the susceptibility of the specimen was again measured, and this heat treatment was repeated until the last determination was made on a completely recovered alloy.

The last measurement was made in a wide interval of temperature, beginning at about 750° C, where the specimens were annealed for 30 minutes, enclosed in evacuated quartz tubes.

From the force, working on the specimens when the magnetic field was applied, it is possible to calculate a value of the paramagnetic atomic susceptibility. From this value the experimental diamagnetic susceptiblity of the base metal has been subtracted; no allowance has been made for the diamagnetism of the transition metal, as the available methods for calculations, e.g. by SLATER (5) do not appear to be very reliable for Mn atoms in a metallic structure. The diamagnetism of the transition metals should, moreover, be of small account in our case, where the paramagnetism of the alloys is very strong. The paramagnetic susceptibility of the alloy, x_P, is thus calculated from the expression

$$x_P = x_A - x_D(1-\alpha)$$

where α is the atomic concentration of Mn, and x_D is the diamagnetic susceptibility of the base metal. All the susceptibilities are calculated per gram atom of the alloy.

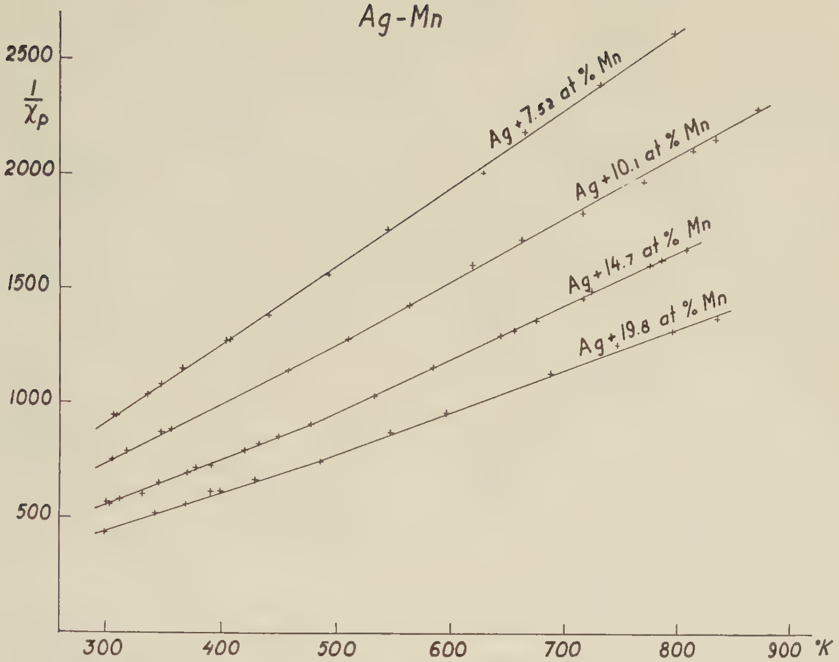

Fig. 1. The reciprocal of the paramagnetic susceptibility of the Mn atom in AgMn alloys as a function of the temperature.

The results

1. AgMn alloys

In Figs. 1–2 the inverse paramagnetic susceptibility $1/x_P$, has been represented as a function of the absolute temperature. The results of measurements on the finally annealed alloys are shown in Fig. 1. Only in the case of the alloy containing 7.52 at% Mn was it possible to draw a straight line through the experimental points, so the most dilute alloy was the only one which followed Curie-Weiss' law throughout the whole temperature interval. For the sake of simplicity, the curves for other alloys have been drawn as broken straight lines. As in many other investigations, it is not easy to decide whether the slope of the $1/x_P - T$ curves gradually changes from the value in the lower temperature range to a somewhat smaller value at higher temperatures, or if the transition between the two ranges occurs discontinuously. This question has been discussed thoroughly on several occasions (6).

In Fig. 2 the results of the measurements on cold-worked and successively annealed specimens are shown. The results agree with the corresponding measurements on AuCr and CuMn alloys (3) with regard to the considerable decrease in the paramagnetic susceptibility due to cold-working. The reduction of the slope of the curves with continued recovery, determined on cold-worked AuCr and CuMn alloys, did not occur in the AgMn system. From the curves in Fig. 2 it will be seen that the slopes of the straight lines, from which the atomic moments are calculated, did not change within the accuracy of the measurements, when the time of annealing was increased.

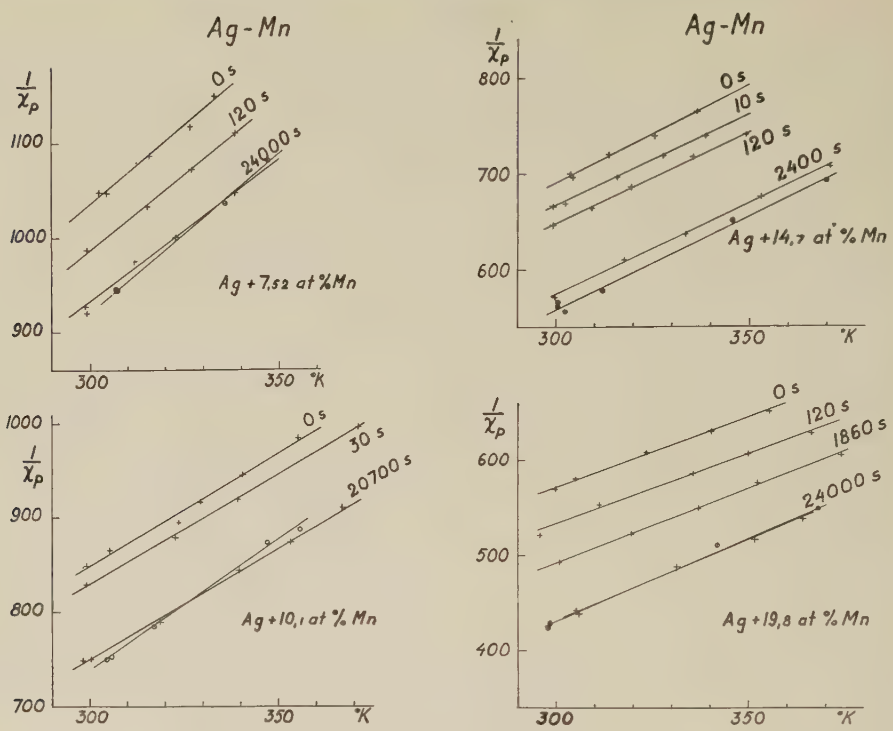

Fig. 2. Influence of cold-working on the paramagnetic susceptibility of AgMn alloys. Annealing temperature 200° C. Annealing times marked on the curves except for the lowest curves marked with rings, which correspond to continued annealing at about 800° C.

The magnetic atomic moment, μ, has been calculated from the constant C in Curie-Weiss' law

$$1/x_P = T/C - \Theta/C$$

using the expression

$$\mu = \sqrt{3kC/N\alpha}$$

where k is the Bolzmann constant, α is the atomic concentration of the transition metal, and N is the Avogadro number. From the "spin-only" formula

$$\mu = \mu_B \sqrt{4S(S+1)} \quad (\mu_B = \text{the Bohr magneton})$$

it is possible to calculate a value of the total spin quantum number of the Mn atom, S, and the number of the vacant 3 d electrons, $2S$.

The results of these calculations, which are shown in Table 1, have been plotted in Fig. 3, representing the average magneton values μ/μ_B, as a function of the Mn content. Three sets of values, which differ especially at higher Mn concentrations, have been determined for temperatures between 600 and 1000° K, between 300 and 600° K, and finally for the cold-worked and annealed specimens between 300 and 600° K. In the last case the calculated average magneton value from the determina-

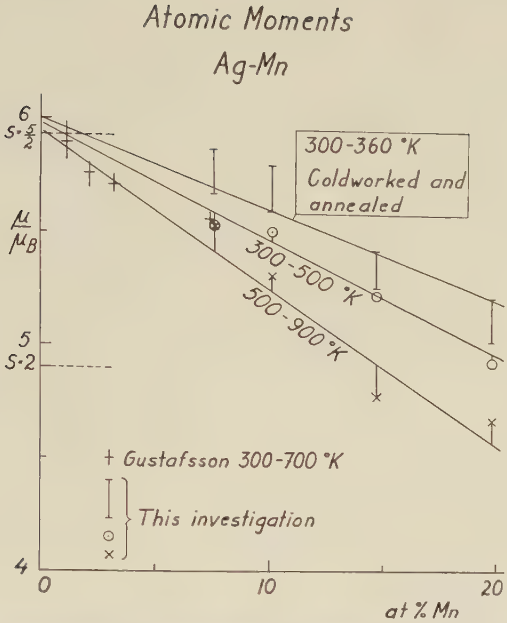

Fig. 3. AgMn alloys. Dependence of the calculated average magnetic moments of the Mn atoms on the concentration of Mn. As indicated by the marks the uncertainty of the determinations at very low concentrations and small intervals of temperature is considerable.

tions after different annealing times has been plotted for each alloy. The results from GUSTAFSSON's investigation (between 300 and 700° K) (2) mentioned in the introduction, have also been plotted in Fig. 3. Our measurements and GUSTAFSSON's agree very well; the investigation by NÉEL (1), on the other hand, gives quite different results.

The magneton values as a function of the Mn concentration for the different ranges of temperature seem to form straight lines, which converge at zero Mn concentration to a calculated magneton number 5.95 corresponding to a "spin-only" value of $S \sim 5/2$.

2. AuMn alloys

Previously, Gustafsson investigated some AuMn alloys up to 5 at% Mn (1). In the present work two alloys with the concentrations 9.73 and 14.65 at% Mn have been examined. The measurements were made in the same way for as the AgMn alloy. The 14.65 at% alloy has been influenced by an ordered phase of the composition Au_3Mn. In Fig. 5, containing the results from the whole temperature range, the fully-drawn line, ending in a point obtained for the quenched alloy, shows the susceptibility of the homogenous alloy. The curve obtained for a slowly cooled alloy, drawn with short dashes, shows the susceptibility, influenced by the order process. The deviating values of the susceptibility of the slowly cooled alloy, which are also dependent on the applied magnetic field, indicate the existence of ferromagnetism, which presumably refers to the ordered phase Au_3Mn. It is known from the Heusler alloys that Mn can show ferromagnetism in certain compounds.

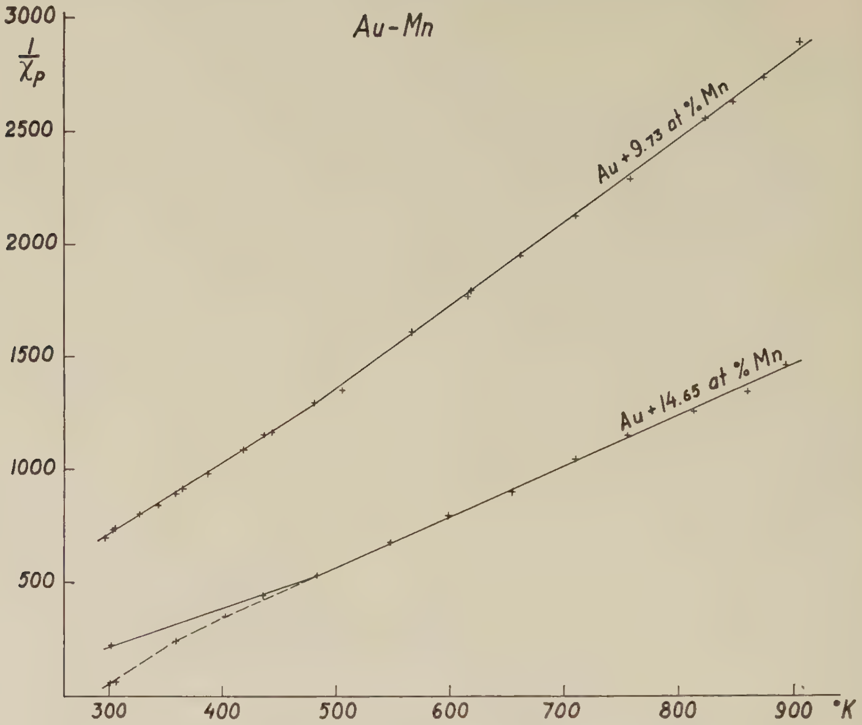

Fig. 4. The reciprocal of the paramagnetic susceptibility of the Mn atom in AuMn alloys plotted against the temperature.

The cold-worked AuMn alloys show the same properties as the cold-worked AgMn alloys, as appears from Fig. 5, the magnetic atomic moment not changing when the originally cold-worked alloys were annealed. The change of the interaction energy term, Θ/C, in Curie-Weiss' law was very evident also in the AuMn alloys.

Also in the case of AuMn alloys there is a slight bend in the susceptibility curves, indicating different average magneton values at low and high temperatures. These values are shown in Table 1. In the corresponding diagram of the calculated magne-

Table 1. Number of magnetons per atom.

Alloy	Mn concentration	Temperature range		
		300°–700° C	20°–300° C	20°–80° C
AgMn	7.52 at %	5.54	5.54	5.77
	10.1 »	5.31	5.51	5.70
	14.7 »	4.77	5.23	5.34
	19.8 »	4.67	4.93	5.12
AuMn	9.73 at %	4.78	4.97	5.22
	14.7 »	4.98	5.66	—

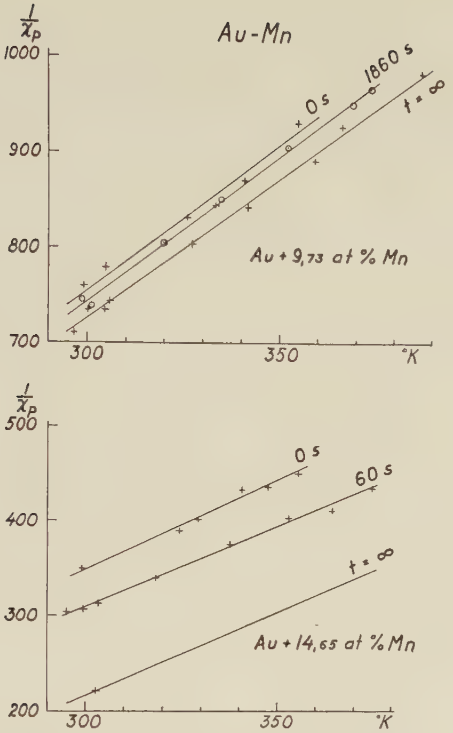

Fig. 5. Influence of cold-working on the paramagnetic susceptibility of AuMn alloys. Annealing temperature 200° C. Annealing times marked on the curves. $t = \infty$ means continued annealing at about 800° C.

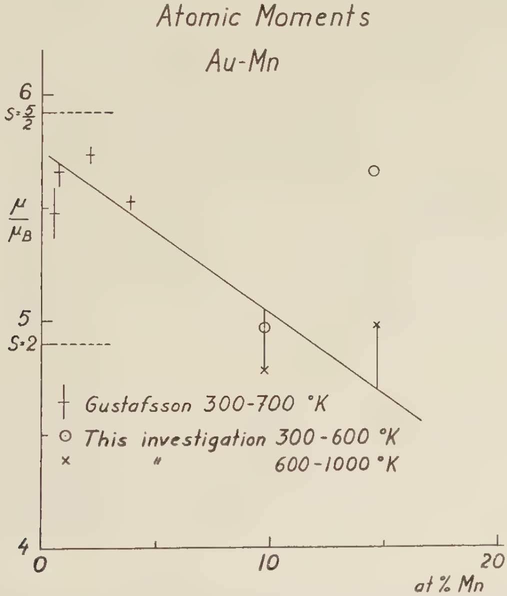

Fig. 6. AuMn alloys. Dependence of the atomic moments of the Mn atoms as functions of the Mn content. The high value of the atomic moment of the AuMn alloy with 14.65 at % Mn in the temperature range 300–600° K was due to a quenched alloy.

ton values in Fig. 6, Gustafsson's points have been plotted together with ours. The high temperature magneton values as a function of the Mn content appear even here to lie on a straight line, even if some of the points deviate rather considerably. However, if a straight line is drawn through the points, it has the same slope as the corresponding line for the AgMn alloys, but lies somewhat lower. The two lines give an average value of $\mu/\mu_B = 5.85$ and $S \approx 5/2$ at zero Mn concentration.

Discussion of the variation of the magneton number

The large decrease of the atomic moment with the concentration, which also appears for other similar alloys, e.g. AuCr and CuMn alloys (3) (1), remains to be interpreted. The paramagnetism of the pure metals Mn and Cr is rather weak and does not change very much with the temperature. Such paramagnetism has been explained as anti-ferromagnetism, superimposed with Curie-Weiss' paramagnetism (7). The occurrence of both negative and positive interaction is probably due to different distances between the 3 d shells. The Mn lattice has two parameters, and interactions between the nearest and the second nearest neighbours can possibly contribute. Now, Mn and Cr atoms in dilute solutions and salts can produce a strong temperature-dependent paramagnetism of the Curie-Weiss type, corresponding to a "spin-only" value of the spin quantum number of the transition metal atom of as high as 2–5/2, the latter value being the highest possible in the iron group. This fact is easily accounted for by the rather large distances between the transition metal atoms in the dilute alloys, which leave the magnetic carriers free to orientate in a magnetic field. This should give a Curie-Weiss paramagnetism, which actually appears in most of the alloys.

With increasing concentration of the transition metal atoms in the alloy, the average distance between them becomes smaller, and in order to account for the observed decrease in the average atomic moment it is natural to assume an increasing contribution from anti-ferromagnetic interactions, which give a tendency towards an anti-parallel orientation of the atomic moments. The temperature dependence of the calculated average magneton number of the alloys is probably caused by one or perhaps both of the following two reasons. On the one hand, NÉEL has explained the change in slope of the $1/x_P$ curves for AgMn by assuming the above mentioned anti-ferromagnetic interaction at low temperatures, thus causing a decrease in the susceptibility below the Curie-Weiss values, which are asymptotically approached at high temperatures (8). On the other hand, it is possible that, at least to some extent, the observed variation of the magnetic value is caused by changes in the electron configuration in the transition metal atom, the number of vacant 3 d electrons being decreased at high temperatures. This is most probable in cases where the temperature variations of the reciprocal of the susceptibilities are broken lines, which hardly can be explained by Néel's theory.

The authors wish to express their gratitude to Professor G. BORELIUS, Director of the Physical Department I of the Royal Institute of Technology in Stockholm, for his great interest in this work and for valuable discussions. The work has been subventioned by Statens Naturvetenskapliga Forskningsråd.

SUMMARY

The temperature dependence of the magnetic susceptibility has been determined for AgMn and AuMn alloys. The results from these and previous measurements show that the average atomic moment of the Mn atom decreases approximately linearly, when the concentration of Mn increases in the alloys. The extrapolated moment for infinite dilution is about 6 Bohr magnetons, corresponding to $S \approx 5/2$. The influence of cold-working on the paramagnetic susceptibility was fairly large; only the interaction energy changed, however, and the average atomic moment of the Mn atoms was not affected.

LITERATURE

1. L. NÉEL, Journ. de Phys. *3* (1932) 160.
2. G. GUSTAFSSON, Ann. d. Physik *25* (1936) 545.
3. E. KRONQVIST, Arkiv f. mat., astr. och fysik 34 B, No. 7 (1947).
4. J. O. LINDE, Arkiv f. mat., astr. och fysik 36 A, No. 10 (1948).
5. J. C. SLATER, Phys. Rev. *36* (1930), 57.
6. Le Magnétisme. 3. Paramagnétisme. Collection Scientifique. Inst. International de Coopération Intellectuelle (Paris 1940) 232 and 304.
7. G. FOEX, Journ. de Phys. *12* (1951) 153.
8. L. NÉEL, Proc. of the Phys. Soc. 395 A (1952) 870.

Tryckt den 30 november 1953

Uppsala 1953. Almqvist & Wiksells Boktryckeri AB

ARKIV FÖR FYSIK Band 7 nr 27

Mitgeteilt am 8. April 1953 durch G. Borelius und O. H. Faxén

Zur Kohlenstoffausscheidung aus dem α-Eisen

Von O. Krisement[1]

Mit 2 Figuren im Text

Im System Eisen-Kohlenstoff verläuft die Kohlenstoffausscheidung aus dem α-Eisen unterhalb A_1 (721° C) durchweg nicht nach dem stabilen System Eisen-Graphit, sondern nach dem metastabilen System Eisen-Eisenkarbid Fe_3C. Die Phasengrenze wurde einmal durch Dämpfungsmessungen von verschiedenen Autoren[2], zum anderen durch kalorimetrische Untersuchungen bestimmt[3]. Bei tieferen Temperaturen (200° und darunter) wird die Ausscheidung des Zementits Fe_3C durch die Ausscheidung eines anderen Karbids abgelöst. Durch Elektronenbeugungs-Untersuchungen[4] wurde festgestellt, dass bei 100 und 200° C im α-Eisen übersättigt gelöster Kohlenstoff als ε-Karbid Fe_2C, bei 300° C und darüber als Zementit Fe_3C ausgeschieden wird.

Durch kalorimetrische Untersuchungen[5] sollte festgestellt werden, in welchem Temperaturgebiet die Fe_3C-Ausscheidung durch die Ausscheidung eines anderen Karbides abgelöst wird. Es wurden Proben aus deutschen Armco-Eisen mit der Analyse

C	Si	Mn	P	S	Cr	Mo	Ni	N
0,020	0.001	0,010	0,013	0,045	0,012	0,01	0,008	0,002

sowie aus schon früher benutztem schwedischen technisch reinem Eisen ähnlicher Zusammensetzung[6] verwendet. Die Proben wurden bei 700° C in einer Stickstoffatmosphäre ca. 30 Min. homogenisiert, in Eiswasser abgeschreckt, anschliessend bei verschiedenen Temperaturen zwischen 188 und 230° geglüht, wieder in Eiswasser abgeschreckt, dann in etwa 2 Min. auf Thermostattemperatur erwärmt (103° C) und in den Thermostaten eingesetzt. Die Messungen der bei der Ausscheidung entwickelten Wärmemenge erfolgte in einem Wasserdampfthermostaten, dessen Messzelle 30 in Reihe geschaltete Kupfer-Konstantan-Thermoelemente enthielt.[7]

---

[1] Wissenschaftlicher Mitarbeiter des Max-Planck-Instituts für Eisenforschung, Düsseldorf.

[2] Vgl. z. B. L. J. Dijkstra: Journal of Metals *1* (1950) S. 1242; J. K. Stanley: Journal of Metals *1* (1949) S. 752.

[3] G. Borelius u. S. Berglund: Arkiv för Fysik *4* (1951) S. 173.

[4] A. L. Tsou, J. Nutting u. J. W. Menter: J. Iron Steel Inst. *172*, part 2 (1952) S. 163.

[5] Zur Beschreibung der kalorimetrischen Methoden siehe 3).

[6] Analyse siehe Probe 7 in 3).

[7] Dieselbe Anordnung wie in 3) beschrieben.

Tabelle 1. Glühtemperaturen, Glühzeiten und Wärmeentwicklung Q bei 103° C durch Kohlenstoffausscheidung aus dem α-Eisen.

°C	Glühzeit	Q in Ws/Mol
188	20 min	(0,5)
188		0,52
200	30 »	1,16
206	20 »	0,86
218	20 »	1,00
230	20 »	0

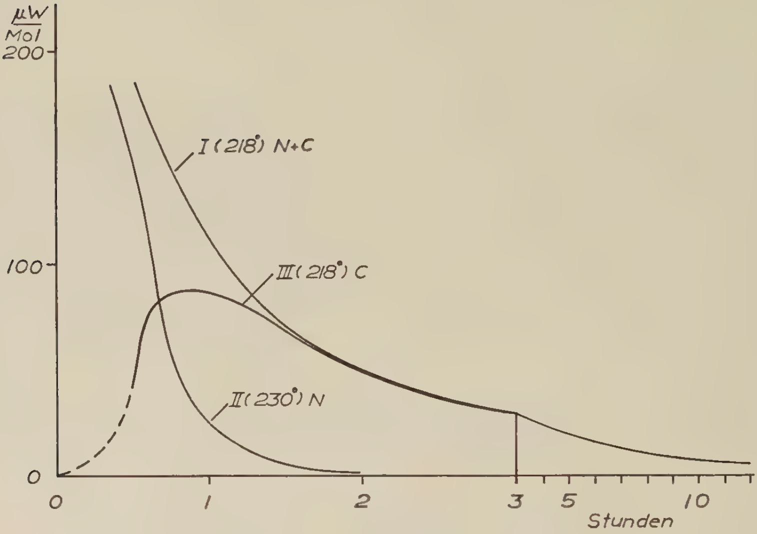

Abb. 1: Kurven der Wärmeentwicklung.

Das Glühen erfolgte so, dass die abgeschreckte Probe in einem kleinen Ofen in rund 60 min. auf die Glühtemperatur erwärmt und dann, abgesehen von einem Falle, rund 20 Min. (die sich durch einen Vorversuch als ausreichend dafür erwiesen, dass sich kein Kohlenstoff mehr in übersättigter Lösung befindet) bei ihr gehalten wurde. Ob und wie weit bei dieser Glühzeit neben der Ausscheidung des ε-Karbids schon eine Fe_3C-Ausscheidung stattgefunden hat, bleibt offen. Tabelle 1 gibt Aufschluss über die verschiedenen angewandten Glühtemperaturen und Glühzeiten. Kurve I in Abb. 1 zeigt die pro Zeiteinheit entwickelte Wärmemenge der bei 218° geglühten Probe, wobei die zeitliche Trägheit der Messanordnung bereits korrigiert ist. Bei den ersten vier in Tabelle 1 genannten Glühtemperaturen zeigten die Kurven der Wärmeentwicklung ein ganz ähnliches Bild wie Kurve I, nach etwa 10 Std. sank die Wärmeentwicklung unter die Messgenauigkeit ab. Dagegen verlief die Wärmeentwicklung der bei 230° geglühten Probe ganz anders, hier war der Prozess bereits nach ca. 2 Std. unter die Messgenauigkeit abgesunken (Kurve II in Abb. 1). Schreibt man diese Wärmeentwicklung der Stickstoffausscheidung zu (was auch mit früheren

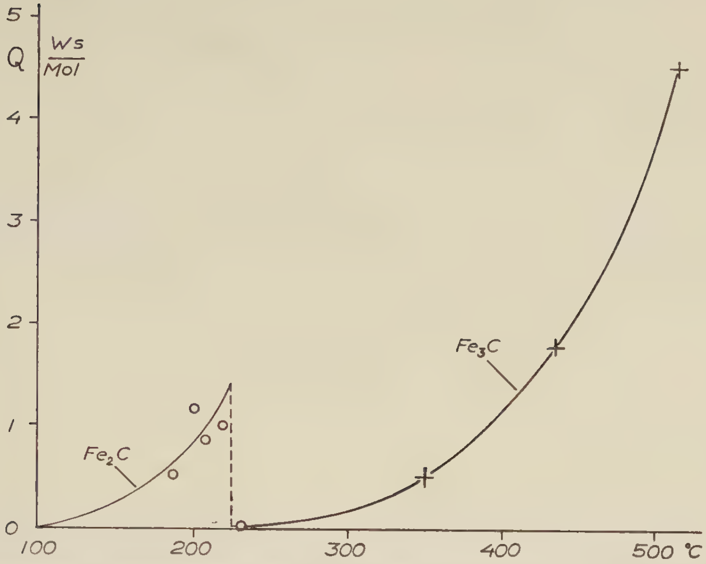

Abb. 2: Entwickelte Wärmemengen bei der Kohlenstoffausscheidung. × nach G. Borelius u. S. Berglund. ⊙ nach der vorliegenden Arbeit.

Versuchen, die zu 3) ausgeführt wurden, vereinbar ist), so ergibt sich, da wegen des kleinen Stickstoffgehaltes der Stickstoff bei den verschiedenen Glühtemperaturen vollständig gelöst ist, dass bis zu Glühtemperaturen von 218° C eine Wärmeentwicklung durch Kohlenstoffausscheidung bemerkbar ist, während sie bei 230° verschwindend klein wird. Subtrahiert man die der Stickstoffausscheidung zugeordnete Wärmemenge von der beobachteten, so erhält man für die bei 218° geglühte Probe die Kurve III in Abb. 1. Dasselbe wurde für die anderen Versuche gemacht, und durch Integration ergaben sich die in Tab. 1 genannten Wärmemengen Q für die Kohlenstoffausscheidung.

Diese Q-Werte sind sehr unsicher, da die Effekte nicht weit über der Empfindlichkeit der Messanordnung liegen und ausserdem die Korrektur für den Stickstoff enthalten. Schon die numerische Bestimmung der Q-Werte aus den Messresultaten hat eine Unsicherheit von etwa ± 30 %. Die Q-Werte sind in Abb. 2 zusammen mit den früher bei höheren Temperaturen gemessenen Werten[3] eingetragen. Da sie zusammen mit diesen nicht auf einer einzigen monotonen Kurve liegen, kann das Ergebnis so gedeutet werden, dass die Übergangstemperatur zwischen der Fe_3C-Ausscheidung und der Ausscheidung eines anderen Karbids zwischen 218 und 230° C liegt. Dieser angegebene Temperaturbereich wird natürlich noch von der Art der Glühbehandlung abhängen können.

Für die gastfreundliche Aufnahme an seinem Institut möchte ich auch an dieser Stelle Herrn Prof. Borelius meinen aufrichtigsten Dank sagen.

Stockholm, Physikalisches Institut der Technischen Hochschule.

Tryckt den 30 november 1953

Uppsala 1953. Almqvist & Wiksells Boktryckeri AB

ARKIV FÖR FYSIK Band 7 nr 28

Communicated 8 April 1953 by G. Borelius and H. Alfvén

Time dependence of boron absorption coefficient for neutrons slowed down in water at room temperature

By G. von Dardel

With 9 Figures in the text

I. Introduction

The life time of neutrons in a moderator may be divided into three periods. During the initial, *epicadmium*, period the neutrons are slowed down from their initial energy to the cadmium absorption limit of about 0.3 eV and are not appreciably influenced by the thermal excitation and chemical binding of the moderating molecules. In the *transition* period the neutrons approach thermal equilibrium with the moderator. After this equilibrium has been established no further change occurs in the neutron spectrum during the final, *thermal*, period which extends until the neutrons have disappeared by absorption or leakage.

The energy distribution of the neutrons from a moderator has been extensively studied using neutron spectrometers (1), (2). The energy spectrum obtained in these experiments is the average spectrum for the whole lifetime of the neutrons in the moderator. The low energy portion of the measured energy distributions could be fitted quite well to a Maxwellian distribution corresponding to an effective temperature about 100° above the temperature of the moderator.

Measurements of the effective temperature of the neutrons in a reactor (3), (4) have also been performed and shown it to be appreciably above the temperature of the moderator.

The Maxwellian component of the measured neutron energy spectrum is due to neutrons emitted mainly during the transition and thermal periods, and the disagreement between the measured neutron temperature and the moderator temperature indicates that the approach to thermal equilibrium during the transition period occupies a substantial part of the total life-time of the neutrons in the geometry used by the experimenters.

It is the object of this investigation to study the time scale for the slowing down process and the approach to thermal equilibrium. The technique of the pulsed neutron source and gated detector, which has been developed mainly for time-of-flight measurements (1), was used to select neutrons leaving the moderator at certain time delays after the injection of fast neutrons. The energy distribution of the neutrons had to be determined by a method not requiring long paths, which would introduce time-of-flight separation of the spectrum emitted at a particular time. The simplest technique is the boron absorption technique (5), using a "bad" geometry.

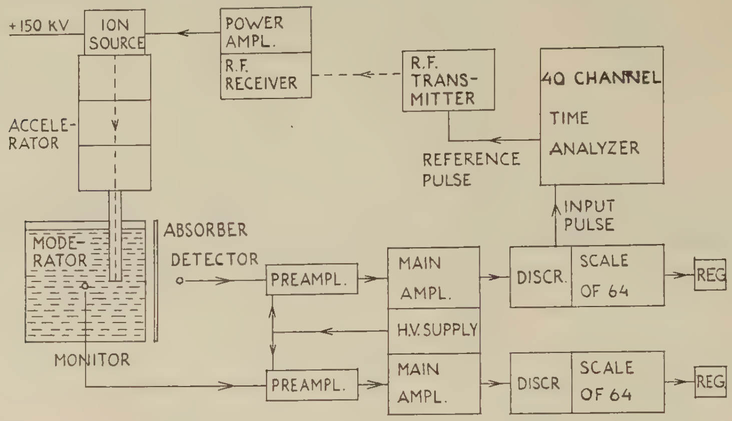

Fig. 1. Block diagram of the experimental apparatus.

This article will describe the experimental apparatus and some of the measurements performed with this new technique on neutrons slowed down in water of room temperature. A more detailed discussion of these and other measurements, and of the theory, will be given elsewhere in a thesis by the author (12).

II. Apparatus

A block diagram of the apparatus is shown in fig. 1.

The 40 channel time analyzer described in a separate publication (6) emits a reference pulse which is transmitted to the high voltage side of a small 150 kV accelerator by a radio-frequency transmission link (7), and modulates the ion source. A burst of neutrons is produced by the D-D-reaction in a target. The neutrons are slowed down in the moderator, and the leakage flux is detected by a small BF_3-chamber. The pulses are amplified, discriminated and counted in a scale of 64. The pulses from the discriminator are further analyzed in the time analyzer. The number of counts are referred to a constant number of neutrons counted in an identical monitoring channel.

Accelerator and target

The accelerator was designed by Mr E. Blomsjö and will be described in more detail in a coming article. It is connected to the 150 kV generator of a standard Philips industrial X-ray set. The accelerating tube is mounted on a movable stand fitted with a winch mechanism by means of which the height of the target can easily be adjusted, a feature which appreciably facilitated the experiment.

The target to be used for the D-D-reaction offers some problems. Conventional targets involve the use of heavy ice or heavy phosphoric acid, and have to be cooled, usually by immersion of the target in a Dewar flask containing liquid air or dry ice and alcohol. These targets would be very unsuitable for the present investigation, since part of the slowing down process would occur in the coolant. The temperature of the moderating materials would not be uniform, absorption would occur in the Dewar flask and the coolant, and the level of the coolant would have to be kept rigorously constant in order to obtain reliable measurements. In some of the measurements targets were therefore used which do not require cooling, such as palladium saturated with heavy hydrogen by electrolysis, and deuterated zirconium targets (8). The author is grateful to Mr E. Blomsjö for providing the zirconium targets. Both these types of target have to be regenerated quite frequently.

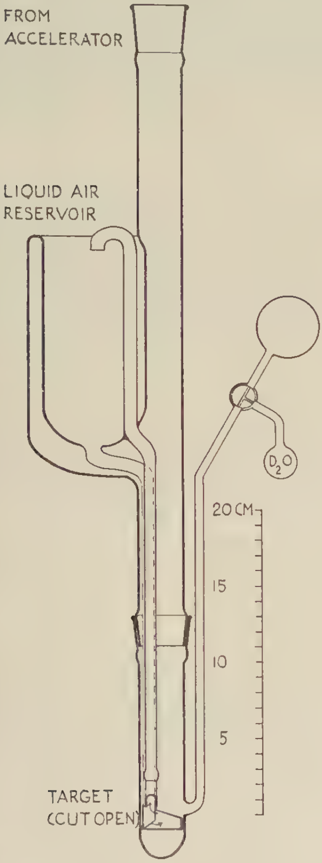

Fig. 2. Target assembly for the D-D-reaction.

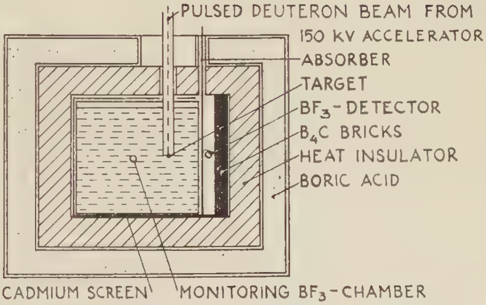

Fig. 3. Experimental geometry for transmission experiments.

A more satisfactory target was found in the form of a heavy ice target cooled by liquid air which was circulated from a Dewar flask, placed some distance away. A drawing of the target assembly is shown in fig. 2. The copper target chamber is suspended from the bottom of the Dewar flask by the glass feed tubes in such a way that it is not in contact with the surrounding target tube. Good heat insulation is thus provided by the vacuum of the accelerator. The exhaust tube of the target starts at the top of the sloping target surface, so that the evolved gas bubbles will readily escape, and protrudes above the surface of the liquid air in the Dewar flask. The gas bubbles rising through the exhaust tube will give rise to a pumping action,

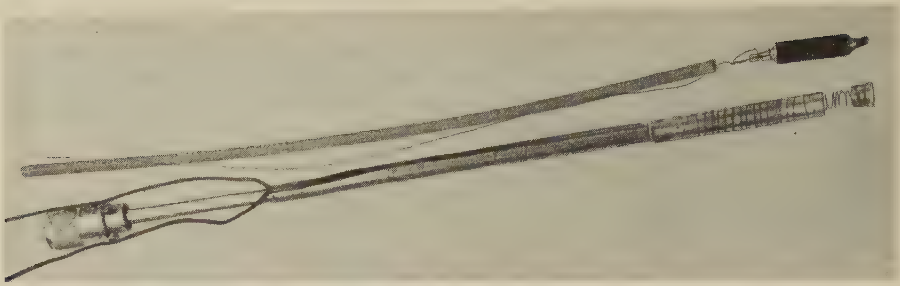

Fig. 4. Boron trifluoride chamber and probe (demounted).

and liquid air will circulate through the target chamber more rapidly at higher beam power. This circulation should improve the cooling at high power loading. While in the present experiment the ion beam is pulsed, and the average beam power small (of the order of one watt), the target has been found to work efficiently at power dissipations as high as 60 watts. A few other advantages of the target assembly should perhaps be pointed out. The beam from the accelerator passes between the two glass walls of the Dewar flask, which thus acts as a cold trap insulating the target assembly from the rest of the vacuum system. This serves the dual purpose of condensing oil vapours from the pump, which might otherwise poison the target, and water vapour evolved at the target, which might otherwise cause breakdowns in the accelerating tube. Another advantage is the fact that essentially only the target plate is at low temperature, and heavy water vapour introduced into the target tube will therefore condense mainly on the target plate, and regenerate the target.

Experimental geometry

The experiments were performed in the arrangement shown in fig. 3. The water is contained in a copper vessel of dimensions 18.7 × 19 × 19 cm, which is surrounded by a double-walled plywood box, the interspace being filled with boric acid for protection against stray neutrons from outside. Since some experiments were performed at temperatures other than room temperature, the moderator tank can further be surrounded by a 5 cm thick heat-insulating layer of "Styrofoam". The moderator is screened against neutrons diffusing in the Styrofoam by 0.5 mm cadmium sheets except at the face where the absorption experiment is made. At this face there is a space (3 cm deep) between the moderator tank and the Styrofoam, for the detector and interposed absorber. Behind the detector the space is lined with 2 cm thick bricks made of boron carbide bound with sulfur. These bricks are almost black to neutrons. The monitoring chamber is introduced in a central channel through the tank, where it is not influenced by the absorber.

Detectors

The detector and monitor were identical chambers filled to one atmosphere with boron trifluoride enriched in B^{10}. The author is indebted to Mr C. Taylor for filling the chambers and to Mr K. E. Holmberg for the enriched boron. In order to reduce time-of-flight delays in the chambers their dimensions had to be kept small, the total volume being 1 cm³. The detector is shown demounted in fig. 4. The chamber is a thin-walled soda glass bulb, external diameter 0.8 cm, with external aquadag cathode (9), (10). The central collector, a stainless steel wire, is connected to a low capacity probe which is made from a piece of coaxial cable of which the central wire has been replaced by a 0.01 cm wire. The chamber was surrounded by a thin-walled aluminium hood, and the probe was screened by an aluminium tube. The probe is joined directly to the preamplifier input, using coaxial connectors with the insulators removed, since these gave spurious pulses with high voltage. Contact is made to the end of the probe by a spring. 1000 volt is applied to the probe through a 100 MΩ resistor, and the pulses are coupled to the input of the amplifier by a condenser.

The amplifiers are of conventional design, having a rise-time of about 0.5 μsec and gain stabilization by inverse feedback. The output is fed to a diode discriminator. The discriminated pulses are connected to a conventional scale of 64, having a second discriminator circuit, which however is set at a low bias, so that essentially all the pulses from the first discriminator are registered by the second. The output pulses of the second discriminator, which are of uniform height and rise-time and at a low impedance, are coupled by a coaxial cable to the input of the time analyzer.

Absorbers

The combinations of "$1/v$"-absorbers used during the experiment for the study of the energy distribution of the neutrons are tabulated in table 1.

Table 1. "$1/v$"-absorbers

No.	Material	g B/cm²	k_0*) cm/sec	$k_0^2 \cdot \frac{m}{2k}$ °K
B 1	Boron carbide	0.0110	$0.97 \cdot 10^5$	56
B 2	"Hysil" glass	0.0244	$2.12 \cdot 10^5$	270
B 3	"Hysil" glass	0.0248	$2.16 \cdot 10^5$	279
B 1 + B 2		0.0354	$3.09 \cdot 10^5$	572
B 2 + B 3		0.0492	$4.28 \cdot 10^5$	1100

*) Calculated on the basis of $\sigma_B = 710 \cdot 10^{-24}$ cm² for a neutron velocity of $2.2 \cdot 10^5$ cm/sec.

The macroscopic cross section of the absorbers is expressed, in column 4 of the table, as that velocity k_0, at which the transmission for perpendicular incidence is $1/e$. The 5th column lists the corresponding neutron temperature, which is convenient to know for the conversion of transmission data to neutron temperatures. B2 and B3 are 0.28 ± 0.02 cm thick plates of "Hysil" glass, which by chemical analysis was shown to contain 12.2 ± 0.1% of B_2O_3. Since the boron content is rather low, deviations from a pure $1/v$-law can be expected, especially for neutrons of high energy, due to the scattering power of the other constituents. At thermal energies the total scattering cross section is only about 7% of the absorption cross section, and in the "bad" geometry of the experiment the effect of scattering on the transmission is expected to be much less than this. At higher neutron energies, where the

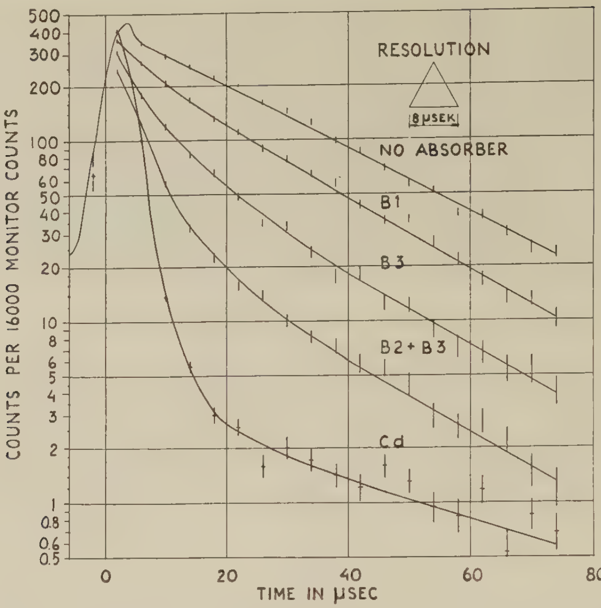

Fig. 5. Experimental data, referred to 16 000 monitor counts. Channel width: 4 μsec. Repetition cycle: 80 μsec.

absorption is less important, scattering may have to be taken into account for accurate measurements, but in the present more qualitative investigation this was not considered necessary.

Absorber B 1 was produced, essentially according to the method of BAKER, BACHER and MACDANIEL (11) by sifting powdered boron carbide, analyzed to contain 69% boron, through a sieve from a height of about 2 meters onto a flat tray of 0.005 cm aluminium foil. The tray was filled with a solution of about 0.5 gram of polyvinyl-acetate in acetone. The powder was distributed as uniformly as possible over a fairly large area, in the center of which the tray was situated. After the acetone has evaporated the carbide adhered firmly to the backing, the polyvinyl-acetate serving as a binder. The absorbing surface was protected by a 0.003 cm aluminium foil. After the measurements had been concluded the absorber was divided into 8 pieces and the carbide removed with acetone. The density of boron carbide on each piece was determined by weighing the pieces before and after the removal of the carbide. The value cited in table 1 is the mean for all 8 pieces, but the extreme values differed from the mean by over 15%. Linear variations in thickness should cancel out in the first approximation if the measurement is made near the centre of the absorber. For more accurate experiments the absorbers should however be chosen with greater care for uniformity.

Measurements were also made on a cadmium sheet of 0.05 cm thickness (0.438 g/cm^2).

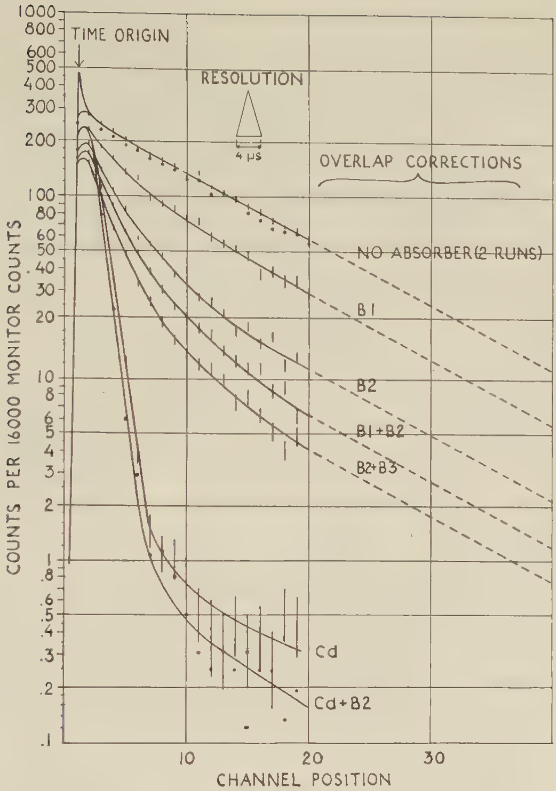

Fig. 6. Experimental data, referred to 16 000 monitor counts. Channel width: 2 μsec. Repetition cycle: 40 μsec.

III. Measurements

Preliminary measurements showed that the transmission of neutrons through the absorbers varies only during the first 40 μsec after the neutron burst. After this time the transmission is constant within the statistical fluctuations, indicating that the neutrons have become thermal. To extend the measurement beyond 40 μsec would only reveal the exponential decay of the neutron density.

The rate at which the measurement can be repeated depends on the rate of decay of the neutron flux from the moderator, and on the amount of overlapping between cycles which can be tolerated. With pure water the neutron flux will decay with a mean life of about 70 μsec in our geometry, as is shown by the data of fig. 9, and in order to avoid excessive overlap it would thus with pure water be necessary to let about 200 μsec elapse between neutron bursts. Only a small portion of the cycle, about 40 μsec, would be of interest for the present problem. In order to be able to use a faster repetition rate and thus get higher counting rates, the mean life in the moderator was decreased to a value of 23 μsec by the addition of about 20 grams of boric acid per liter water. The boric acid content will not appreciably affect the slowing down properties of the solution, and since it is a $1/v$-absorber the velocity distribution will not be changed.

The neutron flux emerging from the moderator was studied in two sets of measurements, with channel widths of 2 and 4 μsec. In each case the length of the neutron burst equalled the channel width, which is the normal mode of operation of the time analyzer, and gives optimum resolution for a given counting rate. With this choice the resolution function is a triangle, two channel widths wide at the base.

The number of counts registered in the channels, referred to a constant number of monitor counts, are shown in fig. 5 and 6. The length of the vertical lines through the experimental points indicates the standard statistical errors, calculated in the usual manner from the number of counts.

The measurements with 4 μsec channel width were made using a deuterated zirconium target. For the 2 μsec curves the new heavy ice target was used. The total measuring time for the latter curves was about 6 hours.

In the measurements with 4 μsec channel width the measuring cycle was repeated after 20 channel widths, or 80 μsec. The neutron flux had time to decay to 3% of its initial value before the next cycle started, and the overlap correction was thus quite small. In the measurements with 2 μsec channel widths the measuring cycle was also 20 channel widths, or 40 μsec, and the spectrum will decay only to 17% of the initial value. The overlap correction is in this case quite large. On the other hand the measurements with 4 μsec channel width indicate that all the curves decay exponentially with a period of 23 μsec after the first 40 μsec have elapsed. The overlap correction for the 2 μsec data could thus be calculated quite accurately simply by extrapolating the curves exponentially with this period into the next cycle, as has been done in fig. 6. The accuracy of the data will not be appreciably decreased by the correction, and the counting rate is twice as high as if the longer repetition cycle had been chosen.

Since the time analyzer has 40 channels, while the repetition cycle was only 20 channel widths, each channel could be duplicated and a very rigorous check on the reliability of the data was thus obtained. For each run it was also checked that the sum of the counts registered in all the channels agreed within narrow limits with the total number of counts registered by the external scale of 64 in the detecting channel.

Time origin

In order to establish the time origin for the data, several procedures can be adopted. One is to measure the delays in the various parts of the circuits of fig. 1. Delays occur in the output circuits of the time analyzer, in the R. F. link for transmitting the pulses to the high voltage side of the accelerator, and in the ion source itself. Further delays occur in the BF_3-chamber, amplifier and discriminator. Finally there is a delay in the input circuits of the time analyzer, before the pulses are analyzed. If all these delays are measured and added, the position of the origin within the measuring cycle can be determined. A convenient way of measuring the total delay in the circuits up to the input of the time analyzer is to remove the detector, and connect the input of the preamplifier to the target of the accelerator through an attenuator. The deuteron current pulse on the target produces a voltage pulse, which is attenuated to approximately the size of the pulses from the detector. The delay of the input pulse to the time analyzer will then include delays of all the circuits up to that point, with the exception of the short collection time for the elec-

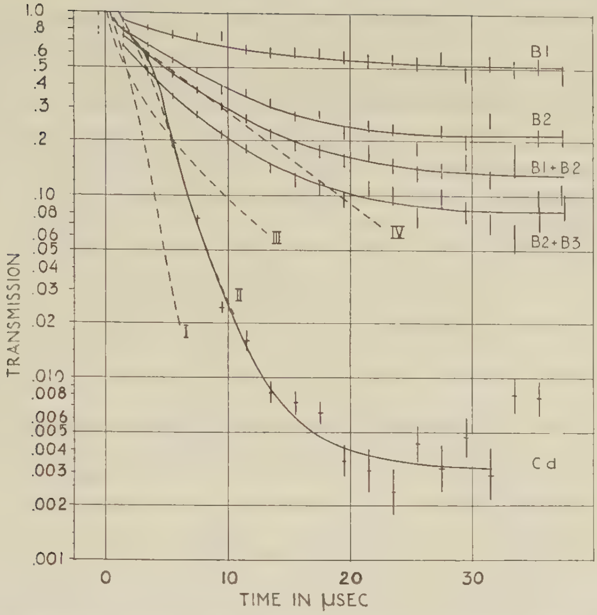

Fig. 7. Full curves: Measured transmission against time for 4 combinations of $1/v$-absorber and for cadmium. Dashed curves: Theoretical transmission through cadmium, with no time-of-flight delay (curve I), and with a time-of-flight delay, corresponding to a source-detector distance of one mean free path (curve II). Curves III and IV are the corresponding theoretical curves for the transmission through the "$1/v$"-absorber B2.

trons in the detector. The delay in the input circuit of the time analyzer must be determined in a separate measurement, with pulses from a pulse generator.

A more convenient way of determining the time origin from the experimental data themselves has however been adopted in this investigation. The experimental points near the sharp rise of the time distribution depend very sensitively on the position of the time origin. We first assumed the true behaviour at the origin to be a step function increase of the neutron flux to a stationary value. A triangular resolution function was then applied to this assumed curve, and the resulting curves compared to the experimental points. It turned out however that the experimental points were not compatible with a step function behaviour but required a sharp peak to be superimposed on the edge of the step function. This behaviour is indeed to be expected, as the leakage of fast neutrons during the first instants of time would give a rapid decrease of the neutron density in the water moderator. We therefore fitted the experimental points with the curves which result if a step function with a superimposed δ-function is viewed through a triangular window. A good fit was obtained with the experimental points if the area of the δ-function equalled the area under 2 μsec of the step function curve. The accuracy of the method is about 0.2 channel widths.

Treatment of the data

The experimental results were first corrected for the extrapolated overlap correction. From the measurements with and without absorber the transmission as a function of channel number was then calculated. Since the measurements with 2 μsec channel width have higher resolution, and, at the same time, due to the higher yield of the heavy ice target, give higher statistical accuracy than the data with 4 μsec resolution, only the treatment of the former will be discussed here. The calculated transmission curves for this case are shown in fig. 7. The transmission curves from the data with 4 μsec resolution were almost identical except for the measurements with cadmium, where the presence of a small background made itself noticeable, due to the low counting rate.

A. The epicadmium period

In the epicadmium period the greater part of the neutrons have energies above the cadmium cut-off energy at about 0.3 eV. Since this is higher than or of the same order as the quantum energy of the strongest bonds in water, the protons can, as far as the slowing down process is concerned, be regarded essentially as free protons, and it should be possible to apply the results derived for this case in the author's thesis (12).

Cadmium absorption

If we assume cadmium to transmit all neutrons with velocities above $7.5 \cdot 10^5$ cm/sec and to absorb all neutrons with lower velocities, the transmission can easily be obtained by integrating from the cut-off velocity to infinity the theoretical velocity spectrum of neutrons slowed down by free protons (ref. (12) eq. (8)). For the mean free path in water we take a value of 0.7 cm (13). In this way the theoretical curve I in fig. 7 is obtained. According to this curve we would expect that less than 10 % of the neutrons will be transmitted by cadmium after 3 μsec, and we should thus expect the length of the slowing down period to be of this order. The experimental results indicate that it takes about 6.5 μsec for the transmission to fall below 10%. The theoretical curve I is however valid only if the detector dimensions and the detector-to-moderator distance are negligible. In practice this is not the case. The detector has a finite radius of about 0.4 cm, and since some space is also needed for inserting the absorbers, the center of the detector cannot be brought closer to the moderator surface than about 0.8 cm. The transmission curves to be expected if the time-of-flight of the neutrons over this distance is taken into account have been calculated. It has been assumed that the detector is a point detector at a distance of one mean free path from the moderator. The result of the calculation is shown as the dashed curve II of fig. 7. It is seen that agreement between this curve and the experimental curve is quite satisfactory.

$1/v$-absorbers

Further information on the neutrons within the epicadmium period can be obtained from a study of the transmission curves through $1/v$-absorbers of various thicknesses. A theoretical curve has been calculated in (12) for the variation with time or absorber thickness of the transmission through a $1/v$-absorber, if the neutrons are slowed down by free protons. This curve has been replotted in fig. 7 (dashed curve III) for absorber B2, which has an absorption constant k_0 of $2.12 \cdot 10^5$ cm per sec. As with cadmium, the experimental curve drops much less rapidly with time than the theoretical curve.

A new curve, corrected for time-of-flight, has been derived and is shown as the dashed curve IV. It is seen that this corrected curve fits the experimental data better, but that the measured transmission curve is still a little higher than the theoretical curve derived on the assumption that the protons of the moderator are free. A deviation in this direction may be expected since the transmission through the rather thin $1/v$-absorber B2 will depend on the shape of the energy spectrum below 0.3 eV, where the chemical bond begins to be important. The effect of the bond would be expected to decrease the number of very slow neutrons, and thus the transmission in boron would be expected to be larger than for a moderator of free nuclei.

Basis for theoretical predictions

While the experimental results are thus in essential agreement with the theoretical predictions, it would probably be unwise to try to draw any more detailed conclusions concerning the epicadmium period from the present data. In order to arrive at the theoretical curves, shown dashed in fig. 7, it was necessary to make a number of simplifying assumptions, and the final curves are therefore rough approximations only. These simplifying assumptions will now be discussed.

In the first place it has been assumed that the slowing down process in water is the same as that in a moderator with constant mean free path, consisting of free protons at rest. The free proton cross section is constant up to about 100 keV, and any influence of the decreasing scattering cross section above this energy will have had ample time to disappear before the neutrons have been slowed down to the 1 eV region, where the measurement is made. The presence of the oxygen atoms is expected to have a negligible effect, since collisions with them occur only in 10% of the cases, and produce little energy change.

For low neutron energies the effect of the chemical bonds have to be considered. The vibrational energies of the water molecule, which are virtually unchanged by the physical state of the substance, occur at 0.46, 0.45 and 0.20 eV (14). Even when the neutron is incapable of exciting these vibrations, it can, in the vapour, transfer energy relatively freely to the rotational degrees of freedom, the rotational quanta being about 0.02 eV. While these rotations are hindered to some extent in the solid and liquid state (15), they still remain as a degree of freedom with low quanta, which should be very efficient for removing energy from the neutron. It has been shown elsewhere (12) that the slowing down process against incompletely bound nuclei proceeds almost unaffected by the bond until the neutron energies are of the same order as the lowest vibrational quanta. It can thus be expected that above the cadmium cut-off at 0.3 eV the chemical bond may safely be neglected.

A further assumption, which has been made and which is open to question, is that the velocity distribution of the neutron flux emitted from the surface of a finite moderating geometry with a localized neutron source is the same as that of the flux inside an infinite moderator with a constant density of neutron sources, which is the case treated by the theory. Qualitatively one might expect that the neutron spectrum in a finite geometry would be depleted in high energy neutrons compared to the spectrum in an infinite medium.

The angular distribution of the neutrons emitted from a surface element was assumed to be proportional to $(\cos\vartheta + \sqrt{3}\cdot\cos^2\vartheta)$, as derived by FERMI (16), cf. (17). With this emission law the detector will receive neutrons having the angular distribution $(1 + \sqrt{3}\cdot\cos\vartheta)$, if the neutron emission is uniform and the surface infinite. In the case of our finite moderator this angular distribution will be modified, since the neutrons received by the detector at an oblique angle originate near the edge of the surface, where the neutron flux is lower. These modifications to the angular distribution due to the finite dimensions of the moderator will also depend on the detector-to-moderator distance. It is, however, believed that the errors caused by deviations from the angular distribution $(1 + \sqrt{3}\cdot\cos\vartheta)$ are not serious, since good agreement between experimental and theoretical results in the thermal period was obtained using this angular distribution.

Improved measurement

It is believed that improved experiments, specially designed for the study of the slowing down period, could yield valuable information concerning the epicadmium period. Improvements should, in the author's opinion, aim to eliminate the need for time-of-flight corrections. This can be done in two ways.

First the flight paths of the neutrons can be reduced by the use of a detector of smaller geometrical dimensions. A flat thin detector would be more suitable than the cylindrical chamber used in the present investigation. An ideal solution would be a scintillation detector using a thin layer of a mixture of a boron compound and a fast phosphor (18). The absorbers should also be as thin as possible, and the glass absorbers of low boron content used in this investigation should be replaced by absorbers with boron in a more concentrated form.

The time-of-flight effect can also be decreased by extending the time scale of the slowing down process. This can be done by increasing the neutron mean free path for scattering in the moderator artificially without otherwise changing the slowing down properties. The moderator may be "diluted" by a heavy substance such as lead, which does not, in comparison to the hydrogenous material, contribute appreciably to the slowing down process. In some cases the moderating material can be produced as a foam. A further advantage of this extension of the time scale for the slowing down process, is that it allows better resolution to be obtained.

It should perhaps be pointed out that the time-of-flight effect is serious chiefly for hydrogenous materials due to the speed of the slowing down process in these materials. In other moderators the mean free path is longer, and the change in neutron velocity per collision smaller, so that the process is much slower than in a hydrogenous material.

B. The transition period

After about 3 μsec the neutrons have been slowed down below the cadmium cut-off energy. The subsequent approach to thermal equilibrium will occur much more slowly. Since the approach is gradual it is difficult to define a definite time when the neutrons have become thermal and the transition period has ended. The experimental curves of figs. 5 and 7 indicate, that the transmissions in the boron absorbers reach stable values after 30 μsec, and we can take this to be the length of the transition period at room temperature.

Theory

In the transition period the neutron energy is of the same order as the thermal energies and of the quantum energies of the chemical and mechanical bonds which keep the atoms together. Conditions are therefore much more complicated than in the epicadmium period, where definite theoretical predictions concerning the process can be made. While water is of considerable practical interest as a moderator, it is from the theoretical point of view (15) an exceedingly complicated substance, and a correct theoretical treatment of the transition region seems almost hopeless.

In connection with the present investigation we must content ourselves with a phenomenological discussion, or at most with exceedingly simplified theoretical arguments. For a more detailed treatment a substance having a simple and well-known structure would be preferable.

At least in the latter stage of the transition period the problem is closely similar to those treated by the kinetic theory of gases. The neutrons can be regarded as a very rarefied gas, which interacts with the moderator. For the final approach to thermal equilibrium the gas kinetic methods of treating phenomena in mixtures of gases may give useful results. Unfortunately the time dependence of the kinetic processes in gases has not received much attention, probably due to the fact that in gases at ordinary pressures the times concerned are so short as to have little practical interest.

Bearing in mind this analogy it may be fruitful to see if the neutrons may be regarded as a gas in a quasi-stationary state, having essentially a Maxwellian velocity distribution. From the transmission measurements this assumption about the velocity distribution may be given a rough test, and a temperature assigned to the neutron "gas". Using the transmission data we can follow the gradual cooling of the neutron gas until it comes into thermal equilibrium with the moderator. The "temperature" of the neutron gas may be expected to approach the equilibrium temperature exponentially, to a first approximation. The rate at which temperature equilibrium is attained is a measure of the heat transfer between the two systems.

Following these lines, an approximate theory was derived in ref. (12) for the time dependence of the mean neutron energy or neutron temperature, on the assumption that the water molecules appear as rigid structures and that the bonds between them can be neglected.

Boron absorption measurements

In order to transform the transmission data for the boron absorbers to effective neutron temperatures we need to know the transmission through the absorbers for a Maxwellian neutron velocity spectrum, and for an angular distribution proportional to $(1+\sqrt{3}\cdot\cos\vartheta)$. This problem is treated in the author's thesis (12). The transmission is there calculated as a function of the dimensionless parameter $x = k_0(m/2kT)^{\frac{1}{2}}$. The effective temperature is defined as $k_0^2 m/2kx^2$, where $k_0^2 m/2k$ is listed in Table 1, for the various combinations of absorbers.

The results for the various absorbers are shown in fig. 8. The effective neutron temperatures calculated from the transmission through the thicker absorbers agree with each other within the limits of the experimental errors, indicating that the neutrons have indeed an essentially Maxwellian spectrum during the transition period.

The thinnest absorber B1, however, yielded effective temperatures, which were consistently higher than the temperatures derived from the other measurements. In the thin absorber, only the low energy part of the neutron spectrum is absorbed. The result thus indicates that it takes a longer time for the low energy part than for the main part of the spectrum to adjust itself to the proper Maxwellian distribution. The process is not concluded within the 40 μsec covered by the 2 μsec resolution measurements shown in fig 7.

These conclusions concerning the lag of the low energy part of the neutron spectrum with respect to the rest of the spectrum seem reasonable since it becomes increasingly difficult for the neutrons to loose more energy when their energy is already low. Too much weight should not be given to the results with the thin absorber, however, since in the first place the conversion from transmission to effective neutron temperature becomes increasingly less accurate as the transmission approaches unity, and in the second place the absorber was not very uniform.

The range of time over which time-of-flight effects must be taken into account may be estimated from a series of measurements in which the time distribution was measured with the detector at various distances from the moderator surface. The results of the measurements are shown in fig. 9. The channel width was 11 μsec, and the moderator was water containing no boric acid. It is seen that with the detector in its normal position, at a distance of about 1 cm from the moderator, the time-of-flight effect is appreciable only during the first 20 μsec or so. It is thus not necessary to take it into account during the final part of the transition period and during the thermal period.

Cadmium absorption measurements

The measurements with Cd absorber are rather inaccurate, due to the extremely low counting rates obtained, which resulted in low statistical accuracy and made the measurement sensitive to any background of stray neutrons, and to spurious counts. In the measurements with 2 μsec resolving time the apparent transmission reaches an approximately stationary value of about $3 \cdot 10^{-3}$ after 20 μsec. In the measurements with 4 μsec channel width the transmission does not drop below 10^{-2}, and there is evidence for a constant background in the shape of the time distribution (fig. 5). In these measurements the intensity of the neutron source was lower than in the 2 μsec measurements and we would thus expect the background to assume more relative importance.

In order to investigate what part of the observed transmission in the measurements with the 2 μsec channel width corresponded to transmitted neutrons, and what part was caused by stray neutrons and background, a measurement was made with cadmium and the boron absorber B2. The absorber B2 decreased the transmission after the first 20 μsec by a factor of 0.7 ± 0.2. The neutrons emerging from the cadmium absorber will be those of near perpendicular incidence, since the oblique neutrons will traverse much more absorber and thus be almost entirely absorbed. If the neutrons are thermal neutrons of room temperature we would expect (12) the boron absorber to cause an extra attenuation of about 0.38. Combining this with the observed attenuation we conclude that roughly one half of the intensity registered behind the cadmium absorber can be expected to be real, the rest being caused by background counts and stray neutrons. The latter effects would thus correspond to

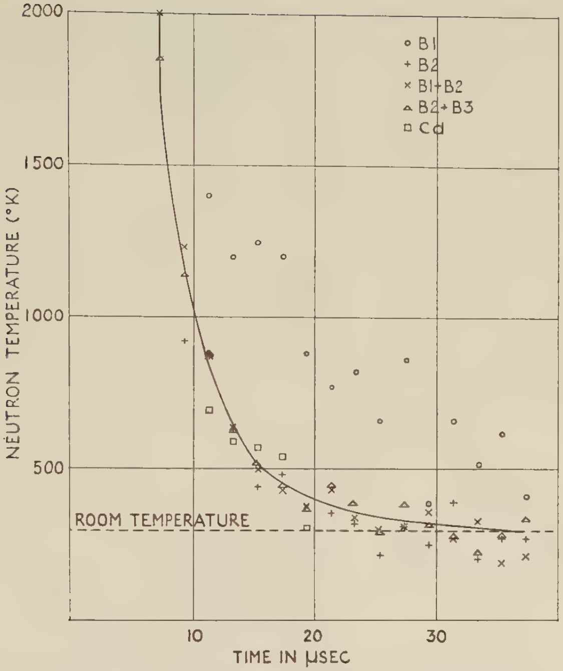

Fig. 8. Effective temperature of neutrons as calculated from transmission data through various absorbers as a function of time.

a transmission of about $1.5 \cdot 10^{-3}$, which is negligible compared to the measured ransmission in all absorbers except cadmium.

The transmission of neutrons through cadmium can be calculated quite easily if he cross section is assumed to be constant up to a certain cut off energy, and zero bove this energy. For the constant cross section we take the value $2300 \cdot 10^{\ 24}$ cm², orresponding to a macroscopic cross section for our cadmium absorber of 5.4 cm²/cm². For the cut off energy we assume the value 0.3 eV.

For neutrons below the cut off energy and having the angular distribution $1 + \sqrt{3} \cdot \cos \vartheta)$ we find (ref. (12), appendix II) an expected transmission of about 0^{-3}. For thermal neutrons of room temperature the fraction having energies above he cut off energy is much smaller than this value, and the theoretical transmission hould thus be 10^{-3}, in agreement with the rough experimental value of $1.5 \cdot 10^{-3}$. Vith increasing neutron temperature the fraction of epicadmium neutrons in the hermal spectrum increases, and at a temperature of about 450° K the transmission lue to these high energy neutrons equals that of the lower energy neutrons. Above his temperature the transmission increases rapidly and becomes a sensitive measure f the neutron temperature. The neutron temperatures determined from the cadmium ransmission measurements, corrected for a background "transmission" of $1.5 \cdot 10^{-3}$, n the assumption of a Maxwellian velocity spectrum during the transition region re plotted in fig. 8, and are seen to be in rough agreement with the temperatures letermined from the boron measurements.

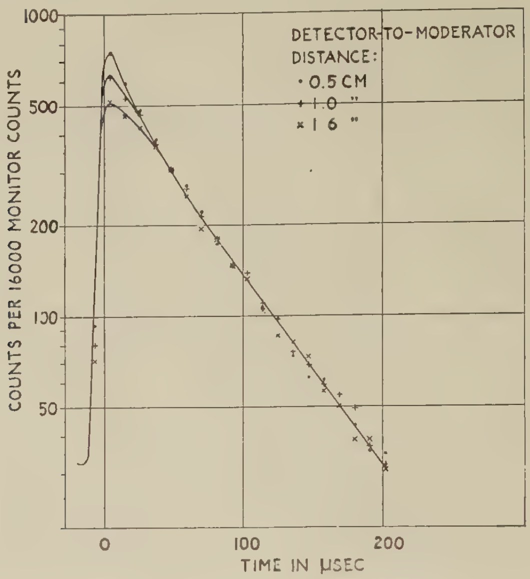

Fig. 9. Normalized time distribution of flux from a water moderator for various moderator-to-detector distances.

Conclusion

We conclude that in the transition period the neutrons behave approximately as a gas in a quasi-stationary state, having at each moment a Maxwellian velocity distribution corresponding to a momentary temperature which decreases rapidly towards the temperature of the moderator. There are however indications that the low energy portion of the spectrum is less pronounced than in the proper Maxwellian spectrum. The effective neutron temperatures approach the equilibrium temperature along a curve (fig. 8), which can be approximated by an exponential approach with a time constant of about 7 µsec. The accuracy attributed to this value is however low, about ± 3 µsec. During the initial part of the transition period the approach is more rapid. The curve agrees closely with the approximate theoretical behaviour derived for neutrons in a gas of free water molecules (12).

C. Thermal period

The measurements described in this article were performed with special emphasis on the slowing down and transition periods. The amount of thermal neutrons was reduced deliberately by the addition of boric acid to the water, and the repetition time was chosen so short that most of the thermal period was overlapped by the next cycle. The measurements of fig. 5 show that the spectrum is indeed constant after the end of the transition period, and for at least another 40 µsec. The effective neutron temperature curves of fig. 8 show that at the end of the transition region the neutrons are in thermal equilibrium with the moderator. The agreement between neutron temperatures found using different absorber thicknesses shows that the velocity distribution in the moderator is approximately Maxwellian, since this distribution was assumed in converting from transmission to neutron temperature. More sensitive experiments designed to investigate the thermal period in more detail will be described in ref. (12).

Acknowledgements

The author wishes to express his thanks to Dr S. EKLUND in whose laboratory the present investigation was made, and to Prof. L. HULTHÉN and Dr N. SVARTHOLM for many stimulating discussions concerning the interpretation of the experimental results. The technical assistance of Mr P. HOLMÉN is gratefully acknowledged.

AB Atomenergi, Department of Physics, Stockholm.

REFERENCES

1. L. J. RAINWATER, W. W. HAVENS Jr., Phys. Rev. *70*, 136 (1946).
2. J. H. MANLEY, L. J. HAWORTH, E. A. LUEBKE, Phys. Rev. *69*, 405 (1946).
3. H. L. ANDERSON, E. FERMI, A. WATTENBERG, G. L. WEIL, W. H. ZINN, Phys. Rev. *72*, 16 (1947).
4. W. J. STURM, Phys. Rev. *71*, 757 (1947).
5. H. A. BETHE, Rev. Mod. Phys. *9*, 134 (1937).
6. G. VON DARDEL, Appl. Sci. Res. *133*, 209 (1953).
7. G. VON DARDEL, E. HELLSTRAND, C. TAYLOR, Appl. Sci. Res. *B3*, 35 (1953).
8. E. R. GRAVES, A. A. RODRIGUES, M. GOLDBLATT, D. I. MEYER, Rev. Sci. Instr. *20*, 579 (1949).
9. R. MAZE, J. de Physique *7*, 164 (1946).
10. M. L. MACKNIGHT, R. L. CHASSON, Rev. Sci. Instr. *22*, 700 (1951).
11. R. F. BACHER, C. P. BAKER, B. D. MACDANIEL, Phys. Rev. *69*, 443 (1947).
12. G. VON DARDEL: The interaction of neutrons with matter, studied with a pulsed neutron source. Diss. Tekn. Högskolan, Stockholm (in press).
13. E. MELKONIAN, Phys. Rev. *76*, 1744 (1949).
14. G. HERZBERG, Infrared and Ramanspectra of Polyatomic Molecules, New York (1947).
15. NIELS BJERRUM, K. Dansk. Vid. Selsk. Mat.fys. Medd. *27: 1* (1951).
16. E. FERMI, Ric. Sci. *7*, 13 (1936).
17. G. PLACZEK, Phys. Rev. *72*, 556 (1947).
18. D. E. ALBURGER, Rev. Sci. Instr. *23*, 769 (1952).

Tryckt den 2 december 1953

Uppsala 1953. Almqvist & Wiksells Boktryckeri AB

ARKIV FÖR FYSIK Band 7 nr 29

Communicated 3 June 1953 by OSKAR KLEIN and IVAR WALLER

On the scattering of slow neutrons by crystals near the Bragg angles

By ALF SJÖLANDER

With 5 figures in the text

Formulas for the diffuse temperature scattering of neutrons by an isotropic cubic crystal are derived, holding when the Laue interference conditions are approximately fulfilled. The singularities of the scattering cross section are studied for anisotropic cubic crystals, and relations between the singular directions and the elastic constants of the crystal are given. Finally some general results about the intensity of the scattering are derived.

In this paper some general results concerning diffuse temperature scattering of slow neutrons by small single crystals will be given. The deviation from the Laue interference conditions is assumed to be small, and the main results refer to neutron velocities which do not exceed the velocities of sound. Only crystals of cubic symmetry have been studied, but the methods used here are not restricted to this case.

Methods of wide applicability for this problem have been developed by WALLER, who investigated the diffuse temperature scattering of X-rays.[1] Some of the most characteristic qualitative properties for the scattering of neutrons have been pointed out by SEEGER and TELLER[2] and later a more close quantitative investigation has been carried out by WALLER[3] and FRÖMAN[4]. The results are in broad outline the same as in the case of X-ray diffraction, but there are some characteristic differences, especially for neutron velocities of the same order of magnitude as sound velocities. Replacing the mass of the neutron by zero, all results in I are transformed into the corresponding results for X-rays.

Introduction

The general problem concerns the scattering of neutrons by a crystal. The incident neutrons are supposed to be represented by a monochromatic plane wave of particles, the wave vector of which is denoted by $\boldsymbol{k}$. The scattered neutrons emerge radially from the crystal, and they can be represented by a superposition of monochromatic waves. We will denote by $\boldsymbol{n}$ the unit vector for the direction in which the emergent neutrons are considered. Scattering dependent on magnetic interaction, isotopic disorder and spin dependence will be neglected.[1]

---

[1] I. WALLER, Interferenz- und Dispersionstheorie der Röntgenstrahlen, Thesis, Uppsala 1925.

[2] R. J. SEEGER–E. TELLER, Phys. Rev., 62, 37 (1942).

[3] I. WALLER–P. O. FRÖMAN, Arkiv för Fysik, band 4 nr. 5. (In the text this paper will be refered to as I.)

[4] P. O. FRÖMAN, Arkiv för fysik, band 4 nr. 6.

The only crystals dealt with are so small that absorption can be neglected.[2] Nevertheless the number of atoms in the crystal can be taken as very large. A nucleus is characterized by a cellular index $l=(l_1, l_2, l_3)$ and a basic index p, the latter indicating the nuclei in a single cell. N denotes the number of unit cells in the crystal. For crystals of cubic symmetry the basic vectors of the lattice can be chosen as $a\,\boldsymbol{e}_1$, $a\,\boldsymbol{e}_2$, $a\,\boldsymbol{e}_3$, where a is the lattice parameter and $\boldsymbol{e}_1$, $\boldsymbol{e}_2$, $\boldsymbol{e}_3$ are unit vectors along the principal axes of the crystal. It is convenient to introduce the reciprocal lattice, the basic vectors of which are $b\,\boldsymbol{e}_1$, $b\,\boldsymbol{e}_2$, $b\,\boldsymbol{e}_3$, where b is the reciprocal value of a.

Owing to thermal vibrations, the crystal deviates from the ideal form. All other causes of imperfections are neglected. The nuclei perform approximately harmonic vibrations around their mean positions, and the vibrations of the crystal can be considered as a superposition of its eigen vibrations. If the surface distortion is neglected, these eigen vibrations are progressive, monochromatic waves. Denoting by $\boldsymbol{u}_l^p$ the deviation from the mean position of the nucleus, characterized by (p, l), we may write an eigen vibration of the crystal in the form

$$\boldsymbol{u}_l^p=\boldsymbol{C}_{\varkappa j}^p\, e^{i(\boldsymbol{\varkappa}\cdot \boldsymbol{A}_l-\omega_{\varkappa j} t)} \quad j=1, 2, \ldots 3\,s. \tag{1}$$

$\boldsymbol{\varkappa}$ is the wave vector. $\boldsymbol{A}_l=a\,(l_1\,\boldsymbol{e}_1+l_2\,\boldsymbol{e}_2+l_3\,\boldsymbol{e}_3)$ is the position vector of the lattice point, indicated by l. $\boldsymbol{C}_{\varkappa j}^p$ denotes the complex amplitude, and $\omega_{\varkappa j}$ are the eigen frequencies. j refer to $3\,s$ waves associated with a definite wave vector, where s is the number of nuclei in a cell. The wave vectors lie very close together in the reciprocal cell $(l_1, l_2, l_3)=0$, and their end points are uniformly distributed in this cell. The number of eigen vibrations is the same as the number of degrees of freedom of the crystal. The eigen vibrations can be separated into acoustic waves, which correspond to the elastic vibrations in the crystal, and optical waves, which are unimportant for this investigation.[3]

Considering only acoustic waves and $\boldsymbol{\varkappa}$-vectors, small in comparison with a reciprocal basic vector, we may write the motion of the nuclei in the form

$$\boldsymbol{u}_l^p=\boldsymbol{C}_{\varkappa j}^p\, e^{i(\boldsymbol{\varkappa}\cdot \boldsymbol{A}_l-\omega_{\varkappa j} t)} \quad j=1, 2, 3. \tag{1'}$$

where $C_{\varkappa j}$ and $\omega_{\varkappa j}$ are determined from the following linear system of equations.[4]

$$\left(\omega_{\varkappa j}^2-\frac{c_{44}}{\varrho}\varkappa^2\right)\boldsymbol{C}_{\varkappa j}=\frac{c_{11}-c_{44}}{\varrho}\,\varkappa^2\,\boldsymbol{\Gamma}\,\boldsymbol{C}_{\varkappa j} \tag{2}$$

---

[1] The effect of isotopic disorder and spin dependence on the scattering has been studied by FRÖMAN, among others. P. O. FRÖMAN, Arkiv för Fysik, band 6 nr. 11.

[2] This is justifiable if the linear dimension of the crystal is 10^{-4} cm or smaller. See: W. H. ZACHARIASEN, Theory of X-ray diffraction in crystals, p. 103.

[3] M. BORN, Dynamik der Kristallgitter (1915). See also: W. H. ZACHARAISEN, Theory of X-ray diffraction in crystals, p. 192–197 (1944).

[4] Cf. M. BORN, Atomtheorie des festen Zustandes, Enc. Mat. Wiss. V 3, p. 648.

where $\mathbf{\Gamma}$ is a tensor, c_{11}, c_{12}, c_{44} are the elastic constants, and ϱ is the mass density. We denote by $(x y z)$ the direction cosines of the wave vectors relative to the principal axes. $\mathbf{\Gamma}$ has the following form

$$\mathbf{\Gamma} = \begin{pmatrix} x^2 & K x y & K x z \\ K y x & y^2 & K y z \\ K z x & K z y & z^2 \end{pmatrix}. \tag{2'}$$

The symbol K is defined by

$$K = \frac{c_{12} + c_{44}}{c_{11} - c_{44}}. \tag{2''}$$

For an isotropic crystal $K = 1$.

$\boldsymbol{C}_{\varkappa j}$ is ortho-normalized in the following way

$$\boldsymbol{C}^*_{\varkappa j} \cdot \boldsymbol{C}_{\varkappa j'} = \frac{2}{N M} \delta_{j j'} \tag{2'''}$$

where M denotes the total mass in a unit cell.

If the isotropy condition is fulfilled, the solutions of (2) are of very simple form. Even in the general case it is possible to give an exact solution, but then the expressions are too complicated to be used in the following reasoning. In an appendix we have calculated the limits of each of the three branches of the eigen frequencies, when $(x y z)$ lies on the unit sphere, and these values will be used later.

Following the methods developed by WALLER, the differential scattering cross section can be expanded in a series

$$\sigma(\boldsymbol{k}, \boldsymbol{n}) = \sum_{i=0}^{\infty} \sigma_i (\boldsymbol{k}, \boldsymbol{n})$$

where σ_0 gives the intense coherent scattering when the Laue conditions are exactly fulfilled.

$$\boldsymbol{K} - \boldsymbol{k} = 2 \pi \boldsymbol{\tau} \qquad \boldsymbol{K} = |\boldsymbol{k}| \, \boldsymbol{n}. \tag{3}$$

Here $\boldsymbol{\tau}$ denotes the position vector of a reciprocal lattice point.

σ_0 is of importance only for vectors $\frac{1}{2\pi}(\boldsymbol{K} - \boldsymbol{k})$ in an extremely narrow region around a reciprocal lattice point. On the other hand, the sum $\sum_{i=2}^{\infty} \sigma_i (\boldsymbol{k}, \boldsymbol{n})$ is shown by WALLER to be negligible in the case of X-ray diffraction, when the Laue conditions are approximately fulfilled, and the same conclusion may be drawn in this case.[1] Our task in this paper is to study the term σ_1. As the

---

[1] WALLER (l. c.) $\sigma_1 \approx \alpha \frac{K}{\delta^2}, \quad \sigma_2 \approx \alpha \frac{K^2}{\delta}$

$$K \approx \frac{4 \pi k_B}{3 a^3} \frac{2 c_{11} + c_{44}}{c_{11} \; c_{44}} \left(\frac{a \sin \theta}{\lambda} \right)^2 T.$$

starting point of our investigation we will take the expression for the differential cross section given by WALLER and FRÖMAN in I, p. 185, formula (6).

$$\sigma_1(\boldsymbol{k}, \boldsymbol{n}) = N^2 \sum_{pp'} f_p f_{p'}^* \, e^{i 2\pi \boldsymbol{\tau} \cdot (\boldsymbol{r}_p - \boldsymbol{r}_{p'})} \, e^{-M_p(2\pi\boldsymbol{\tau}) - M_{p'}(2\pi\boldsymbol{\tau})} \cdot \sum_{\substack{\varkappa, j, \varepsilon \\ (k'\boldsymbol{n} - \boldsymbol{k} - 2\pi\boldsymbol{\tau} - \boldsymbol{\varkappa} = 0)}} \frac{1}{2} (2\pi\boldsymbol{\tau} \cdot \boldsymbol{C}_{\varkappa j}^{p}) (2\pi\boldsymbol{\tau} \cdot \boldsymbol{C}_{\varkappa j}^{*p'}) \frac{1}{2} \left(g(\omega_{\varkappa j}) + \frac{\varepsilon \hbar}{2\omega_{\varkappa j}} \right) \frac{1}{|J|} \tag{4}$$

$$J = 1 + \frac{\varepsilon}{v} \boldsymbol{n} \cdot \operatorname{grad} \omega_{\varkappa j} \qquad v = \text{neutron velocity.} \tag{4'}$$

$\boldsymbol{r}_p$ gives the mean position of the p:th nucleus in the unit cell defined by $(l_1, l_2, l_3) = 0$. f_p is the scattering length of the nucleus characterized by the index p. M_p signifies the DEBYE-WALLER temperature factor, well known in the theory of X-rays.[1] $g(\omega_{\varkappa j})$ can be approximated with $\frac{1}{\vartheta \omega_{\varkappa j}^2} = \frac{k_B T}{\omega_{\varkappa j}^2}$, if T is not too low.[2] Here k_B denotes Boltzmann's constant and T is the absolute temperature. Owing to the factor $\frac{1}{\omega_{\varkappa j}^2}$, the contribution from the optical waves can be neglected if the $\boldsymbol{\varkappa}$-vectors included in (4) are small compared with a reciprocal basic vector.[3] Only a few eigen vibrations of the crystal contribute to the scattering in this approximation. The $\boldsymbol{\varkappa}$-vectors to be put into (4) are determined from the following relation, given for a special case in I (8)–(9).

$$\boldsymbol{\varkappa} = \boldsymbol{\eta} - \varepsilon \frac{\omega_{\varkappa j}}{v} \boldsymbol{n} \tag{5}$$

where[4]

$$\boldsymbol{\eta} = \boldsymbol{K} - \boldsymbol{k} - 2\pi\boldsymbol{\tau} \qquad \boldsymbol{K} = |\boldsymbol{k}|\,\boldsymbol{n}.$$

The summation is extended over the three vibrations, indicated by $j = 1, 2, 3$, and $\varepsilon = \pm 1$, corresponding to absorption and emission of energy by the neutrons respectively.

The relation (5) is of great importance for the following. Its geometrical meaning will be clear from Figs. 1 and 2.

For many crystals, $K \lesssim 2.10^{-5}\, T p^2$; p is the order of reflexion. This suggests that at room temperature and for $p \lesssim 4$, $\sum_{i=2}^{\infty} \sigma_i$ might be neglected, if $\delta = \frac{\eta}{b} \lesssim 1$. The notation is given in the text.

[1] WALLER (l. c.), p. 35 formula (56′). See also: FRÖMAN (l. c.), p. 197.

[2] The error is smaller than 10 per cent, if $\frac{\hbar \omega_{\varkappa j}}{k_B T} \approx \frac{\Theta}{T} \frac{\varkappa}{\pi b} \lesssim 1$. Θ is the Debye temperature. In the following we use the notation ϑ for $1/k_B T$.

[3] It might be sufficient that $\frac{\varkappa}{\pi b} \lesssim \frac{1}{4}$.

[4] $k' = \left(1 - \varepsilon \frac{2\omega_{\varkappa j}}{v|\boldsymbol{k}|}\right)^{1/2} |\boldsymbol{k}|$ has been approximated with $|\boldsymbol{k}| - \varepsilon \frac{\omega_{\varkappa j}}{v}$.

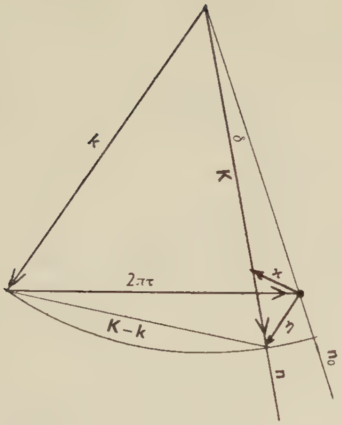

Fig. 1.

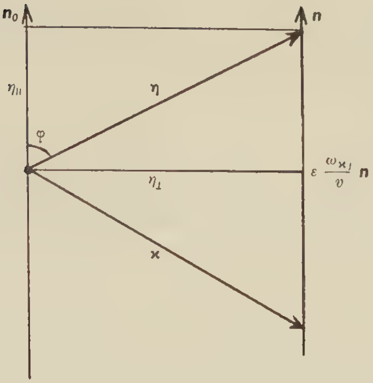

Fig. 2.

n_0 may be taken $\parallel$ n.

I contains explicit expressions for the scattering in a Debye crystal with one sound velocity. Two remarkable results are obtained. The scattering is independent of the neutron velocity, if $v > c$ (c = velocity of sound). For $v < c$ the intensity is extremely high in certain directions of $\boldsymbol{n}$, and when the deviation from a Bragg angle exceeds that for the directions mentioned above, the scattering cross section abruptly vanishes. The neglected part of the cross section does make a contribution, but only a small one. The directions with the high intensity are determined by

$$\operatorname{tg} \varphi = \frac{1}{\sqrt{\beta^2 - 1}} \quad \beta = \frac{c}{v} \cdot \quad \text{(See fig. 2.)} \tag{6}$$

The corresponding vectors $\boldsymbol{\eta}$ generate a circular cone. A surface generated by $\boldsymbol{\eta}$-vectors and defining directions for extremely high intensity will in the following be denoted by an η-cone.

Isotropic crystals

In this section it will be shown that the results above can be generalized for an isotropic crystal. The solution of equation (2) is easily obtained. We get two sound velocities $c_{\parallel}$ and $c_{\perp}$, corresponding to longitudinal and transversal waves, and these are independent of $\boldsymbol{\varkappa}$. The amplitudes are

$$\boldsymbol{C}_{\varkappa j} = \left(\frac{2}{NM}\right)^{1/2} \boldsymbol{e}_{\varkappa j}$$

where $\boldsymbol{e}_{\varkappa_1}$, $\boldsymbol{e}_{\varkappa_2}$, $\boldsymbol{e}_{\varkappa_3}$ are three mutually orthogonal unit vectors, and $\boldsymbol{e}_{\varkappa_1}$ is parallel to $\boldsymbol{\varkappa}$. For each of the sound velocities we find in exactly the same manner as in I a solution of (5)

$$|\boldsymbol{\varkappa}| = \frac{\pm\bar{\eta} - \varepsilon\beta\eta_{\parallel}}{1-\beta^2}, \quad \beta = \begin{cases} \dfrac{c_{\parallel}}{v} = \beta_{\parallel} \\ \dfrac{c_{\perp}}{v} = \beta_{\perp} \end{cases} \tag{7}$$

where

$$\bar{\eta} = \eta_{\parallel}\sqrt{1+(1-\beta^2)\,\mathrm{tg}^2\,\varphi}.$$

The signs $\pm$ and $\varepsilon = \pm 1$ must be chosen to make $|\boldsymbol{\varkappa}| > 0$.

By using the relations (4′), (5) and (7), J is transformed as follows

$$J = 1 + \varepsilon\beta\frac{\eta_{\parallel}}{|\boldsymbol{\varkappa}|} - \beta^2 = \pm\frac{\bar{\eta}}{|\boldsymbol{\varkappa}|}. \tag{8}$$

Using the expressions for J, $|\boldsymbol{\varkappa}|$ and $\boldsymbol{C}_{\boldsymbol{\varkappa}j}$ given above we get the following expression for the scattering cross section

$$\begin{aligned} \sigma_1(\boldsymbol{k}, \boldsymbol{n}) = N|F|^2\frac{1}{2M\vartheta}\left[\frac{1}{\bar{\eta}_1}\frac{1}{c_{\parallel}^2}\sum\left(\frac{(2\pi\boldsymbol{\tau}_{\parallel}\boldsymbol{\varkappa})^2}{|\boldsymbol{\varkappa}|}\right)_{\parallel} + \frac{1}{\bar{\eta}_2}\frac{1}{c_{\perp}^2}\sum\left(\frac{2\pi\boldsymbol{\tau}_{\perp}\boldsymbol{\varkappa})^2}{|\boldsymbol{\varkappa}|}\right)_{\perp}\right] + \\ + N|F|^2\frac{\hbar}{4M}\left[\frac{1}{\bar{\eta}_1}\frac{1}{c_{\parallel}}\sum(\varepsilon(2\pi\boldsymbol{\tau}_{\parallel}\boldsymbol{\varkappa})^2)_{\parallel} + \frac{1}{\bar{\eta}_2}\frac{1}{c_{\perp}}\sum(\varepsilon(2\pi\boldsymbol{\tau}_{\perp}\boldsymbol{\varkappa})^2)_{\perp}\right] \end{aligned} \tag{9}$$

where

$$\bar{\eta}_1 = \eta_{\parallel}\sqrt{1+(1-\beta_{\parallel}^2)\,\mathrm{tg}^2\,\varphi}, \quad \bar{\eta}_2 = \eta_{\parallel}\sqrt{1+(1-\beta_{\perp}^2)\,\mathrm{tg}^2\,\varphi}$$

$$F = \sum_p f_p\, e^{i2\pi\boldsymbol{\tau}\cdot\boldsymbol{r}_p}\, e^{-M_p(2\pi\boldsymbol{\tau})}$$

$\tau_{\parallel}\boldsymbol{\varkappa}$ and $\tau_{\perp}\boldsymbol{\varkappa}$ denote the component of $\boldsymbol{\tau}$ parallel and perpendicular to $\boldsymbol{\varkappa}$. $(\ )_{\parallel}$ and $(\ )_{\perp}$ signify that the values of $\boldsymbol{\varkappa}$ inside are to be those obtained from (7), when $\beta = \beta_{\parallel}$ and $\beta = \beta_{\perp}$ respectively. The summation is extended over the $\boldsymbol{\varkappa}$-vectors in accordance with (7). For $c_{\parallel} = c_{\perp}$ the formula reduces to that given by WALLER and FRÖMAN (I p. 189).

From (9) it is clear that the scattering cross section will be infinite in certain directions, when $\beta_{\parallel}$ or $\beta_{\perp} > 1$, and that the corresponding $\boldsymbol{\eta}$-vectors generate two circular $\boldsymbol{\eta}$-cones, defined by

$$\mathrm{tg}\,\varphi = \frac{1}{\sqrt{\beta_{\parallel}^2 - 1}}, \quad \mathrm{tg}\,\varphi = \frac{2}{\sqrt{\beta_{\perp}^2 - 1}}. \tag{10}$$

As a continuous dependence on the vector $\boldsymbol{\eta}$ has been assumed in deriving (4), we can only conclude that the intensity will be extremely high in those directions for which (9) becomes infinite.

For neutron velocities larger than both of the sound velocities, that part of (9) which depends on the neutron velocity vanishes. The calculations are elementary but rather lengthy; therefore, only the result will be given here:

$$\sigma_1(\boldsymbol{k}, \boldsymbol{n}) = N|F|^2|2\pi\boldsymbol{\tau}|^2\frac{1}{M\vartheta}\left[\frac{1}{c_{\parallel}^2}\left(\frac{\eta_{\parallel\boldsymbol{\tau}}}{\eta}\right)^2 + \frac{1}{c_{\perp}^2}\left(\frac{\eta_{\perp\boldsymbol{\tau}}}{\eta}\right)^2\right]\frac{1}{\eta^2}, \quad \eta = |\boldsymbol{\eta}|. \tag{11}$$

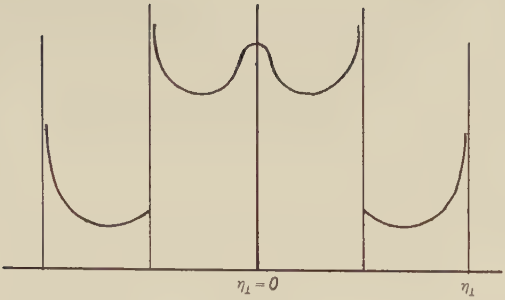

Fig. 3.

The two new symbols $\eta_{\parallel \boldsymbol{\tau}}$ and $\eta_{\perp \boldsymbol{\tau}}$ in (11) denote the components of $\boldsymbol{\eta}$ parallel and perpendicular to the vector $\boldsymbol{\tau}$.

When the neutron velocity does not exceed either $c_\parallel$ or $c_\perp$ the differential cross section depends on v. This dependence is clear from the following formula, which has been derived from (9); $v < c_\parallel$ and $c_\perp$.

$$\sigma_1(\boldsymbol{k}, \boldsymbol{n}) = N\,|F|^2 \frac{1}{M\vartheta}\left[\frac{\alpha_1(\boldsymbol{k}, \boldsymbol{n})}{v} + \frac{\alpha_2(\boldsymbol{k}, \boldsymbol{n})}{v^3}\right]\frac{1}{\eta^2} + N\,|F|^2 \frac{\hbar}{4M}\,\frac{\alpha_3(\boldsymbol{k}, \boldsymbol{n})}{v^2}\,\frac{1}{\eta} \qquad (12)$$

and

$$\alpha_i(\boldsymbol{k}, \boldsymbol{n}) = \frac{g_i(\boldsymbol{k}, \boldsymbol{n})}{\bar{\eta}_1} + \frac{h_i(\boldsymbol{k}, \boldsymbol{n})}{\bar{\eta}_2}$$

where g_i and h_i are independent of v. To get numerical values of the scattering cross section, formula (9) might be the most convenient one to use.

Conclusion (Isotropic crystals)

When the neutron velocity exceeds the two velocities of sound, the scattering is independent of the neutron velocity. The intensity is given by formula (11), which agrees exactly with the corresponding formula for X-rays. In other cases the scattering depends on the neutron velocity, according to (12). The intensity is high for directions defined by $\eta_\perp = 0$ $(\eta_\parallel \leqslant 2\pi b)$ and for directions determined from the relation (10) (see Figs. 1 and 2). Outside these exceptional directions the scattering abruptly decreases.

Fig. 3 gives an idea how the intensity depends on $\eta_\perp$, when $\eta_\parallel$ is kept fixed and $v < c_\parallel$ and $c_\perp$.

Anisotropic crystals.

In most real crystals the deviations from isotropy are considerable, and a brief account of some qualitative results valid in the general case may therefore be of interest. For sufficiently slow neutrons there are three η-cones corresponding

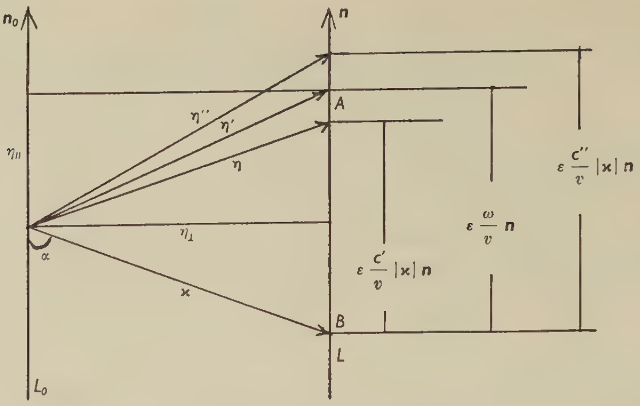
n_0
n
A
η''
η'
η
$\eta_{\parallel}$
$\varepsilon \frac{c''}{v} |\varkappa| n$
$\varepsilon \frac{\omega}{v} n$
$\eta_{\perp}$
α
$\varepsilon \frac{c'}{v} |\varkappa| n$
$\varkappa$
B
L
L_0

Fig. 4.

to each component of the sound velocities[1] The analytical characters of these surfaces are in general very complicated. We will surround each of them with circular cones in such a manner that there are simple relations between the apical angles of these cones and the elastic constants of the crystal. By choosing the orientation of the crystal relative to the incident neutrons in a suitable way, it is possible to arrange that an η-cone will touch, at least approximately, one of its surrounding circular cones. In this way, even some quantitative relations valid for the anisotropic crystal may be obtained.

The singularities of the scattering cross section, when $\eta_{\perp} \neq 0$ (see Fig. 2), are due to the vanishing of J.

The figure above is the same as Fig. 2. The new quantities introduced are explained below.

The index $(\varkappa j)$ in $\omega_{\varkappa j}$ will be dropped from now on, and we consider a special branch j.

From equation (2) we conclude that the form of ω is

$$\omega = c(xyz)\,|\boldsymbol{\varkappa}|$$

where $c(xyz)$ depends only on the direction of $\boldsymbol{\varkappa}$. We determine those $\boldsymbol{\varkappa}$-vectors that correspond to vectors $\boldsymbol{\eta}$, the end points (A) of which are located on the straight line L, where L may be allowed to rotate about L_0 (Fig. 4). Because of the homogeneity of (5), the solution for arbitrary $\boldsymbol{\eta}$ may then be obtained by simply introducing a scale factor.

$c(xyz)$ is bounded; the limits are denoted by

$$c' = \inf c(xyz), \quad c'' = \sup c(xyz). \tag{13}$$

Let us first decide whether (5) can be satisfied for every $\boldsymbol{\eta}$. Let the point B (Fig. 4) describe L, and consider the motion of A. For large values of v, A will move along the whole line, but for sufficiently small v the variation of A is restricted to one side of a certain limit point. The vector $\boldsymbol{\eta}$ corresponding to this limit point will be denoted by $\boldsymbol{\eta}_L$. We will suppose that there is at most one turning point of A, when B moves in a definite direction.[1]

---

[1] As mentioned above, we include three eigen vibrations under each wave vector $\boldsymbol{\varkappa}$.

The vector $\boldsymbol{\varkappa}$ corresponding to $\boldsymbol{\eta}_L$ is determined from the relation

$$\frac{\varepsilon}{v}(\boldsymbol{n}\cdot\operatorname{grad}\omega)+1=0. \tag{14}$$

The lefthand side of (14) is identical with J, and for this reason (14) gives the η-cone.

The vectors, $\boldsymbol{\eta}'$ and $\boldsymbol{\eta}''$, are constructed (Fig. 4). We note that $\boldsymbol{\eta}$ will always take an intermediate position between them. Our intention is to make a comparison with two Debye crystals having the sound velocities c' and c''. From the construction it is immediately clear, that the η-cones of the Debye crystals, denoted by η'_D and η''_D cones, surround the corresponding η-cone of our anisotropic crystal. Formula (6) gives the apical angles of these surrounding cones. The surfaces generated by $\boldsymbol{\varkappa}$-vectors corresponding to the η_D-cones may be denoted by $\varkappa'_D$ and $\varkappa''_D$ cones respectively, and their apical angles are given by

$$\cos\alpha=\frac{1}{\beta} \tag{15}$$

where β is $\begin{cases}\dfrac{c'}{v}\\[1ex] \dfrac{c''}{v}\end{cases}$.

For a vector $\boldsymbol{\varkappa}$ satisfying the relation $c(xyz)=c'$ and located on the $\varkappa'_D$-cone, $\boldsymbol{\eta}'=\boldsymbol{\eta}'_D=\boldsymbol{\eta}=\boldsymbol{\eta}_L$. The η-cone will touch the outer η_D-cone. For a $\boldsymbol{\varkappa}$ satisfying $c(xyz)=c''$ and located on the $\varkappa''_D$-cone, $\boldsymbol{\eta}''=\boldsymbol{\eta}''_D=\boldsymbol{\eta}$, and $\boldsymbol{\eta}=\boldsymbol{\eta}_L$ when the first infinitesimal variation of $c(xyz)$ vanishes. The conditions for the η-cone to touch its outer or inner η_D-cone can be formulated as follows:

I. *To get an η-cone touching its outer η_D-cone, we have to rotate the crystal, or choose the neutron velocity so that one of the unit vectors (fixed in the crystal) determined by the relation*

$$c(xyz)=c' \tag{16}$$

lies on the $\varkappa'_D$-cone. The condition for touching the inner η_D-cone is expressed in the same way by simply changing the indices ($c'\rightarrow c''$, $\varkappa'_D\rightarrow\varkappa''_D$) and in addition providing $\delta c(xyz)=0$.[2]

---

[1] The author has not succeeded in justifying this. However, the study of isotropic crystals suggests that our supposition might be valid for most directions of $\boldsymbol{n}_0$, at least for crystals not too far from isotropy.

[2] See appendix. $\delta c(xyz)=0$ is automatically fulfilled in the directions defined by $c(xyz)=c''$ except for the lowest branch of the eigen frequencies in the directions (± 1, ± 1, ± 1) and the case $K>1$.

The directions defined by the relation (16) or the corresponding relation where $c' \to c''$, are denoted by L', L'' respectively and are given in an appendix.

We can draw some conclusions about the η-cones and the intensity of the scattering from the symmetry properties of the crystal.[1] Some results obtained immediately are given below.[2]

When the direction of $\boldsymbol{n}$ varies the intensity can be visualized in a plane normal to the vector $\boldsymbol{n}_0$ (see Figs. 1 and 2). We get singular curves, which are approximately the intersections of the η-cones and the plane defined by $\eta_{\parallel} = \text{constant}$. For isotropic crystals these curves are circles, and for anisotropic crystals we have surrounded each singular curve with two concentric circles.

The following theorem is obtained directly:

II. *If the crystal is rotated so that* $\boldsymbol{n}_0$ *lies along one of the following directions*

a) $(\pm 1, 0, 0)$, $(0, \pm 1, 0)$, $(0, 0, \pm 1)$

b) $(\pm 1, \pm 1, 0)$, $(\pm 1, 0, \pm 1)$, $(0, \pm 1, \pm 1)$

c) $(\pm 1, \pm 1, \pm 1)$

the singular curves have

a) 4   *b*) 2   *c*) 3

axes of symmetry.

In accordance with this we note that the differential cross section, which in the approximations used here can be written in the form

$$\sigma_1(\boldsymbol{k}, \boldsymbol{n}) = N^2 |F|^2 \sum_{\substack{\boldsymbol{\varkappa}, j, \varepsilon \\ \left(\boldsymbol{\varkappa} + \varepsilon \frac{\omega_{\varkappa j}}{v} \boldsymbol{n} - \boldsymbol{\eta} = 0\right)}} |2\pi \boldsymbol{\tau} \cdot \boldsymbol{C}_{\varkappa j}|^2 \frac{1}{4} \left(\frac{1}{\vartheta \omega_{\boldsymbol{\varkappa} j}^2} + \frac{\varepsilon \hbar}{2 \omega_{\boldsymbol{\varkappa} j}} \right) \frac{1}{|J|} \tag{17}$$

has no such axes of symmetry, owing to the factor $|2\pi \boldsymbol{\tau} \cdot \boldsymbol{C}_{\varkappa j}|$. In the following special case, however, we get the theorem:

III. *When the condition*

$$2\pi \boldsymbol{\tau} \cdot \boldsymbol{n}_0 = 0$$

is fulfilled and $\boldsymbol{n}_0$ *lies along* (1, 0, 0), (1, 1, 0) *or the equivalent directions, the scattering cross section has the same magnitude in directions symmetric relative to* $\boldsymbol{n}_0$.

Another similar conclusion, also obtained directly from the symmetry, is the following:

IV. *For temperatures so high, that* $\frac{\varepsilon \hbar}{2 \omega_{\boldsymbol{\varkappa} j}}$ *can be neglected in* (17), *the intensity is the same for the* $\boldsymbol{\eta}$*-vectors symmetric relative to a Laue interference point* $2\pi \boldsymbol{\tau}$.

---

[1] See Fig. 5 in the appendix.

[2] The author is grateful to FRÖMAN for suggesting this special study.

Because of the homogeneity of (2) and (5), we can write the differential cross section, when the direction of $\boldsymbol{\eta}$ is kept fixed and $|\boldsymbol{\eta}|$ varies, in the following form $\left(\frac{\varepsilon \hbar}{2\,\omega_{\varkappa j}}\text{ is neglected}\right)$:

$$\sigma_1(\boldsymbol{k}, \boldsymbol{n}) = \frac{\text{const.}}{\eta^2}. \tag{18}$$

The intensity of the scattering decreases abruptly when the angle φ between $\boldsymbol{n}_0$ and $\boldsymbol{\eta}$ (Fig. 2) exceeds the apical angle of an $\boldsymbol{\eta}$-cone, and for vectors $\boldsymbol{\eta}$ outside all η-cones the scattering cross section vanishes. It can easily be shown, that when $\boldsymbol{\eta}$ approaches an η-cone from the inside in the direction of $\eta_\perp$, the scattering cross section increases as $\frac{1}{\sqrt{\eta_\perp^L - \eta_\perp}}$; $\eta_\perp^L$ denotes the value of $\eta_\perp$ on an η-cone.

In Table I the explicit formulas for c_j' and c_j'' and the corresponding directions L' and L'' are given $(j = 1, 2, 3)$.[1] The η_D-cones are determined by the formula

$$\operatorname{tg}\varphi = \frac{1}{\sqrt{\beta^2 - 1}}, \quad \beta = \begin{cases} \dfrac{c'}{v} \\ \dfrac{c''}{v} \end{cases} \tag{19}$$

and in a similar way the $\varkappa_D$-cones are given by

$$\cos\alpha = \frac{1}{\beta} \tag{19'}$$

Table I

j	(1)	(2)	(3)	(4)
1	$\frac{c_{44}}{\varrho}$	$(0, y, z)$, $(x, 0, z)$ $(x, y, 0)$[2]	$\frac{c_{11} - c_{12} + c_{44}}{3\,\varrho}$	$(\pm 1, \pm 1, \pm 1)$
2	$\frac{c_{44}}{\varrho}$	$(\pm 1, 0, 0)$, $0, \pm 1, 0)$ $(0, 0, \pm 1)$	$\frac{c_{11} - c_{12}}{2\,\varrho}$	$(\pm 1, \pm 1\ 0)$, $(\pm 1, 0, \pm 1)$ $(0, \pm 1, \pm 1)$
3	$\frac{c_{11} + 2\,c_{12} + 4\,c_{44}}{3\,\varrho}$	$(\pm 1, \pm 1, \pm 1)$	$\frac{c_{11}}{\varrho}$	$(\pm 1, 0; 0)$ $(0, \pm 1, 0)$ $(0, 0, \pm 1)$

$K < 1$: (1) gives $(c')^2$, (2) gives L', (3) gives $(c'')^2$ and (4) gives L''.
$K < 1$: (1) gives $(c'')^2$, (2) gives L'', (3) gives $(c')^2$ and (4) gives L'.

---

[1] See appendix.

[2] $(0, y, z)$ denotes a direction with vanishing x-component.

Table II. 10^5 cm/sec

	K	c_1'	c_1''	c_2'	c_2''	c_3'	c_3''
Ag[1]	1.8	1.2	2.0	1.5	2.0	3.3	3.8
Al[2]	1.2	2.8	3.3	3.0	3.3	6.3	6.6
Cu[2]	2.1	1.6	2.9	2.1	2.9	4.4	5.2
Na[1]	8.3	0.8	2.1	1.4	2.1	2.3	3.2
NaCl[2]	0.7	2.4	2.8	2.4	2.9	4.4	4.8
KCl[2]	0.4	1.8	2.6	1.8	2.9	3.7	4.6
LiF[3]	2.3	3.3	4.6	3.8	4.6	6.0	7.1

[1] R. F. S. HARMON, Rev. Mod. Phys., 18, 409 (1946).
[2] D. LAZARUS, Phys. Rev., 76, 545 (1949).
[3] H. B. HUNTINGTON, Phys. Rev., 72, 321 (1947).

Table II gives numerical values of K, c_j' and c_j'' for some crystals.

For the Laue interference conditions to be approximately fulfilled, it is necessary that $|\boldsymbol{k}| \gtrsim \pi/a$. For the η-cones to exist it is thus necessary that the neutron velocity is restricted within the interval

$$\frac{\pi\hbar}{m_0 a} \lesssim v < c_3'' \qquad m_0 = \text{neutron mass.}$$

Approximate numerical values of the boundaries for some crystals are given in Table III.[4]

Table III

	Lower boundary			Upper boundary		
	v 10^5 cm/sec	E 10^{-2} eV	λ 10^{-8} cm	v 10^5 cm/sec	E 10^{-2} eV	λ 10^{-8} cm
Ag	0.48	0.12	8.2	3.8	7.8	1.0
Al.	0.48	0.12	8.1	6.5	22.1	0.6
Cu	0.54	0.15	7.2	5.2	14.2	0.8
Na	0.45	0.11	8.6	3.2	5.5	1.2
NaCl	0.35	0.06	11.2	4.7	11.7	0.8
KCl	0.31	0.05	12.5	4.5	10.5	0.9
LiF	0.49	0.13	8.1	7.1	26.3	0.5

Conclusion (Anisotropic crystals)

For real crystals there are in every direction three sound velocities, the magnitude of which depends on the direction of the sound wave. The regions in which these velocities vary are given in Table I and II. It should be noted that the region of c_3 lies completely outside the overlapping regions of c_1 and

---

[4] $E = \frac{1}{2} m_0 v^2$; $\lambda = \frac{h}{m_0 v}$.

Table II suggests that in some respects many crystals may be considered s isotropic with rather good accuracy.

When the neutron velocity exceeds c_3'', the scattering cross section varies moothly with $\eta_\perp$. Ordinarily, the intensity decreases as $\eta_\perp$ increases in a cer- ain direction (see Figs. 1 and 2, cf. 11). For smaller neutron velocities, singular irections appear and for $c_2'' < v < c_3'$ there is one singular cone, outside of which he intensity abruptly decreases without vanishing. When $\pi \hbar / m_0 a \lesssim v < c_1'$, we et three singular cones, of which the two outer ordinarily lie rather close ogether. Thus Fig. 3 might in the anisotropic case give an idea of how the ntensity varies, with the modifications that the outer singularity is broadened nd the scattering angle varies when rotating around the direction $\boldsymbol{n}_0$.

In theorems (II)–(IV) we have given some results regarding the intensity nd the symmetry properties of the singular surfaces.

Ordinarily the singular cones are not circular, but we get an idea of their ppearance and widths by surrounding each cone with two circular cones, the pical angles of which are given by (19). In theorem (I) we get the conditions or a singular cone to touch one of its surrounding ones. In this case the rela- ion between the elastic constants of the crystal and the width of a singular one is given by (19).

Application to Al

In order to find the order of magnitude of the angles to be measured to etect the η-cones, we apply our results to Al. This crystal is a convenient one, artly because magnetic interaction, isotopic disorder and spin dependence can e neglected[1] and furthermore because the elastic anisotropy is negligible. We ave carried out the calculation for the following neutron velocities: $\lambda = 1.057$ Å nd $\lambda = 1.315$ Å, corresponding to $v = 3.698\ 10^5$ cm/sec and $v = 2.973\ 10^5$ cm/sec espectively.[1]

For $\lambda = 1.057$ Å, only one η-cone appears and the angle φ, determining this cone, aries in the very small interval $34^\circ.4 \leq \varphi \leq 36^\circ.2$. The angle δ (Fig. 1) varies ith $\eta_\parallel$ as follows:

$$\delta = 0.093\ \mu \lesssim 0.019\ \ (1^\circ.1), \quad \mu = \frac{\eta_\parallel}{\pi b} \lesssim \frac{1}{5}.$$

For $\lambda = 1.315$ Å there is one fully developed η-cone and one cone which is nly partly developed. The corresponding angles φ_3 and φ_2 vary in the inter- als: $27^\circ.0 \leq \varphi_3 \leq 28^\circ.3$, $66^\circ.5 \leq \varphi_2 \leq 90^\circ$; and δ_3, δ_2 have the values

$$\begin{aligned} &\delta_3 = 0.085\ \mu \lesssim 0.009\ \ (0^\circ.5) \\ &\delta_2 \geq 0.373\ \mu\ (\lesssim 0.037;\ 2^\circ.1) \end{aligned} \qquad \mu = \frac{\eta_\parallel}{\pi b} \lesssim \frac{1}{10}.$$

The author wishes to express his gratitude to Professor Ivar Waller for uggesting this investigation and for much good advice during the work.

Institute for Mechanics and Mathematical Physics, University of Uppsala, ppsala.

---

[1] C. G. Shull–E. O. Wollan, Phys. Rev. 81, 527 (1951).

Appendix

The eigen frequencies $\omega_{\varkappa j}$ are determined from the secular equation corresponding to the system (2). The expressions may be simplified by introducing a new variable u.

$$\varkappa^2 u = \left(\omega^2 - \frac{c_{44}}{\varrho}\varkappa^2\right)\frac{\varrho}{c_{11}-c_{44}}.$$

The secular equation transforms into

$$u^3 - u^2 + a(xyz)\,u - b(xyz) = 0 \tag{A}$$

where

$$\begin{aligned} a(xyz) &= (1-K^2)(x^2y^2+y^2z^2+z^2x^2) \\ b(xyz) &= (1-K)^2(1+2K)\,x^2y^2z^2. \end{aligned} \tag{B}$$

Let us consider $K>0$, which corresponds to $c_{11}>c_{44}$. The case $K=1$ has already been treated (isotropic case). The roots u_1, u_2, u_3 are ordered in magnitude, and the boundaries of each u_j may be determined. Because of the symmetry we may restrict ourselves to the case $(xyz)\geq 0$.

Supposing the Jacobian $\dfrac{d(a,b)}{d(x_i x_j)} \neq 0$ $(i \neq j)$, we may take (a,b) as independent parameters instead of (x_i, x_j), and all the Jacobians vanish simultaneously only for $x=y$, $y=z$ or $z=x$ (Fig. 5). The case when (xyz) lies on these exceptional curves (γ') will be treated separately.

When (xyz) runs over the whole unit sphere, (a,b) represented as a point in an (a,b) plane will vary in a domain which is bounded by a curve γ. γ corresponds to (xyz) values of the circles P_1P_2, P_2P_3, P_3P_1 and the circles

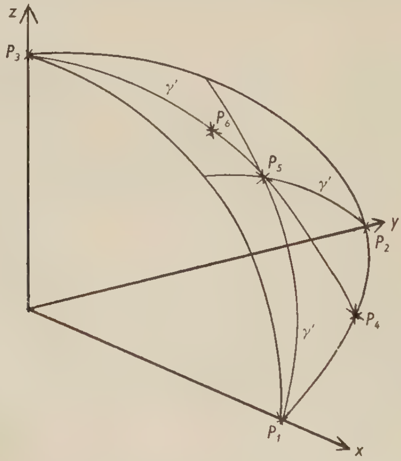

Fig. 5.

denoted by γ'. In this connection we note that because of the symmetry we need only solve (A) for (xyz) in the triangle $P_1 P_5 P_4$.

Considering (xyz) inside the triangle $P_1 P_5 P_4$ and choosing a, b as parameters, we can immediately show that in no points do the two derivatives of u_j, $\partial u_j / \partial a$ and $\partial u_j / \partial b$, vanish. As the derivatives of u_j with regard to a and b may not exist where (A) has double or triple roots, extreme values of u_j may occur in these points. We can however show that no triple roots exist, and the double roots are examined as follows. Denoting a double root by ξ, the equation (A) gives

$$\xi = \frac{1}{3} \pm \frac{1}{3}(1-3a)^{1/2}. \tag{C}$$

Then the following relation between a and b must exist

$$b = \frac{a}{3} - \frac{2}{27} \mp \frac{2}{27}(1-3a)^{1/2}. \tag{D}$$

The lower sign corresponds to ξ being the smallest root, the upper sign to ξ being the largest root. It will be seen from (C) that ξ takes its extreme values on the boundaries of a. We can also show, that the largest root never coincides with any of the other roots. Thus the extreme values must appear for a point (xyz) on γ' or $P_1 P_2$, $P_2 P_3$, $P_3 P_1$.

For (xyz) on $P_1 P_2$, $P_2 P_3$, $P_3 P_1$, the solutions of (A) have a simple analytical form. Because of the symmetry we need only consider the circle $P_1 P_2$, and then we have

$$\begin{aligned} u_1 &= 0 \\ u_2 &= \frac{1}{2} - \sqrt{\frac{1}{4} - (1-K^2)\,x^2 y^2} \qquad K<1 \\ u_3 &= \frac{1}{2} + \sqrt{\frac{1}{4} - (1-K^2)\,x^2 y^2}\,. \end{aligned}$$

For $K>1$ $u_1 \rightleftharpoons u_2$.

The extreme values of u_2 and u_3 are reached in the points $P_1\,(P_2)$ and P_4, and u_1 vanishes everywhere on the circle $P_1 P_2$.

Finally, let us examine the roots on γ'. We need only consider the curve $P_3 P_4$. Taking x as independent parameter, (B) becomes

$$\begin{aligned} a\,(xyz) &= (1-K^2)\,(2-3x^2)\,x^2 \\ b\,(xyz) &= (1-K)^2\,(1+2K)\,(1-2x^2)\,x^4. \end{aligned} \tag{B$'$}$$

We apply the same reasoning as before In the point defined by $x^2 = \dfrac{1+K}{3+5K}$ (P_6), the root $\dfrac{(1-K)(1+2K)}{3+5K}$ (u_2 for $K<1$, u_1 for $K>1$) is a real maximum $(K<1)$ or a real minimum $(K>1)$; the other roots are $\dfrac{1-K^2}{3+5K}$ and $\dfrac{1+4K+3K^2}{3+5K}$. In P_5

the root u_3 has a minimum $(K<1)$ or a maximum $(K>1)$. A rather lengthy but elementary calculation shows that at the point P_5 the two smallest roots coincide and that no other double roots exist.

We may now conclude that all extreme values are to be found at the points P_1, P_4, P_5 and P_6, and thus we need only choose the largest and the smallest root for each j at these points.

$\delta c_j(xyz)$ $(\omega = c(xyz)|\varkappa|)$ vanishes at all points where u_j has its extreme values, except for u_1 in the point P_5; here u_1 and u_2 have a peak.

Table IV gives the boundaries of u_j and the corresponding directions of $\varkappa$.

$K<1$

Table IV

	(1)	Dir.	(2)	Dir.
u_1	0	$(0, y, z)$ $(x, 0, z)$ $(x, y, 0)$	$\frac{1}{3}(1-K)$	$(1, 1, 1)$
u_2	0	$(1, 0, 0)$ $(0, 1, 0)$ $(0, 0, 1)$	$\frac{1}{2}(1-K)$	$(1, 1, 0)$ $(1, 0, 1)$ $(0, 1, 1)$
u_3	$\frac{1}{3}(1+2K)$	$(1, 1, 1)$	1	$(1, 0, 0)$ $(0, 1, 0)$ $(0, 0, 1)$

(1) and (2) are the lower and upper limits respectively. For $K>1$ the table above gives the result, if $u_1 \rightleftharpoons u_2$ and lower $\rightleftharpoons$ upper.

Tryckt den 4 december 1953

Uppsala 1953. Almqvist & Wiksells Boktryckeri AB

ARKIV FÖR FYSIK Band 7 nr 30

Communiqué le 9 Septembre 1953 par M. SIEGBAHN et E. HULTHÉN

Etude de la radioactivité de Sb_{51}^{125}

Par JEAN MOREAU

Avec 6 figures dans le texte

Introduction

La désintégration de Sb_{51}^{125} a déjà donné lieu à plusieurs études, les plus importantes faites avec l'emploi de spectromètres sont celles de K. SIEGBAHN et W. FORSLING [1] d'une part et B. KERN, A. MITCHELL et D. ZAFFARANO [2], d'autre part. Sb_{51}^{125} décroit avec une période de 2,7 ans par émission $\beta^- \gamma$, et donne naissance à Te_{52}^{125} ou à son état métastable de période 58 jours. Les résultats publiés par K. SIEGBAHN et B. KERN sont reportés dans le tableau I. Les résultats sont, en général en assez bon accord et les deux auteurs ont pu proposer un schéma uniquement prouvé par des considérations énergétiques.

Les prévisions de la théorie des couches pour les états quantiques de Sn_{50}^{125} (9,4 j.) Sb_{51}^{125} (2,7 a.) et Te_{52}^{125} (58 j.) sont respectivement $h_{11/2}$, $g_{7/2}$, $h_{11/2}$ [3]. Le spectre β^- (2.330 kev) de Sn_{50}^{125} a une forme et une valeur de log ft (8,9) correspondant à une transition de première interdiction et $\Delta I = 2$ oui [4]: cette transition est donc en accord avec les attributions de $h_{11/2}$, $g_{7/2}$. Le spectre β^- (616 kev) le plus énergique de Sb_{51}^{125} a une valeur log $ft = 9{,}4$ mais sa forme d'après les résultats publiés [1–2] ne correspondant pas à une transition $\Delta l = 1$, $\Delta I = 2$ oui, était en désaccord avec les prévisions $g_{7/2}$ $h_{11/2}$.

Tableau I

Auteur	Spectre β^- Energie en keV	Intensité	Rayonnement γ Energie en keV Identification $\begin{cases} ce^- & \text{conversion interne} \\ pe^- & \text{photoélectron} \end{cases}$
K. SIEGBAHN	616	18 %	35 (ce^-) – 110 (ce^-) – 175 (ce^- pe^-)
	299	49 %	425 (ce^- pe^-) – 465 (pe^-) – 601 (ce^- pe^-) 637 (pe^-)
	128	33 %	
B. KERN	621	33 %	110 (ce^-) – 125 (ce^-) – 174 (ce^- pe^-)
	288	66 %	431 (ce^- pe^-) – 466 (pe^-) – 609 (ce^- pe^-) 646 (pe^-)

Il était donc intéressant d'étudier la désintégration de Sb_{51}^{125} par une méthode de coïncidence pour prouver que le spectre de 616 kev aboutissait bien à Te_{52}^{125} (58 j.) et, d'autre part, pour voir si la forme de ce spectre n'était pas modifiée par la présence d'un autre spectre peu intense.

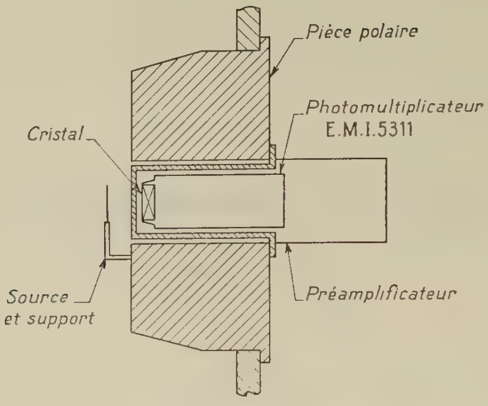

Figure 1. Disposition du photomultiplicateur.

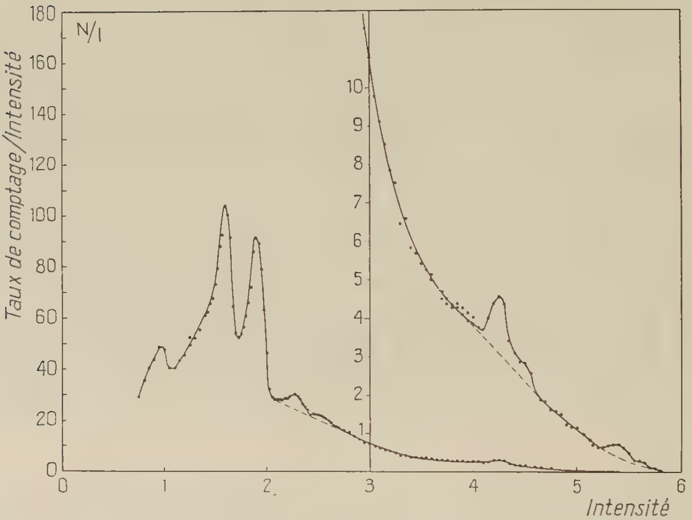

Figure 2. Spectre β^- de Sb_{51}^{125}.

Dispositif expérimental

Le spectromètre β à image intermédiaire de H. SLÄTIS et K. SIEGBAHN [5] a été utilisé pour l'étude du spectre β^- et des raies de conversion interne. Il a été utilisé également pour les coïncidences $\beta^- \gamma$ et $e^- \gamma$ avec une pièce polaire modifiée contenant un photomultiplicateur E.M.I. 5311 et un cristal de 1 Na (Tl) (figure 1): le photomultiplicateur était alors situé dans le cylindre de fer qui constitue un blindage magnétique; dans la position représentée, aucune perturbation dans son fonctionnement ne fut enregistrée, le champ magnétique à l'intérieur du cylindre était, pour l'énergie maximum focalisée dans le spectromètre, donc très faible sur l'ensemble des dynodes.

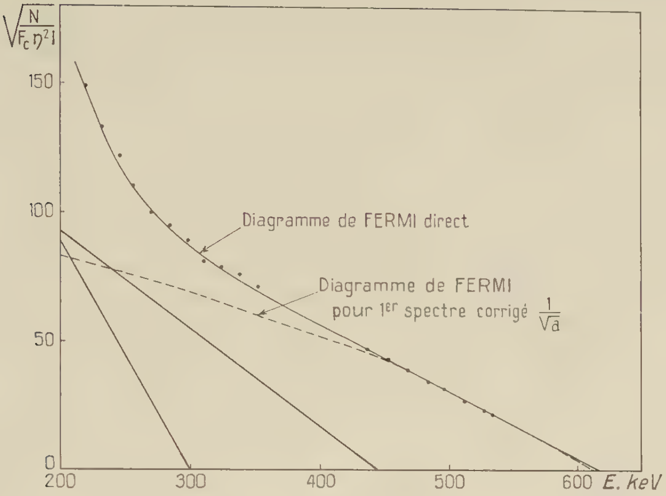

Figure 3. Diagramme de Ferni.

Le circuit à coïncidence [6] utilisé était un système symétrique prévu pour l'étude des coïncidences d'impulsions provenant de deux compteurs à scintillations; dans le cas présent, le compteur G.M. était connecté à l'une des entrées, le temps de résolution était $0{,}5 \cdot 10^{-6}$ sec. Il fut possible, avec ce dispositif de compter les coïncidences entre particules β ou e^- et les rayons γ détectés au compteur à scintillations après sélection ou discrimination.

Spectre β

La figure 2 donne le spectre continu β d'une source de Sb_{51}^{125} préparée suivant la méthode décrite par W. Forsling, les deux raies intenses appartiennent à Te_{52}^{125} provenant de la désintégration de Sb_{51}^{125} (ce tellure n'ayant pas été chimiquement séparé); ce spectre est identique à celui publié par B. Kern, Mitchell et Zaffarano. Les énergies des rayons γ obtenus à partir des raies de conversion interne sont en accord avec les valeurs connues, un diagramme de Fermi (figure 3) a été calculé, les valeurs utilisées de la fonction de Fermi sont celles publiées par le National Bureau of Standards.

Spectre γ

Un spectre γ (figure 4) a été obtenu à l'aide du compteur à scintillations utilisé pour les expériences en coïncidence: un premier pic correspond au γ de 175 kev, le suivant aux deux rayons γ non séparés d'énergie 425 465 kev et le dernier au groupe de deux rayons γ également non séparés d'énergie 601–637 kev; les valeurs des énergies des rayons γ n'ont pas été déterminées à nouveau, ce sont celles de K. Siegbahn.

Coïncidences β–γ

1°. Les coïncidences entre particules β et l'ensemble du rayonnement γ (seuil de discrimination pratiquement nul) ont été étudiées. Un diagramme de Fermi des spectres en coïncidence est représenté (figure 5).

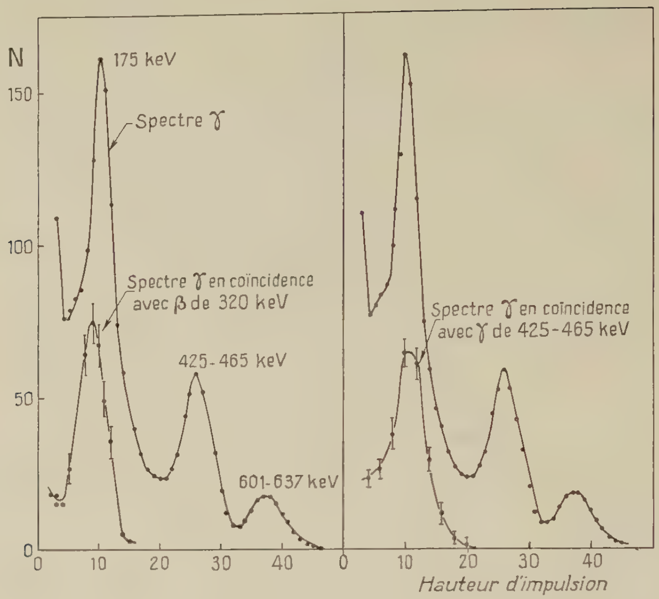

Figure 4. Spectre γ.

2°. Les coïncidences entre particules β et les rayons γ d'énergie supérieure à 175 kev ont été étudiées. Un diagramme de Fermi des spectres en coïncidence est représenté (figure 5).

3°. Les coïncidences entre particules β et le rayon γ de 175 kev ont été également étudiées; un diagramme de Fermi du spectre obtenu en coïncidence est représenté (figure 4).

4°. Les coïncidences entre les rayons γ et les particules β d'énergie 320 kev ont été étudiées, le spectre de rayonnement γ en coïncidence est représenté (figure 4).

5°. Les coïncidences entre particules β et les rayons γ d'énergie supérieure à 465 kev ont été étudiées mais les très faibles taux de comptage obtenus n'ont pas permis d'obtenir un diagramme de Fermi des spectres en coïncidence.

D'après l'examen des droites de Fermi nous pouvons conclure:

a. Le spectre connu d'énergie maximum 616 kev conduit à l'état fondamental ou métastable du tellure puisqu'il n'apparait pas en coïncidence avec le rayonnement γ.

b. Un nouveau spectre d'énergie maximum 444 ± 6 kev a été mis en évidence. Il est en coïncidence avec les γ de 175 kev (figure 3).

c. Le spectre connu d'énergie maximum 300 kev est en coïncidence avec au moins un des rayons γ d'énergie 425–465 kev.

d. Le spectre à basse énergie (environ 125 kev) est en coïncidence avec au moins un des rayons γ d'énergie 601–637 kev.

Coïncidences γγ

Les coïncidences entre les différents rayons γ ont été recherchées en employant 2 compteurs à scintillations (cristaux INa (Tl) et tubes E.M.I. 5311) associés au même circuit électronique que ci-dessus.

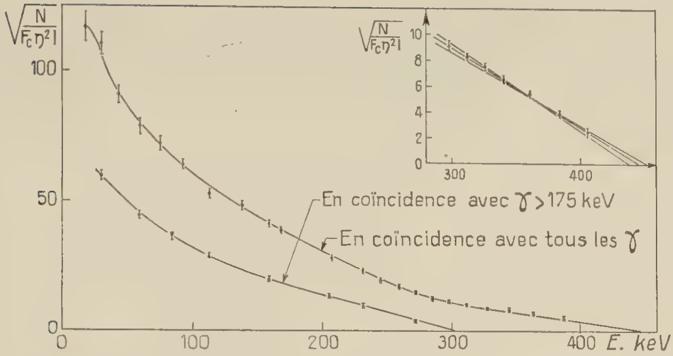

Figure 5. Diagramme de Fermi de spectres en coïncidence.

Des coïncidences ont été trouvées entre les rayons γ d'énergie 425 465 kev et des rayons γ d'énergie 175 kev (fig. 4).

Coïncidences $e^-\gamma$

1°. Les coïncidences entre les électrons de conversion interne du rayon γ d'énergie 175 kev et l'ensemble des rayons γ ont été recherchées, seule une très faible fraction de la raie de conversion interne peut être en coïncidence avec l'ensemble des rayons γ.

2°. Les coïncidences entre les électrons de conversion interne du rayon γ d'énergie 425 kev et l'ensemble des rayons γ ont été recherchées, seule également, une faible fraction de la raie de conversion interne peut être en coïncidence avec l'ensemble des rayons γ.

Résultats – Schéma de désintégration

La forme du diagramme de Fermi du spectre le plus énergique obtenu directement, qu'on ne peut étudier qu'entre 440 et 616 kev, ne permet pas de conclure s'il s'agit d'une transition ($\Delta l = 1$, $\Delta I = 2$ oui). Dans une aussi faible étendue en énergie, il n'est pas possible avec le pouvoir séparateur utilisé de mettre en évidence la courbure caractéristique du diagramme de Fermi d'une telle transition interdite, mais les mesures de coïncidences indiquent l'existence du second spectre et son intensité relative est connue, car l'efficacité totale du compteur à scintillations a été déterminée avec le γ de As_{33}^{71} [7] d'énergie très voisine de 175 kev.

Une nouvelle décomposition du spectre direct peut être faite en retranchant le nouveau spectre et l'on obtient alors pour le spectre énergique la forme interdite caractéristique dont le diagramme de Fermi peut être rendu linéaire en appliquant le coefficient de correction $a = W^2 - 1 + (W_0 - W)^2$.

Cette nouvelle décomposition donne 4 spectres dont les énergies limites, les intensités et log ft sont reportés dans le tableau II.

L'énergie limite et l'intensité du quatrième spectre sont des valeurs assez imprécises car la présence des raies du tellure et la diffusion due à l'épaisseur de la source ne permettent qu'une très mauvaise décomposition vers cette énergie.

Il est nécessaire, pour proposer un schéma de désintégration en accord avec les mesures antérieures sur Te_{52}^{125} et ces dernières mesures, d'admettre l'existence de

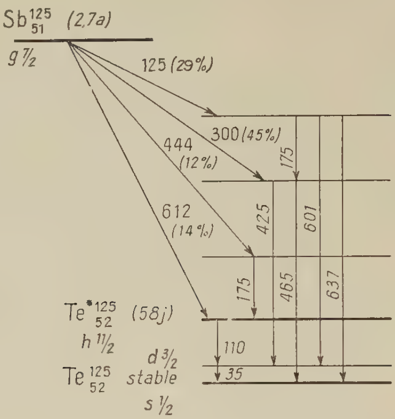

Figure 6. Schéma de désintégration proposé.

Tableau II

	Energie limite	Intensité	log *ft* [8]
Premier spectre	612	14 %	9,4
Deuxième spectre	444	12 %	9,1
Troisième spectre	300	45 %	7,8
Quatrième spectre	125	29 %	6,9

deux rayons γ d'énergie voisine de 175 kev. En effet, nous avons trouvé que le rayon γ de 175 kev était en coïncidence avec le deuxième spectre β. Nous avons trouvé aussi que ce rayon γ était en coïncidence avec le groupe de rayons γ de 425 -465 kev, ces derniers rayons γ étant en coïncidence avec le troisième spectre: s'il n'y avait qu'un seul rayon γ de 175 kev, le premier et le troisième spectre ne pourraient appartenir au même isotope tous les deux, ce qui est très improbable; cependant, il n'a pas été possible de séparer les deux rayons γ par leurs raies K de conversion interne; si l'on conserve donc l'hypothèse de l'existence de deux rayons γ il faut aussi admettre qu'ils sont d'énergie très voisine (2 à 3 kev de différence).

Le schéma proposé (figure 6) tient compte de cette hypothèse, une comparaison entre les taux de comptage en coïncidence βγ et γγ permet aussi d'établir que le rayon en coïncidence avec le groupe 425–465 kev est assez peu intense.

Conclusion

La nouvelle décomposition du spectre total de Sb_{51}^{125} conduit donc pour le premier spectre en accord avec sa valeur de log *ft* à une forme de première interdiction $\Delta I = 2$ oui, ce qui confirme les états $g_{7/2}$ de Sb_{51}^{125} et $h_{11/2}$ de Te^{*125}_{52}. Le second spectre, pour lequel log *ft* est également élevé, n'a pu être étudié du point de vue de la forme, les troisième et quatrième spectres pourraient, d'après leur valeur de log *ft*, être considérés comme interdits du premier ordre.

Ce travail a été effectué au Nobel Institutet för Fysik; je remercie vivement le rofesseur Manne Siegbahn qui m'a assuré dans cet Institut des possibilités de ravail excellentes, je remercie également le Professeur Kai Siegbahn qui m'a irigé au cours de ce travail et M. Björn Åström, Ingénieur électronicien, pour ses onseils continus.

REFERENCES

. Kai Siegbahn et Wilhelm Forsling — Ark. för Fys. B 1 nr 24, p. 505 (1949).
. B. Kern, A. Mitchell et D. Zaffarano — Phys. Rev. *76*, 94 (1949).
. M. Goldhaber et R. D. Hill — Rev. Mod. Phys. *24*, n° 3, p. 179 (1952).
. C. M. Nelson, G. E. Boyd et B. H. Ketelle — Oakridge National Laboratory O.R.N.L. 828 (1951).
. H. Slätis, K. Siegbahn — Arkiv för Fysik h. 4, p. 339 (1949).
. B. Åström — à paraître.
. A paraître.
. Moskowski — Phys. Rev. *82*, p. 35 (1951).

Tryckt den 3 december 1953

Uppsala 1953. Almqvist & Wiksells Boktryckeri AB

ARKIV FÖR FYSIK Band 7 nr 31

Communicated 14 October 1953 by Bengt Edlén

Point corona against a plane covered by an insulating film

By C. H. Hertz

With 1 figure in the text

If in a point-plane corona arrangement the plane is covered by a thin insulating film, for example a thin lacquer layer, the corona current in air has been found to be much higher than without such a film. The current-voltage characteristics of a

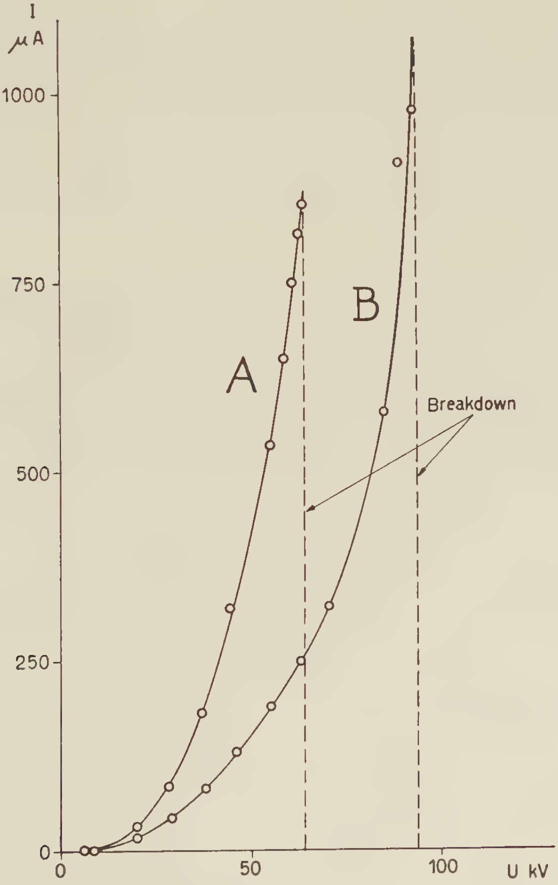

Fig. 1. Corona current vs. gap voltage. In curve A the plane was covered by a thin film of shellac, curve B was without shellac.

negative point-plane corona in air at 760 mm Hg are shown in fig. 1, the point-plane distance being 7.5 cm. With smaller point-plane distances (ca. 5 mm) the difference in corona current is much more marked. As can be seen from fig. 1 the breakdown voltage using a lacquer covered plane is much lower than without such a layer. Similar behaviour was observed when the point was replaced by a highly polished brass sphere 38 mm in diameter, but the breakdown voltage differed in the two cases only if a corona current could be observed before the breakdown occurred.

This somewhat unexpected behaviour is due to the presence of very small holes in the lacquer layers. In the case of a negative corona the insulating lacquer layer around the minute holes is charged by the negative ions coming from the point. Thereby a region of high electric field intensity is created in the holes where the bearers of negative charge coming from the point are able to ionize the gas. The positive ions thereby created in the holes are attracted to the point where they increase the electron emission from the point by ion impact. They also decrease the negative space charge between the point and the plate which probably also has an effect on the corona current. The holes in the lacquer layer can be seen glowing in darkness, therefore this method can be used for testing lacquer layers etc. for holes. The explanation given for the effect described above can be tested for example in the following way. Common writing paper and some plastic films will stop the corona current entirely if placed on the plane of the point-plane arrangement if they do not possess any holes. If some holes are made in these materials by perforating them with a thin needle a corona current can be observed again and a glow be seen in each hole. Under certain circumstances the presence of electronegative gases may change the results appreciably.

Even for positive corona points the current has been found to be larger if the cathode plane is covered by an insulating film, but the difference in breakdown voltage is not so large. The effect can also be found using AC at the point.

Trichel pulses have also been observed with a negative corona, the frequency of which was slightly larger than those found without lacquer layers (and independent of the kind of layer used). In contrast to the usual Trichel pulses the frequency was much more constant. This result is in agreement with the theory for the Trichel pulse mechanism given by LOEB (1) if the explanation of the effect described in this paper is accepted.

Because of the corona current and breakdown characteristics of the effect described it might be of importance in high voltage engineering.

Physics Department, University of Lund, Sweden. August 13, 1953.

REFERENCE

1. LOEB, Journ. Appl. Ph. *19*, 882 (1948).

Tryckt den 19 januari 1954

Uppsala 1954. Almqvist & Wiksells Boktryckeri AB

ARKIV FÖR FYSIK Band 7 nr 32

Communicated 3 June 1953 by LISE MEITNER

On the radioactivity of Rb^{87}

By J. FLINTA and S. EKLUND

With 8 figures in the text

Summary

The radioactive radiation from Rb^{87} has been investigated, and the maximum energy of the β-spectrum found to be 250 ± 25 keV, by means of absorption in aluminium. The absorption curve shows an excess of low-energy β-particles, in agreement with the assumption that the β-decay is triply forbidden. No γ or X radiations were found.

The mean value found for the total β-radiation from rubidium was 42.2 ± 0.7 β-decays/min/mg Rb, corresponding to a half-life of $(6.1 \pm 0.2) \cdot 10^{10}$ years for Rb^{87}.

I. Intensity of radiation as a function of source thickness

The GM counter (Fig. 1) used for the measurements was the same as that used in a previous investigation (EKLUND [1]). The cathode of the counter was made of wire gauze, and the source could be placed in the volume occupied by the filling gas (90 torr H_2 + 10 torr C_2H_5OH). Sources of 0.11–2.05 mg RbCl/cm² evaporated onto thin (about 0.9 mg/cm²) zapon films were used. The results of the measurements

Table 1. Source area 22.56 cm².

Weight mg RbCl/cm²	Intensity pulses/min/mg Rb	Origin of source material
0.11	1.99 ± 0.07	E. Merk
0.174	1.95 ± 0.04	Johnson & Matthey (spectroscopic standard)
0.267	1.88 ± 0.04	E. Merk
0.394	1.80 ± 0.03	Mackay
0.495	1.74 ± 0.03	New Metal
0.683	1.67 ± 0.03	British Drug House
0.863	1.64 ± 0.02	,,
0.955	1.58 ± 0.02	New Metal
1.13	1.53 ± 0.014	,,
1.42	1.486 ± 0.014	,,
2.05	1.391 ± 0.009	,,

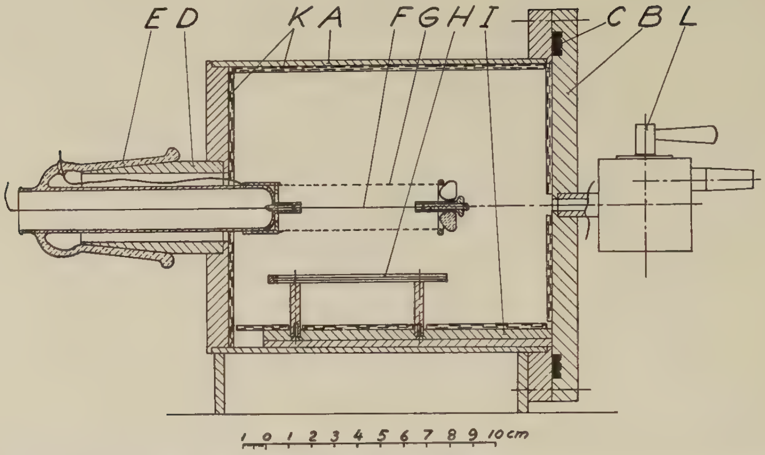

Fig. 1. The brass tube A with the cover B and rubber gasket C serves as a vacuum-tight vessel for the GM filling gas. D is a brass cone for vacuum-tight connection to the glass joint E, through which the electric connections are made, and which carries the anode wire F and the gauze cathode G, which is at negative potential with respect to the tube A. The sample table H may be withdrawn by the slide I, in order to change the sample. To reduce the reflexion as much as possible from the inside of the walls there is a lining K of polystyrene. The brass tap L is for evacuating and filling the GM-vessel with the gas mixture 10 torr C_2H_5OH and 90 torr H_2.

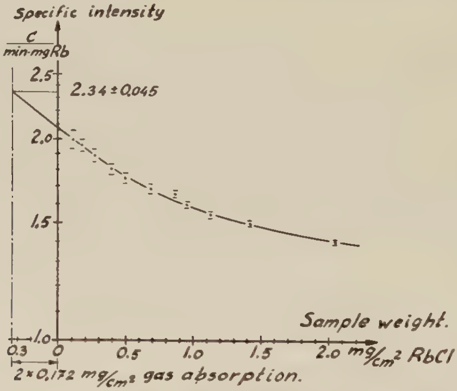

Fig. 2. The specific intensity of the radiation from samples of RbCl. The $H_2 + 10\,\%\ C_2H_5OH$ counter gas in the space between the GM gauze cathode and the sample amounts to 0.135 mg/cm², equivalent to 0.172 mg RbCl/cm². Twice this value has been taken when extrapolating to zero gas absorption (see Aten [2], Feather [3] and Bleuler & Zünti [4]).

are given in Table 1 and Fig. 2. The effective solid angle ω subtended at the source by the GM counter has been measured by several different methods, as shown in Table 2.

Measurements were made with the counter gas enclosure lined with different materials, in order to evaluate a correction factor for particles scattered from the walls. Similar measurements were made with various thicknesses of the zapon support. These corrections gave together a factor of −3.5%. By extrapolation to

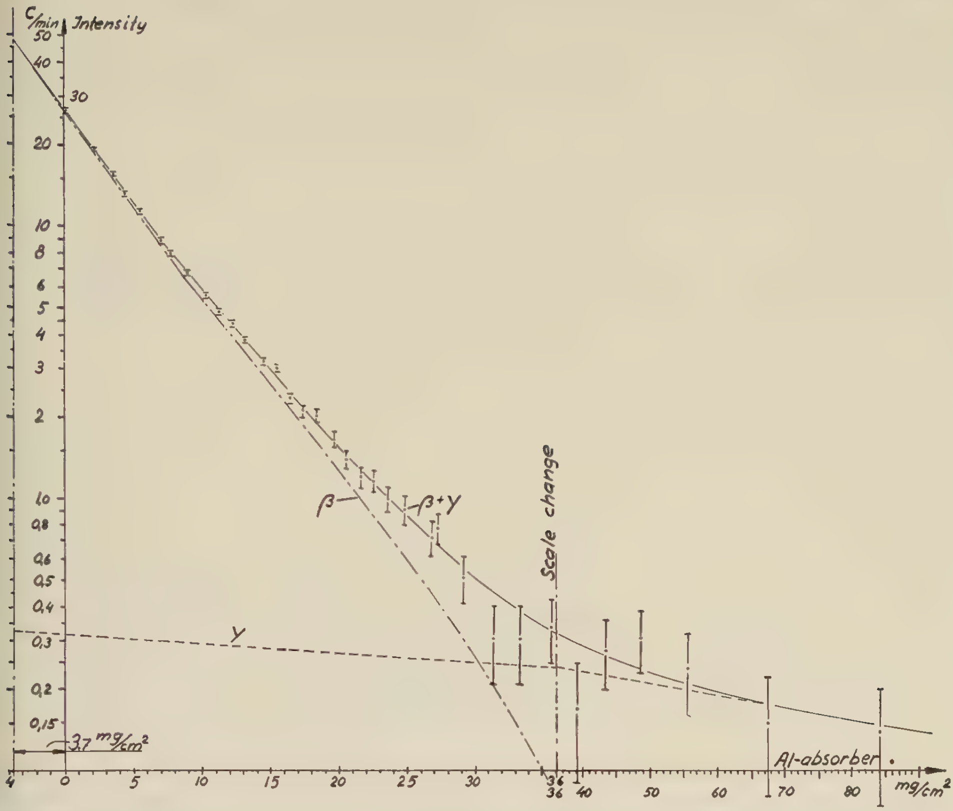

Fig. 3. Absorption of the radiation from Rb^{87} in Al. Sample: 2.05 mg RbCl/cm² mounted on a 0.9 mg/cm² zapon film. The slope of the Y curve is taken from Fig. 4.

Table 2.

Method	Percentage of 4π
α-particles from Po	5.6 ± 0.2
α from U	5.4 ± 0.3
α+β from U	5.8 ± 0.6
α+β ,, ...	5.4 ± 0.2
β from RaD+E	5.5 ± 0.4
Measurements with Rb source in ordinary position, and inside sensitive volume of GM counter	5.4 ± 0.3
The same, for another Rb source . .	5.4 ± 0.3
Graphical calculation	5.1 ± 0.8
Mean value	5.45 ± 0.07

ource thickness 0 mg/cm² and to absorber thickness (the gas) 0 mg/cm² (Fig. 2), ve find the counting rate 2.34 ± 0.045 pulses/min/mg Rb/ω. Making corrections

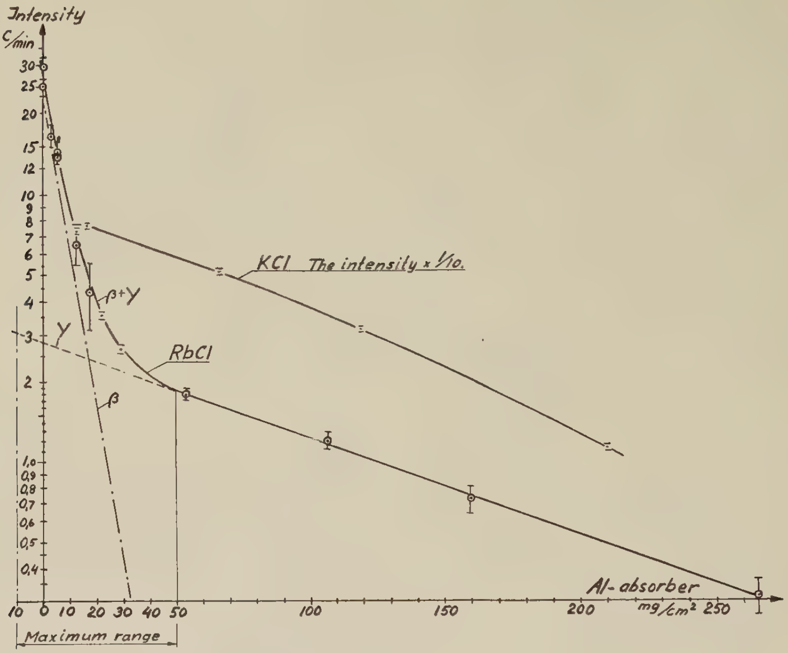

Fig. 4. Absorption of the radiation from Rb^{87} and K^{40} in Al. Sample: 250 mg RbCl/cm² on the backing 6.6 mg Al/cm². Sample: 290 mg KCl/cm² on the backing 6.6 mg Al/cm².

for gas absorption and scattering from the walls and the support, the total decay rate into solid angle 4π is 41.4 ± 1.2 β-pulses/min/mg Rb. The measurements described in the following sections were made to investigate whether these pulses are due only to β-radiation from Rb^{87} or whether there is also any contribution due to X-rays or Auger electrons.

II. Absorption measurements

a. Investigation of the whole spectrum

A GM counter of the bell type with a 1.7 mg/cm² mica window was used. Aluminium foils were used as absorbers. The measurement was first made with a source of 2.05 mg/cm² RbCl evaporated onto a zapon film (Fig. 3), and then with 250 mg/cm² of powdered RbCl in a 6.6 mg/cm² aluminium container (Fig. 4). The distances between the sources and the mica window corresponded to 1.0 mg/cm² and 1.9 mg/cm² of air respectively. From Fig. 4 the range of the rubidium β-radiation is clearly of the order of 60 mg/cm², and we also deduce that there is a much more penetrating component, having an absorption half-thickness of 83 ± 7 mg/cm² Al, corresponding either to a 15.0 ± 1.3 keV X-ray, or to a 1.5 ± 0.2 MeV β-ray, using the data of GLENDENIN [5] and KATZ *et al.* [6].

A source of 290 mg/cm² KCl was investigated in the same apparatus. The aluminium absorption curve is shown in Fig. 4. The similarity between this curve and

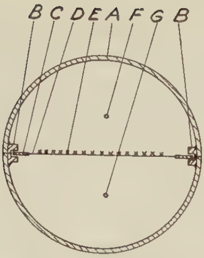

ig. 5. Schematic drawing of double GM counter (see Fig. 6 for details). The cathode A is made two halves and is fitted with insulated end plugs at both ends. B are track guides for the sample slide C. D sample backing. E sample. F and G are anode wires.

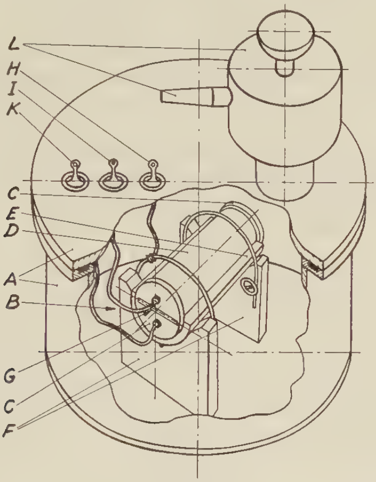

ig. 6. The vacuum vessel A (made for other experiments) encloses the GM-tube B. The inner iameter of the cathode is 31.0 mm, and the sensitive length 55 mm, between the inner surfaces f the polystyrene end-plugs C which fix the two anode wires. The cathode half-cylinders D nd E (in this case brass with wall thickness 2 mm and graphite of thickness 10 mm respectvely) are exchangeable, and are held in place on polystyrene holders F with brass straps. The ample frame is guided in tracks in the cathode walls where the two half-cylinders meet. The ample is introduced through the slit G in one of the end plugs. The cathode and the two anode ires are connected to the Stupakoff lead-throughs H, I, and K, all with screened cables. L is a rass tap for evacuating and filling the vessel with the gas mixture, in this case 10 torr C_2H_5OH and 90 torr Ar.

he one representing the penetrating component shows that this latter consists in he main of 1.35 MeV β-radiation from K^{40} impurity in the rubidium chloride due o the fact that Rb is very similar chemically to K. The intensity of 0.67% (see elow) corresponds to 3.4% of KCl by weight in the RbCl-source. A spectral analysis f the RbCl-source showed 2.5 to 4.5% K in the RbCl.[1]

Measurements on a spectroscopically pure sample of 270 mg/cm² RbCl from JOHN- ON & MATTHEY showed a counting rate due to the K^{40} β-radiation and possibly -radiation of only 0.07 ± 0.09 pulses/min, when the Rb β-radiation was eliminated

---

[1] Carried out by G. TYDÉN, AB Atomenergi, Department of Chemistry.

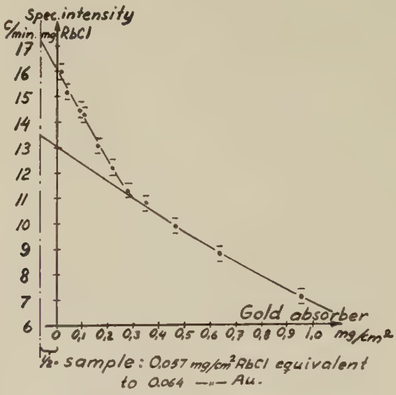

Fig. 7. The absorption in Au of the radiation from Rb^{87}. Sample: 0.114 mg RbCl/cm², equivalent in absorption to 0.128 mg Au/cm².

by an aluminium absorber of 66 mg/cm². The many differing results in the literature (see for example FAZZINI & FRANCHETTI [7]) for measurements on the radioactive radiations from Rb would thus seem to be at least partly due to potassium contamination.

In Fig. 3 the absorption curve for the K^{40} radiation marked Y has been drawn (the dashed line). This curve was constructed using the absorption half-thickness of the K^{40} radiation and the range of the Rb β-radiation, from Fig. 4. By extrapolation to zero absorber thickness we find a counting rate of 0.32 pulses/min, or 0.67% of the total β-intensity, which latter is taken to be the difference between the total intensity and the K^{40} radiation, and is shown as the dot-dash curve. For absorber thicknesses less than 8 mg/cm² the curve has a steeper slope, indicating an excess of low-energy β-particles. This energy distribution makes it impossible to make an accurate comparison between the Rb^{87} β-radiation and another β-active source of about the same maximum energy and a known intensity. For the same reason a Feather analysis [5] of the whole curve gives an uncertain result. Using only the part of the curve corresponding to absorber thicknesses greater than 8 mg/cm² Al a Feather analysis gives the value 55 ± 6 mg/cm² for the range, a more accurate value than that given above, which was obtained directly by inspection from Fig. 4. This value is equivalent to a maximum energy of 250 ± 25 KeV using Glendenin's range-energy relation. With the n-th power method given by KATZ and PENFOLD we find 248 KeV.

b. Investigation of the low-energy component

In order to investigate the low-energy part of the absorption curve, measurements were made with a double GM counter (see Figs. 5 and 6, and section III a below), gold absorbing layers being evaporated onto the sources. Two sources were used, of 0.114 and 0.071 mg/cm² RbCl, both on 6.65 mg/cm² aluminium foils. The absorption measurements were made in the brass half of the double counter. The reflection coefficient of a thick aluminium support for electrons and β-particles has been taken as 15%, using the results of EKLUND [1] and YANKWICH [8]. The reflection coefficient for a 6.65 mg/cm² support and the β-energy in question here was estimated to be about 14%. An aluminium support was used because a zapon film would not withstand the repeated evaporations. For the 0.114 mg/cm² RbCl source, the absorber thickness was increased in steps up to 0.952 mg/cm² Au, with the results shown in Fig. 7. With the other source only two points were taken, as a check. The other half of the GM counter was used as a background monitor.

The absorption curve shows a soft component with range 0.34 mg/cm² Au, corresponding to a 12 keV β-ray, according to GLENDENIN [5], or to an X-ray of about 1 keV (see COMPTON and ALLISON [9]). The intensity of this very soft component, as found by extrapolating the curve of Fig. 7 to zero absorber thickness, is (17.2–13.6) : 17.2 = 21% of the total intensity.

c. Investigation of the γ-radiation

An unsuccessful attempt was made to detect a γ-radiation. For this investigation a source of 1.55 g/cm² RbCl in an aluminium container of wall thickness 0.053 g/cm² Al was used. The β-radiation and any soft X-radiation which might be present (see section II a) was entirely eliminated by a copper absorber of 0.890 g/cm². Measurements were made with a gold radiator (0.046 g/cm² Au) between the source container and the mica window of the GM counter, and with an aluminium absorber (0.053 mg/cm² Al) in the same position. The results of the measurements are collected in Table 3.

Table 3.

Sample	Absorber	Counts/min.	Increase
Without sample	Without absorber	8.36 ± 0.02 } 8.37	
,, ,,	Absorber 0.890 g Cu/cm²	8.38 ± 0.02	
With sample 1.55 g RbCl/cm²	,, ,, ,, + 0.053 g Al/cm²	8.39 ± 0.034	0.02 ± 0.05
With sample 1.55 g RbCl/cm²	Absorber 0.890 g Cu/cm² + 0.046 g Au/cm²	8.30 ± 0.027	− 0.07 ± 0.05

The lower limit of the sensitivity of this method is about 100 keV and the measurements show that if there are any γ:s at all their number must be small.

d. Investigation of influence of chemical structure

An exploratory aluminium absorption measurement was made with a source consisting of 210 mg/cm² RbF, using the same apparatus as that described in section II above. The absorption curve agreed with that of Fig. 4, i.e. some potassium contamination was present here too.

e. Investigation of X-radiation

According to SIEGBAHN [10 (p. 467)] the absorption energies for the K and L electron shells of the decay product Sr are 16.1 and 2.19 keV respectively, so that we might expect 13.9 keV X-rays and 11.7 keV Auger electrons. As was stated in section II b above, Fig. 7 may be interpreted as showing the presence of a soft electron radiation making up 21% of the total radiation. If this soft component consists of Auger electrons, some 60% of the primary X-radiation should not be converted to Auger electrons (MASSEY [11]), and should therefore be detectable.

Selective X-ray measurements were performed by means of absorption measurements in solids and gases.

1. Solids

Pt, Au, Br and Se absorb this X-radiation strongly, while Sr does not. Absorption measurements with this method gave, however, no accurate result because of the high background of the K^{40} radiation.

2. Gases

A GM-counter filled with Ar is, for the X-rays in question, about 150 times more sensitive than one filled with H_2 (cf the method used by GRAF [12]). The spectroscopically pure sample used in section II a above gave less than 0.07 pulses/min in the Ar-filled counter which should register about 4.8% of the incoming X-rays. If most of those pulses came from X-rays we get 0.5% of the β-radiation as an upper limit for the primary X-radiation.

III. Investigation of the low-energy β or e^-

a. Reflection from the inner walls of the GM counter

In their coincidence measurements with a double GM counter, HAXEL and HOUTERMAN [13] claimed to have detected a very low-energy β-particle or electron. These coincidences could, however, also be due to β-particles reflected from the inner walls of the counter, passing back through the thin source mounting into the other half of the counter. In order to investigate this scattering from the walls, the double GM counter with exchangeable counter halves mentioned in II b above was used (see Figs. 5 and 6). The halves of the counter were made of brass and graphite, having the same inner diameter and the same wall density in weight per cm². The back scattering coefficient of 100–300 keV electrons from graphite has been given as 5–6% (EKLUND and YANKWICH). For copper, the same authors give 23–30%. The coincidence rate for the two halves was measured, and also their individual counting rates. The measurements were made with three sources, marked 1, 2 and 3 of 0.059, 0.120 and 0.250 mg/cm² RbCl respectively, mounted on zapon films of 0.875, 0.80 and 0.95 mg/cm² respectively. The sources were covered by evaporated gold absorber layers of thicknesses 0.102, 0.11 and 0.14 mg/cm² respectively. The proportion of back-scattered electrons found in the measurements will be lower than the values for the coefficient given above, since about half of the scattered electrons will strike the walls a second time, instead of passing back through the source. Some will also be absorbed in the filling gas. On the other hand, a low-energy electron in coincidence with the β-radiation would increase the value. From the results collected in Table 4 we find, assuming no such low-energy electrons, a back-scattering coefficient in this geometry of (16.1 ± 3.2)% for brass, and (2.4 ± 1.0)% for graphite. In calculating these values allowance was made for absorption in the source and source mounting.

The measurements show that there is without doubt a back-scattering effect which depends on the wall material, although they alone are not sufficiently precise to exclude definitely the existence of HAXEL and HOUTERMAN's low energy electrons.

Table 4. Intensity (pulses/min) measurements in a double GM counter, the two halves having exchangeable wall materials (graphite and brass). C indicates a graphite section, B a brass section, S the source side, U the side under the source, and K coincidences. The background has been subtracted. C/B means that the measurement was made with the graphite half opposite the source, and the brass side opposite the backing.

Source	1			2			3		
Arrangement	Measurement								
	S	U	K	S	U	K	S	U	K
C/C	25.7 ± 0.5	10.0 ± 0.5	0.5 ± 0.3	48.4 ± 0.4	18.7 ± 0.7	1.1 ± 0.3			
C/B	27.5 ± 0.4	10.4 ± 0.7	2.2 ± 0.3	54.0 ± 1.6	23.6 ± 1.2	3.0 ± 1.1	24.5 ± 0.3	5.4 ± 0.7	0.2 ± 0.3
B/C	25.5 ± 0.7	12.6 ± 0.3	2.6 ± 0.3	51.1 ± 0.7	26.1 ± 0.4	4.2 ± 0.6	23.8 ± 0.8	8.0 ± 0.3	2.2 ± 0.5
B/B	26.9 ± 1.3	16.6 ± 1.3	4.8 ± 1.0	58.6 ± 1.5	31.7 ± 1.3	7.1 ± 1.8			

b. No auger electrons

As was mentioned in Section II e, we find no X-radiation with energy in the region of 14 keV, and thus no Auger electrons can be emitted.

c. Conversion electrons

The absence of 14 keV X-radiation does not exclude the possibility that there may be 12 keV electron emission, as discussed above in section II b, since there might be total conversion in the L-shell. This would result mainly in the fluorescent radiation (L–M) = 1.8 keV. An attempt was made to detect this radiation by selective absorption in the filling gas of the GM counter. From COMPTON and ALLISON one may estimate that 82% of radiation of this kind is absorbed in an argon-filled counter of the type used, while only 4.7% is absorbed in a hydrogen filling. The source (2.83 mg/cm² RbCl spread over an area of 7 cm²) was mounted inside the sensitive volume of the counter, because of the short range of the radiation. If 21% of the β-decays (see Fig. 7) are followed by fluorescence radiation from conversion electrons, one may estimate that there will be about 22 X-rays pulses + 240 β-pulses per minute with argon as counter gas, and 1.5 X-ray + 240 β-pulses per minute with hydrogen. The results of the measurements are shown in Fig. 8. Since the design of the GM counter used was not suitable for the relatively high voltage required by the H_2 filling, the full plateau characteristic of the counter was taken in both cases. The measurement gives no reason to believe that there is any 1.8 keV fluorescence radiation.

Conclusion

Since the attempts to detect an X-radiation were not successful, the soft radiation of energy 12 keV which is evident from Fig. 7 must belong to the β-spectrum. The

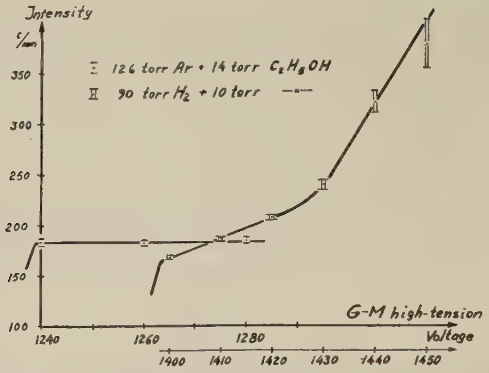

Fig. 8. The characteristics of the GM-bell-counter for two different filling gases. Sample: 2.83 mg RbCl/cm² spread over 7 cm², inside the counter window.

transition from Rb^{87}, with spin p 3/2, to the ground state of Sr^{87}, with spin g 9/2, corresponds to a spin change of 3 with change of parity, i.e. to a triply forbidden transition [14]. This is consistent with the observed shift in the maximum of the β-spectrum towards low energies [7, 20 and 23]. The absorption curve of Fig. 7 should therefore be extrapolated to zero absorber and source thickness (half the source thickness, see Fig. 2), which gives, for the β-intensity into solid angle 2π, the value 17.2 ± 0.2 pulses/min/mg RbCl. Correcting for reflection, we find that the total radiation intensity from natural Rb is 42.6 ± 0.8 β/min/mg Rb. Using the result of section I, 41.4 ± 1.2 β/min/mg Rb, the weighted mean is 42.2 β/min/mg Rb, with an estimated error of 2%. Assuming that natural Rb contains 27.5 ± 0.2% of Rb^{87} (taking the mean of the results given in references [15], [16], and [17] and corrected for the potassium radiation, the half life of Rb^{87} is

$$T = (6.1 \pm 0.2) \cdot 10^{10} \text{ years.}$$

Table 5 shows the results of some of the more recent measurements on rubidium.

Table 5.

Author	(Half-life) · 10^{10} years	Maximum energy (keV)
EKLUND [1]	5.8 ± 1.0	–
HAXEL and HOUTERMAN [13] . . .	6.9 ± 0.7	–
KEMMERICH [18]	6.0 ± 0.6	–
BELL, CASSIDY, DAVYS [19]	–	270
CURRAN, DIXON, WILSON [20] . . .	6.15 ± 0.3	275
MACGREGOR, WIEDENBECK [21] . .	6.23 ± 0.3	–
BÄHNISCH, HUSTER, WALCHER [22]	>4.8	–
LEWIS [23]	5.90 ± 0.3	275
FLINTA, EKLUND	6.1 ± 0.2	250 ± 25

Acknowledgements

The authors want to thank Dr. T. Graf for many discussions and Mr. S. Berglund, who made the first measurements in the present investigation.

The work has been supported by a grant to one of us (S. E.) from The Swedish Natural Science Research council.

AB Atomenergi, Department of Physics, Stockholm, Sweden.

LITERATURE

1. S. Eklund, Arkiv f. Mat., Astr. o. Fysik, Bd 33A.
2. A. H. W. Aten Jr, Nucleonics *6*, 70 (1950).
3. N. Feather, BDDA 114 Supplement to 346/1949 BDDA16.
4. E. Bleuler a. W. Zünti, Helv. Ph. Acta, XIX 375 (1946).
5. L. Glendenin, Nucleonics *2*, 27 (1948).
6. L. Katz and A. S. Penfold, Rev. Mod. Ph. *24*, 28 (1951).
7. T. Fazzini and S. Franchetti, Il Nuovo Cimento 311 (1948) V.N.4.
8. E. Yankwich and J. Weight, Science *107* 651, (1948).
9. Compton and Allison, X-rays in theory and experiment (1934).
10. M. Siegbahn, Spektroskopie der Röntgenstrahlen (1931).
11. H. S. W. Massey, E. H. S. Burhop, Proc. Roy. Soc., Ser A *153*, 661 (1936).
12. T. Graf, Arkiv f. Fysik, Band 3 nr 13 (1951).
13. O. Haxel and F. G. Houterman, ZS. f. Physik *124*, 705 (1948).
14. Y. Tomozawa, M. Umezawa, S. Nakamura, Phys. Rev. *86* 791, (1952).
15. A. K. Brewer, Phys. Rev. *49*, 867 (1936).
16. A. O. Nier, Phys. Rev. *50*, 1041 (1936).
17. W. Z. Paul, ZS. f. Physik *124*, 244 (1948).
18. M. Kemmerich, ZS. f. Physik *126*, 399 (1949).
19. Bell, Cassidy, Davys ORNL–694 (1950).
20. S. C. Curran, D. Dixon, H. W. Wilson, Phys. Rev. *84*, 151 (1951).
21. M. H. MacGregor & M. L. Wiedenbeck, Phys. Rev. *86* 420, (1952).
22. I. Bähnisch, E. Huster, W. Walcher, Naturwiss. *39* 379, (1952).
23. G. M. Lewis, Phil. Mag., *43* 1070, (1952).

Tryckt den 19 januari 1954

Uppsala 1954. Almqvist & Wiksells Boktryckeri AB

ARKIV FÖR FYSIK Band 7 nr 33

Communicated 14 October 1953 by Bengt Edlén

Improved wavelengths for some infrared lines in the arc spectrum of carbon

By Lennart Minnhagen

In the course of an investigation of the spectra of argon some infrared carbon lines accidentally appeared as impurity lines and could be accurately measured. As the wavelengths found differ somewhat from those given by Kiess (1), and show an improved average agreement with the wavelengths observed in the solar spectrum (2) the results seem worth being reported.

The light source was an electrodeless discharge tube, containing argon and a small amount of neon, at a total pressure of a few hundreths of a mm, excited by means of a high frequency oscillator. The spectra were recorded with a 21′ grating in stigmatic mounting (Jarrell-Ash, type Ja 70–15 m), the dispersion being 5 A/mm. The carbon lines were measured on three or four spectrograms against Ne I and A I lines, emitted from the discharge tube, as standards. The interferometer wavelengths of the neon lines were taken from the list of Burns, Adams and Longwell (3), additional lines being calculated from the same list. A few interferometer wavelengths by Meggers and Humphreys (4) were used in the range of longest wavelengths, and some A I lines were calculated from unpublished interferometer measurements kindly furnished by Drs Burns and Adams. The uncertainty of the carbon wavelengths, collected in Table 1, is estimated to be about ± 0.01 A for lines given to

Table 1. Wavelengths of infrared carbon lines

Int.	λ, present obs.	λ, Kiess	λ, Sun	σ (cm^{-1})	Combination
calc.	9 658.43[1]	.49	.40	10 350.81	3s $^3P_2 - 3p\ ^3S_1$
2	9 620.785	.86	.98	10 391.31	$^3P_1 - \ ^3S_1$
1	9 603.032	.09	.143	10 410.52	$^3P_0 - \ ^3S_1$
5	9 405.735	.77	.74	10 628.90	$^1P_1 - \ ^1D_2$
2	9 111.80	.85	.877	10 971.77	$^3P_2 - \ ^3P_1$
3	9 094.83[2]	.89	.82	10 992.24	$^3P_2 - \ ^3P_2$
2	9 088.509	.57	masked	10 999.89	$^3P_1 - \ ^3P_0$
1	9 078.292	.32	.28	11 012.27	$^3P_1 - \ ^3P_1$
2	9 062.473	.53	.48	11 031.49	$^3P_0 - \ ^3P_1$
2	9 061.433	.48	.443	11 032.75	$^3P_1 - \ ^3P_2$
4	8 335.148	.19	.150	11 994.09	$^1P_1 - \ ^1S_0$

[1] Wavelength calculated from the level values of Table 2, the carbon line being masked by the strong argon line 9 657.78 A.

[2] Observation possibly affected by a neighbouring argon line 9 095.10 A.

Table 2. Relative level values of C I

Desig.	Level	Interval	Desig.	Level	Interval
3s $^3P_0$	60 333.78	19.22	3p $^3S_1$	70 744.31	
3s $^3P_1$	60 353.00	40.50	3p $^3P_0$	71 352.89	12.38
3s $^3P_2$	60 393.50		3p $^3P_1$	71 365.27	20.48
			3p $^3P_2$	71 385.75	

three decimals and somewhat greater for the two lines given to two decimals. Fo comparison, the values given by KIESS as well as those from the solar spectrur table have been included. It appears that the wavelengths now obtained are systematically smaller than those reported by KIESS, the mean difference being about 0.05 A Kiess used a higher pressure (5 mm) in his experiments, but it seems difficult t explain the whole difference as due to a pressure shift. The agreement between th new carbon wavelengths and the corresponding solar wavelengths is good, except i three cases, where it might be assumed that the solar lines are blends or their measurements affected by neighbouring lines.

The vacuum wave-numbers and the term combinations of the C I lines measure are given in the last two columns of Table 1. The vacuum corrections were made b means of EDLÉN's dispersion formula (5). Improved values for some triplet levels i C I were calculated from the new measurements, using as a starting point the valu for 3s$^3P_1$ given in "Atomic Energy Levels" (6), as shown in Table 2.

REFERENCES

1. KIESS, C. C., J. Res. Nat. Bur. Std. *20*, 33 (1938).
2. BABCOCK, H. D. and MOORE, C. E., Carnegie Inst. Wash. Publ. *579* (1947).
3. BURNS, K., ADAMS, K. B., and LONGWELL, J., J. Opt. Soc. Am. *40*, 339 (1950).
4. MEGGERS, W. F., and HUMPHREYS, C. J., J. Res. Nat. Bur. Std. *13*, 293 (1934).
5. EDLÉN, B., J. Opt. Soc. Am. *43*, 339 (1953).
6. MOORE, C. E., "Atomic Energy Levels", Vol. I, Circular 467, Nat. Bur. Std., Washingto (1949).

Tryckt den 19 januari 1954

Uppsala 1954. Almqvist & Wiksells Boktryckeri AB

ARKIV FÖR FYSIK Band 7 nr 34

Communicated 11 November 1953 by AXEL E. LINDH and HARALD NORINDER

Synthetic sodium chloride crystals; refractive index and lattice constant

By GÖTE ERICSSON

With 5 figures in the text

This paper is a report on experiments in the preparation of synthetic crystals, primarily of NaCl, which were carried out at the Physics Laboratory. Preliminary determinations of the refractive indices of the crystals prepared have been made for certain wavelengths, and, in addition, the lattice constant for the crystals has been determined.

Preparation of the crystals

The synthetic crystals were prepared in accordance with the method described by KYROPOULOS (1). The principle of the method is that a seed crystal is caused to crystallize in contact with molten salt by cooling it, at the same time as it is gradually raised (and perhaps rotated). A furnace as shown in Fig. 1 was used, with the molten salt in an unglazed porcelain crucible. The furnace is fitted with six heating elements connected in series. These are spirals of chromium-nickel wire, resting on shelves of fire bricks and easy to exchange. The power consumption for the preparation of sodium chloride crystals (melting point 802° C) is about 2000 watts.

The crystal holder (Fig. 2) consists of a water-cooled jacket surrounding a rotating tube. Inside this tube is another tube, the upper end of which is connected to a rotating mechanism and to a vacuum pump. The seed crystal is fastened to the closed end of a short nickel tube (at the bottom of Fig. 2), which is inserted into the rotating tube in such a way that it can easily be removed when the crystal is ready. The vacuum pump draws a stream of air through the bottom of the holder, providing effective cooling.

When the seed crystal is first lowered into the molten bath, this should have a temperature some 20–30° C above the melting point. The rate of cooling is lowered sufficiently for the seed crystal to begin melting at the contact surface, thereby exposing a fresh surface at which crystallization takes place when the rate of cooling is increased.

The crystal is lifted by winding up the two wires on which the holder hangs, at a rate of 8 mm per hour, by means of a worm-geared synchronous motor. This also produces the rotation, at a rate of one revolution per hour. Even lower speeds of lifting have been recommended; A. C. MENZIES and J. SKINNER (2) state 2–4 mm per hour.

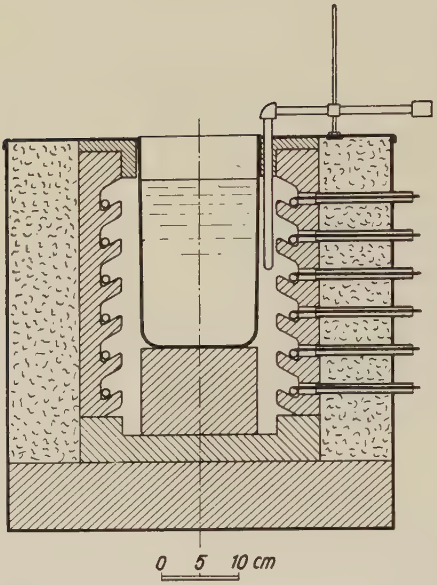

Fig. 1. The furnace used for preparation of the crystals. The insulating material is kieselguhr.

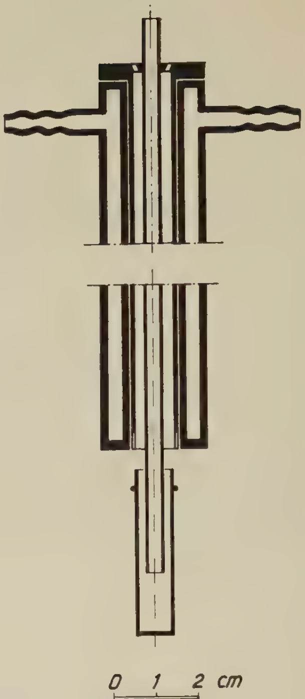

Fig. 2. The crystal holder — total length 20 cm.

In order to cool the grown crystal to room temperature after preparation, it i transferred to a second furnace, which has been heated in advance to a temperatur just below the melting point. The furnaces run on rails, and the transfer can thus b accomplished by changing furnaces under the lifted crystal. In the cooling furnac the temperature is gradually reduced to room temperature during the course of week. This is done by a clockwork mechanism connected to the rotary regulator o the variable transformer supplying the furnace.

It is of course of great importance that the temperature should be constant, onc favourable conditions for crystallization have been obtained. For that reason th furnace is supplied from a constant-voltage transformer, further stabilized by a electronic magnetic stabilizer[1] (Fig. 3). Here the regulating device is a reactor (trans ductor (3)), magnetized with direct current. The reactor consists of two transformer used as chokes with d.c. windings; these d.c. windings are coupled in opposition t one another, to cancel the induced alternating e.m.f.'s induced in them. Increasin the direct current raises the magnetic flux in the choke cores towards the saturatio value, thus lowering the reactance; a decrease in the direct current has the opposit effect. Thus, for constant alternating current, the a.c. voltage drop across the reacto is regulated by the direct current. In the present stabilizer this direct current i

---

[1] I am grateful to Lic. REUTERSWÄRD for the design of the stabilizer.

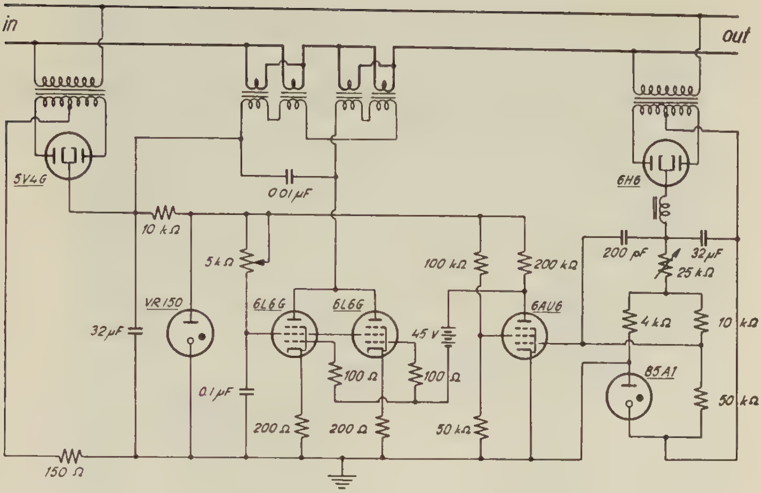

Fig. 3. Circuit of the stabilizer.

controlled by the voltage drop across the furnace. For this purpose, the latter is rectified (6H6) and compared with a constant voltage (Philips reference tube 85A1). The difference is amplified in a pentode stage (6AU6), after which the regulating current is drawn from two power tubes (6L6G). With this stabilizing, the temperature in the furnace can be kept constant to within 1° C.

To measure the temperature of the furnace a chromel-alumel thermocouple is used, the e.m.f. of which is determined by means of a potentiometer, calibrated in degrees centigrade.

The crystals grown have had sizes up to 10 cm diameter and 10 cm height and have been of good optical quality.

Determination of refractive indices

For these determinations the crystals were sawn to 60° prisms with faces 5 × 5 cm. These rough prisms were then polished according to the directions given by R. C. Lord, R. S. McDonald and F. A. Miller (4) ("Notes on the Practice of Infrared Spectroscopy"). The refractive indices were determined for the C and F lines of the hydrogen spectrum (6563 A and 4861 A respectively) and for the d line of the helium spectrum (5876 A), using a precision spectrometer. For comparison, a determination was also carried out on a prism of natural rock salt. The margin of error in the determinations was estimated to be $4 \cdot 10^{-5}$. The variation in temperature during the measurements did not exceed 0.1° C.

The results are shown in Table 1, which also contains the corresponding values for rock salt as given by Landolt and Börnstein's tables. It will be seen that the refractive indices of the artificial crystals are somewhat lower than those of natural rock salt.

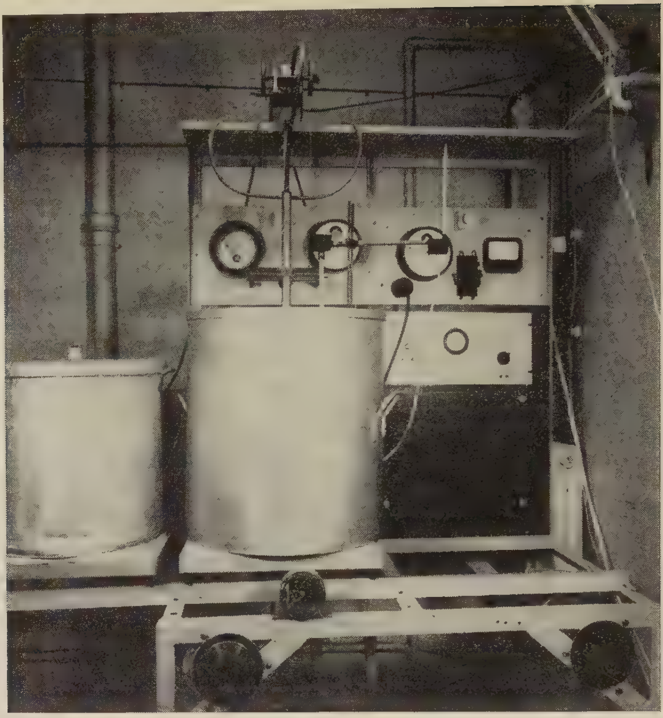

Fig. 4. View of the entire design, the melting furnace to the right with the crystal holder lowered into it, and the cooling furnace to the left.

Table 1. Refractive indices of artificial and natural rock salt at 20° C.

	C-line 6563 A	d-line 5876 A	F-line 4861 A
Artificial rock salt prism 1 . . .	1.54054	1.54429	1.55326
,, ,, ,, ,, 2 . . .	1.54056	1.54432	1.55328
,, ,, ,, ,, 3 . . .	1.54055	1.54430	1.55326
Natural rock salt prism	1.54061	1.54435	1.55332
Natural rock salt (according to LANDOLT and BÖRNSTEIN) . .	1.54062	—	1.55334

Determination of the lattice constant

The lattice constant was determined with a tube spectrometer by the commo "Umlegemethode". The spectrometer and its adjustments have previously bee described in detail by A. LARSSON (5).

The measurements were made on crystal plates of size 12 × 20 × 1 mm, whic could easily be obtained from the crystals by cleavage. The initial material for th

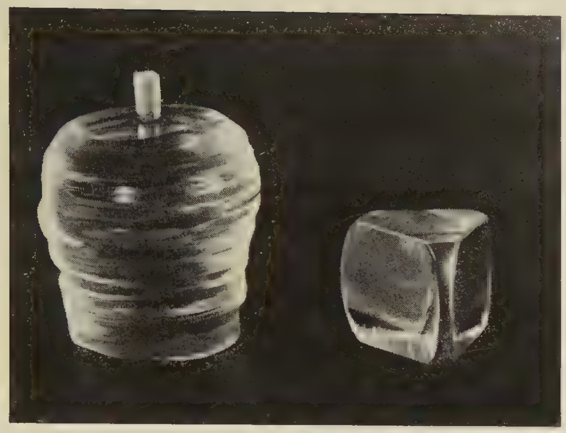

Fig. 5. A crystal as drawn from the melt and after sawing and polishing to a 60° prism.

crystallizing melt in this case was sodium chloride pro analysi ("Merck"), with the following maximum limits of impurities:

Unsolved	0.005 %	Heavy Metals (Pb)	0.0008 %
Alkalinity (as NaOH)	0.0025 %	Iron (Fe)	0.0003 %
Acidity (as HCl)	0.0023 %	Barium (Ba)	0.001 %
Sulphate (SO_4)	0.002 %	Calcium (Ca)	0.004 %
Phosphate (PO_4)	0.0005 %	Magnesium (Mg)	0.001 %
Bromide (Br)	0.01 %	Potassium (K)	0.01 %
Total Nitrogen (N)	0.001 %	Arsenic (As)	0.00005 %
		Total	0.04 %

The exposures were made with the Cu $K\alpha_1$ line of the first order (20 kV and 20 mA). In the calculations, the wavelength of this line was taken to be 1537.399 X.U. As the sharpness of the lines was not of the highest order, the measurements of the distance between the lines of the double exposure could not be carried out with an accuracy greater than 0.005 mm, which introduces an uncertainty of 0.04 X.U. in the lattice constant. The tube length was 771.0 mm. The variation in temperature during the exposures was kept within 0.1° by a thermostat. The linear expansion coefficient of sodium chloride was taken to be $4.04 \cdot 10^{-5}$. Table 2 gives the values obtained, referred to 18° C.

As sodium chloride crystallizes in a face-centred cubic lattice, the length of the edge of the elementary cell is twice the lattice constant. Thus, for the above value of d_∞, the length of the edge is

$$a = 5627.70 \text{ X.U.}$$

For purposes of comparison, Table 3 gives other determinations of the edge-ength of natural and artificial rock salt. STRAUMANIS and IEVINŜ's determinations were made by the powder method (DEBYE-SCHERRER method), on rock salt and sodium chloride pro analysi (Kahlbaum).

Table 2. Measured values of the lattice constant, referred to 18° C.

Plate no.	d_t	temp.	$d_{18.0}$
50	2813.96	21.0	2813.62
51	2814.00	21.6	59
66	.39	25.5	54
67	.49	25.8	61
72	.38	24.4	65
73	.39	24.3	67
75	.37	24.6	63
77	.43	25.0	62
79	.38	24.9	60
80	.34	24.9	56
81	.38	24.5	64
82	.41	25.5	56
83	.33	24.8	56
96	.41	25.6	55
97	.42	25.6	56
98	.44	25.6	58

Mean value . . . . 2813.60 X. U.
Correction for refraction . . . . + 0.25
$d_\infty = 2813.85$ X. U.

Table 3. Determinations of the edge-length of the cell of natural and artificial rock salt.

	Natural rock salt	Artificial rock salt and NaCl
Tu (6)	5627.79	
van Bergen (7)		5628.23
Straumanis and Ievinŝ (8) .	5627.67	5627.37

The value 5627.70 X.U. found in the present investigation thus agrees well with the values for natural rock salt but differs considerably from the determinations for artificial rock salt. As regards the value obtained by Straumanis and Ievinŝ, the discrepancy might be accounted for by the different process used in preparing the crystals examined (precipitation of a saturated solution). On the other hand, van Bergen's determinations were made with crystals prepared by the same method as in the present investigation, and it thus seems as if crystals made by the same method under somewhat different conditions may give different values of the lattice constant As an investigation of the quality of the crystals concerned would be of great interest in this connection, such an investigation has been started using a more extensive crystal material. The results are to be published in the near future.[1]

I wish to express my sincere thanks to the head of the Institute, Professor Axel E Lindh, for valuable help and for the interest he has shown while I was engaged in this work. I also thank Dr. Constantin Kurylenko, who at the beginning of the work taught me how to prepare artificial crystals.

Physics Laboratory, University of Uppsala, September 1953.

---

[1] Brogren and Ericsson, to be published.

REFERENCES

. Kyropoulos, Z. anorg. Chemie *154*, 308 (1926).
. Menzies and Skinner, Disc. Far. Soc. *5*, 306 (1949).
. Lamm, Aseas Tidning *31*, 18 (1939).
. Lord, McDonald and Miller, J. Opt. Soc. Am. *42*, 149 (1952).
. Larsson, Phil. Mag. (7) *3*, 1136 (1927).
. Tu, Phys. Rev. *40*, 673 (1932).
. van Bergen, Ann. d. Physik *39*, 553 (1941).
. Straumanis and Ievinŝ, Zs. f. Physik *102*, 353 (1936).

Tryckt den 20 januari 1954

Uppsala 1954. Almqvist & Wiksells Boktryckeri AB

ARKIV FÖR FYSIK Band 7 nr 35

Communicated 9 September 1953 by MANNE SIEGBAHN

Internal conversion of the zero-zero transition in RaC′

By DAVID E. ALBURGER[1] and ARNE HEDGRAN

With 1 figure in the text

Of the three known cases (1) of zero-zero, no parity change nuclear transitions he 6 Mev first excited state of O^{16} decays predominantly by internal pair formation vhile the 0.7 and 1.4 Mev transitions in Ge^{72} and RaC′ respectively may be observed y the resulting internal conversion electrons. Unconverted gamma-rays do not ccur because of the strictly forbidden nature of direct gamma emission between tates of zero spin having the same parity.

The zero-zero transition has been the subject of theoretical considerations (1, 2) y DRELL and ROSE. At low energies where pair production is not important the onversion depends on the size of the orbital electron wave functions within the ucleus and it is possible to calculate the relative amounts of conversion in the arious shells. In the RaC′ case the theoretical value (3) for the K to L ratio should e 5.5 while the K to L + M ratio should be 4.3 both with an uncertainty of 10 percent wing to inexact knowledge of the nuclear radius. It is also predicted that the conersion should take place mostly in the K, L_I, and M_I subshells with a small amount f L_{II} and negligible L_{III}.

Two measurements have been reported on the RaC′ conversion lines, the first by ATYSHEV (4) who obtained a K to L + M ratio of 4.1. Later Latyshev and co-workers 5) resolved the M line and found a K to L ratio of 5.4 and a K to L + M ratio of .3 in agreement with the theoretical values. Their resolution was not sufficient to tudy the relative conversion in the various subshells.

In connection with precision measurements (6) on Co^{60} gamma-radiation we have ad occasion to use sources of RaC in the 50 cm radius double-focusing spectrometer. o examine these conversion lines at high resolution the sources were 1×10 mm² n size and were made by electrostatic collection on copper backings from 500 mC mpules of radon. The spectrometer resolution baffles were set for an opening of .8 × 4 cm² (corresponding to a solid angle of $\sim 3 \times 10^{-4}$) compared with a full opening f 10 × 10 cm² while the exit slit in front of the counter was 1 mm wide. A resolution f 0.085 percent was obtained under these conditions. In order to correct for decay NaI gamma-ray monitor counter was biased in such a manner that it was sensitive nly to the higher energy lines of the 20 min RaC activity. It was determined that the istance between the monitor and the edges of the spectrometer poles (~ 1 meter) as sufficient so that the range of variation of the magnetic field did not measurably lter the counting characteristics.

---

[1] National Science Foundation fellow on leave from Brookhaven National Laboratory.

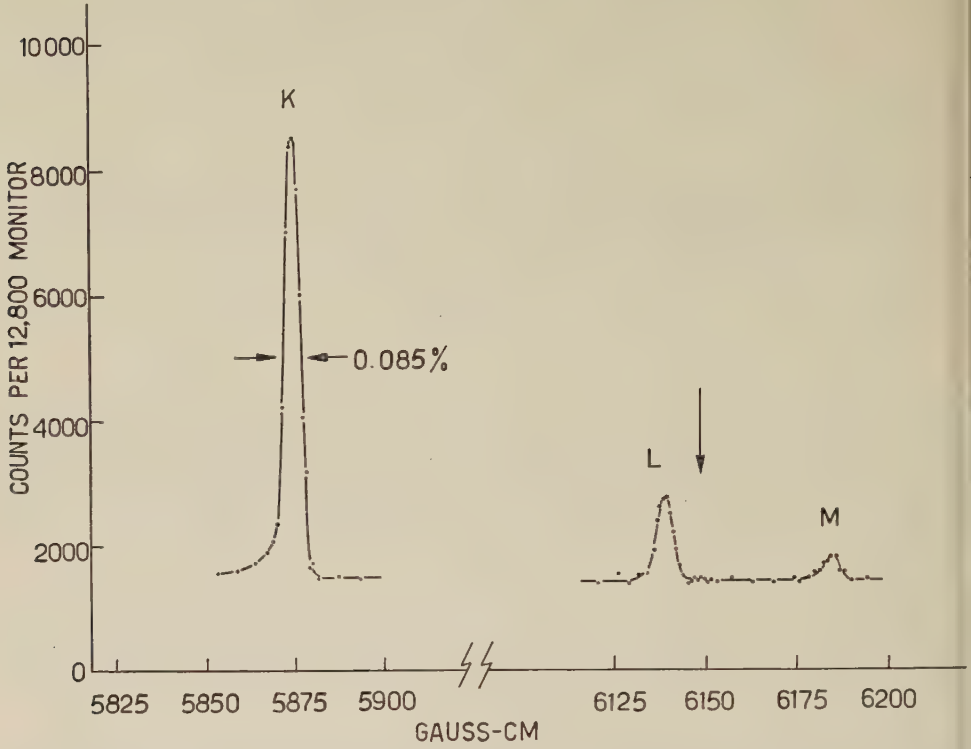

Fig. 1. Internal conversion lines associated with the 1.4158 Mev zero-zero transition in RaC′. The arrow indicates the expected position of an L_{III} component.

From Fig. 1, which shows the conversion lines corresponding to the 1.42 Mev RaC′ transition, it is seen that the ratio of the peaks to the beta-ray background is rather favorable at this resolution. The L line appears to be simple as tested by matching it to the K line. Using a calibration constant derived from the K line, the L line has a position which agrees with that expected of L_{I} to within 1 part in 10^4 whereas it differs from the L_{II} position by 3 parts in 10^4. We believe that the line is predominantly L_{I} although an L_{II} component with a relative strength of up to 20 percent could be present and still not be detected. As indicated by the arrow an L_{III} line would be completely resolved but none appears. If this line exists it has an intensity less than 5 percent of the L_{I} line. The M line also seems to have the same half-width as the K line and its position closely corresponds to M_{I} or $_{II}$.

The K to L ratio, 5.3 ± 0.3, and the K to L + M ratio, 4.25 ± 0.3, are both in excellent agreement with the calculations of Drell. Taken together with the apparent absence of L_{III} electrons the results lend additional support to the theoretical predictions for zero-zero transitions.

We would like to thank professor MANNE SIEGBAHN for his interest in this work and for the hospitality of the Nobel Institute extended to the first-named author during 1952–53.

Nobel Institute of Physics, Stockholm 50.

REFERENCES

1. For a review of these cases see S. D. Drell and M. E. Rose, Prog. in Theor. Phys. *7*, 125 (1952).
2. S. D. Drell, Phys. Rev. *81*, 656 (A) (1951) and Oak Ridge Nat. Lab. Rept ORNL 792 (unpublished)
3. —— private communication.
4. G. D. Latyshev, Rev. Mod. Phys. *19*, 132 (1947).
5. Latyshev, Sliv, Barchuk, and Bashilov, see Physics Abstracts No. 7253 (1949).
6. Lindström, Hedgran and Alburger, Phys. Rev. *89*, 1303 (1953).

Tryckt den 20 januari 1954

Uppsala 1954. Almqvist & Wiksells Boktryckeri AB

ARKIV FÖR FYSIK Band 7 nr 36

Communicated 28 October 1953 by MANNE SIEGBAHN and BENGT EDLÉN

Scintillation spectrometry of continuous γ- and x-ray spectra below 1 MeV

By K. LIDÉN and N. STARFELT

With 12 figures in the text

Contents

Page

Summary 428

I. Introduction 429

II. Essential experimental details of the method 429

- a. Spectrometer design: crystal material and electronic components 429
- b. Geometry source-detector 431
- c. Backscatter 432
  - 1. General considerations 432
  - 2. Theoretical evaluation 433
  - 3. Experimental measurements 434
- d. Resolving power 436

III. Absorption of γ-rays in a NaI crystal 436

- a. Absorption processes 436
- b. Electron escape 437
  - 1. Escape of primary photoelectrons 437
  - 2. Escape of electrons contributing to the secondary photoelectric pulses 442
- c. K x-ray escape 443

IV. Evaluation of the continuous γ-spectrum from the observed pulse height distribution, involving corrections for: 447

- a. Electronic apparatus 448
- b. Background 448
- c. Energy resolution 448
- d. Compton and escape electrons 449
- e. K x-ray escape 451
- f. Backscatter 452
- g. γ-detection and geometrical efficiency of the crystal 453

V. Discussion 455

References 457

Summary

In an analysis of the factors involved in the scintillation spectrometer method used for quantitative evaluation of continuous gamma- and x-ray spectra in the energy range 0–1 MeV, experimental and theoretical observations suggested that the usefulness and accuracy of the method could be improved by paying careful attention to the following essential points.

1. The long term stability of the apparatus must be very good, especially the zero point and the channel width of the discriminator and the energy calibration of the spectrometer; perfect linearity of response is also important.

2. Backscattered photons from the multiplier window is an undesirable additional contribution to the spectrum in the range 100–300 keV. Using deduced formulas the spectrum is corrected for the backscatter with an accuracy of 1–2 %. However, if a strong source is available, the use of a collimated beam parallel to the window and directed to the centre of the crystal effectively reduces the backscatter.

3. The *K* x-radiation at 73–88 keV from lead diaphragms sometimes causes appreciable errors in this part of a spectrum; this disturbance can be eliminated by lining the hole in the diaphragm and its multiplier side with 1.5 mm Sn + + 0.5 mm Cu.

4. Accurate correction for the Compton electron distribution is very important, and it is performed by means of deduced formulas, based on experimental analysis of the spectra of some single γ-ray lines. For example, in a study of the internal bremsstrahlung from P^{32} with a NaI crystal $\varnothing$ 1.5×1.5 cm the Compton electron contribution was found to be 30 % of the observed intensity at 500 keV.

5. The magnitude of the escape of iodine *K* x-rays from the various surfaces of the crystal is calculated, whereby the fluorescence yield ω_K and the fraction δ_K of the photoelectric absorption processes occurring in the *K*-shell are taken into account. For a crystal $\varnothing$ 1.5×1.5 cm the escape fraction is almost independent of the energy above 200 keV and equal to 3 % of the number of photopeak pulses.

6. Theoretical calculations showed that the electron escape fraction is small at low energies; at 1000 keV and a crystal $\varnothing$ 1.5×1.5 cm it is 7 % of the number of photopeak pulses. Furthermore, the method described for Compton electron correction of an experimental pulse height distribution necessarily includes the electron escape effect. However, this effect must be considered in the performance of purely theoretical calculations of the γ-detection efficiency of crystals of various dimensions.

7. The error in the effective photoelectric efficiency is almost entirely transferred to the final result. The measured values at a crystal $\varnothing$ 1.5×1.5 cm have an error less than 5 % up to 700 keV and probably this accuracy can be improved. The correction for decreasing geometrical efficiency at increasing energy of the primary photons when irradiating the entire crystal has also been calculated; for example, at 200 keV and a distance of 10 cm between the source and the crystal mentioned above this correction is 10 %.

Finally, it is concluded, that the high γ-detection efficiency of the NaI(Tl) cintillation spectrometer, in most cases, can be combined with a high degree f accuracy when measuring continuous spectra in the region of interest 0–1 MeV.

I. Introduction

The high γ- and x-ray efficiency and the proportionality between photon nergy and pulse height of a scintillation counter provided with suitable inorganic rystals have permitted the elaboration of a new technique for the study of - and x-ray spectra. Hitherto such spectra have been studied with ionization hambers, photographic materiels or Geiger counters as detectors, the sensitivity f which is much lower than that of the scintillation counter. Further, it is ometimes difficult to measure the spectral sensitivity of such detectors. The pectral sensitivity of the scintillation spectrometer at least below 1 MeV can, owever, be accurately determined.

Only few investigations of continuous γ- and x-ray spectra by methods using scintillation spectrometer are on record. Johansson (1952) measured continuous -ray spectra and reported this as an example of the usefulness of the scintillaion spectrometer. Novey (1951) and Madansky & Rasetti (1951) investigated he internal bremsstrahlung from P^{32} and RaE. Maeder & Preiswerk (1951) nd Bell, Jauch & Cassidy (1952) measured the internal bremsstrahlung acompanying the K-capture in Fe^{55}. In a study of the disintegration of Tl^{204} er Mateosian & Smith (1952) also investigated the internal bremsstrahlung rom this nucleus.

At this laboratory the scintillation spectrometer has now been used for two ears in the study of the internal and external bremsstrahlung and in the nvestigation of primary and secondary x-radiations (Lidén & Starfelt 1953 (a) b)). The method itself was critically analysed especially with respect to the uantitative evaluation of continuous spectra. The result of this analysis and bservations made on application of the method are described and discussed elow.[1]

II. Essential experimental details of the method

a. Spectrometer design: crystal material and electronic components

The investigation of continuous γ- and x-ray spectra below 1 MeV requires:

1. high γ-detection efficiency,
2. good resolving power,
3. linear response to electrons (photons), and
4. very good electrical and mechanical stability.

1. The efficiency of the spectrometer depends upon the photoelectric absorpion coefficient τ of the crystal material. τ is approximately proportional to

---

[1] A preliminary report of this investigation was given at the sixth meeting of *the Swedish ational Committee for Physics,* held in Stockholm on Sept. 25–27, 1952.

the fourth power of the atomic number Z. Only certain inorganic crystals are suitable, e.g. the thallium-activated crystals of NaI, KI, CsI and CaI_2 or the crystals of $CaWO_4$ and $CdWO_4$ (Gillette 1950). The tungstates have the greatest density and the largest τ of these crystals, but they are difficult to grow synthetically. Large crystals of NaI(Tl) and KI(Tl) are, however, readily obtainable. As yet CaI_2 has only been investigated in a polycrystalline form (Van Scriver & Hofstadter (1951)).

2. The resolving power is intimately related to the fluorescence efficiency of the crystal. The fluorescence efficiency of NaI and CaI_2 is much greater than that of the other iodides[1]; the tungstates are also somewhat inferior to NaI and CaI_2 in this respect.

KI has an additional background from the natural activity of K^{40}.

NaI thus appears to be the most suitable crystal available for the study of γ- and x-ray spectra. In addition its decay time is shorter than that of the other crystals and its optical properties are superior. The only disadvantage of NaI is its sensitivity to moisture.

3. The proportionality of the scintillation response of NaI(Tl) to the electron energy is very good from 1 keV to several MeV (Taylor *et al.* (1951)). In investigations of continuous spectra this linearity should be maintained by the photo-multiplier and by the electronic components. Cumulative experience has shown that photo-multipliers of the EMI 5311 type give good proportionality between energy and pulse height for energies below 1 MeV, if the output pulse height is kept sufficiently small. With larger pulses the energy vs pulse height curve is concave towards the energy axis (Raffle & Robbins (1952)). The linearity of electrostatically-focused photo-multipliers of the RCA 5819 type is less dependent on the voltage than is the EMI type.

A continuous spectrum often gives rise to pulses of very different heights. Therefore, the amplifier should possess good overload characteristics so that overloading of the amplifier with large pulses will not distort the pulse height distribution at low energies.

A single channel differential discriminator may conveniently be used as a pulse analyzer, especially because the counting time may be adjusted to the intensity and the same statistical accuracy throughout the spectrum thereby secured. This is not the case with the method in which the channel is continuously moved through the spectrum and the counting rate is plotted vs pulse height on a recorder. Finally, mention should be made of the method of photographing the pulse distribution on a cathode-ray oscillograph. Owing to the limited accuracy of photographic intensity measurements, the method is in general only suitable for survey measurements.

4. The experimental study of continuous spectra usually requires long observation. Therefore the apparatus must be stable and the measurements must be reproducible over a long period. The geometry of source, collimator, crystal with reflector, and photo-multiplier must be kept constant during observation. The voltage of the photo-multiplier must be accurately stabilised; experience has shown that a stability of 0.5 volts per 1000 volts is desirable. Long-term stability of the photo-multiplier voltage is also necessary in order to maintain

---

[1] Concerning CsI see p. 457.

the energy calibration. In general, the calibration must be checked at intervals of a few hours.

In order to secure stability of the amplifier, of the discriminator and of the high-voltage supply the apparatus must be warmed up 1–2 hours before use. Its temperature should then be kept constant. In the present study it was necessary regularly to measure the channel width of the differential discriminator (Elmore & Sand (1950)) at intervals of about one hour. Furthermore, it was found necessary to stabilise the line voltage for the entire apparatus with a regulated power supply.

b. Geometry source-detector

The efficiency of the spectrometer can be increased by increasing the crystal thickness t and/or by increasing the solid angle Ω_c of source-crystal.

The upper limit of t is dictated, at least partly, by the fact that the light output from the crystal decreases with increasing distance between the scintillation point and the photo-cathode. This means that the resolving power R_c decreases, too.

The solid angle Ω_c can be increased by using a crystal with a large diameter ϕ_c. With the crystal cemented to the window of the photo-multiplier ϕ_c cannot exceed the diameter of the photo-cathode, ϕ_{ph}. A conical light guide permits the use of $\phi_c > \phi_{ph}$, but this reduces R_c at the same time. Ω_c can also be increased by reducing the distance L between the source and the crystal.

However, a large Ω_c complicates the conditions, as all the corrections of the experimental results are most easily calculated for a collimated primary beam normally incident. The usual procedure employs a collimating arrangement which sufficiently reduces disturbing scattered secondary radiation within the entire range of the spectrum observed. When observing intense radiation sources it is possible to use a narrow beam, falling only on the centre of the crystal. That part of the resolving power depending on the crystal is then the best achievable, because the scintillations originate from a small part of the crystal, and because photoelectrons can escape only through those two surfaces through which the beam enters and leaves the crystal (see Sect. III).

In the observation of high intensity radiation sources (e.g. x-ray tubes) it may be difficult to obtain a sufficient reduction in intensity. Large distance L and a collimator with accurately centered diaphragms are necessary; for $E\gamma < 100$ keV the absorption in the air must be considered. For low intensities the collimator system must be constructed so that the beam covers the entire crystal. When investigating spectra with roughly equal intensities at both low and high photon energies, all radiation outside the defined solid angle must be efficiently absorbed (by narrow beam geometry) in order to exclude from the spectra scatter from nearby objects.

Using a lead collimator, lead K x-rays may be obtained with measurable ntensity. This disturbance is eliminated by lining the hole in the diaphragm and its multiplier side with 1.5 mm Sn + 0.5 mm Cu. Other lead shields close to the crystal must be avoided.

c. Backscatter

1. General considerations

Experience has shown that the largest pulse height and the best resolving power are obtained when the crystal is mounted directly on the window of the photo-multiplier. However, if the source is placed on the extension of the axis of the multiplier, this arrangement causes maximal secondary radiation as backscatter from the different parts of the photo-multiplier. The energy of photons scattered between 90° and 180° from a 100–1000 keV primary beam lies between 72 and 340 keV. Thus these backscatter photons, emitted mainly from the photo-multiplier window immediately below and beside the crystal, are fairly effectively absorbed by the crystal. A pulse height distribution of the Cs^{137} 662 keV γ-ray line clearly shows this backscatter as a peak at about 200 keV (*Fig. 1*). 662 keV photons scattered at 180° have an energy of 185 keV. In this case the beam covered the entire window of the photo-multiplier.

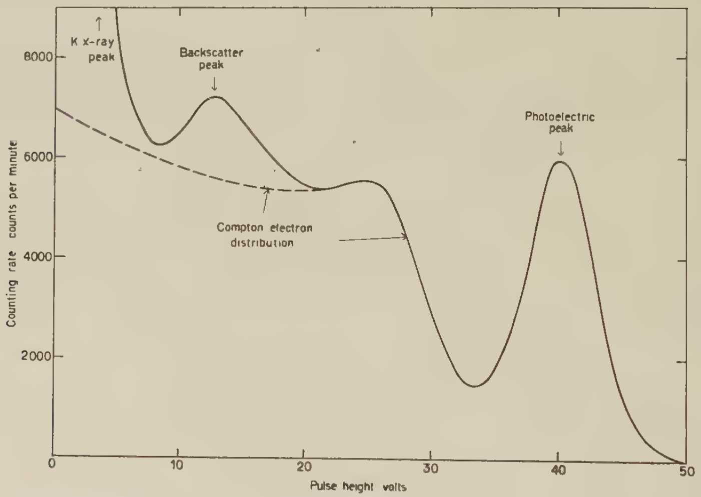

Fig. 1. Pulse height distribution of Cs^{137} 662 keV γ-ray line; NaI(Tl) crystal ∅ 1.5 × 1.5 cm source-crystal distance 10 cm.

The backscatter effect can be considerably reduced by allowing a narrow beam to fall on the central part of the crystal in a direction *parallel* to the window of the photo-multiplier. This is possible with strong sources. With weak sources a larger solid angle must be used, and then the entire crystal is irradiated. It is evident that the latter is not much better than the arrangement with the beam perpendicular to the photo-multiplier window. In both cases a light guide may be used to reduce the number of backscattered photons from that part of the photo-multiplier not covered by the crystal. The fact that the light guide reduces the pulse height and thus the resolving power is a serious disadvantage attending this arrangement.

2. Theoretical evaluation of the backscatter

The number of photons with energy E_γ incident on a surface element dS (*Fig. 2*) of the window of the photo-multiplier is $n_w\,dS$, the following number of which is scattered at the angle θ within the solid angle $d\Omega = \sin\theta\, d\theta\, d\varphi$:

$$n_w\,dS\,(1-e^{-\mu_a a})\frac{1}{\mu_a}\left(\frac{d\sigma_\theta}{d\Omega}\right)_a \sin\theta\, d\theta\, d\varphi \tag{1}$$

where a is the thickness of the window, μ_a the total absorption coefficient of the window materiel and $\left(\frac{d\sigma_\theta}{d\Omega}\right)_a$ its differential Compton scattering coefficient. All scattering in the multiplier window is assumed to occur in a plane half way between the surfaces of the window. The total number of photons with primary energy E_γ, scattered from dS and absorbed by the crystal is $n_b\,dS$. One obtains

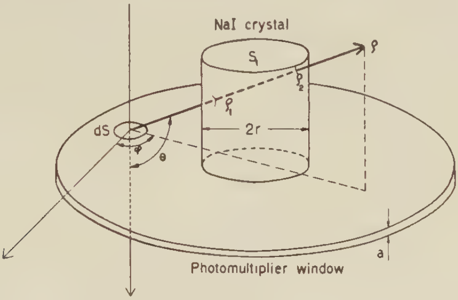

Fig. 2. Diagram for calculating the backscatter.

$$n_b\,dS = n_w\,dS\,(1-e^{-\mu_a a})\int\!\!\int\!\!\int \frac{1}{\mu_a}\left(\frac{d\sigma_\theta}{d\Omega}\right)_a \exp\left(\mu_a' \frac{a}{2\cos\theta}\right)\mu' \exp\left[-\mu'(\varrho-\varrho_1)\right]\times$$
$$\times\, d\varrho\, \sin\theta\, d\theta\, d\varphi. \tag{2}$$

The prime refers to the scattered photon; μ is the absorption coefficient of the crystal. The integral is taken over the entire volume of the crystal.

The total number of scattered photons absorbed by the crystal, $\int_S n_b\,dS$, can be calculated by integrating (2) over the total surface S, irradiated by the primary beam. For a collimated beam containing n_0 photons with energy E_γ, with the cross section ΔS and normally incident on the centre of the surface S_1 of a cylindrical crystal with radius r, the backscatter $n_b\,\Delta S$ is now calculated. In this case $n_w\,dS$ in (1) has to be replaced by $n_0 e^{-\mu t}$. Owing to the cylindrical symmetry the differential solid angle is $2\pi\sin\theta\, d\theta$ and (2) is integrated from $\varrho_1(\theta)$ to $\varrho_2(\theta)$. Finally the following expression for $n_b\,\Delta S$ is obtained:

$$n_b\,\Delta S = n_0 e^{-\mu t}(1-e^{-\mu_a a})\frac{1}{\mu_a}\int_{\theta_1}^{\pi}\left(\frac{d\sigma_\theta}{d\Omega}\right)_a \exp\left(\mu_a' \frac{a}{2\cos\theta}\right)\{1-\exp[-\mu'(\varrho_2-\varrho_1)]\}\times$$
$$\times\, 2\pi\sin\theta\, d\theta \tag{3}$$

where $\theta_1 = \frac{\pi}{2} + \mathrm{arctg}\,\frac{a}{2r}\cdot$ This equation can be numerically integrated. In that case where the entire surface S_1 entered by the beam is irradiated, $\int\limits_{S_1} n_b\, dS$ is approximately equal to $n_b \Delta S$ as calculated from (3).

In *Fig. 3* the backscatter from that part of the multiplier window covered by the crystal is shown as a function of the primary energy E_γ. $\frac{1}{n_0}\int\limits_{S_1} n_b\, dS$ is calculated for two crystal sizes and $\frac{1}{n_p}\left[\int\limits_{S_1} n_b\, dS\right]_p$ for the crystal size ⌀ 1.5× ×1.5 cm. The subscript p denotes effective photoelectric absorption (see Sect. III a). Here n_p is the number of primary photons, effectively absorbed photoelectrically in the crystal.

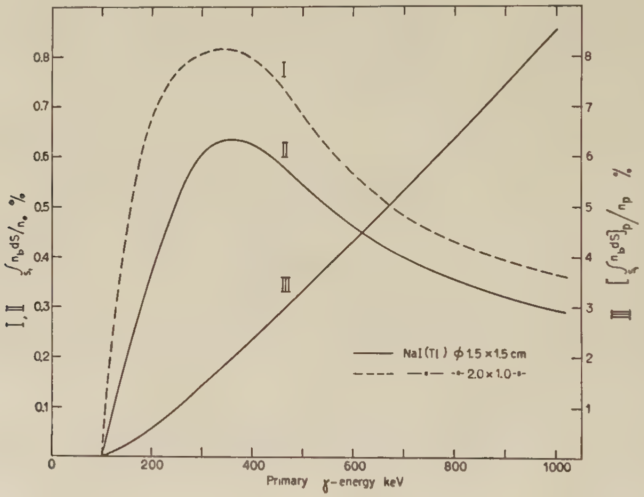

Fig. 3. Backscatter from the part of the photo-multiplier window covered by the crystal as calculated from (3). I and II: number of backscattered photons, absorbed in the crystal per primary photon incident on the crystal. III: number of backscattered photons effectively absorbed photoelectrically by the crystal per pulse in the primary photo-peak.

This calculation has to be considered as a first approximation. In a more accurate calculation the backscatter from photons first scattered in the crystal and then in the window must be taken into account. Measurements of the backscatter using a collimated beam of Cs^{137} 662 keV γ-rays gave a value which is about 40 % greater than that given by (3).

3. Experimental measurement of the backscatter

The number $\int\limits_{F} n_b\, dS$ of photons, scattered from that part F of the window outside the crystal, which is irradiated, can be calculated from (2), but it can also be determined experimentally from a study of some single γ-ray lines. At energies < 500 keV the pulse distribution of the photoelectrons from absorbed backscattered photons coincides with the peak of the Compton electron distribution of the primary γ-ray line and thus the former cannot be measured directly. However, the increased backscatter effect and the corresponding variation of the pulse distribution caused by adding a thin disc of the mass ΔM of low atomic number to the part F of the photo-multiplier window can be studied. The pulse distribution of a single γ-ray line is recorded both with and without ΔM added. In (2) the only factor in the integrand depending on the mass of the window is $\exp\left(\mu_a' \frac{a}{2\cos\theta}\right)$. In each case the average of this factor within the actual range of θ can be estimated with sufficient accuracy. The unknown mass independent factor of $\int_F n_b\, dS$ is obtained from the measured difference between the two pulse distributions. Finally as the other factors of the integral are known the actual value of $\int_F n_b\, dS$ can be calculated. The error in $\int_F n_b\, dS$ caused by the approximate value of $\exp\left(\mu_a' \frac{a}{2\cos\theta}\right)$ mentioned above is probably less than ± 10 %.

The ratio $\frac{1}{n_p}\left[\int_F n_b\, dS\right]_p$ has been determined as described above using a NaI(Tl) crystal ⌀ 1.5×1.5 cm and an EMI 5311 photo-multiplier (*Fig. 4*). The entire photo-multiplier window was irradiated. The γ-ray lines Cr^{51} 330 keV, and Cs^{137} 662 keV were used. The point at 145 keV in *Fig. 4* is obtained from a direct analyse of the backscatter "peak" at about 100 keV of the Ce^{141} γ-ray line. A direct calculation of the backscatter of Cs^{137} 662 keV (Ba K x-rays

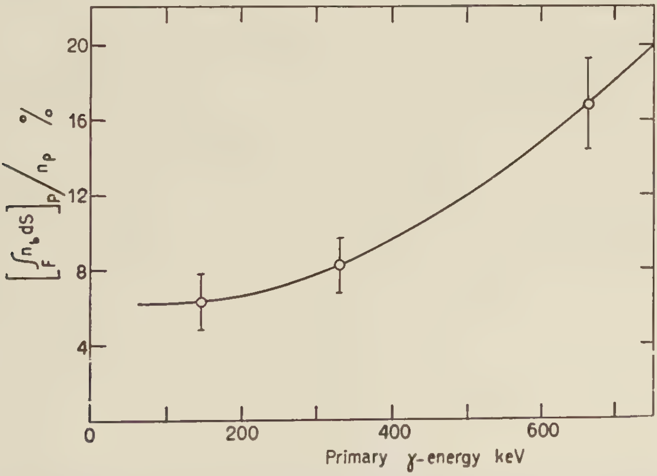

Fig. 4. Measured backscatter from the part of the photo-multiplier window outside the crystal; ratio of backscattered photons, effectively absorbed photoelectrically by the crystal, to the number of pulses in the primary photo-peak.

critically absorbed) from a measured pulse distribution similar to *Fig. 1* gives the same result as the method described above. The error in the backscatter fraction $\frac{1}{n_p}\left[\int\limits_F n_b\, dS\right]_p$ obtained from *Fig. 4*, may be about ±20 %.

The backscatter correction of a continuous spectrum is treated in Sect. IV.

d. Resolving power: the mounting of the crystal and the channel width

A detailed investigation of a continuous spectrum requires good resolving power of the experimental equipment. As to the scintillation spectrometer, the efficiency of the photo-cathode is the factor of greatest importance. This property is invariable for a particular multiplier and it is then necessary to collect and direct as much scintillation light as possible towards the photo-cathode. The crystal has to be cemented to the window and surrounded by an effective reflector, the walls of which must be sufficiently thin to avoid absorption of low energy photons. It is known that the resolving power can be improved by the application of a thin layer of magnesium oxide to the aluminium reflector and by roughening all the crystal surfaces except that adjacent to the window and/or coating them with a thin layer of magnesium oxide. NaI(Tl) crystals must be carefully protected from moisture by storing them in liquid paraffin or silicon oil or in a sealed container. Immediately before the crystal is mounted the crystal surfaces have to be carefully cleaned, e.g. with methylethyl ketone, in order to maintain the resolving power.

If rapid intensity variations in the spectrum investigated are expected, originating from γ-ray lines and absorption edges for example, the channel width must not be larger than one third of the half width for the actual energy (KELLEY 1952).

III. Absorption of γ-rays in a NaI crystal

a. Absorption processes

The scintillation spectrometry in the energy region under consideration (< 1 MeV) is based on the photoelectric absorption process for γ- and x-rays. This process is an interaction between a γ-ray photon with the energy E_γ and an iodine atom. The energy E_γ is transferred partly to the ejected photoelectron and partly to the ionized atom. The latter returns to its ground state by emission of characteristic x-rays and/or Auger electrons. If all the photoelectrons and the x-ray photons are absorbed within the crystal a scintillation arises, the size of which is proportional to the energy E_γ. However, not all the photoelectric absorption processes in NaI give this result. 80 % of these processes occur in the K-shell, and part of the emitted K x-ray photons escape from the crystal. A corresponding γ-ray photon is then recorded, on the average with an energy $E_\gamma - E_K$, where E_K is the mean value of the K x-ray lines (in iodine 29 keV) weighted according to their intensities. In the simple case with one single γ-ray line, this line is recorded as a photoelectric peak at E_γ and an escape-peak at $E_\gamma - E_K$. This K x-ray escape effect is treated in Sect. III c.

The limited dimensions of the crystal mean that certain photoelectrons, produced near the crystal surface, deliver only part of their energy to the crystal. The energy corresponding to such a pulse lies in the interval $0 - E_\gamma$. Der Mateosian & Smith (1952) calculated the magnitude of this electron escape effect in the case of a β-emitter homogeneously distributed in the crystal. Here the electrons are emitted isotropically and the electron ranges are small in relation to the dimension of the crystal. They also assumed that the electron paths were straight. However, the photoelectron distribution is not isotropic, but most of the electrons come off in forward directions, especially at high energies; e.g. at 400 keV the bipartition angle is 34° (Davisson & Evans (1952)). See further Sect. III b.

It is impossible experimentally to distinguish between the pulse distribution caused by the escaped photoelectrons and that caused by Compton electrons.

Some γ-ray photons interact with free electrons in Compton collisions the photon going off with decreased energy E_γ^C and the electron recoiling with the remaining energy $E^C = E_\gamma - E_\gamma^C$. The Compton scattered photon may either be absorbed within the crystal or escape. The spectral distribution of the Compton electrons for a single γ-ray energy can be calculated with the Klein-Nishina formula. However, if the scattered photon is photoelectrically absorbed in the crystal, it will together with the recoil electron cause one single scintillation corresponding to the energy E_γ. Then the photo-peak is increased by such processes, in this paper called *secondary photoelectric processes*, and the pulse distribution of the Compton electrons is correspondingly decreased. In what follows all processes involving absorption of a γ-ray photon E_γ and causing a scintillation corresponding to E_γ are regarded as *effective photoelectric processes.*

It appears from what is said above that the pulse distribution caused by the photoelectrons from a continuous γ-spectrum is distorted by other absorption processes occurring in NaI. On the one hand, the photoelectric peak will be increased by multiple processes, on the other the photoelectron distribution at lower energies will be overlapped by a Compton electron distribution and an escape electron distribution caused by γ-ray photons of higher energies. In order to determine the correct spectral distribution $N_0(E_\gamma)$ of the radiation incident on the crystal all pulses of the height ε, which are not caused by a γ-ray photon of the corresponding energy E_γ, must first be subtracted from the experimental pulse distribution. Once the effective photoelectric absorption coefficient of the crystal is known, the distribution $N_0(E_\gamma)$ can be calculated. For details see Sect. IV.

b. Electron escape

1. Escape of primary photoelectrons

In the volume element $\Delta S\,dx$ at a distance x from an arbitrary crystal surface S (i.e. making any angle with the incident beam), through which electrons escape (*Fig. 5*), $n_{pe}(E_0)\,\Delta S\,dx$ photoelectrons are produced per second. Here $n_{pe}(E_0)$ is the number of photoelectrons with energy $E_0 = E_\gamma - W_0$ produced per

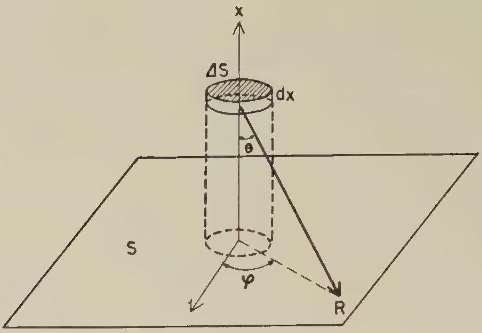

Fig. 5. Diagram for calculating the electron escape.

cm³ and second, E_γ is the energy of the primary photon and W_0 is the ionization energy of the iodine atom; 80 % of the photoelectric absorption processes occur in the K-shell where $W_0 = 33$ keV.

The number of electrons, ejected from $\Delta S\, dx$ in the solid angle $\sin\theta\, d\theta\, d\varphi$, is

$$n_{pe}(E_0)\, \Delta S\, dx\, g(\theta, \varphi, E_0) \sin\theta\, d\theta\, d\varphi \tag{4}$$

where $g(\theta, \varphi, E_0)$ is the distribution function for photoelectrons with energy E_0.

A fast electron first travels fairly straight in matter but as its energy decreases the deviation from the initial direction increases due to multiple scattering.

When the electron has penetrated a small thickness ξ the most probable scattering angle λ is, according to BOTHE (1933),

$$\lambda(E_0, \xi) = \frac{0.8\,(E_0 + m_0c^2)}{E_0(E_0 + 2m_0c^2)}\, Z \left(\frac{\varrho\,\xi}{A}\right)^{1/2}. \tag{5}$$

Here E_0 is given in MeV, ϱ is the density of the absorber and A its atomic weight. Thus λ first increases in proportion to $\xi^{1/2}$ but after sufficient scattering the distribution becomes diffuse. According to BLEULER and ZÜNTI (1946) diffusion sets in at $\lambda = 0.576$, giving $\xi = \xi_d$ in (5). The number of electrons penetrating a thickness ξ decreases continuously as ξ increases. In the diffusion region this occurs exponentially. The corresponding absorption cofficient α increases with increasing ξ due to the decreasing electron energy. If the probability of an electron penetrating the layer ξ is $p(E_0, \xi)$, we have

$$dp/p = -\alpha\, d\xi = -1.3\,(\lambda^2/\xi)\, d\xi \tag{6}$$

Using this relation one can calculate an average range R_0 of electrons with energy E_0. FOWLER, LAURITSEN, and LAURITSEN (1948) give the expression

$$R_0(E_0) = \int_0^{R_{\max}} p(E_0, \xi)\, d\xi \tag{7}$$

Here $R_{\max}$ is the total distance along the path of an electron. The absorption coefficients of aluminium as calculated from the scattering theory agree reasonably well with the experimental values, but for greater Z the theoretical results seem to be too high (BOTHE (1933)). Scattering but also $R_{\max}$ increases with increasing Z.

In a calculation of the electron escape effect in NaI crystals straight electron paths of the length R_0 are assumed. Since reliable values of R_0/ϱ for heavy elements are not available, aluminium data are used for NaI. Electrons which are emitted at the distance x from the surface S (*Fig. 5*) at an angle $\theta < \theta_1$, where $\theta_1 = \arccos\,(x/R_0)$, then escape. Concerning the angular distribution of the straight paths of the electrons two extreme cases must be considered: a) the directional distribution given by the theory of photoelectric processes and b) isotropic distribution. At higher energies case a) will give reliable results. At lower energies ξ_d is very small, giving diffusion immediately with no correlation to the initial directions of the photoelectrons (case b). At higher energies, however, where the values ξ_d and R_0 are of the same order of magnitude, the approximation b) is less accurate, since here a fairly large fraction of the escaping electrons has a range $< \xi_d$ within the crystal.

Case a) is treated in detail; calculations according to b) are also performed, using the method of DER MATEOSIAN & SMITH (1952). In *Table 1* the results of both methods are compared.

Assuming straight paths and isotropic distribution of the electrons DER MATEOSIAN & SMITH have shown that electrons of initial energy E_0 which escape from the crystal are degraded with equal probability into all energies below E_0. It can be shown that this is valid for electrons with an arbitrary angular distribution. In both cases n_{pe} of (4) has to be independent of x, and E_0 must be greater than about 200 keV, the specific energy loss being approximately constant.

In order to obtain the total number of photoelectrons, n_{esc}, escaping from an arbitrary surface S, (4) is first integrated with respect to φ and θ:

$$n_{\text{esc}} = \int_{x=0}^{R_0} n_{pe}\,\Delta S\,dx \int_{\varphi=0}^{2\pi}\int_{\theta=0}^{\theta_1} g(\theta,\varphi)\sin\theta\,d\theta\,d\varphi = \Delta S \int_{x=0}^{R_0} n_{pe}\,A\,dx. \qquad (8)$$

Here A denotes the fraction of the photoelectrons of energy E_0, emitted from $\Delta S\,dx$ within the cone of half-angle $\theta_1 = \arccos \dfrac{x}{R_0}$ and with the axis perpendicular to the crystal surface S.

For the surface S_2 through which the beam leaves the crystal, the calculation is performed for a collimated beam with the cross section ΔS. In this case, n_{pe} is obtained from the following equation:

$$n_{pe}\,\Delta S\,dx = n_0\,e^{-\mu(t-x)}\,\tau\,dx \qquad (9)$$

where n_0 is the number of photons per second, normally incident on the crystal surface S_1, and τ is the linear photoelectric absorption coefficient of NaI. The corresponding $A = A_1$ is equal to $M(\theta_1)$, $M(\alpha)$ being the fraction of photoelectrons, emitted in the cone of half-angle α and with the axis parallel to the incident beam. $M(\alpha)$ is given by DAVISSON & EVANS (1952), Fig. 22, where $N_\theta \equiv M(\alpha)$. With these values inserted in (8), n_{esc} is obtained by numerical integration.

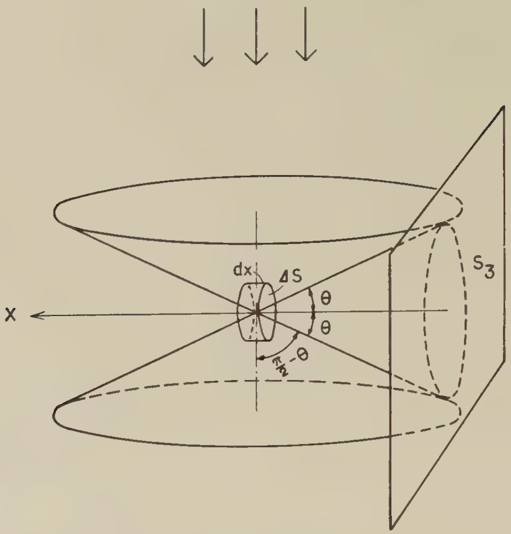

Fig. 6. Diagram for calculating the electron escape from the side surface S_3 of the crystal.

If the primary beam covers the whole crystal, photoelectrons can escape through the side surfaces of the crystal, too. When calculating n_{esc} for a side surface $S_3 = tl$ (*Fig. 6*), all photoelectric processes G in $S_3\,dx$ are assumed to take place in the small cylinder $\Delta S\,dx$, whose axis passes perpendicularly through the centre of S_3.

$$G = \frac{n_0}{S_1}\,l\,dx\,(1-e^{-\mu t})\,\frac{\tau}{\mu}. \tag{10}$$

In (8) the number of photoelectric processes $n_{pe}\,\Delta S\,dx$ in $\Delta S\,dx$ is replaced by G. The fraction $M\left(\frac{\pi}{2}+\theta_1\right) - M\left(\frac{\pi}{2}-\theta_1\right)$ of all the photoelectrons from the volume element $\Delta S\,dx$ is emitted outside the double cone of half-angle $\left(\frac{\pi}{2}-\theta_1\right)$. The fraction $\frac{1-\cos\theta_1}{2\sin\theta_1}$ of these photoelectrons is emitted within the cone of half-angle θ_1. This gives:

$$A = A_2 = \frac{1-\cos\theta_1}{2\sin\theta_1}\left[M\left(\frac{\pi}{2}+\theta_1\right) - M\left(\frac{\pi}{2}-\theta_1\right)\right].$$

n_{esc} is obtained by numerical integration of (8) with these values inserted.

The escape factor P for primary photoelectrons for the entire crystal, i.e. the number of escape electrons $\sum n_{esc}$ per pulse in the photo-peak, is calculated for a cylindrical crystal with radius r. In (10) l has to be replaced by $2\pi r$ and S_1 is equal to πr^2.

$$P = \frac{\sum n_{esc}}{n_p} = \tau\,\frac{n_0}{n_p}\int_0^{R_0} e^{-\mu(t-x)} A_1\,dx + \frac{2}{r}\,(1-e^{-\mu t})\,\frac{\tau\,n_0}{\mu\,n_p}\int_0^{R_0} A_2\,dx \tag{11 a}$$

where n_p is the number of pulses in the photo-peak.

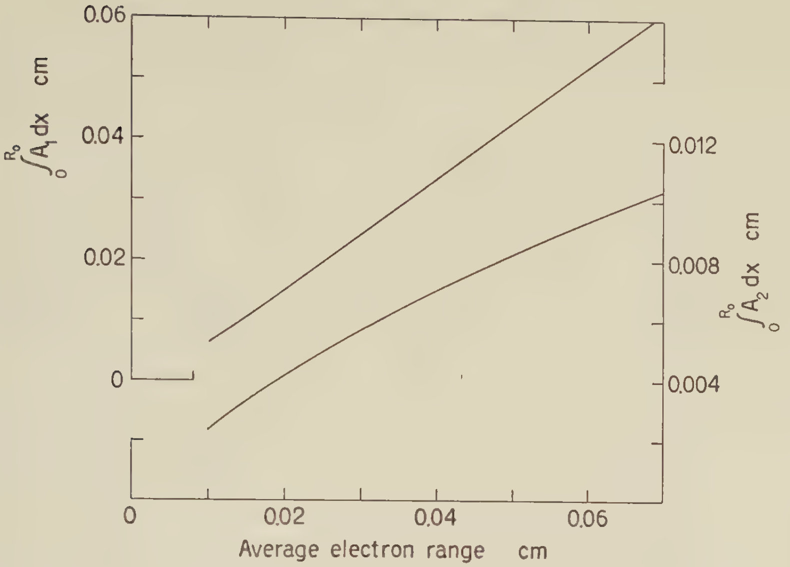

Fig. 7 a. The factors $\int_0^{R_0} A_1\,dx$ and $\int_0^{R_0} A_2\,dx$ in (11) used in the calculation of the electron escape fractions.

If R_0 be negligible in relation to t one obtains

$$P = \tau e^{-\mu t} \frac{n_0}{n_p} \int_0^{R_0} A_1\,dx + \frac{2}{r}\left(1 - e^{-\mu t}\right) \frac{\tau}{\mu} \frac{n_0}{n_p} \int_0^{R_0} A_2\,dx. \tag{11 b}$$

Here the escape of photoelectrons from the surface, entered by the beam, is not taken into account. This assumption is permissible, because the photoelectrons are ejected mainly in the forward direction.

$\int_0^{R_0} A_1\,dx$, $\int_0^{R_0} A_2\,dx$ and P as functions of R_0 and E_γ respectively for a crystal ⌀ 1.5×1.5 cm is shown in *Fig. 7 a* and *7 b*. The different parts of P are given in *Table 1*, where S_3 is the cylindrical surface of the crystal.

Table 1. Escape fractions of primary photoelectrons for a NaI crystal ⌀ 1.5×1.5 cm assuming the directional distribution of the electrons: a) as given by the theory of photoelectric processes; b) as isotropic.

E keV	$(n_{esc})_{S_1}/n_p$, %		$(n_{esc})_{S_2}/n_p$, %		$(n_{esc})_{S_3}/n_p$, %	
	a	b	a	b	a	b
500	0	0.3	0.6	0.2	0.8	1.0
1000	0	0.7	1.9	0.5	1.5	2.5

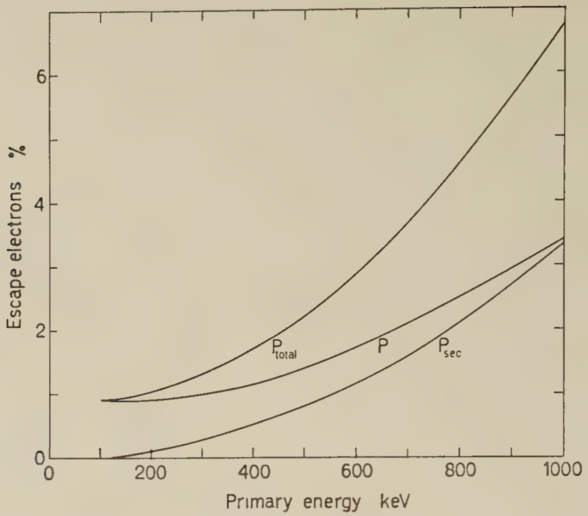

Fig. 7 b. Per cent escape electrons per pulse in the photoelectric peak for a NaI crystal ∅ 1.5 × 1.5 cm. P is the part due to primary photoelectric processes, P_{sec} the part due to secondary photoelectric processes and $P_{\text{total}} = P + P_{\text{sec}}$.

2. Escape of electrons contributing to secondary photoelectric pulses

In the volume element $\Delta S\,dx$ (*Fig. 5*), $n_{ce}\Delta S\,dx$ Compton electrons, contributing to the photo-peak, i.e. the corresponding Compton photon is completely absorbed in the crystal (in the following the abbreviation *sp-Compton electrons* is used) are produced by primary photons with energy E_γ. In the solid angle $\sin\theta\,d\theta\,d\varphi$ the following number of sp-Compton electrons is ejected:

$$n_{ce}\,\Delta S\,dx\,h(\theta,\varphi)\,\sin\theta\,d\theta\,d\varphi \tag{12}$$

where $h(\theta,\varphi)$ is the distribution function for such electrons. From a cylinder with the base ΔS, n'_{esc} sp-Compton electrons escape through S.

Provided that the primary beam leaves the crystal perpendicularly to the escape surface S_2, θ is the angle between the primary beam and the Compton electron direction. Integrating (12) one obtains $(n'_{\text{esc}})_{S_2}$:

$$(n'_{\text{esc}})_{S_2} = \int_{\theta=0}^{\pi/2}\int_{\varphi=0}^{2\pi}\int_{x=0}^{R_0(\theta)\cos\theta} n_{ce}\,\Delta S\,h(\theta)\,\sin\theta\,d\theta\,d\varphi\,dx \tag{13}$$

where $R_0(\theta)$ is the average range in NaI of a Compton electron in the direction θ. As R_0 is small in relation to the thickness of the crystal, n_{ce} is almost independent of x. Here h is independent of φ and proportional to the product of the number of electrons in the direction θ (Klein-Nishina formula) and the probability that the corresponding Compton photon is completely absorbed in the crystal. From simple geometrical considerations this probability can be calculated for a collimated beam passing through the centre of the crystal surface S_2. For the actual crystal ∅ 1.5×1.5 cm one obtains the values of $(n'_{\text{esc}})_{S_2}/n_p$ given in *Table 2*. This result is also approximately valid for a beam irradiating the entire crystal.

The escape of sp-Compton electrons through a crystal surface S_3, parallel to the incident beam can be calculated in a similar way. However, this calculation is more complicated as h in this case is a function of φ. $(n'_{\text{esc}})_{S_3}$ can be obtained with sufficient accuracy from a calculation of the volume of the thin layer of the crystal from which Compton electrons with the direction θ (corresponding energy E) can escape. It can be shown that the fraction $1/\pi$ of the Compton electrons produced in the layer escapes. The thickness of this layer is almost independent of the Compton electron energy for a certain value of E_γ. It follows that the fraction q of the Compton electrons with the energy E which escape is roughly independent of E. A mean value of q is used in the calculation of the number $(n'_{\text{esc}})_{S_3}$ of sp-Compton electrons which escape.

For the actual crystal ∅ 1.5×1.5 cm one obtains the values of $(n'_{\text{esc}})_{S_3}/n_p$ given in *Table 2*.

Escape of photoelectrons, produced by photoelectric absorption of Compton photons is here calculated assuming isotropic distribution of the electrons and using an estimated mean value of the Compton photon energy. This electron escape effect, n''_{esc}, contributes only slightly to the total electron escape factor, P_{total}.

For a crystal ∅ 1.5×1.5 cm one obtains the values of n''_{esc}/n_p given in *Table 2*.

Table 2. Escape fractions of electrons contributing to secondary photoelectric pulses for a NaI crystal ∅ 1.5×1.5 cm.

E keV	$(n'_{\text{esc}})_{S_2}/n_p$, %	$(n'_{\text{esc}})_{S_3}/n_p$, %	n''_{esc}/n_p, %
500	0.3	0.2	0.3
1 000	2.5	0.5	0.4

Fig. 7 b shows $P_{\text{sec}} = \dfrac{(n'_{\text{esc}})_{S_2} + (n'_{\text{esc}})_{S_3} + n''_{\text{esc}}}{n_p}$ and also $P_{\text{total}} = P + P_{\text{sec}}$.

c. *K* x-ray escape

The K-escape factor $f(E_\gamma)$ for a crystal surface is defined as

$$f(E_\gamma) = \frac{n^K_{\text{esc}}(E_\gamma)}{n_0(E_\gamma)} \tag{14}$$

where $n_0(E_\gamma)$ is the number of incident photons with the energy E_γ and $n^K_{\text{esc}}(E_\gamma)$ is the corresponding number of K x-ray photons escaping through the surface in question.

$f(E_\gamma) = f_1(E_\gamma)$ is first calculated for the surface S_1 on which a collimated beam with the cross section ΔS is normally incident. The calculation is valid for a surface, the linear dimensions of which are large compared with the mean free path of the K x-rays of iodine. In the volume element $\Delta S\,dx$ at the distance x from S_1, $d n_0$ photons are absorbed in photoelectric processes in the K-shell:

$$d n_0 = n_0 e^{-\mu x} \tau \delta_K d x. \tag{15}$$

Here δ_K is the fraction of the photoelectric processes taking place in the K-shell. A number $d n_{\text{esc}}^K$ of the K x-ray photons, emitted in $\Delta S\,dx$, escape from the crystal surface

$$d n_{\text{esc}}^K = \omega_K d n_0 \frac{1}{2} \int_0^{\pi/2} \exp\left(-\mu_K \frac{x}{\cos\theta}\right) \sin\theta\, d\theta \tag{16}$$

where μ_K is the linear absorption coefficient of the K x-rays of iodine and ω_K the K-fluorescence yield of iodine. $\pi-\theta$ is the angle between the direction of the K x-ray photon and the beam. From (16) one obtains

$$n_{\text{esc}}^K = \int_{x=0}^{t} d n_{\text{esc}}^K \tag{17}$$

where t is the thickness of the crystal. When integrating, t may be replaced by ∞, as $d n_{\text{esc}}^K$ is very small when $x > 0.5$ cm. $f_1(E_\gamma)$ is obtained from (14):

$$f_1(E_\gamma) = \frac{1}{2} \omega_K \delta_K \frac{\tau}{\mu} \left[1 - \frac{\mu_K}{\mu} \ln\left(1 + \frac{\mu}{\mu_K}\right)\right]. \tag{18}$$

BURHOP (1952) gives the value $\omega_K = 0.84$. A good mean value of δ_K is 0.80 (HALL (1936), LATYSHEW (1947), HEDGRAN & LIND (1952)). As μ_K is essentially different for the K_α- and K_β-groups, the calculations of $f_{1\alpha}$ and $f_{1\beta}$ have been performed with the following values of the mean energy E_{K_α} and E_{K_β} of these groups, and the corresponding linear absorption coefficients:

$$E_{K_\alpha} = 28.6 \text{ keV} \qquad \mu_{K_\alpha} = 24.3 \text{ cm}^{-1}$$

$$E_{K_\beta} = 32.5 \text{ keV} \qquad \mu_{K_\beta} = 17.1 \text{ cm}^{-1}.$$

Fig. 8 shows $f_{1\alpha}$, $f_{1\beta}$ and f_1, where the intensity ratio $K_\alpha : K_\beta = 100:26$ has been used in calculating f_1.

At higher energies, K x-rays escape also from the surface through which the beam leaves the crystal. The escape factor f_2 of this surface is always less than f_1. A calculation similar to that of f_1 gives:

$$f_2 = \frac{1}{2} \omega_K \delta_K e^{-\mu t} \frac{\tau}{\mu} \left[\frac{\mu_K}{\mu} \ln \frac{\mu_K}{\mu_K - \mu} - 1\right]. \tag{19 a}$$

At energies above 200–300 keV,

$$f_2 = f_1 e^{-\mu t} \tag{19 b}$$

is a good approximation.

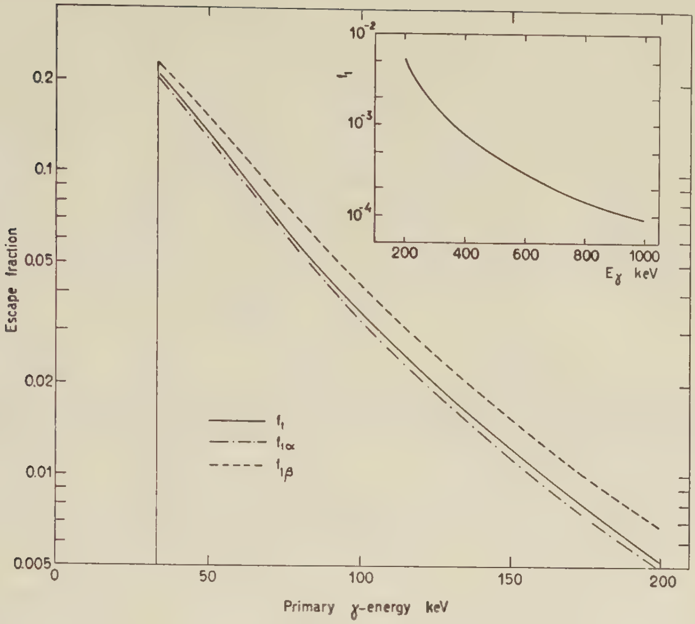

Fig. 8. K_α and K_β x-ray escape fractions $f_{1\alpha}$ and $f_{1\beta}$ as calculated from (18), i.e. the number of K x-ray photons escaping per incident photon, for the surface entered by the beam, and their weighted mean value f_1.

The ratio of the number of pulses degraded by escape through the surface S_2 to the number of pulses in the photo-peak, $f_2 \dfrac{n_0}{n_p}$, is less than 0.5 % for $E_\gamma < 1$ MeV and the crystal thickness $t > 0.5$ cm. See also *Table 3.*

If the whole crystal is irradiated by the beam, K x-rays escape through the side surface too. $f_3(E)$ of the surface S_3 in *Fig. 9* is calculated as follows. In the volume element $l \times t \times dy$, dn_0 photons of the energy E are photoelectrically absorbed in the K-shell

$$d n_0 = \int_{x=0}^{t} \frac{n_0}{S_1}\, l\, d y\, e^{-\mu x}\, \tau\, \delta_K\, d x. \tag{20}$$

(20) inserted in (16) gives $d n_{\text{esc}}^{K}$ and thus $f_3(E)$ with the same approximation as above, i.e. all the photoelectric processes are assumed to take place near the centre of the surface, the linear dimensions of which are assumed to be much greater than the mean free path of the K x-rays.

$$d n_{\text{esc}}^{K} = \frac{l n_0}{S_1}\, \omega_K \delta_K \frac{\tau}{\mu}\left(1 - e^{-\mu t}\right) \frac{1}{2} \int_{y=0}^{d} \int_{\theta=0}^{\pi/2} \exp\left(-\mu_K \frac{y}{\cos\theta}\right) d y \sin\theta\, d\theta. \tag{21}$$

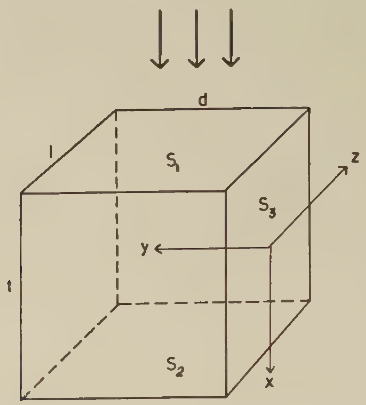

Fig. 9. Diagram for the calculation of the K x-ray escape fraction for the side surface of the crystal.

If $d > 0.5$ cm the value of the integral in (21) is $\frac{1}{2\mu_K}$, which gives

$$f_3(E_\gamma) = \frac{1}{4d}\,\omega_K \delta_K \frac{\tau}{\mu\,\mu_K}(1 - e^{-\mu t}). \tag{22 a}$$

For a cylindric crystal with $S_1 = \pi r^2$ and $l = 2\pi r$, the escape fraction f_3 for the cylindric surface is given by:

$$f_3 = \frac{1}{2r}\,\omega_K \delta_K \frac{\tau}{\mu\,\mu_K}(1 - e^{-\mu t}) \tag{22 b}$$

which is valid with good accuracy if $r > 0.5$ cm.

For a NaI(Tl) crystal ⌀ 1.5×1.5 cm the ratio of escape pulses caused by K-escape through the cylindrical surface S_3 to the number of pulses in the photo-peak, $\frac{f_3 n_0}{n_p}$, is given in *Table 3.*

Photoelectric absorption of scattered photons from Compton processes in the crystal also gives rise to K x-ray emission. As the secondary photoelectric absorption contributes appreciably to the photo-peak only at higher energies ($E_\gamma > 200$ keV), the corresponding escape factor f_{sec} is calculated as if the photoelectric absorption processes of scattered photons were equally spaced in the crystal. f_{sec} is defined as

$$f_{\text{sec}} = \frac{{}^*n^K_{\text{esc}}}{n_0} = \frac{{}^*n^K_{\text{esc}}}{n_{\text{sec}}} \times \frac{n_{\text{sec}}}{n_0} \tag{23 a}$$

where n_{sec} is the total number of secondary photoelectric processes in the crystal and ${}^*n^K_{\text{esc}}$ the total number of K x-ray photons escaping from the crystal after being emitted in such processes. The calculation gives

$$f_{\mathrm{sec}} = \frac{\omega_K \delta_K}{4\mu_K} \times \frac{\sum S}{V} \times \frac{n_{\mathrm{sec}}}{n_0} \tag{23 b}$$

where $\sum S$ is the entire surface of the crystal and V the volume of the crystal. *Table 3* shows some values of $f_{\mathrm{sec}} \frac{n_0}{n_p}$ for a crystal ⌀ 1.5 × 1.5 cm.

The total escape factor $F(E_\gamma)$ is defined as the ratio of the total number of escaped K x-ray photons to the number of effective photoelectric processes.

$$F(E_\gamma) = (f_1 + f_2 + f_3 + f_{\mathrm{sec}})\, n_0/n_p. \tag{24}$$

F for a cylindrical crystal ⌀ 1.5 × 1.5 cm is given in *Table 3*.

Above, the escape factor has been calculated for large surfaces and collimated beams. For finite crystals entirely within the beam the values calculated above must be corrected for the edge effect. An analysis shows that the value of the total theoretical escape factor is a little too large. For example, with a cubic crystal of 1 cm³ and $E_\gamma = 33.2$ keV the correction is −8 %. It decreases with increasing energy and crystal size.

Table 3. The number of K x-ray photons escaped per pulse in the photo-peak for a NaI(Tl) crystal ⌀ 1.5 × 1.5 cm. f_1, f_2, f_3 refer to K-escape from true photoelectric processes, through the top, bottom and side surfaces respectively. f_{sec} refers to the total K-escape in secondary photoelectric processes. F is the sum of the different escape fractions.

E_γ keV	50	200	500	1000
$f_1 \frac{n_0}{n_p}$	0.134	0.008	0.004	0.004
$f_2 \frac{n_0}{n_p}$	0.000	0.001	0.002	0.003
$f_3 \frac{n_0}{n_p}$	0.020	0.015	0.011	0.011
$f_{\mathrm{sec}} \frac{n_0}{n_p}$	0.000	0.008	0.014	0.012
F	0.154	0.032	0.031	0.030

IV. Evaluation of the continuous γ-spectrum from the observed pulse height distribution

It is clear from the preceding sections that the experimental pulse height distribution $N_{\mathrm{exp}}(\varepsilon)$, where ε is the pulse height, must be subjected to a series of corrections before the true radiation spectrum is obtained. A survey of these calculations is given in this section.

a. Electronic apparatus

A dead-time (τ) in the pulse analyzer causes coincidence losses. The input pulse rate R is calculated according to the formula $R = \frac{R_{\exp}}{1 - R_{\exp}\tau}$, where $R_{\exp}$ is the observed counting rate.

If the resolving power has been reduced by the use of a channel width larger than the maximum value given in Sect. II d but still smaller than the half width of a single γ-ray line, then the pulse height distribution can be corrected accordingly. The interval between the experimental points must not be larger than the channel width. The true pulse height distribution is first estimated and the expected counting rates for the channels used are calculated. This estimation is then adjusted until the calculated counting rates are equal to the experimental ones.

b. Background

The background counting rate measured with removed source is subtracted.

c. Energy resolution

Because of the statistical nature of the emission of electrons from the cathode and the dynodes of the photo-multiplier the scintillations ε_γ of a γ-ray line are recorded as a Gaussian pulse-height distribution $g(\varepsilon)$:

$$g(\varepsilon) = (2\pi K \varepsilon_\gamma)^{-\frac{1}{2}} \exp\left[-\frac{(\varepsilon_\gamma - \varepsilon)^2}{2K\varepsilon_\gamma}\right]. \tag{25}$$

The constant K and the experimentally observable half widths $2W(\varepsilon_\gamma)$ are related by

$$K = W^2(\varepsilon_\gamma)/2\varepsilon_\gamma \ln 2. \tag{26}$$

The value of K depends mainly on the photoelectric conversion efficiency of the cathode. To obtain the correct "scintillation distribution", $N_3(\varepsilon_\gamma)$, the pulse height distribution $N_2(\varepsilon)$, corrected according to Sect. IV a, b, must be corrected for the limited resolution of the apparatus. The following relation holds:

$$N_2(\varepsilon) = \int_0^\infty \frac{N_3(\varepsilon_\gamma)}{(2\pi K \varepsilon_\gamma)^{1/2}} \exp\left[-\frac{(\varepsilon_\gamma - \varepsilon)^2}{2K\varepsilon_\gamma}\right] d\varepsilon_\gamma. \tag{27}$$

According to MORTON (1952) series expansion and integration using suitable approximations give a fairly simple expression:

$$N_3(\varepsilon_\gamma) = N_2(\varepsilon) - \frac{K\varepsilon}{4} \times \frac{d^2 N_2(\varepsilon)}{d\varepsilon^2}. \tag{28}$$

This expression is valid in case of good resolution, i.e. at high energies.

The difficulties at lower energies can be avoided by numerical evaluation of the integral (27) in the following way. A first approximation $N_3(\varepsilon_\gamma)^{\mathrm{I}}$ for $N_3(\varepsilon_\gamma)$ is estimated directly from $N_2(\varepsilon)$ (or simply N_2 may be used). A point on the corresponding $N_2(\varepsilon)^{\mathrm{I}}$ is calculated by numerical integration of (27). The Gaussian distribution $(2\pi K\varepsilon_\gamma)^{-\frac{1}{2}} \exp\left[-\frac{(\varepsilon_\gamma-\varepsilon)^2}{2K\varepsilon_\gamma}\right]$ is multiplied point by point by $N_3(\varepsilon_\gamma)^{\mathrm{I}}$. The area below the curve thus obtained, is calculated. This gives *one* point on $N_2(\varepsilon)^{\mathrm{I}}$. In this way a sufficient number of points on $N_2(\varepsilon)^{\mathrm{I}}$ are determined. If now $N_2(\varepsilon)^{\mathrm{I}}$ does not coincide with $N_2(\varepsilon)$ the approximation $N_3(\varepsilon_\gamma)^{\mathrm{I}}$ has to be improved to $N_3(\varepsilon_\gamma)^{\mathrm{II}}$ with knowledge of the difference $N_2(\varepsilon)-N_2(\varepsilon)^{\mathrm{I}}$. This procedure is repeated till $N_2(\varepsilon)^n \equiv N_2(\varepsilon)$. Then $N_3(\varepsilon_\gamma)^n = N_3(\varepsilon_\gamma)$. Observations made show that two successive approximations are practically always sufficient to determine $N_3(\varepsilon_\gamma)$ with sufficient accuracy.

d. Compton and escape electrons

If $n_0(E_\gamma)$ photons with the energy E_γ are incident on the crystal, a certain number $n_p(E_\gamma)$ transfer all their energy to the crystal (i.e. effective photoelectric absorption). Then $\varepsilon_p = \text{const} \times E_\gamma$ holds for the corresponding pulse height ε_p. Furthermore, $n_e(E_\gamma)$ photons give rise to pulses $\varepsilon_e < \varepsilon_p$ (escape and Compton electrons). Here the K-escape effect is neglected. The maximum energy of the Compton scattered electron, E_γ^*, is given by:

$$E_\gamma^* = \frac{2E_\gamma^2}{m_0c^2\left(1+2\frac{E_\gamma}{m_0c^2}\right)}. \tag{29}$$

The expressions for n_p and n_e are:

$$n_p = n_0(E_\gamma)(1-e^{-\mu t})\,k(E_\gamma) \tag{30}$$

$$n_e = n_0(E_\gamma)(1-e^{-\mu t})(1-k(E_\gamma)) \tag{31}$$

where μ is the total linear absorption coefficient of NaI and t is the thickness of the crystal. If the electron escape and the absorption in the crystal of Compton scattered photons could be neglected, $k(E_\gamma)$ and $1-k(E_\gamma)$ would have the values $\frac{\tau}{\mu}$ and $\frac{\sigma}{\mu}$ respectively, where τ and σ are the linear photoelectric and linear Compton absorption coefficients of NaI respectively. The actual value of $k(E_\gamma)$ can be determined from the experimental pulse height distribution of a number of single γ-ray lines in the energy region of interest, 100–1000 keV. (30) and (31) give:

$$k(E_\gamma) = \frac{n_p(E_\gamma)}{n_p(E_\gamma)+n_e(E_\gamma)} \tag{32}$$

Then $n_p(E_\gamma)$ is equivalent to the area of the observed photo-peak and $n_e(E_\gamma)$ is equivalent to the area of the remainder of the pulse height distribution (Compton and escape electrons). When determining $k(E_\gamma)$ it is necessary to use such isotopes, from which it is possible to obtain, either directly or by critical absorption, a single γ-ray line incident on the crystal. The following γ-ray lines have been used in this investigation: Ce^{141} 145 keV, Hg^{203} 280 keV, Cr^{51} 330 keV, Au^{198} 412 keV, Cs^{137} 662 keV and Rb^{86} 1080 keV. *Fig. 1* shows a record of the Cs^{137} γ-ray line with a NaI crystal ⌀ 1.5 × 1.5 cm, 10 cm distance between the source and the crystal and a lead diaphragm, 17 mm thick and with a hole of ⌀ 24 mm, half way between source and crystal. Here no additional filters were used. Determination of $n_e(E_\gamma)$ from this special diagram is difficult, as the Compton electron distribution is overlapped by the K x-rays of barium at 30 keV and distorted by the backscatter peak at about 210 keV. However, the K x-rays from Ba can be critically absorbed, the backscatter peak can be subtracted from the curve (see Sect. II), and, since the high energy part of the Compton electron distribution is undistorted, the curve can be determined with sufficient accuracy. The determination of $n_e(E_\gamma)$ for Au^{198} 412 keV, Cr^{51} 330 keV and Hg^{203} 280 keV is more difficult, because the backscatter is superimposed mainly along the peak of the Compton electron distribution. However it is possible to make a satisfactory correction for this backscatter disturbance according to the method described in Sect. II. Finally, the non-availability of a convenient γ-ray line at about 200 keV is unfortunate, because here the $k(E_\gamma)$ curve is fairly steep.

Fig. 10 shows $k(E_\gamma)$ experimentally determined for a crystal ⌀ 1.5 × 1.5 cm With this curve, $k(E_\gamma)$ can be estimated with an accuracy of ±5 %.

So far only the absorption of single γ-ray lines has been discussed.

In the treatment of a continuous γ-ray spectrum, the following definitions are now used. On the crystal, $N_0(E_\gamma)\,dE_\gamma$ photons with energies between E_γ and $E_\gamma + dE_\gamma$ are incident. $N_p(E_\gamma)\,dE_\gamma$ photons are recorded as photoelectric pulses and $N_e(E_\gamma)\,dE_\gamma$ photons are to be found in the corresponding continuum

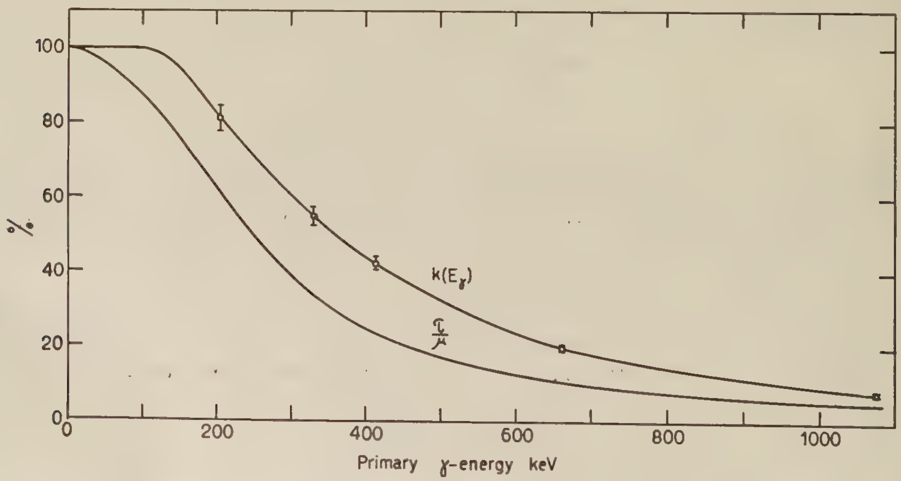

Fig. 10. The experimental ratio $k(E_\gamma)$ of photo-peak pulses to the total number of pulses, NaI(Tl) ⌀ 1.5 × 1.5 cm. The point at 200 keV is calculated theoretically. For comparison $\frac{\tau}{\mu}$ is also given.

of Compton and escape electrons. The probability that such an electron, produced by a γ-ray photon of energy E_γ has an energy between E and $E+dE$ is put equal to $C(E, E_\gamma)dE$. In the continuum of Compton and escape electrons, superimposed on N_p, the total number of electrons with energies between E and $E+dE$ is $N_c(E)dE$. It follows that

$$N_c(E)=\int_0^\infty C(E, E_\gamma)N_e(E_\gamma)dE_\gamma. \tag{33}$$

In the calculation of $N_c(E)$ the functions $C(E, E_\gamma)$ may be approximated with:

$$\left.\begin{aligned} &C(E, E_\gamma)=C(E_\gamma)=\frac{1}{E_\gamma^*} && 0<E<E_\gamma^* \\ &C(E, E_\gamma)=C(E_\gamma)=0 && E>E_\gamma^*. \end{aligned}\right\} \tag{34}$$

This approximation gives sufficient accuracy because: firstly, the escape electrons are few in relation to the Compton electrons (Sect. III b); secondly, the actual functions $C(E, E_\gamma)$ are smoothed out at the high energy end compared to the functions, calculated according to the Klein-Nishina formula, because the corresponding scattered photons with low energy are readily absorbed within the crystal. This absorption together with the Compton electron thus gives rise to a pulse, falling within the photo-peak.

For the distribution N_3 obtained in Sect. IV c, the following expression holds:

$$N_3(E)=N_c(E)+N_p(E) \tag{35}$$

$N_c(E)$ is obtained from (33) by numerical integration. $N_e(E_\gamma)$ is obtained from (30) and (31), giving:

$$N_e(E_\gamma)=N_p(E_\gamma)\frac{1-k(E_\gamma)}{k(E_\gamma)} \tag{36}$$

$N_c(E)$ is zero for $E^*_{\gamma\,\max}<E<E_{\gamma\,\max}$, $E_{\gamma\,\max}$ being the maximum energy of the investigated γ-ray spectrum. Then (35) gives $N_3(E)=N_p(E)$ in this energy interval. $N_c(E)$ for $E^{**}_{\gamma\,\max}<E<E^*_{\gamma\,\max}$ is given by (33) with (36) inserted. Now $N_p(E)$ can be calculated from (35) in this interval. This procedure is then repeated throughout the spectrum.

e. *K* x-ray escape

Now the distribution $N_p(E)$ obtained above is corrected for the effect of the K x-ray escape. The following expression is valid:

$$N_p(E)=N_4(E)[1-F(E)]+N_4(E+E_K)F(E+E_K). \tag{37}$$

Here N_4 is the distribution corrected for K x-ray escape and E_K the mean value of the energies of the K x-rays of iodine. N_4 is obtained from (37):

$$N_4(E) = \frac{N_p(E) - N_4(E+E_K)\,F(E+E_K)}{1-F(E)}. \tag{38}$$

When carrying out the calculation of N_4 one starts with the high-energy end of the spectrum where $N_4(E+E_K)=0$. At energies near E_K the influence of the limited resolving power must be considered.

f. Backscatter

If N_5 is the pulse distribution corrected for the backscatter and N_β the distribution of the absorbed, backscattered γ-ray photons, then

$$N_4 = N_5 + N_\beta.$$

The probability that a backscattered photon of primary energy E_γ will give a pulse between E and $E+dE$, is $B(E, E_\gamma)\,dE$. From Sect. II c one then obtains

$$N_\beta(E) = \int_0^\infty B(E, E_\gamma)\left[\frac{1}{n_p}\int_S n_b\,dS\right] N_p(E_\gamma)\,dE_\gamma. \tag{39}$$

(39) is integrated numerically. Approximately, $B(E, E_\gamma)$ is taken equal to zero for $E<E_1$ and $E>E_2$ and equal to the straight line

$$B = \frac{2}{(E_2-E_1)^2}(E_2-E); \qquad E_1 \leqq E \leqq E_2 \tag{40}$$

where E_1 and E_2 are the energies of photons of primary energy E_γ scattered at 180° and 90° respectively. The distribution $B_{S_1}(E, E_\gamma)$ for photons scattered

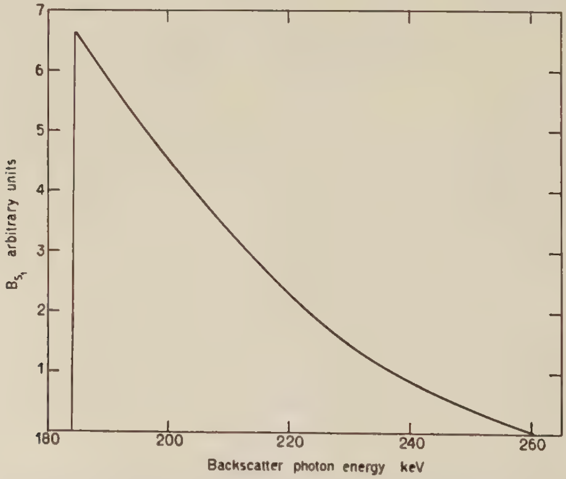

Fig. 11. Calculated spectral distribution of the effectively photoelectrically absorbed photons, which have been scattered from that part of the photo-multiplier window, covered by the crystal, ⌀ 1.5 × 1.5 cm; primary γ-energy 662 keV.

from that part S_1 of the photo-multiplier window, which is covered by the crystal is shown in *Fig. 11* for $E_\gamma = 662$ keV and a NaI(Tl) crystal ⌀ 1.5 × 1.5 cm. The distribution $B_F(E, E_\gamma)$ of the photons scattered from the part F of the window outside the crystal has a similar shape. However, at the high energy end B_F is somewhat larger than B_{S_1}.

g. γ-detection and geometrical efficiency of the crystal

In the case of narrow beam geometry the spectral distribution of the radiation normally incident on the crystal is obtained directly from the photoelectric efficiency of the crystal according to (30). If the entire crystal surface $S_1 = \pi r^2$ is irradiated from a source at a distance L, (30) has to be generalized with respect to the divergence of the beam. Low energy photons are absorbed close to S_1, while the absorption processes of high energy photons are approximately equally distributed throughout the entire crystal, i.e. the effective solid angle of the crystal decreases with increasing energy E_γ. Then $N_p(E_\gamma)$ is obtained from the following expression using polar coordinates with origo in the source:

$$N_p(E_\gamma) = \iiint\limits_V \frac{d N_S}{d\Omega} \sin\theta \, d\theta \, d\varphi \, e^{-\mu(\varrho \quad \varrho_1)} \mu \, d\varrho \, k(E_\gamma). \tag{41 a}$$

Here the integral is taken over the entire volume V of the crystal. ϱ_1 is the radius vector of a photon entrance point of the crystal and $\dfrac{d N_S(E_\gamma, \theta, \varphi)}{d\Omega} dE_\gamma$ is the number of photons emitted from the source in the energy interval between E_γ and $E_\gamma + dE_\gamma$ per unit solid angle in the direction θ, φ. If the solid angle subtended by the crystal is small, (41 a) gives:

$$N_p(E_\gamma) = \frac{d N_S}{d\Omega} k(E_\gamma) \int\limits_0^t \frac{S_1}{(x+L)^2} e^{-\mu x} \mu \, dx \tag{41 b}$$

where x is the distance from S_1. That part $N_0(E_\gamma) dE_\gamma$ of $N_S(E_\gamma) dE_\gamma$ irradiating the crystal surface S_1 is:

$$N_0(E_\gamma) = \frac{d N_S}{d\Omega} \frac{S_1}{L^2}. \tag{42}$$

Partial integration of (41 b) then gives:

$$N_p(E_\gamma) = N_0(E_\gamma) k(E_\gamma) \mu L^2 \left[\frac{1}{L} - \frac{e^{-\mu t}}{t+L} - \mu e^{-\mu L} \int\limits_{\mu L}^{\mu(L+t)} \frac{e^{-x}}{x} dx \right] =$$

$$= N_0(E_\gamma) k(E_\gamma) D(E_\gamma, L, t). \tag{41 c}$$

The exponential integral $-Ei(-a) = \int\limits_a^\infty \dfrac{e^{-x}}{x} dx$ is obtained from numerical tables.

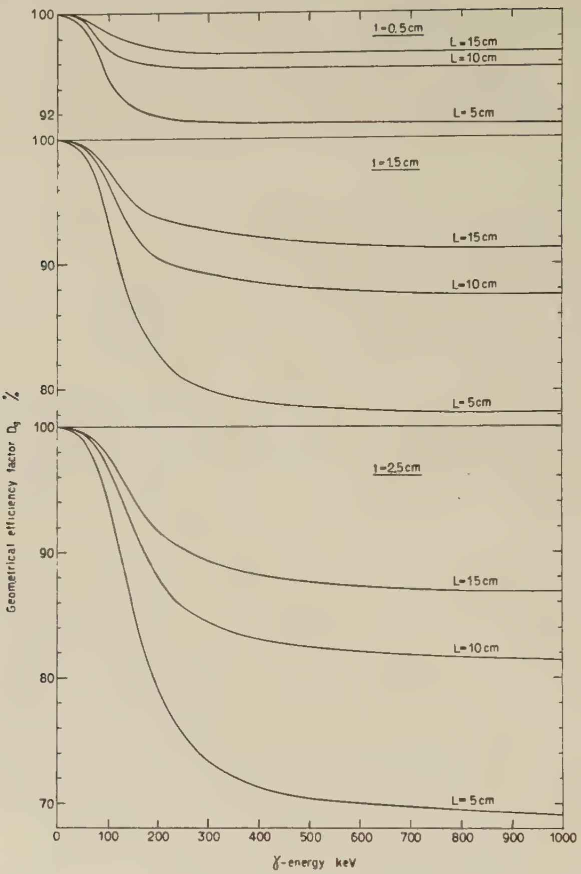

Fig. 12 a. Geometrical efficiency factor D_g, i.e. the ratio of N_0 calculated for a large distance L between source and crystal (Eq. (30)) to N_0 calculated for finite value of L (Eq. (41)), N_p being the same in both cases. t is the thickness of the crystal.

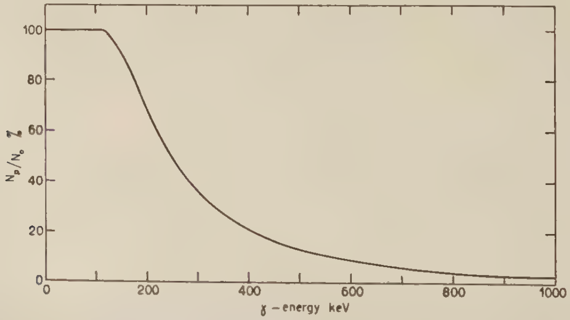

Fig. 12 b. Effective photoelectric γ-detection efficiency N_p/N_0 (Eq. (30)) for a NaI(Tl) crystal ∅ 1.5 × 1.5 cm and a large source-crystal distance L.

If $a > 10$, it is best to calculate $-Ei(-a)$ from the corresponding semiconvergent series. From (41 c) and (42) $N_S(E_\gamma)$ may be calculated using $N_p(E_\gamma)$ determined in Sect. IV d. *Fig. 12* (*a*) shows the geometrical correction factor $D_g = \frac{D}{1-e^{-\mu t}}$ as a function of E_γ for various L and t. *Fig. 12* (*b*) shows the effective photoelectric γ-detection efficiency N_p/N_0 for a NaI(Tl) crystal ⌀ 1.5 × 1.5 cm and $L = \infty$, calculated from (30) using the measured values of $k(E_\gamma)$ (*Fig. 10*).

V. Discussion

The usefulness and the achievable accuracy of the described method for quantitative evaluation of continuous γ-spectra mainly depends on two limiting factors.

1. the poor resolving power of the scintillation spectrometer at low energies,
2. the accuracy of the determination of the effective photoelectric absorption in the crystal and of the correction for the Compton electron distribution.

The best resolving power of a scintillation spectrometer hitherto claimed is equivalent to a half width of about 8 % at $E_\gamma = 662$ keV and about 20 % at $E_\gamma = 100$ keV. It may therefore sometimes be difficult to analyse irregularities in the spectrum, e.g. x-ray lines or absorption edges at energies less than 100 keV. However, it is often known beforehand that a single γ- or x-ray line or a K-absorption edge will appear in the spectrum to be studied, and then the difficulties can be overcome. In the case with a single line for example, the intensity of the line is simply determined from its more or less pronounced peak or bump in the pulse distribution. A subtraction of a correct Gaussian plot of the line from this distribution then gives the pulse distribution of the continuous spectrum.

As shown by Johansson (1952) the maximum energy of a continuous x-ray spectrum from an x-ray tube can be fairly accurately determined.

The accuracy of the correction for the Compton electron distribution is closely related to the size of the crystal and to the shape of the spectrum. According to Sect. IV d, $1-k(E_\gamma)$ decreases with increasing dimensions of the crystal for all energies, i.e. $N_c(E_\gamma)/N_p(E_\gamma)$ decreases. Since the correction term $N_c(E_\gamma)$ is determined solely by the intensity of energies *greater* than E_γ, the value of N_c/N_p will be smaller for spectra the intensity of which rapidly decreases with increasing energy E_γ than for spectra with about the same intensity at all energies, for example. Further, as $1-k(E_\gamma)$ increases with increasing energy E_γ, $N_c(E_\gamma)$ increases rapidly with maximum energy of similar spectra.

The correction for the Compton electron distribution can be performed with a good degree of accuracy using the approximation $C(E, E_\gamma) = \text{const}$, (Sect. IV d), provided that the spectrum to be analysed is of the same type as the internal bremsstrahlung from P^{32}. In this case the error in the corrected distribution will be smaller than ±5 %. In certain other cases it may be necessary to represent $C(E, E_\gamma)$ more exactly.

At the final calculation from Eqs. (41) of the spectral distribution of the radiation, incident on the crystal, the accuracy of the result depends mainly on μ and $k(E_\gamma)$. It can be shown that the relative error caused by the uncertainty $\Delta\mu$ of μ, is always less than $|\Delta\mu/\mu|$. For an energy region where μ is accurately determined, the accuracy of the final result depends on k. In the experimental determination of k for a NaI(Tl) crystal ⌀ 1.5 × 1.5 cm, described in Sect. IV d, the maximum error is less than ±10 %; for energies below 700 keV the accuracy is probably better than ±5 %.

The analysis of the backscatter effect in Sect. II shows that this effect readily gives rise to considerable errors for which correction is not easy. Therefore backscatter must also be considered; if the intensity available is sufficiently high (see also Sect. II c) such backscatter should be diminished with suitable geometry.

Finally it may be pointed out that the problems of measuring the intensities of γ-ray lines often are the same as for continuous spectra. Thus many deductions made in this paper are applicable to such measurements.

When this paper was nearly ready for the press, some articles on scintillation spectrometer measurements appeared. MAEDER & WINTERSTEIGER (1952) reported theoretical calculations of the Compton electron distribution and of the effective photoelectric absorption for various γ-ray energies and crystal sizes. They also compared the result with experimental data.

The above mentioned investigations of the internal bremsstrahlung from P^{32} and RaE by NOVEY (1951) and by MADANSKY & RASETTI (1951) have now been described in detail in two recent papers, one by NOVEY (1953) and the other by BOLGIANO, MADANSKY & RASETTI (1953). The present authors also studied the internal bremsstrahlung from P^{32}, using the method described in the present paper, and an account of this investigation together with results from the measurements of the external bremsstrahlung from various elements is being prepared.[1] In his recent paper NOVEY gives a short account of the necessary corrections of the measurements, obtained by his apparatus. In several respects his treatment of the experimental results seems to agree with the method described above. A few divergences may be mentioned. The Compton electron distribution is ignored by NOVEY; this approximation causes an error of about 5–10 % in the energy region below 250 keV. In the calculation of the K-escape effect the fluorescence yield ω_K and the K-absorption jump δ_K are not considered; this gives a K-escape factor 30 % too high. Finally, the energy dependence of the geometrical efficiency is not taken into account. In the case with a distance of 15 cm between the source and the crystal, however, this factor introduces an efficiency difference of 6 % between low energies and 250 keV.

As well as the present authors, BOLGIANO, MADANSKY & RASETTI have noticed the risk of reradiated K x-rays from the lead shielding. They have included ω_K in the K-escape calculation but δ_K is not discussed. Otherwise the lack of details concerning the corrections prevents further discussions.

In a very recent paper by ANDERSON *et al.* (1953) dealing with scintillation spectrometer measurements of internal bremsstrahlung following K-capture in A^{37} with a maximum energy of 815 keV a considerable inaccuracy must arise from neglecting the corrections for the Compton electron distribution and from the use of inappropriate values of the crystal efficiency.

---

[1] A preliminary report of this investigation was given at the sixth meeting of *the Swedish National Committee for Physics*, held in Stockholm on Sept. 25–27, 1952.

Recent investigations by HAHN (1953) and HAHN & ROSSEL (1953) show high fluorescence efficiency of CsI crystals at 77° K for α-particles. It seems probable that this discovery will become important for γ-ray spectroscopy.

Acknowledgments

The present investigation has mainly been carried out at the Department of Physics, University of Lund. The authors wish to express their gratitude to Professor B. EDLÉN and Professor S. VON FRIESEN for their interest and support in this work and to Dr S. A. E. JOHANSSON for many valuable discussions. For assistance with electronic equipment we are indebted to Dr L. STIGMARK. The authors are also very grateful to Professor F. W. SPIERS, University of Leeds, England, who kindly read and commented the manuscript.

Radiation Physics Department, University of Lund, Sweden. October 1953.

REFERENCES

ANDERSON, C. E., WHEELER, G. W., WATSON, W. W., 1953, Phys. Rev. *90*, 606.
BELL, P. R., JAUCH, J. M., CASSIDY, J. M., 1952, Science *115*, 12.
BLEULER, E., ZÜNTI, W., 1946, Helv. Phys. Acta *19*, 375.
BOLGIANO, P., MADANSKY, L., RASETTI, F., 1953, Phys. Rev. *89*, 679.
BOTHE, W., 1933, Handbuch der Physik (Berlin: Julius Springer) *22*, Part 2, p. 1.
BURHOP, E. H. S., 1952, *The Auger Effect and Other Radiationless Transitions.* (Cambridge: University Press).
DAVISSON, C. M., EVANS, R. D., 1952, Rev. Mod. Phys. *24*, 79.
ELMORE, W. C., SANDS, M., 1949, *Electronics Experimental Techniques.* (New York: McGraw Hill Book Company, Inc.).
FOWLER, W. A., LAURITSEN, C. C., LAURITSEN, T., 1948, Rev. Mod. Phys. *20*, 236.
GILLETTE, R. H., 1950, Rev. Sci. Instr. *21*, 294.
HAHN, B., 1953, Phys. Rev. *91*, 772.
HAHN, B., ROSSEL, J., 1953, Helv. Phys. Acta *26*, 271.
HALL, H., 1936, Rev. Mod. Phys. *8*, 358.
HEDGRAN, A., LIND, D., 1952, Arkiv för Fysik *5*, 29.
JOHANSSON, S. A. E., 1952, Arkiv för Fysik *3*, 533.
KELLEY, G. G., 1952, Nucleonics *10*, No. 4, 34.
LATYSHEW, G. D., 1947, Rev. Mod. Phys. *19*, 132.
LIDÉN, K., STARFELT, N., 1953, (a) Arkiv för Fysik *7*, 109.
—— 1953, (b) Arkiv för Fysik *7*, 193.
MADANSKY, L., RASETTI, F., 1951, Phys. Rev. *83*, 187.
MAEDER, D., PREISWERK, P., 1951, Phys. Rev. *84*, 595.
MAEDER, D., WINTERSTEIGER, V., 1952, Physica *18*, 1147.
DER MATEOSIAN, E., SMITH, A., 1952, Phys. Rev. *88*, 1186.
MORTON, G. A., 1952, Advances in Electronics *4*, 69.
NOVEY, T. B., 1951, Phys. Rev. *84*, 145.
—— 1953, Phys. Rev. *89*, 672.
RAFFLE, J. F., ROBBINS, E. J., 1952, Proc. Phys. Soc. *65 B*, 320.
VAN SCRIVER, W., HOFSTADTER, R., 1951, Phys. Rev. *84*, 1062.
TAYLOR, C. J., JENTSCHKE, W. K., REMLEY, M. E., EBY, F. S., KRUGER, P. G., 1951, Phys. Rev. *84*, 1034.
WHITE, G. R., 1952, *X Ray Attenuation Coefficients from 10 keV to 100 MeV.* National Bureau of Standards Report 1003.

Tryckt den 1 mars 1954

Uppsala 1954. Almqvist & Wiksells Boktryckeri AB

ARKIV FÖR FYSIK Band 7 nr 37

Communicated 25 November 1953 by MANNE SIEGBAHN and ERIK HULTHÉN

The reaction energy of Ne^{22} (d, p) Ne^{23} and the atomic mass of Ne^{23}

By KATARINA AHNLUND

With 2 figures in the text

Introduction

The mass of Ne^{23} has been inaccessible to mass spectroscopic precision measurements due to its short half-life to β^--decay, 40.2 seconds. However, by nuclear reactions there are two ways by which its mass may be linked to existing mass data for adjacent nuclei, either from the mass difference evaluated as energy in the ground state transition Ne^{22} (d, p) Ne^{23}, or from the maximum β-energy in the decay from Ne^{23} to Na^{23}. (Fig. 1). The former reaction has

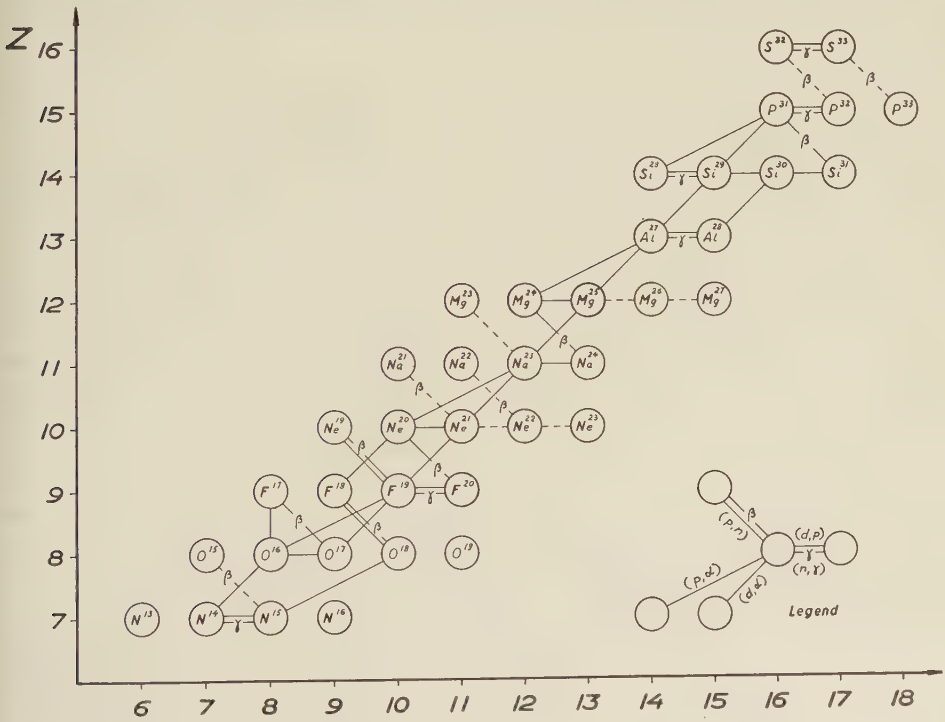

Fig. 1. Nuclei and nuclear reactions between nitrogen and sulphur.

been studied by VAN PATTER, SPERDUTO, ENDT, BUECHNER and ENGE 195 (Ref. 1) and the latter by PEREZ-MENDEZ and BROWN 1950 (Ref. 2). Their result show a discrepancy in the mass of Ne^{23} of 194×10^{-6} atomic mass units—th cycle Ne^{23} (β^-) Na^{23}, Na^{23} (d, α) Ne^{21}, Ne^{21} (d, p) Ne^{22}, Ne^{22} (d, p) Ne^{23} fails t close by 180 keV. The errors were quoted to 7 keV and 50 keV for Ref. and Ref. 2 respectively.

A new determination of the reaction energy of Ne^{22} (d, p) Ne^{23} is presente here.

Experimental procedure

Descriptions of the experimental arrangements have been given earlier (Ref 3, 4). Deuterons of 875 keV from the Nobel Institute Cockcroft-Walton accele rator were used to bombard a thin target of Ne^{22} separated onto a thick silve backing. The target layers were investigated by elastic scattering. The proton leaving the target in an angle of 4° at 135° to the deuteron beam were analyse by the magnetic nuclear spectrometer and detected by nuclear emulsion plates The energy scale of the spectrometer was calibrated with protons from th ground state transition C^{12} (d, p) C^{13} leaving the target at 61°.4 to the inciden beam. The Q-value of this reaction is known to within ± 5 keV. (Ref. 5).

The reaction Ne^{22} (d, p) Ne^{23} has a small cross-section at 875 keV. We ob tained 1 proton track per 30 μC deuterons to the target, which corresponds t

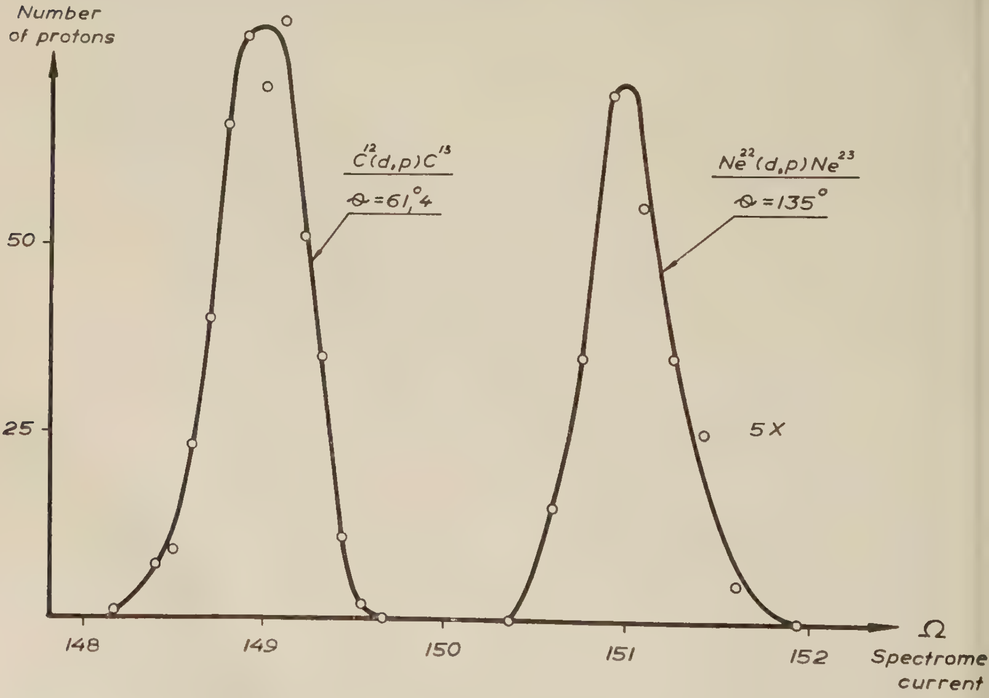

Fig. 2. Spectrum of protons from the reactions C^{12} (d, p) C^{13} at $\Theta = 61.4°$ and Ne^{22} (d, p) Ne^{23} a $\Theta = 135.0°$. $E_d = 876.5$ keV. Photographic detection. $1\ \Omega = 45$ keV.

1 track per minute as the deuteron current had necessarily to be kept low in order not to gas away the Ne-layer from the target. It is evident that the use of photographic detection is essential for work on reactions which give such low intensity.

The identity of the proton group which we have assigned to Ne^{22} (d, p) Ne^{23} has been checked in the following ways. In the first place the spectrometer angle was varied from 135° to 90° to the incident beam, and the resulting change in proton energy agreed with the value calculated from the impulse laws. This procedure however gives insufficient discrimination between nuclei with a small difference in mass number. As we also expect Ne^{20} to give a proton group in this energy region—the exact position of this group is so far unknown—and as some amount of Ne^{20} (as hydride) is inevitable on a separated Ne^{22}-target, a special control run on a Ne^{20}-target was made. No proton groups from the Ne^{20}-target was found corresponding to the one assigned to Ne^{22} (d, p) Ne^{23}.

Results

The two proton groups from Ne^{22} and C^{12} are given in Fig. 2. From the positions of the maxima, corrected for target thicknesses, and from data for deuteron energy and spectrometer angles, we obtain the reaction energy of *Ne*^{22} (d, p) *Ne*^{23}: $Q = 2.968$ *MeV*.

The probable errors entering the determination are given in Table 1.

Table 1.

Source of Error	Probable error	Contribution to Q
Q-value of C^{12} (d, p) C^{13}	5 keV	Total 8 keV
Deuteron energy	2 keV	
Each spectrometer angle	0.2°	
Evaluation of each proton peak . .	3 keV	
Dispersion in the photographic plate	3 keV	

In Table 2 a comparison is given between Ref. 1 and the present result.

Table 2.

Reaction	$E_d = 1.8$ MeV, $\Theta = 90°$	$E_d = 0.88$ MeV, $\Theta = 135°$
Ne^{22} (d,p) Ne^{23}	$Q = 2.964 \pm 0.007$ MeV (v. PATTER et al. 1952)	$Q = 2.968 \pm 0.008$ MeV (Present work)

Thus agreement was obtained. The combination of deuteron energy and spectrometer angle was different for the two cases.

The atomic mass of Ne^{23}

To be able to calculate the mass of Ne^{23} from the Q-value, one must b sure that this belongs to the transition to the ground state. The discrepancy of 180 keV between the two determinations mentioned in the introduction woul of course disappear if the Q-value belonged to a level in Ne^{23} with 180 keV excitation. It should therefore be stressed that no other proton group was foun in the energy region up to 250 keV above the measured group.

We calculate the atomic mass of Ne^{23} from

$$Ne^{22} + d = Ne^{23} + p + Q$$

The mass defects are (Ref. 6):

Ne^{22}	-1.529 ± 0.023 MeV
d	13.7203 ± 0.006 MeV
p	7.5815 ± 0.0027 MeV

With $Q = 2.968$ MeV we get the atomic mass of

$$Ne^{23} = 23.001763 \pm 0.000027 \ a.m.u.$$

The largest contribution to the error comes from the inaccuracy in the mass of Ne^{22}. The mass of Ne^{23} is increased by 2 a.m.u. if we use the mean between v. PATTERS and our Q-value.

Acknowledgements

My thanks are due to Professor M. SIEGBAHN for furnishing the working facilities and to Tekn. lic. S. THULIN for preparing the separated Ne-targets.

Nobel Institute of Physics, Stockholm 50, Sweden.

REFERENCES

1. VAN PATTER, D. M., SPERDUTO, A., ENDT, P. M., BUECHNER, W. W., and ENGE, H. A. Phys. Rev. *85*, 142 (1952).
2. PEREZ-MENDEZ, V., and BROWN, H., Phys. Rev. *78*, 812 (1950).
3. MILEIKOWSKY, C., Ark. f. Fys. *7*, nr 8 (1953).
4. AHNLUND, K., Ark. f. Fys. *7*, nr 14 (1953).
5. VAN PATTER, D. M., M. I. T. Technical Report nr 57 (jan. 1952).
6. AJZENBERG, F., and LAURITSEN, T., Rev. Mod. Phys. *24*, 321 (1952).

Tryckt den 2 mars 1954

Uppsala 1954. Almqvist & Wiksells Boktryckeri AB

ARKIV FÖR FYSIK Band 7 nr 38

Communicated 9 September 1953 by G. Borelius and H. Alfvén

Design study of a strong-focusing electron-synchrotron

By Erik Smårs and Olle Wernholm

With 5 figures in the text

I. Introduction

The principle of the strong-focusing synchrotron which was stated by Courant *et al.*[1] for the acceleration of heavy particles up to the 100 GeV range can probably also be applied advantageously to accelerate electrons. For electrons, however, one cannot expect to reach higher energies than with the conventional synchrotron owing to the fact that the limit of about 1000 MeV for both constructions is set by radiation losses from the electrons. A considerable reduction in material costs (iron and storage condensers) and r.f. energy seems to be obtainable with the new principle. But at present it seems that this reduction is obtained at the expense of the precision required for the alignment of the magnets.

A strong-focusing electron synchrotron will presumably be a good tool to test the focusing properties of this type of machine. The design is in many respects relatively simple. For instance no radio frequency modulation has to be applied, provided that synchrotron acceleration is started at an energy of a few MeV. The pre-acceleration technique for electrons is also much simpler than for heavy particles.

An electron moving in a circular orbit radiates an energy per revolution

$$\frac{e}{3\,\varepsilon_0\cdot r}\cdot\left(\frac{E}{E_0}\right)^4=\frac{6.03\cdot 10^{-9}}{r}\cdot\left(\frac{E}{E_0}\right)^4\,\mathrm{eV} \tag{1}$$

where r is the orbit radius in meters, E is the total energy, and E_0 the rest energy of the electron. These losses have to be supplied by the radio frequency resonator. For a peak flux density 1.1 Vs/m^2 at the orbit these losses amount to 3.7 keV at 500 MeV and 32 keV at 1000 MeV.

In this paper we have considered an electron-synchrotron with two alternatives as regards the particle energy, viz. 500 MeV and 1000 MeV. The required radio frequency voltage for the latter would not be too difficult to obtain.

---

[1] Courant, Livingstone and Snyder, Phys. Rev. *80*, 1190.

II. The strong-focusing principle

In conventional synchrotrons and betatrons the magnetic flux density is independent of the azimuth angle. Stability for the motion of the particles is achieved when

$$-1 < \frac{r}{B} \cdot \frac{\partial B}{\partial r} < 0. \qquad (2)$$

The focusing forces are approximately proportional to $\left|\frac{r}{B} \cdot \frac{\partial B}{\partial r}\right|$ for axial oscillations and to $\left(1 - \left|\frac{r}{B} \cdot \frac{\partial B}{\partial r}\right|\right)$ for radial oscillations.

Courant *et al.*[1] have shown that a very strong focusing effect can be obtained both for axial and radial oscillations by alternating large positive and negative values of $\frac{\partial B}{\partial r}$ in successive sectors of the magnet. A rapid decrease of the flux density with radius in one sector is followed by a rapid increase in the next sector. The magnetic field strength is thus independent of the azimuth angle only for one value of the radius, $r = r_0$. Compared to those in the conventional machines the oscillation amplitudes are considerably reduced, which means that the dimensions of the magnet poles and of the whole magnet can also be reduced. The conditions for stable motion of the particles have been given by Courant *et al.*[1]

In practice it may be necessary to have a number of relatively long field-free sections between the magnet sectors, where radio frequency resonator, pre-acceleration components and, if necessary, correction lenses can be placed. Such straight sections will change the stability conditions. The general case has been treated by Lundquist.[2] His results will be briefly recalled here.

For odd sectors we suppose that the field gradient is negative $\frac{\partial B}{\partial r} < 0$ and for even sectors positive $\frac{\partial B}{\partial r} > 0$, and introduce

$$n = -\frac{r_0}{B_0} \cdot \frac{\partial B}{\partial r} = n_1 \text{ for odd sectors} \qquad (3\text{ a})$$

$$n = -\frac{r_0}{B_0} \cdot \frac{\partial B}{\partial r} = -n_2 \text{ for even sectors} \qquad (3\text{ b})$$

where n_1 and n_2 are positive quantities not necessarily equal. Index 0 refers to values at the radius $r = r_0$. With a linear field, i.e., the field gradients $\frac{\partial B_z}{\partial r}$ and $\frac{\partial B_r}{\partial z}$ are constant, axial (z) and radial ($x = r - r_0$) oscillations are described by the equations

---

[1] Courant, Livingstone and Snyder, Phys. Rev. *80*, 1190.

[2] Phys. Rev. Vol. 91, No 4, 981—983, Aug. 15, 1953.

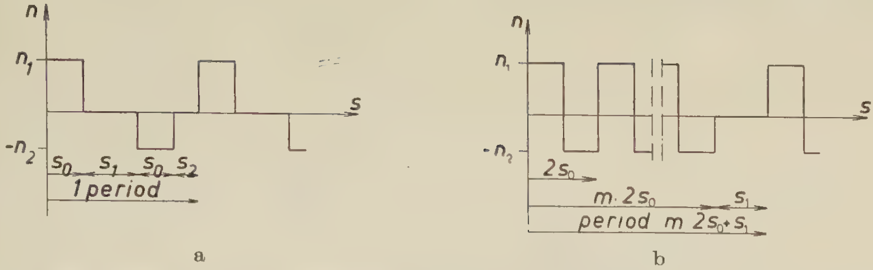

Fig. 1. Field index n as a function of the azimuth coordinate (a) with straight sections between every magnet sector (b) with m double sectors between every straight section.

$$\frac{d^2 z}{d s^2}+\frac{n_1}{r_0^2}\cdot z=0; \quad \frac{d^2 x}{d s^2}+\frac{1-n_1}{r_0^2}\cdot x=0 \quad \text{(odd sectors)} \tag{4 a}$$

$$\frac{d^2 z}{d s^2}+\frac{-n_2}{r_0^2}\cdot z=0; \quad \frac{d^2 x}{d s^2}+\frac{1+n_2}{r_0^2}\cdot x=0 \quad \text{(even sectors)} \tag{4 b}$$

where s is the coordinate along the equilibrium orbit.

The condition for stability when we introduce straight sections between every one of the N magnet sectors, the length of these sections alternating between s_1 and s_2 according to Fig. 1 a, is given by the relation

$$|\cos \mu|=\left|\cos \varphi+\frac{s_1+s_2}{s_0}\cdot \beta-\frac{s_1 s_2}{s_0^2}\cdot \gamma\right|<1. \tag{5 a}$$

In this expression $s_0=2\pi r_0/N$ is the length of the magnet sectors,

$$\cos \varphi=\cos \alpha_1 \cosh \alpha_2-\frac{\alpha_1^2-\alpha_2^2}{2\,\alpha_1\,\alpha_2} \sin \alpha_1 \sinh \alpha_2,$$

$$\beta=\frac{\alpha_2}{2} \cos \alpha_1 \sinh \alpha_2-\frac{\alpha_1}{2} \sin \alpha_1 \cosh \alpha_2$$

$$\gamma=\frac{1}{2}\, \alpha_1 \alpha_2 \sin \alpha_1 \sinh \alpha_2$$

$$\alpha_1=2\pi \frac{\sqrt{n_1}}{N}$$

for axial oscillations

$$\alpha_2=2\pi \frac{\sqrt{n_2}}{N}$$

$$\alpha_1=2\pi \frac{\sqrt{n_1-1}}{N}$$

for radial oscillations

$$\alpha_2=2\pi \frac{\sqrt{n_2+1}}{N}.$$

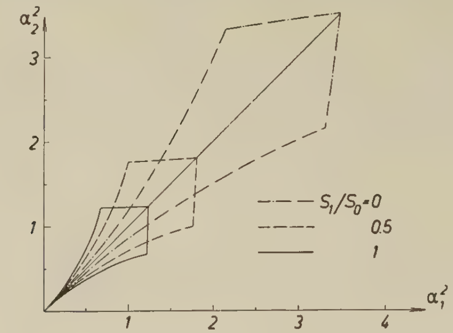

Fig. 2 a. Graph showing the stable regions for the case in Fig. 1 a with $s_1 = s_2$.

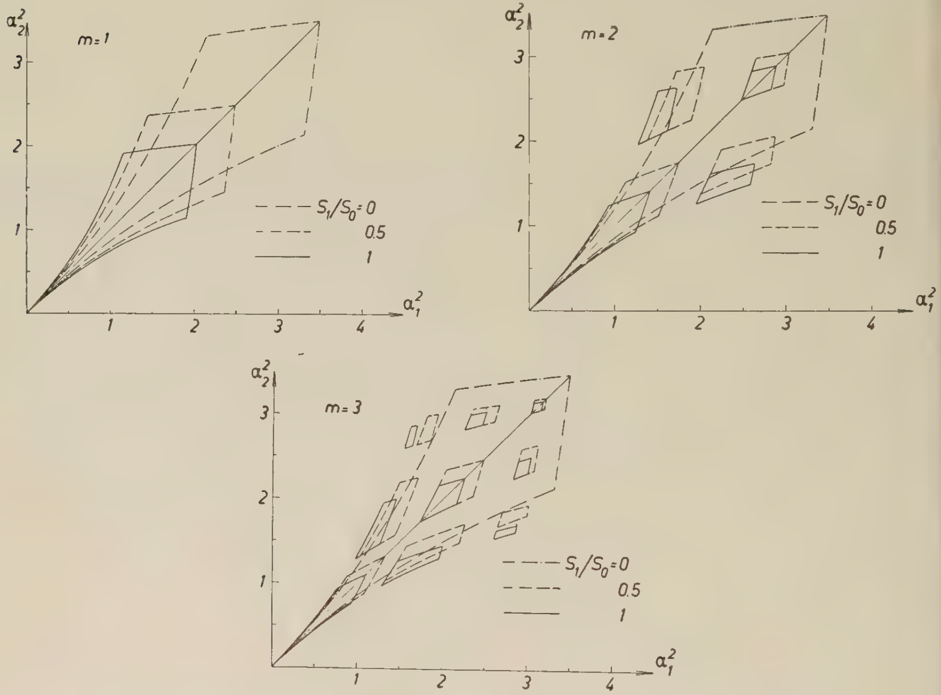

Fig. 2 b. Graph showing the stable regions for the case in Fig. 1 b with $m = 1$, 2, and 3.

The stable regions in the α_1^2, α_2^2 plane are shown in Fig. 2 a for some different values of $s_1/s_0 = s_2/s_0$ and for the case that $N \gg 1$.

If we introduce straight sections s_1 according to Fig. 1 b, i.e., with m pairs of magnet sectors between every straight section, the condition for stability is

$$|\cos \mu| = \left| \cos m\varphi + \varkappa \frac{\sin m\varphi}{\sin \varphi} \right| < 1 \tag{5 b}$$

where $\varkappa = \beta \cdot s_1/s_0$. The stable regions in this case are given in Fig. 2 b.

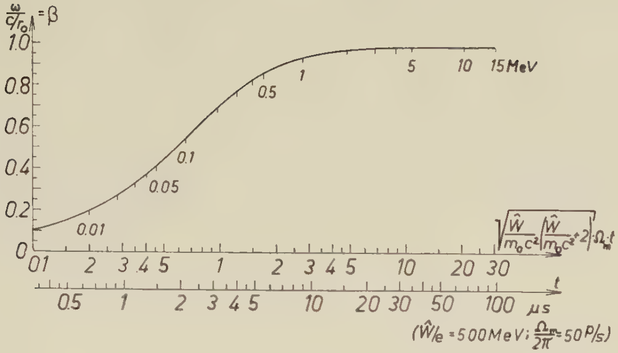

Fig. 3. The time variation of orbital frequency and kinetic energy of the electrons.

In both these cases, (5 a) and (5 b), the number of betatron oscillations in one revolution is $Q = \mu N / 4\pi$. The operation point should be chosen in the center of the stable region, i.e., where $n_1 = n_2$ and $\cos \mu \approx 0$.

The choice of the parameters s_1, s_2, m, n, and N depend on the size and kind of machine in consideration.

III. The acceleration mechanisms

The angular frequency ω of an electron moving in a magnetic field of flux density B is

$$\omega = \frac{e \cdot B}{m} = \frac{e c^2 \cdot B}{m_0 c^2 + W} \tag{6}$$

where $m_0 c^2$ is the rest energy of the electron and W its kinetic energy. The relation between W, B and the radius r_0 of the orbit, which is considered as constant, is

$$W (W + 2 m_0 c^2) = (e c B \cdot r_0)^2. \tag{7}$$

If B is supposed to vary sinusoidally with time ($B = \hat{B} \sin \Omega_m t$), the time dependence of ω can be derived from (6) and (7) as

$$\omega = \frac{c}{r_0} \cdot \beta = \frac{c}{r_0} \left\{ 1 + \frac{1}{\frac{\hat{W}}{m_0 c^2} \left(\frac{\hat{W}}{m_0 c^2} + 2 \right) \sin^2 \Omega_m t} \right\}^{-\frac{1}{2}} \tag{8}$$

where $\hat{W}$ is the peak kinetic energy of the electron. This relation is shown graphically in Fig. 3 for small values of $\Omega_m t$, i.e., for the beginning of the acceleration cycle. The microsecond time scale is valid for a peak energy of 500 MeV and $\frac{\Omega m}{2\pi} = 50$ c/s.

Equation (7) gives

$$W = m_0 c^2 \left\{ \sqrt{1 + \left(\frac{\hat{W}}{m_0 c^2} \cdot \sin \Omega_m t \right)^2} - 1 \right\}. \tag{9}$$

Thus the electron energy in the relativistic range increases as B. For lower energies the time dependence of W is indicated along the curve in Fig. 3.

The energy that has to be delivered to the electron is, per revolution,

$$\Delta W = \frac{dW}{dt} \cdot \frac{2\pi r_0}{c \cdot \beta}$$

which can be rewritten in the form

$$\Delta W = \hat{W} \frac{2\pi r_0}{c} \cdot \Omega_m \cos \Omega_m t. \tag{10}$$

The peak value of ΔW is 4.9 keV for 500 MeV and 19.7 keV for 1000 MeV with $r_0 = 1.5$ m and 3.0 m, respectively.

The acceleration at a constant radio frequency cannot be started until the electrons have reached a velocity near that of light. There are two possibilities available for the preacceleration from injector voltages of some 100 kV to the energies of some MeV, either betatron acceleration or frequency-modulated radiofrequency acceleration. In the latter case the frequency has to be modulated according to Fig. 3. It is also possible to inject the electrons from a linear accelerator or a van de Graff machine.

A fractional deviation $\frac{\Delta f}{f}$ from the orbital frequency given by (8) will cause a fractional change $\frac{\Delta T}{T} = \frac{\Delta f}{f}$ in the time of revolution of the particle. The allowable limit of the change is set by the maximum allowable change in the radial position of the orbit.

If L is the circumference of the orbit

$$\frac{\Delta f}{f} = \frac{\Delta T}{T} = \frac{\Delta L}{L} - \frac{\Delta v}{v} = \left\{ 1 - \frac{1}{\varepsilon} \left(\frac{E_0}{E} \right)^2 \right\} \frac{\Delta L}{L}, \tag{11}$$

v is the velocity, E and E_0 the total and rest energy of the particle. ε is defined by

$$\frac{\Delta L}{L} = \varepsilon \cdot \frac{\Delta p}{p} \tag{12}$$

where p is the particle momentum. The value of the "momentum compaction" coefficient ε for the case with equal straight sections s_1 between every magnet sector is approximately given by

$$\varepsilon \left(1 + \frac{s_1}{s_0} \right) = \frac{-2 + n_1 - n_2}{2(n_1 - 1)(n_2 + 1)} + \frac{N}{2\pi} \cdot \frac{(n_1 + n_2)^2}{[(n_1 - 1)(n_2 + 1)]^{3/2}} \cdot \frac{1}{-\sqrt{n_1 - 1} \cot \frac{\alpha_2}{2} + \sqrt{n_2 + 1} \coth \frac{\alpha_1}{2} + \frac{s_1}{r_0} \sqrt{(n_1 - 1)(n_2 + 1)}}. \tag{13}$$

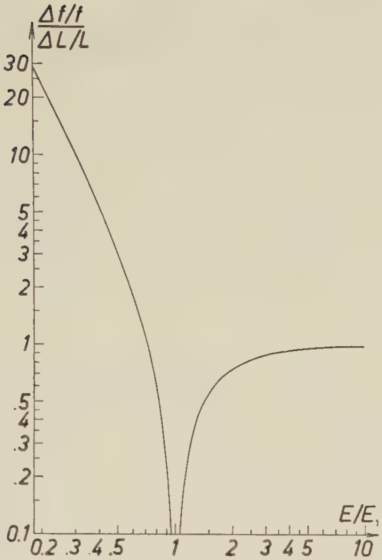

Fig. 4. Frequency tolerance as a function of the kinetic energy of the electrons.

Equation (11) shows that at a particular energy $E_1 = E_0 \sqrt{\frac{1}{\varepsilon}}$ the frequency tolerance is zero. At this energy the equilibrium phase angle shifts from rising to falling slope of the resonator voltage wave. The relation (11) is shown in Fig. 4.

In our case the critical energy E_1 has to be passed during the pre-acceleration and for this reason frequency modulation must be excluded. Betatron pre-acceleration seems to be much simpler.

The transition to constant frequency acceleration has to occur at such an energy E_{tr} that approximately $1-\beta \leq 2\,\frac{\Delta f}{f}$ which together with equation (11) gives the condition

$$\mathrm{E}_{tr} > E_0 \sqrt{\frac{1}{\varepsilon} + \frac{1}{4\,\Delta L/L}}\,. \tag{14}$$

The frequency stability of the oscillators is assumed to be much better than $\frac{\Delta f}{f}$. The maximum value of ΔL is determined by the radial aperture of the magnetic field and the vacuum chamber.

For the radio frequency acceleration one or several high Q doughnut type resonators can be used and placed in straight sections of the orbit. Their size may be reduced by using a harmonic of the orbital frequency, which also reduces the radial amplitude of the synchrotron oscillations by a factor $M^{-\frac{1}{2}}$, where M is the harmonic.[3]

---

[3] Brobeck, Rev. Sci. Instr. *19*, 545.

The betatron voltage is not very critical in the strong-focusing machine due to the "momentum compaction". The relations (12) and (13) show that the fractional change in particle momentum $\frac{\Delta p}{p}$ may be much larger than in the conventional synchrotron. Separate betatron cores can be used constructed as pulse transformers in which the secondary is the electron orbit. The primary will be fed from hard tube pulsers. The total voltage that has to be generated in the orbit is according to the betatron flux condition about 5 kV and 20 kV in the two alternatives with pulse durations of about 20 μs and 15 μs, respectively, the time in which the electrons reach the transition energy. The total weight of the betatron cores will be about 400 kg and 1100 kg, respectively.

IV. Choice of machine parameters

Several factors will influence the choice of the n-value. For lowest costs of iron and storage condensers n should be chosen as high as possible. However, as Lawson and others have pointed out, the required engineering tolerances in the magnet are approximately proportional to $1/n$. Small errors in the alignment of the individual sectors can cause large oscillations to build up, so that the electrons hit the vacuum chamber walls. The alignment errors have to be made so small that the particles clear the walls for several revolutions. Furthermore, resonances and subresonances occur, for certain values of Q which cause unlimited oscillations to build up. These Q-values are grouped as "stop-bands" around integer and half-integer values of Q. Therefore operation should be maintained between two such "stop-bands" during the whole acceleration cycle. It might be possible to make Q amplitude-dependent by introducing non-linearities in the magnetic field and in this way avoid these resonances, but then coupling between horizontal and vertical oscillations might introduce new resonances.

In determining the value of the field index n we have to consider on the one hand the costs of iron, copper, and condensers, and on the other hand the following facts:

a) The required accuracy in manufacturing and aligning the magnets decreases with decreasing n.

b) The available space between two "stop-bands" increases with decreasing n.

c) Saturation effects and other causes for inhomogeneities in the magnetic field decrease with decreasing n.

d) The critical energy E_1, at which the frequency tolerance is zero, decreases with decreasing n and as a result of this also the necessary peak energy of the pre-accelerator.

e) With lower n-values the magnet sectors will be longer, and the fringing fields at the sector ends will be less influential.

A field gradient of about 10 $\mathrm{Vs/m^2/m}$ (1000 gauss/cm) would be suitable. Then an alignment accuracy of about 0.1 mm should be sufficient to keep the amplitudes of the oscillations well below tolerable values.

The number of magnet sectors N and the field index n should be chosen so that the values of Q for both axial and radial oscillations differ as much as possible from the two neighbouring "stop-bands". When the pole tips saturate in the later part of the acceleration cycle, Q thus may change slightly without entering a stop-band.

Table 1

Peak electron energy	500	1000	MeV
Peak magnetic flux density in the equil. orbit, B_0	1.1	1.1	Vs/m²
Orbit radius, r_0	1.5	3.0	m
Number of magnet sectors, N	20	28	
Length of sector, s_0	0.47	0.67	m
Length of straight sections, $s_1 = s_2$	0.75. $s_0 = 0.35$	0.60. $s_0 = 0.40$	m
Total length of orbit	16.5	30.2	m
Field index, n	11.4	24.3	
Field gradient, $\frac{\partial B}{\partial r}$	8.36	8.91	Vs/m²/m
Ampl. of betatron oscillations for an angular spread of β radians at equil. orbit, A_β	2.3	$3.3\,\beta$	m
Momentum compaction coefficient, ε	0.165	0.078	
Teoretical max. in momentum deviation, $\left(\frac{\Delta p}{p}\right)_{\max}$	7	8	%
Critical energy, W_1	0.75	1.3	MeV
Transition energy from pre-acc. to synchr. acc. (theoretical minimum), W_{tr}	2.2	3.2	MeV
Required alignment accuracy for clearance of 1 revolution, Δ_1	0.6	0.5	mm
Orbital frequency	18.2	10.0	Mc/S
Iron weight	10	20	ton
Copper weight	1.2	2.4	ton
Ampere turns	50 000	50 000	At
Power losses for 12.5 pulses/sec.	25	50	kW

In Table 1 are given the numerical values of the machine parameters that will be subject to further investigations.

V. Magnet construction

The magnet consists of 20 and 28 sectors in the two alternatives. A constant magnetic field gradient (linear field) in the acceleration space may be realized by using a four-pole magnet with hyperbolic polefaces. Two of the poles can be replaced by a neutral pole. The flux density varies from zero at this pole to 2 B_0 at the opposite edge of the pole, where B_0 is the flux density in the equilibrium orbit. However, calculations of the amplitudes of the particle oscillations indicate that it is not necessary to use the whole space. Therefore the hyperboles could be cut and the neutral pole omitted. Fig. 5 shows the pole form thus obtained.

If all sectors are made of identical laminations, the circumferential alternation in n may be accomplished by an alternation of the magnetic return circuit of the C:s on both sides of the orbit. The pole fronts of the inside sectors have then to be made slightly convex and those of the outside sectors slightly concave.

The fringing fields at the ends of a sector will change its effective length. The total deflection of the particle by passing through the magnet and its

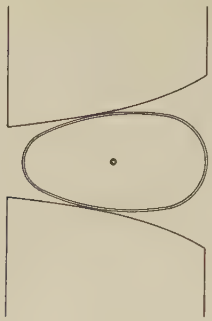

Fig. 5. Cross-section diagram showing the pole form.

fringing fields must be $2\pi/N$. The actual length of a sector then has to be made so that

$$\int B\,d\,s = B_0\,r_0\,\frac{2\,\pi}{N}$$

where the integral is taken along the orbit through the sector with its fringing fields, and B_0 and r_0 refer to the flux density and orbit radius in the ideal case of an abruptly changing field.

Also the field index n does not change abruptly as in the ideal case. From measurements on a model it will be possible to calculate how much the effective value differs from the actual value in the sector center. Such a.c. model tests will also be made in order to establish field irregularities, flux leakage, and saturation effects in the iron.

Royal Institute of Technology, Stockholm.

Tryckt den 2 mars 1954

Uppsala 1954. Almqvist & Wiksells Boktryckeri AB

ARKIV FÖR FYSIK Band 7 nr 39

Communicated 25 November 1953 by ERIK HULTHÉN

The energy of dissociation of BeO

By ALBIN LAGERQVIST

Recently DRUMMOND and BARROW (1) have given a value for the energy of dissociation of BeO from thermochemical calculations. They report D_{BeO} to be 127 ± 5 kcal/mol (or 5.51 ± 0.22 eV). At one point in their treatment they have to extrapolate the heat capacity of BeO_{cryst} beyond the range of known values: this was done by comparison with the corresponding values for MgO_{cryst} and CaO_{cryst}. How much this estimation influences the accuracy of the determination is difficult to predict — probably very little. BREWER (2) calculates using a similar method $D_{BeO} \leq 125$ Kcal mol (5.42 eV). The spectroscopic value for D_{BeO} is usually given as 3.9 eV. Here is shown that a value 4.8 eV can be determined from spectroscopic data.

The spectroscopic determination of the energy of dissociation demands the knowledge of the energy of the dissociation limit above the ground state and the products of dissociation at this limit. In the band-spectrum of BeO the lowest known electronic state is a $^1\Sigma$ state. This state cannot dissociate into the ground states of beryllium (^1S_g) and oxygen (^3P_g), for this atom pair correlates to $^3\Sigma$ and $^3\Pi$ states in BeO. The lowest excited pair giving birth to a $^1\Sigma$ state is $Be(^1S_g) + O(^1D_g)$. The excitation energy is here 1.97 eV. The dissociation limit for $^1\Sigma$, determined from $v = 0$ and $J = 0$, is about 47500 cm^{-1}. Considering this state being the ground state we obtain the value mentioned above 3.9 eV for D_{BeO}.

Thorough rotational and vibrational analyses (3) have been made of three singlet states in BeO; the (probable) ground state X $^1\Sigma$, the state A $^1\Pi$ ($T_0 = 9235$ cm^{-1}) and the state B $^1\Sigma$ ($T_0 = 21197$). It seems to me quite probable that A $^1\Pi$ as well as X $^1\Sigma$ dissociates into $Be(^1S_g) + O(^1D_g)$ and not to higher excited states. Assuming this we can obtain a more accurate value of D_{BeO}, as in X $^1\Sigma$ the vibrational energy function $G(v)$ is known only up to $v = 16$, while in A $^1\Pi$ it is known as far as $v = 25$. The dissociation limit for A $^1\Pi$ is reached at about 45500 cm^{-1}. A plot of $\Delta G(v)$ against v for the A $^1\Pi$ state forms a curve somewhat concave upwards and that is the reason why we get a fairly high value of the dissociation limit. The calculation gives $D_{BeO} = 4.8$ (4.82) eV.

The value 4.8 eV agrees rather well with those obtained through thermochemical calculations. In the spectra of MgO, CaO and SrO only a few vibrational states are known for the lowest states, so that the spectroscopic method here gives very uncertain values of the energy of dissociation.

REFERENCES

1. G. DRUMMOND and R. F. BARROW, Trans. Faraday Soc. *49*, 599 (1953).
2. L. BREWER, Chem. Reviews *52*, No. 1 (1953).
3. A. LAGERQVIST, Dissertation, Stockholm, 1948.

Tryckt den 2 mars 1954

Uppsala 1954. Almqvist & Wiksells Boktryckeri AB

ARKIV FÖR FYSIK Band 7 nr 40

Communicated 25 November 1953 by Manne Siegbahn and Bengt Edlén

Photo-electric determination of the charge of heavy primaries in the cosmic radiation

By Berndt Waldeskog

With 9 figures in the text

Summary

A method of determining the charge of heavy nuclei in the cosmic radiation is described. It depends on measuring with the photo-electric method mean track widths of tracks ending in a photographic emulsion. It is shown that the particles are easily divided into groups representing different values of the charge even if a track length of only 300 microns is used. No definitely primary particles with charge $Z = 3$, 4 or 5 have been found. The possibility of finding such particles in the plate packet is discussed. The statistical material available is not enough to decide whether particles with charge 3, 4 or 5 are present in the primary radiation or not.

The exposure of the plates

A dozen Ilford G-5 emulsions 10 × 10 cm, 400 μ thick were sent up with a Darex-balloon J-1900, to obtain heavy primaries. The guaranteed minimum altitude for the balloon with the load carried during this experiment was 34000 m. The altitude was measured with an altimeter designed by Kristiansson (1). On analysing the diagram obtained, it was found that the balloon had been 10 hours above 15000 m and 7 hours above 29000 m. The maximum altitude was 34000 m. A preliminary scanning of the plates showed about 100 particles per cm^3 longer than 800 μ, and with an ionization greater than that of α-particles near the end of their range. Scanning was then concentrated on particles ending in the emulsion. Up till now about 50 of these have been found. These particles show the characteristic tapering at the end of the track (Fig. 9).

Arrangement of the experiment and measuring method

Formerly, Perkins (2), among others, tried to measure the charge of these slow particles. He used mainly two methods. One was based on determining the position of the maximum width of the track, and the other on determining the "thin-down" length. Both methods are not very reliable. For example, the position of the maximum width is very indefinite, because the maximum is very flat.

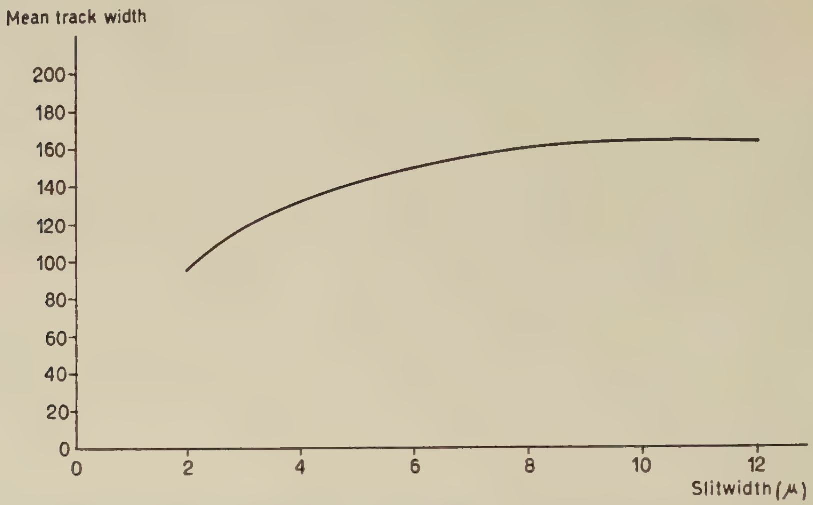

Fig. 1. The observed mean track width of a certain part of a track, measured with different slit widths, as a function of slit width.

A method has been worked out, whereby the charge of these particles can be determined with the help of photo-electric measurements.

The apparatus used was of the same type as described by VON FRIESEN and KRISTIANSSON (3), though slightly modified. The output current from the photo-multiplier tube was connected through a linear amplifier to a Speedomax recorder (4) instead of, as previously, direct to a galvanometer. The slit-width was varied from 0.3 to 2.0 mm corresponding to 3 to 20 microns in the object plane. The slit length was kept constant at 3 mm, which corresponds to 30 microns in the object plane. The exact slit width was measured by calibrating it with an object micrometer. The error in the determination of the slit width was 0.5 %.

The measurements were made in the same way as previously described (3). A measurement was made first with the track in the slit and then on the background on each side of the track. Since the ionization of the track increases greatly from the range $R - 0$ and backwards to the point of maximum track width, the slit width must be increased by degrees as the ionization increases. If a slit width, which is too large, is used at the beginning of the track, then the difference between the measurement for the background and for the track in the slit is small, and the uncertainty is greater. The slit width was chosen so that the track always took up about the same proportion of the total slit area. When the slit width was changed the same piece of track was measured first with the smaller slit and then with the larger one. If the same value of the mean track width was obtained for both measurements, it was a criterion that the smaller slit was wide enough for the range in question.

At the end of a track the length and the number of δ-rays is small, and there is no difficulty in putting the whole track into the slit. On the other hand, for that part of the track where ionization reaches a maximum, the number of long δ-rays is much larger. It is then practically impossible to use a slit that is wide enough to measure all the δ-rays. An investigation was made to determine the error which arises from

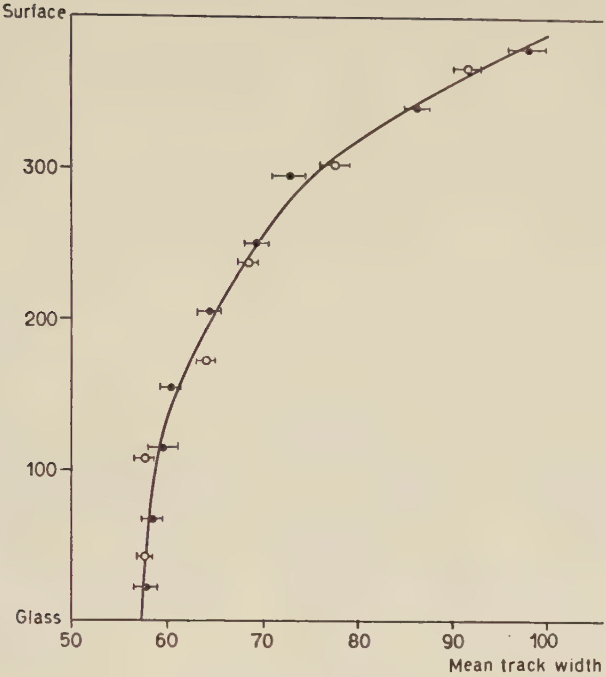

Fig. 2. Correction curve derived from two "heavy" tracks.

this. In the energy interval which was used for the measurements, the contribution that should have been given by the long δ-rays to the total mean track width was relatively constant. A certain part of the track in the neighbourhood of the maximum width was measured with different slit widths (Fig. 1). From the figure is seen that, if the slit width exceeds a certain value which varies with the charge of the particle, the mean track width becomes constant, and the contribution of the long δ-rays to the mean track width is less than the errors of measurement. This "plateau value" was used in the calculations.

Determination of the depth-correction in the emulsion

The mean track widths obtained must be corrected for the depth in the emulsion. A method, simpler than that of KRISTIANSSON (5), was worked out to obtain the correction curves. It is rather tedious work, when protons are used to obtain these curves, to find protons ending at different depths in the emulsion. In this investigation a track from a fast heavy primary particle is used, which traverses the emulsion from the surface to the glass. The length of the tracks used was 4000–5000 microns. The ionization for a fast particle of this range can be regarded as constant. The correction curves were obtained by plotting the mean track widths as a function of the depth in the emulsion. As a check that the correction curve obtained was correct, in other words, that the ionization did not vary along the track, at least two such tracks were measured on each plate. To find the effect caused by a change in the

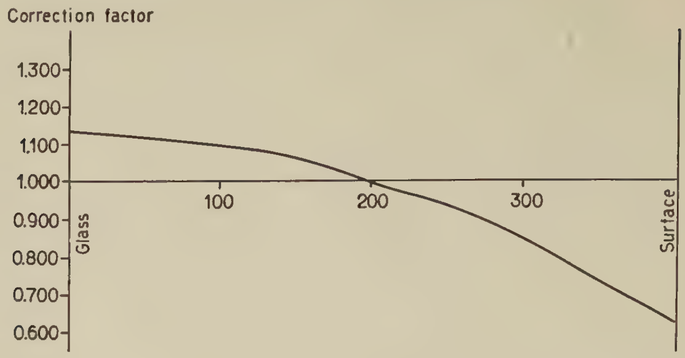

Fig. 3. The depth-correction as calculated from the curve in Fig. 2.

ionization, these tracks were chosen so that one travelled from the surface to the glass and the other from the glass to the surface. The direction could be determined because the vertical orientation of the plates during the exposure was known. The resulting correction curves for the two tracks show a very good agreement (Fig. 2). The correction factors for different depths in the emulsion were calculated from the correction curves (Fig. 3). For the reasons causing the slope of the correction curves see KRISTIANSSON (5).

Measurement results

In Fig. 4 the logarithm of the total track area for different numbers of slit lengths (= different total ranges), counted from the end of the track, have been plotted in a histogram.

In the initial scanning only such tracks were searched for that definitely did not emanate from stars in the emulsion itself. It then appeared that there was an exceptionally large gap between the α-particle group and the next heavier particle group. This group cannot be due to Li-particles, since it can be calculated approximately where a possible Li-group will lie. Scanning was then turned towards the "heavy" tracks, with a minimum length of 300 microns, emanating from stars in the emulsion. These tracks are very rare, and up to now only a few have been found which have been measured. They have been marked with a white dot in Fig. 4.

The particles are clearly divided into groups, representing different values of the charge, already for 10 slit lengths, i.e. a range of 300 microns. The histograms corresponding to 15 and 20 slit lengths are also shown in Fig. 4.

As a check on whether particles from different plates may be compared, the protons and α-particles measured were chosen at random from different plates. From the distribution of the protons and α-particles the conclusion was drawn that the use of tracks from different plates did not introduce any error. The proton group is here a mixture of protons, deuterons and tritons. The length of the tracks measured ($\leq$ 600 microns) is too short for separating these particles.

In Fig. 5 the mean value of the logarithm of the total track area is plotted as a function of the assumed charge Z. In Fig. 5*a* the range is 300 microns, in Fig. 5*b* 450 microns. The curve is for lower values of Z nearly a straight line, but for higher Z

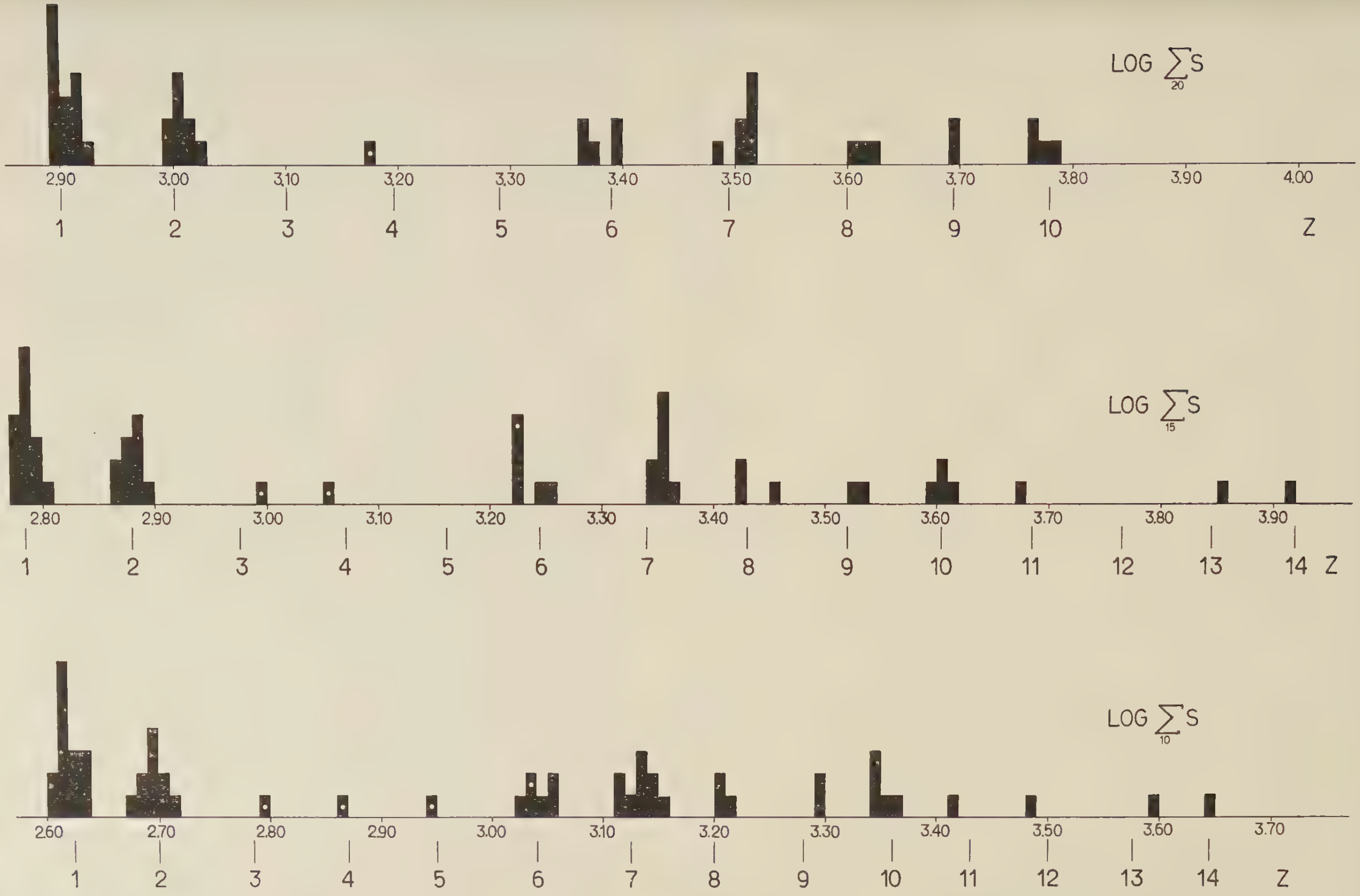

Fig. 4. Number of particles versus the logarithm of the total track area for different numbers of slit lengths (= different total range). The three parts refer to 600 μ, 450 μ and 300 μ total range.

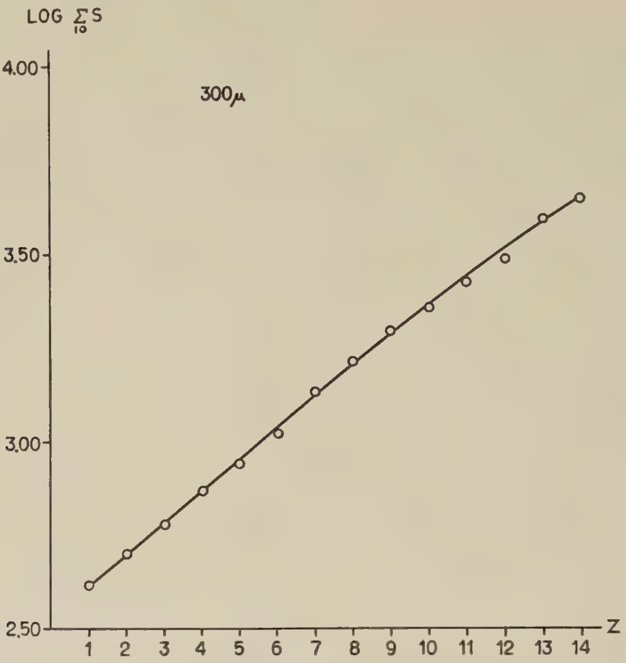

Fig. 5 a. The logarithm of the total track area for 10 slit lengths (= 300 μ) versus the assumed charge.

it tends towards the Z-axis. This means that for higher Z the overlapping is greater, so that the resolution is not so good for the high values of the charge. The resolving power of this method has proved to be sufficient to separate charges at least up to $Z = 14$, which till now is the highest value found for the charge.

Some of the tracks measured were much longer than 600 microns. These were measured in the same way as the shorter tracks. In Fig. 6 the mean track width is plotted as a function of the range. The four particles shown in the figure are chosen at random from the groups of charge $Z = 6$ and $Z = 7$. The steeply sloping part of the curves between the range $R = 0$ and $R \simeq 500$ microns shows the tapering of the tracks. The track width then reaches a very flat maximum. Evidently it is also possible to determine the charge of a particle by measuring the mean track width for instance between $R = 1000$ and $R = 1500$ microns. For tracks with a length of about 1500 microns or more the resolving power is then very good.

The tracks ending in the emulsion were followed backwards. Identification of heavy primaries from one emulsion to another is very simple. The total length of the track in the emulsion + the glass, i.e. the total range of the particle in the plate packet was measured. The range in glass was divided by a factor 1.18 to get the equivalent range in emulsion. A total number of 21 particles with $Z \geq 3$ were observed. In Fig. 7 the number of particles, which definitely entered the plate packet from the outside, has been plotted against track length. The maximum track length observed was 8 cm and the mean length was 3.1 cm. The numbers in the squares indicate the charge of the particle.

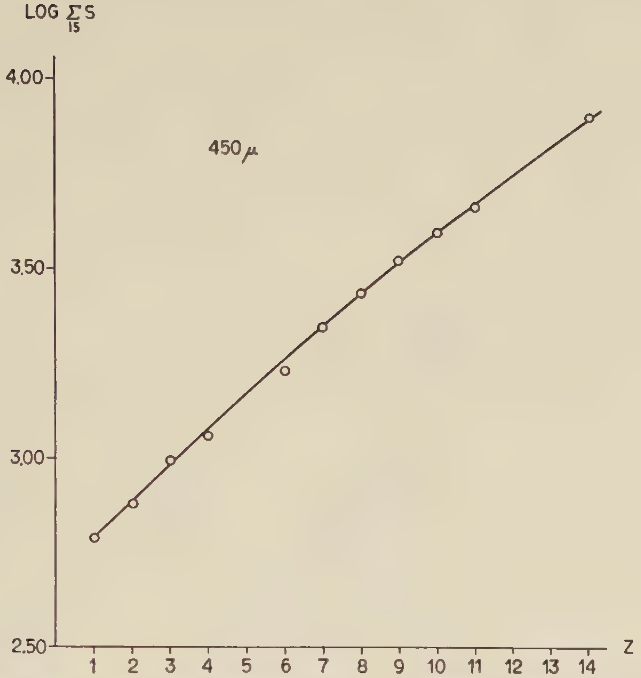

Fig. 5 b. The logarithm of the total track area for 15 slit lengths ($= 450\ \mu$) versus the assumed charge.

Since no particles with $Z = 3$, 4 or 5 and of definitely primary origin have been found, a calculation was made to find the probability for these particles to come to rest in the plate packet. According to Störmer's theory the smallest momentum a particle must have to force its way through the earth's magnetic field is $p = 14.9 \times \cos^4\lambda$ BeV/c, where λ is the geomagnetic latitude of the place. The balloon was sent up at $\lambda = 56°$. For a proton the lowest energy possible under these conditions is 0.80 BeV, and for particles with $Z \geq 2$ the limit is approximately 0.25 BeV/nucleon.

The following calculations have been made for an altitude of 30000 m and for particles entering from the zenith. The emulsion equivalent for overlying atmosphere at this altitude is 3.9 cm.

A proton with an energy of 0.80 BeV has a range of the order of 100 cm in emulsion. When the proton reaches the plate packet, it must travel about 96 cm in the emulsion before it is finally brought to rest. Consequently, the protons which were measured cannot have been primaries.

An α-particle ($Z = 2$, $M = 4$) with an energy of 0.25 BeV/nucleon has a range of 15 cm in the emulsion, and again, for the same reason as for protons, the α-particles measured were certainly secondaries.

A Li-particle ($Z = 3$, $M = 7$) with an energy of 0.25 BeV/nucleon has a range of 11.5 cm in the emulsion. Such a particle traverses $(11.5–3.9) = 7.6$ cm of emulsion before it is brought to rest. The corresponding figures for particles with larger Z may be found in Table 1, where L is the total range of a particle with energy 0.25 BeV/nucleon and $L' = L–3.9$ cm.

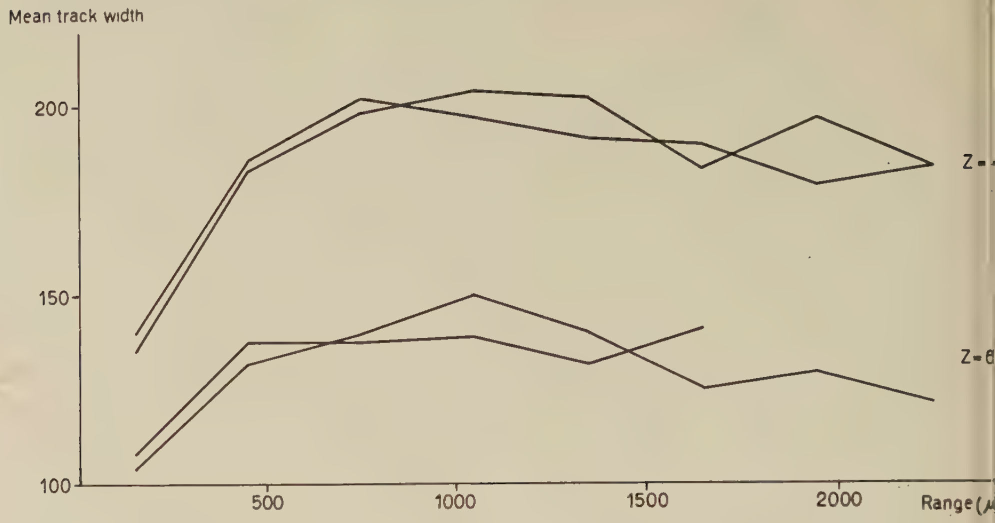

Fig. 6. The mean track width versus the range of particles with charges 6 and 7.

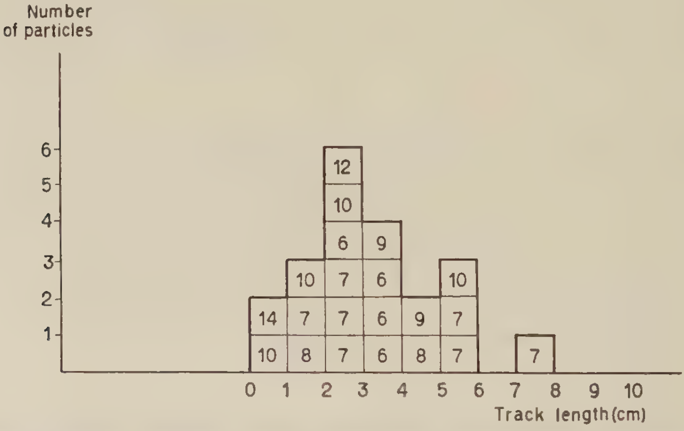

Fig. 7. Number of observed particles versus total range of the tracks in the plate packet. The numbers in the squares indicate the charge of the particle.

Table 1.

	He_2^4	Li_3^7	Be_4^9	B_5^{11}	C_6^{12}	N_7^{14}	O_8^{16}	F_9^{19}	Ne_{10}^{20}
L (cm)	15.0	11.5	8.3	5.9	4.9	4.3	3.7	3.3	2.9
L' (cm)	11.1	7.6	4.4	2.0	1.0	0.4	—	—	—

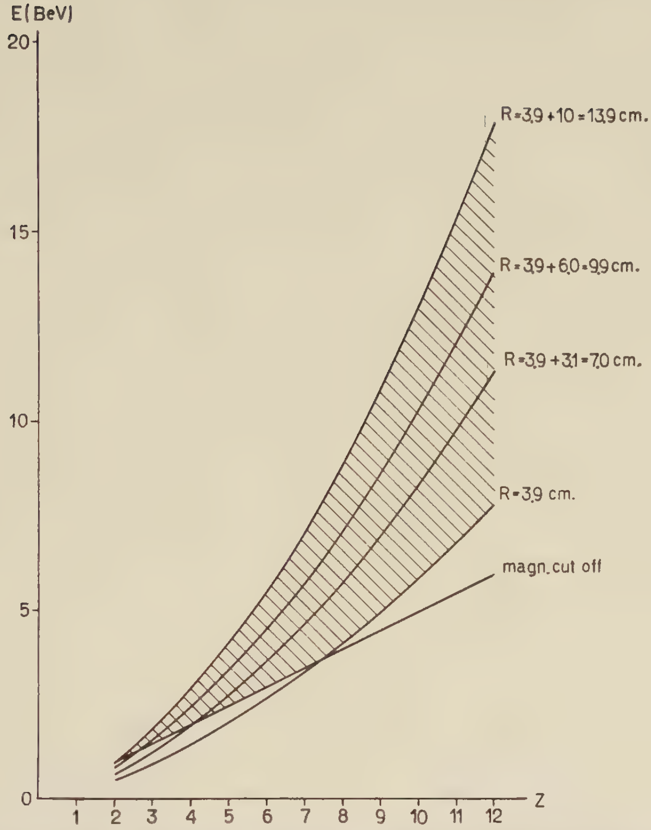

Fig. 8. The magnetic cut-off energy and the energy for certain given ranges versus the charge of the particles.

If the maximum range of a particle in the plate packet is set at 10 cm, then, according to Table 1, particles with $Z = 3$, 4 or 5 and minimum energy should also be found in the plates.

The energy interval, within which a particle must lie to come to rest in the plate packet, varies with Z depending on the fact that the slowing down of a particle in emulsion is a function of the charge. In Fig. 8 is plotted the magnetic cut-off energy and the energy for given ranges in the emulsion as a function of the charge. From the figure can be seen that particles with $Z \leq 7$ and minimum energy have ranges greater than 4 cm and thus reach the plate packet (collisions in the overlying atmosphere are disregarded), while for particles with $Z \geq 8$ the minimum energy is not sufficient for the particles to reach the plate packet. To be brought to rest in the plate packet the particle must lie in the shaded area of Fig. 8, if the maximum range in the plate packet is set at 10 cm. The figure shows that the permissible energy interval increases with Z.

In this calculation it was assumed that the balloon floated at an altitude of 30000 m, and that all particles came from the zenith direction. Since the actual altitude varied

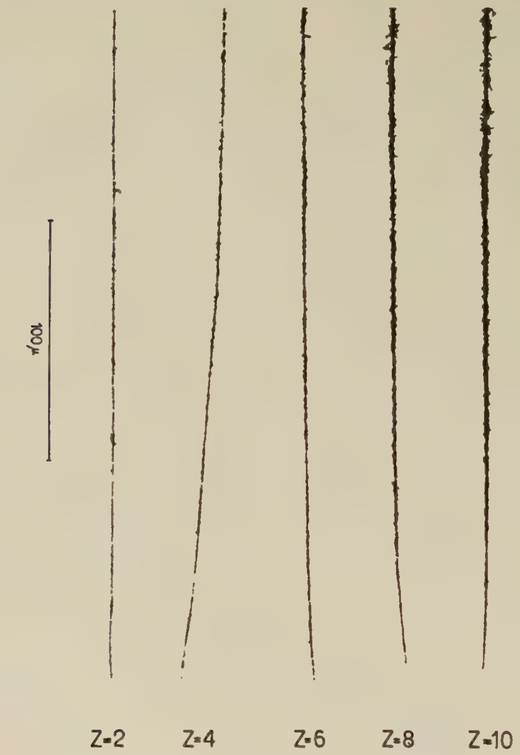

Fig. 9. Microphotographs of 5 tracks with charges 2, 4, 6, 8 and 10.

roughly between 27000 and 34000 m, the result will be correspondingly modified. Also, the directions of the particles varied. If the angle with the zenith direction is assumed to be 45° and the altitude 30000 m, then the particle must traverse an air layer equivalent to 5.5 cm emulsion before reaching the plate packet. This means that the particle has a range in the plate packet that is correspondingly shorter, and the probability of finding it will be greater.

The statistical material available so far is not enough to decide whether particles with charge $Z = 3$, 4 or 5, are present in the primary radiation or not.

The main purpose of this paper has been to describe the method. The investigation is being continued with a modified method to get better statistical material. It can be foreseen that it will be possible to determine the charge of a particle even if the end of the track is not known.

Acknowledgments

The present investigation has been carried out at the *Department of Physics of the University of Lund.* The author wishes to express his sincere thanks to Professor Sten von Friesen for his unfailing interest and continued encouragement in this work.

REFERENCES

1. KRISTIANSSON, Arkiv f. Fysik *6*, 317, 1953.
2. PERKINS, Proc. Roy. Soc. *A 203*, 399, 1950.
3. VON FRIESEN and KRISTIANSSON, Arkiv f. Fysik, *4*, 505, 1952.
4. VON FRIESEN, unpublished.
5. KRISTIANSSON, Phil. Mag. Ser. 7, *44*, 267, 1953.

Tryckt den 3 mars 1954

Uppsala 1954. Almqvist & Wiksells Boktryckeri AB

ARKIV FÖR FYSIK Band 7 nr 41

Read 14 October 1953

On a class of spherically symmetric solutions of Einstein's gravitational equations

By O. Klein

Introduction

In the discussion of stellar equilibria the theory of socalled polytropic gas pheres plays an important and wellknown rôle [1]. This theory, which is based n the study of the Lane-Emden differential equation is founded on Newtonian ravitational theory. Now in problems related with the formation of the elements and with cosmology we meet with similar problems concerning systems f different degree of superstellar size, where, due to high density of matter nd radiation or to large dimensions, the relativistic deviations from Newtonian heory may be very considerable. In order to obtain a general survey of these problems a comparatively simple and adequate generally relativistic generalization f the theory of polytropic equilibria is strongly needed. The following pages conain an attempt in this direction.

As wellknown, the polytrope theory depends on the assumption that the presure p of the substance in question is proportional to a power of the density ϱ, i.e.

$$p = K \varrho^{\frac{n+1}{n}}, \tag{1}$$

where K and n are positive constants. The latter is the socalled polytropic ndex and need not be an integer. This relation is then combined with the ondition for gravitational equilibrium

$$\frac{dp}{dr} = -\frac{\gamma M(r)}{r^2} \varrho, \tag{2}$$

where γ is the gravitational constant, r the distance of the point in question rom the centre and $M(r)$ the mass inside the sphere of radius r, so that

$$\frac{dM(r)}{dr} = 4\pi r^2 \varrho. \tag{3}$$

For the following purpose it is good to split equation (2) into two equations by the introduction of the gravitational potential V, namely

$$\frac{dp}{dr} = -\varrho \frac{dV}{dr}, \tag{4}$$

$$\frac{dV}{dr} = \frac{\gamma M(r)}{r^2}. \tag{5}$$

We shall now regard the pressure p as a function of the potential V, as i will become if r is eliminated between p and V. Then according to (4) als ϱ is defined as a function of V by the relation

$$\varrho = -\frac{dp}{dV}. \tag{6}$$

From (3) and (5) we have the Poisson equation

$$\frac{1}{r^2}\frac{d}{dr}\left(r^2 \frac{dV}{dr}\right) = 4\pi\gamma\varrho, \tag{7}$$

where V is regarded as a function of r. Let us now assume the polytropi condition (1). Together with (6) this gives

$$dV = -\frac{dp}{\varrho} = -K\frac{n+1}{n}\varrho^{\frac{1}{n}-1}\,d\varrho,$$

which after integration gives

$$V_0 - V = K(n+1)\,\varrho^{\frac{1}{n}}$$

or

$$\varrho = \left(\frac{V_0 - V}{K(n+1)}\right)^n \tag{8}$$

and

$$p = \frac{(V_0 - V)^{n+1}}{K^n (n+1)^{n+1}}. \tag{8 a}$$

Here V_0 is the potential at the point, where ϱ vanishes. We put

$$\chi = V_0 - V, \tag{9}$$

and substitute this and (8) into (7), whereby we get

$$\frac{1}{r^2}\frac{d}{dr}\left(r^2 \frac{d\chi}{dr}\right) = -\frac{4\pi\gamma}{[K(n+1)]^n}\chi^n$$

or with

$$\chi = V_0 \psi, \quad r = \left[\frac{[K(n+1)]^n}{4\pi\gamma V_0^{n-1}}\right]^{1/2} \xi, \tag{10}$$

$$\frac{1}{\xi^2}\frac{d}{d\xi}\left(\xi^2 \frac{d\psi}{d\xi}\right) = -\psi^n, \tag{11}$$

which is the Lane-Emden equation of index n where instead of the usual dimensionless temperature variable we have used the potential measured in the unit V_0.

While this choice of the dependent variable would not seem important in the ordinary theory its counterpart in relativity theory presents a definite advantage. This is mainly due to the circumstance, that what is needed for the integration of the Einstein equations is not in the first place a relation between the density and the pressure but both these quantities expressed as functions of the line element coefficient corresponding to V. It is true, that by means of the relativistic equation corresponding to (4), the relationship between p and ϱ being given, we may find these functions in a way similar to that used above in order to express ϱ and p as functions of V. It is more convenient, however, to make for these functions a simple choice instead of using the more complicated expressions obtained from (1). It must be remembered that the very use of the concept of polytropy is a mere matter of convenience.

§ 1. General relativistic formulation of the problem

We proceed now to the general relativistic analogon of the procedure just developed, the square of the line element being given by

$$-\alpha\, d r^2 - r^2 (d\vartheta^2 + \sin^2\vartheta\, d\varphi^2) + \beta c^2\, d t^2,$$

where ϑ and φ are polar angles, t the time variable and c the vacuum velocity of light. In the static case, which alone we shall consider here, α and β are functions of r only.

Let now u be the energy density in the local geodesic coordinate system, and p again the pressure. Then the Einstein equations may, as shown by Tolman [2], be written in the following form

$$\varkappa p = \frac{1}{\alpha}\left(\frac{1}{r\beta}\,\frac{d\beta}{dr} + \frac{1}{r^2}\right) - \frac{1}{r^2}, \tag{12 a}$$

$$\varkappa u = \frac{1}{\alpha}\left(\frac{1}{r\alpha}\,\frac{d\alpha}{dr} - \frac{1}{r^2}\right) + \frac{1}{r^2}, \tag{12 b}$$

$$\frac{dp}{dr} = -\frac{u+p}{2}\,\frac{1}{\beta}\,\frac{d\beta}{dr} \tag{12 c}$$

where

$$\varkappa = \frac{8\pi\gamma}{c^4}.$$

Now in the limit of Newtonian theory the gravitation potential, chosen in the usual way so as to be zero at infinity, is small compared to c^2, and we have approximately

$$\beta \approx 1 + \frac{2V}{c^2}. \tag{13}$$

Since any function of β, which is regular for $\beta = 1$, would in the same approximation be a linear function of V, we may choose the relativistic analogon of V rather freely, and different choices may prove practical under differen circumstances. The choice made here would seem to recommend itself by its close relation to the problem of unordered radiation, which on the one hand is a typically and even extremely relativistic problem, and which on the other hand presents a close analogy to Emden's isothermic gas sphere [3]. In that case p and u are inversely proportional to the square of β. We shall thus put

$$p = A(\varepsilon - \varepsilon_0)^{n+1}, \quad (14$$

with

$$\varepsilon = 1/\beta$$

which in the nonrelativistic limit goes over to the expression (8 a), if the constant A is connected with K in (1) by means of

$$A = \left[\frac{c^2}{2(n+1)}\right]^{n+1} K^{-n}. \quad (15)$$

Regarding now p as a function of ε, we have from (12 c)

$$u = 2\varepsilon \frac{dp}{d\varepsilon} - p, \quad (16)$$

and thus with the aid of (14)

$$u = A(\varepsilon - \varepsilon_0)^n ((2n+1)\varepsilon + \varepsilon_0). \quad (17)$$

§ 2. Definition of mass and basic equations

With (14) and (17) equations (12 a) and (12 b) become differential equations in α and ε, by means of which these quantities may be determined as functions of r, as soon as their values are given for a given value of r. Before considering this problem, we shall see that its solution under the conditions assumed in the thermodynamic theory of the abundance of the elements wil also give the composition of the substance for every value of r. Thus, if al sorts of nuclear reactions are possible with sufficient velocity the concentrations of a specific kind of nuclei will be determined by the temperature and the two chemical potentials of the neutrons and the protons respectively. Further with a plausible assumption about the neutrinos the concentration of electrons and positrons will also be determined by these same quantities. The condition of electrical equilibrium (in practice electrical neutrality) will now provide a relation between the three parameters mentioned [4]. Finally the unordered, electromagnetic radiation will be completely determined by the temperature alone Thus the composition of the substance and the quantities u and p will be determined by two parameters, say the temperature and the neutron chemica potential. If now u and p are given as functions of ε, we may solve for the two parameters in question and express them as functions of ε, so that the composition will be given in terms of ε. Having then obtained ε as a function of r the composition will also be given for every value of r.

Returning now to the equations (12 a) and (12 b) we shall first show that the mass of the system may be determined in a way which is very similar to that based on the classical equation (3). In order to let the analogy appear as directly as possible we shall put

$$M(r)=\frac{4\pi}{\varkappa c^2}\,r\left(1-\frac{1}{\alpha}\right), \tag{18}$$

from which follows

$$\alpha=\left(1-\frac{\varkappa c^2}{4\pi}\,\frac{M(r)}{r}\right)^{-1}. \tag{19}$$

From (12 b) we now get

$$\frac{d\,M(r)}{d\,r}=4\pi r^2\frac{u}{c^2}, \tag{20}$$

or, since $M(0)=0$

$$M(r)=\int\limits_0^r 4\pi r^2\frac{u}{c^2}\,d\,r. \tag{21}$$

Let us now assume that for $r\geq r_0$, $u=0$, $p=0$. Then outside r_0 we shall have $M(r)=\text{konst.}=M$, with which (19) goes over into the Schwarzschild solution outside of a mass of magnitude M. Since this solution ought to be the direct continuation of that valid for $r<r_0$ we get

$$M=\int\limits_0^{r_0} 4\pi r^2\frac{u}{c^2}\,d\,r \tag{22}$$

for the total mass of the system, a formula which bears a close formal analogy to the corresponding classical formula.

It should be noted, that $M(r)$ is not in general the mass of the substance within a sphere of radius r, which is given by the Tolman integral [5]

$$M=\frac{1}{\sqrt{\alpha(r)\,\beta(r)}}\int\limits_0^r 4\pi r^2\sqrt{\alpha\,\beta}\,\frac{(u+3\,p)}{c^2}\,d\,r.$$

Due to its greater simplicity, the expression (22), however, is more convenient for practical puposes. If u and p have no finite zeropoint but go to zero rapidly enough, when r_0 goes to infinity, to make the integrals converge, formula (22) is still valid with the upper limit equal to infinity. Indeed, from equations (12) it follows that

$$\frac{1}{\sqrt{\alpha(r)\,\beta(r)}}\int\limits_0^r 4\pi x^2\sqrt{\alpha(x)\,\beta(x)}\,\frac{u(x)+3\,p(x)}{c^2}\,d\,x=$$

$$=\frac{4\pi}{\varkappa c^2}\,\frac{r^2}{\alpha\beta}\,\frac{d\beta}{d\,r}=\frac{4\pi}{\varkappa c^2}\left[r\left(1-\frac{1}{\alpha}\right)\right]+\frac{4\pi\,p}{c^2}\,r^3=M(r)+\frac{4\pi\,p(r)}{c^2}\,r^3 \tag{23}$$

from which the above statements follow.

We proceed now with the relativistic field equations for our generalized polytropic equilibria. Without lack of generality we may assume $\alpha=\beta=1$ for $r=$ and we shall denote the value of p at that point by p_0. Then we have

$$p=p_0\left(\frac{\varepsilon-\varepsilon_0}{1-\varepsilon_0}\right)^{n+1}, \quad u=p_0\,\frac{(\varepsilon-\varepsilon_0)^n\,((2n+1)\,\varepsilon+\varepsilon_0)}{(1-\varepsilon_0)^{n+1}}. \qquad (24$$

At the same time we shall introduce the following dimensionless variable instead of r

$$s=\varkappa\,p_0\,r^2. \qquad (25$$

With this we get

$$\begin{aligned}\left(\frac{\varepsilon-\varepsilon_0}{1-\varepsilon_0}\right)^{n+1}&=\frac{1}{\alpha}\left(-\frac{2}{\varepsilon}\frac{d\varepsilon}{ds}+\frac{1}{s}\right)-\frac{1}{s}\\ \frac{(\varepsilon-\varepsilon_0)^n\,((2n+1)\,\varepsilon+\varepsilon_0)}{(1-\varepsilon_0)^{n+1}}&=\frac{2}{\sqrt{s}}\,\frac{d}{ds}\left[\sqrt{s}\left(1-\frac{1}{\alpha}\right)\right].\end{aligned} \qquad (26$$

With $n=1$, $\varepsilon_0=0$ these equations are seen to be identical with those governing the gravitational equilibrium of unordered radiation [3]. Indeed, equations (24 give in this case

$$p=p_0/\beta^2, \quad u=3\,p_0/\beta^2.$$

If, on the other hand, ε and ε_0 are both very close to unity the equations go over to the corresponding classical equations, whereby

$$K=\left[\frac{c^2\,(1-\varepsilon_0)}{2\,(n+1)}\right]^{\frac{n+1}{n}}p_0^{-\frac{1}{n}}. \qquad (27$$

§ 3. The case $\varepsilon_0=0$

The case $\varepsilon_0=0$ presents a close analogy to that of unordered radiation also for arbitrary n-values. Thus it is easily seen that the equations (26) and (24 have then the following singular solution

$$\left.\begin{aligned}\alpha&=\frac{n^2+4n+2}{(n+1)^2}\\ \beta&=[(n^2+4n+2)\,\varkappa\,p_0\,r^2]^{1/n+1}\\ p&=\frac{1}{\varkappa\,(n^2+4n+2)\,r^2}\\ u&=\frac{2n+1}{\varkappa\,(n^2+4n+2)\,r^2}\end{aligned}\right\}, \qquad (28$$

which with $n=1$ gives the singular solution for the case of unordered radiation [3].

The complete treatment of this case is quite analogous to that given for the radiation equilibrium [3]. Thus we may put

$$\xi = \frac{\beta^{n+1}}{s}, \quad x = \frac{\beta^{n+1}}{(n+1)^2 \alpha s}, \tag{29}$$

from which follows

$$\alpha = \frac{\xi}{(n+1)^2 x}, \quad \beta = \frac{1}{\varepsilon} = s^{\frac{1}{n+1}} \xi^{\frac{1}{n+1}}. \tag{30}$$

Introducing this into equations (26) with $\varepsilon_0 = 0$ we get after some algebraic reductions

$$\xi = \frac{(n+1)^2}{n+2} \left\{ (n+4) x + \frac{dx}{d\tau} + \frac{n}{(n+1)^2} \right\}, \tag{31}$$

where we have put

$$s = e^{2\tau}, \tag{32}$$

and further

$$x \left(\frac{d^2 x}{d\tau^2} + \frac{n+6}{n+2} \frac{dx}{d\tau} \right) = \frac{n+1}{n+2} \left(\frac{dx}{d\tau} \right)^2 + \frac{3n+2}{(n+1)(n+2)} \frac{dx}{d\tau} - \\ - \frac{2(n+4)}{n+2} x^2 + \frac{2(n^3 + 6n^2 + 8n + 4)}{(n+1)^2 (n+2)} x + \frac{2n}{(n+1)^2 (n+2)}. \tag{33}$$

As in the paper mentioned we put

$$y = -\frac{dx}{d\tau}, \tag{34}$$

and, taking x as independent variable, we obtain the following first order equation

$$x y \frac{dy}{dx} = -\frac{2(n+4)}{n+2} x^2 + \frac{(n+6)}{n+2} x y + \frac{n+1}{n+2} y^2 + \frac{2(n^3 + 6n^2 + 8n + 4)}{(n+1)^2 (n+2)} x - \\ - \frac{3n+2}{(n+1)(n+2)} y + \frac{2n}{(n+1)^2 (n+2)}, \tag{35}$$

With $x = 1$, $y = 0$ this equation is satisfied, which, as shown by (30) and (31), corresponds to the singular solution discussed above. Starting with $\alpha = 1$, $\beta = 1$ for $s = 0$ we get by means of the equations (26) the following expansions valid for small s

$$\frac{1}{\alpha} = 1 - \frac{2n+1}{3} s + \frac{(n+1)(n+2)(2n+1)}{15} s^2 - \\ - \frac{n(n+1)(n+2)(2n+1)(8n^2 + 17n + 14)(n+8)}{630} s^3 + \cdots,$$

$$\beta^{n+1} = 1 + \frac{(n+1)(n+2)}{3} s + \frac{(n+1)(n+2)(2n+1)(n+6)}{90} s^2 + \\ + \frac{(n+1)(n+2)(2n+1)(4-n)}{2835} s^3 \cdots, \tag{36}$$

which correspond to the following expansion of y as a function of x, whic may be directly obtained by means of (35)

$$y=2x-\frac{2(n^2+n+1)}{3(n+1)^2}-\frac{2(2n+1)(n+2)^2}{45(n+1)^3}\frac{1}{x}-\frac{2(2n+1)(n+2)^2(6n^2+11n+7)}{945(n+1)^5}\frac{1}{x^2}\cdots. \quad (37$$

All these formulae go over to those of the former paper by putting $n=1$ Just as there the expansion (37) must be continued to smaller values of x b numerical integration of (35), the result being a curve enclosing the point $x=1$ $y=0$ by smaller and smaller coils.[1] This means that the solution in questio tends asymptotically towards the singular solution (28). From this it follow that there is no finite mass distribution in the case $\varepsilon_0=0$.

§ 4. Closer consideration of the case $\varepsilon_0 \neq 0$

Returning now to the case $\varepsilon_0 \neq 0$ we may conveniently put

$$\varepsilon=\varepsilon_0\,\eta,\quad s=\left(\frac{1-\varepsilon_0}{\varepsilon_0}\right)^{n+1} z^2,\quad \mu=z\left(1-\frac{1}{\alpha}\right), \quad (38$$

whereby the equations (26) take the form

$$\begin{aligned} -\frac{1}{\eta}\frac{d\eta}{dz}&=z^2\,\frac{(\eta-1)^{n+1}+\mu/z^3}{z-\mu} \\ \frac{d\mu}{dz}&=z^2(\eta-1)^n\,[(2n+1)\,\eta+1]. \end{aligned} \quad (39)$$

Further it follows from (18), (25) and (38) that

$$M(r)=\frac{4\pi}{c^2}\,\varkappa^{-3/2},\,p_0^{-1/2}\left(\frac{1-\varepsilon_0}{\varepsilon_0}\right)^{\frac{n+1}{2}}\mu,\quad r=\varkappa^{-1/2}\,p_0^{-1/2}\left(\frac{1-\varepsilon_0}{\varepsilon_0}\right)^{\frac{n+1}{2}} z. \quad (40)$$

We see, that the equations (39) are independent of ε_0, but this quantity reappears in the initial conditions, which are now

$$\eta=\eta_0=\frac{1}{\varepsilon_0}>1,\quad \mu=0 \quad \text{for } z=0. \quad (41)$$

It is easily seen, that these conditions determine η and μ uniquely as a powe series in z valid for small z, whereby we are of course only interested in positive values of the independent variable. Thus a straightforward calculation gives

---

[1] This problem will be more closely studied in a paper by fil. lic. P. O. OLSSON, who kindly pointed out to me that this behaviour is altered, when n becomes smaller than $-2+\frac{4}{\sqrt{7}}$, which, however, is outside of the range of n-values considered here. (Note added to proof).

$$\eta = \eta_0 - \frac{1}{3}\eta_0((n+2))\eta_0 - 1)(\eta_0 - 1)^n z^2 + \cdots$$

$$\mu = \frac{1}{3}[(2n+1)\eta_0 + 1](\eta_0 - 1)^n z^3 - \frac{1}{15}(n+1)\eta_0[(n+2)\eta_0 - 1][(2n+1)\eta_0 - 1] \cdot \cdot (\eta_0 - 1)^{2n-1} z^5 \cdots. \tag{42}$$

We shall now prove, that, how large we may choose η_0, the value $\eta = 1$ will always be reached for a finite value of z. From the second equation (39) we see that μ will be positive for positive z, $\frac{d\mu}{dz}$ being positive as long as the point $\eta = 1$ is not yet reached and zero at that point. Therefore the right side of the first equation (39) will be positive and finite if only $z - \mu > 0$. We shall thus fix our attention on the latter quantity, putting

$$\nu = z - \mu. \tag{43}$$

As is seen from (42), ν is positive for small, positive z-values. In order to have ν negative the point $\nu = 0$ must be reached, when z increases. Since, when this point is approached, $-\frac{d\eta}{dz}$ will increase without limit, it is probable beforehand that η will decrease to the value 1 before the point $\nu = 0$ is reached. We shall now show that this is necessarily so.

From (39) we get

$$\frac{-d\nu}{(\eta - 1)^n[(2n+1)\eta + 1] - 1/z^2} = z^2\,dz = \frac{-\nu\,d\eta}{\eta(\eta - 1)^{n+1} + \eta\mu/z^3}. \tag{44}$$

Now, trouble could only arise if for a certain value ν_1, of ν this quantity would decrease with increasing z, which will only occur, when the denominator of the left expression of (44) is positive. Since, further, both terms of the right hand denominator are positive we obtain from (44) the following inequality valid for positive dz

$$\frac{-d\nu}{(\eta - 1)^n[(2n+1)\eta + 1]} < z^2\,dz < \frac{-\nu\,d\eta}{\eta(\eta - 1)^{n+1}}, \tag{45}$$

from which follows

$$-\frac{d\nu}{\nu} < -\left(\frac{2(n+1)}{\eta - 1} - \frac{1}{\eta}\right) d\eta,$$

and, after integration

$$\nu > \nu_1 \frac{\eta_1}{\eta}\left(\frac{\eta - 1}{\eta_1 - 1}\right)^{2(n+1)}, \tag{46}$$

η_1 being the η-value corresponding to ν_1. From this inequality we see, that we shall never reach the value $\nu = 0$, not even when η reaches the value 1. Consequently the right side of the first equation (39) will stay finite and positive for increasing z including the point, where $\eta = 1$, which will thus be reached for a finite value z_0 of z. The result just obtained would at first sight seem to contradict the fact that classical polytropes lead to finite mass-values only for a certain range of n-values. It must be remembered, however, that in a case, where no finite mass is possible, the general relativistic corrections to the equations in question will become very large for large r-values thus invalidating the conclusions drawn from the classical polytrope theory.

We can now compute the mass M and radius r_0 of a polytropic model fulfilling the initial conditions (41), M being equal to $M(r_0)$. Thus from (40) and (39) we get

$$\begin{aligned} M &= \frac{4\pi}{c^2} \varkappa^{-3/2} p_0^{-1/2} (\eta_0 - 1)^{\frac{n+1}{2}} \int_0^{z_0} z^2 (\eta - 1)^n \left[(2n+1)\eta + 1\right] dz \\ r_0 &= \varkappa^{-1/2} p_0^{-1/2} (\eta_0 - 1)^{\frac{n+1}{2}} z_0. \end{aligned} \tag{47}$$

Since η is uniquely determined by the initial conditions, the integral in the expression for M will be a function of η_0 alone. We see further that both M and r_0 are inversely proportional to the squareroot of the pressure at the centre of the model.

We are now planning to make numerical integrations of the equations (39) for a number of values of η_0.

Stockholms Högskolas Institut för mekanik och matematisk fysik, October 1953.

REFERENCES

1. S. Chandrasekhar, An Introduction to the Study of Stellar Structure, Chicago 1938.
2. R. C. Tolman, Relativity, Thermodynamics and Cosmology, Oxford 1934, p. 246.
3. O. Klein, Arkiv f. mat. astr. o. fys. Bd. 34 A, No. 19, 1947.
4. G. Beskow and L. Treffenberg, Arkiv f. mat. astr. o. fys. Bd. 34 A, No. 17, 1947.
5. R. C. Tolman, Relativity, Thermodynamics and Cosmology, Oxford 1934, p. 248.

Tryckt den 2 mars 1954

Uppsala 1954. Almqvist & Wiksells Boktryckeri AB

ARKIV FÖR FYSIK Band 7 nr 42

Communicated 25 November 1953 by NILS ZEILON and BENGT EDLÉN

On a mathematical model of a photographic emulsion

By CARL-ERIK FRÖBERG

With 2 figures in the text

Summary

The paper gives a model in tabular form of a photographic emulsion. From this model tracks can be obtained similar to those formed by cosmic rays. The number of grains per unit length is computed under different assumptions. Lastly a method for obtaining corrections due to secondary high-energy δ-rays is sketched, all procedures being based on a simple Monte Carlo-technique.

In connection with investigations on cosmic rays which are made visible as tracks in photographic emulsions, some problems arise which cannot easily be handled by ordinary methods. In some cases it has turned out that a Monte Carlo-technique can be successfully applied and for this reason a mathematical model of the photographic emulsion is needed. This model will here be constructed under the following assumptions:

1. The grains are equal in size and spherical in shape.
2. The grains are distributed at random in the emulsion.
3. The grains occupy 50 % of the total volume.

Two methods have been tried, but only one of them seems to be satisfactory. The other method, however, might be used as a complement to the first one, and both of them will be described below.

The first method is more or less straight forward. A finite volume was chosen rather deliberately: $0 \leq x \leq 10$, $0 \leq y \leq 10$, $0 \leq z \leq 120$ and the radius of the spheres $R = 2.5$. Since any two spheres must not intersect, we have the condition $|\vec{r_i} - \vec{r_k}| \geq 5$, where $\vec{r_k}$ is the coordinate vector of the k:th center. Suppose m spheres have already been chosen. Then the next one must enter the volume in a random manner but also fulfilling the condition above, which means that certain regions are blocked by the m present spheres. However, there is still one difficulty. It turns out that the centers have a strong tendency of gathering in the corners of the xy-square, consequently violating assumption (3). This can be avoided by making the whole configuration periodic. Thus we introduce the alternative condition:

Table 1.

x	y	z	x	y	z
4.05	1.05	0.10	6.65	4.45	60.66
2.55	5.75	1.14	1.70	6.50	60.80
8.70	2.30	2.51	5.90	9.45	61.00
6.30	7.90	3.74	9.40	0.15	64.53
1.50	5.00	6.00	1.35	5.85	67.02
3.20	0.30	7.07	6.60	4.10	67.43
6.65	4.15	7.30	5.25	9.05	67.68
8.45	8.85	8.20	0.65	1.35	69.23
3.60	6.67	10.50	2.65	7.45	71.69
0.70	2.60	10.76	6.50	1.15	72.05
5.55	1.45	11.40	7.65	6.15	72.23
9.35	7.65	14.36	1.85	2.15	74.02
3.10	4.20	14.90	5.55	8.55	76.36
8.30	2.80	15.40	6.50	3.50	76.48
2.65	2.60	19.66	1.70	5.55	77.69
4.20	7.60	19.90	0.40	0.40	78.50
9.20	6.50	20.07	7.05	4.85	81.27
7.45	1.45	20.55	4.50	0.40	81.63
1.05	9.60	23.54	2.00	4.80	83.91
4.50	5.60	24.51	7.70	8.50	85.09
9.75	4.10	26.00	2.55	9.15	86.53
7.25	8.15	27.95	8.55	3.15	87.32
3.95	1.85	29.73	3.60	4.40	88.64
3.45	6.70	31.00	9.05	7.55	89.85
9.45	0.55	31.79	9.25	2.05	92.15
8.65	5.55	32.01	3.25	7.15	92.86
5.10	0.25	34.33	4.25	2.05	93.02
1.85	6.65	35.74	8.05	6.20	94.69
6.40	4.60	36.43	2.30	4.50	97.01
0.75	1.75	36.51	8.95	8.35	99.35
8.70	7.90	39.43	3.80	0.30	99.60
4.75	1.00	39.50	8.05	3.35	99.72
3.50	6.85	42.00	2.75	5.85	102.14
2.35	2.25	43.71	7.50	6.30	103.75
7.25	3.65	43.86	4.75	1.65	104.20
9.25	8.21	44.39	9.75	0.80	104.62
4.05	7.85	46.92	1.00	5.30	107.19
9.65	1.65	48.01	5.85	5.45	108.48
5.00	3.40	49.00	6.85	0.45	108.84
9.85	6.95	50.57	1.85	9.75	109.55
5.60	9.40	52.01	1.20	3.85	112.58
1.45	2.50	52.61	8.15	7.85	112.95
7.35	3.25	55.45	3.30	8.60	114.25
4.45	7.35	56.47	4.85	4.05	116.02
9.60	8.90	56.81	0.15	2.65	117.34
2.75	2.70	57.65	9.35	7.65	117.80

$$[(\xi_i-\xi_k)^2+(\eta_i-\eta_k)^2+(\zeta_i-\zeta_k)^2]^{1/2}\geq 5;\quad \xi_i=\begin{cases}x_i\\ x_i\pm 10\end{cases}\quad \eta_i=\begin{cases}y_i\\ y_i\pm 10\end{cases}\quad \zeta_i=\begin{cases}z_i\\ z_i\pm 120.\end{cases}$$

With the aid of a table over random numbers, 92 spheres, corresponding to 50.18 % of the total volume, were distributed and the configuration of Table 1 was obtained. The work is simple in principle but tedious and time-consuming. Choosing different straight lines in the z-direction in the final model, we obtain

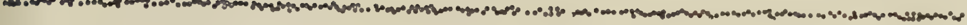

Fig. 1 a. Model track.

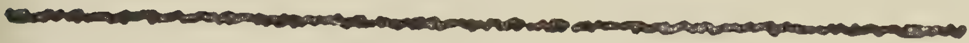

Fig. 1 b. Same, out of focus.

different tracks which can be combined into longer ones. These tracks can be manipulated in many ways by introducing various complementary conditions (e.g. as to energy distribution, formation of secondary rays of different range and so on). Fig. 1 shows a track obtained in this way.

The second method works in the following way. Let r be the radius of the spheres and consider a symmetric configuration of closest packing where the centers of the spheres form a mesh of squares in parallel planes, the distance between two adjacent planes being $r\sqrt{2}$. Taking a large volume V_0 and denoting by V the volume occupied by spheres, we find

$$\frac{V}{V_0} = \frac{\pi\sqrt{2}}{6} = 0.74048.$$

Now suppose that all spheres shrink from radius r to radius R, then the volume ratio V/V_0 will decrease to f and we get:

$$R = r \cdot \left(\frac{6f}{\pi\sqrt{2}}\right)^{1/3}.$$

We will start from this completely symmetric configuration and step by step change the positions of the spheres.

Choose a suitable domain containing N spheres enumerated from 1 to N, We take a random sphere and give it a random displacement repeating the procedure a suitable number of times. Introducing four stochastic variables x_1 x_2 x_3 and x_4 with a rectangular distribution in the interval (0,1) we can describe the process in the following way:

1. Choose a sphere (number n) at random: $n = N x_1$
2. Choose a random azimuth angle $\varphi = 2\pi x_2$
3. Choose a random polar angle $\theta = \arccos\,(1-2x_3)$

4. In this direction the sphere (n) can move only a limited distance a before collision with some other sphere (m). Let the coordinates of the centers be $(x_n\, y_n\, z_n)$ and $(x_m\, y_m\, z_m)$ and further $(\xi,\ \eta,\ \zeta) = (x_m - x_n,\ y_m - y_n,\ z_m - z_n)$. We easily find $a = p - \sqrt{p^2 - \xi^2 - \eta^2 - \zeta^2 + 4R^2}$ with $p = \xi \sin\theta \cos\varphi + \eta \sin\theta \sin\varphi + \zeta \cos\theta$. Then the displacement q is obtained by $q = a x_4$.

5. The new coordinates of (n) are computed by

$$x_n' = x_n + q \sin\theta \cos\varphi$$

$$y_n' = y_n + q \sin\theta \sin\varphi$$

$$z_n' = z_n + q \cos\theta.$$

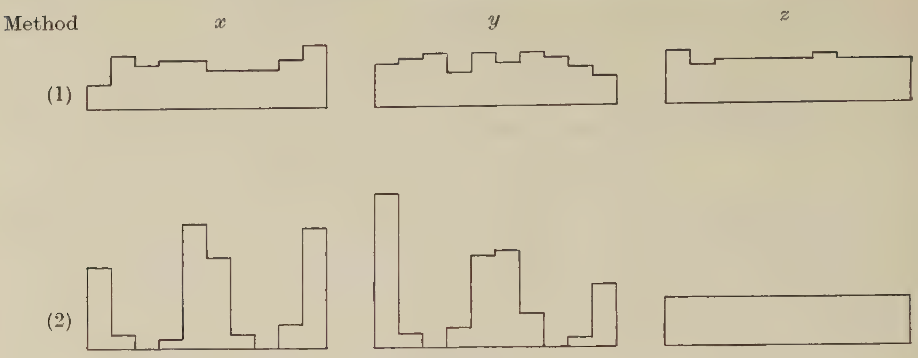

Fig. 2. Frequency diagram for sphere center coordinates.

This procedure was tried on 100 spheres with the value $f = \frac{1}{2}$ and 250 displacements.[1] However, an examination of the distribution of x, y, and z-values revealed a marked inhomogeneity. On the other hand the corresponding check on Table 1 disclosed a more satisfactory homogeneity (Fig. 2).

Another question of some interest will also be treated here. A primary particle passing through the emulsion will give rise to secondary δ-rays by ionization. With no secondaries only the grains coming into contact with the primary ray will be developed. Now we introduce a cylinder with the primary track as axis. The radius $a \cdot R$ is chosen in such a way that all grains in contact with this (immaterial) cylinder are developed with probability 1, while grains outside and sufficiently close to the cylinder are developed with a probability < 1 (depending on the distance from the axis). In this way the great number of small-energy δ-rays are taken into account, while we have to apply a correction afterwards due to the small number of high-energy δ-rays. Now we want to compute the number of grains per unit length without the correction just mentioned.

For this purpose consider a sphere with radius 1 and an intersecting cylinder with radius a. The distance between the center of the sphere and the axis of the cylinder is denoted by r and the common volume by $V(r, a)$. Let the equations be:

$$x^2 + y^2 + z^2 = 1$$

$$x^2 + (z - r)^2 = a^2.$$

Then $V(r, a) = 2 \cdot \iint_S \sqrt{1 - x^2 - z^2} \cdot dx\, dz$ where S is the common part of the circles $x^2 + z^2 = 1$ and $x^2 + (z - r)^2 = a^2$. We distinguish between three different cases: (I) $r \leq 1 - a$; (II) $1 - a < r < 1$; (III) $1 \leq r \leq 1 + a$. In case (I) we get putting

$$\begin{cases} x = \varrho \sin \varphi \\ z = r - \varrho \cos \varphi \end{cases} \qquad k = \sqrt{\frac{4 r \varrho}{1 - (r - \varrho)^2}}$$

---

[1] The numerical work was performed by Miss FEDRA NEFTIDJI and is hereby gratefully acknowledged.

$$V(r,a)=4\cdot\int_0^a \varrho\cdot d\varrho\int_0^\pi \sqrt{1-r^2-\varrho^2+2r\varrho\cos\varphi}\;d\varphi=8\int_0^a \varrho\sqrt{1-(r-\varrho)^2}\;E(k)\,d\varrho.$$

In case (II) we obtain: $V(r,a)=8\int_0^{1-r}\varrho\sqrt{1-(r-\varrho)^2}\;E(k)\,d\varrho+$

$$+8\int_{1-r}^{a}\sqrt{\frac{\varrho}{4r}}\cdot\{4r\varrho\,E(k^{-1})-[(r+\varrho)^2-1]\cdot K(k^{-1})\}\,d\varrho$$

and in case (III):

$$V(r,a)=8\int_{r-1}^{a}\sqrt{\frac{\varrho}{4r}}\cdot\{4r\varrho\,E(k^{-1})-[(r+\varrho)^2-1]\cdot K(k^{-1})\}\,d\varrho$$

where E and K are the usual complete elliptic integrals. $V(r,a)$ has been computed for $a=0$, 0.1, 0.2, 0.3, and 0.4. It is now easy to find the mean value $\overline{V}_a$ and the number of spheres n_a per unit length:

$$\overline{V}_a=\int_0^{1+a} r\cdot V(r,a)\,dr\Big/\int_0^{1+a} r\,dr$$

$$n_a=\tfrac{1}{2}\pi a^2/\overline{V}_a\,.$$

n_a appears in Table 2.

Table 2.

a	n_a
0	0.375
0.1	0.454
0.2	0.540
0.3	0.627
0.4	0.735

Lastly we also sketch briefly how the correction for the high-energy δ-rays can be applied. On the track obtained from Table 1 we choose a random point and a random direction:

$$\begin{cases} z=120\,x_1\\ \varphi=2\,\pi x_2\\ \theta=\arccos\,(1-2\,x_3)\end{cases}$$

Then we choose the energy in agreement with the well-known Mott formula:

$$f(E)=c\,(1/E-1/E_m);\; c=\frac{E_0\,E_m}{E_m-E_0}\,.$$

E_0 is the lower energy limit (corresponding to the radius of the cylinder), E_m is the maximum impact energy and $f(E)$ is the relative number of δ-rays with energy $>E$ (normalized in such a way that $f(E_0)=1$). Taking a new stochastic variable x_4 with rectangular distribution over (0,1) we get:

$$E=\frac{E_0 E_m}{E_m-(E_m-E_0)\,x_4}.$$

Experimentally known relations between energy and range (for AgBr and gelatine) make it possible to follow the path of the ray in the emulsion, and we can see directly whether a new grain is developed or not. The number of such rays with energy between E_0 and E_m depends on the energy of the primary particle and is also known from experiments. As an example the number of new grains was computed close to the end of a proton track when the cylinder radius was $\frac{1}{5}$ of the grain radius ($a=0.2$). The result was about 6 %. It is obvious that the errors in such computations may become considerable, but nevertheless it should be possible to obtain important information if the method is used with skill and good judgement.

Institute of Theoretical Physics, Lund.

Tryckt den 2 mars 1954

Uppsala 1954. Almqvist & Wiksells Boktryckeri AB

ARKIV FÖR FYSIK Band 7 nr 43

Communicated 3 June 1953 by MANNE SIEGBAHN

Acceleration of heavy ions in the 225-cm cyclotron at the Nobel Institute of Physics

Preliminary note

BY HUGO ATTERLING

With 1 figure in the text

Cyclotrons are usually used for the production of high-energy protons, deuterons and alpha particles. During the last few years the acceleration of heavy ions—which in this connexion means ions heavier than alpha particles—has been given much attention in some laboratories.

In 1940 ALVAREZ (1) succeeded in accelerating carbon nuclei, using the 37-inch cyclotron at Berkeley. The work on carbon acceleration was continued with the Berkeley 60-inch cyclotron by other investigators (2–8). MILLER *et al.* (6) report that they used a hooded capillary ion source fed with carbon dioxide; they obtained $^{12}C^{6+}$ and $^{13}C^{6+}$ ions of maximum energy 115 and 122 MeV respectively. MILLER (8) mentions that G. B. ROSSI improved the carbon beam by a factor of ten by using an uncooled ion source of graphite, exposed to the cyclotron radio-frequency field. In the synchro-cyclotron at Chicago CHOU *et al.* (9) have accelerated carbon nuclei to energies of 1,100 MeV.

Recently WALKER and FREMLIN (10) published a communication on some of their work on heavy ion acceleration with the 60-inch cyclotron at Birmingham. In this communication they report studies concerning the resonances of various heavy ions from $^{9}Be^{4+}$ to $^{20}Ne^{9+}$. Later these investigators increased the internal beam currents of, in particular, $^{14}N^{6+}$ and $^{16}O^{6+}$ ions to intensities sufficient for the production of activities of useful strengths (11, 12). By the introduction of argon into the cyclotron chamber they increased very markedly the intensity of high-energy six-charged ions (11). They found that nitrous oxide was the best source of both nitrogen and oxygen ions (11).

WYLY and ZUCKER (13) report that a 63-inch cyclotron has been constructed at the Oak Ridge National Laboratory to accelerate $^{14}N^{3+}$ ions to an energy of about 25 MeV. At maximum radius beam currents of approximately 1 μA are obtained.

The possibility of using accelerated heavy ions as a means of studying nuclear structure has been considered in a paper by BREIT *et al.* (14).

The following note gives briefly preliminary results of some experiments going on at the Nobel Institute of Physics. From the beginning of 1953 the fixed-frequency 225-cm cyclotron has been used for heavy ion acceleration; $^{12}C^{6+}$ ions, and, in particular, $^{14}N^{6+}$ and $^{16}O^{6+}$ ions have been accelerated. As already mentioned in a communi-

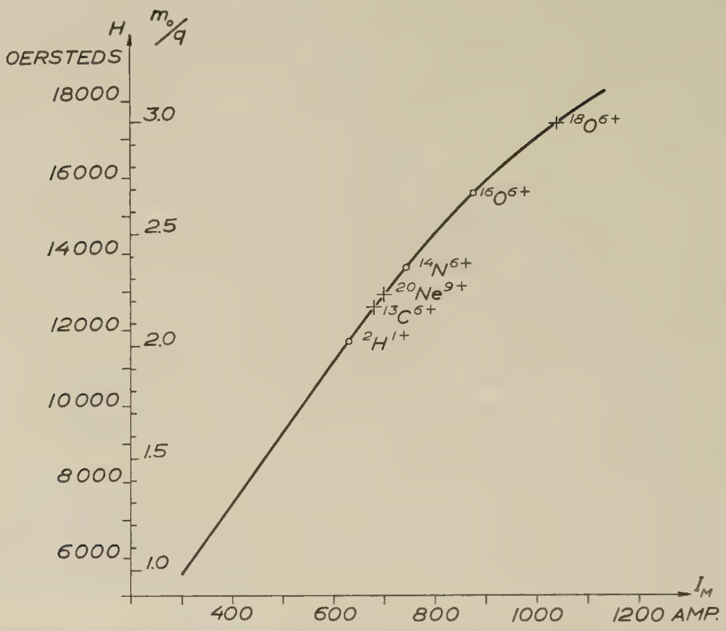

Fig. 1. The central magnetic field H plotted as a function of the magnet current I_M for the Stockholm 225-cm cyclotron. The fields for resonance at the cyclotron frequency of 8.7 megacycles per sec. are indicated for some particles. A scale for m_0/q is also given (m_0 = rest mass of ion in mass units; q = charge carried by ion in units of the positron charge). The circles represent some observed resonances. The crosses are calculated points (the resonance of $^{20}Ne^{9+}$ has been located in preliminary experiments).

cation on this cyclotron (15), the machine has such dimensions that the magnetic field used for the production of 25 MeV deuterons (for which the cyclotron was primarily designed) is only about 2/3 of the maximum obtainable field. It will be seen from the following that this fact makes the Stockholm 225-cm cyclotron a useful tool for the acceleration of heavy ions.

For a given frequency of the dee voltage the maximum energy of particles in resonance with the radio-frequency field is approximately proportional to the atomic mass number A. With the present frequency (8.7 megacycles per sec.) the 225-cm cyclotron at Stockholm can accelerate ions to maximum energies of about 12.5 × × A MeV (12.5 MeV protons, 25 MeV deuterons, 50 MeV alpha particles, 150 MeV ^{12}C ions, and so on). The magnetic field at the centre of the acceleration chamber is—for resonance at fixed frequency—approximately proportional to m_0/q, where m_0 is the rest mass of the accelerated ion and q its charge. In Fig. 1 the central magnetic field is plotted as a function of the magnet current for the 225-cm Stockholm cyclotron. The fields corresponding to resonance for some particles are indicated. A scale for m_0/q gives the mass-to-charge ratios for which resonance can be obtained. In general, fixed-frequency cyclotrons are designed for acceleration of deuterons, for which m_0/q is about 2. The amount by which m_0/q can exceed 2, and resonance still be obtained at unchanged frequency, depends on how much the magnetic field can be increased above the value for deuteron resonance.

The mechanism for the production of high-energy heavy ions by utilizing the third harmonic pre-acceleration of ions in the doubly-charged state has been outlined by MILLER (8) and by WALKER and FREMLIN (10). Thanks to this pre-acceleration it is possible to produce high-energy six-charged ions of, for instance, nitrogen and oxygen, provided that the magnetic field can be adjusted to give resonance for the corresponding m_0/q-value. As may be seen from Fig. 1, particles with mass-to-charge ratios as high as 3 can be accelerated in the Stockholm 225-cm cyclotron. This machine, therefore, can be used for the acceleration of a variety of heavy ions.

In the experiments carried out with the Stockholm cyclotron doubly-charged ions have been produced in an arc ion source with a hood made of Elkonite (a copper-tungsten alloy) (16). The high-energy ions have been collected by a target inside a windowed probe which can be inserted to different radii. The window opening of this probe is covered with a thin metal foil (aluminium or platinum) to absorb all doubly-charged ions, the maximum energy of which is only 1/9 of that of the six-charged ions. Due to the way in which the six-charged ions are formed, the internal beam of these ions has a continuous energy distribution up to the maximum energy. By use of the windowed probe the current of ions reaching the target with energies exceeding a certain value can be measured. This has so far been achieved by means of a current sensitive galvanometer connected to the target, which is insulated from the surrounding probe.

To improve the stripping of ions to the six-charged state the above-mentioned method, consisting of the introduction of argon into the cyclotron chamber, as used in the Birmingham experiments (11), has been adopted. With argon in the chamber the pressure (measured in one of the dee stem tanks) is increased from about 5×10^{-6} mm Hg to a value in the range from 1×10^{-5} to 1.5×10^{-5} mm Hg. By switching off the argon flow when the machine has been running it has been proved that the presence of argon in the cyclotron chamber improves the beam of high-energy six-charged ions. No accurate quantitative investigation of this increase of the beam intensity has been made. Some preliminary experiments indicate that the beam of $^{14}N^{6+}$ ions with energies ranging from 60 to 175 MeV is increased by the argon gas by a factor between 2 and 5.

To check that the beam reaching the target, measured by the galvanometer, really consists of high-energy heavy ions, gold foils have been bombarded and the induced alpha activity measured. When accelerating, for instance, nitrogen ions, this alpha activity can be produced only by particles with energies higher than about 70 MeV, which corresponds to the Coulomb barrier of gold.

Table 1. Energies and beam-strengths of $^{12}C^{6+}$, $^{14}N^{6+}$ and $^{16}O^{6+}$ ions, accelerated in the Stockholm 225-cm cyclotron. The energies given are the maximum attainable energies corresponding to a radius of 90 cm. The beam currents have been measured at a radius of about 88.5 cm.

Particle	Max. energy (MeV)	Internal beam	Source gas
$^{12}C^{6+}$	150	10^{11} ions/sec. with energies > 50 MeV	CO_2
$^{14}N^{6+}$	175	1×10^{10}—5×10^{10} ions/sec. with energies > 60 MeV	N_2O
$^{16}O^{6+}$	200	10^{9} ions/sec. with energies > 60 MeV	N_2O

Internal beams of strengths high enough for the production of useful amounts of activities have been obtained of $^{12}C^{6+}$, $^{14}N^{6+}$ and $^{16}O^{6+}$ ions. The source gas has been carbon dioxide when accelerating carbon ions. In the first experiments with nitrogen ions the ion source was fed with nitrogen gas. The successful use of nitrous oxide (N_2O) in the Birmingham cyclotron (11) suggested trying this gas, and in the continued Stockholm experiments both nitrogen and oxygen ions have been produced from N_2O. Using neon gas in the ion source a preliminary investigation of the $^{20}Ne^{9+}$ resonance has been made. The intensity of the neon beam, however, has not been adequate for producing detectable activities in heavy targets.

A summary of data is given in Table 1.

Further details of the work on heavy ion acceleration with the 225-cm cyclotron will be published later.

I wish to acknowledge the technical assistance of several members of the 225-cm cyclotron group.

Nobel Institute of Physics, Stockholm 50.

REFERENCES

1. ALVAREZ, L. W., Phys. Rev. *58*, 192 (A), 1940.
2. TOBIAS, C., Thesis, University of California, Berkeley, 1942.
3. TOBIAS, C. and SEGRÈ, E., Phys. Rev. *70*, 89 (L), 1946.
4. CONDIT, R., Thesis, University of California, Berkeley, 1942, and Phys. Rev. *62*, 301 (A), 1942.
5. YORK, H., HILDEBRAND, R., PUTNAM, T., and HAMILTON, J. G., Phys. Rev. *70*, 446 (A), 1946.
6. MILLER, J. F., HAMILTON, J. G., PUTNAM, T. M., HAYMOND, H. R., and ROSSI, G. B., Phys. Rev. *80*, 486 (L), 1950.
7. MILLER, J. F., Phys. Rev. *83*, 1261 (L), 1951.
8. MILLER, J. F., Thesis, University of California, Berkeley, 1952.
9. CHOU, C. N., FRY, W. F., and LORD, J. J., Phys. Rev. *87*, 671 (L), 1952.
10. WALKER, D. and FREMLIN, J. H., Nature *171*, 189, 1953.
11. Private communication from Dr. J. H. FREMLIN.
12. CHACKETT, K. F., FREMLIN, J. H., and WALKER, D., Proc. Phys. Soc. *A 66*, 495 (L), 1953.
13. WYLY, L. D. and ZUCKER, A., Phys. Rev. *89*, 524 (L), 1953.
14. BREIT, G., HULL, M. H., and GLUCKSTERN, R. L., Phys. Rev. *87*, 74, 1952.
15. ATTERLING, H. and LINDSTRÖM, G., Nature *169*, 432, 1952.
16. Concerning this type of ion source reference is made to COWIE, D. B. and KSANDA, C. J., Rev. Sci. Instr. *16*, 224, 1945.

Tryckt den 27 februari 1954

Uppsala 1954. Almqvist & Wiksells Boktryckeri AB

ARKIV FÖR FYSIK Band 7 nr 44

Communicated 2 December 1953 by OSKAR KLEIN and HILDING FAXÉN

On the temperature jump in a rarefied gas

By PIERRE WELANDER

With 11 Figures in the text

Contents

		Page
	Summary	507
I.	Introduction	508
II.	Survey of the literature	510
III.	Discussion of the old theory	512
IV.	Fundamental equations	514
V.	Collision mechanism	523
VI.	Determination of the distribution function	526
VII.	Equations for the density and temperature gradients	528
VIII.	Numerical calculations	533
IX.	Final results	538
App. I.	Treatment of viscous slip	542
App. II.	The theory of Wiener and Levinson	545
App. III.	Computation of the integrals J_n and L_{mn}	549
	References	553

Summary

A theoretical investigation is made of the conditions in a rarefied monatomic gas having heat exchange with an adjacent wall. The calculations have been carried out on the assumption that the rate of change of the molecular distribution function owing to the inter-molecular collisions is proportional to the deviation from the Maxwellian state, and that the gas molecules which impinge on the wall are reflected back in Maxwellian distribution.

The resulting temperature distribution in the gas shows an infinite gradient at the wall. The temperature jump differs from that given previously by SMOLUCHOWSKI and others in that the factor $\frac{2-a}{a}$ is replaced by $\frac{2-ka}{a}$, where k is a constant. Its value is calculated as 0.827.

It may be expected that the results apply quite well for polyatomic gases, also.

I. Introduction

In the conduction of heat between a highly rarefied gas mass and an adjacent wall, a difference has been observed between the temperature T_0 of the gas next to the wall and the wall temperature T_w. This difference is of the order of $\lambda\left(\frac{\partial T}{\partial n}\right)_w$, where $\left(\frac{\partial T}{\partial n}\right)_w$ is the normal component of the temperature gradient in the gas as calculated by the ordinary theory of heat conduction, and λ is the mean free path of the gas molecules. Moreover, the temperature in the gas does not vary linearly near the wall, but deviates from a linear distribution in the manner indicated in fig. 1. The deviation is appreciable over a region which stretches up to a distance of a few λ from the wall, and which in the following will be called *the transition region.*

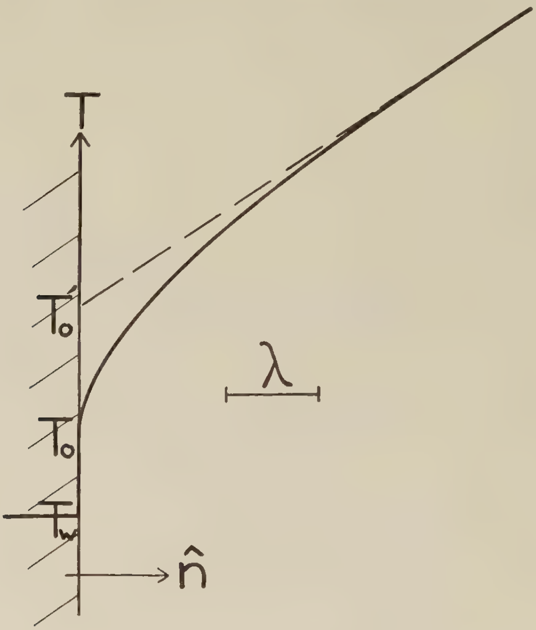

Fig. 1. Temperature distribution near a wall.

These phenomena are partly due to the fact that the gas molecules reflected from the wall have never attained complete temperature equilibrium with it, and thus have a temperature T_{0_+} differing somewhat from the wall temperature T_w. However, the purely geometrical restrictions which the wall exercises on the movement of the gas molecules also play an important rôle. The explanation of this is obvious if we consider that the molecules which cross in one direction an imaginary plane in the gas parallel with the wall do not have the actual temperature there, but instead have the temperature corresponding roughly to the region where they last suffered an impact. We thus find, *e.g.*, n the case where the molecules are reflected from the wall in temperature quilibrium with it, that the temperature T_0 is the mean of the wall temperature and the temperature existing at a distance $\approx \lambda$ from the wall.

By *the temperature jump* is usually meant the difference between the temperature T_0', arising at the wall from a linear extrapolation of the temperature curve ust beyond the transition region, and the wall temperature T_w (*cf.* fig. 1). As the transition region has a diffuse bound, this definition is only applicable when, according to the ordinary theory, the temperature curve may be considered as linear over distances of the order of λ, that is to say, when

$$\left| \frac{\lambda \left(\frac{\partial^2 T}{\partial n^2} \right)_w}{\left(\frac{\partial T}{\partial n} \right)_w} \right| \ll 1.$$

In practice the wall often is a circular-sectioned filament (hot-wire manometer). If its radius is r, we get from the heat flow equation in a cylindrically symmetrical case

$$\frac{\left(\frac{\partial^2 T}{\partial n^2} \right)_w}{\left(\frac{\partial T}{\partial n} \right)_w} = - \frac{1}{r},$$

and the condition above may then be written $\lambda \ll r$.

Now, measurements of the temperature jump are carried out with the object of determining indirectly, by comparison with a theoretical jump value, the degree of heat exchange between the wall and the gas molecules. This is usually characterized by *the accommodation coefficient*, which enters into the theoretical jump value as an unknown parameter. The reliability of such a determination depends to a large extent, then, on the reliability of the theoretical value. Up to now, however, it has not been possible to advance a correct theory, and all that one has to go on is a rough calculation, given essentially by SMOLUCHOWSKI [26] in 1899, in which the transition region is entirely ignored.

The main difficulty in developing a more advanced theory is that use cannot be made of the precise method of calculation developed by CHAPMAN and ENSKOG [3, 5]. This method is found to be quite successful under ordinary conditions, but it fails when applied to the transition region.[1]

Another problem arising here concerns the reflection of the gas molecules from the wall. Whereas in the old theory it is found sufficient to characterize the reflection mechanism by the accommodation coefficient only, this mechanism must in an advanced theory necessarily be described in detail, and we still have not the factual foundation on which to base such a description.

---

[1] A new general method of calculation, known as *the 13-moment method*, has recently been presented by H. GRAD [9] and applied successfully to the transition region. His calculation of the temperature jump is carried out only in a first approximation with the result agreeing with that of the old theory, but it should be possible, in principle at least, to extend his results further.

The treatment of which an account is to be given here cannot pretend to furnish any complete and systematic penetration into the problem; the assumptions made are in part rather special and the way of reasoning is found to be essentially an intuitive one. Nevertheless, it does appear as if the results are physically sound and in reasonable agreement with the experimental evidence where such is available, and we can hope to have achieved here a picture that is principally correct concerning the conditions prevailing in the transition region.

As in the theory of CHAPMAN and ENSKOG, the start is made from the Boltzmann equation for a rarefied monatomic gas. This equation is applied to the transition region under certain simplifying assumptions, analogous to those made in the boundary layer theory of hydrodynamics. The collision integral in the equation is further assumed to be proportional to the deviation from the Maxwellian equilibrium state, and the gas molecules reflected from the wall are assumed to have a Maxwellian distribution.

In the last stage of our calculations we are met with a pair of integral equations for the density and temperature gradients. These equations have been solved numerically with the aid of the digital computer BARK at the Swedish Board of Computing Machinery. After the temperature gradient was determined, the temperature distribution in the gas and the temperature jump could easily be found.

A brief report is given in an appendix of the corresponding treatment of *the viscous slip*, a related phenomenon arising when the gas has a mass velocity along the wall.

II. Survey of the literature

The occurrence of a temperature jump in a rarefied gas was first suggested by KUNDT and WARBURG [16]. The effect was ascertained experimentally by SMOLUCHOWSKI [25], who also presented two theoretical calculations of the jump value [26]. His first calculation was based on the rough *method of mean free path*, whereas in his second calculation the starting point were the results which MAXWELL [20] had arrived at earlier in his investigation of a gas composed of molecules repelling each other inversely as the fifth power of the distance (*Maxwell-gas*).

In this latter case, assuming that of the gas molecules which impinge on the wall a certain fraction f is reflected specularly and the remainder is reflected in Maxwellian distribution, SMOLUCHOWSKI found a jump value

$$\Delta T = \frac{15}{16}\sqrt{2\pi}\,\frac{2-f}{f}\,\frac{\eta}{\sqrt{p\varrho}}\left(\frac{\partial T}{\partial n}\right)_w = \frac{75\pi}{128}\,\frac{2-f}{f}\,\lambda\left(\frac{\partial T}{\partial n}\right)_w . \tag{1 a}$$

Here η is the coefficient of viscosity, p the pressure and ϱ the density. λ will have the meaning of *equivalent mean free path of heat conduction* [14].

More recently another parameter, *the accomodation coefficient*, has been introduced to characterize the reflection mechanism at the wall [12]. The accommodation coefficient is defined as

$$a = \frac{E_{0_-} - E_{0_+}}{E_{0_-} - E_w} \cdot \tag{2}$$

Iere E_{0_-} represents the energy which is brought up to the wall per unit area nd second by the incident stream of gas molecules, while E_{0_+} and E_w re-resent the corresponding energies carried away from the wall by the reflected tream of molecules in the actual case and the case where this stream forms Maxwellian distribution at the wall temperature T_w. $a=0$ corresponds to the ase of no heat exchange taking place at the wall, $a=1$ to the case of the eat exchange being complete.

If we now introduce the accomodation coefficient in the calculation, we ob-ain the jump value

$$\Delta T = \frac{75\pi}{128} \frac{2-a}{a} \lambda \left(\frac{\partial T}{\partial n}\right)_w , \tag{1 b}$$

vhich is the same as before, apart from f being replaced by a. It should be bserved, however, that the last result is of much more general application, as n this case no special assumptions are made regarding the distribution of the eflected molecules.

The jump value commonly given in more recent literature is, for a monatomic as,

$$\Delta T = \frac{15}{8} \frac{2-a}{a} \lambda \left(\frac{\partial T}{\partial n}\right)_w . \tag{1 c}$$

his corresponds to a value of $\frac{5}{4}$ for the quotient $\frac{K}{\varrho \bar{v} \lambda c_v}$, instead of the value $\frac{5\pi}{64} \approx 1.23$ for a Maxwell-gas (K is the coefficient of heat conduction, $\bar{v}$ the nean speed of the gas molecules and c_v the specific heat per gram). As may e seen the difference is slight.

Attempts to generalize the theory so as to apply also for polyatomic gases ave been made by GREGORY [10], FREDLUND [7], KENNARD [14] and WEBER [29]. he three former authors present essentially the same arguments, leading up o a result which in its most general form may be written

$$\Delta T = \frac{4}{\gamma + 1} \frac{K}{\varrho \bar{v} \lambda c_v} \frac{2-a}{a} \lambda \left(\frac{\partial T}{\partial n}\right)_w . \tag{1 d}$$

Iere γ is the ratio of the specific heats at constant pressure and at constant olume. WEBER, however, arrives at a different and rather surprising result, inding that the jump value calculated for a monatomic gas should apply without ny changes also for polyatomic gases. He considers this to be supported by he experimental results.

Measurements of the temperature jump and determinations from these of the ccommodation coefficient in different cases are abundantly reported in the terature. Mention may be made here of SMOLUCHOWSKI [25], GEHRCKE [8], Lazareff [17], Mandell and West [19], Dickins [4], Archer [1], Weber [29], Grilly, Taylor and Johnstone [11] and v. Ubisch [28].

In general only the heat flow in the gas is measured, after which the jump value is calculated from a simply corrected heat flow equation. Lazareff and Mandell-West, however, have directly measured the temperature distribution in the gas. As their measurements also cover the transition region these are of special interest here.

III. Discussion of the old theory

In the theory given by Smoluchowski and his successors it is assumed that the temperature varies linearly near the wall, and that the conditions in the stream of gas molecules falling on the wall are the same as are found in the ordinary theory of heat conduction.

Now, these assumptions are not realistic. We know that the temperature curve in reality bends away near the wall as is indicated in fig. 1, and we can also realize that the distribution of the incident stream of gas molecules must be appreciably modified by the collisions with the molecules just reflected from the wall and cannot be correctly described by the ordinary theory, where the situation is taken to be entirely symmetrical. In spite of that, if we identify, in (1 b) or (1 c), ΔT with the temperature jump in the definition previously given, and further identify $\left(\frac{\partial T}{\partial n}\right)_w$ with the normal component of the temperature gradient just beyond the transition region, then the result appears to be fairly correct, the values of the accommodation coefficient determined from it being on the whole in agreement with values calculated in other ways and lying always below the limit 1.

From a theoretical point of view, however, we find it hard to accept this result without further argumentation, and a more thorough treatment of the whole problem, comprising also an investigation of the conditions prevailing in the transition region, must in any case be regarded as highly desirable.

In the efforts to extend the old theory so as to apply also for polyatomic gases, one has encountered the same difficulties as in the ordinary theory of heat conduction, and it has become natural to take over from this the well-known reasoning of Eucken [6]. However, it does not appear quite clear how the calculation actually is to be carried out in this case, as conflicting results occur in the literature, and we shall therefore discuss the subject briefly.

Eucken's argument applies to a model of the gas where the translatory and the internal parts of the molecular energy are exchanged only individually and entirely independent of the other part. Thus the flow of translatory energy in the gas will be the same as in a monatomic gas, and the internal energy will be distributed over the molecules without any correlation to the molecular velocity. If subscripts t and i designate parts belonging respectively to the translatory and the internal energy, it is then found that (very closely)

$$K_t = \frac{5}{2}\eta\, c_{v_t} = \frac{15}{4}\eta R, \quad K_i = \eta\, c_{v_i},$$

where η is the coefficient of viscosity and R is the gas constant per gram.

Now, in the kinetic theory of gases the temperature is defined only through he translatory energy[1], and all we need to do then is to replace the accommodation coefficient a in the result applying to a monatomic gas by the part t. Moreover, experiments performed by KNUDSEN [13] have indicated that a_i nd a_t must be in close agreement. If we put $a_i = a_t$ it follows that also $a = a_t$, s is easily seen by writing out the expressions in full, and we will then come o the conclusion that *the jump value is the same for polyatomic gases as for a mona- omic gas.* WEBER [29] has earlier arrived at the same conclusion after somewhat engthy calculations.

There is, however, another way of reasoning which may be studied in KEN- ARD [14], and which leads to the differing result (1 d). In this case it is asumed that the stream of gas molecules falling on the wall brings with it the nergy

$$E_{0-} = S\left(\frac{4}{3}\cdot\frac{3}{2}RT_0 + c_{v_i}T_0\right) + \frac{1}{2}K\left(\frac{\partial T}{\partial n}\right)_w,$$

where S is the grams of gas transported, all reckoned per unit area and second. The first term in the above expression represents the contribution from the Maxwellian effusion flow and the second term the contribution from the real heat flow. The factor 4/3 standing before the translatory energy per gram $\frac{3}{2}RT_0$ arises from the positive correlation between this part of the energy and the molecular velocity, whereas there is no such factor before the internal energy per gram $c_{v_i}T_0$ in agreement with EUCKEN's reasoning.

However, there is a point here that seems somewhat doubtful, *viz.* the assumption that the temperature corresponding to the internal energy in the Maxwellian effusion flow should equal the actual temperature T_0. If we are to have $a_i = a_t$ the temperature of the internal energy *a fortiori* will lie nearer to the wall temperature T_w than does T_0, seeing that "the persistence of energy" s less for the internal part than for the translatory part.

We find, in fact, making up the calculations for the translatory and the internal energy separately, that KENNARD's assumption leads to the relations

$$\Delta T = \left(\frac{1}{a_t} - \frac{1}{2}\right)\frac{K_t\left(\frac{\partial T}{\partial n}\right)_w}{2SR} = \left(\frac{1}{a_i} - \frac{1}{2}\right)\frac{K_i\left(\frac{\partial T}{\partial n}\right)_w}{Sc_{v_i}}.$$

These then give, using EUCKEN's values for K_t and K_i,

$$\frac{\frac{1}{a_i} - \frac{1}{2}}{\frac{1}{a_t} - \frac{1}{2}} = \frac{15}{8}.$$

---

[1] See foot-note pp. 11–12.

This is not in agreement with KNUDSEN's result; it is easy to see, however, that we can get $a_i = a_t$ and obtain again our previous result by introducing an appropriate accommodation of the temperature of the internal energy towards the wall temperature.

IV. Fundamental equations

A correct theory for the temperature jump must be based on the Boltzmann equation for the molecular distribution function. For a rarefied monatomic gas, free from the action of external forces and in a stationary state, this equation reads [3]

$$\boldsymbol{v} \cdot \frac{\partial f}{\partial \boldsymbol{r}} + I(f f_1) = 0.$$

$f(\boldsymbol{r}, \boldsymbol{v})\, \boldsymbol{d r}\, \boldsymbol{d v}$ gives the number of molecules in the volume element $(\boldsymbol{r}, \boldsymbol{d r})$ with their velocities in the range $(\boldsymbol{v}, \boldsymbol{d v})$, and $I(f f_1)\, \boldsymbol{d r}\, \boldsymbol{d v}$ gives the net number of these molecules which disappear per second from the region owing to the inter-molecular collisions. $\frac{\partial}{\partial \boldsymbol{r}}$ stands for the gradient operator, $\boldsymbol{d r}$ for the volume element $dx\, dy\, dz$, $(\boldsymbol{r}, \boldsymbol{d r})$ for the same element near a specified point $\boldsymbol{r}(x, y, z)$ and so on.

The collision integral $I(f f_1)$ written out explicitly is

$$I(f f_1) = \int_{\boldsymbol{v}_1} \int_{b=0}^{\infty} \int_{\varepsilon=0}^{2\pi} [f(\boldsymbol{r}, \boldsymbol{v})\, f(\boldsymbol{r}, \boldsymbol{v}_1) - F(\boldsymbol{r}, \boldsymbol{v})\, F(\boldsymbol{r}, \boldsymbol{v}_1)]\, g\, b\, db\, d\varepsilon\, \boldsymbol{d v}_1.$$

$F(\boldsymbol{r}, \boldsymbol{v})$ here stands for the distribution function after an inter-molecular collision. This function contains also the parameters determining the collision situation: the magnitude g of the relative velocity $\boldsymbol{g} = \boldsymbol{v}_1 - \boldsymbol{v}$ before the collision, and the polar coordinates b and ε as shown in fig. 2. The integration over b should strictly go up only to some appropriate finite value. It is found, however, that no serious error is introduced if the integration for the sake of analytical convenience is extended up to infinity. The integral symbol $\int_{\boldsymbol{v}}$ is written for $\int_{v_x=-\infty}^{\infty} \int_{v_y=-\infty}^{\infty} \int_{v_z=-\infty}^{\infty}$; we also, for example, write in the following $\int_{v_x>0}$ for $\int_{v_x=0}^{\infty} \int_{v_y=-\infty}^{\infty} \int_{v_z=-\infty}^{\infty}$.

The following remarks concerning the assumptions should be stated:

That the gas is to be rarefied means that the distance within which the molecules appreciably influence each other in their paths, and which we may call *the effective radius of influence* (σ), should be much less than λ.[1] This ra-

---

[1] Statements of this kind must of course be interpreted statistically, being valid not for all molecular constellations occurring but only for the great mass of them.

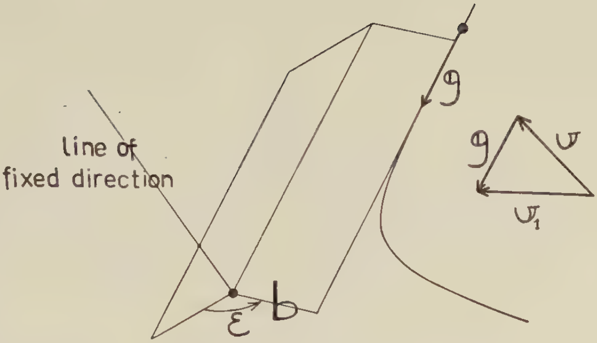

Fig. 2. Definition of the coordinates b and ε.

ius depends not only on the density of the gas but also on the temperature, iminishing in fact when the temperature increases. Thus even a very dense as is to be considered as rarefied in this meaning if the temperature is suffi- iently high. The condition is well fulfilled in most cases occurring in prac- ice.

That the gas is to be monatomic means that the molecules should be well epresented by mass points exerting a spherically symmetrical field of forces. s before, we may generalize the theory so as to apply also for polyatomic ases, in the Eucken approximation.

That the gas is to be free from the action of external forces may appear nrealistic, as the force of gravity is in fact always present and, as is well nown, causes convection flows in the gas when temperature differences are reated. In experimental investigations of heat conduction such effects, how- ver, are generally well eliminated by an appropriate construction of the ap- aratus, and our approximation is then justified. It is implied that there should lso be no mass flows due to other causes, so that the gas can be considered o be in a state of perfect mass equilibrium.

We shall now confine ourselves to the case where it is possible to delimit ear the wall a region in the gas which has linear dimensions much greater han λ but much less than the radii of curvature ϱ_1, ϱ_2 of the wall, and also uch less than any distance parallel to the wall over which the conditions in e gas alter appreciably. This is our rigorously expressed condition. However, s it is found that even distances of, say, 5 to 6 λ are here practically to be onsidered as "much greater than λ", we shall henceforth use instead the phrase a few λ", and also simply express the condition above as that "λ shall be much ss than the radii of curvature, etc."

Furthermore, we shall assume that the temperature gradient in this region directed normal to the wall. In cases occurring in practice the situation is sually such that this is valid. (Even when there is a temperature drop in the as along the wall, the temperature gradient near the wall will lie almost in e normal direction, because its normal component, as will be found later on, creases very rapidly when we approach the wall through the transition region, hereas its tangential component on the whole remains the same throughout (fig. 4)).

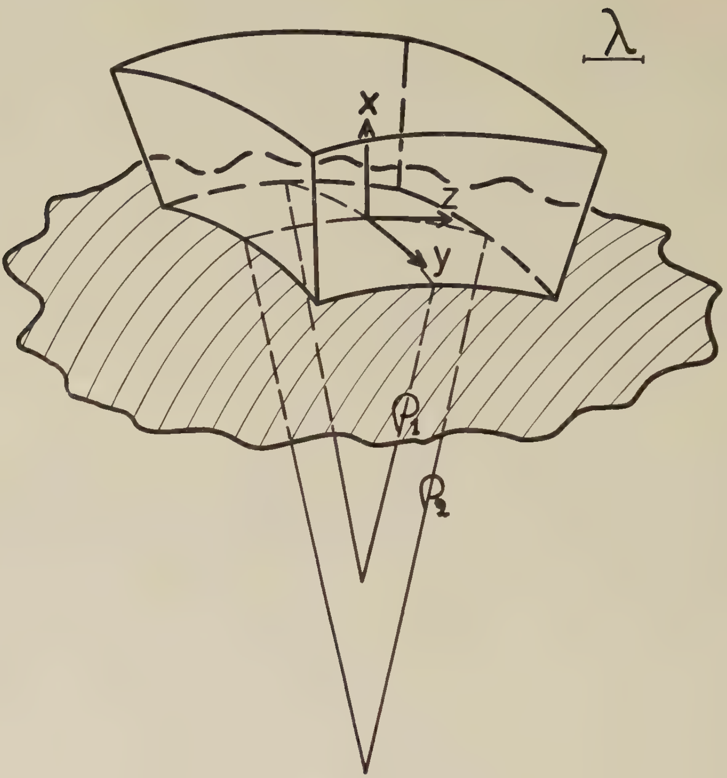

Fig. 3. Delimitation of the gas.

A closer analysis shows that the results we will derive hold good, in a first order approximation, also in this more general case, if only we substitute in these results the corresponding partial derivatives for the total derivatives.

With the conditions set up here, the definition of the temperature jump as previously given has certainly a meaning.

In our delimited region we can now apply the simplified Boltzmann equation

$$v_x \frac{\partial f}{\partial x} + I(f f_1) = 0,$$

with $f = f(x, \boldsymbol{v})$. We use here rectangular axes of reference, laying the x-axis in the normal direction out from the wall and the y-z-axes along the wall.

f is split up into two terms:

$$f = f^{(0)} + f^{(1)}.$$

$f^{(0)}$ is the Maxwellian distribution at the actual but at present unknown values for the number of molecules per unit volume $n(x)$ and for the temperature $T(x)$, *i.e.*,

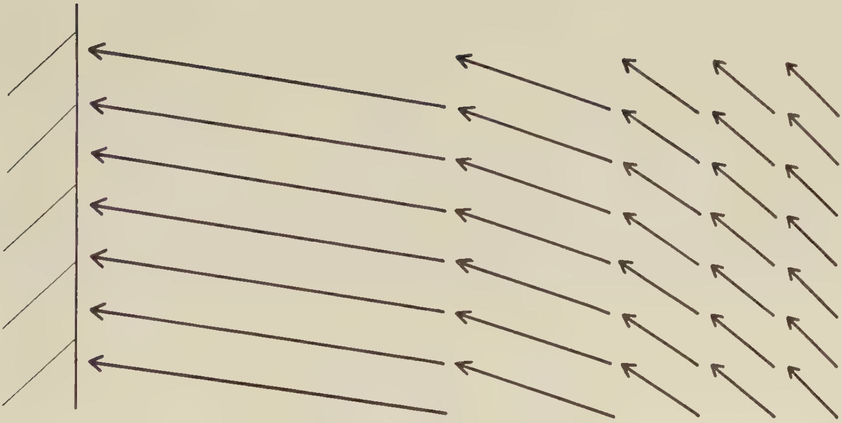

Fig. 4. Temperature gradients near a wall.

$$f^{(0)} = n(x)\left[\frac{m}{2\,\pi\,k\,T(x)}\right]^{3/2} e^{-\frac{m\,v^2}{2\,k\,T(x)}}, \tag{3 a}$$

($v^2 = v_x^2 + v_y^2 + v_z^2$, m is the molecular mass and k is the Boltzmann constant). $f^{(1)}$ is a correction term which we assume to be small. We can then write for the collision integral

$$I(f\,f_1) = I(f^{(0)}\,f_1^{(0)}) + I(f^{(0)}\,f_1^{(1)} + f^{(1)}\,f_1^{(0)}) + I(f^{(1)}\,f_1^{(1)}) = I(f^{(0)}\,f_1^{(1)} + f^{(1)}\,f_1^{(0)}),$$

since the collisions between the molecules in the equilibrium distribution $f^{(0)}$ do not contribute at all, and the collisions between the molecules in $f^{(1)}$ only contribute with a negligible term of the second order.[1]

The equation is then found to be

$$v_x\frac{\partial f^{(1)}}{\partial x} + I(f^{(0)}\,f_1^{(1)} + f^{(1)}\,f_1^{(0)}) = -v_x\frac{1}{n}\frac{d\,n}{d\,x}f^{(0)} + v_x\frac{1}{T}\left(\frac{3}{2} - \frac{m\,v^2}{2\,k\,T}\right)\frac{d\,T}{d\,x}f^{(0)}. \tag{4 a}$$

In the ordinary theory of heat conduction the term $v_x\dfrac{\partial f^{(1)}}{\partial x}$ is entirely neglected, and furthermore it is assumed that $\dfrac{1}{n}\dfrac{d\,n}{d\,x} = -\dfrac{1}{T}\dfrac{d\,T}{d\,x}$, corresponding to the scalar pressure p being constant [3, 5, 14].[2] However, these simplifications cannot be

---

[1] The phrase "the collisions between the molecules in $f^{(1)}$" has of course only a formal meaning. Strictly speaking, $f^{(1)}$ does not contain any molecules at all, since $\int\limits_{\boldsymbol{v}} f^{(1)}\,d\boldsymbol{v} = 0$.

[2] In the kinetic theory of gases the pressure tensor for a rarefied gas is defined as

$$p_{ij} = \int\limits_{\boldsymbol{v}} m\,(v_i - \bar{v}_i)\,(v_j - \bar{v}_j)\,f\,d\boldsymbol{v} = n\,m\,\overline{(v_i - \bar{v}_i)\,(v_j - \bar{v}_j)}.$$

The temperature is defined through the relation made here. It is true that we have assumed $f^{(1)}$ to be a relatively small term, but even very small variations, when pressed into our microscopic transition region, may give rise to appreciable gradient values which must be considered. Nor can we prescribe any algebraic relation between $\frac{1}{n}\frac{dn}{dx}$ and $\frac{1}{T}\frac{dT}{dx}$; such a relation would necessarily make our final equations inconsistent.

Now, it may appear a little strange that the gas, which is assumed to be in a state of perfect mass equilibrium, should not have a constant scalar pressure. We note, however, that the conditions of equilibrium do not in themselves require this. These conditions, which read

$$\frac{\partial p_{xx}}{\partial x}+\frac{\partial p_{xy}}{\partial y}+\frac{\partial p_{xz}}{\partial z}=0,$$

$$\frac{\partial p_{xy}}{\partial x}+\frac{\partial p_{yy}}{\partial y}+\frac{\partial p_{yz}}{\partial z}=0,$$

$$\frac{\partial p_{xz}}{\partial x}+\frac{\partial p_{yz}}{\partial y}+\frac{\partial p_{zz}}{\partial z}=0,$$

will in fact, regarding our conditions of symmetry, only give that

$$p_{xx}=\text{constant},$$

$$p_{xy}=p_{xz}=\text{constant},$$

$$p_{yz}=0.$$

At large distances from the wall we should expect normal conditions to hold, thus

$$p_{xx}=p_{yy}=p_{zz}=p_\infty,$$

$$p_{xy}=p_{xz}=p_{yz}=0.$$

In the transition region we therefore must have $p_{xx}=p_\infty$ and no tangential stresses. There is, however, nothing to prevent variations of p_{yy} and p_{zz} according to x, if only in some way these variations could be maintained against the smoothing tendency of the molecular movement. This now occurs through the heat flow itself, which introduces extra stresses $\Delta p_{yy}(x)$ and $\Delta p_{zz}(x)$ in

---

$$\frac{3}{2}nkT=\int_{\boldsymbol{v}}\frac{1}{2}m\,|\boldsymbol{v}-\bar{\boldsymbol{v}}|^2 f\,d\boldsymbol{v}=\frac{1}{2}nm\overline{|\boldsymbol{v}-\bar{\boldsymbol{v}}|^2}.$$

(We also speak of the temperatures corresponding to special groups of molecules, as *e.g.* the temperatures T_{0-} and T_{0+} of respectively the stream of molecules falling on the wall and the stream of molecules reflected from it. In calculating these temperatures it is to be noted that $\bar{\boldsymbol{v}}$ in the formula should have still the meaning of the total mean velocity).

The scalar pressure is

$$p=\frac{1}{3}(p_{11}+p_{22}+p_{33})=\frac{1}{3}nm\overline{|\boldsymbol{v}-\bar{\boldsymbol{v}}|^2}=nkT,\ \text{(the gas law)}.$$

the gas. The presence of such temperature stresses is well known [3, 5, 20], and it is in fact quite correct that these should appear here regarding the degree of approximation used in our calculation.[1]

The simplifications in the ordinary theory of heat conduction earlier mentioned only correspond to the second approximation in the general method of solution given by CHAPMAN and ENSKOG, and we will also say something about how this method works here when it is applied in full.

The method, as it is developed by ENSKOG, corresponds to an expansion in series of the terms in the Boltzmann equation according to descending powers of the density. The identification of the coefficients gives a system of equations successively solvable for the terms in the expansion of the distribution function $f = f^{(0)} + f^{(1)} + f^{(2)} + \cdots$:

$$\begin{aligned} &\varphi^{(0)}\,(f^{(0)}) = 0, \\ &\varphi^{(1)}\,(f^{(0)},\, f^{(1)}) = 0, \\ &\varphi^{(2)}\,(f^{(0)},\, f^{(1)},\, f^{(2)}) = 0, \\ &\quad \cdot\ \cdot\ \cdot\ \cdot\ \cdot \end{aligned}$$

Like the original Boltzmann equation, a sub-equation $\varphi^{(k)} = 0$ is built up by derivative terms and a collision integral. There enter into it all terms in the development of f up to $f^{(k)}$. Of these, $f^{(0)}, f^{(1)}, \ldots, f^{(k-1)}$ can be calculated from the preceding equations, while $f^{(k)}$ appears as a new unknown term in the collision integral of the equation.

It can be shown that the set of approximations

$$\begin{aligned} &f = f^{(0)}, \\ &f = f^{(0)} + f^{(1)}, \\ &f = f^{(0)} + f^{(1)} + f^{(2)}, \\ &\quad \cdot\ \cdot\ \cdot\ \cdot\ \cdot \end{aligned}$$

in general converges towards a so-called *normal solution* of the Boltzmann equation (a solution which depends only on the values of n, T and $\bar{v}$ in the gas).

This procedure, however, does not work well in our case. In the transition region the derivative terms of the Boltzmann equation are dominating and the collision integral is of relatively small importance, as will be seen later on. To take account of the new f-term in the collision integral of the sub-equation but neglect it in the derivative terms would then be to "strain at a

---

[1] According to the theory of CHAPMAN and ENSKOG we find in our case the temperature stresses

$$\Delta p_{yy} = \Delta p_{zz} = p_\infty \left[l_1^2 \frac{1}{T^2} \left(\frac{dT}{dx} \right)^2 + l_2^2 \frac{1}{T} \frac{d^2 T}{dx^2} \right],$$

where l_1 and l_2 are characteristic lengths of the order of λ. However, in the transition region the correct connection between the temperature stresses and the temperature derivatives must be a more complicated one; we find in fact that the above result will be absurd in that it gives infinite stresses at the wall.

gnat and swallow the camel". The convergence must necessarily be very poor, and it is possible that the method breaks down entirely.

Let us now consider the boundary conditions. At the wall we must obviously prescribe some law giving us the distribution of the reflected gas molecules. Most generally we could describe the reflection mechanism by a probability function $P(\boldsymbol{v}, \boldsymbol{v}_1)$, where $P(\boldsymbol{v}, \boldsymbol{v}_1)\, \boldsymbol{dv}$ gives the probability that a gas molecule impinging on the wall with the velocity $\boldsymbol{v}_1$ would be reflected with a velocity lying in the range $(\boldsymbol{v}, \boldsymbol{dv})$. Owing to the condition of dynamic reversibility it should be valid that $P(\boldsymbol{v}, \boldsymbol{v}_1) = P(-\boldsymbol{v}_1, -\boldsymbol{v})$.

The number of molecules in the range $(\boldsymbol{v}_1, \boldsymbol{dv}_1)$ which impinge on the wall is now $-v_{1_x} f(0, \boldsymbol{v}_1)\, \boldsymbol{dv}_1$ and the number of molecules which are reflected in the range $(\boldsymbol{v}, \boldsymbol{dv})$ thus

$$v_x f(0, \boldsymbol{v})\, \boldsymbol{dv} = -\int_{v_{1_x}<0} P(\boldsymbol{v}, \boldsymbol{v}_1)\, v_{1_x} f(0, \boldsymbol{v}_1)\, \boldsymbol{dv}_1\, \boldsymbol{dv},$$

all reckoned per unit area and second. We can then write the boundary condition

$$\underset{v_x>0}{f(0, \boldsymbol{v})} = -\int_{v_{1_x}<0} \frac{v_{1_x}}{v_x} P(\boldsymbol{v}, \boldsymbol{v}_1) f(0, \boldsymbol{v}_1)\, \boldsymbol{dv}_1. \tag{5 a}$$

As it is assumed that no gas molecules diffuse away through the wall, we should have that

$$\int_{v_x>0} P(\boldsymbol{v}, \boldsymbol{v}_1)\, \boldsymbol{dv} = 1,$$

or

$$\int_{\boldsymbol{v}} v_x f(0, \boldsymbol{v})\, \boldsymbol{dv} = 0. \tag{6}$$

In the outer parts of the transition region we should require that the temperature gradient has the prescribed value $\left(\frac{dT}{dx}\right)_w$. From a macroscopic point of view this equals the value found just at the wall. In our microscopic observation of the transition region, however, it is to be identified with the gradient value at infinite distance from the wall:

$$\underset{x\to\infty}{\frac{dT}{dx}(x)} = \left(\frac{dT}{dx}\right)_w. \tag{7}$$

This formulation is to be regarded as correct under the assumptions being made in the problem.

The approximate values of the density and the temperature in the transition region are also to be considered as prescribed. We shall make the assumption that $n(x)$ and $T(x)$ have there such small relative variations that we may consider them as constants in the Boltzmann equation, equal to given values $\bar{n}$

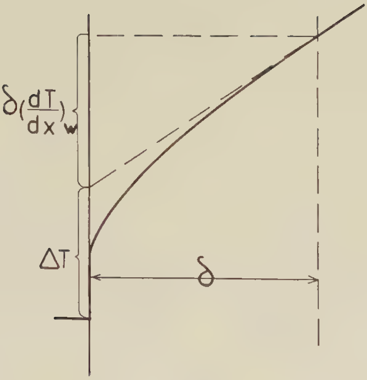

Fig. 5. Temperature variation in the transition region.

and $\overline{T}$, and take account of the x-dependence only in the gradients $\frac{dn}{dx}$ and $\frac{dT}{dx}$. More rigorously the reasoning runs as follows:

Assume that $\left|\frac{\lambda}{\overline{T}}\left(\frac{dT}{dx}\right)_w\right| \ll 1$. As the temperature jump is of the order of $\lambda\left(\frac{dT}{dx}\right)_w$, and the thickness δ of the transition region is of the order of λ, it is clear that the relative variation of the temperature over the transition region is also to be considered as small. However, to legitimate our simplifications in the Boltzmann equation we must demand that this variation is small not only as compared to 1, but also as compared to the relative variation of $\frac{dT}{dx}$.

Now, for a given kind of gas, the values of $\bar{n}$, $\overline{T}$ and $\left(\frac{dT}{dx}\right)_w$, or λ, $\overline{T}$ and $\left(\frac{dT}{dx}\right)_w$, will determine the whole situation. The temperature distribution function must thus be of the form

$$T(x) = f\left(\frac{x}{\lambda}, \frac{\lambda}{\overline{T}}\left(\frac{dT}{dx}\right)_w\right)\lambda\left(\frac{dT}{dx}\right)_w .$$

When $\frac{\lambda}{\overline{T}}\left(\frac{dT}{dx}\right)_w$ is small, this will be simplified to the form

$$T(x) = g\left(\frac{x}{\lambda}\right)\lambda\left(\frac{dT}{dx}\right)_w .$$

It follows that

$$\frac{\frac{dT}{dx}(x)}{\left(\frac{dT}{dx}\right)_w} = g'\left(\frac{x}{\lambda}\right).$$

From this we infer that the relative variation of $\frac{dT}{dx}$ over the transition region will be the same whatever are the conditions of the gas. The analogous result holds for $\frac{dn}{dx}$. Since it should be valid that $\frac{1}{n}\left(\frac{dn}{dx}\right)_w = -\frac{1}{\overline{T}}\left(\frac{dT}{dx}\right)_w$, we thus find our simplifications certainly being legitimate if only $\frac{\lambda}{\overline{T}}\left(\frac{dT}{dx}\right)_w$ is taken to be sufficiently small.

Equation (4 a) together with the boundary conditions should now be sufficient for the determination of $f^{(1)}$ as a function of x, $\frac{dn}{dx}(x)$, $\frac{dT}{dx}(x)$ and $\boldsymbol{v}$. We should expect our solution to agree with the solution given by the ordinary theory of heat conduction, when $x \to \infty$.

We must yet determine $\frac{dn}{dx}(x)$ and $\frac{dT}{dx}(x)$. For this we have at our disposal the two equations which express the fact that the density and the temperature shall agree in f and $f^{(0)}$. These equations may be written

$$\left.\begin{aligned} \int_{\boldsymbol{v}} f^{(1)}\, d\boldsymbol{v} &= 0, \\ \int_{\boldsymbol{v}} v^2 f^{(1)}\, d\boldsymbol{v} &= 0. \end{aligned}\right\} \tag{8 a}$$

After $\frac{dT}{dx}(x)$ being calculated we may find the temperature distribution from

$$T(x) = T_0 + \int_0^x \frac{dT}{dx}(t)\, dt, \tag{9 a}$$

and the temperature jump from

$$\Delta T = T_0' - T_w = T_0 - T_w + \int_0^\infty \left[\frac{dT}{dx}(t) - \left(\frac{dT}{dx}\right)_w\right] dt. \tag{10 a}$$

The calculation of the constant $T_0 - T_w$ in the general case will not be discussed. In the special case which we are going to examine further, it is split up into the two terms $T_{0_-} - T_w$ and $T_{0_+} - T_0$. The first of these can be expressed directly in terms of the accomodation coefficient, whereas the other will enter our final equations as an eigen-parameter.

Looking back on the calculation procedure sketched out here it may appear as if this has been made unnecessarily complicated by our special choice of $f^{(0)}$. If we had chosen $f^{(0)}$ not at the actual unknown values of the density and the temperature in the gas, but instead at some neighbouring prescribed values $n^*(x)$ and $T^*(x)$, then after solving the Boltzmann equation we might have calculated the differences $\Delta n(x) = n(x) - n^*(x)$ and $\Delta T = T(x) - T^*(x)$ directly from

$$\Delta n(x) = \int_{\boldsymbol{v}} f^{(1)} \, d\boldsymbol{v},$$

$$\frac{3}{2} k \left[\bar{n} \, \Delta T(x) + \bar{T} \, \Delta n(x)\right] = \int_{\boldsymbol{v}} \frac{1}{2} m v^2 f^{(1)} \, d\boldsymbol{v}\,.$$

In our case, on the other hand, we have to solve a pair of integral equations given by (8 a), which are not found to be particularly simple. Nevertheless, our choice of $f^{(0)}$ is justified because it gives us the possibility of introducing essential simplifications of the collision integral in the Boltzmann equation, the solution of which appears to be very difficult in a more general case (one may compare with the treatment of viscous slip given by KRAMERS [15]).

We close this chapter by summarizing the assumptions that have been made in the problem:

a. A rarefied monatomic gas in a state of mass equilibrium,
b. λ much less than the radii of curvature of the wall, and also much less than any distance parallel to the wall over which the conditions in the gas alter appreciably,
c. the temperature gradient directed normal to the wall,
d. small deviations from the Maxwellian state, and
e. $\left| \frac{\lambda}{T} \left(\frac{dT}{dx} \right)_w \right| \ll 1.$

V. Collision mechanism

To evaluate the collision integral in the Boltzmann equation one must introduce the forces acting between two colliding gas molecules. Generally one must be content then with using relatively simple models for which the calculations can be carried out without too much difficulty. In the theory of CHAPMAN and ENSKOG, for example, the calculations are performed only for the cases where the molecules are represented as hard elastic spheres or as mass points exerting forces proportional to some negative power of the distance (also a few combinations of these, as the models of SUTHERLAND and LENNARD-JONES).

Now, the mathematical difficulties in our case will become very great even for the most simple models. We will therefore attack the problem in another way and attempt to set up directly some reasonably simplified expression for the collision integral, without troubling too much as to how the corresponding collision mechanism works in detail. However, we shall necessarily require that the mechanism is a physical one to the extent that the total mass, momentum and energy of the molecules are preserved at the collisions, these being the fundamental collision laws both in the classical and in the quantum mechanics description.

If we have an arbitrary molecular property ϕ, then the integral $\int_{\boldsymbol{v}} \phi \, I(f f_1) \, d\boldsymbol{v}$ gives the rate of change of this property due to the inter-molecular collisions, reckoned per unit volume. Thus the conditions demanded may be written

$$\int_{\boldsymbol{v}} \phi\, I\,(f^{(0)} f_1^{(1)} + f^{(1)} f_1^{(0)})\, d\boldsymbol{v} = 0 \tag{11}$$

for $\phi = m$, $m\boldsymbol{v}$ and $\frac{1}{2} m v^2$, or, since the masses of the gas molecules are all the same, as well for $\phi = 1$, $\boldsymbol{v}$ and v^2.

Our collision integral is now a linear integral-function of $f^{(1)}$, and the simplest physically justified assumption we can make is that it is proportional to $f^{(1)}$ itself:

$$I\,(f^{(0)} f_1^{(1)} + f^{(1)} f_1^{(0)}) = \theta f^{(1)}, \tag{12}$$

where θ should be a positive constant. This corresponds to a case where the inter-molecular collisions change the molecular distribution function in the direction towards the Maxwellian form (3 a) at a rate proportional to the deviation from this.

It is immediately clear that the conditions (11) are satisfied in this case. For $\phi = 1$ and v^2 we obtain precisely the equations (8 a), and for $\phi = \boldsymbol{v}$ we obtain the condition that the gas shall have no net flow of mass, which was assumed to be valid from the start.

The relation (12) is already known in the ordinary theory [3, 14], where it holds for a Maxwell-gas with a value for the constant of proportionality

$$\theta = \frac{8}{15} \frac{\bar{v}}{\lambda},$$

corresponding to $f^{(1)}$ losing about one molecule in every second collision. Since we want a connection with the ordinary theory in the outer parts of the transition region, it would be natural simply to take over this value. Then, for the sake of consistency, we also take the Maxwellian values for the other constants entering into our equations. Further, we take (1 b) as the old jump value with which our result should be compared.

It would be reasonable to suppose that (12) corresponds to the collision mechanism of a Maxwell-gas in our case, too, but this does not seem to be the case. However, it has not yet been possible to find out "the back way" how the molecular model implied here would correctly appear.

To set up the boundary condition at the wall we will also need a description of the reflection mechanism there. Now, we know very little about how such a mechanism functions in detail. It has been found that the gas molecules impinging on a wall in general are reflected back in an almost diffuse manner according to the cosine-law, but that the temperature accommodation varies much with the properties of the gas and the wall [14, 18]. If, *e.g.*, the wall surface is smooth, the molecules are reflected back at the first impact on the wall and only a moderate accommodation will occur, whereas if the surface is rough or porous, the molecules collide several times with the wall before escaping and the accommodation will then be more complete. The attractive surface forces from the wall also play an important rôle here. Sometimes these forces cause a real condensation of the gas in the form of a thin film over the wall surface, and in such cases we may of course expect that the reflected molecules, or here better re-evaporated molecules, are almost in mplete temperature equilibrium with the wall. In addition, the accommoda- on varies appreciably with the mass ratio of the gas and the wall molecules. ccording to the ordinary collision laws we might expect that, under conditions herwise unchanged, the energy exchange and thus also the temperature ac- mmodation becomes smaller to the same extent as the relative difference of e masses increases in magnitude [2]; this seems also on the whole to be in reement with the experimental evidence.

That the reflection of the gas molecules in all cases appears to be almost iffuse may be explained by their weak directional persistence. Already after e or two impacts on the wall their original direction tendencies are practically iped out, while in contrast their temperature is appreciably accommodated wards the wall temperature only after a comparatively great number of im- acts.

The velocity distribution of gas molecules reflected from a wall at a differing mperature has been determined by Ornstein and van Wyk [22] from mea- rements of the spectral Doppler effect. It was found, surprisingly enough, at the distribution was practically Maxwellian also when temperature equilib- um was not attained (the accommodation coefficient was in this experiment timated to 0.32). A slight deficiency in the low-speed region was found, how- er, when the molecules were reflected from a hotter wall.

We then might find it reasonable to set up as our boundary condition at e wall simply

$$\underset{v_x>0}{f}(0,\,\boldsymbol{v}) = n_{0_+}\left(\frac{m}{2\pi k T_{0_+}}\right)^{3/2} e^{-\frac{m v^2}{2 k T_{0_+}}},$$

here n_{0_+} and T_{0_+} stand for respectively twice the number of molecules per nit volume and the temperature in the reflected stream of molecules. As $\frac{{}_{0_+}-n_0}{\bar{n}}$ and $\frac{T_{0_+}-T_0}{\bar{T}}$ are assumed to be much less than 1, we may write with ufficient accuracy

$$\underset{v_x>0}{f^{(1)}}(0,\,\boldsymbol{v}) = \frac{n_{0_+}-n_0}{\bar{n}} f^{(0)} - \frac{T_{0_+}-T_0}{\bar{T}}\left(\frac{3}{2}-\frac{m v^2}{2 k \bar{T}}\right) f^{(0)}. \tag{5 b}$$

ow, this boundary condition is strictly justified only to the extent the devia- ons from the Maxwellian state actually observed can be considered as being the second order, since the temperature jump which we are to calculate de- ends itself directly on the first order deviations. In reality the deviations, owever, are not found to be small in this meaning, and we may fear that ur condition is not realistic as regards small values of the accommodation efficient. It seems not possible to draw from the experiments any definite nclusions regarding the corrections to be applied in this case.[1]

---

[1] The boundary condition proposed by Maxwell and Smoluchowski [20, 26], where a cer- in fraction of the impinging gas molecules is reflected specularly and the remainder is re- ected in Maxwellian distribution at the wall temperature, may be considered to be of a more lvanced type than ours. It is, however, unrealistic in so far as the accommodation of the ngential momentum and of the energy of the gas molecules are assumed to be the same; in ality the momentum accommodation is much smaller.

VI. Determination of the distribution function

With the simplifications that we have introduced, the Boltzmann equation takes on the form

$$v_x \frac{\partial f^{(1)}}{\partial x} + \theta f^{(1)} = - v_x \frac{1}{\bar{n}} \frac{d n}{d x}(x) \bar{f}^{(0)} + v_x \frac{1}{\bar{T}} \left(\frac{3}{2} - \frac{m v^2}{2 k \bar{T}}\right) \frac{d T}{d x}(x) \bar{f}^{(0)}, \tag{4 b}$$

where

$$\bar{f}^{(0)} = \bar{n} \left(\frac{m}{2 \pi k \bar{T}}\right)^{3/2} e^{-\frac{m v^2}{2 k \bar{T}}}. \tag{3 b}$$

It defines $f^{(1)}$ as a function of x, $\frac{d n}{d x}(x)$, $\frac{d T}{d x}(x)$, v_x and v. Integrating along the characteristics we find

$$f^{(1)}(x, \boldsymbol{v}) = C(v_x, v)\, e^{-\frac{\theta x}{v_x}} - \frac{1}{\bar{n}} \int\limits_{\alpha(v_x, v)}^{x} \frac{d n}{d x}(t)\, e^{\frac{\theta}{v_x}(t-x)}\, d t \cdot \bar{f}^{(0)} +$$

$$+ \frac{1}{\bar{T}} \left(\frac{3}{2} - \frac{m v^2}{2 k \bar{T}}\right) \cdot \int\limits_{\alpha(v_x, v)}^{x} \frac{d T}{d x}(t)\, e^{\frac{\theta}{v_x}(t-x)}\, d t \cdot \bar{f}^{(0)},$$

where $C(v_x, v)$ and $\alpha(v_x, v)$ are arbitrary functions.

The molecular distribution function is generally required to be finite. Moreover, such integrals as define density, temperature and the like must converge. We shall assume that $\frac{d n}{d x}$ and $\frac{d T}{d x}$ are bounded, and that they tend towards constant (non-zero) values at infinity. The conditions above are then satisfied throughout our region $0 \leq x < \infty$ if we put

$$C(v_x, v) = 0 \quad \text{for } v_x < 0,$$

$$\alpha(v_x, v) = 0 \quad \text{for } v_x > 0,$$

$$\alpha(v_x, v) = \infty \quad \text{for } v_x < 0,$$

and define

$$f^{(1)}(x, \boldsymbol{v}) = 0 \ \text{ for } v_x = 0.$$

Then only $\underset{v_x \to 0}{C}(v_x, v)$ remains to be considered. This, however, is precisely $\underset{v_x \to 0}{f^{(1)}}(0, \boldsymbol{v})$, which is given by our boundary condition (5 b). The complete expression for $f^{(1)}$ thus reads

$$\left.\begin{aligned}
&{}^{1)}_{>0}(x,\,\boldsymbol{v})=\left[\frac{n_{0+}-n_0}{\bar n}\,e^{-\frac{\theta x}{v_x}}-\frac{1}{\bar n}\int\limits_0^x\frac{dn}{dx}(t)\,e^{\frac{\theta}{v_x}(t-x)}\,dt\right]f^{(0)}-\\
&\qquad-\left(\frac{3}{2}-\frac{m v^2}{2k\bar{\bar T}}\right)\left[\frac{T_{0+}-T_0}{\bar{\bar T}}\,e^{-\frac{\theta x}{v_x}}-\frac{1}{\bar{\bar T}}\int\limits_0^x\frac{dT}{dx}(t)\,e^{\frac{\theta}{v_x}(t-x)}\,dt\right]f^{(0)},\\
&{}^{1)}_{<0}(x,\,\boldsymbol{v})=\frac{1}{\bar n}\int\limits_x^\infty\frac{dn}{dx}(t)\,e^{\frac{\theta}{v_x}(t-x)}\,dt\cdot f^{(0)}-\left(\frac{3}{2}-\frac{m v^2}{2k\bar{\bar T}}\right)\frac{1}{\bar{\bar T}}\int\limits_x^\infty\frac{dT}{dx}(t)\,e^{\frac{\theta}{v_x}(t-x)}\,dt\cdot f^{(0)},\\
&{}^{1)}_{=0}(x,\,\boldsymbol{v})=0.
\end{aligned}\right\}\qquad(13\text{ a})$$

It is of interest to see how $f^{(1)}$ behaves when $x\to\infty$. We anticipate here the elation $\frac{1}{\bar n}\frac{dn}{dx}(\infty)=-\frac{1}{\bar{\bar T}}\frac{dT}{dx}(\infty)$, being verified further on. Now,

$$\frac{1}{\bar n}\int\limits_{\substack{x\\ x\to\infty}}^{\infty}\frac{dn}{dx}(t)\,e^{\frac{\theta}{v_x}(t-x)}\,dt=\frac{1}{\bar n}\frac{dn}{dx}(\infty)\int\limits_{\substack{x\\ x\to\infty}}^{\infty}e^{\frac{\theta}{v_x}(t-x)}\,dt=\frac{v_x}{\theta}\,\frac{1}{\bar n}\frac{dn}{dx}(\infty)\qquad\text{for } v_x<0,$$

lso

$$\int\limits_{\substack{0\\ \to\infty}}^{x}\frac{dn}{dx}(t)\,e^{\frac{\theta}{v_x}(t-x)}\,dt=\frac{1}{\bar n}\int\limits_{\substack{0\\ x\to\infty}}^{\frac{x}{2}}\frac{dn}{dx}(t)\,e^{\frac{\theta}{v_x}(t-x)}\,dt+\frac{1}{\bar n}\int\limits_{\substack{\frac{x}{2}\\ x\to\infty}}^{x}\frac{dn}{dx}(t)\,e^{\frac{\theta}{v_x}(t-x)}\,dt=$$

$$=\frac{1}{\bar n}\frac{dn}{dx}(\xi)\int\limits_{\substack{0\\ x\to\infty}}^{\frac{x}{2}}e^{\frac{\theta}{v_x}(t-x)}\,dt+\frac{1}{\bar n}\frac{dn}{dx}(\infty)\int\limits_{\substack{\frac{x}{2}\\ x\to\infty}}^{x}e^{\frac{\theta}{v_x}(t-x)}\,dt=\frac{v_x}{\theta}\,\frac{1}{\bar n}\frac{dn}{dx}(\infty)\qquad\text{for } v_x>0,$$

nd analogously for the integrals of $\frac{dT}{dx}$. Observing that the boundary condiion terms in (13 a) tend to zero, we then have, for all values of v_x,

$$\underset{x\to\infty}{f^{(1)}}(x,\,\boldsymbol{v})=\frac{v_x}{\theta}\left(\frac{5}{2}-\frac{m v^2}{2k\bar{\bar T}}\right)\frac{1}{\bar{\bar T}}\frac{dT}{dx}(\infty)\,f^{(0)}.\qquad(13\text{ b})$$

his is precisely the CHAPMAN-ENSKOG result for a Maxwell-gas.

As will be found later on, $\frac{dn}{dx}$ and $\frac{dT}{dx}$ become very large close to the wall, whereas their values integrated over the transition region are only moderate. Further, the constants $\frac{n_{0+}-n_0}{\bar{n}}$ and $\frac{T_{0+}-T_0}{\bar{T}}$ are found to be of the order of $\lambda\left(\frac{dT}{dx}\right)_w$. It follows then that close to the wall $v_x \frac{\partial f^{(1)}}{\partial x}$ is much greater than $\theta f^{(1)}$, that is to say, $\lambda \frac{\partial f^{(1)}}{\partial x}$ is much greater than $f^{(1)}$, while the condition is just the opposite at large distances from the wall. This, as mentioned earlier, is the reason for the failure in the transition region of the CHAPMAN-ENSKOG method of solution.

VII. Equations for the density and temperature gradients

The unknown functions $\frac{dn}{dx}(x)$ and $\frac{dT}{dx}(x)$ entering into $f^{(1)}$ are to be determined from the equations (8 a). The constants $\frac{n_{0+}-n_0}{\bar{n}}$ and $\frac{T_{0+}-T_0}{\bar{T}}$ are obtained from the additional conditions (6) and (7). All these equations may be replaced by

$$\left.\begin{aligned} &\int_{\boldsymbol{v}} v_x f^{(1)} \, d\boldsymbol{v} = 0, \\ &\int_{\boldsymbol{v}} \frac{1}{2} m v_x v^2 f^{(1)} \, d\boldsymbol{v} = -K\left(\frac{dT}{dx}\right)_w, \end{aligned}\right\} \tag{14 a}$$

where K stands for the coefficient of heat conduction for a Maxwell-gas, as calculated by the ordinary theory. For if (4 b) is integrated over the velocity space, we get

$$\frac{\partial}{\partial x}\int_{\boldsymbol{v}} v_x f^{(1)} \, d\boldsymbol{v} + \theta \int_{\boldsymbol{v}} f^{(1)} \, d\boldsymbol{v} = 0,$$

also, if the same equation is multiplied by $\frac{1}{2} m v^2$ before the integration

$$\frac{\partial}{\partial x}\int_{\boldsymbol{v}} \frac{1}{2} m v_x v^2 f^{(1)} \, d\boldsymbol{v} + \frac{1}{2} m \theta \int_{\boldsymbol{v}} v^2 f^{(1)} \, d\boldsymbol{v} = 0,$$

since the right-hand sides, being odd functions of v_x, will disappear in the integration. We find that (14 a) will imply (8 a), and we also can see that (6) and (7) will be automatically satisfied. Since there are then no additional conditions set up for $\frac{n_{0+} - n_0}{\bar{n}}$ and $\frac{T_{0+} - T_0}{\bar{T}}$, these constants must here be assumed to play the rôle of eigen-parameters, permitting a solution of our equations for one given pair of values only.

Our expression (13 a) for $f^{(1)}$ is now to be inserted into (14 a). We introduce the non-dimensional variables:

$$\xi = \frac{16}{15\sqrt{\pi}} \frac{x}{\lambda},$$

$$\boldsymbol{V} = \sqrt{\frac{m}{2\,k\,T}}\,\boldsymbol{v},$$

$$\varphi(\xi) = \frac{1}{\bar{n}} \frac{d\,n}{d\,\xi}(\xi),$$

$$\chi(\xi) = \frac{1}{\bar{T}} \frac{d\,T}{d\,\xi}(\xi) \text{ with especially } \chi_w = \frac{1}{\bar{T}}\left(\frac{d\,T}{d\,\xi}\right)_w,$$

and define the functions

$$L_{m\,n}(\xi) = \int\limits_{V_x > 0} V_x\, V^{2\,m} \left(\frac{3}{2} - V^2\right)^n e^{-\frac{\xi}{V_x} - V^2}\, \boldsymbol{d\,V},$$

$$(V^2 = V_x^2 + V_y^2 + V_z^2).$$

Remembering that $\theta = \frac{8}{15} \frac{\bar{v}}{\lambda}$, $\bar{v} = \frac{2}{\sqrt{\pi}} \sqrt{\frac{2\,k\,\bar{T}}{m}}$ and $K = \frac{25\,\pi}{64} \varrho\, \bar{v}\, \lambda\, c_v$ we find then, after a change of the order of integration, the following pair of integral equations:

$$\frac{n_{0+} - n_0}{\bar{n}} L_{00}(\xi) - \frac{T_{0+} - T_0}{\bar{T}} L_{01}(\xi) - \int_0^{\xi} L_{00}(\xi - \tau)\,\varphi(\tau)\,d\tau + \int_0^{\xi} L_{01}(\xi - \tau)\,\chi(\tau)\,d\tau -$$
$$- \int_{\xi}^{\infty} L_{00}(\tau - \xi)\,\varphi(\tau)\,d\tau + \int_{\xi}^{\infty} L_{01}(\tau - \xi)\,\chi(\tau)\,d\tau = 0$$

$$\frac{n_{0+} - n_0}{\bar{n}} L_{10}(\xi) - \frac{T_{0+} - T_0}{\bar{T}} L_{11}(\xi) - \int_0^{\xi} L_{10}(\xi - \tau)\,\varphi(\tau)\,d\tau + \int_0^{\xi} L_{11}(\xi - \tau)\,\chi(\tau)\,d\tau -$$
$$- \int_{\xi}^{\infty} L_{10}(\tau - \xi)\,\varphi(\tau)\,d\tau + \int_{\xi}^{\infty} L_{11}(\tau - \xi)\,\chi(\tau)\,d\tau = -\frac{5}{4}\pi\sqrt{\pi}\,\chi_w.$$

We again introduce new variables:

$$\varphi^*(\xi) = -\frac{\varphi(\xi)}{\chi_w},$$

$$\chi^*(\xi) = \frac{\chi(\xi)}{\chi_w},$$

and the parameters

$$\mu_0 = \frac{n_{0_+} - n_0}{\bar{n}\,\chi_w},$$

$$\mu_1 = -\frac{T_{0_+} - T_0}{\bar{T}\,\chi_w},$$

and have, after rearranging the integrals,

$$\left.\begin{aligned} &\int_0^\infty L_{00}(|\xi-\tau|)\,\varphi^*(\tau)\,d\tau + \int_0^\infty L_{01}(|\xi-\tau|)\,\chi^*(\tau)\,d\tau = -\mu_0 L_{00}(\xi) - \mu_1 L_{01}(\xi),\\ &\int_0^\infty L_{10}(|\xi-\tau|)\,\varphi^*(\tau)\,d\tau + \int_0^\infty L_{11}(|\xi-\tau|)\,\chi^*(\tau)\,d\tau = -\mu_0 L_{10}(\xi) -\\ &\qquad\qquad\qquad\qquad -\mu_1 L_{11}(\xi) - \frac{5}{4}\pi\sqrt{\pi}.\end{aligned}\right\} \quad (14\,\mathrm{b})$$

The appearance of the functions $L_{mn}(\xi)$ occurring here will be seen from fig. 11. More precise values can be computed from Table 4, using (32) and (35).

(14 b) is to be classified as a system of Wiener-Hopf's equations of the first kind. In principle, such equations may be solved by applying certain Fourier transforms and using arguments from the theory of a complex variable [30, 31]. This analytic method is of value to verify that a solution does really exist and to find out how the eigen-parameters enter into the problem, but it does not seem to be very well adapted for a numerical calculation of the solution. Therefore, we have here preferred to tackle the equations directly by a numerical method. However, the analytical method is briefly discussed in App. II, where the exact values of the eigen-parameters are also calculated.

When $\xi \to \infty$, then

$$\int_0^\infty L_{mn}(|\xi-\tau|)\,\varphi^*(\tau)\,d\tau \to \varphi^*(\infty)\int_0^\infty L_{mn}(|\xi-\tau|)\,d\tau \to 2\,\varphi^*(\infty)\int_0^\infty L_{mn}(\tau)\,d\tau$$

and analogously for the integrals of χ^*. Making use of the formulae (31), (33) and (35) and noting that the parameter terms tend to zero, we find then that the system (14 b) at infinity is reduced to

$$\varphi^*(\infty) - \chi^*(\infty) = 0,$$

$$\varphi^*(\infty) - 2\,\chi^*(\infty) = -1,$$

or $\varphi^*(\infty)=\chi^*(\infty)=1$. This means that $\frac{1}{\bar{n}}\frac{dn}{dx}(\infty)=-\frac{1}{\bar{T}}\frac{dT}{dx}(\infty)=-\frac{1}{\bar{T}}\left(\frac{dT}{dx}\right)_w$, as is to be expected.

Another case of interest is when $\xi\to 0$. To find out what happens in this case we consider the equations of the second kind obtained from (14 b) by a twofold differentiation

$$2L'_{00}(0)\,\varphi^*(\xi)+2L'_{01}(0)\,\chi^*(\xi)+\int_0^\infty L''_{00}(|\xi-\tau|)\,\varphi^*(\tau)\,d\tau+$$
$$+\int_0^\infty L''_{01}(|\xi-\tau|)\,\chi^*(\tau)\,d\tau=-\mu_0 L''_{00}(\xi)-\mu_1 L''_{01}(\xi),$$

$$2L'_{10}(0)\,\varphi^*(\xi)+2L'_{11}(0)\,\chi^*(\xi)+\int_0^\infty L''_{10}(|\xi-\tau|)\,\varphi^*(\tau)\,d\tau+$$
$$+\int_0^\infty L''_{11}(|\xi-\tau|)\,\chi^*(\tau)\,d\tau=-\mu_0 L''_{10}(\xi)-\mu_1 L''_{11}(\xi).$$

When $\xi\to 0$ the functions $L''_{mn}(\xi)$ in these equations will increase without bound, whereas the integrals $\int_0^\infty L''_{mn}(\tau)\,d\tau$ are finite, and we find the essential part of the system to be

$$\mu_0 L''_{00}(\xi)+\mu_1 L''_{01}(\xi)=0,$$
$$\mu_0 L''_{10}(\xi)+\mu_1 L''_{11}(\xi)=0,$$

provided that φ^* and χ^* are finite.

However, the quotients $\frac{L''_{00}(\xi)}{L''_{10}(\xi)}$ and $\frac{L''_{01}(\xi)}{L''_{11}(\xi)}$ tend towards different limits and the system will thus be inconsistent, apart from the trivial case $\mu_0=\mu_1=0$.

This must mean that φ^* and χ^* cannot in actual fact be finite throughout our region but must have some point of infinity. It is easy to see that this point can be no other than $\xi=0$. From a physical point of view it may perhaps seem surprising that the density and temperature gradients become infinite at the wall. The result, however, is not unreasonable in any way, if only the density and the temperature themselves remain finite at the wall, *i.e.*, if the integrals $\int_0^\varepsilon \varphi^*(\tau)\,d\tau$ and $\int_0^\varepsilon \chi^*(\tau)\,d\tau$ converge $(\varepsilon>0)$. That such is the case is easily seen, also. For if the integrals were infinite, the essential part of (14 b) would be included in

$$L_{00}(\xi)\int_0^\varepsilon \varphi^*(\tau)\,d\tau+L_{01}(\xi)\int_0^\varepsilon \chi^*(\tau)\,d\tau=0,$$

$$L_{10}(\xi)\int_0^\varepsilon \varphi^*(\tau)\,d\tau+L_{11}(\xi)\int_0^\varepsilon \chi^*(\tau)\,d\tau=0,$$

which system is not consistent.

Now, we have in our earlier reasonings assumed the density and temperature gradients to be finite throughout our region. However, it is easy to see that the introducing of such a point of infinity as is actually found here will cause no trouble, and our conclusions still hold.

On the other hand, we may ask whether the Boltzmann equation itself is valid near the point of infinity. It is known that this equation holds good when the distribution function varies appreciably over distances of the order of λ, but that it ceases to apply when the variations become noticeable even over distances comparable with the effective radius of influence σ [9]. Now, the distribution function is continuous in ξ throughout our region. Its relative variation over a distance of, say, $\Delta x = \sigma$ can always be made as small as we please by taking λ sufficiently large compared to σ, λ appearing here only in the variable ξ. Thus, if the gas is to be taken sufficiently rarefied, the Boltzmann equation is certainly valid in all points, including the point of infinity.

Finally, we will here give the temperature distribution and the temperature jump in terms of our new variables:

$$T(\xi) = T_0 + \int_0^{\xi} \chi^*(\tau)\, d\tau \cdot \left(\frac{dT}{d\xi}\right)_w , \tag{9 b}$$

where

$$T_0 = T_w + (T_{0_+} - T_w) + \mu_1 \left(\frac{dT}{d\xi}\right)_w ,$$

$$\begin{aligned} \Delta T = T_0 - T_w + \int_0^{\infty} [\chi^*(\tau) - 1]\, d\tau \cdot \left(\frac{dT}{d\xi}\right)_w = \\ = T_{0_+} - T_w + \left[\mu_1 + \int_0^{\infty} [\chi^*(\tau) - 1]\, d\tau\right] \left(\frac{dT}{d\xi}\right)_w . \end{aligned} \tag{10 b}$$

The constant $T_{0_+} - T_w$ occurring here may be expressed in terms of the accommodation coefficient. We have, using earlier notations,

$$E_{0_+} - E_w = 2SR(T_{0_+} - T_w) = \frac{1}{2} \varrho \bar{v} R (T_{0_+} - T_w),$$

$$E_{0_-} - E_{0_+} = K \left(\frac{dT}{dx}\right)_w = \frac{75\pi}{128} R \varrho \bar{v} \lambda \left(\frac{dT}{dx}\right)_w = \frac{5\sqrt{\pi}}{8} R \varrho \bar{v} \left(\frac{dT}{d\xi}\right)_w ,$$

$$a = \frac{E_{0_-} - E_{0_+}}{E_{0_-} - E_w} = \frac{1}{1 + \dfrac{E_{0_+} - E_w}{E_{0_-} - E_{0_+}}} .$$

The combination of these will give

$$T_{0_+} - T_w = \frac{5\sqrt{\pi}}{4} \frac{1-a}{a} \left(\frac{dT}{d\xi}\right)_w . \tag{15}$$

t appears that the temperature jump is here, as in the old theory, proporional to both λ and $\left(\frac{dT}{dx}\right)_w$.

VIII. Numerical calculations

When the system (14 b) is to be solved numerically, it is found preferable irst to eliminate the point of infinity. For that we choose a positive number , so small that we may put with sufficient accuracy

$$\int_0^{\varepsilon} L_{m\,n}(|\xi-\tau|)\,\varphi^*(\tau)\,d\tau = L_{m\,n}(\xi)\int_0^{\varepsilon}\varphi^*(\tau)\,d\tau,$$

nd analogously for the integrals of χ^*. We can then in our equations change he lower limit of the integrals from 0 to ε. This merely means that we relace the eigen-parameters μ_0 and μ_1 by the new values

$$\mu_0^* = \mu_0 + \int_0^{\varepsilon}\varphi^*(\tau)\,d\tau$$

nd

$$\mu_1^* = \mu_1 + \int_0^{\varepsilon}\chi^*(\tau)\,d\tau.$$

Furthermore, we formally eliminate the eigen-parameters by solving for them t $\xi = 0$, from

$$\left.\begin{aligned} L_{00}(0)\,\mu_0^* + L_{01}(0)\,\mu_1^* &= -\int_{\varepsilon}^{\infty} L_{00}(\tau)\,\varphi^*(\tau)\,d\tau - \int_{\varepsilon}^{\infty} L_{01}(\tau)\,\chi^*(\tau)\,d\tau, \\ L_{10}(0)\,\mu_0^* + L_{11}(0)\,\mu_1^* &= -\int_{\varepsilon}^{\infty} L_{10}(\tau)\,\varphi^*(\tau)\,d\tau - \int_{\varepsilon}^{\infty} L_{11}(\tau)\,\chi^*(\tau)\,d\tau - \frac{5}{4}\pi\sqrt{\pi}, \end{aligned}\right\} \quad (14\text{ c})$$

nd putting them back into the equations again. These may then be written

$$\left.\begin{aligned} \int_{\varepsilon}^{\infty} L_{00}^*(\xi,\tau)\,\varphi^*(\tau)\,d\tau + \int_{\varepsilon}^{\infty} L_{01}^*(\xi,\tau)\,\chi^*(\tau)\,d\tau &= L_0(\xi), \\ \int_{\varepsilon}^{\infty} L_{10}^*(\xi,\tau)\,\varphi^*(\tau)\,d\tau + \int_{\varepsilon}^{\infty} L_{11}^*(\xi,\tau)\,\chi^*(\tau)\,d\tau &= L_1(\xi), \end{aligned}\right| \quad (14\text{ d})$$

vhere

$$L_{m\,n}^*(\xi,\tau) = L_{m\,n}(|\xi-\tau|) - L_{m\,0}(\xi)\left[\frac{3}{\pi}L_{0\,n}(\tau) - \frac{1}{2\pi}L_{1\,n}(\tau)\right] - \\ - L_{m\,1}(\xi)\left[\frac{2}{\pi}L_{0\,n}(\tau) - \frac{1}{\pi}L_{1\,n}(\tau)\right],$$

$$L_0(\xi) = -\frac{5}{4}\pi\sqrt{\pi}\left[\frac{1}{2\pi}L_{00}(\xi) + \frac{1}{\pi}L_{01}(\xi)\right],$$

$$L_1(\xi) = -\frac{5}{4}\pi\sqrt{\pi}\left[1 + \frac{1}{2\pi}L_{10}(\xi) + \frac{1}{\pi}L_{11}(\xi)\right].$$

The values of $L_{mn}(0)$ are obtained from (33) and (35).

The functions $L^*_{mn}(\xi, \tau)$ now have their largest values in the region $\tau \approx \xi$, and this would seem to make possible the following iterative method of solution:

Assume that φ^*_n, χ^*_n is a known approximate solution. We write

$$\varphi^* = \varphi^*_n + \Delta\varphi^*_n,$$

$$\chi^* = \chi^*_n + \Delta\chi^*_n,$$

and put

$$\int_\varepsilon^\infty L^*_{mn}(\xi,\tau)\,\varphi^*(\tau)\,d\tau = \int_\varepsilon^\infty L^*_{mn}(\xi,\tau)\,[\varphi^*_n(\tau) + \Delta\varphi^*_n(\tau)]\,d\tau \approx$$

$$\approx \int_\varepsilon^\infty L^*_{mn}(\xi,\tau)\,\varphi^*_n(\tau)\,d\tau + \Delta\varphi^*_n(\xi)\int_\varepsilon^\infty L^*_{mn}(\xi,\tau)\,d\tau$$

and analogously for the integrals of χ^*. The correction terms $\Delta\varphi^*_n$ and $\Delta\chi^*_n$ may then be computed approximately from a pair of linear equations, which we write in the form

$$\left.\begin{aligned}
\Delta\varphi^*_n(\xi)\,K_{00}(\xi) + \Delta\chi^*_n(\xi)\,K_{01}(\xi) &= f_0(\xi) - \int_\varepsilon^\infty L^*_{00}(\xi,\tau)\,[\varphi^*_n(\tau) - 1]\,d\tau \\
&\quad - \int_\varepsilon^\infty L^*_{01}(\xi,\tau)\,[\chi^*_n(\tau) - 1]\,d\tau, \\
\Delta\varphi^*_n(\xi)\,K_{10}(\xi) + \Delta\chi^*_n(\xi)\,K_{11}(\xi) &= f_1(\xi) - \int_\varepsilon^\infty L^*_{10}(\xi,\tau)\,[\varphi^*_n(\tau) - 1]\,d\tau \\
&\quad - \int_\varepsilon^\infty L^*_{11}(\xi,\tau)\,[\chi^*_n(\tau) - 1]\,d\tau,
\end{aligned}\right\} \quad (14\,\mathrm{e})$$

where

$$K_{mn}(\xi) = \int_\varepsilon^\infty L^*_{mn}(\xi,\tau)\,d\tau,$$

$$f_m(\xi) = L_m(\xi) - K_{m0}(\xi) - K_{m1}(\xi).$$

The procedure is then repeated again, starting from the new approximate solution

$$\varphi^*_{n+1} = \varphi^*_n + \Delta\varphi^*_n,$$

$$\chi^*_{n+1} = \chi^*_n + \Delta\chi^*_n,$$

and so on.

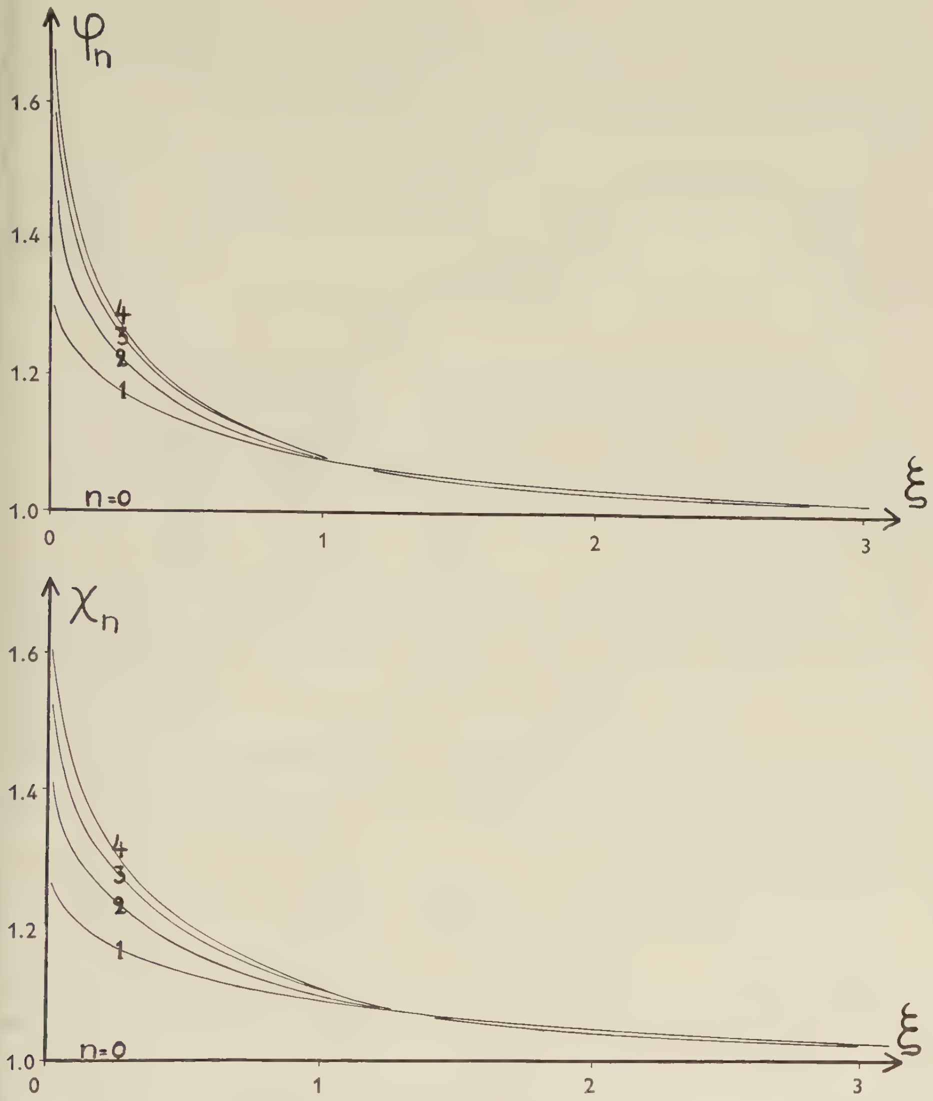

Fig. 6–7. First five approximate solutions of φ^* and χ^*.

With each approximate solution φ_n^*, χ_n^* there are associated values of the eigenparameters $(\mu_0^*)_n$, $(\mu_1^*)_n$, as computed from (14 c). In practice the method is found to converge.

The actual computations, which to the main part were performed with the BARK, run in short as follows:

First, for 32 arguments from $\xi = \varepsilon = 1/64$ up to $\xi = 14$, the occurring functions L_{mn}, K_{mn} and f_m were computed (as will be further described in App. III). Successive approximations of φ^* and χ^* were then computed for the same arguments from (14 e), starting with the asymptotic solution, $\varphi_0^* = \chi_0^* = 1$. The integrals in the right-hand sides of these equations were estimated by a numerical quadrature, based essentially on the Simpson rule. With only 32 values of the argument (this number was set by the limited memory capacity of BARK), it was not possible to ensure an adequate accuracy if these values were equally spaced, and therefore they had to be taken closer spaced in the region of small ξ, where the occurring functions vary most rapidly. This caused a deal of trouble, since in the computation of a convolution integral such as $\int_{\varepsilon}^{\infty} L_{mn}(|\xi-\tau|)[\varphi^*(\tau)-1]\,d\tau$ it was necessary to introduce an interpolation procedure both for $L_{mn}(|\xi-\tau|)$ (in the region of small τ) and for $\varphi^*(\tau)$ (in the region $\tau \approx \xi$).

The iterative procedure was not applied strictly throughout, but some experiments were made with extrapolations of the approximate solutions obtained in order to bring down the number of iterations. The points above $\xi = 10$ were excluded in the last iteration as the values there did not appear wholly reliable. The convergence of the φ^* and χ^* values was quite good, except in the region of small ξ (however, the convergence in a direction *normal* to the solution curves was good even there, *cf.* fig. 6–7. The total number of iterations was 13.

Our final numerical values of φ^* and χ^* and of the eigen-parameters μ_0^* and μ_1^* are given in Table 1, taking in those figures which were found to be steady in the last iteration. Graphs of the first five approximate solutions are given in fig. 6–7. All the approximate values of the constants μ_1^* and $\int_{\varepsilon}^{\infty}[\chi^*(\tau)-1]\,d\tau$, which are to be used in the computation of the temperature jump, are given in Table 2.

It is of interest to compare our final values of μ_0^* and μ_1^* with the correct values of μ_0 and μ_1 from (30). We find

$$\mu_0^* - \mu_0 = \int_0^{\varepsilon} \varphi^*(\tau)\,d\tau = 0.147,$$

$$\mu_1^* - \mu_1 = \int_0^{\varepsilon} \chi^*(\tau)\,d\tau = 0.237\,.$$

These values are surprisingly large, indicating a considerable temperature drop in the narrow region from $\xi = 0$ to ε (*cf.* fig. 8).

The errors which affect our computations are the following:

a) Errors owing to the introduction of ε (< 0.0005),
b) errors owing to the integrations not being extended to infinity (< 0.001),
c) errors in the computation of the functions L_{mn}, K_{mn} and f_m (< 0.00001),
d) errors in the interpolation and in the numerical quadrature (< 0.001),
e) errors owing to the number of iterations being finite (< 0.001).

The numerical values given in a–b and d–e refer to the absolute errors in the right-hand sides of (14 e), taken in mean over the ξ-range.[1] Regarding our values of φ^*, χ^*, μ_0^* and μ_1^* given in Table 1, the total error in each value appears to be at most one or two units in the last figure taken in.

Table 1. Final values of φ^*, χ^*, μ_0^* and μ_1^*.

ξ	φ^*	χ^*	ξ	φ^*	χ^*
0	∞	∞	0.75	1.106	1.145
0.015625	2.5	2.8	1	1.076	1.108
0.03125	2.0	2.1	1.25	1.057	1.081
0.046875	1.8	1.9	1.5	1.045	1.063
0.0625	1.68	1.75	1.75	1.036	1.050
0.078125	1.60	1.67	2	1.030	1.041
0.09375	1.55	1.62	3	1.014	1.019
0.109375	1.51	1.59	4	1.007	1.011
0.125	1.48	1.55	5	1.004	1.006
0.1875	1.364	1.435	6	1.002	1.004
0.25	1.295	1.366	7	1.001	1.002
0.3125	1.246	1.317	8	1.001	1.001
0.375	1.210	1.279	9	1.000	1.001
0.4375	1.183	1.247	10	1.000	1.000
0.5	1.162	1.220			

$\mu_0^* = 0.429 \quad \mu_1^* = 0.895$

---

[1] Concerning the estimation of the errors we note the following:

a) The error made by putting $\int_0^\varepsilon L_{mn}(|\xi-\tau|)\,\varphi^*(\tau)\,d\tau = L_{mn}(\xi)\int_0^\varepsilon \varphi^*(\tau)\,d\tau$ is of the magnitude $|L_{mn}(\xi-\theta\varepsilon) - L_{mn}(\xi)|\,(\mu_0^* - \mu_0)$, where $0 \leq \theta \leq 1$, and the same error will affect our term $\int_\varepsilon^\infty L^*_{mn}(\xi,\tau)\,[\varphi^*(\tau)-1]\,d\tau$. The corresponding mean absolute error is $\approx \frac{1}{10}\,\theta\,\varepsilon\,|L_{mn}(0)|\cdot$ $\cdot(\mu_0^* - \mu_0)$. The analogous result holds for the integrals of χ^*.

b) The error made in $\int_\varepsilon^\infty L^*_{mn}(\xi,\tau)\,[\varphi^*(\tau)-1]\,d\tau$ by cutting off the integration at $\tau = 10$ is of the magnitude $\left|\int_{10}^\infty L^*_{mn}(\xi,\tau)\,[\varphi^*(\tau)-1]\,d\tau\right| < [\varphi^*(10)-1]\left|\int_{10}^\infty L^*_{mn}(\xi,\tau)\,d\tau\right| < [\varphi^*(10)-1]\,|K_{mn}(\xi)|$, and analogously for the integrals of χ^*.

c) See App. III.

d) The error in the interpolation, which was carried out in the parabolic approximation, is $\frac{y'''}{6}(\tau-\tau_0)(\tau-\tau_1)(\tau-\tau_2)$. Here $y(\tau)$ is the interpolated function, known at τ_0, τ_1 and τ_2. The error in the Simpson rule is $\frac{y^{(4)}\,h^5}{90}$, where h is the argument interval. The derivatives occurring in these terms may be estimated from the differences of the corresponding order.

e) These errors are given by the values of the right-hand sides of (14 e) when our last approximate solution is substituted.

We finally note that the rounding-off errors are negligible (BARK calculates with an accuracy corresponding to about seven decimal points).

Table 2. Approximate values of the constants μ_1^* and $\int_\varepsilon^\infty [\chi^*(\tau) - 1]\, d\tau$.

n	$(\mu_1^*)_n$	$\int_\varepsilon^\infty [\chi_n^*(\tau) - 1]\, d\tau$
0	1.1232	0.0000
1	1.0119	0.2990
2	0.9808	0.3293
3	0.9566	0.3553
4*	0.9427	0.3739
5	0.9217	0.3926
6	0.9142	0.4001
7	0.9101	0.4049
8*	0.9074	0.4087
9	0.8966	0.4171
10	0.8957	0.4186
11	0.8952	0.4197
12	0.8950	0.4203
13	0.8947	0.4205

* After the 4th and the 8th iteration there was performed an extrapolation of the φ^* and χ^* values.

IX. Final results

The temperature distribution in the gas and the temperature jump were finally computed, making use of the results presented in the preceding chapter. In fig. 8 is shown the appearance of the temperature curve

$$X(\xi) = \int_0^\xi \chi^*(\tau)\, d\tau = \frac{T(\xi) - T_0}{\left(\frac{dT}{d\xi}\right)_w}. \tag{16}$$

In the same figure have been plotted some of the temperature values which were measured by LAZAREFF [17] in an air gap between two plates held at different temperatures. $\left(\frac{dT}{dx}\right)_w$ has been taken as the temperature gradient valid at a point midway between the plates, and furthermore T_0 is chosen so that the temperature at the same point will fall on the theoretical curve. As Lazareff did not use a monatomic gas but air, and moreover the distance between his plates was so small that the transition regions at the two plates will noticeably overlap, it may be difficult to make here a quite fair comparison with our theoretical result. It appears, however, that the agreement on the whole is good.

Measurements similar to those of LAZAREFF have been performed more recently by MANDELL and WEST [19], but these, according to WEBER [29], are not to be considered as wholly reliable. In any case, they seem to be of little interest to us, as the temperature differences were kept too large for our theory

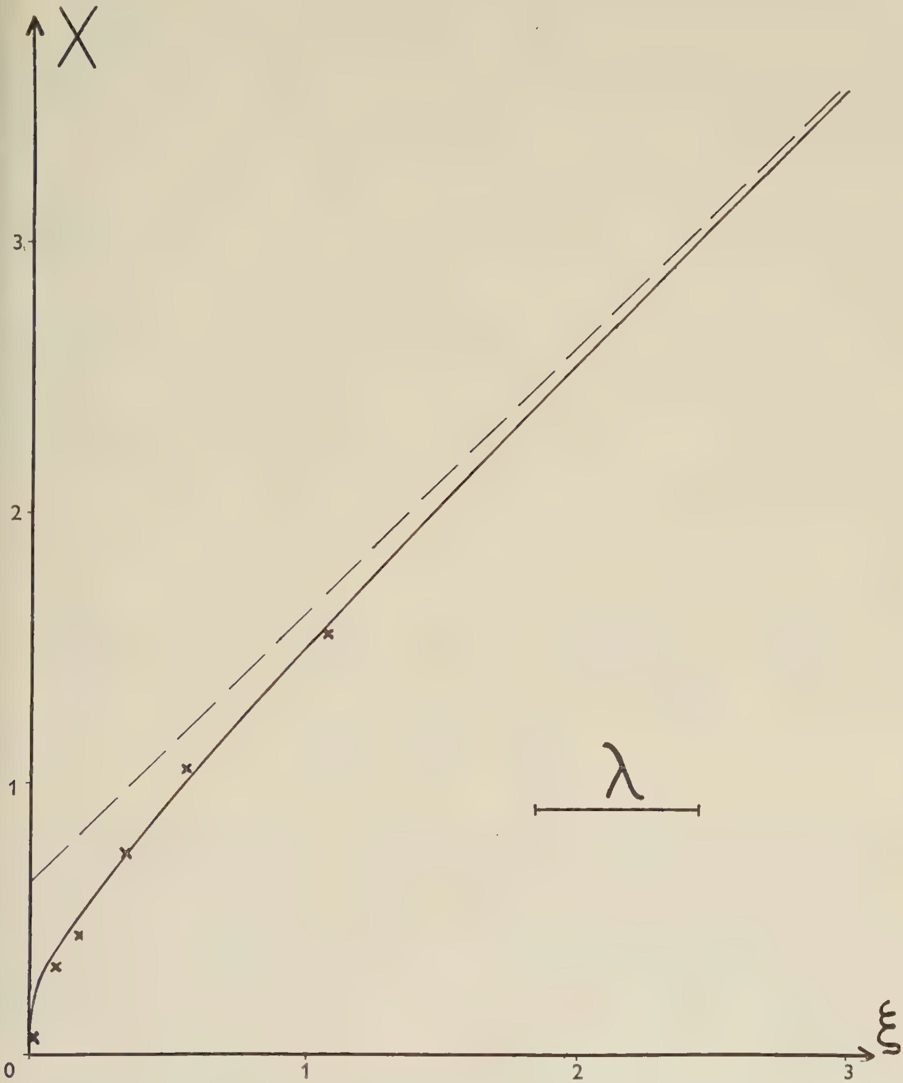

Fig. 8. Theoretical temperature distribution in the gas. The crosses give some of the temperature values measured by LAZAREFF [17] (in air of the pressure 0.019 mm Hg, distance between the plates 9 mm).

to be applicable. It would be of interest to have further temperature measurements in the transition region, especially at distances from the wall of some hundredths of a λ and smaller, where according to our theory we should expect a considerable temperature drop.

Using (10 b) and (15) we can write the expression for the temperature jump in the form

$$\Delta T = \frac{5\sqrt{\pi}}{8}\,\frac{2-ka}{a}\left(\frac{dT}{d\xi}\right)_w = \frac{75\pi}{128}\,\frac{2-ka}{a}\,\lambda\left(\frac{dT}{dx}\right)_w, \tag{1 e}$$

where k is a constant, the value of which is given by

$$k = 2 - \frac{8}{5\sqrt{\pi}}\left\{\mu_1 + \int_0^\infty [\chi^*(\tau)-1]\,d\tau\right\} = 2 - \frac{8}{5\sqrt{\pi}}\left\{\mu_1^* - \varepsilon + \int_\varepsilon^\infty [\chi^*(\tau)-1]\,d\tau\right\}.$$

We see that (1 e) agrees with the result (1 b) of the old theory, except for the replacement of the factor $\frac{2-a}{a}$ by $\frac{2-ka}{a}$. For our first approximate solution $\chi_0^* = 1$, which has an associate parameter value $(\mu_1^*)_0 = \frac{5\sqrt{\pi}}{8} + \varepsilon$, we find $k=1$ and thus arrive precisely at (1 b).

For our final solution there is computed the numerical value

$$k = 0.827.$$

The value appears to be correct to within one or two units in the last figure. The value of the temperature jump would thus finally be

$$\Delta T = \frac{75\pi}{128}\,\frac{2-0.827\,a}{a}\,\lambda\left(\frac{dT}{dx}\right)_w. \tag{1 f}$$

This is the main result of our investigation.

Of immediate interest is the correction that is to be applied to a value of the accommodation coefficient determined by the formula of the old theory to ensure it being correct according to our new result. This correction is represented in fig. 9. Its magnitude seems to be quite reasonable. We would recall, however, that with the boundary condition (5 b) our theory cannot claim to be realistic for small a-values, so that the result must then be taken with some reservation.

We find from fig. 9 that a value of $a = 0.92$ according to the old theory corresponds to a corrected value very near 1. If our result is correct, this former value should thus be about the upper limit for the values of the accommodation coefficient earlier reported in the literature, so far as they have come out from temperature jump measurements. Such a limit can now in fact be detected, although some isolated higher values appear. The tendency is most evident in the extensive and carefully performed investigation reported by DICKINS [4]. DICKINS' determinations of the accommodation coefficient have been criticized by KENNARD [14], who points out that he has made use of an older doubtful value of the temperature jump. However, in combination with the older value of λ also used by DICKINS this jump value will correspond precisely to (1 c), and we thus have no reason to consider his results as un-

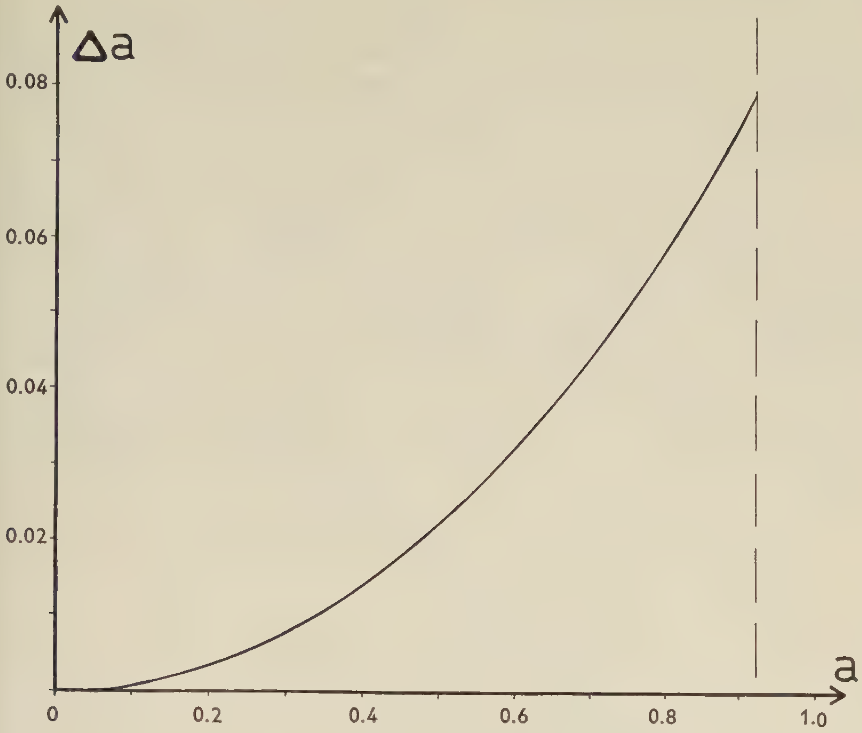

Fig. 9. $\Delta a = \dfrac{a^2}{\dfrac{2}{1-k} - a}$.

Correction for values of the accommodation coefficient being determined according to the old theory.

Table 3. DICKINS' values of the accommodation coefficient.

H_2–Pt	0.35	N_2O–Pt	0.90
He–Pt	0.51	Air–Pt	0.90
Ar–Pt	0.88	CO–Pt	0.91
NH_3–Pt	0.88	CO_2–Pt	0.92
N_2–Pt	0.90	SO_2–Pt	0.95
O_2–Pt	0.90		

reliable from the standpoint of the old theory. All of DICKINS' values of the accommodation coefficient are listed in Table 3.

It will be seen that the values, with the exception of those for the gases H_2, He and SO_2, lie closely assembled at the limit value predicted. Normally the values for different gases are found to be rather dispersed, and the assembling tendency observed would only seem capable of an explanation by assuming that the wall in this case exerts a very strong accommodation action, so that all kinds of gas molecules, except the very lightest (H_2 and He), will be reflected from it in temperature equilibrium. The fact that the agreement is so good for the polyatomic gases would seem to indicate that the reasoning of EUCKEN is well applicable here (Ch. III).

App. I. Treatment of viscous slip

When a gas has a mass velocity V along a wall there arises at the wall a viscous slip ΔV, which is of the order of $\lambda \left(\frac{\partial V}{\partial n}\right)_w$. This phenomenon is entirely analogous with the temperature jump.

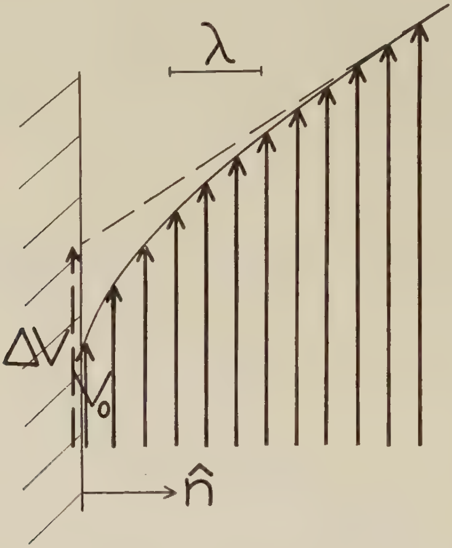

Fig. 10. Mass velocity distribution near a wall.

The classical theory for the viscous slip was developed by MAXWELL [20], and has later on been generalized by MILLIKAN [21] and others. The results corresponding to (1 b) and (1 c) in the temperature jump theory are respectively

$$\Delta V = \frac{5\pi}{16} \frac{2-f}{f} \lambda \left(\frac{\partial V}{\partial n}\right)_w \tag{17 a}$$

and

$$\Delta V = \frac{2-f}{f} \lambda \left(\frac{\partial V}{\partial n}\right)_w . \tag{17 b}$$

f stands here for the fraction of tangential momentum given up to the wall by the incident stream of gas molecules. Efforts to arrive at a more correct theory on the basis of the Boltzmann equation have recently been made by

KRAMERS [15], GRAD [9] and ROSE [23], but as far as is known, no new slip value has yet been reported.

Now, it is possible to treat the viscous slip in the same way as we previously have treated the temperature jump. The reasoning is quite analogous and will not be repeated here in detail, but we wish to state briefly the assumptions to be made and the equations arising.

We assume a rarefied gas streaming along a wall having radii of curvature much greater than λ. The conditions in the gas are to be practically unchanged along the wall over distances of a few λ. The mass velocity V is to be much less than $\bar{v}$ and must vary only in the direction normal to the wall. Finally, the density and the temperature in the gas are to be constant. This last condition cannot of course be applied strictly, since the viscous dissipation will always produce temperature variations in the gas. However, this effect is practically negligible for moderate values of the mass velocity.

As before we use a rectangular coordinate system with the x-axis in the normal direction out from the wall; the y-axis is laid in the direction of the mass velocity. The Boltzmann equation corresponding to (4 a) then reads

$$v_x \frac{\partial f^{(1)}}{\partial x} + I\left(f^{(0)} f_1^{(1)} + f^{(1)} f_1^{(0)}\right) = -\frac{m}{kT} v_x (v_y - V) \frac{dV}{dx} f^{(0)}, \tag{18}$$

where

$$f^{(0)} = n \left(\frac{m}{2\pi k T}\right)^{3/2} e^{-\frac{m}{2kT}\left[v_x^2 + (v_y - V)^2 + v_z^2\right]}. \tag{19 a}$$

As before we put

$$I\left(f^{(0)} f_1^{(1)} + f^{(1)} f_1^{(0)}\right) = \theta f^{(1)}. \tag{20}$$

However, θ has now the value $\frac{4}{5}\frac{\bar{v}}{\lambda}$.

The solution of the equation will become, in the same degree of approximation as is used in the temperature jump theory,

$$f^{(1)}(x, \boldsymbol{v}) = C(v_x, v_y, v_z)\, e^{-\frac{\theta x}{v_x}} - \frac{m}{kT} v_y \int\limits_{\alpha(v_x, v_y, v_z)}^{x} \frac{dV}{dx}(t)\, e^{\frac{\theta}{v_x}(t-x)}\, dt \cdot f^{(0)},$$

where

$$f^{(0)} = n \left(\frac{m}{2\pi k T}\right)^{3/2} e^{-\frac{m v^2}{2kT}}. \tag{19 b}$$

The functions $\underset{v_x<0}{C}$ and α are to be chosen as before.

Regarding the boundary condition at the wall, we assume that the gas molecules are reflected diffusely ($f = 1$) and Maxwellian. We may then write, with sufficient accuracy,

$$\underset{v_x>0}{f^{(1)}}(0, \boldsymbol{v}) = -\frac{m}{kT} v_y V_0 f^{(0)}. \tag{21}$$

The complete expression for $f^{(1)}$ is

$$\left.\begin{aligned} \underset{v_x>0}{f^{(1)}}(x, \boldsymbol{v}) &= -\frac{m}{kT} v_y \left[V_0 e^{-\frac{\theta x}{v_x}} + \int_0^x \frac{dV}{dx}(t)\, e^{\frac{\theta}{v_x}(t-x)}\, dt\right] \cdot f^{(0)}, \\ \underset{v_x<0}{f^{(1)}}(x, \boldsymbol{v}) &= \frac{m}{kT} v_y \int_x^\infty \frac{dV}{dx}(t)\, e^{\frac{\theta}{v_x}(t-x)}\, dt \cdot f^{(0)}; \\ \underset{v_x=0}{f^{(1)}}(x, \boldsymbol{v}) &= 0. \end{aligned}\right\} \tag{22}$$

The equations which determine $\frac{dV}{dx}(x)$ and V_0 are

$$\left.\begin{aligned} \int_{\boldsymbol{v}} v_y f^{(1)}\, \boldsymbol{dv} &= 0, \\ \underset{x\to\infty}{\frac{dV}{dx}(x)} &= \left(\frac{dV}{dx}\right)_w. \end{aligned}\right\} \tag{23}$$

Equivalent to these is

$$\int_{\boldsymbol{v}} m v_x v_y f^{(1)}\, \boldsymbol{dv} = -\eta \left(\frac{dV}{dx}\right)_w, \tag{24 a}$$

where η stands for the coefficient of viscosity for a Maxwell-gas, as calculated by the ordinary theory.

We introduce the variables

$$\xi = \frac{8}{5\sqrt{\pi}} \frac{x}{\lambda},$$

$$\psi^*(\xi) = \frac{\frac{dV}{d\xi}(\xi)}{\left(\frac{dV}{d\xi}\right)_w},$$

the functions

$$J_n(\xi) = \int_0^\infty x^n e^{-\frac{\xi}{x} - x^2}\, dx,$$

and the parameter

$$\nu = \frac{V_0}{\left(\frac{dV}{d\xi}\right)_w}.$$

The equation which corresponds to (14 b) in the temperature jump theory is found to be

$$\int_0^\infty J_1(|\xi-\tau|)\,\psi^*(\tau)\,d\tau = -\nu J_1(\xi)+\frac{\sqrt{\pi}}{2}. \tag{24 b}$$

Values of the function $J_1(\xi)$ will be found in Table 4.

As before, it is easily verified that $\psi^*\to 1$ when $\xi\to\infty$ and that $\psi^*\to\infty$ when $\xi\to 0$, but that $\int_0^\varepsilon \psi^*(\tau)\,d\tau$ converges. A discussion of (24 b) according to the theory of Wiener and Levinson [30] is given in App. II.

Expressed in the variables introduced above, the mass velocity distribution will be

$$V(\xi)=\left[\nu+\int_0^\xi \psi^*(\tau)\,d\tau\right]\left(\frac{dV}{d\xi}\right)_w, \tag{25}$$

and the viscous slip

$$\Delta V=\left\{\nu+\int_0^\infty [\psi^*(\tau)-1]\,d\tau\right\}\left(\frac{dV}{d\xi}\right)_w. \tag{26}$$

Numerical computations are being made, using an iterative method of solution analogous to that described in Ch. VIII. A preliminary result has been the slip value

$$\Delta V = 1.21\,\lambda\left(\frac{dV}{dx}\right)_w.$$

To this there corresponds in the formula (17 a) of the old theory the value $f=0.90$, which may be compared with those reported in the literature (see *e.g.* Kennard [14], p. 299).

A complete account of the numerical computations will be given in a later report.

App. II. The theory of Wiener and Levinson

A fundamental theory for integral equations of the type we are concerned with in (14 b) and (24 b) has been given by Wiener and Hopf [31]. In this theory it is required, however, that the kernels vanish at least exponentially at infinity, which condition is not fulfilled here according to (34) and (35). On the other hand, it is possible to use the modified theory given by Wiener and Levinson [30], and we will here briefly discuss the application of this theory to our case. For the sake of simplicity, we shall for the present confine ourselves to the consideration of the equation (24 b).

To start with, we eliminate the asymptotic part of the equation by the substitution $\psi^*=1+Z$. This gives

$$\int_0^\infty J_1(|\xi-\tau|)\,Z(\tau)\,d\tau = -\nu J_1(|\xi|) + J_2(|\xi|), \quad (\xi \geq 0). \tag{24 c}$$

For the sake of symmetry, we have written $|\xi|$ for the argument in the right-hand side. Only those solutions $Z(\xi)$ which belong to the class $L_1(0, \infty)$[1] will be investigated.

Let us introduce the Fourier transforms of $J_n(|\xi|)$

$$j_n(u) = \int_{-\infty}^{\infty} e^{i\xi u} \int_0^\infty x^n e^{-\frac{|\xi|}{x}-x^2}\,dx\,d\xi = \int_0^\infty x^n e^{-x^2} \int_{-\infty}^{\infty} e^{-\frac{|\xi|}{x}+i\xi u}\,d\xi\,dx =$$

$$= 2\int_0^\infty \frac{x^{n+1}}{1+x^2u^2}\,e^{-x^2}\,dx.$$

For $n>0$, which is the only case of interest here, $j_n(u)$ are bounded and >0 (u real), and have the following asymptotic expressions when $|u| \to \infty$:

$$j_1(u) \sim 2J_0(0)\cdot\frac{1}{u^2} + O\left(\frac{1}{u^3}\right),$$

$$j_2(u) \sim 2J_1(0)\cdot\frac{1}{u^2} + O\left(\frac{\log|u|}{u^4}\right),$$

$$j_n(u) \sim 2J_{n-1}(0)\cdot\frac{1}{u^2} + O\left(\frac{1}{u^4}\right) \quad \text{for } n>2.$$

We can now, according to a known theorem, split up $j_1(u)$ into two complex factors,

$$j_1(u) = i_1(u)\cdot i_2(u),$$

such that $i_1(u+iv)$ and $i_2(u+iv)$ are bounded, analytic and free from zeros for respectively $v>0$ and $v<0$.[2] On the real axis we may put

$$|i_1(u)|^2 = |i_2(u)|^2 = j_1(u).$$

---

[1] $Z(\xi)$ belongs to the class $L_n(a,b)$ if $\int_a^b |Z(\xi)|^n\,d\xi < \infty$.

[2] The possibility of such a factorization is secured by the relations

$$j_1(u)>0, \quad j_1(-u)=j_1(u) \quad \text{and} \quad \int_{-\infty}^{\infty} \frac{|\log j_1(u)|}{1+u^2}\,du < \infty.$$

The factors are given by

$$i_1(u+iv) = \exp\frac{1}{2\pi}\int_{-\infty}^{\infty}\frac{\log j_1(s)}{i[s-(u+iv)]}\,ds, \quad i_2(u+iv) = \bar{i}_1(u-iv),$$

where the bar indicates the conjugate complex quantity.

Ve note that $i_1(u)$ and $i_2(u)$ belong to $L_2(-\infty, \infty)$. Thus we have the con-olution form [27]

$$J_1(|\xi|) = \int_{-\infty}^{\infty} I_2(s)\, I_1(\xi - s)\, ds, \tag{27}$$

vhere $I_1(\xi)$ and $I_2(\xi)$ are the inverse Fourier transforms of respectively $i_1(u)$ nd $i_2(u)$. Moreover, we have

$$I_1(\xi) = 0 \quad \text{for} \quad \xi < 0,$$

$$I_2(\xi) = 0 \quad \text{for} \quad \xi > 0,$$

s is found by closing the paths of integration of the transform integrals in espectively the upper and the lower half plane and making use of the Cauchy ntegral theorem.

We further define a function $a(u)$ through the equation

$$a(u) \cdot i_2(u) = -\nu\, j_1(u) + j_2(u).$$

s $j_1(u)$ is always positive, $i_2(u)$ has no zeros and we find that also $a(u)$ elongs to $L_2(-\infty, \infty)$. Again we have a convolution form,

$$\int_{-\infty}^{\infty} A(\xi - s)\, I_2(s)\, ds = -\nu\, J_1(|\xi|) + J_2(|\xi|), \tag{28}$$

vhere $A(\xi)$ is the inverse Fourier transform of $a(u)$.

By introducing (27) and (28) into our equation (24 c) we find, after a change f the order of integration,

$$\int_{-\infty}^{0} I_2(s)\, F(\xi - s)\, ds = 0, \quad (\xi \geq 0),$$

r, putting $\xi - s = t$,

$$\int_{\xi}^{\infty} I_2(\xi - t)\, F(t)\, dt = 0, \quad (\xi \geq 0), \tag{24 d}$$

vhere

$$F(\xi) = \int_{0}^{\infty} I_1(\xi - \tau)\, Z(\tau)\, d\tau - A(\xi).$$

his implies

$$F(\xi) = 0, \quad (\xi \geq 0). \tag{24 e}$$

ultiplying here by $e^{iu\xi}$ and integrating from $\xi = 0$ to ∞, we have, introducing he integrals

$$z(u) = \int_{0}^{\infty} Z(\xi)\, e^{iu\xi}\, d\xi,$$

$$a_1(u) = \int_0^\infty A(\xi)\, e^{iu\xi}\, d\xi,$$

that

$$i_1(u) \cdot z(u) = a_1(u). \tag{24 f}$$

These steps are legitimate when $Z(\xi)$ belongs to $L_1(0, \infty)$ and $F(\xi)$ thus belongs to $L_2(0, \infty)$ [24, 27].

The problem of finding $a_1(u)$ from $a(u)$ is equivalent to the problem of splitting up $a(u)$ into two complex terms $a_1(u)$ and $a_2(u)$, being analytic and bounded in respectively the upper and the lower half plane. Introducing the exponentials

$$\alpha(u) = e^{a(u)},$$

$$\alpha_1(u) = e^{a_1(u)},$$

$$\alpha_2(u) = e^{a_2(u)},$$

we are again met with the factorization problem. Now, at infinity $|a_1(u)|$ is of the order of $|a(u)|$. Since $|a(u)|$ and $|i_1(u)|$ will both vanish as $\frac{1}{u}$, we find then that $z(u)$ does not tend to zero, and thus no integrable solution $Z(\xi)$ can exist. There is, however, one exception: if we choose for the eigen-parameter ν the special value

$$\nu = \lim_{u\to\infty} \frac{j_2(u)}{j_1(u)} = \frac{J_1(0)}{J_0(0)} = \frac{1}{\sqrt{\pi}}\,(\approx 0.564), \tag{29}$$

where is used (33), then $|a(u)|$ will vanish as $\frac{1}{u^2}$ and $z(u)$ belongs to $L_2(-\infty, \infty)$. Moreover, it can be shown that $z(u)$ is bounded and analytic in the upper half plane. This means that $z(u)$ is the complete Fourier transform of a solution $Z(\xi)$, being zero for $\xi < 0$. Thus

$$Z(\xi) = \frac{1}{2\pi} \int_{-\infty}^{\infty} z(u)\, e^{-i\xi u}\, du.$$

Since $z(u)$ is bounded at $u = 0$ this solution is certainly integrable, also it seems possible to show that it is absolutely integrable.

For the system (14 b) we find by an analogous reasoning, which is not given here, that a solution exists only when the eigen-parameters μ_0 and μ_1 have the special values

$$\left.\begin{aligned} \mu_0 &= \lim_{u\to\infty} \frac{-h_0(u)\, l_{11}(u) + h_1(u)\, l_{01}(u)}{l_{00}(u)\, l_{11}(u) - l_{10}(u)\, l_{01}(u)} = \frac{1}{2\sqrt{\pi}}\,(\approx 0.282), \\ \mu_1 &= \lim_{u\to\infty} \frac{h_0(u)\, l_{10}(u) - h_1(u)\, l_{00}(u)}{l_{00}(u)\, l_{11}(u) - l_{10}(u)\, l_{01}(u)} = \frac{7}{6\sqrt{\pi}}\,(\approx 0.658), \end{aligned}\right\} \tag{30}$$

where are used (31), (33) and (35). Here $l_{mn}(u)$ and $h_m(u)$ are the Fourier transforms

$$l_{mn}(u) = \int_{-\infty}^{\infty} L_{mn}(|\xi|)\, e^{i\xi u}\, d\xi,$$

$$h_m(u) = \int_{-\infty}^{\infty} \left[\int_0^{\infty} L_{m0}(|\xi - \tau|)\, d\tau + \int_0^{\infty} L_{m1}(|\xi - \tau|)\, d\tau \right] e^{iu\xi}\, d\xi.$$

App. III. Computation of the integrals J_n and L_{mn}

The integrals

$$J_n(\xi) = \int_0^{\infty} x^n e^{-\frac{\xi}{x} - x^2}\, dx$$

have been computed with the BARK for $n = 1$, 2 and 3 in the range $0 \leq \xi \leq 10$.[1]

We have the recurrence formulae

$$J_n' = -J_{n-1}, \tag{31}$$

$$J_n = \frac{n-1}{2} J_{n-2} + \frac{\xi}{2} J_{n-3}, \ (\xi > 0, \text{ and } \xi = 0,\ n > -1). \tag{32}$$

Special values of interest are

$$\left.\begin{aligned} J_0(0) &= \frac{\sqrt{\pi}}{2}, \\ J_{2k-1}(0) &= \frac{(k-1)!}{2}, \qquad\qquad (k = 1, 2, \cdots) \\ J_{2k}(0) &= \frac{(2k-1)(2k-3)\cdots 1}{2^{k+1}} \sqrt{\pi}. \end{aligned}\right\} \tag{33}$$

---

[1] Putting $x = \xi^{1/3} t^{1/2}$ we find

$$J_n(\xi) = \frac{1}{2} \xi^{\frac{n+1}{3}} \int_0^{\infty} t^{\frac{n-1}{2}} e^{-\xi^{2/3}(t + t^{-1/2})}\, dt.$$

The last integral is of the type $\int_0^{\infty} e^{-y(t + t^{-\mu})}\, t^{\nu}\, dt$, which has been investigated by H. FAXÉN (Arkiv f. Mat. Astr. Fys. 15, n:o 13, 1920). FAXÉN gives an expansion in series of this integral, which could be used to calculate values of $J_n(\xi)$ near the singular point $\xi = 0$.

For large positive ξ we find by the method of saddle points

$$J_n \sim \sqrt{\frac{\pi}{3}} \left(\frac{\xi}{2}\right)^{\frac{n}{3}} e^{-3\left(\frac{\xi}{2}\right)^{\frac{2}{3}}}. \tag{34}$$

The functions $J_n(\xi)$ are finite for $\xi > 0$, but infinite at $\xi = 0$ for $n \leq -1$.

The computations were performed by applying step-by-step a Taylor expansion

$$J_n(\xi + h) = \sum_{k=0}^{\infty} \frac{h^k}{k!} J_n^{(k)}(\xi) = \sum_{k=0}^{\infty} (-1)^k \frac{h^k}{k!} J_{n-k}(\xi),$$

combined with (32). Initial values were computed to seven correct decimal points at $\xi = 1$ by a numerical quadrature. The computed values up to $\xi = 10$ are given in Table 4. They are correct in all the figures reproduced, except in the range $\xi < 0.125$, where there may be an error of 1 or 2 units in the last figure. Extension of the table in the direction of n is easily performed using (32).

The integrals

$$L_{mn}(\xi) = \int_{x>0} x\, r^{2m} \left(\frac{3}{2} - r^2\right)^n e^{-\frac{\xi}{x} - r^2} \boldsymbol{dr}, \quad (r^2 = x^2 + y^2 + z^2)$$

were also computed at the same points, for $m, n = 0,1$. These functions may directly be expressed as linear combinations of J_n:

$$\left.\begin{aligned}
L_{00} &= \pi J_1, \\
L_{01} &= \frac{\pi}{2} J_1 - \pi J_3, \\
L_{10} &= \pi J_1 + \pi J_3, \\
L_{11} &= -\frac{\pi}{2} J_1 - \frac{\pi}{2} J_3 - \pi J_5.
\end{aligned}\right\} \tag{35}$$

They are presented graphically in fig. 11.

We finally give here the corresponding functions

$$K_{mn}(\xi) = \int_{\varepsilon}^{\infty} L_{mn}^{*}(\xi, \tau)\, d\tau$$

and

$$f_m(\xi) = L_m(\xi) - K_{m0}(\xi) - K_{m1}(\xi),$$

as expressed in terms of J_n. Using the approximate formula

$$K_{mn}(\xi) \approx \int_0^{\infty} L_{mn}^{*}(\xi, \tau)\, d\tau - \frac{\varepsilon^2}{2} \frac{\partial L_{mn}^{*}}{\partial \tau}(\xi, 0),$$

which is sufficiently accurate for our purpose, and the formulae (31), (33) and (35), these are found to be

$$K_{00} = \frac{\pi\sqrt{\pi}}{2} - \frac{3}{8}\pi\sqrt{\pi}\,J_1 - \pi\,J_2 - \frac{1}{8}\pi\sqrt{\pi}\,J_3 - \frac{\varepsilon^2}{2}\left(\pi\,J_0 + \frac{5}{4}\pi\sqrt{\pi}\,J_1 - \frac{1}{4}\pi\sqrt{\pi}\,J_3\right),$$

$$K_{01} = -\frac{1}{2}\pi\sqrt{\pi} - \frac{1}{4}\pi\sqrt{\pi}\,J_1 - \frac{\pi}{2}J_2 + \frac{3}{4}\pi\sqrt{\pi}\,J_3 + \pi\,J_4 -$$

$$-\frac{\varepsilon^2}{2}\left(\frac{\pi}{2}J_0 + \frac{3}{4}\pi\sqrt{\pi}\,J_1 - \pi\,J_2 - \frac{3}{4}\pi\sqrt{\pi}\,J_3\right),$$

$$K_{10} = \frac{5}{4}\pi\sqrt{\pi} - \frac{\pi\sqrt{\pi}}{2}J_1 - \pi\,J_2 - \frac{\pi\sqrt{\pi}}{2}J_3 - \pi\,J_4 - \frac{\pi\sqrt{\pi}}{8}J_5$$

$$-\frac{\varepsilon^2}{2}\left(\pi\,J_0 + \pi\sqrt{\pi}\,J_1 + \pi\,J_2 + \pi\sqrt{\pi}\,J_3 - \frac{\pi\sqrt{\pi}}{4}J_5\right),$$

$$K_{11} = -\frac{5}{2}\pi\sqrt{\pi} + \frac{\pi\sqrt{\pi}}{2}J_1 + \frac{\pi}{2}J_2 + \frac{\pi\sqrt{\pi}}{2}J_3 + \frac{\pi}{2}J_4 + \frac{3\pi\sqrt{\pi}}{4}J_5 + \pi\,J_6 +$$

$$+\frac{\varepsilon^2}{2}\left(\frac{\pi}{2}J_0 + \frac{\pi}{2}J_2 + \pi\,J_4 + \frac{3}{4}\pi\sqrt{\pi}\,J_5\right),$$

Table 4. $J_n(\xi) = \int\limits_0^\infty x^n\, e^{-\frac{\xi}{x} - x^2}\, dx.$

ξ	J_1	J_2	J_3	ξ	J_1	J_2	J_3
0	0.500000	0.443113	0.500000	1	0.146564	0.168488	0.221587
0.015625	0.486741	0.435408	0.493139	1.25	0.114216	0.136093	0.183683
0.03125	0.474318	0.427900	0.486394	1.5	0.090026	0.110704	0.152959
0.046875	0.462548	0.420582	0.479766	1.75	0.071629	0.090599	0.127892
0.0625	0.451336	0.413443	0.473250	2	0.057446	0.074539	0.107324
0.078125	0.440615	0.406475	0.466845	3	0.025263	0.035643	0.054871
0.09375	0.430338	0.399671	0.460547	4	0.011930	0.017959	0.029167
0.109375	0.420464	0.393025	0.454355	5	0.005927	0.009409	0.015978
0.125	0.410962	0.386530	0.448264	6	0.003064	0.005082	0.008969
0.1875	0.376178	0.361957	0.424886	7	0.001638	0.002811	0.005141
0.25	0.345686	0.339419	0.402978	8	0.000902	0.001581	0.003006
0.3125	0.318659	0.318674	0.382421	9	0.000508	0.000895	0.001801
0.375	0.294510	0.299526	0.363110	10	0.000289	0.000507	0.001118
0.4375	0.272797	0.281810	0.344950				
0.5	0.253177	0.265383	0.327857				
0.75	0.190792	0.210358	0.268713				

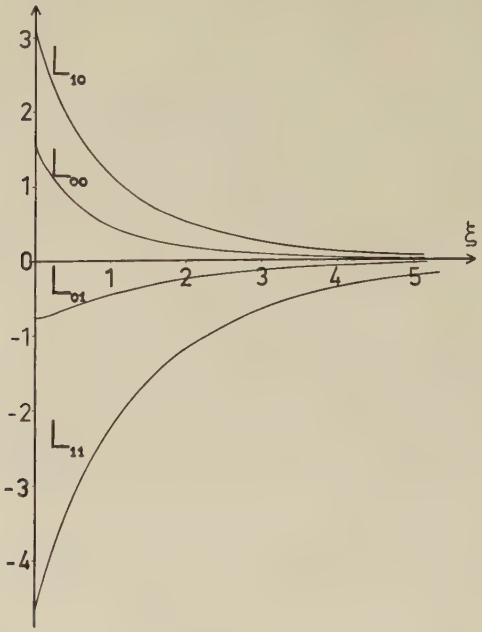

Fig 11. $L_{mn}(\xi) = \int\limits_{x>0} x\, r^{2m} \left(\frac{3}{2} - r^2\right)^n e^{-\frac{\xi}{x} - r^2}\, d\boldsymbol{r}, \; (r^2 = x^2 + y^2 + z^2).$

$$f_0 = -\frac{5}{8}\pi\sqrt{\pi}\, J_1 + \frac{3}{2}\pi J_2 + \frac{5}{8}\pi\sqrt{\pi}\, J_3 - \pi J_4 + \\ + \frac{\varepsilon^2}{2}\left(\frac{3}{2}\pi J_0 + 2\pi\sqrt{\pi}\, J_1 - \pi J_2 - \pi\sqrt{\pi}\, J_3\right),$$

$$f_1 = \frac{\pi}{2} J_2 + \frac{\pi}{2} J_4 + \frac{5}{8}\pi\sqrt{\pi}\, J_5 - \pi J_6 + \\ + \frac{\varepsilon^2}{2}\left(\frac{\pi}{2} J_0 + \pi\sqrt{\pi}\, J_1 + \frac{\pi}{2} J_2 + \pi\sqrt{\pi}\, J_3 - \pi J_4 - \pi\sqrt{\pi}\, J_5\right).$$

Note added in proof: It has become known to the author that the integrals studied in App. III have been investigated earlier in connection with the problem of thermal neutron absorption. Reference is given to Journ. Math. Phys. 32, p. 188 (1953).

Research Institute of National Defence, Stockholm, October 1953.

REFERENCES

1. C. T. Archer, Proc. Roy. Soc. A 165, p. 474 (1938).
2. B. Baule, Ann. Physik 44, p. 145 (1914).
3. S. Chapman and T. Cowling, The Theory of Non-Uniform Gases, pp. 1–133, 151–198, 259–272, Cambr. Un. Press (1939).
4. B. G. Dickins, Proc. Roy. Soc. A 143, p. 517 (1933).
5. D. Enskog, Kinetische Theorie der Vorgänge in mässig verdünnten Gasen, Upsala (1917).
6. A. Eucken, Phys. Zeits. 14, p. 324 (1913).
7. E. Fredlund, Ann. Physik 28, p. 319 (1937).
8. E. Gehrcke, Ann. Physik 2, p. 102 (1900).
9. H. Grad, Commun. Pure Appl. Math. 2: 4, p. 331 (1949).
10. H. S. Gregory, Phil. Mag. 22, p. 257 (1936).
11. E. R. Grilly, W. J. Taylor and H. E. Johnstone, J. Chem. Phys. 14, p. 435 (1946).
12. M. Knudsen, Ann. Physik 34, p. 593 (1911).
13. ——, Ann. Physik 6, p. 129 (1930).
14. E. H. Kennard, Kinetic Theory of Gases, pp. 162–184, 291–327, McGraw Hill Book C:o, New York (1938).
15. H. A. Kramers, Nuovo Cimento 6, Suppl. (1949).
16. A. Kundt and E. Warburg, Pogg. Ann. 156, p. 177 (1875).
17. P. Lazareff, Ann. Physik 37, p. 233 (1912).
18. L. Loeb, Kinetic Theory of Gases, pp. 240–279, 308–337, McGraw Hill Book C:o, New York (1927).
19. W. Mandell and J. West, Proc. Phys. Soc. 37, p. 20 (1925).
20. J. C. Maxwell, Collected Works 2, pp. 26–78, 681–712, Cambr. Un. Press (1927).
21. R. A. Millikan, Phys. Rev. 21, p. 217 (1923).
22. L. S. Ornstein and W. R. van Wyk, Zeits. Phys. 78, p. 734 (1932).
23. M. Rose, Note in Bull. Am. Phys. Soc. 28: 3 (1953).
24. W. Schmeidler, Integralgleichungen mit Anwendungen in Physik und Technik 1, pp. 1–242, Akad. Verl. Geest & Portig, Leipzig (1950).
25. M. v. Smoluchowski, Wied. Ann. 64, p. 101 (1898).
26. ——, Akad. Wiss. Wien 107, p. 304 (1898), and 108, p. 5 (1899).
27. E. C. Titmarsch, Introduction to the Theory of Fourier Integrals, pp. 1–95, Clarendon Press, Oxford (1948).
28. H. v. Ubisch, Appl. Sci. Res. A 2, 5–6, p. 403 (1951).
29. S. Weber, Kgl. Danske Vidensk. Selsk. Medd. 16: 9 (1939).
30. N. Wiener, The Extrapolation, Interpolation and Smoothing of Stationary Time Series, pp. 52–68, 153–160, Mass. Inst. Techn. Press (1949).
31. N. Wiener and E. Hopf, Über eine Klasse singulärer Integralgleichungen, Akad. Wiss. Berlin, pp. 696–706 (1931), also in Am. Math. Soc. Coll. Publ. 21, p. 49 (1934).

Tryckt den 6 april 1954

Uppsala 1954. Almqvist & Wiksells Boktryckeri AB

ARKIV FÖR FYSIK Band 7 nr 45

Communicated 27 January 1954 by Oskar Klein and Hilding Faxén

Heat conduction in a rarefied gas: the cylindrically symmetrical case[1]

By Pierre Welander

With 4 figures in the text

For studying heat conduction in gases at low pressures a hot-wire gauge is often used, heat being produced electrically in a thin wire and conducted through the gas to a surrounding coaxial tube. When the pressure of the gas is successively lowered from the atmospheric level while the temperatures of the wire and the tube are held constant, we find at first that the heat flow remains constant, as is predicted by the ordinary kinetic theory. However, when the pressure has become so low that the mean free path λ of the gas molecules cannot be completely neglected as compared to the radius of the wire, the effect of the temperature jump at the wire surface will appear, and the heat flow decreases with a further lowering of the pressure.

As long as λ is still small as compared to the radius of the wire, it is possible to calculate the heat flow theoretically according to the formula

$$Q = \frac{2\pi K (T_1 - T_2)}{\ln \frac{r_2}{r_1} + \varkappa_1 \frac{\lambda}{r_1} + \varkappa_2 \frac{\lambda}{r_2}}. \tag{1}$$

Here Q is the heat flow from the wire per unit length, K is the coefficient of heat conduction of the gas, r_1 and r_2 are the radii of the wire and the tube, T_1 and T_2 the corresponding temperatures, and $\varkappa_1$ and $\varkappa_2$ the corresponding temperature jump numbers. The temperature jump numbers are defined according to the formulae

$$\Delta T_1 = \varkappa_1 \lambda \left(\frac{\partial T}{\partial n}\right)_{w_1} = -\varkappa_1 \frac{\lambda}{r_1} \frac{Q}{2\pi K},$$

$$\Delta T_2 = \varkappa_2 \lambda \left(\frac{\partial T}{\partial n}\right)_{w_2} = \varkappa_2 \frac{\lambda}{r_2} \frac{Q}{2\pi K}.$$

Applying the temperature jump value previously calculated we find

---

[1] This paper is written as a supplement to the preceding paper: "On the temperature jump in a rarefied gas", to which the reader is referred throughout.

$$\varkappa = \frac{75\,\pi}{128}\,\frac{2 - k\,a}{a},$$

where a is the accommodation coefficient and k is a pure number ≈ 0.827.

When λ becomes comparable with r_1, the temperature jump theory fails because the ordinary temperature curve cannot be considered to vary linearly in the transition region at the wire. Still more complicated conditions appear when λ becomes comparable to the radius r_2 of the tube and the transition region fills up the whole space in the tube. However, at extremely low pressures, where λ is much greater than r_2 and the intermolecular collisions become rare as compared to the collisions between the gas molecules and the walls, we again meet with a comparatively simple case (free molecule conduction) which can be handled theoretically [4, 5].

Attempts to explain theoretically the intermediate region have been made by several authors [2, 3, 6, 7, 8]. In all these calculations the same basic approach is used: it is assumed that a free molecule conduction takes place in certain intervals $(r_1, r_1 + \Delta r_1)$ and $(r_2 - \Delta r_2, r_2)$, while the ordinary theory should apply in the interval $(r_1 + \Delta r_1, r_2 - \Delta r_2)$. WEBER [8] puts for a monatomic gas $\Delta r_1 = \Delta r_2 = \frac{15}{8}\lambda$ and arrives at an expression for the heat flow which he considers to be fairly correct for all values of $\frac{\lambda}{r_1}$. However, his main formula is in fact derived under the tacit assumption that $\frac{\lambda}{r_1}$ and $\frac{\lambda}{r_2}$ are small quantities, and his derivation from this formula of the free molecule result is apparently unjustified.[1] SCHÄFER–RATING–EUCKEN [6] introduce for Δr_1 and Δr_2 certain corrective factors, which are functions of $\frac{\lambda}{r_1}$ and $\frac{\lambda}{r_2}$, respectively. This seems to improve the theory a great deal and their result is found to apply quite well over a large pressure range.

However, to develop a quite correct theory it is necessary to abandon the simple model where the gas mass is sharply divided up into a region of free molecule conduction and a region of ordinary heat conduction, and examine the transition region more closely.

We will here make a preliminary study of this problem, working along the same lines as in the theory of the temperature jump presented previously. The treatment is confined to the important case where λ is small as compared to $r_2 - r_1$ but of any magnitude as compared to r_1. In such a case we find it convenient to introduce a *generalized temperature jump* $\Delta' T_1$, defined as the difference between the temperature T_0' found at the surface of the wire by an extrapolation of the temperature curve from the region of ordinary heat conduction according to the relation $r\frac{d\,T}{d\,r} = -\frac{Q}{2\,\pi\,K} = \text{const.}$, and the temperature T_1 of the wire (Fig. 1). Writing the jump in the form $\Delta' T_1 = -\varkappa_1' \frac{\lambda}{r_1}\frac{Q}{2\,\pi\,K}$

---

[1] Formulae (3) and (5), pp. 6–7.

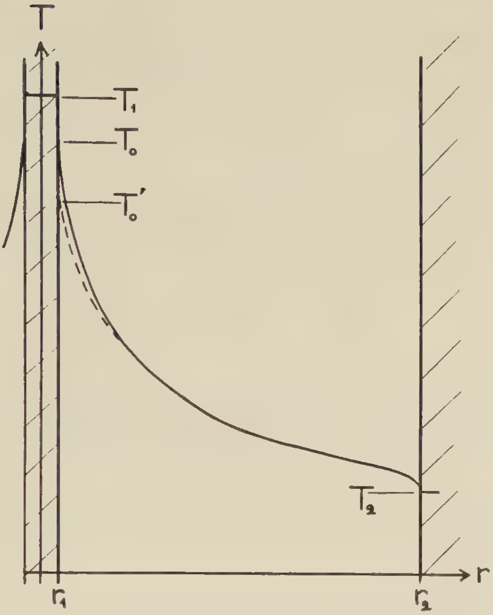

Fig. 1. Temperature distribution in the gas.

we find the formula (1) again being applicable, if only $\varkappa_1$ is replaced by $\varkappa_1'$. Our main task is then to determine $\varkappa_1'$.

We start our investigation from the Boltzmann equation, and first derive the form of this equation when expressed in cylindrical coordinates r, φ and z (Fig. 2).

Assume that the number of gas molecules in the volume element $(\boldsymbol{r}, \boldsymbol{dr})$ having their velocities in the range $(\boldsymbol{v}, \boldsymbol{dv})$ is $f(r, \varphi, z, v_r, v_\varphi, v_z)\, \boldsymbol{dr}\, \boldsymbol{dv}$. We follow such a group of molecules from time t to $t+dt$. If no molecular collisions occur, the group at the later time will have the coordinates

$$r(t+dt) = r(t) + v_r\, dt,$$

$$\varphi(t+dt) = \varphi(t) + \frac{v_\varphi}{r}\, dt,$$

$$z(t+dt) = z(t) + v_z\, dt,$$

and the velocity components

$$v_r(t+dt) = v_r(t) + \frac{v_\varphi^2}{r}\, dt,$$

$$v_\varphi(t+dt) = v_\varphi(t) - \frac{v_r\, v_\varphi}{r}\, dt,$$

$$v_z(t+dt) = v_z(t),$$

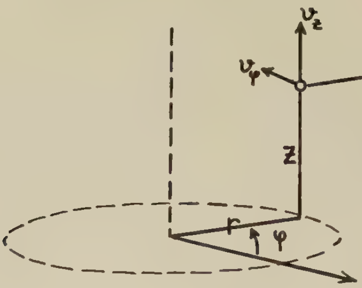

Fig. 2. Coordinate system.

and fills up elements $\boldsymbol{dr}$ and $\boldsymbol{dv}$ of the same magnitude as before. If further a net number of molecules $I(f f_1)\ \boldsymbol{dr}\ \boldsymbol{dv}\ dt$ disappears from the group by molecular collisions during the time interval dt, it follows that

$$f\left(r+v_r\,dt,\ \varphi+\frac{v_\varphi}{r}\,dt,\ z+v_z\,dt,\ v_r+\frac{v_\varphi^2}{r}\,dt,\ v_\varphi-\frac{v_r\,v_\varphi}{r}\,dt,\ v_z\right)\boldsymbol{dr}\,\boldsymbol{dv}=$$

$$f(r,\varphi,z,v_r,v_\varphi,v_z)\,\boldsymbol{dr}\,\boldsymbol{dv}-I\,(f f_1)\,\boldsymbol{dr}\,\boldsymbol{dv}\,dt.$$

Or, introducing differential quotients,

$$v_r\frac{\partial f}{\partial r}+\frac{v_\varphi}{r}\frac{\partial f}{\partial \varphi}+v_z\frac{\partial f}{\partial z}+\frac{v_\varphi^2}{r}\frac{\partial f}{\partial v_r}-\frac{v_r\,v_\varphi}{r}\frac{\partial f}{\partial v_\varphi}+I\,(f f_1)=0. \tag{2 a}$$

In our case the situation is taken to be cylindrically symmetrical, so that $\dfrac{\partial f}{\partial \varphi}=\dfrac{\partial f}{\partial z}=0$.

We introduce here the same kind of approximations as before. Thus, f is divided into two terms,

$$f=f^{(0)}+f^{(1)},$$

where $f^{(0)}$ is the Maxwellian distribution at the actual values of the number of molecules per unit volume $n(r)$ and of the temperature $T(r)$, and $f^{(1)}$ is a small correction term. $n(r)$ and $T(r)$ are replaced by constant values $\bar{n}$ and $\overline{T}$ except in the gradients; this is justified when $\left|\dfrac{Q}{2\pi K T_1}\dfrac{\lambda}{r_1}\right|\ll 1$. Furthermore, we put for the collision integral

$$I\,(f f_1)=I\,(f^{(0)} f_1^{(1)}+f^{(1)} f_1^{(0)})=\Theta f^{(1)},$$

where we may take for θ the value $\dfrac{8}{15}\dfrac{\bar{v}}{\lambda}$, as valid for a Maxwell-gas in the ordinary theory of heat conduction.

The Boltzmann equation then becomes

$$v_r \frac{\partial f^{(1)}}{\partial r} + \frac{v_\varphi^2}{r} \frac{\partial f^{(1)}}{\partial v_r} - \frac{v_r v_\varphi}{r} \frac{\partial f^{(1)}}{\partial v_\varphi} + \theta f^{(1)} = v_r g(r, v), \tag{2 b}$$

where

$$g(r, v) = -\frac{1}{\bar{n}} \frac{d n}{d r}(r) f^{(0)} + \frac{1}{\bar{T}} \left(\frac{3}{2} - \frac{m v^2}{2 k \bar{T}}\right) \frac{d T}{d r}(r) f^{(0)}.$$

It determines $f^{(1)}$ as a function of r, $\frac{d n}{d r}(r)$, $\frac{d T}{d r}(r)$, v_r, v_φ, and v_z. $\frac{d n}{d r}(r)$ and $\frac{d T}{d r}(r)$ are to be determined from the equations

$$\left.\begin{aligned} &\int_{\boldsymbol{v}} f^{(1)} \, \boldsymbol{d v} = 0, \\ &\int_{\boldsymbol{v}} v^2 f^{(1)} \, \boldsymbol{d v} = 0. \end{aligned}\right\} \tag{3}$$

Now, multiplying the Boltzmann equation (2 b) by r and integrating over the velocity space we have

$$r \frac{\partial}{\partial r} \int_{\boldsymbol{v}} v_r f^{(1)} \, \boldsymbol{d v} + \int_{\boldsymbol{v}} v_\varphi^2 \frac{\partial f^{(1)}}{\partial v_r} \boldsymbol{d v} - \int_{\boldsymbol{v}} v_r v_\varphi \frac{\partial f^{(1)}}{\partial v_\varphi} \boldsymbol{d v} + r \theta \int_{\boldsymbol{v}} f^{(1)} \, \boldsymbol{d v} = 0,$$

since the right hand side of (2 b) is an odd function of v_r. Further

$$\int_{\boldsymbol{v}} v_\varphi^2 \frac{\partial f^{(1)}}{\partial v_r} \boldsymbol{d v} = \int_{\boldsymbol{v}} \frac{\partial}{\partial v_r} (v_\varphi^2 f^{(1)}) \, \boldsymbol{d v} = \int_{v_\varphi = -\infty}^{\infty} \int_{v_z = -\infty}^{\infty} \Big[v_\varphi^2 f^{(1)} \Big]_{v_r = -\infty}^{\infty} d v_\varphi \, d v_z = 0,$$

and

$$\int_{\boldsymbol{v}} v_r v_\varphi \frac{\partial f^{(1)}}{\partial v_\varphi} \boldsymbol{d v} = \int_{\boldsymbol{v}} v_\varphi \frac{\partial}{\partial v_\varphi} (v_r f^{(1)}) \, \boldsymbol{d v} = \int_{v_r = -\infty}^{\infty} \int_{v_z = -\infty}^{\infty} \Big[v_\varphi v_r f^{(1)} \Big]_{v_\varphi = -\infty}^{\infty} d v_r \, d v_z -$$

$$- \int_{\boldsymbol{v}} v_r f^{(1)} \, \boldsymbol{d v} = - \int_{\boldsymbol{v}} v_r f^{(1)} \, \boldsymbol{d v},$$

and we find that

$$\frac{\partial}{\partial r} \Big(r \int_{\boldsymbol{v}} v_r f^{(1)} \, \boldsymbol{d v}\Big) + r \theta \int_{\boldsymbol{v}} f^{(1)} \, \boldsymbol{d v} = 0.$$

The equation $\int_{\boldsymbol{v}} f^{(1)} \, \boldsymbol{d v} = 0$ can thus be replaced by the equation $r \int_{\boldsymbol{v}} v_r f^{(1)} \, \boldsymbol{d v} =$ const., and in the same way we see that the equation $\int_{\boldsymbol{v}} v^2 f^{(1)} \, \boldsymbol{d v} = 0$ can be replaced by the equation $r \int_{\boldsymbol{v}} v_r v^2 f^{(1)} \, \boldsymbol{d v} =$ const. We have especially to take here

$$\left.\begin{aligned} &\int_{\mathbf{v}} v_r\, f^{(1)}\, d\mathbf{v} = 0, \\ &\tfrac{1}{2}\, m\, r \int_{\mathbf{v}} v_r\, v^2\, f^{(1)}\, d\mathbf{v} = -\frac{Q}{2\pi}. \end{aligned}\right\} \tag{4}$$

To the partial differential equation (2 b) there is associated a set of characteristic equations

$$\frac{d\,r}{v_r} = \frac{r}{v_\varphi^2}\, d\, v_r = -\frac{r}{v_r\, v_\varphi}\, d\, v_\varphi = \frac{d\, v_z}{0} = \frac{d\, f^{(1)}}{v_r\, g\,(r, v) - \theta\, f^{(1)}}.$$

It follows that

$$\begin{aligned} &v_\varphi\, d\, r + r\, d\, v_\varphi = 0, \\ &v_r\, d\, v_r + v_\varphi\, d\, v_\varphi = 0, \\ &v_r\, d\, v_r + v_\varphi\, d\, v_\varphi + v_z\, d\, v_z = 0, \end{aligned}$$

from which appear the integrals

$$\begin{aligned} r\, v_\varphi &= C_1, \\ v_r^2 + v_\varphi^2 &= C_2, \\ v^2 &= C_3. \end{aligned}$$

Using these we have

$$v_r\,(r)\, \frac{d\, f^{(1)}}{d\, r} + \theta\, f^{(1)} = v_r\,(r)\, g_1\,(r),$$

where

$$v_r\,(r) = \pm \sqrt{C_2 - \frac{C_1^2}{r^2}},$$

$$g_1\,(r) = \left\{ -\frac{1}{\bar{n}}\, \frac{d\, n}{d\, r}\,(r) + \frac{1}{\bar{T}} \left(\frac{3}{2} - \frac{m\, C_3}{2\, k\, \bar{T}} \right) \frac{d\, T}{d\, r}\,(r) \right\} \bar{n} \left\{ \frac{m}{2\, \pi\, k\, \bar{T}} \right\}^{3/2} e^{-\frac{m\, C_3}{2\, k\, \bar{T}}},$$

and that gives us

$$f^{(1)} = C\, e^{-\theta \int_a^r \frac{dt}{v_r(t)}} + \int_b^r g_1\,(t)\, e^{-\theta \int_t^r \frac{du}{v_r(u)}}\, d\, t.$$

C, a and b are in the general case arbitrary functions of C_1, C_2 and C_3. Observing that

$$\int_a^r \frac{d\, t}{v_r\,(t)} = \pm \frac{1}{C_2} \left(\sqrt{C_2\, r^2 - C_1^2} - \sqrt{C_2\, a^2 - C_1^2} \right)$$

we find finally, after insertion of the expressions for C_1, C_2 and C_3, the general solution of (2 b):

$$f^{(1)} = C \exp\left\{-\theta \frac{r\,v_r}{v_r^2+v_\varphi^2}\left[1-\sqrt{1+\frac{(a^2-r^2)\,(v_r^2+v_\varphi^2)}{r^2\,v_r^2}}\right]\right\}+$$

$$+\int\limits_b^r g\,(t,v)\exp\left\{-\theta\frac{r\,v_r}{v_r^2+v_\varphi^2}\left[1-\sqrt{1+\frac{(t^2-r^2)\,(v_r^2+v_\varphi^2)}{r^2\,v_r^2}}\right]\right\}d\,t.$$

In the interval $r_1 \leq r < \infty$ we now demand that $f^{(1)}$ be real and finite, and that such integrals as define density, temperature and the like converge. These conditions are fulfilled by choosing

$$a = b = r_1 \qquad \text{for } v_r > 0 \text{ and } \frac{r^2}{r_1^2} \leq \frac{v_r^2+v_\varphi^2}{v_\varphi^2},$$

$$a = b = \frac{r\,v_\varphi}{\sqrt{v_r^2+v_\varphi^2}} \qquad \text{for } v_r > 0 \text{ and } \frac{r^2}{r_1^2} > \frac{v_r^2+v_\varphi^2}{v_\varphi^2},$$

$$a = b = \infty \qquad \text{for } v_r < 0.$$

Regarding the boundary condition we assume that the gas molecules reflected from the surface of the wire are distributed Maxwellian at n_{0+}, T_{0+}, giving

$$f^{(1)}_{\substack{r=r_1\\ v_r>0}} = \left\{\frac{n_{0+}-n_0}{\bar{n}} - \frac{T_{0+}-T_0}{\overline{T}}\left(\frac{3}{2}-\frac{m\,v^2}{2\,k\,T}\right)\right\} f^{(0)}.$$

Our solution is then, written out in full,

$$\frac{+v_\varphi^2}{v_\varphi^2} \quad = \left\{\frac{n_{0+}-n_0}{\bar{n}} - \frac{T_{0+}-T_0}{\overline{T}}\left(\frac{3}{2}-\frac{m\,v^2}{2\,k\,\overline{T}}\right)\right\}\exp\left\{-\theta\frac{r\,v_r}{v_r^2+v_\varphi^2}\left[1-\sqrt{1-\frac{(r^2-r_1^2)\,(v_r^2+v_\varphi^2)}{r^2\,v_r^2}}\right]\right\} f^{(0)}+$$

(I

$$+\int\limits_{r_1}^{r}\left\{\frac{1}{\bar{n}}\frac{d\,n}{d\,r}(t)-\frac{1}{\overline{T}}\left(\frac{3}{2}-\frac{m\,v^2}{2\,k\,\overline{T}}\right)\frac{d\,T}{d\,r}(t)\right\}\exp\left\{-\theta\frac{r\,v_r}{v_r^2+v_\varphi^2}\left[1-\sqrt{1-\frac{(r^2-t^2)\,(v_r^2+v_\varphi^2)}{r^2\,v_r^2}}\right]\right\}d\,t\,f^{(0}$$

$$\frac{+v_\varphi^2}{v_\varphi^2} \quad = \left\{\frac{n_{0+}-n_0}{\bar{n}} - \frac{T_{0+}-T_0}{\overline{T}}\left(\frac{3}{2}-\frac{m\,v^2}{2\,k\,\overline{T}}\right)\right\}\exp\left\{-\theta\frac{r\,v_r}{v_r^2+v_\varphi^2}\right\} f^{(0)}+$$

(II

$$\int\limits_{\frac{v_\varphi}{{}^2+v_\varphi^2}}^{r}\left\{\frac{1}{\bar{n}}\frac{d\,n}{d\,r}(t)-\frac{1}{\overline{T}}\left(\frac{3}{2}-\frac{m\,v^2}{2\,k\,\overline{T}}\right)\frac{d\,t}{d\,r}(t)\right\}\exp\left\{-\theta\frac{r\,v_r}{v_r^2+v_\varphi^2}\left[1-\sqrt{1-\frac{(r^2-t^2)\,(v_r^2+v_\varphi^2)}{r^2\,v_r^2}}\right]\right\}d\,t\,f^{(0)},$$

$$= -\int\limits_{r}^{\infty}\left\{\frac{1}{\bar{n}}\frac{d\,n}{d\,r}(t)-\frac{1}{\overline{T}}\left(\frac{3}{2}-\frac{m\,v^2}{2\,k\,\overline{T}}\right)\frac{d\,T}{d\,r}(t)\right\}\exp\left\{-\theta\frac{r\,v_r}{v_r^2+v_\varphi^2}\left[1-\sqrt{1+\frac{(t^2-r^2)\,(v_r^2+v_\varphi^2)}{r^2\,v_r^2}}\right]\right\}d\,t\,f^{(0}$$

(III

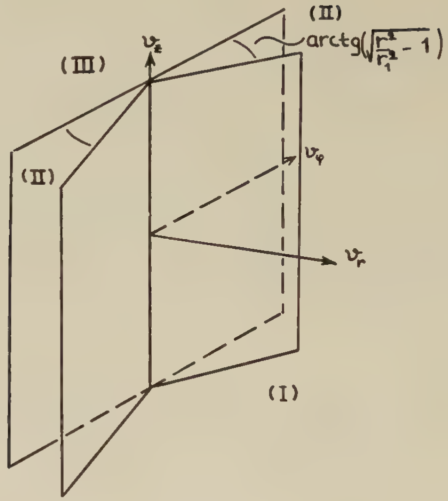

Fig. 3. Regions of the solution.

The regions of the velocity space occupied by the different parts of the solution are indicated in Fig. 3.

The solution in the plane case previously investigated is found again in the regions I and III by putting $r = r_1 + x$ and expanding the exponents under the assumption that $r_1 \to \infty$ and $\frac{x}{r_1} \to 0$. The region II will disappear entirely in the limit.[1]

If we insert the solution (5) in the equations (4) and introduce the following non-dimensional variables and parameters:

$$\xi = \frac{r}{\lambda},$$

$$V = \sqrt{\frac{m}{2\,k\,\bar{T}}}\,v,$$

---

[1] The region $v_r = 0$ is not included in our solution. The functional determinant of the characteristics will vanish there, and the solution becomes singular [1]. We note that

$$\underset{v_r \to +0}{f^{(1)}} = \begin{cases} \left[\dfrac{n_{0+} - n_0}{\bar{n}} - \dfrac{T_{0+} - T_0}{\bar{T}}\left(\dfrac{3}{2} - \dfrac{m\,v^2}{2\,k\,\bar{T}}\right)\right]\bar{f}^{(0)} & \text{for} \quad v_\varphi \neq 0, \\ 0 & \text{for} \quad v_\varphi = 0, \quad \text{and} \end{cases}$$

$$\underset{v_r \to -0}{f^{(1)}} = -\int_r^\infty g\,(t,\,v)\,\exp\left\{-\frac{\theta}{|v_\varphi|}\sqrt{t^2 - r^2}\right\}dt\,.$$

In the plane case it should be valid that $\underset{v_r \to \pm 0}{f^{(1)}} = 0$. This limit comes out correctly from (5) by increasing r_1 indefinitely for sufficiently small fixed values of v_r.

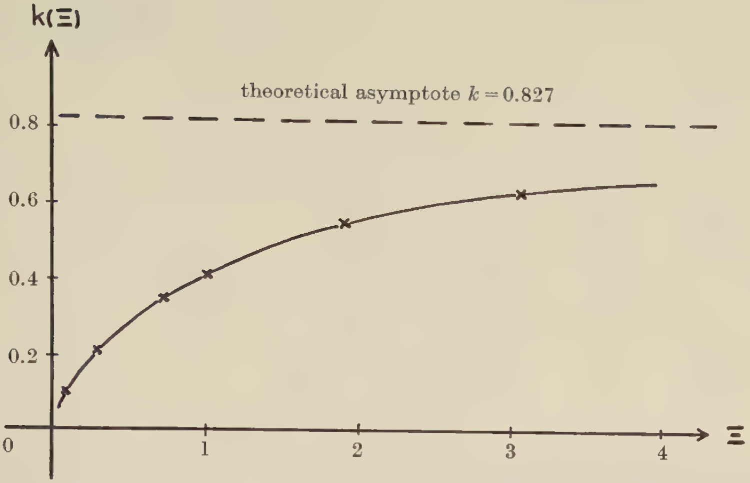

Fig. 4. Variation of k (Ξ).

$$\varphi = \frac{1}{\bar{n}} \frac{d\,n}{d\,\xi} \frac{K\,T}{Q},$$

$$\chi = -\frac{1}{\bar{T}} \frac{d\,T}{d\,\xi} \frac{K\,T}{Q},$$

$$\Xi = \frac{r_1}{\lambda},$$

$$\mu_0 = -\frac{n_{0+} - n_0}{\bar{n}} \frac{K\;T}{Q},$$

$$\mu_1 = \frac{T_{0+} - T_0}{\bar{T}} \frac{K\,T}{Q},$$

we get a pair of integral equations containing only the variables φ, χ, the parameters Ξ, μ_0, μ_1, and the independent variable ξ. Then, in analogy with our previous result, we should expect a solution $\varphi(\xi, \Xi)$, $\chi(\xi, \Xi)$ to exist only when μ_0, μ_1 take on some special values $\mu_0(\Xi)$, $\mu_1(\Xi)$.

Our generalized temperature jump is

$$\Delta' T = T_0' - T_1 = T_0 - T_1 + \int_{r_1}^{\infty} \left[\frac{d\,T}{d\,r}(t) + \frac{Q}{2\,\pi\,K}\frac{1}{t}\right] d\,t =$$

$$= T_{0+} - T_1 - \frac{Q}{K}\left\{\mu_1(\Xi) + \int_{\Xi}^{\infty} \left[\chi(\tau, \Xi) - \frac{1}{2\,\pi}\frac{1}{\tau}\right] d\,\tau\right\},$$

and using the relation

$$T_{0+} - T_1 = -\frac{75\,\pi}{64}\,\frac{1-a}{a}\,\frac{Q}{2\,\pi K} \qquad (cf.\ \text{formula (15), p. 532})$$

we may bring it into the form

$$\Delta' T = -\frac{75\,\pi}{128}\,\frac{2-k(\Xi)\,a}{a}\,\frac{1}{\Xi}\,\frac{Q}{2\,\pi K}, \tag{6}$$

where

$$k(\Xi) = 2 - \frac{256}{75}\,\Xi\left\{\mu_1 + \int\limits_{\Xi}^{\infty}\left[\chi(\tau,\Xi) - \frac{1}{2\,\pi}\,\frac{1}{\tau}\right]d\tau\right\}.$$

Thus we have

$$\varkappa_1' = \frac{75\,\pi}{128}\,\frac{2-k(\Xi)\,a}{a}. \tag{7}$$

No attempts have been made yet to determine $k(\Xi)$ from the integral equations. However, the function has been estimated by comparing our theoretical heat flow formula with experimental data. A typical result is shown in Fig. 4 (experimental data from SCHÄFER–RATING–EUCKEN [6], Table 1, p. 188).

Research Institute of National Defence, Stockholm, December 1953.

REFERENCES

1. COURANT, R., and HILBERT, D., Methoden der Matematischen Physik II, pp. 51–63, Verlag Julius Springer, Berlin (1937).
2. FREDLUND, E., Ann. Physik *28*, 319 (1937).
3. GREGORY, H. S., Phil. Mag. *22*, 257 (1936).
4. KNUDSEN, M., Ann. Physik *34*, 593 (1911).
5. SMOLUCHOWSKI, M. v., Ann. Physik *35*, 983 (1911).
6. SCHÄFER, K., RATING, W., and EUCKEN, A., Ann. Physik *42*, 176 (1942).
7. UBISCH, H. v., Appl. Sci. Res. A 2, *5–6*, 403 (1951).
8. WEBER, S., Kgl. Danske Vidensk. Selsk. Medd. *19: 11* (1942).

Tryckt den 5 april 1954

Uppsala 1954. Almqvist & Wiksells Boktryckeri AB

ARKIV FÖR FYSIK Band 7 nr 46

Communicated 11 November 1953 by OSKAR KLEIN and BENGT EDLÉN

On the renormalization of the Salpeter-Bethe equation.

By ARNE CLAESSON

With 8 figures in the text

Summary

In order to study the renormalization of the Salpeter-Bethe equation up to the fourth order in the coupling constant, the renormalization terms are introduced in the corresponding Lagrangian according to the methods given by KÄLLÉN. Equations are obtained for the determination of the renormalization constants which are computed by power series expansion in the coupling constant. When these values are introduced into the Salpeter-Bethe equation, a finite result is obtained.

1. Introduction

The equation of SALPETER and BETHE[1] describes the interaction of two or more Fermi-Dirac particles relativistically. The aim of this paper is to study the divergences occurring in the fourth order terms of the equation and to show how they can be removed. Up till now no attempts have been made to renormalize the Salpeter-Bethe equation. However, CINI[2] has just published a covariant form of TAMM-DANCOFF's relativistic two body equation with the intention of discussing a renormalization procedure in a forthcoming paper, and MACKE[3] has transformed the Salpeter-Bethe equation into a one time equation with four components in order to deal with the renormalization of the interaction operator.

2. Renormalized field equations

In this paper we consider a field operator $\psi(x)$ for protons and a field $\varphi(x)$ for neutrons coupled to each other by a real scalar meson field $A(x)$. We start with the following unrenormalized Lagrangian

$$L^{\mathrm{ur}} = L_{\psi} + L_{\varphi} + L_{A} + L_{\mathrm{int}} \tag{1}$$

where

---

[1] SALPETER and BETHE, Phys. Rev. *84*, 1232 (1951), GELL-MANN and LOW, Phys. Rev. *84*, 350 (1951).

[2] M. CINI, Il nuovo cimento, *10*, 526 (1953).

[3] W. MACKE, Il nuovo cimento, *10*, 1198 (1953).

$$
\begin{aligned}
L_\psi &= -\frac{1}{4}\left[\bar{\psi}(x), \left(\gamma\frac{\partial}{\partial x}+m\right)\psi(x)\right]-\frac{1}{4}\left[-\frac{\partial\bar{\psi}(x)}{\partial x}\gamma+m\bar{\psi}(x), \psi(x)\right]\\
L_\varphi &= -\frac{1}{4}\left[\bar{\varphi}(x), \left(\gamma\frac{\partial}{\partial x}+m\right)\varphi(x)\right]-\frac{1}{4}\left[-\frac{\partial\bar{\varphi}(x)}{\partial x}\gamma+m\bar{\varphi}(x), \varphi(x)\right]\\
L_A &= -\frac{1}{2}\left[\frac{\partial A(x)}{\partial x_\nu}\frac{\partial A(x)}{\partial x_\nu}+\mu^2 A^2(x)\right]\\
L_{\text{int}} &= \frac{ig}{2}A(x)\left([\bar{\psi}(x)\psi(x)]+[\bar{\varphi}(x)\varphi(x)]\right).
\end{aligned}
\tag{2}
$$

To this we add, using the methods given by KÄLLÉN[4], the renormalization terms, (δm for protons and neutrons, $\delta\mu$ for the mesons and the "charge" renormalization L)

$$L = L^{\text{ur}}+\tfrac{1}{2}\delta m\left([\bar{\psi}(x)\psi(x)]+[\bar{\varphi}(x)\varphi(x)]\right)+\tfrac{1}{2}A^2(x)\,\delta\mu-\mathrm{L}\,L_A. \tag{3}$$

From this Lagrangian we obtain the equations of motion

$$
\begin{aligned}
&\left(\gamma\frac{\partial}{\partial x}+m\right)\psi(x)=igA(x)\psi(x)+\delta m\,\psi(x)\equiv f^P(x)\\
&\left(\gamma\frac{\partial}{\partial x}+m\right)\varphi(x)=igA(x)\varphi(x)+\delta m\,\varphi(x)\equiv f^N(x)\\
&(\Box-\mu^2)A(x)=-\frac{ig}{2(1-\mathrm{L})}\left([\bar{\psi}(x)\psi(x)]+[\bar{\varphi}(x)\varphi(x)]\right)-\frac{\delta\mu}{1-\mathrm{L}}A(x)\equiv-j(x).
\end{aligned}
\tag{4}
$$

Further we define the normalization constants N and M from the conditions

$$
\begin{aligned}
<0|\psi(x)|q_P> &= N<0|\psi^{(0)}(x)|q_P>\\
<0|\varphi(x)|q_N> &= N<0|\varphi^{(0)}(x)|q_N>\\
<0|A(x)|k> &= M<0|A^{(0)}(x)|k>
\end{aligned}
\tag{5}
$$

where $<0|$ is the vacuum state, $|q>$ a state with one proton or neutron present and $|k>$ a state with one meson.

If we now introduce new operators $\psi'=\frac{1}{N}\psi$, $\varphi'=\frac{1}{N}\varphi$, and $A'=\frac{1}{M}A$ we can write the integral equations of motion as

$$
\begin{aligned}
\psi(x) &= \frac{1}{N}\psi^{(0)}(x)-\int S_R^P(x-x')\,f^P(x')\,dx'\\
\varphi(x) &= \frac{1}{N}\varphi^{(0)}(x)-\int S_R^N(x-x')\,f^N(x')\,dx'\\
A(x) &= \frac{1}{M}A^{(0)}(x)+\int \Delta_R(x-x')\,j(x')\,dx'
\end{aligned}
\tag{6}
$$

---

[4] G. KÄLLÉN, Helvetica Physica Acta 25, 417 (1952).

where we have dropped the dash and where

$$
\begin{aligned}
j(x) &= \frac{i\,g\,N^2}{2\,M\,(1-\mathrm{L})}\,\{[\bar{\psi}(x)\,\psi(x)]+[\bar{\varphi}(x)\,\varphi(x)]\}+\frac{\delta\mu}{1-\mathrm{L}}\,A(x)\\
f^{\left\{ P \atop N \right\}}(x) &= i\,g\,M\,A(x)\begin{Bmatrix}\psi(x)\\ \varphi(x)\end{Bmatrix}+\delta m\begin{Bmatrix}\psi(x)\\ \varphi(x)\end{Bmatrix}.
\end{aligned}
\tag{7}
$$

The Lagrangian is now

$$
L = N^2\,(L_\psi + L_\varphi) + M^2\,L_A + M\,N^2\,L_{\mathrm{int}} + \frac{1}{2}\,\delta m\,N^2\,([\bar{\psi}\,\psi]+[\bar{\varphi}\,\varphi]) +
+\frac{\delta\mu}{2}\,M^2\,A^2 - \mathrm{L}\,M^2\,L_A. \tag{8}
$$

To get finite expressions for the coefficients in a formal expansion of the S-matrix in powers of the coupling constant (there is one infinite quantity arising from the scattering of one free meson by another through virtual nucleon pair creation), we have to add a term $\lambda\cdot A^4(x)$ to the Lagrangian where λ is a new renormalization constant.[5] As will be seen, this term is of no importance in this paper.

From L we obtain the "commutators" for equal time coordinates

$$
\begin{aligned}
&\{\bar{\psi}(x)\,\psi(x')\} = N^{-2}\,\gamma_4^P\,\delta(\bar{x}-\bar{x}')\\
&\{\bar{\varphi}(x),\,\varphi(x')\} = N^{-2}\,\gamma_4^N\,\delta(\bar{x}-\bar{x}') \qquad (x_0 = x_0')\\
&\left[\frac{\partial A(x)}{\partial x_0},\,A(x')\right] = \frac{-i}{M^2\,(1-\mathrm{L})}\,\delta(\bar{x}-\bar{x}')\\
&\{\psi(x),\,\varphi(x')\} = \cdots = 0.
\end{aligned}
\tag{9}
$$

According to the paper by KÄLLÉN[4] mentioned above, we obtain the follow- ng formulas for the renormalization constants

$$
\begin{aligned}
&\frac{\delta m}{N^2} = \bar{\Sigma}_1(-m^2)\\
&\frac{N-1}{N^2} = -\frac{1}{2}\,\{\bar{\Sigma}_2(-m^2) + 2\,m\,\bar{\Sigma}_1'(-m^2)\}\\
&\frac{\delta\mu}{M^2\,(1-\mathrm{L})^2} = \bar{\pi}(-\mu^2)\\
&\frac{\mathrm{L}}{1-\mathrm{L}} = 2\,(M-1) + M^2\,\bar{\pi}'(-\mu^2).
\end{aligned}
\tag{10}
$$

Here

$$
\bar{\Sigma}_i(-m^2) = \int_{(m+\mu)^2}^{\infty} \frac{\Sigma_i(-a)}{a-m^2}\,da, \quad \bar{\Sigma}_i'(-m^2) = -\int_{(m+\mu)^2}^{\infty} \frac{\Sigma_i(-a)}{(a-m^2)^2}\,da \tag{11}
$$

---

[5] P. T. MATTHEWS, The Phil. Mag., *41*, 185 (1950).

where Σ_i is given by

$$< 0 \,|\, \{\bar{f}_\alpha(x')\, f_\beta(x)\} \,|\, 0 > = \frac{-1}{(2\pi)^3} \int d\,p\, e^{i\,p\,(x-x')}\, \varepsilon(p)\, \{\Sigma_1(p^2) + (i\,\gamma\, p + m)\, \Sigma_2(p^2)\}_{\beta\alpha} \tag{12}$$

and

$$\bar{\pi}(-\mu^2) = P \int\limits_{\mu^2}^{\infty} \frac{\pi(-a)}{a-\mu^2}\, d\,a, \quad \bar{\pi}'(-\mu^2) = P \int\limits_{\mu^2}^{\infty} \frac{\pi(-a)}{(a-\mu^2)^2}\, d\,a \tag{13}$$

where π it defined by

$$< 0 \,|\, [j(x)\, j(x')] \,|\, 0 > = \frac{-1}{(2\pi)^3} \int d\,p\, e^{i\,p\,(x'-x)}\, \pi(p^2)\, \varepsilon(p). \tag{14}$$

$\varepsilon(x)$ is defined by equation (56).

We thus have four equations and five unknown constants. Another equation is obtained by regarding the matrix element $< q \,|\, j(x) \,|\, q' >$ where $< q \,|$, $|\, q' >$ are proton (or neutron) states. An expression for $< q \,|\, j(x) \,|\, q' >$ may be obtained from

$$< 0 \,|\, \{[j(x)\, \psi^{(0)}(x')]\, \bar{\psi}^{(0)}(x'')\} \,|\, 0 > \tag{15}$$

considered as an identity in x' and x''. We get[6]

$$\begin{aligned} < q \,|\, j(x) \,|\, q' > = < q \,|\, j^{(0)}(x) \,|\, q' > \Bigg[& \frac{1 + 2\,(N-1)}{M\,(1-L)} + \\ & + M \left\{ \frac{\bar{\pi}((q-q')^2) - \bar{\pi}(-\mu^2) + i\,\pi\,\varepsilon(q-q')\,\pi((q-q')^2)}{(q-q')^2 + \mu^2} \right\} \Bigg] + \\ & + i\,g < q \,|\, \bar{\psi}^{(0)}(x) \,|\, 0 > \Lambda(q\,q') < 0 \,|\, \psi^{(0)}(x) \,|\, q' > \end{aligned} \tag{16}$$

where

$$\begin{aligned} \frac{i\,g}{(2\pi)^8} \int d\,p\, d\,p'\, e^{i\,p'(3\,x) + i\,p\,(x\,4)}\, \Lambda(p'\,p) = & \\ = - N^2\, \theta(x\,3)\, \theta(34) < 0 \,|\, [j(x)\, \{f(3)\, \bar{f}(4)\}] \,|\, 0 > + & \\ + N^2\, \theta(x\,3)\, \theta(x\,4) < 0 \,|\, \{f(3)\, [j(x)\, \bar{f}(4)]\} \,|\, 0 > . & \end{aligned} \tag{17}$$

Concerning the definition of $\theta(x)$ see equation (56).

Writing

$$\Lambda(q\,q') = \sum_{\varrho\varrho'=0}^{1} (i\,\gamma\, q + m)^{\varrho}\, F^{\varrho\varrho'}(q\,q')\, (i\,\gamma\, q' + m)^{\varrho'} \tag{18}$$

we obtain

$$\begin{aligned} i\,g < q \,|\, \bar{\psi}^{(0)}(x) \,|\, 0 > \Lambda(q\,q') < 0 \,|\, \psi^{(0)}(x) \,|\, q' > = & \\ = < q \,|\, j^{(0)}(x) \,|\, q' > [R_1((q'-q)^2) + i\,\varepsilon(q'-q)\, R_2((q'-q)^2)] & \end{aligned} \tag{19}$$

where

$$\begin{aligned} & R_1((q'-q)^2) + i\,\varepsilon(q'-q)\, R_2((q'-q)^2) = F^{00} \Big|_{\substack{q^2 = q'^2 = -m^2 \\ q_0 > 0,\; q_0' > 0}} \\ & R_2 \neq 0 \quad \text{if} \quad (q'-q)^2 < 0. \end{aligned} \tag{20}$$

---

[6] G. KÄLLÉN, Det Kgl. Danske Videnskabernes Selskab, *27*, nr. 12 (1953).

e now normalize the expectation value of the current according to

$$\lim_{q\to q'} < q\,|\,j(x)\,|\,q' > = \lim_{q\to q'} < q\,|\,j^{(0)}(x)\,|\,q' > \tag{21}$$

d get as our fifth equation

$$1 = \frac{1+2(N-1)}{M(1-\mathrm{L})} + M\,\frac{\overline{\pi}(0)-\overline{\pi}(-\mu^2)}{\mu^2} + R_1(0). \tag{22}$$

We expand the normalization constants in powers of the coupling constant g, d here we are interested only in terms up to the second order in g, e.g.

$$\delta m = \Sigma\, g^n\,\delta m^{(n)} = g^2\,\delta m^{(2)}. \tag{23}$$

rom the condition

$$< 0\,|\,f(x)\,|\,q > = 0 \tag{24}$$

here $< 0|$ is the vacuum state and $|q>$ a state with only one proton or eutron present, we can determine $\delta m^{(2)}$. The left side of (24) is equal to

$$i\,g < 0\,|\,A\;(x)\,\psi(x)\,|\,q> + \delta m < 0\,|\,\psi(x)\,|\,q> = 0. \tag{25}$$

riting

$$\begin{aligned} \psi(x) &= \Sigma\, g^n\,\psi^{(n)}(x) \\ A\,(x) &= \Sigma\, g^n\,A^{(n)}(x) \end{aligned} \tag{26}$$

e get

$$i\,g^2 < 0\,|\,A^{(1)}(x)\,\psi^{(0)}(x) + A^{(0)}(x)\,\psi^{(1)}(x)\,|\,q> + g^2\,\delta m^{(2)} < 0\,|\,\psi^{(0)}(x)\,|\,q> = 0. \tag{27}$$

ow

$$A^{(1)}(x) = \frac{i}{2}\int dx'\,\Delta_R(x-x')\,\{[\psi^{(0)}(x')\,\psi^{(0)}(x')] + [\overline{\varphi}^{(0)}(x')\,\varphi^{(0)}(x')]\}. \tag{28}$$

bstituting this and the corresponding equation for $\psi^{(1)}(x)$ in (27), we obtain

$$\begin{aligned} & g^2\,\delta m^{(2)} < 0\,|\,\psi^{(0)}(x)\,|\,q> = \\ & \frac{g^2}{2}\int dx'\,[\Delta_R(x-x')\,S^{(1)}(x-x') + S_R(x-x')\,\Delta^{(1)}(x-x')] < 0\,|\,\psi^{(0)}(x')\,|\,q> \\ & \frac{g^2}{2}\,\frac{1}{(2\pi)^7}\int dx'\,dp\,dk\,e^{i(p+k)(x-x')}\,(i\gamma\,p-m)\left\{\frac{\delta(p^2+m^2)}{k^2+\mu^2} + \frac{\delta(k^2+\mu^2)}{p^2+m^2}\right\} < 0\,|\,\psi^{(0)}(x')\,|\,q> \\ & \frac{-g^2\,e^{iqx}}{2(2\pi)^3}\int dp\int_0^1 d\alpha\,(i\gamma\,p-m)\,\delta'\,[(p^2+m^2)\,\alpha + ((q-p)^2+\mu^2)(1-\alpha)] < 0\,|\,\psi^{(0)}\,|\,q> \qquad (29) \\ & \frac{g^2}{2}\,\frac{m}{(2\pi)^3}\,e^{iqx}\int_0^1 d\alpha\,(1+\alpha)\int dp\,\delta'(p^2+B) < 0\,|\,\psi^{(0)}\,|\,q> \end{aligned}$$ [7]

---

[7] J. SCHWINGER, Phys. Rev., *76*, 790 (1949).

where

$$B = \mu^2 \alpha + m^2 (1-\alpha)^2. \tag{30}$$

Thus

$$\delta m^{(2)} = \frac{-m}{2(2\pi)^3} \int_0^1 d\alpha\,(1+\alpha) \int dp\, \delta'(p^2 + B). \tag{31}$$

As δm and M are the only renormalization constants which appear in our approximation of the Salpeter-Bethe equation, we calculate only these and get for M from (22) and (10) in the g^2 approximation

$$M - 1 = -2(N-1) - R_1^{(0)}(0) + \frac{\bar{\pi}^{(0)}(-\mu^2) - \bar{\pi}^{(0)}(0)}{\mu^2} - \bar{\pi}'^{(0)}(-\mu^2). \tag{32}$$

The last terms are easily proved to be finite. We have according to (13)

$$\frac{\bar{\pi}(-\mu^2) - \bar{\pi}(0)}{\mu^2} - \bar{\pi}'(-\mu^2) = P \int_{\mu^2}^{\infty} da\, \frac{\pi(-a)\cdot(-\mu^2)}{a(a-\mu^2)^2}. \tag{33}$$

Calculating $\pi^{(0)}(p^2)$ from (14), we get

$$\pi^{(0)}(p^2) = \frac{1}{2(2\pi)^2}(p^2 + 4m^2)\sqrt{1 + \frac{4m^2}{p^2}}\left[1 - \frac{p^2 + 4m^2}{|p^2 + 4m^2|}\right] \tag{34}$$

and introducing this in (33), we may integrate and obtain a finite result. To obtain $R_1^{(0)}(0)$ we use the expression for $\Lambda(p'p)$ in (17), where we substitute $f(3) = f^{(0)}(3) = i g A^{(0)} \psi_1^{(0)} \ldots$ and get, omitting terms of order higher than the second in g

$$\begin{aligned} \Lambda(pp') = -\frac{g^2}{2} \int dx^3\, dx^4\, e^{-i[p(3x) + p'(x4)]} [& S_A(3x)\, S_R(x4)\, \Delta^{(1)}(34) + \\ & + S_A(3x)\, S^{(1)}(x4)\, \Delta_R(34) + S^{(1)}(3x)\, S_R(x4)\, \Delta_A(34)]. \end{aligned} \tag{35}$$

Transforming this to momentum space we get

$$\begin{aligned} \Lambda(pp') = -\frac{g^2}{2} \int dq\, & [i\gamma(p-q) - m]\,[i\gamma(p'-q) - m] \cdot \\ & \cdot \left\{ \frac{1}{(2\pi)^3} \int_0^1 d\alpha \int_0^\alpha d\beta\, \delta''[(q - \beta p' - (\alpha-\beta)p)^2 + B'] + \right. \\ & + \frac{1}{8\pi}\, \delta((p-q)^2 + m^2)\, \delta((p'-q)^2 + m^2)\, \delta(q^2 + \mu^2) \cdot \\ & \cdot [\varepsilon(p-q)\,\varepsilon(p'-q) + \varepsilon(p-q)\,\varepsilon(q) + \varepsilon(p'-q)\,\varepsilon(q)] + \\ & + \frac{i}{2(2\pi)^2} \left[\frac{\delta((p-q)^2 + m^2)\, \delta((p'-q)^2 + m^2)\, (\varepsilon(p'-q) - \varepsilon(p-q))}{q^2 + \mu^2} + \right. \\ & \left.\left. + \frac{\delta((p'-q)^2 + m^2)\, \delta(q^2 + \mu^2)\, (\varepsilon(q) - \varepsilon(q-p'))}{(p-q)^2 + m^2} - \frac{\delta((p-q)^2 + m^2)\, \delta(q^2 + \mu^2)\, (\varepsilon(q) - \varepsilon(q-p))}{(p'-q)^2 + m^2} \right] \right\} \end{aligned} \tag{36}$$

where

$$B' = p'^2 \beta + p^2 (\alpha - \beta) - (p' \beta + p (\alpha - \beta))^2 + m^2 \alpha + \mu^2 (1 - \alpha). \tag{37}$$

The last two terms are different from zero only if[8]

$$p'^2 < -(m+\mu)^2 \quad \text{and} \quad p^2 < -(m+\mu)^2. \tag{38}$$

But here $p^2 = p'^2 = -m^2$, and thus (38) are not fulfilled. In the same way the term

$$\frac{\delta((p-q)^2 + m^2)\, \delta((p'-q)^2 + m^2)\, (\varepsilon(p'-q) - \varepsilon(p-q))}{q^2 + \mu^2} \tag{39}$$

is zero if $-(p-p')^2 \leq 4m^2$, and thus this term vanishes at least when $p = p'$. Integrating it, one finds that it is of the form $\varepsilon(p-p') f((p-p')^2)$ and it thus belongs to R_2 in (19). The second term in (36) is also equal to zero when $p^2 = p'^2 = -m^2$. Introducing $q' = q - \beta p' - (\alpha - \beta) p$ and observing that a term of the form $\int dq\, q\, \delta''(q^2 + B')$ vanishes by reason of symmetry and that $\int dq\, \delta''(q^2 + B')$ is finite[7], we obtain

$$R_1^{(0)}((p-p')^2) = \frac{g^2}{2(2\pi)^3} \int dq' \int_0^1 d\alpha \int_0^\alpha d\beta\, q'^2 \delta''(q'^2 + B') + \text{finite terms}. \tag{40}$$

But

$$x\, \delta^{(n)}(x) = -n\, \delta^{(n-1)}(x) \tag{41}$$

and thus

$$R_1^{(0)}((p-p')^2) = -\frac{g^2}{(2\pi)^3} \int dq \int_0^1 d\alpha \int_0^\alpha d\beta\, \delta'(q^2 + B') + \text{finite terms}. \tag{42}$$

Putting $p = p'$, and with $p^2 = p'^2 = -m^2$ we get $B' = m^2 \alpha^2 + \mu^2 (1-\alpha)$. Thus B' is independent of β, and in (42) we may integrate with respect to β. The result is

$$R_1^{(0)}(0) = -\frac{g^2}{(2\pi)^3} \int dq \int_0^1 d\alpha\, \alpha\, \delta'(q^2 + B') + \text{finite terms} =$$

$$= -\frac{g^2}{(2\pi)^3} \int dq \int_0^1 d\alpha\, (1-\alpha)\, \delta'(q^2 + B) + \text{finite terms}. \tag{43}$$

In the g^2-approximation $N-1$ is, according to (10),

$$N - 1 = -\tfrac{1}{2} \{\bar{\Sigma}_2^{(0)}(-m^2) + 2m\, \bar{\Sigma}_1'^{(0)}(-m^2)\} \tag{44}$$

where $\bar{\Sigma}_i(p^2)$ may be calculated from the equation

$$-\frac{i}{2} \varepsilon(12) < 0 | \{\bar{f}(2) f(1)\} | 0 > = \frac{1}{(2\pi)^4} \int dp\, e^{ip(12)} \{\bar{\Sigma}_1(p^2) + (i\gamma p + m)\, \bar{\Sigma}_2(p^2)\}. \tag{45}$$

---

[8] G. Källén, Arkiv för fysik, *2*, 37 (1950).

Transforming to momentum space we get

$$\begin{aligned}\bar{\Sigma}_1^{(0)}(p^2) &= -\frac{m\,g^2}{2\,(2\pi)^3}\int dq\int_0^1 d\alpha\,(1+\alpha)\,\delta'\,(q^2+p^2\,\alpha\,(1-\alpha)+\mu^2\,\alpha+m^2\,(1-\alpha))\\ \bar{\Sigma}_2^{(0)}(p^2) &= \frac{g^2}{2\,(2\pi)^3}\int dq\int_0^1 d\alpha\,\alpha\,\delta'\,(q^2+p^2\,\alpha\,(1-\alpha)+\mu^2\,\alpha+m^2\,(1-\alpha)).\end{aligned} \tag{47}$$

As $\bar{\Sigma}_1'(-m^2)=\frac{d}{dp^2}\,(\bar{\Sigma}_1(p^2))\,|_{p^2=-m^2}$[4], we have

$$\bar{\Sigma}_1'^{(0)}(-m^2) = -\frac{m\,g^2}{2\,(2\pi)^3}\int_0^1 d\alpha\,\alpha\,(1-\alpha^2)\int dq\,\delta''\,(q^2+B)=\text{finite}. \tag{48}$$

Thus

$$N-1=-\frac{g^2}{4\,(2\pi)^3}\int dq\int_0^1 d\alpha\,\alpha\,\delta'\,(q^2+B)+\text{finite terms} \tag{49}$$

and

$$2\,(M-1)=\frac{g^2}{(2\pi)^3}\int dq\int_0^1 d\alpha\,(2-\alpha)\,\delta'\,(q^2+B)+\text{finite terms}. \tag{50}$$

3. The Salpeter-Bethe equation

The Salpeter-Bethe equation is obtained from the wave function

$$\chi_n(12)=<0\,|\,[\psi(1)\,\varphi(2)]\,|\,n>,\quad \psi(1)=\psi(x^1)=\psi(x_1^1\,x_2^1\,x_3^1\,x_4^1) \tag{51}$$

where $<0|$ is the vacuum state and $|n>$ is an arbitrary state with no free mesons. This definition of the wave function is somewhat different from the definition given by Gell-Man and Low who use the P-symbol. The commutator is sometimes found to be more convenient. Operating on χ_n with the Dirac operators for protons and neutrons, we get

$$\left(\gamma^P\frac{\partial}{\partial x^1}+m\right)\left(\gamma^N\frac{\partial}{\partial x^2}+m\right)\chi_n(12)=<0\,|\,[f^P(1)\,f^N(2)]\,|\,n>. \tag{52}$$

We now approximate the right hand side by expanding it in powers of the operator $A^{(0)}(x)$, defined by the integral equation for $A(x)$ with

$$(\Box-\mu^2)\,A^{(0)}(x)=0 \tag{53}$$

and

$$\begin{gathered}[A^{(0)}(x)\,A^{(0)}(x')]=-i\,\Delta\,(x'-x)\\ <0\,|\,\{A^{(0)}(x)\,A^{(0)}(x')\}\,|\,0>=\Delta^{(1)}(x-x').\end{gathered} \tag{54}$$

In Bethe and Salpeter's original work, all diagrams are classified by the number of meson lines. Algebraically this corresponds to the number of operators $A^{(0)}$ or, according to (54), to the number of Δ, $\Delta^{(1)}$ or $\bar{\Delta}$ functions. We thus rewrite the right hand side of (52) with the help of the equations (6), omitting all terms with more than two Δ factors (or four $A^{(0)}$, or one Δ and two $A^{(0)}$ etc.). Then all $A^{(0)}$ factors can be transformed to Δ functions with the help of formulas of the following type where we suppose that $F_i(x^i)$ commute with A and $\frac{\partial A}{\partial x_0}$ for equal time coordinates.

$$
\begin{aligned}
&<0|A^{(0)}(x)\,F_1(x^1)\,F_2(x^2)\dots F_\lambda(x^\lambda)|n> = \\
&= \sum_{\nu=1}^{\lambda} i \int d\,x^{\lambda+1}\,\theta(x^\nu - x^{\lambda+1}) <0|F_1(x^1)\dots F_{\nu-1}(x^{\nu-1})\,[F_\nu(x^\nu)\,j(x^{\lambda+1})]\times \\
&\qquad\qquad \times F_{\nu+1}(x^{\nu+1})\dots F_\lambda(x^\lambda)|n> <0|A^{(0)}(x)\,A^{(0)}(x^{\lambda+1})|0> \\
&<0|F_1\dots F_\lambda\,A^{(0)}|n> = \\
&= \sum_{\nu=1}^{\lambda} i \int d\,x^{\lambda+1}\,\theta(x^\nu - x^{\lambda+1}) <0|F_1\dots[F_\nu j]\dots F_\lambda|n> <0|A^{(0)}(x^{\lambda+1})\,A^{(0)}(x)|0> \qquad (55) \\
&\quad <0|F_1\,A^{(0)}\,F_2\dots F_\lambda|n> = <0|A^{(0)}\,F_1\dots F_\lambda|n> - <0|[A^{(0)}F_1]\,F_2\dots F_\lambda|n> \\
&\qquad\quad [A^{(0)}(x)\,F_\nu(x^\nu)] = \int d\,x^{\lambda+1}\,\theta(x^\nu - x^{\lambda+1})\,\Delta(x - x^{\lambda+1})\,[j(x^{\lambda+1})\,F_\nu(x^\nu)] \quad \text{etc.}
\end{aligned}
$$

where

$$
\theta(x) = \tfrac{1}{2}(1 + \varepsilon(x)) = \begin{cases} 1, & x_0 > 0 \\ 0, & x_0 < 0. \end{cases} \qquad (56)
$$

In this way we obtain the same number of Δ factors in every term, except for those of the first order. We now have, in each term, matrix elements of the type $<0|F_1\dots[F_\nu j]\dots F_\lambda|n>$ where F is either ψ, $\bar{\psi}$, φ or $\bar{\varphi}$. Rewriting these functions, we replace every F, and ψ etc. in $j(x)$, by its zero approximation $\psi^{(0)}$ etc., except one ψ and one φ in every term, and these are joined to give the wave function $\chi_n(x^i x^j)$. Finally we sum over every i and j. This means that in the diagrams inner lines are represented by S-functions and all exterior lines by χ_n.[9]

With definition (7) for $f(x)$, we obtain

$$
\begin{aligned}
<0|[f^P(1)\,f^N(2)]|n> &= -g^2 M^2 <0|[A(1)\,\psi(1),\ \ A(2)\,\varphi(2)]|n> + \\
&+ i\,g\,M\,\delta m\,(<0|[\psi(1),\ A(2)\,\varphi(2)]|n> + <0|[A(1)\,\psi(1),\ \varphi(2)]|n>) + \qquad (57) \\
&+ (\delta m)^2\,\chi_n(12).
\end{aligned}
$$

In order to find an expansion of the first commutator in (57), we write it in the following way

$$
\begin{aligned}
[A(1)\,\psi(1),\ A(2)\,\varphi(2)] = \tfrac{1}{2}(\{A(1)\,A(2)\}\,[\psi(1)\,\varphi(2)] + [A(1)\,A(2)]\,\{\psi(1)\,\varphi(2)\}) + \\
+ A(1)\,[\psi(1)\,A(2)]\,\varphi(2) + A(2)\,[A(1)\,\varphi(2)]\,\psi(1). \qquad (58)
\end{aligned}
$$

---

[9] R. KARPLUS and A. KLEIN, Phys. Rev., *87*, 848 (1952).

For the first term we have

$$\begin{aligned} \langle 0|\{A(1)\,A(2)\}\,[\psi(1)\,\varphi(2)]\,|n\rangle &= \langle 0|\{A(1)\,A(2)\}|\,0\rangle\,\chi_n(12) + \\ &+ \sum_{|z\rangle \neq |0\rangle} \langle 0|\{A(1)\,A(2)\}\,|z\rangle\,\langle z|\,[\psi(1)\,\varphi(2)]\,|n\rangle \end{aligned} \tag{59}$$

where $|z\rangle$ is an arbitrary state. Writing

$$\langle 0|\,A^{(0)}(x)\,|k\rangle = \frac{1}{M}\langle 0|\,A^{(0)}(x)\,|k\rangle + \left(1-\frac{1}{M}\right)\langle 0|\,A^{(0)}(x)\,|k\rangle \tag{60}$$

we obtain

$$\begin{aligned} \langle 0|\{A(1)\,A(2)\}|\,0\rangle &= \Delta^{(1)}(12)\,\frac{1+2\,(M-1)}{M^2} + \\ &+ \int dx^3\,dx^4\,\theta(13)\,\theta(24)\,\Delta(13)\,\Delta(24)\,\langle 0|\{j(3)\,j(4)\}|\,0\rangle. \end{aligned} \tag{61}$$

The second term in (59) may be divided as follows

$$\begin{aligned} &\sum_{|z\rangle \neq |0\rangle} \langle 0|\{A(1)\,A(2)\}\,|z\rangle\,\langle z|\,[\psi(1)\,\varphi(2)]\,|n\rangle = \\ &\quad = \frac{1}{M^2}\sum_{|k,\,k'\rangle} \langle 0|\{A^{(0)}(1)\,A^{(0)}(2)\}\,|k\,k'\rangle\,\langle k\,k'|\,[\psi(1)\,\varphi(2)]\,|n\rangle - \\ &- \frac{1}{M}\sum_{|z\rangle \neq |0\rangle}\int dx^3\,\theta(13)\,\Delta(13)\,\langle 0|\{j(3)\,A^{(0)}(2)\}\,|z\rangle\,\langle z|\,[\psi(1)\,\varphi(2)]\,|n\rangle - \\ &- \frac{1}{M}\sum_{|z\rangle \neq |0\rangle}\int dx^3\,\theta(23)\,\Delta(23)\,\langle 0|\{A^{(0)}(1)\,j(3)\}\,|z\rangle\,\langle z|\,[\psi(1)\,\varphi(2)]\,|n\rangle + \\ &+ \sum_{|z\rangle \neq |0\rangle}\int dx^3\,dx^4\,\theta(13)\,\theta(24)\,\Delta(13)\,\Delta(24)\,\langle 0|\{j(3)\,j(4)\}\,|z\rangle\,\langle z|\,[\psi(1)\,\varphi(2)]\,|n\rangle \end{aligned} \tag{62}$$

where $|k\,k'\rangle$ is a state with two mesons. The last term is already of the second order in Δ and after some calculations (using the method described above) it can be shown that the matrix element is

$$\begin{aligned} &\sum_{|z\rangle \neq |0\rangle} \langle 0|\{j(3)\,j(4)\}\,|z\rangle\,\langle z|\,[\psi(1)\,\varphi(2)]\,|n\rangle = \\ &\quad = \frac{g^2}{2}\,[(i\,S^P(14) - S^{1P}(14))\,S^{1P}(43)\,\chi_n(32) + \\ &+ (i\,S^N(23)) - S^{1N}(23))\,S^{1N}(34)\,\chi_n(14) + (i\,S^N(24) - S^{1N}(24))\,S^{1N}(43)\,\chi_n(13) + \\ &+ (i\,S^P(13) - S^{1P}(13))\,S^{1P}(34)\,\chi_n(42) - \\ &- (i\,S^P(14) - S^{1P}(14))\,(i\,S^N(23) - S^{1N}(23))\,\chi_n(43) - \\ &- (i\,S^N(24) - S^{1N}(24))\,(i\,S^P(13) - S^{1P}(13))\,\chi_n(34)]. \end{aligned} \tag{63}$$

So far as the second and third terms of (62) are concerned, we observe that we still need one factor $A^{(0)}$. This can be found in $j(3)$ or in $< z\,|\,[\psi(1), \varphi(2)]\,|\,n >$. Consider

$$[A^{(0)}(1)\,[\bar{\psi}(3)\,\psi(3)]] = [\bar{\psi}(3)\,[A^{(0)}(1)\,\psi(3)]] + [[A^{(0)}(1)\,\bar{\psi}(3)]\,\psi(3)]. \tag{64}$$

Since

$$\begin{aligned} M^{-1} A^{(0)}(x) = \int^{x'} d\,x''\,\Delta(x-x'')\,j(x'') - \\ - \int_{x_0''=x_0'} d^{(3)}\,\bar{x}''\,[\dot{A}^{(0)}(x'')\,\Delta(x-x'') + A(x'')\,\dot{\Delta}(x-x'')] \end{aligned} \tag{65}$$

and A and $A^{(0)}$ commute with ψ when the time coordinates are equal, we get

$$[A^{(0)}(1)\,[\bar{\psi}(3)\,\psi(3)]] = M \int^{x^3} d\,x^4\,\Delta(14)\,\{[\bar{\psi}(3)\,[j(4)\,\psi(3)]] + [[j(4)\,\bar{\psi}(3)]\,\psi(3)]\}. \tag{66}$$

But

$$\begin{aligned} [j(4)\,\psi(3)] = \int_{x^4}^{x^3} d\,x^5\,S^P(15)\,[j(4)\,f^P(5)] - i \int_{x^5_0=x^4_0} d^{(3)}\,\bar{x}^5\,S^P(35)\,\gamma_4\,[j(4)\,\psi(5)] = \\ = -\frac{g}{M(1-\mathrm{L})}\,S^P(34)\,\psi(4) + \text{terms of order } \Delta. \end{aligned} \tag{67}$$

Thus

$$\begin{aligned} [A^{(0)}(1)\,[\bar{\psi}(3)\,\psi(3)]] = \\ = -\frac{g}{(1-\mathrm{L})} \int^{x^3} d\,x^4\,\Delta(14)\,\{S^P(34)\,[\bar{\psi}(3)\,\psi(4)] - S^P(43)\,[\bar{\psi}(4)\,\psi(3)]\}. \end{aligned} \tag{68}$$

Regarding this as an identity in x^1, we obtain

$$\begin{aligned} < 0\,|\,[\bar{\psi}(3)\,\psi(3)]\,|\,z > = \frac{i\,g}{(1-\mathrm{L})} \int^{x^3} d\,x^4\,\{S^P(34) < 0\,|\,A^{(0)}(4)\,[\bar{\psi}(3)\,\psi(4)]\,|\,z > - \\ - S^P(43) < 0\,|\,A^{(0)}(4)\,[\bar{\psi}(4)\,\psi(3)]\,|\,z > \} \end{aligned} \tag{69}$$

and

$$\begin{aligned} &< 0\,|\,\{j(3)\,A^{(0)}(1)\}\,|\,z > = \\ &= \frac{i\,g\,N^2}{2\,M\,(1-\mathrm{L})}\,(< 0\,|\,\{[\bar{\psi}(3)\,\psi(3)]\,A^{(0)}(1)\}\,|\,z > + < 0\,|\,\{[\bar{\varphi}(3)\,\varphi(3)]\,A^{(0)}(1)\}\,|\,z >) = \\ &= \frac{-g^2\,N^2}{2\,M\,(1-\mathrm{L})^2} \int^{x^3} d\,x^4\,\Delta^{(1)}(41)\,\{S^P(34) < 0\,|\,[\bar{\psi}(3)\,\psi(4)]\,|\,z > - \\ &\qquad - S^P(43) < 0\,|\,[\bar{\psi}(4)\,\psi(3)]\,|\,z > + \\ &+ S^N(34) < 0\,|\,[\bar{\varphi}(3)\,\varphi(4)]\,|\,z > - S^N(43) < 0\,|\,[\bar{\varphi}(4)\,\varphi(3)]\,|\,z > \}. \end{aligned} \tag{70}$$

The previously described technique which we applied to derive (63) can again be used with the following result

$$\sum_{|z>\neq|0>} <0|[\psi(3)\,\psi(4)]|z>\;<z|[\psi(1)\,\varphi(2)]|n> = (i\,S^{P}(13) - S^{1P}(13))\,\chi_{n}(42). \tag{71}$$

If we consider the commutator

$$[A^{(0)}(1)\,[\psi(1)\,\varphi(2)]]. \tag{72}$$

instead of (64), we obtain

$$\begin{aligned} <z|[\psi(1)\,\varphi(2)]|n> = \frac{i g}{(1-\mathrm{L})}\Bigg\{\int^{x^2} d x^4\, S^{N}(24) <z|A^{(0)}(4)\,[\psi(1)\,\varphi(4)]|n> + \\ + \int^{x^1} d x^4\, S^{P}(14) <z|A^{(0)}(4)\,[\psi(4)\,\varphi(2)]|n>\Bigg\}. \end{aligned} \tag{73}$$

Combining (70), (71) and (73) we finally get

$$\begin{aligned} &\sum_{|z>\neq|0>} <0|\{j(3)\,A^{(0)}(1)\}|z>\;<z|[\psi(1)\,\varphi(2)]|n> = \\ &= -\frac{g^2}{2}\int d x^4\,\{\theta(34)\,\Delta^{(1)}(41)\,[S^{P}(34)\,(i\,S^{P}(13) - S^{1P}(13))\,\chi_{n}(42) - \\ &\qquad - S^{P}(43)\,(i\,S^{P}(14) - S^{1P}(14))\,\chi_{n}(32) + \\ &+ S^{N}(34)\,(i\,S^{N}(23) - S^{1N}(23))\,\chi_{n}(14) - S^{N}(43)\,(i\,S^{N}(24) - S^{1N}(24))\,\chi_{n}(13)] + \\ &+ \theta(24)\,(\Delta^{(1)}(41) - i\,\Delta(41))\,S^{N}(24)\,[(i\,S^{P}(13) - S^{1P}(13))\,\chi_{n}(34) + \\ &\qquad + (i\,S^{N}(43) - S^{1N}(43))\,\chi_{n}(13)] + \\ &+ \theta(14)\,(\Delta^{(1)}(41) - i\,\Delta(41))\,S^{P}(14)\,[(i\,S^{P}(43) - S^{1P}(43))\,\chi_{n}(32) + \\ &\qquad + (i\,S^{N}(23) - S^{1N}(23))\,\chi_{n}(43)]\} \end{aligned} \tag{74}$$

where we have choosen the zero order approximation of the renormalization constants as the term is already of the fourth order in $A^{(0)}$ when inserted in (62). From (73) we obtain further

$$\begin{aligned} &<k k'|[\psi(1)\,\varphi(2)]|n> = \\ &= -g^2\int d x^3\, d x^4 <k k'|A^{(0)}(3)\,A^{(0)}(4)|0>\{\theta(23)\,\theta(34)\,S^{N}(23)\,S^{N}(34)\,\chi_{n}(14) + \\ &+ \theta(23)\,\theta(14)\,S^{N}(23)\,S^{P}(14)\,\chi_{n}(43) + \theta(13)\,\theta(34)\,S^{P}(13)\,S^{P}(34)\,\chi_{n}(42)\}. \end{aligned} \tag{75}$$

Thus the first term of (58) is now expanded to the second order in Δ functions, and in the second term

$$\begin{aligned} \{\psi(1)\,\varphi(2)\} = -g^2\int_{x^1}^{x^2} d x^3 \int_{x^3}^{x^1} d x^4\, S^{P}(14)\,S^{N}(23)\,[A(4)\,A(3)]\,[\psi(4)\,\varphi(3)] + \\ + \text{terms of order } A^4, \end{aligned} \tag{76}$$

thus

$$
\begin{aligned}
<0|[A(1)\,A(2)]\,\{\psi(1)\,\varphi(2)\}\,|n> = g^2 \int dx^3\,dx^4\,[\theta(23)-\theta(13)]\,[\theta(14)-\theta(34)]\times \\
\times\,\Delta(12)\,\Delta(34)\,S^P(14)\,S^N(23)\,\chi_n(43).
\end{aligned}
\tag{77}
$$

The third term of (58) is expanded in the following way. We observe that

$$
[\psi(1)\,A(2)] = -\int_{x^1}^{x^2} dx^3\,\Delta(23)\,[\psi(1)\,j(3)]
\tag{78}
$$

since $[\psi(1), A(2)]=0$ when the time coordinates are equal. This gives us

$$
\begin{aligned}
<0|A(1)\,[\psi(1)\,A(2)]\,\varphi(2)\,|n> = -\int_{x^1}^{x^2} dx^3\,\Delta(23) <0|A^{(0)}(1)\,[\psi(1)\,j(3)]\,\varphi(2)\,|n> + \\
+\int_{x^1}^{x^2} dx^3 \int^{x^1} dx^4\,\Delta(23)\,\Delta(14) <0|j(4)\,[\psi(1)\,j(3)]\,\varphi(2)\,|n>.
\end{aligned}
\tag{79}
$$

Finally, according to (67), we get

$$
\begin{aligned}
<0|A(1)\,[\psi(1)\,A(2)]\,\varphi(2)\,|n> = \frac{i\,g^4}{4}\int dx^3\,dx^4\,[\theta(24)-\theta(14)]\times \\
\times\{[\theta(13)-\theta(43)]\,S^P(13)\,S^P(34)\,(\Delta^{(1)}(31)-i\,\Delta(31))\,\chi_n(42)+ \\
+\,\theta(23)\,S^P(14)\,S^N(23)\,(\Delta^{(1)}(31)-i\,\Delta(31)]\,\chi_n(43)- \\
-\,\theta(13)\,\Delta(13)\,S^P(14)\,(i\,S^N(23)-S^{1N}(23))\,\chi_n(43)+ \\
+\,\theta(43)\,S^P(14)\,S^P(43)\,(\Delta^{(1)}(31)-i\,\Delta(31))\,\chi_n(32)- \\
-\,\theta(13)\,\Delta(13)\,S^P(14)\,(i\,S^P(43)-S^{1P}(43))\,\chi_n(32)\}.
\end{aligned}
\tag{80}
$$

Similarly, we obtain the last term of (58) and the renormalization terms in (57) are expanded in an analogous way, i.e.

$$
\begin{aligned}
<0|[\psi(1), A(2)\,\varphi(2)]\,|n> = \\
= \frac{i\,g}{2}\int dx^3\,\{\theta(23)\,[\Delta^{(1)}(32)\,S^N(23)-\Delta(32)\,S^{1N}(23)]\,\chi_n(13)+ \\
+\,[\theta(13)\,\Delta^{(1)}(32)\,S^P(13)-\theta(23)\,\Delta(32)\,S^{1P}(13)]\,\chi_n(32)\}.
\end{aligned}
\tag{81}
$$

$$
\begin{aligned}
<0|[A(1)\,\psi(1), \varphi(2)]\,|n> = \\
= \frac{i\,g}{2}\int dx^3\,\{\theta(13)\,[\Delta^{(1)}(31)\,S^P(13)-\Delta(31)\,S^{1P}(13)]\,\chi_n(32)+ \\
+\,[\theta(23)\,\Delta^{(1)}(31)\,S^N(23)-\theta(13)\,\Delta(31)\,S^{1N}(23)]\,\chi_n(13)\}.
\end{aligned}
\tag{82}
$$

Collecting the terms, we now have

$$
\begin{aligned}
&< 0 \,|\, [f^P(1)\, f^N(2)] \,|\, n > = - \\
&- \frac{g^2}{2} [1 + 2(M-1)]\, \Delta^{(1)}(12)\, \chi_n(12) - \\
&- \frac{g^2}{2} \int dx^3\, dx^4\, \theta(13)\, \theta(24)\, \Delta(13)\, \Delta(24) < 0 \,|\, \{j(3)\, j(4)\} \,|\, 0 > \chi_n(12) - \\
&- \frac{g^4}{2} \int dx^3\, dx^4\, [\theta(24) - \theta(14)]\, [\theta(13) - \theta(43)]\, \Delta(12)\, \Delta(43)\, S^P(13)\, S^N(24)\, \chi_n(34) + \\
&+ \frac{g^4}{4} \int dx^3\, dx^4\, \{[(\theta(13) - \theta(23))\, (\theta(24) - \theta(14))\, S^P(14)\, S^N(23)\, \Delta(31)\, \Delta(42) - \\
&- i\,\theta(23)\, \theta(14)\, S^P(14)\, S^N(23)\, \Delta(31)\, \Delta^{(1)}(42) - i\,\theta(14)\, \theta(23)\, S^P(14)\, S^N(23)\, \Delta(42)\, \Delta^{(1)}(31) \\
&+ \theta(14)\, \theta(23)\, S^P(14)\, S^N(23)\, \Delta^{(1)}(31)\, \Delta^{(1)}(42) - \theta(13)\, \theta(14)\, S^P(14)\, S^{1N}(23)\, \Delta(31)\, \Delta^{(1)}(42) - \\
&- \theta(23)\, \theta(24)\, S^{1P}(14)\, S^N(23)\, \Delta(42)\, \Delta^{(1)}(31) + \theta(13)\, \theta(24)\, S^{1P}(14)\, S^{1N}(23)\, \Delta(31)\, \Delta(42)]\, \chi_n(43) \\
&+ [\theta(13)\, (\theta(24) - \theta(34))\, S^N(23)\, S^N(34)\, \Delta(31)\, \Delta(42) + \theta(23)\, \theta(34)\, S^N(23)\, S^N(34)\, \Delta^{(1)}(31)\, \Delta^{(1)}(42) \\
&- \theta(23)\, \theta(24)\, S^N(23)\, S^{1N}(34)\, \Delta(42)\, \Delta^{(1)}(31) - \theta(13)\, \theta(34)\, S^{1N}(23)\, S^N(34)\, \Delta(31)\, \Delta^{(1)}(42) + \\
&+ \theta(24)\, \theta(43)\, S^{1N}(23)\, S^N(34)\, \Delta^{(1)}(31)\, \Delta(42) + \theta(13)\, \theta(24)\, S^{1N}(23)\, S^{1N}(34)\, \Delta(31)\, \Delta(42)]\, \chi_n(14) \\
&+ [\theta(23)\, (\theta(14) - \theta(34))\, S^P(13)\, S^P(34)\, \Delta(32)\, \Delta(41) + \theta(13)\, \theta(34)\, S^P(13)\, S^P(34)\, \Delta^{(1)}(32)\, \Delta^{(1)}(41) \\
&- \theta(13)\, \theta(14)\, S^P(13)\, S^{1P}(34)\, \Delta(41)\, \Delta^{(1)}(32) - \theta(23)\, \theta(34)\, S^{1P}(13)\, S^P(34)\, \Delta(32)\, \Delta^{(1)}(41) + \\
&+ \theta(14)\, \theta(43)\, S^{1P}(13)\, S^P(34)\, \Delta(41)\, \Delta^{(1)}(32) + \theta(14)\, \theta(23)\, S^{1P}(13)\, S^{1P}(34)\, \Delta(32)\, \Delta(41)]\, \chi_n(32) \\
&+ [\theta(13)\, \theta(34)\, S^N(24)\, S^N(43)\, \Delta(31)\, \Delta(42) + \theta(24)\, \theta(43)\, S^N(24)\, S^N(43)\, \Delta^{(1)}(31)\, \Delta^{(1)}(42) \\
&- \theta(13)\, \theta(24)\, S^N(24)\, S^{1N}(43)\, \Delta(31)\, \Delta^{(1)}(42) + \theta(13)\, \theta(34)\, S^{1N}(24)\, S^N(43)\, \Delta(31)\, \Delta^{(1)}(42) \\
&- \theta(24)\, \theta(43)\, S^{1N}(24)\, S^N(43)\, \Delta^{(1)}(31)\, \Delta(42) + \theta(13)\, \theta(24)\, S^{1N}(24)\, S^{1N}(43)\, \Delta(31)\, \Delta(42)]\, \chi_n(13) \\
&+ [\theta(24)\, \theta(43)\, S^P(13)\, S^P(34)\, \Delta(31)\, \Delta(42) + \theta(13)\, \theta(34)\, S^P(13)\, S^P(34)\, \Delta^{(1)}(31)\, \Delta^{(1)}(42) \\
&- \theta(13)\, \theta(24)\, S^P(13)\, S^{1P}(34)\, \Delta^{(1)}(31)\, \Delta(42) + \theta(24)\, \theta(43)\, S^{1P}(13)\, S^P(34)\, \Delta^{(1)}(31)\, \Delta(42) \\
&- \theta(13)\, \theta(34)\, S^{1P}(13)\, S^P(34)\, \Delta(31)\, \Delta^{(1)}(42) + \theta(13)\, \theta(24)\, S^{1P}(13)\, S^{1P}(34)\, \Delta(31)\, \Delta(42)]\, \chi_n(42) \\
&+ [S^P(13)\, \Delta^{(1)}(31) - S^{1P}(13)\, \Delta(31)]\, [S^N(24)\, \Delta^{(1)}(42) - S^{1N}(24)\, \Delta(42)]\, \theta(13)\, \theta(24)\, \chi_n(34)\} \\
&- \frac{g^2}{2} \delta m \int dx^3\, \{\theta(23)\, [\Delta^{(1)}(32)\, S^N(23) - \Delta(32)\, S^{1N}(23)]\, \chi_n(13) + \\
&\qquad\qquad + [\theta(13)\, \Delta^{(1)}(32)\, S^P(13) - \theta(23)\, \Delta(32)\, S^{1P}(13)]\, \chi_n(32) \\
&+ \theta(13)\, [\Delta^{(1)}(31)\, S^P(13) - \Delta(31)\, S^{1P}(13)]\, \chi_n(32) + \\
&\qquad\qquad + [\theta(23)\, \Delta^{(1)}(31)\, S^N(23) - \theta(13)\, \Delta(31)\, S^{1N}(23)]\, \chi_n(13)\} \\
&+ (\delta m)^2\, \chi_n(12).
\end{aligned}
$$

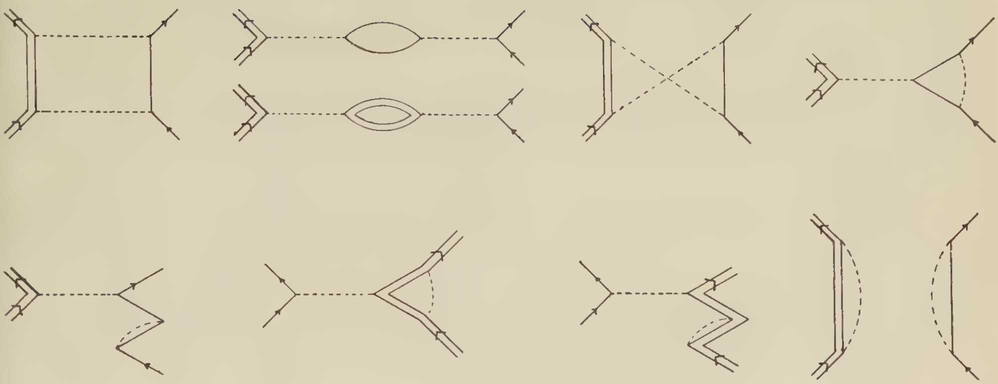

Fig. 1.

This shows that we get contributions from the above Feynman diagrams where ordinary lines refer to neutrons, double lines to protons and dotted lines to mesons.

We now transform (83) to momentum space by wellknown formulas

$$\Delta(x) = \frac{-i}{(2\pi)^3} \int dp\, e^{ipx}\, \delta(p^2+m^2)\, \varepsilon(p) \tag{84}$$

$$\Delta^{(1)}(x) = \frac{1}{(2\pi)^3} \int dp\, e^{ipx}\, \delta(p^2+m^2) \tag{85}$$

$$\bar{\Delta}(x) = -\frac{1}{2}\varepsilon(x)\,\Delta(x) = \frac{1}{(2\pi)^4} P \int dp \frac{e^{ipx}}{p^2+m^2} \tag{86}$$

$$S(x) = \left(\gamma \frac{\partial}{\partial x} - m\right) \Delta(x). \tag{87}$$

Introducing the centre of gravity coordinate $X = \frac{x^1+x^2}{2}$ and the relative coordinate $x = x^1 - x^2$, we write the wave function in the following way

$$\chi_n(12) = e^{i\frac{k}{2}(x^1+x^2)} \int dr\, f(r)\, e^{ir(x^1-x^2)}. \tag{88}$$

Using formulas (84) to (88), we transform the term corresponding to the diagram in fig. 2

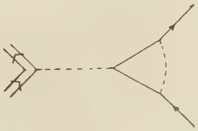

Fig. 2.

and get

$$\frac{g^4}{4}\frac{1}{(2\pi)^6}\int d p_1\, d p_2\, d q_1\, d q_2\, d r\, f(r)\, e^{i\frac{k}{2}(x^1+x^2)+i(r+q_1)(x^1-x^2)}(i\gamma p_1-m)(i\gamma p_2-m)\times$$
$$\times\delta(p_1-p_2+q_1)\,\delta\left(p_2+q_2-\frac{k}{2}+r\right)\Big\{-\pi^2\delta(p_1^2+m^2)\,\delta(p_2^2+m^2)\,\delta(q_1^2+\mu^2)\,\delta(q_2^2+\mu^2)\times$$
$$\times[\varepsilon(p_1)\varepsilon(p_2)+\varepsilon(p_1)\varepsilon(q_2)+\varepsilon(p_2)\varepsilon(q_1)+\varepsilon(q_1)\varepsilon(q_2)-\varepsilon(p_2)\varepsilon(q_2)]-$$
$$-i\pi\,\delta(p_1^2+m^2)\,\delta(p_2^2+m^2)\frac{\delta(q_1^2+\mu^2)}{q_2^2+\mu^2}[\varepsilon(p_1)\varepsilon(p_2)\varepsilon(q_1)+\varepsilon(p_2)-\varepsilon(q_1)-\varepsilon(p_1)]+$$
$$+i\pi\frac{\delta(p_1^2+m^2)}{p_2^2+m^2}\delta(q_1^2+\mu^2)\,\delta(q_2^2+\mu^2)[\varepsilon(p_1)\varepsilon(q_1)\varepsilon(q_2)+\varepsilon(p_1)+\varepsilon(q_1)+\varepsilon(q_2)]+ \qquad (89)$$
$$+i\pi\,\delta(p_2^2+m^2)\,\delta(q_2^2+\mu^2)\left[\frac{\delta(q_1^2+\mu^2)}{p_1^2+m^2}+\frac{\delta(p_1^2+m^2)}{q_1^2+\mu^2}\right][\varepsilon(p_2)+\varepsilon(q_2)]+$$
$$+\frac{\delta(p_1^2+m^2)\,\delta(p_2^2+m^2)}{(q_1^2+\mu^2)(q_2^2+\mu^2)}[1-\varepsilon(p_1)\varepsilon(p_2)]+\frac{\delta(p_1^2+m^2)\,\delta(q_2^2+\mu^2)}{(p_2^2+m^2)(q_1^2+\mu^2)}[1+\varepsilon(p_1)\varepsilon(q_2)]+$$
$$+\delta(q_1^2+\mu^2)\left[\frac{\delta(p_1^2+m^2)}{(p_2^2+m^2)(q_2^2+\mu^2)}+\frac{\delta(p_2^2+m^2)}{(p_1^2+m^2)(q_2^2+\mu^2)}+\frac{\delta(q_2^2+\mu^2)}{(p_1^2+m^2)(p_2^2+m^2)}\right]\Big\}.$$

Regarding the second last term in (89), we find that it contains the factor

$$\int d q\frac{\left[i\gamma\left(q-\frac{k}{2}+s\right)+m\right]\left[i\gamma\left(q-\frac{k}{2}+r\right)+m\right]}{\left(q-\frac{k}{2}+r\right)^2+m^2}. \qquad (90)$$
$$\cdot\,\delta\left[\left(q-\frac{k}{2}+s\right)^2+m^2\right]\delta(q^2+\mu^2)\left[1-\varepsilon(q)\,\varepsilon\left(q-\frac{k}{2}+s\right)\right]$$

where $s=r+q_1$. Integrating this we get a finite result. The integration is easily performed by introducing a system where $\frac{1}{2}\bar{k}-\bar{s}=0$. In a similar way we find that all the other terms of (89) are finite except the last one which gives us[7]

$$\frac{g^4}{4(2\pi)^6}e^{i\frac{k}{2}(x^1+x^2)}\int d s\, e^{i s(x^1-x^2)}\, d r\, f(r)\,\delta[(s-r)^2+\mu^2]\, d q\left[i\gamma\left(-q+\frac{k}{2}-s\right)-m\right)\times$$
$$\times\left[i\gamma\left(-q+\frac{k}{2}-r\right)-m\right]\int_0^1 d\alpha\int_0^{\alpha} d\beta\,\delta''\Big\{(q^2+\mu^2)\beta+ \qquad (91)$$
$$+\left[\left(q-\frac{k}{2}+r\right)^2+m^2\right](\alpha-\beta)+\left[\left(q-\frac{k}{2}+s\right)^2+m^2\right](1-\alpha)\Big\}.$$

Introducing

$$B' = \left[\left(\frac{k}{2}-r\right)^2+m^2\right](\alpha-\beta)+\left[\left(\frac{k}{2}-s\right)^2+m^2\right](1-\alpha)-$$

$$-\left\{\left(\frac{k}{2}-r\right)(\alpha-\beta)+\left(\frac{k}{2}-s\right)(1-\alpha)\right\}^2+\mu^2\beta$$

$$Q_1 = \left(\frac{k}{2}-r\right)\beta+(r-s)\,\alpha \tag{92}$$

$$Q_2 = \left(\frac{k}{2}-r\right)\beta+(r-s)(1+\alpha)$$

we may write (91)

$$\frac{g^4}{4(2\pi)^6}e^{i\frac{k}{2}(x^1+x^2)}\int ds\,dr\,dq\,e^{is(x^1-x^2)}f(r)\,\delta[(s-r)^2+\mu^2]\,[i\gamma(-q+Q_1)-m]\times$$

$$\times[i\gamma(-q+Q_2)-m]\int_0^1 d\alpha\int_0^\alpha d\beta\,\delta''(q^2+B')=$$

$$=\frac{g^4}{4(2\pi)^6}e^{i\frac{k}{2}(x^1+x^2)}\int ds\,dr\,dq\,e^{is(x^1-x^2)}f(r)\,\delta[(s-r)^2+\mu^2]\int_0^1 d\alpha\int_0^\alpha d\beta\,2\,\delta'(q^2+B')+ \tag{93}$$

$$+\text{finite terms,}$$

according to (40) and (41).

However, B' in (93) is rather complicated. But from relation[7]

$$\int dq\,[\delta'(q^2+B')-\delta'(q^2+B)] = 2\pi\log\frac{B'}{B} \tag{94}$$

it follows that if we choose in B', $r=s$, $\left(\frac{k}{2}-r\right)^2=\left(\frac{k}{2}-s\right)^2=-m^2$, we obtain a term with

$$B' = B = \mu^2\beta+m^2(1-\beta)^2 \tag{95}$$

which differs from the original expression by a finite quantity. B is thus independent of α and in (93) we may integrate with respect to α. The infinite term of (89) corresponding to the diagram in fig. 2 is thus

$$\frac{g^4}{4(2\pi)^6}e^{i\frac{k}{2}(x^1+x^2)}\int ds\,dr\,dq\,e^{is(x^1-x^2)}f(r)\,\delta[(s-r)^2+\mu^2]\int_0^1 d\alpha\,2(1-\alpha)\,\delta'(q^2+B). \tag{96}$$

Similarly, we can obtain the infinite part of the diagram in Fig. 3:

$$\frac{-g^4}{4(2\pi)^6}e^{i\frac{k}{2}(x^1+x^2)}\int ds\,dr\,dq\,e^{is(x^1-x^2)}f(r)\left[\frac{\delta\left[\left(\frac{k}{2}-s\right)^2+m^2\right]}{(s-r)^2+\mu^2}+\frac{\delta[(s-r)^2+\mu^2]}{\left(\frac{k}{2}-s\right)^2+m^2}\right]\times \tag{97}$$

$$\times\int_0^1 d\alpha\left[\left(i\gamma\alpha\left(\frac{k}{2}-s\right)-m\right]\left[i\gamma\left(\frac{k}{2}-s\right)-m\right]\delta'(q^2+B).$$

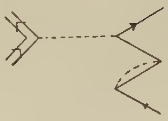

Fig. 3.

Finally the term contributed by the mass renormalization of the neutron is

$$\frac{-g^2\,\delta m}{2\,(2\pi)^3}\,e^{i\frac{k}{2}(x^1+x^2)}\int dr\,dq\,f(r)\,e^{ir(x^1-x^2)}\int_0^1 d\alpha\left[i\gamma\alpha\left(\frac{k}{2}+r\right)-m\right]\delta'(q^2+B)+$$

$$+\frac{g^2\,\delta m}{2\,(2\pi)^3}\,e^{i\frac{k}{2}(x^1+x^2)}\int ds\,dr\,e^{is(x^1-x^2)}f(r)\left[i\gamma\left(\frac{k}{2}-s\right)-m\right]\cdot \tag{98}$$

$$\cdot\left[\frac{\delta\left[\left(\frac{k}{2}-s\right)^2+m^2\right]}{(s-r)^2+\mu^2}+\frac{\delta[(s-r)^2+\mu^2]}{\left(\frac{k}{2}-s\right)^2+m^2}\right].$$

According to (83) we now add the terms in (96), (97), and the second term in (98) and get, introducing (31) for $\delta m^{(2)}$,

$$\frac{g^4}{4\,(2\pi)^6}\,e^{i\frac{k}{2}(x^1+x^2)}\int ds\,dr\,dq\,e^{is(x^1-x^2)}f(r)\left\{\delta(s-r)^2+\mu^2]\int_0^1 d\alpha\,2\,(1-\alpha)\,\delta'(q^2+B)-\right.$$

$$-\left[\frac{\delta\left[\left(\frac{k}{2}-s\right)^2+m^2\right]}{(s-r)^2+\mu^2}+\frac{\delta[(s-r)^2+\mu^2]}{\left(\frac{k}{2}-s\right)^2+m^2}\right]\cdot \tag{99}$$

$$\left.\cdot\left[i\gamma\left(\frac{k}{2}-s\right)-m\right]\int_0^1 d\alpha\left[\left[i\gamma\alpha\left(\frac{k}{2}-s\right)-m\right]+m\,(1+\alpha)\right]\delta'(q^2+B)\right\}\cdot$$

Writing

$$i\gamma\alpha\left(\frac{k}{2}-s\right)-m=\left[i\gamma\left(\frac{k}{2}-s\right)+m\right]\alpha-(1+\alpha)\,m \tag{100}$$

we obtain for the last part of (99)

$$\int_0^1 d\alpha\left\{\left[i\gamma\alpha\left(\frac{k}{2}-s\right)-m\right]+m\,(1+\alpha)\right\}\delta'(q^2+B)=\left[i\gamma\left(\frac{k}{2}-s\right)+m\right]\int_0^1 d\alpha\,\alpha\,\delta'(q^2+B).$$

Thus (99) may be written

$$\frac{g^4}{4(2\pi)^6} e^{i\frac{k}{2}(x^1+x^2)} \int ds\, dr\, dq\, e^{is(x^1-x^2)} f(r) \Big\{ \delta[(s-r)^2+\mu^2] \int_0^1 d\alpha\, 2(1-\alpha)\, \delta'(q^2+B) +$$

$$+ \left[\left(\frac{k}{2}-s\right)^2+m^2\right] \left[\frac{\delta\left[\left(\frac{k}{2}-s\right)^2+m^2\right]}{(s-r)^2+\mu^2} + \frac{\delta[(s-r)^2+\mu^2]}{\left(\frac{k}{2}-s\right)^2+m^2} \right] \int_0^1 d\alpha\, \alpha\, \delta'(q^2+B) \Big\} = \qquad (102)$$

$$= \frac{g^4}{4(2\pi)^6} e^{i\frac{k}{2}(x^1+x^2)} \int ds\, dr\, dq\, f(r)\, \delta[(s-r)^2+\mu^2] \int_0^1 d\alpha\, (2-\alpha)\, \delta'(q^2+B).$$

We find immediately that the two diagrams of fig. 4 give the same infinite contribution to our expansion (83) as (102)

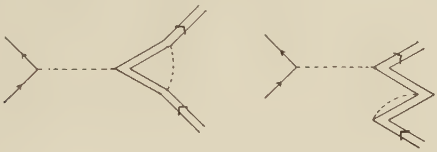

Fig. 4.

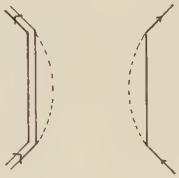

Fig. 5.

The term represented by fig. 5 is, in *p*-space, given by

$$\frac{g^4}{4(2\pi)^6} e^{i\frac{k}{2}(x^1+x^2)} \int dr\, e^{ir(x^1-x^2)} f(r) \int_0^1 d\alpha \int dq_1 \left[i\gamma\alpha\left(\frac{k}{2}+r\right)-m\right] \delta'(q_1^2+B) \times$$

$$\times \int_0^1 d\beta \int dq_2 \left[i\gamma\beta\left(\frac{k}{2}-r\right)-m\right] \delta'(q_2^2+B) + \text{finite terms.} \qquad (103)$$

Using (100) we write this as follows

$$\frac{g^4}{4(2\pi)^6} e^{i\frac{k}{2}(x^1+x^2)} \int dr\, e^{ir(x^1-x^2)} \cdot$$

$$\cdot f(r) \left\{ \left[i\gamma\left(\frac{k}{2}+r\right)+m\right] \left[i\gamma\left(\frac{k}{2}-r\right)+m\right] \left[\int_0^1 d\alpha\, \alpha \int dq\, \delta'(q^2+B)\right]^2 - \right.$$

$$- m\left[i\gamma\left(\frac{k}{2}-r\right)+m\right] \int_0^1 d\alpha\, (1+\alpha) \int dq_1\, \delta'(q_1^2+B) \int_0^1 d\beta\, \beta \int dq_2\, \delta'(q_2^2+B) - \qquad (104)$$

$$- m\left[i\gamma\left(\frac{k}{2}+r\right)+m\right] \int_0^1 d\alpha\, \alpha \int dq_1\, \delta'(q_1^2+B) \int_0^1 d\beta\, (1+\beta) \int dq_2\, \delta'(q_2^2+B) +$$

$$\left. + m^2 \left[\int_0^1 d\alpha\, (1+\alpha) \int dq\, \delta'(q^2+B)\right]^2 \right\}.$$

Now

$$\left[i\gamma\left(\frac{k}{2}+r\right)+m\right]\left[i\gamma\left(\frac{k}{2}-r\right)+m\right]f(r) \tag{105}$$

corresponds in configuration space to

$$\left(\gamma^{P}\frac{\partial}{\partial x^{1}}+m\right)\left(\gamma^{N}\frac{\partial}{\partial x^{2}}+m\right)\chi_{n}(12)=-\frac{g^{2}}{2}\Delta^{(1)}(12)\,\chi_{n}(12)+\ldots \tag{106}$$

and is thus of order Δ. The first term in (104) may therefore be neglected. The other terms of (104), together with the remaining mass renormalization terms (the first term of (98), the corresponding term for the proton, and the last term of (83)) give

$$\begin{aligned}
&\frac{g^{4}}{4(2\pi)^{6}}e^{i\frac{k}{2}(x^{1}+x^{2})}\int d r\, e^{i r(x^{1}-x^{2})} f(r)\left\{m^{2}\left[\int_{0}^{1} d\alpha\,(1+\alpha)\int d q\,\delta'(q^{2}+B)\right]^{2}-\right.\\
&-m\left[i\gamma\left(\frac{k}{2}-r\right)+m\right]\int_{0}^{1} d\alpha\,(1+\alpha)\int d q_{1}\,\delta'(q_{1}^{2}+B)\int_{0}^{1} d\beta\,\beta\int d q_{2}\,\delta'(q_{2}^{2}+B)-\\
&-m\left[i\gamma\left(\frac{k}{2}+r\right)+m\right]\int_{0}^{1} d\alpha\,\alpha\int d q_{1}\,\delta'(q_{1}^{2}+B)\int_{0}^{1} d\beta\,(1+\beta)\int d q_{2}\,\delta'(q_{2}^{2}+B)-\\
&-\frac{2(2\pi)^{3}}{g^{2}}\delta m\int_{0}^{1} d\alpha\int d q\left[i\gamma\alpha\left(\frac{k}{2}+r\right)-m\right]\delta'(q^{2}+B)-\\
&\qquad\left.-\frac{2(2\pi)^{3}}{g^{2}}\delta m\int_{0}^{1} d\beta\int d q\left[i\gamma\beta\left(\frac{k}{2}-r\right)-m\right]\delta'(q^{2}+B)+\frac{4(2\pi)^{6}}{g^{4}}(\delta m)^{2}\right\}.
\end{aligned} \tag{107}$$

Here again we use (100) and introduce $\delta m=g^{2}\,\delta m^{(2)}$, according to (31). The result of this is that (107) vanishes.

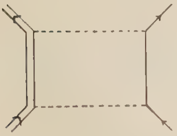

Fig. 6.

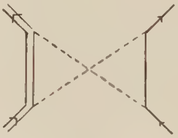

Fig. 7.

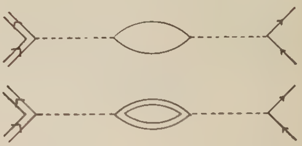

Fig. 8.

It is obvious that the term corresponding to fig. 6 gives a finite contribution and the same is true for the terms corresponding to fig. 7 and fig. 8. This may be proved by transformation to momentum space. The reason why the vacuum polarization terms of fig. 8 are finite is that here we use the commutator to define the wave function. The P-symbol would have given divergences and thus more trouble in the renormalization.

There is still one renormalization term left in (83) which depends on the normalization of the meson field. Together with the remaining infinite term of (102) and the corresponding term from the proton field we get

$$\frac{g^4}{2\,(2\,\pi)^6}\,e^{i\,\frac{k}{2}(x^1+x^2)}\int d\,s\,d\,r\,e^{i\,s\,(x^1-x^2)}\cdot$$
$$\cdot f(r)\,\delta\,[(s-r)^2+\mu^2]\left\{\int_0^1 d\,\alpha\,(2-\alpha)\int d\,q\,\delta'\,(q^2+B)-\frac{(2\,\pi)^3}{g^2}\,2\,(M-1)\right\}\cdot \tag{108}$$

But according to (50) this is equal to zero. Thus all divergences have been compensated.

I wish to express my gratitude to professor T. Gustafson for the great interest he has shown in this work. My thanks are further due to Dr. G. Källén who suggested this investigation, for many valuable discussions and good advice.

Department of Theoretical Physics and Mechanics, University of Lund.

Tryckt den 6 april 1954

Uppsala 1954. Almqvist & Wiksells Boktryckeri AB

THE UNIVERSITY OF ILLINOIS AT CHICAGO
3 8198 314 370 063